



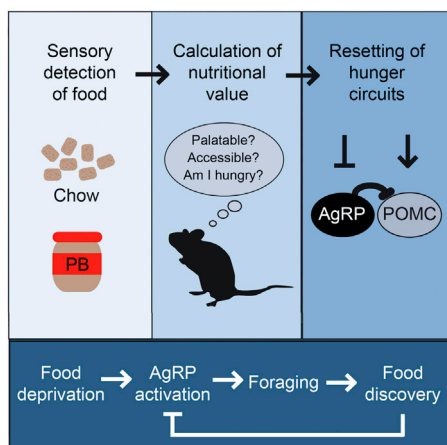
Cell

Volume 160
Number 5

February 26, 2015

www.cell.com

Immunity against Marburg



Just Looking at Food...

PAGE 829

Feeding and hunger states are regulated by the AgRP and the POMC neurons. By optically recording their activity in mice, Chen et al. make the unexpected observation that simply presenting food to a hungry mouse resets the neuronal activation state from one associated with hunger to one associated with satiety, even if no food is consumed. This sensory regulation suggests that role of this circuit is not restricted to responding to internal energy states.

A Landscape for Longevity

PAGE 842

Energy homeostasis is coordinated both locally in peripheral tissues and distally by the nervous system. Examining the relative contributions of these local and distal effects to healthy aging, Burkewitz et al. show that AMPK locally and cell-autonomously increases longevity; however, to slow aging, AMPK must

inactivate CRTC-dependent transcription in neurons to generate a systemic catecholamine signal that creates a permissive transcriptional and mitochondrial landscape for longevity.

Speed Dating for DNA

PAGE 856

DNA recombination requires matching up homologous sequences, but doing this efficiently is a challenge given the vast amount of DNA in the genome to be sampled. Using single-molecule imaging with ssDNA curtains, Qi et al. find that DNA recombinases kinetically discriminate between different lengths of microhomology, using eight nucleotide tracts to interrogate and align homologous DNA sequences.

Framing Ribosome Excursions

PAGE 870

Frameshift-programming mRNAs regulate the translation of alternative protein products from a single transcript. Yan et al. find that *E. coli* ribosomes shift reading frames via multiple translocation attempts induced by flanking mRNA structural barriers. These dynamic excursions permit ribosomes to access alternative codon:anticodon base-pairing along the mRNA, thereby unlocking a broad range of frameshift pathways.

Protein Bet Hedging

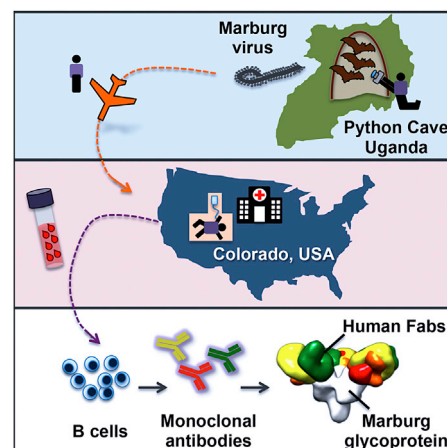
PAGE 882

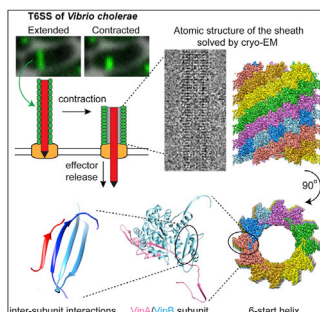
Stiffler et al. explore the origins of evolvability by systematically analyzing all single amino acid mutants in an enzyme under selection for a wild-type function (ampicillin resistance) and a new function (cefotaxime resistance). The results suggest that fluctuating environments select for enzymes with excess activity relative to the strength of selection.

Viral Lessons from the Survivors

PAGE 893 and PAGE 904

Flyak et al. characterize a panel of neutralizing antibodies from a human survivor of Marburg virus hemorrhagic fever and report that all antibodies bind to a single major antigenic site in the viral glycoprotein (GP). Hashiguchi et al. determine the crystal structure of the viral GP in complex with one of these antibodies and show that the binding site overlaps with the GP binding site to its cellular receptor. Remarkably, the same antibodies can also bind to Ebola GP, despite the differences in protein sequence among the glycoprotein in the two viruses, providing a critical template for development of immunotherapeutics and inhibitors of viral entry.





Totally Tubular Protein Delivery Vehicle

PAGE 952 and PAGE 940

Bacterial Type VI secretion systems (T6SS) deliver proteins into target cells by a rapid contraction of a long sheath assembly. Two papers in this issue unveil the structural organization for tube-like contractile sheaths determined by atomic resolution cryoelectron microscopy. Kudryashev et al. report the structure of the *Vibrio cholerae* sheath while Clemens et al. identify and structurally characterize a new T6SS from *Francisella novicida*. The structures providing insight into how bacterial sheaths can be recycled for multiple rounds of protein delivery and define a repeating two-protein substructure that forms the basis for the mesh-like architecture of the sheaths.

Building Bridges Breaks Chromosomes

PAGE 913

Marzec et al. identify a mechanism of telomere-induced genome instability that contributes to developing complex rearrangements in ALT sarcomas. Accumulation of GGGTCA variant repeats on ALT telomeres leads to the aberrant recruitment of NR2C/F nuclear receptors, which, in turn, can bridge to their conventional binding sites through the nuclear space. Homologous recombination can then lead to insertion of telomeric sequences proximal to NR2C/F binding sites, creating potential fragile sites.

Telomere Inactivation in Aging

PAGE 928

Telomerase is required for telomere maintenance and protection. Using single-cell analyses in yeast, Xie et al. identify a new layer of lifespan regulation where they demonstrate that early telomerase inactivation leads to accelerated mother cell aging. This event is distinct from senescence caused by telomere shortening and is associated with a transient DNA damage response.

TGF- β Fuels Resistance

PAGE 963

Understanding the cause of therapeutic resistance is crucial for improving the efficacy of cancer therapy. Oshimori et al. show that perivascular TGF- β suppresses proliferation but promotes invasion and heterogeneity in squamous cell carcinomas stem cells. These cells reprogram anti-oxidant metabolism and resist anti-cancer therapy, leading to tumor recurrence.

Approaching Cancer with Precision

PAGE 977

There is a lack of effective predictive biomarkers to precisely assign optimal therapy to cancer patients. Montero et al. find that drug-induced death signaling measured by Dynamic BH3 Profiling predicts chemotherapy response across many cancer types treated with different drugs, including combinations of chemotherapies, unraveling its potential use as a predictive biomarker for cancer therapy.

Wiring HIV latency

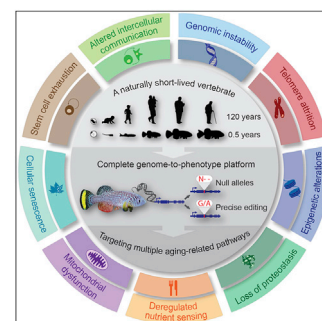
PAGE 990 and PAGE 1002

Establishment of HIV latency is viewed currently as a process that depends on cellular environment and activation state. New work from Razoooky et al. presents results from a synthetic circuit approach suggesting that the latency program can be modulated by Tat expression independent of the cell state, supporting a model in which a hardwired latency circuit can be initiated autonomously. Rouzine et al. build from these findings to focus on the potential benefit of such a circuit for evolution of latency. They develop a mathematical model, consistent with observed patterns during infection, where that initial establishment of latency promotes infectivity at mucosal barriers, suggesting new approaches for therapies focused on eliminating latent virus.

A Killi App for Aging Research

PAGE 1013

Aging is the number one risk factor for many human pathologies, yet it is challenging to study as existing vertebrate models are relatively long lived. Harel et al. have developed an integrative genome-to-phenotype platform in a naturally short-lived vertebrate, the African turquoise killifish, opening the door to high-throughput in vivo modeling of vertebrate aging and complex human diseases.



Unfrozen

This year's winter in Cambridge, Massachusetts—the home of the Cell Press office—has been a humbling experience. It has laid bare how poorly suited we as a species are to cold weather and brings to mind not only ways of keeping warm but also the adaptations of species better suited to the cold that we would emulate if we could.

Like other mammals, we have the ability to produce heat through non-shivering thermogenesis. The molecular underpinnings of this are well known—briefly, upregulation of uncoupling protein 1 (UCP1) in brown adipose tissue helps mitochondria dissipate energy as heat. Although it is known that UCP1 expression is sensitive to cold exposure, the cellular mechanisms of this are unclear. Recently, the lab of Hei Sook Sul has made a significant step forward in identifying a protein that is critical to UCP1 expression and which is induced by cold exposure (Dempersmier et al., 2015). The protein, Zfp516, binds to the *UCP1* promoter and drives its transcription in brown fat, and it further stimulates the browning of subcutaneous white adipose tissue (beige fat). Beyond its role in keeping us warm, these features make Zfp516 a promising target for anti-obesity treatments.

Although UCP1 is particularly effective at heat generation, countless reactions in a cell release energy as heat. New findings by Riedel et al. (2015) suggest that the heat released by catalysis, such as the highly exothermic breakdown of hydrogen peroxide to water and oxygen by the enzyme catalase, has a direct effect on enzyme diffusion. By examining single-molecule behavior of catalase and other enzymes, they show that the heat generated by catalysis increases enzyme diffusion by producing an asymmetric pressure wave that applies a force that is centered away from the protein's center of mass. To imagine a single catalytic event, the force of a recoiling gun might be one analogy, and though an enzyme's cumulative motion would still be Brownian, I nevertheless envision its movement as like a small boat weaving aimlessly through the warm turquoise waters of a Caribbean mangrove. But I digress. The authors suggest that the heat-driven pressure waves may lead to a partial unfolding of part of an enzyme that could temporarily halt its activity, or intriguingly, this force might affect the processivity of molecular complexes such as RNA or DNA polymerase.

For many species, these everyday cellular reactions do not generate enough warmth to counteract the brutal cold of the environments in which they are found. So if homeothermy—or hopping a plane to Florida—isn't an option, what's a species to do? One answer is to embrace the cold. So-called anti-freeze proteins in species ranging from bacteria to vertebrates hinder the formation of macroscopic ice by binding the surface of nascent ice crystals, halting their growth. A



Image from iStockphoto/olada.

recent study of anti-freeze protein type III (AFP-III) from the Antarctic eelpout (a fish that looks a bit like an eel) shows that the protein at temperatures higher than freezing has “ice-like” water layers around the ice binding site of the protein (Meister et al., 2014). This suggests that it is these ordered water molecules and not the protein itself that binds to nascent ice crystals. In other words, polar fish have a protein that “makes” ice for ice fishing. Once you've wrapped your head around that, consider this—the anti-freeze proteins of Antarctic icefish not only inhibit formation of ice crystals at subzero temperatures, they also impede their melting at higher temperatures (Cziko et al., 2014). Meaning, for species that rely on anti-freeze proteins, microscopic ice crystals may persist within them even during periods of above-freezing temperatures. Looking outside at the bleak gray-white cityscape, I can't help but think we could use some of that ice flowing in our veins until spring comes.

REFERENCES

- Cziko, P.A., DeVries, A.L., Evans, C.W., and Cheng, C.H. (2014). *Proc. Natl. Acad. Sci. USA* 111, 14583–14588.
- Dempersmier, J., Sambeat, A., Gulyaeva, O., Paul, S.M., Hudak, C.S.S., Raposo, H.F., Kwan, H.-Y., Kang, C., Wong, R.H.F., and Sul, H.S. (2015). *Mol. Cell* 57, 235–246.
- Meister, K., Strazdaite, S., DeVries, A.L., Lotze, S., Olijve, L.L.C., Voets, I.K., and Bakker, H.J. (2014). *Proc. Natl. Acad. Sci. USA* 111, 17732–17736.
- Riedel, C., Gabizon, R., Wilson, C.A.M., Hamadani, K., Tsekouras, K., Marqusee, S., Pressé, S., and Bustamante, C. (2015). *Nature* 517, 227–230.

Robert Kruger

The Hunger Games

Randy J. Seeley^{1,*} and Kent C. Berridge²

¹Department of Surgery

²Department of Psychology

University of Michigan, Ann Arbor, MI 48109, USA

*Correspondence: seeleyrj@med.umich.edu

<http://dx.doi.org/10.1016/j.cell.2015.02.028>

Although AgRP and POMC neurons in the hypothalamus have long been associated with regulation of food intake, in this issue of *Cell*, Chen et al. use direct imaging in vivo to demonstrate rapid changes in their activity upon food presentation. The rapidity of their altered responses challenges classic notions of their functions and raises new hypotheses.

Food is essential to an organism's survival, and consequently, considerable neural circuitry is dedicated to directing and regulating ingestive behaviors. Hypothalamic AgRP and POMC have been known as the yin/yang of food intake regulation for over a decade (Schwartz et al., 2000). They are targets of molecules indicating energy status such as leptin, ghrelin, and nutrients, with AgRP neurons promoting feeding and POMC neurons decreasing feeding. However, approaches to measuring the activity of these neurons have been technically limited in terms of monitoring them during the act of eating itself.

In the current edition of *Cell*, all of this changes. Chen et al. (2015) used fiber photometry to visualize the activity of both AgRP and POMC neurons while hungry mice began to eat palatable food or interact with food odors in their environment. Given that activating AgRP neurons is thought to cause a robust and rapid increase in food intake (Aponte et al., 2011), a logical expectation might have been that AgRP neuronal activity would be high when animals began to eat, remain high during the early portion of the meal, and gradually decline during eating as appetite ebbed. The exact opposite pattern would be expected in POMC neurons—a low start followed by a gradual rise during eating. What Chen et al. found, however, was that while AgRP neuronal activity was high in fasted mice before encountering food, their AgRP neuronal activity decreased in mere seconds as soon as food was presented and just as eating began. Conversely, POMC activity, while low as expected in hungry mice, rose almost

immediately as soon as the mouse began to eat, even though mice continued to eat avidly for some time more without being inhibited by the initial rise in POMC neuronal activity. If the chow pellet was removed midway through the meal, the AgRP neurons increased again in activity, and the POMC neurons declined. Moreover, if mice were given access to more attractive food, such as chocolate or peanut butter, the rapid decrease in AgRP activity and increase in POMC activity were even more pronounced.

These observations have a number of important implications. The rapid changes in the activity of these neurons could not be the result of signals coming from the body about fuel status. That is, the early POMC rise could not be a physiological satiety signal, nor could the early AgRP decline mean that appetite had disappeared (since the mice continued to eat avidly for some time after both signals changed). At least, if the initial POMC rise were a satiety signal that stops eating, it was a remarkably ineffective one because most of the avid eating occurred afterward. Rather, these changes must reflect inputs onto these neurons that process information about the immediate availability and attractiveness of food in the environment.

What does that mean for understanding the regulatory roles of AgRP or POMC neurons? Chen et al. (2015) suggest one possibility. They note that hunger would promote foraging in addition to eating food actually found and propose that the role of AgRP neurons is specifically the former. A sudden drop in AgRP as soon as food was discovered, they suggest, “provides a mechanism to rapidly

inhibit foraging upon the discovery of food.” In that case, AgRP and POMC would have a role in appetitive food seeking and foraging behaviors but not so much in the consummatory eating phase of actual biting, chewing, and swallowing. Splitting appetite into separate effects on foraging and consummatory behaviors is certainly one way of potentially solving this puzzle. However, that split raises a further puzzle of why earlier studies reported that AgRP and POMC manipulations do powerfully control food consumption, and so it is not limited to foraging behavior (Aponte et al., 2011).

A second way of looking at the rapid changes in activity is that AgRP may still promote the act of eating and intake, and POMC activity inhibits intake, but these signals are only the first links in a long chain. By that view, the rapid changes in AgRP and POMC neuronal activity are not sufficient to inhibit intake on their own but might act as the first topple in a chain of dominos. After some delay, the final domino might be another mechanism that successfully inhibits eating.

A third way of looking at the rapid response of AgRP and POMC neurons is the alternative view that perhaps these signals do not drive eating directly, but rather these neurons modulate and receive powerful input from brain reward circuitry that reacts to cues and foods in the environment and that mediates current motivation to eat (Figure 1). That is, high AgRP (and low POMC) may prime the reactivity of mesocorticolimbic circuitry to the sight, smell, and taste of food, which generates high incentive motivation to eat, rather than simply

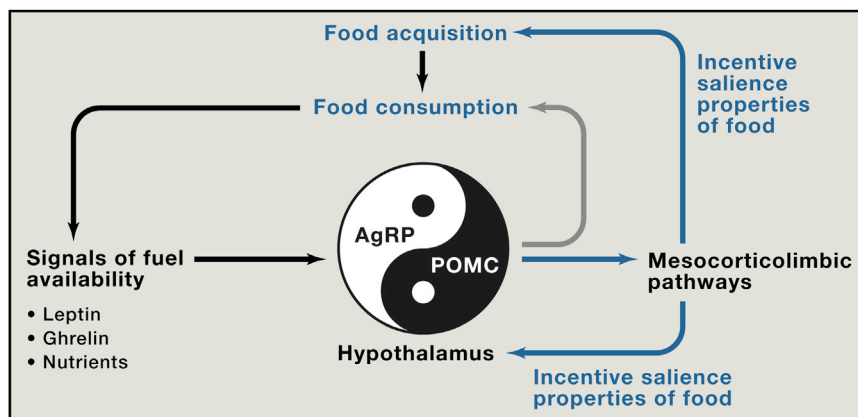


Figure 1. Integrated Model for the Roles for AgRP and POMC Neurons in Food Responsiveness and Energy Homeostasis

Traditional models of hypothalamic regulation of food intake (blue arrows) hypothesize that AgRP and POMC neurons in the hypothalamus are regulated by signals of fuel availability and, in turn, that AgRP activation directly drives eating, whereas POMC activation inhibits eating (hatched blue arrow). [Chen et al. \(2015\)](#) challenge this view and show that these neurons' activity is often disconnected with the act of eating itself. Incorporating findings of [Chen et al. \(2015\)](#) into the incentive interpretation we describe, the activity of these neurons instead primes the motivational/incentive salience mesocorticolimbic circuitry to react to food stimuli, which sustains continued eating, and feeds back to immediately and potentially regulate hypothalamic neuronal activity (yellow arrows). This embeds hypothalamic function to regulate eating into larger circuitry that also incorporates mesocorticolimbic pathways and regulates the varied behaviors involved in acquiring and consuming food in a complex environment.

causing a hunger drive that more directly powers eating. Once eating is triggered by that amplified mesocorticolimbic reaction to food, the high AgRP could be superfluous to appetite and eating behavior and is able to decline without suppressing behavior. Higher mesocorticolimbic reactivity could sustain eating by its own continuing activation, such as by higher dopamine levels or related neuronal signals in nucleus accumbens or related targets (see [Figure 1](#)). In turn, by this view, mesocorticolimbic circuitry must send feedback signals that food is encountered to hypothalamus, causing the early changes in AgRP and POMC neurons, so that their activity immediately reflects the incentive value of food in the moment.

Other data support this modulatory incentive hypothesis. For example, starvation signals similarly increase mesocorticolimbic reactivity to food in both humans and rats ([Berthoud, 2012](#); [DiLeone, 2009](#); [Farooqi et al., 2007](#); [Figuewicz and Sipols, 2010](#)) (though compare [Fulton et al. \[2006\]](#)). Incentive-related feedback from mesocorticolimbic circuitry may also explain another finding

of [Chen et al. \(2015\)](#)—namely, that the rapid AgRP and POMC activity changes triggered by mouse chow can be blocked if the mouse has just eaten a morsel of chocolate or peanut butter 10 min earlier. If the order is reversed, however, eating chow first does not block the neural responses to a subsequent chocolate or peanut butter treat. Eating chocolate first would reduce the incentive value of chow, but that should not occur in reverse, and so the rapid AgRP and POMC changes accordingly remain robust to both foods.

This incentive hypothesis of hypothalamic interaction with mesocorticolimbic circuitry leads to some further predictions. For example, neutral cues in the environment can gain motivational value when paired with food and activate mesocorticolimbic systems as effectively as food itself. The current findings would predict that such previously neutral stimuli would also serve as potent stimuli to rapidly alter the activity of AgRP and POMC neurons if they have been learned as food cues.

The bottom line is that psychologists and neuroscientists have spent decades

investigating the relationship between neural activity and key aspects of our behavior, including motivation, reward, and hunger. [Chen et al. \(2015\)](#) have ushered in a new chapter where molecular markers of activity for the neurons one wishes to observe can be directly related to ingestive behavior. Here, we have learned that these specific neuronal populations respond more rapidly than previously suspected to information about the quality of food in their environment. Given the importance of these neurons beyond ingestive homeostasis ([Dietrich et al., 2012](#); [Matarese et al., 2013](#)), the implications for this work extend to understanding not only how food intake is regulated but to a wide swath of topics around the relationship between brain and behavior.

ACKNOWLEDGMENTS

R.J.S. has received research support from Novo Nordisk, Boehringer Ingelheim, Eisai, Givaudan, and Ethicon Surgical Care. He has also served as a paid consultant for Novo Nordisk, Boehringer Ingelheim, Sanofi, Novartis, Circuit Therapeutics, Nestle, and Takeda.

REFERENCES

- Aponte, Y., Atasoy, D., and Sternson, S.M. (2011). *Nat. Neurosci.* 14, 351–355.
- Berthoud, H.-R. (2012). *Proc. Nutr. Soc.* 71, 478–487.
- Chen, Y., Lin, Y.-C., Kuo, T.-W., and Knight, Z.A. (2015). *Cell* 160, this issue, 829–841.
- Dietrich, M.O., Bober, J., Ferreira, J.G., Tellez, L.A., Mineur, Y.S., Souza, D.O., Gao, X.-B., Picciotto, M.R., Araújo, I., Liu, Z.-W., and Horvath, T.L. (2012). *Nat. Neurosci.* 15, 1108–1110.
- DiLeone, R.J. (2009). *Int. J. Obes. (Lond.)* 33 (2), S25–S29.
- Farooqi, I.S., Bullmore, E., Keogh, J., Gillard, J., O'Rahilly, S., and Fletcher, P.C. (2007). *Science* 317, 1355.
- Figuewicz, D.P., and Sipols, A.J. (2010). *Pharmacol. Biochem. Behav.* 97, 15–24.
- Fulton, S., Pissios, P., Manchon, R.P., Stiles, L., Frank, L., Pothos, E.N., Maratos-Flier, E., and Flier, J.S. (2006). *Neuron* 51, 811–822.
- Matarese, G., Procaccini, C., Menale, C., Kim, J.G., Kim, J.D., Diano, S., Diano, N., De Rosa, V., Dietrich, M.O., and Horvath, T.L. (2013). *Proc. Natl. Acad. Sci. USA* 110, 6193–6198.
- Schwartz, M.W., Woods, S.C., Jr., Porte, D., Jr., Seeley, R.J., and Baskin, D.G. (2000). *Nature* 404, 661–671.

For Longevity, Perception is Everything

Vanisha Lakhina¹ and Coleen T. Murphy^{1,*}

¹Department of Molecular Biology and LSI Genomics, Princeton University, Princeton NJ 08544, USA

*Correspondence: ctmurphy@princeton.edu

<http://dx.doi.org/10.1016/j.cell.2015.02.027>

Aging is a risk factor for chronic diseases, and identifying targets for intervention is a goal of the aging field. Burkewitz et al. now describe a mechanism that mediates the specific role for AMPK in longevity, whereby its activity in neurons modulates metabolism and mitochondrial integrity in peripheral tissues.

Because aging is the primary risk factor for the development of many chronic diseases, it is a fundamental public health problem. Therefore, one goal of the aging field is to identify regulatory mechanisms that could become targets of intervention. Animals adjust their metabolic rates and life schedules according to nutrient status. The highly conserved AMP-activated protein kinase, AMPK, which is activated under low nutrient conditions and is required for lifespan extension with dietary restriction (DR), is an attractive target for such interventions. However, AMPK also affects growth, reproduction, and disease development (Mair et al., 2011). Therefore, identifying mechanisms of AMPK activation that slow aging without deleterious effects is important in moving AMPK pathway drugs to a clinical application. Previously, Mair and colleagues showed that inhibition of the cyclic AMP-responsive element (CREB)-regulated transcriptional co-activator (CRTC-1) is required for AMPK-mediated lifespan extension (Mair et al., 2011). In this issue of *Cell*, Burkewitz et al. (2015) now find that CRTC-1 specifically mediates AMPK's role in longevity, but not growth or reproduction, through its activity in neurons, modulating metabolism and mitochondrial integrity in peripheral tissues. Notably, neuronal AMPK/CRTC-1 status is dominant to the pathway's activity in peripheral tissues, which has implications for the development of AMPK-based therapeutics [Figure 1](#).

To identify the mechanisms underlying the specific effect of CRTC-1 on lifespan, the authors first zeroed in on transcriptional targets that correlated solely with AMPK/CRTC-1-dependent longevity. This set was enriched for mitochondrial metabolism genes, and metab-

olomic analyses demonstrated an increase in TCA cycle intermediates and associated metabolites upon AMPK activation, suggesting a specific coupling of AMPK-mediated metabolic regulation and lifespan extension. Moreover, the authors found that several of these metabolic genes were also regulated by NHR-49, a functional ortholog of the nuclear receptor PPAR α , which activates transcription in low energy states, ultimately acting in an antagonistic manner to CRTC-1.

CRTC-1 is expressed in neurons and intestine, a major site of longevity regulation in *C. elegans* (Libina et al., 2003). Because AMPK is expressed ubiquitously, and many of the factors involved in dietary restriction-mediated longevity, including CRTC-1, are found in peripheral tissues, AMPK and the CRTC-1/CREB complex were previously presumed to directly affect metabolism in tissues in which they are expressed (Mair et al., 2011). However, the authors found that intestinal CRTC-1 had no effect on longevity, while neuronal expression of the constitutively nuclear CRTC-1^{S76A, S179A}, which is refractory to AMPK regulation, was sufficient to suppress the longevity effects and metabolic transcription of AMPK activation, and even caused fragmentation of the mitochondrial network in muscle cells. Similarly, neuronal rescue of NHR-49 in an *nhr-49* null mutant induced metabolic changes in neurons, muscle, and intestine. Therefore, the effects of AMPK on peripheral tissues seemed to be modulated by a neuron-derived signal. Indeed, the authors next identified the neuromodulator octopamine as the AMPK/CRTC-1-mediated signal that alters metabolism in peripheral tissues. AMPK/CRTC-1 signaling regulated the expression of octopamine syn-

thesis enzymes, and loss of octopamine abolished the reduced longevity of CRTC-1^{S76A, S179A} animals. Exogenous octopamine treatment even phenocopied the mitochondrial fragmentation seen in muscle tissue upon neuronal CRTC-1 activation. Thus, octopamine, acting as the AMPK neuronal signal, was able to "override" local AMPK signaling in peripheral tissues.

The exact sites of action for some of these players still remain to be identified. Octopamine synthesis enzymes are expressed in the RIC interneurons, a site of CRTC-1 localization, but CRTC-1 and NHR-49 may also act in additional neurons. The specific receptors and receiving cells of the octopamine signal are also unknown, but given that starvation induces CREB activity in SIA neurons to regulate acetylcholine release, it will be interesting to examine whether SIA neurons and/or acetylcholine activity are also involved in the CRTC-1 longevity response. Additionally, the direct transcriptional targets of neuronal NHR-49 and CREB in this context are not known; AMPK's regulation of growth and reproduction does not involve CRTC-1, and CREB's role in growth is largely due to non-neuronal gene expression (Lakhina et al., 2015). Downstream changes in peripheral tissues may be regulated by the activity of the longevity transcription factors DAF-16 or PQM-1 (Tepper et al., 2013), as the DAF-16 Associated Element (DAE) was overrepresented in the promoters of AMPK/CRTC-1's downstream transcriptional targets. The involvement of these transcription factors also suggests that an insulin may act as an intermediate signal upstream of the peripheral tissues. While these are challenging questions, leveraging

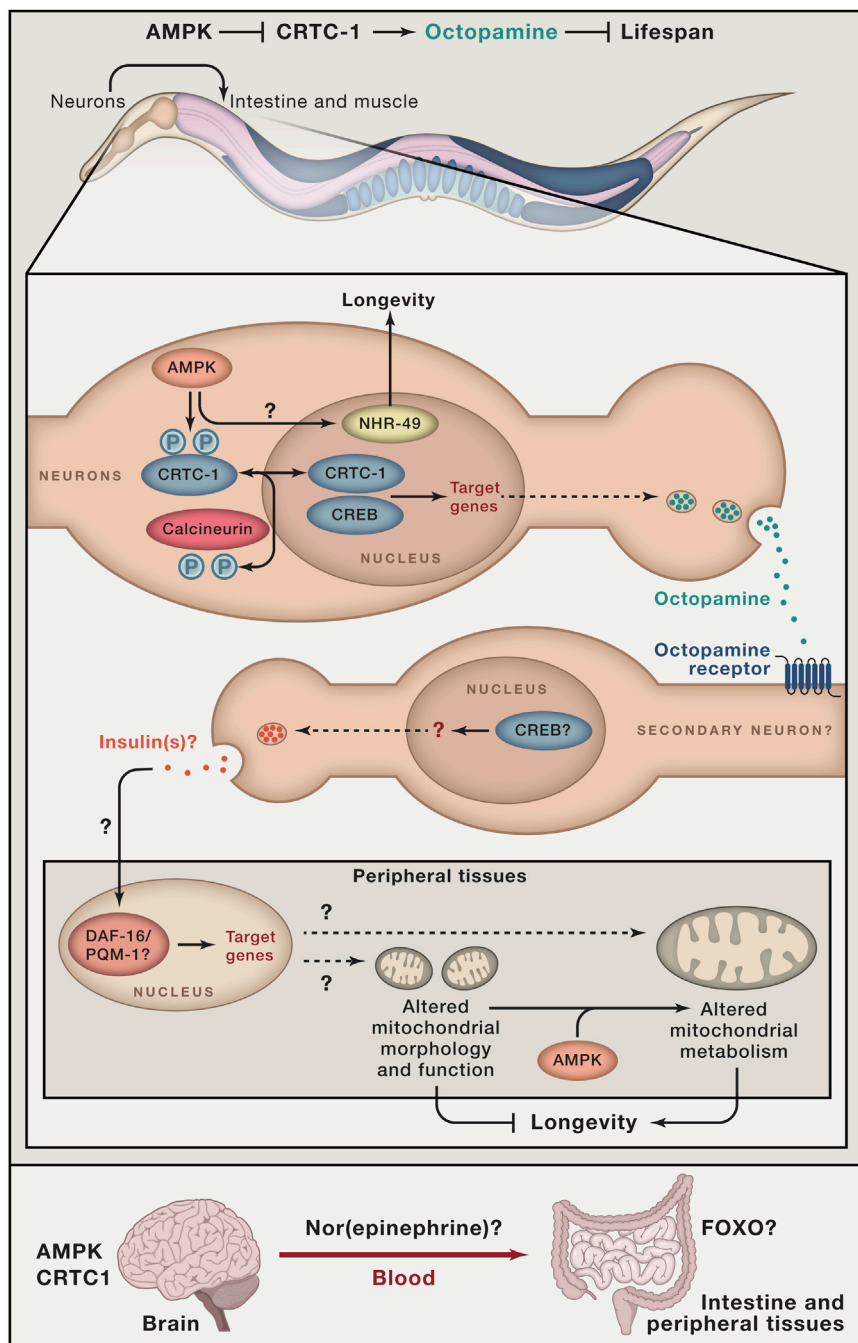


Figure 1. Nutrient Status Sensing in Neurons by AMPK May Relay a Signal between Neurons to Peripheral Tissues

(Top) Upon reduced AMPK activity in neurons, CRTC-1 induces octopamine secretion, which alters metabolic gene expression and causes mitochondrial fragmentation in peripheral tissues, potentially due to the transcriptional activity of DAF-16/PQM-1 within these tissues. Octopamine is most likely sensed by intermediate neurons, which may signal to peripheral cells via secreted cues such as insulins. (Bottom) AMPK/CRTC1 in the human brain may communicate via (nor)epinephrine to the intestine and peripheral tissues to regulate the pro-longevity factors, such as FOXO.

the distinct neuronal and peripheral tissue transcriptional outputs will help untangle them.

Neuronal regulation of peripheral tissue responses has been observed in varied contexts; for example, dietary restriction

activates the transcription factor SKN-1 in ASI neurons, which signals peripheral tissues to increase metabolic activity and whole-body respiration (Bishop and Guarente, 2007), and heat stress activates the AFD thermosensory neurons to elicit serotonin release, which turns on HSF-1-mediated transcription in distant germline tissues (Tatum et al., 2015). Sensory cues can regulate longevity of the whole organism, as loss of ciliated sensory neurons, odorant receptors, and the TRPV1 receptor extend lifespan in worms and mice (Apfeld and Kenyon 1999; Riera et al., 2014). CRTC1 activity in mammalian neurons also affects organismal metabolism (Riera et al., 2014), and upregulation of AMPK in *Drosophila* neurons increases autophagy in the brain as well as intestine (Ulgherait et al., 2014), underscoring the conservation of the signaling logic. The present findings extend this theme of regulation of whole organism and peripheral tissue status by neuronal signaling, but in this case, the activity of neuronal AMPK appears to have the ability to ignore its own signaling elsewhere. At least in worms, it seems that *perception* of nutrient status is more important than the actual status in peripheral tissues themselves. While it is not clear how often these might become uncoupled, this remarkable finding suggests that current therapies aimed primarily at regulating AMPK signaling in peripheral tissues may be altered by neuronal signaling; or, seen in a more promising light, that sensing of AMPK status may be sufficient to induce beneficial metabolic effects. Therefore, future therapeutic investigations should include the consideration of effects on brain AMPK and CRTC1 signaling, in addition to more direct effects in peripheral tissues themselves.

REFERENCES

- Apfeld, J., and Kenyon, C. (1999). *Nature* 402, 804–809.
- Bishop, N.A., and Guarente, L. (2007). *Nature* 447, 545–549.
- Burkewitz, K., Morante, I., Weir, H.J.M., Yeo, R., Zhang, Y., Huynh, F.K., Ilkayeva, O.R., Hirschey, M.D., Grant, A.R., and Mair, W.B. (2015). *Cell* 160, this issue, 842–855.
- Lakhina, V., Arey, R.N., Kaletsky, R., Kauffman, A., Stein, G., Keyes, W., Xu, D., and Murphy, C.T. (2015). *Neuron* 85, 330–345.
- Libina, N., Berman, J.R., and Kenyon, C. (2003). *Cell* 115, 489–502.

Mair, W., Morante, I., Rodrigues, A.P., Manning, G., Montminy, M., Shaw, R.J., and Dillin, A. (2011). *Nature* 470, 404–408.

Riera, C.E., Huising, M.O., Follett, P., Leblanc, M., Halloran, J., Van Andel, R., de Magalhaes Filho,

C.D., Merkwirth, C., and Dillin, A. (2014). *Cell* 157, 1023–1036.

Tatum, M.C., Ooi, F.K., Chikka, M.R., Chauve, L., Martinez-Velazquez, L.A., Steinbusch, H.W., Morimoto, R.I., and Prahlad, V. (2015). *Curr. Biol.* 25, 163–174.

Tepper, R.G., Ashraf, J., Kaletsky, R., Kleemann, G., Murphy, C.T., and Bussemaker, H.J. (2013). *Cell* 154, 676–690.

Ulgherait, M., Rana, A., Rera, M., Graniel, J., and Walker, D.W. (2014). *Cell Rep.* 8, 1767–1780.

Finding the Right Match Fast

Divya Nandakumar¹ and Smita S. Patel^{1,*}

¹Department of Biochemistry and Molecular Biology, Rutgers-Robert Wood Johnson Medical School, 675 Hoes Lane West, Piscataway, NJ 08854, USA

*Correspondence: patelss@rutgers.edu
<http://dx.doi.org/10.1016/j.cell.2015.02.007>

DNA recombinases face the daunting task of locating and pairing up specific sequences among millions of base pairs in a genome, all within about an hour. Qi et al. show that recombinases solve this problem by searching in 8-nt microhomology units, reducing the search space and accelerating the homology search.

Homologous recombination is important for repairing stalled replication forks and ensuring genetic diversity (Lusetti and Cox, 2002). The recombinase that mediates homologous recombination self-assembles into presynaptic helical filaments on single-stranded (ss) DNA to search for a sequence match in double-stranded (ds) DNA, and then the ssDNA displaces the non-complementary strand in dsDNA to form a stable synaptic complex. To ensure genome stability, this process must be fast and accurate, but how this occurs given the size and complexity of genomes has been a mystery (Renkawitz et al., 2014). In this issue, Qi et al. (2015) now show that a minimal homology length requirement reduces the search space and accelerates the search for target homologous sequences through a hierarchical search mechanism.

Recognition of homologous sequence by the recombinase filament occurs via Watson-Crick pairing, and studies of *E. coli* RecA show that 15–18 bases of homology are sufficient for stable synaptic complex formation (Hsieh et al., 1992), long enough to represent a unique site in either the *E. coli* or human genome (~12 nt for *E. coli* and ~17 nt for humans). Given that the entire search

process occurs within an hour, how does the recombinase filament find this unique site? Theoretical studies suggest that dividing the search process into multiple stages and employing smaller groups of bases are effective strategies for fast and accurate searches (Jiang and Prentiss, 2014). Consistent with this, multiple kinetic intermediates and transient complexes between the RecA filament and 6- to 7-nt homology segments in dsDNA have been detected (Ragunathan et al., 2012). However, the shortest unit of homology that can form a stable synaptic complex with the dsDNA remained unclear.

To examine interactions of dsDNA sequences with the presynaptic filament, Qi et al. monitored complexes of dsDNA with the *Saccharomyces cerevisiae* Rad51 filament using single-molecule microscopy. In this method, a curtain of Rad51 filaments with ATP is generated on repeats of M13 ssDNA stretched across a flow chamber and anchored at both ends. The Rad51 filaments are then incubated with fluorophore-labeled dsDNA. After washing away unbound dsDNA, the bound dsDNAs are visualized and the off rates are measured. This method has the advantage of simultaneously monitoring

multiple fluorescent dsDNA complexes on several presynaptic filaments in the curtain.

When such experiments were carried out with non-homologous 70-bp dsDNA, the authors were surprised to find stable complexes with lifetimes as long as ~16 min. Analysis of the dsDNA sequence revealed that each strand contained short tracts of microhomology (3–9 nt in length) with the M13 ssDNA, consistent with a previous study suggesting that 8-nt homology is sufficient for initial base pairing (Hsieh et al., 1992). In contrast, dsDNAs with less than 8 nt microhomology formed unstable complexes, with average half-lives of ~0.5 s.

Strikingly, a ~1,300-fold increase in the lifetime of complexes was observed when the base homology was increased by just one nucleotide, from 7 to 8 nt. This degree of stabilization was not observed when the microhomology was further increased to 9 nt or more. Binding energy increases by 8 k_BT when the microhomology is increased from 7 to 8 nt, but only by 0.4 k_BT when going from 8 to 9 nt. Interestingly, subsequent binding energy increases of ~0.4 k_BT occurred in 3-nt increments, consistent with the triplet base organization of ssDNA observed in the crystal structure of RecA filament

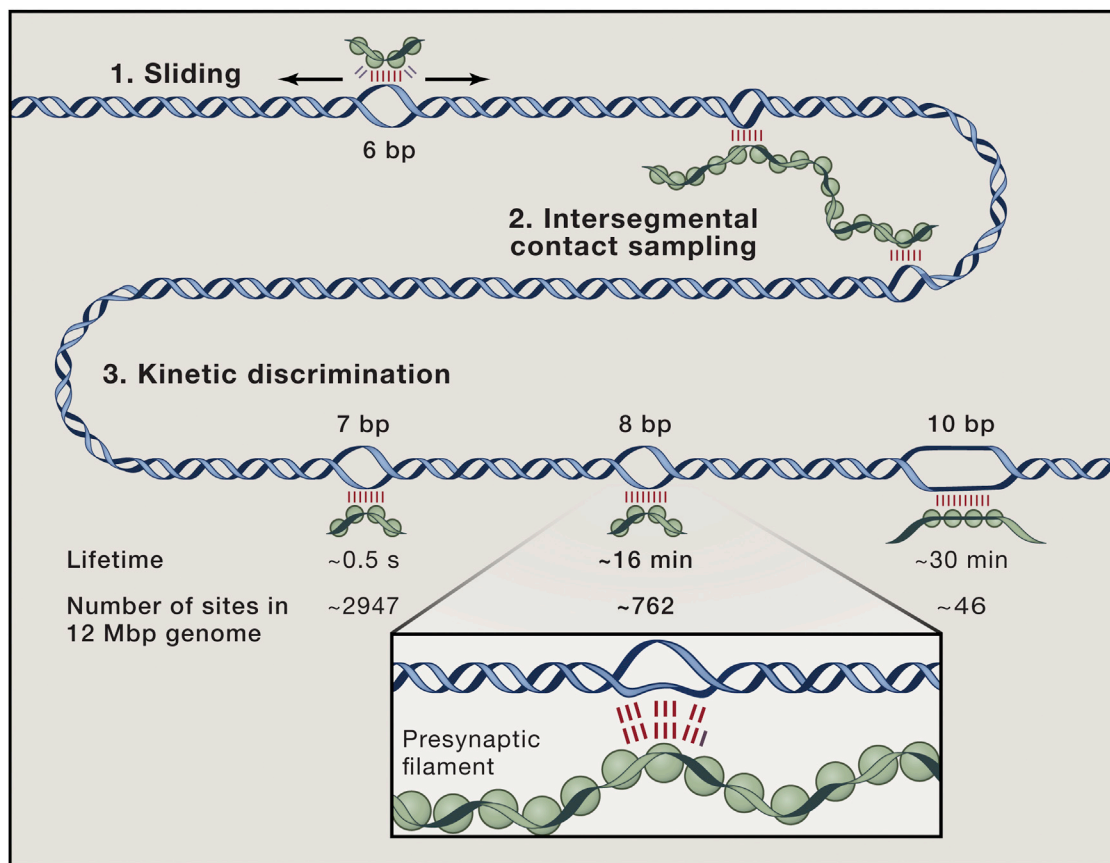


Figure 1. Mechanisms to Accelerate the Homology Search Process

There is experimental evidence for at least three mechanisms that the recombinase presynaptic filament (green) uses to accelerate the search for the homologous sequence in the genome. (1) A short region of the filament binds to dsDNA with no or <8-nt homology and slides along the dsDNA looking for longer tracts of homology (Ragunathan et al., 2012). (2) The presynaptic filament probes multiple segments of the dsDNA that are separated in sequence through intersegmental contact sampling (Forget and Kowalczykowski, 2012). (3) The filament scans and rejects regions with <8-nt homology that occur at high frequencies in the genome. The filament forms relatively stable complexes with 8-nt and longer microhomology dsDNA regions. This decreases the search space and accelerates the homology search process (Qi et al., 2015).

(Chen et al., 2008) and the propagation of initial synaptic filaments in 3-nt increments (Ragunathan et al., 2011). These findings indicate a length-dependent kinetic discrimination against sequences that are less likely to be fully homologous.

Though the genome sizes of different organisms vary dramatically, initial recognition of 8-nt microhomology regions is conserved across the Rad51/RecA family. What is the advantage of searching for homology in 8-nt bits? The likelihood of a given sequence appearing in a genome decreases exponentially as the length of the sequence increases; for example, in the 12 Mbp genome of *Saccharomyces cerevisiae*, a specific 7-nt sequence is expected to appear ~2,947 times, while this figure drops to

~762 times for an 8-nt sequence (Figure 1). A 10-nt sequence appears only ~46 times in the *S. cerevisiae* genome, but the 10 bp synaptic complex is stable for nearly half an hour. Thus, there must be a balance between the number of sites needed to scan the genome and the stability of the synaptic complexes.

Given that binding was relatively stable beyond the microhomology “sweet spot” of 8 nt, there must be mechanisms to dissociate stable complexes that are sampled but incorrect. Indeed, Qi et al. also show that competitor dsDNA can increase the dissociation rates of 8- and 12-nt complexes by as much as 3-fold, suggesting a “facilitated exchange” mechanism. The authors also predict that, while longer filaments have more

sites to interrogate in the genome, increasing the search time, they also permit multiple, simultaneous interactions, which may decrease the search time. In vivo, other factors such as helicases, nuclear organization proteins, and chromosome mobility may aid both the search and dissociation of incorrect complexes. Future studies with added factors will be necessary to refine the homology search models.

Additional mechanisms may work together with kinetic discrimination to accelerate the homology search (Figure 1). For instance, multiple segments of long dsDNA are probed simultaneously by “intersegmental contact sampling” (Forget and Kowalczykowski, 2012). Curiously, this single-molecule approach did not observe stable

synaptic complex formation with extended dsDNA despite the presence of numerous microhomology sites. Short-range sliding of presynaptic filaments on dsDNA substrates has also been observed, which may speed up the search process by ~ 200 fold (Ragunathan et al., 2012).

The advent of elegant single-molecule methods has allowed us to better understand the molecular mechanisms of homologous DNA recombination (Sanchez et al., 2014), but several questions remain. The crystal structure of ssDNA-bound RecA filament shows that the ssDNA has periodic base triplets in nearly B form, followed by an extended bond (Chen et al., 2008), so the structural basis for 8-nt microhomology recognition is not

clear. Similarly, how the dynamics of the presynaptic filament are involved in recognizing dsDNA base pairing is not known. Finally, while the proposed mechanisms for accelerating the homology search may work in concert, they have not been observed simultaneously in a single study. Further work is needed to determine how, or if, the mechanisms function together, as well as the relative contribution of each to accelerating the process.

REFERENCES

- Chen, Z., Yang, H., and Pavletich, N.P. (2008). *Nature* 453, 489–484.
- Forget, A.L., and Kowalczykowski, S.C. (2012). *Nature* 482, 423–427.
- Hsieh, P., Camerini-Otero, C.S., and Camerini-Otero, R.D. (1992). *Proc. Natl. Acad. Sci. USA* 89, 6492–6496.
- Jiang, L., and Prentiss, M. (2014). *Phys. Rev. E Stat. Nonlin. Soft Matter Phys.* 90, 022704.
- Lusetti, S.L., and Cox, M.M. (2002). *Annu. Rev. Biochem.* 71, 71–100.
- Qi, Z., Redding, S., Lee, J.Y., Gibb, B., Kwon, Y., Niu, H., Gaines, W.A., Sung, P., and Greene, E.C. (2015). *Cell* 160, this issue, 856–869.
- Ragunathan, K., Joo, C., and Ha, T. (2011). *Structure* 19, 1064–1073.
- Ragunathan, K., Liu, C., and Ha, T. (2012). *eLife* 1, e00067.
- Renkawitz, J., Lademann, C.A., and Jentsch, S. (2014). *Nat. Rev. Mol. Cell Biol.* 15, 369–383.
- Sanchez, H., Reuter, M., Yokokawa, M., Takeyasu, K., and Wyman, C. (2014). *DNA Repair (Amst.)* 20, 110–118.

ALT Telomeres Get Together with Nuclear Receptors

Eric Aeby¹ and Joachim Lingner^{1,*}

¹Swiss Institute for Experimental Cancer Research (ISREC), School of Life Sciences, Ecole Polytechnique Fédérale de Lausanne (EPFL), 1015 Lausanne, Switzerland

*Correspondence: joachim.lingner@epfl.ch
<http://dx.doi.org/10.1016/j.cell.2015.02.006>

Nuclear receptors bind chromosome ends in “alternative lengthening of telomeres” (ALT) cancer cells that maintain their ends by homologous recombination instead of telomerase. Marzec et al. now demonstrate that, in ALT cells, nuclear receptors not only trigger distal chromatin associations to mediate telomere-telomere recombination events, but also drive chromosome-internal targeted telomere insertions (TTI).

Telomeres, the ends of chromosomes, would look just like the products of DNA double strand breaks if not for their specialized sequences and cohort of protective binding proteins. The cellular overproliferation characteristic of cancer requires some means of maintaining telomeric sequence through successive rounds of replication. For some cells, that involves reactivating telomerase, the enzyme that templates the characteristic telomere repeats. For others, it means relying on a homologous recombination-dependent mechanism termed alternative lengthening of telomeres (ALT). In this

issue of *Cell*, Marzec et al. (2015) identify nuclear receptors as critical components in reprogramming normal telomeres toward ALT.

In most normal human, somatic cells, telomeres shorten with every round of DNA replication due to the DNA end replication problem and the absence of telomerase. Too short telomeres elicit a DNA damage response triggering a permanent cell-cycle arrest termed cellular senescence. Thus, the replicative potential of primary cells is limited, restraining the growth of pre-cancerous lesions that have lost normal growth control. How-

ever, mutations in cell-cycle regulators like p53 and pRB cause senescence bypass and restart the march toward malignancy. Replication under these conditions can lead to further telomere shortening and loss of the proteins that protect chromosome ends from fusion or “repair.” In cases in which telomeres do fuse, cells enter a crisis state in which fused chromosomes that contain multiple centromeres become missegregated or become torn apart during mitosis. Cells can escape crisis either by re-gaining telomerase expression, for instance by mutating the promoter of the human

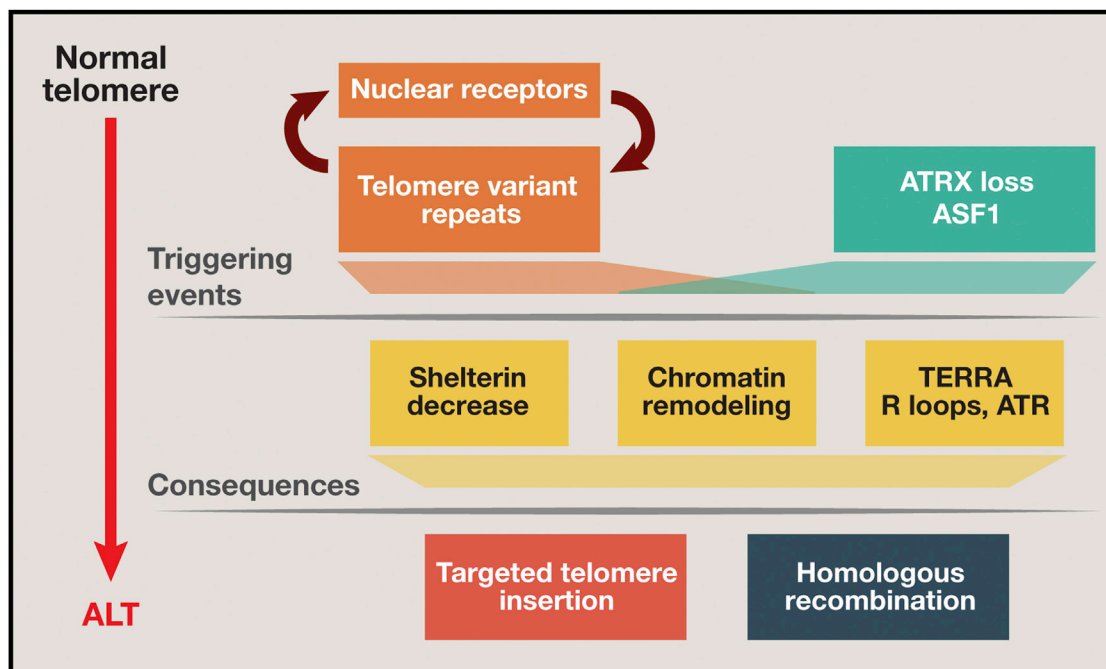


Figure 1. Molecular Events that May Trigger the Alternative Lengthening of Telomeres Pathway

At normal telomeres, HR is repressed by the high abundance of shelterin proteins. For ALT formation, nuclear receptors accumulate at telomeres, binding to variant telomeric repeat sequences. Nuclear receptor binding promotes formation of chromatin clusters that favor HR and spreading of telomeric variant repeats, which in turn will promote further nuclear receptor binding. Nuclear receptors may also promote recruitment of chromatin remodelers, which favor HR protein association and counteract the presence of shelterin. While ATRX loss will also promote telomeric chromatin remodeling, it upregulates the long noncoding RNA TERRA. Misregulated TERRA forms recombination-prone R loops that activate HR. TERRA also perturbs telomeric protein composition favoring association of RPA with telomeric DNA, which activates the ATR checkpoint kinase. Whether ATRX loss and nuclear receptor binding to telomeres are sufficient to trigger ALT remains to be tested.

telomerase reverse transcriptase (hTERT) gene, or by engaging the ALT pathway to maintain telomeres.

ALT is found in ~10% of cancers and is prevalent in sarcomas and glioblastomas. ALT telomeres are maintained by the homologous recombination (HR) machinery. Recombination occurs between telomeres of separate chromosomes. HR and telomere clustering are repressed at normal telomeres by the telomeric shelterin proteins (Sfeir and de Lange, 2012). Critical changes occur in ALT telomeric chromatin to overcome the shelterin-mediated repression of HR.

Orphan nuclear receptors of the NR2C/F class that classically regulate gene expression have also been found at ALT telomeres (Déjardin and Kingston, 2009). Subsequent work demonstrated that the nuclear receptors bind to variant telomeric repeat sequences (5'-GGGTCA-3' instead of the canonical 5'-GGGTTA-3' repeats) that are scarce in normal telomeres but that accumulate at ALT telomeres (Cono-

mos et al., 2012). In the new study, Marzec et al. identified tandem 5'-GGGTCA-3' repeats accumulating at ALT-telomeres bound by NR2C/F nuclear receptors. Importantly, nuclear receptor binding to telomeres induced telomere cluster formation, which is required for HR in ALT cells. Intriguingly, tethering a NR2C2-lacI fusion protein to a single *LacO* array not only led to colocalization of the array with telomeres, but also triggered its rapid amplification and spreading to other sites in the genome. It thus appears that the telomere clusters are sites of highly active recombination, and NR2C/F-mediated recruitment of DNA to this locus is sufficient to make this DNA recombine and spread elsewhere in the genome.

Consistent with this notion, Marzec et al. also discovered that a subset of chromosomal NR2C/F binding sites in ALT cells are locations of targeted telomere insertions (TTI). These newly inserted interstitial telomeric sequences may promote genome instability in ALT cells, as telomeric DNA is fragile and

difficult to replicate. The association of chromosome-internal NR2C/F binding sites with telomeres may explain the spreading of the NR2C/F-bound 5'-GGGTCA-3' repeats into telomeric tracts. Alternatively, the 5'-GGGTCA-3' sequences may amplify from the rare telomeric copies. Thus, the new work suggests a sequence of molecular events that may occur during the evolution of ALT cells from normal cells. Critically short telomeres, missing key shelterin proteins, may expose the scarce 5'-GGGTCA-3' sequences for NR2C/F binding. Binding of NR2C/F at telomeres and its binding at chromosome internal sites would then promote chromatin clustering, HR, and 5'-GGGTCA-3' spreading, which in turn would facilitate further NR2C/F binding, telomere cluster formation, and recombination in a feedforward loop reaction (Figure 1). Thus, in this hypothetical scenario, HR would reinforce itself in ALT once it was triggered by rare initiating events.

Is nuclear receptor binding to telomeres sufficient to trigger ALT? Probably not. Spreading of the receptor binding sites at telomeres using a mutant version of telomerase did not trigger ALT, although it was sufficient to induce some ALT-specific features such as accumulation of single-stranded telomeric (CCCTAA)_(n) DNA circles (C-circles) (Conomos et al., 2012). Recent work has pinpointed additional distinct events required for ALT. These include recruitment or mutation of distinct chromatin remodeling factors that contribute to displacement of shelterin, HR factor binding, and HR activation. Among these, binding of the histone deacetylase NuRD is sustained by nuclear receptors (Conomos et al., 2014). Mutations in other factors may support ALT through mismanagement of histone assembly. For example, depletion of the histone chaperone ASF1 induced ALT features, although this protein is not generally mutated in ALT-utilizing cancers (O'Sullivan et al., 2014). However, a strong correlation was found between ALT status and mutations in the SWI/SNF family ATP-dependent helicase ATRX (Lovejoy et al., 2012), and ATRX-loss was recently intimately linked to the onset of recombination at ALT telomeres (Flynn et al., 2015). ATRX loss leads to upregulation of the telomeric long non-coding RNA TERRA, which may perturb protein association with single-stranded telomeric DNA, coinciding with accumu-

lation of replication protein A (RPA) at telomeres. RPA activates the DNA damage protein kinase ATR, which seems important for ALT as ATR inhibition led to selective killing of ALT cells (Flynn et al., 2015). At the same time, loss of ATRX and TERRA upregulation in S phase may promote the formation of telomeric R loops. In R loops, an RNA strand is base paired with the template DNA strand of a DNA duplex, leaving the displaced non-template DNA single stranded. Telomeric R loops are repressed at normal telomeres (Pfeiffer et al., 2013), but they become prevalent in ALT cells, where they promote recombination between telomeric repeats (Arora et al., 2014). Overall, nuclear receptor accumulation at telomeres and ATRX loss seem to represent two essential triggering events for ALT (Figure 1).

In summary, the new work by Marzec et al. elucidates critical roles for nuclear receptors in mediating telomeric chromatin associations in ALT that are essential for recombination. The work provides a model for how nuclear receptor binding sites spread at telomeres and uncovers TTI as a novel mechanism of genome instability in ALT cells. In combination with other recent results, these findings support the hypothesis that ALT activation depends on several molecular events. Finally, this complexity may explain why telomerase reactivation instead of ALT is the more frequently

selected route toward immortality of cancer cells.

ACKNOWLEDGMENTS

We thank the Swiss Cancer League and the Swiss National Science Foundation for funding.

REFERENCES

- Arora, R., Lee, Y., Wischnewski, H., Brun, C.M., Schwarz, T., and Azzalin, C.M. (2014). *Nat. Commun.* 5, 5220.
- Conomos, D., Stutz, M.D., Hills, M., Neumann, A.A., Bryan, T.M., Reddel, R.R., and Pickett, H.A. (2012). *J. Cell Biol.* 199, 893–906.
- Conomos, D., Reddel, R.R., and Pickett, H.A. (2014). *Nat. Struct. Mol. Biol.* 21, 760–770.
- Déjardin, J., and Kingston, R.E. (2009). *Cell* 136, 175–186.
- Flynn, R.L., Cox, K.E., Jeitany, M., Wakimoto, H., Bryll, A.R., Ganem, N.J., Bersani, F., Pineda, J.R., Suvà, M.L., Benes, C.H., et al. (2015). *Science* 347, 273–277.
- Lovejoy, C.A., Li, W., Reisenweber, S., Thongthip, S., Bruno, J., de Lange, T., De, S., Petrini, J.H., Sung, P.A., Jasin, M., et al.; ALT Starr Cancer Consortium (2012). *PLoS Genet.* 8, e1002772.
- Marzec, P., Armenise, C., Pérot, G., Roumelioti, F.-M., Basyuk, E., Gagos, S., Chibon, F., and Déjardin, J. (2015). *Cell* 160, this issue, 913–927.
- O'Sullivan, R.J., Arnoult, N., Lackner, D.H., Oganesian, L., Haggblom, C., Corpet, A., Almouzni, G., and Karlseder, J. (2014). *Nat. Struct. Mol. Biol.* 21, 167–174.
- Pfeiffer, V., Crittin, J., Grolimund, L., and Lingner, J. (2013). *EMBO J.* 32, 2861–2871.
- Sfeir, A., and de Lange, T. (2012). *Science* 336, 593–597.

Fertile Waters for Aging Research

Adrienne M. Wang,¹ Daniel E.L. Promislow,^{1,2} and Matt Kaeberlein^{1,*}

¹Department of Pathology, University of Washington, Seattle, WA 98195, USA

²Department of Biology, University of Washington, Seattle, WA 98195, USA

*Correspondence: kaeber@uw.edu

<http://dx.doi.org/10.1016/j.cell.2015.02.026>

The quest to slow aging has come far, and what used to be the domain of science fiction writers and snake oil salesmen may soon become science fact. Innovative new approaches, such as the use of the very short-lived African killifish (Harel et al.), are bridging the translational gap and bring the promise of healthy longevity to fruition.

Over the past couple of decades, a tremendous amount has been discovered about the biology of aging from studies largely conducted in classic model organisms: budding yeast, nematode worms, fruit flies, and mice. However, by relying almost exclusively on a single vertebrate model and by focusing on animals maintained under laboratory conditions, we are left with a relatively poor understanding of the extent to which these models translate to other animals and environments and eventually to humans. This has led to a growing recognition in the field that innovative new tools and approaches are needed. In the current issue of *Cell*, Harel et al. (2015) describe just such a new tool: the short-lived African killifish *Nothobranchius furzeri*. We are now entering a period where new animal models and approaches will allow us to delve deeply into the conserved mechanisms of aging and bridge the final translational gap from laboratory models to people.

In many ways, the African killifish combines some of the best features of the major model systems in one animal. With a 4–6 month lifespan that is still comparable to the well-characterized invertebrate aging models, the African killifish is the shortest-lived vertebrate that can be cultivated in the laboratory easily and relatively inexpensively. This naturally compressed lifespan allows for a unique opportunity to study mortality, physiology, and

age-related disease in a vertebrate model with blood, bones, and an adaptive immune system. *Nothobranchius* exhibits many age-dependent phenotypes and pathologies, including decreased fertility, sarcopenia, cognitive decline, and cancer (Di Cicco et al., 2011; Hartmann et al., 2009; Terzibasi et al., 2009), and even has telomeres that resemble humans both in length and in progressive decline. Researchers also benefit from the existence of both inbred and wild-caught strains in this species, providing a useful tool for genetic mapping and comparative genomics studies, as well as a short life cycle, large brood size, and ease of drug administration. All of these attributes make this model an ideal candidate for high-throughput in vivo drug screens.

Until now, research on this burgeoning model has been limited by the lack of a sequenced genome and genetic tools to manipulate gene function and expression. Harel et al. (2015) utilized de novo genome assembly to produce a fully sequenced and annotated genome and CRISPR/Cas9 technology to generate mutant alleles for 13 different genes associated with aging. As proof of principle, they focus on the protein subunit of telomerase (TERT) as a model of telomere attrition. By targeting the catalytic domain of TERT, the authors were able to create a TERT loss-of-function mutant that results in shortened telomeres, reduced fertility, and deficiencies in other proliferative tissues such as blood and intestine. In doing this, the authors achieve in 2 months what

takes several generations in mice (Rudolph et al., 1999) and 6–8 months in zebrafish (Anchelin et al., 2013), generating the fastest vertebrate model of telomere shortening and firmly establishing the killifish as a promising and tractable platform to investigate vertebrate aging.

As Figure 1 shows, the African killifish fills an important evolutionary gap in aging models between mammalian models, which diverged from humans 40–90 million years ago, and the invertebrate models that diverged 900 million years ago or more. Comparative biological approaches that incorporate exceptionally long-lived models such as the naked mole rat and some species of clams

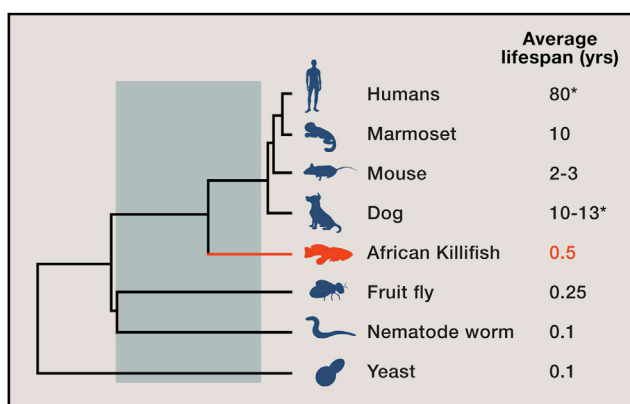


Figure 1. Evolutionary Relationships between Humans and Organisms Frequently Used in Aging Research

Approximate average lifespan shown for each organism. The African killifish (Harel et al., 2015) has an average lifespan comparable to invertebrate models while being much more closely related to people. Ancestors of humans and killifish diverged approximately 400 million years ago (red line). Thus, *Nothobranchius* fills a gap (gray box) between the mammalian models that are separated from humans by ~100 million years and invertebrate models, which diverged ~900 million years ago. The asterisk (*) denotes the shared environment between humans and dogs.

will also undoubtedly play an important role in further contributing to progress in this area. At the same time, two other species are now emerging that we believe may prove crucial to bridging the translational gap to humans. The first of these is the common marmoset, *Callithrix jacchus*. In addition to being a short-lived anthropoid primate, with an average lifespan of about a decade, marmosets suffer from many of the same age-related diseases and declines in function across a variety of tissue and organ systems as people do (Tardif et al., 2011). Marmosets are also becoming more commonly studied in the lab, with a growing set of genomic and transgenic tools available. Research on aging in marmosets is continuing at several primate research centers and should teach us much about the roles of genetic and environmental variation in natural aging processes in primates.

The other animal we believe has the potential to be a “game changer” in aging research is the domestic dog, *Canis lupus familiaris*. Although dogs are as evolutionarily distant from humans as mice are, they share our environment in a way that can't be replicated in the lab. Moreover, the extensive level of pre-existing veterinary knowledge and quality of health care in dogs, including geriatric ones, is

second only to that of humans. Recent studies have described the dramatic differences among breeds in life expectancy, patterns of age-specific mortality, and causes of death (Fleming et al., 2011; Waters, 2011). Aside from the important insights that dogs can provide into human aging, promoting healthier longevity in companion animals has intrinsic value for the millions of people who own them. These features, combined with their genetic and phenotypic diversity, well-characterized breed structure, and (unfortunately!) short lifespans, make companion dogs a compelling choice for both longitudinal and interventional studies of aging.

Traditional laboratory models have led to large advances in our understanding of the basic mechanisms of aging. Despite this progress, the extent to which these mechanisms affect human aging and age-related disease has yet to be determined. Further, the complex effects of environmental and genetic variation make for a large leap from genetically identical organisms in tightly controlled laboratory conditions to genetically diverse humans exposed to many different environments. Studies in non-traditional animal models of aging may hold the key to filling this gap. The addi-

tion of the African killifish as a new aging model, as well as the extension of studies to primates that are more closely related to humans and to canines that share our environment and model phenotypic diversity, holds promise in the ongoing quest to combat aging and age-related diseases.

REFERENCES

- Anchelin, M., Alcaraz-Pérez, F., Martínez, C.M., Bernabé-García, M., Mulero, V., and Cayuela, M.L. (2013). *Dis. Model. Mech.* 6, 1101–1112.
- Di Cicco, E., Tozzini, E.T., Rossi, G., and Cellerino, A. (2011). *Exp. Gerontol.* 46, 249–256.
- Fleming, J.M., Creevy, K.E., and Promislow, D.E. (2011). *J. Vet. Intern. Med.* 25, 187–198.
- Harel, I., Benayoun, B.A., Machado, B., Singh, P.P., Hu, C.-K., Pech, M.F., Valenzano, D.R., Zhang, E., Sharp, S.C., Artandi, S.E., et al. (2015). *Cell* 160, this issue, 1013–1026.
- Hartmann, N., Reichwald, K., Lechel, A., Graf, M., Kirschner, J., Dorn, A., Terzibasi, E., Wellner, J., Platzer, M., Rudolph, K.L., et al. (2009). *Mech. Ageing Dev.* 130, 290–296.
- Rudolph, K.L., Chang, S., Lee, H.W., Blasco, M., Gottlieb, G.J., Greider, C., and DePinho, R.A. (1999). *Cell* 96, 701–712.
- Tardif, S.D., Mansfield, K.G., Ratnam, R., Ross, C.N., and Ziegler, T.E. (2011). *ILAR J.* 52, 54–65.
- Terzibasi, E., Lefrançois, C., Domenici, P., Hartmann, N., Graf, M., and Cellerino, A. (2009). *Aging Cell* 8, 88–99.
- Waters, D.J. (2011). *ILAR J.* 52, 97–105.

Homeostasis, Inflammation, and Disease Susceptibility

Maya E. Kotas^{1,3} and Ruslan Medzhitov^{1,2,*}

¹Department of Immunobiology

²Howard Hughes Medical Institute

Yale University School of Medicine, New Haven, CT USA

³Present address: Department of Medicine, Columbia University, New York, NY USA

*Correspondence: ruslan.medzhitov@yale.edu

<http://dx.doi.org/10.1016/j.cell.2015.02.010>

While modernization has dramatically increased lifespan, it has also witnessed the increasing prevalence of diseases such as obesity, hypertension, and type 2 diabetes. Such chronic, acquired diseases result when normal physiologic control goes awry and may thus be viewed as failures of homeostasis. However, while nearly every process in human physiology relies on homeostatic mechanisms for stability, only some have demonstrated vulnerability to dysregulation. Additionally, chronic inflammation is a common accomplice of the diseases of homeostasis, yet the basis for this connection is not fully understood. Here we review the design of homeostatic systems and discuss universal features of control circuits that operate at the cellular, tissue, and organismal levels. We suggest a framework for classification of homeostatic signals that is based on different classes of homeostatic variables they report on. Finally, we discuss how adaptability of homeostatic systems with adjustable set points creates vulnerability to dysregulation and disease. This framework highlights the fundamental parallels between homeostatic and inflammatory control mechanisms and provides a new perspective on the physiological origin of inflammation.

Introduction

Changes in human ecology—including diet, physical activity, population density, and microbial exposure—have dramatically shifted the spectrum of human diseases over the past century. Genes selected to protect from starvation, infections, injury, and predation may now, in the absence of some of these challenges, contribute to the increasing incidence of “modern human diseases,” including obesity, type 2 diabetes, atherosclerosis, autoimmunity, allergy, and certain psychiatric disorders. Plausible evolutionary explanations for the high prevalence of these diseases in industrialized countries include antagonistic pleiotropy (Williams, 1957) and the mismatch between modern environment and human evolutionary history (Gluckman et al., 2009; Stearns and Koella, 2008).

These modern human diseases seem to have two features in common: they involve disruption of homeostasis, and they are nearly universally associated with chronic inflammation. Despite this well-documented connection between inflammation and diseases of homeostasis, the underlying evolutionary and mechanistic bases remain obscure. In most complex diseases, in contrast to rare Mendelian diseases, the pathological state has a normal, physiological counterpart. The etiology of modern human diseases may therefore point to the physiological rationale connecting inflammation and homeostasis.

Most physiological processes can only operate under a narrow range of conditions, which are maintained by specialized homeostatic mechanisms in the face of variations in the environment, and adjusted in response to changes in

functional demands and biological priorities. Interestingly, only some of these processes are vulnerable to dysregulation and disease. For example, lipid and glucose metabolism can be derailed, leading to dyslipidemia, diabetes, and obesity, while amino acid metabolism seems resistant to homeostatic dysregulation. Here we present a view that may help explain the differential susceptibility of physiological processes to diseases of homeostasis. We explore the fundamental connections between homeostasis and inflammation and discuss an evolutionary perspective on homeostatic diseases.

Homeostatic Variables and Control Circuits

In the 19th century, Claude Bernard articulated the need to maintain a stable internal environment—*milieu interieur*—that would allow biological processes to proceed despite variations in the external environment (Bernard, 1878). Bernard’s concept was further explored, developed, and popularized by Walter Cannon, who coined the term “homeostasis” in describing how key physiological variables are maintained within a predefined range by feedback mechanisms (Cannon, 1929). His contemporary, Curt Richter, expanded the notion of homeostasis to include behavioral responses as an important mechanism by which homeostasis could be regulated in addition to the internal controls systems described by Bernard and Cannon (Moran and Schulkin, 2000; Richter, 1943). Nearly two decades after Cannon, James Hardy proposed a model in which homeostatic mechanisms maintain physiological variables within an acceptable range by comparing

Table 1. Glossary

Term	Definition	Examples
Stock	A system's variable that represents quantity	Blood glucose concentration
Flow	A system's variable that represents a process that changes the stock	Gluconeogenesis, glycogenolysis, glycolysis, gluconeogenesis, glucose transport
Regulated variable	A physiologic variable that is maintained at a stable level (near set point) by homeostatic circuit(s). Regulated variables are stocks	Blood glucose concentration
Controlled variable	A physiologic variable that is manipulated in order to maintain the regulated variable within desired range. Controlled variables are flows	Gluconeogenesis, glycogenolysis, glycolysis, gluconeogenesis, glucose transport
Set point	An optimal value of the regulated variable; divergence from set point value activates homeostatic control mechanisms	Normoglycemia (~5 mM)
Error value $ X - X' $	The difference between the set point and the actual value of the regulated variable	Difference between actual blood glucose concentration and normoglycemia
Controller	A component of the homeostatic circuit that monitors the value of regulated variable	Pancreatic α and β cells
Plant	An effector component of the homeostatic circuit that is activated by the Controller to change the value of regulated variable	Skeletal muscle, white adipose tissue, brown adipose tissue, liver
Controller gain	A characteristic of Controllers that determines the amount of signal produced in response to given error value $ X - X' $	Amount of insulin produced by β -cells in response to a given blood glucose level
Gain tuning of Controller	A method to optimize Controller performance	Changing the amount of insulin produced in response to a given blood glucose level

the actual value of the variable to a desired value or “set point” (Hardy, 1953–1954).

Homeostasis is a unifying theme of modern physiology and much has been elucidated about molecular mechanisms of homeostatic control. However, the term, being intuitively simple, is often used loosely. For the purpose of this discussion, it is important to introduce and review some key definitions and concepts initially developed in control theory and systems dynamics theory, but applicable to homeostatic control in biological systems (see Table 1 for glossary).

First, it is important to distinguish two types of variables that exist in homeostatic systems. The physiological variables that are maintained at a stable level, such as blood glucose or core body temperature, are called *regulated variables*. In contrast, *controlled variables* are activities, or rates, of the processes that contribute to the stability of regulated variables (Cabanac, 2006). For example, blood calcium concentration is a regulated variable, whereas the rate of urinary calcium excretion is a controlled variable that is manipulated in order to regulate blood calcium concentration. Multiple controlled variables typically contribute to the stability of a given regulated variable. Thus, in addition to calcium excretion in the kidney, the rates of intestinal calcium absorption and bone resorption are also controlled variables that contribute to the maintenance of stable blood calcium concentration. In the case of blood glucose concentration (a regulated variable), the controlled variables include the rates of intestinal and renal glucose transport, glycogenolysis, gluconeogenesis, glycolysis, glycogenesis, and glucose transport from the blood into tissues. Thus, regulated variables refer to quantities, whereas controlled variables refer to processes, where process activity or rate is a variable. Put in systems dynamics terms, regulated variables are the *stocks* of the system, while controlled variables are the *flows* of the system: they either

increase (in-flows) or decrease (out-flows) the value of the regulated variable (Figure 1). Notably, while all regulated variables are stocks, not all stocks are regulated variables. For example blood glucose is a regulated variable, whereas blood alcohol is not. Likewise, all controlled variables are flows, but not all flows are controlled variables. Thus heat loss through sweating is a controlled variable, while heat loss through conduction is not. Because these terminologies capture different aspects of system behavior we will use both during this discussion, to emphasize the relevant features of homeostasis.

In order to be maintained within the desired range, the values of regulated variables must be continuously monitored and adjusted. Accordingly, all homeostatic systems have two essential components: *Controllers* and *Plants*. The Controllers monitor the value of the regulated variable (X), compare it to the reference value (or in Hardy's terms, set point) (X'), and generate a signal that is proportional to the absolute value of the difference $|X - X'|$ (the coefficient of proportionality is a characteristic known as the Controller's *gain*) (Åström and Murray, 2008). This signal then acts on the Plant—the effector that creates flows into or out of the system—in order to bring the regulated variable closer to the reference value (Figure 2A). In a classic engineering example of a control system, the thermostat (Controller) compares the actual room temperature (regulated variable) to the desired room temperature (reference value, or set point). If actual room temperature is lower than the set point, a signal is generated and sent to the furnace (the Plant) to increase heat production (the flow) and raise room temperature toward the set point value. In physiology, the Controllers are typically endocrine cells and sensory neurons of the autonomic nervous system, lower brainstem (medulla), and hypothalamus (Hammel, 1968). They monitor deviations in regulated physiologic variables from their set points and generate signals (hormones and

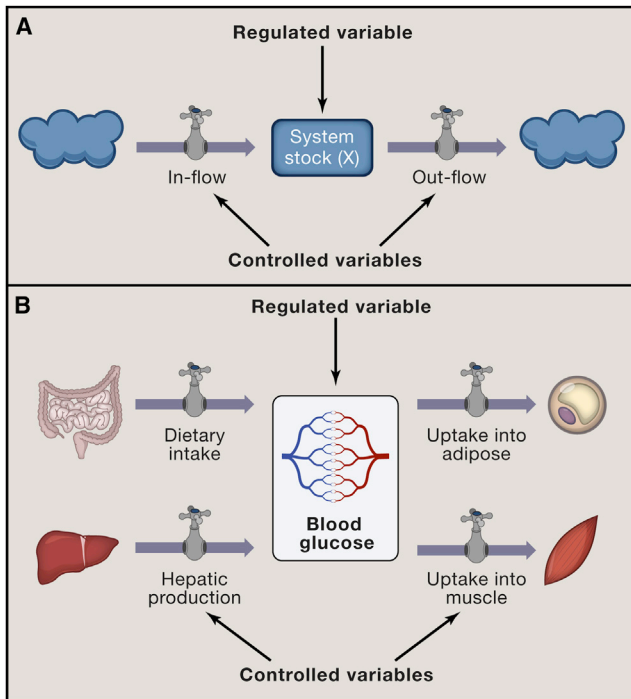


Figure 1. Stock and Flow Model of Homeostasis

(A) Stock and flow model highlights two types of variables in homeostasis: Stock is quantity of a regulated variable - a parameter that is maintained by homeostasis. Flows are the processes that change the value of the stock. Some, but not all flows are controlled variables and targets for homeostatic control signals (graphically represented here as dials). Clouds represent “sources” and “sinks” for regulated variable that are extrinsic to the homeostatic system.

(B) A physiologic example of stock and flow model: dietary glucose uptake, hepatic glucose production, or glucose uptake into adipose and muscle are flows that maintain the stock of blood glucose.

neurotransmitters) that increase or decrease the flows created by various Plants (tissues and organs that can adjust these values) (Figure 2B). For example, pancreatic β -cells (Controller) produce insulin in response to an increase in blood glucose (regulated variable). Insulin acts on skeletal muscle, adipose tissue, and liver (the Plants) to increase glucose uptake and utilization (out-flows) in muscle and fat and to inhibit gluconeogenesis (in-flow) in the liver, thereby reducing plasma glucose level (Figure 2C).

Controllers and Plants are defined with respect to specific regulated variables. For example, pancreatic α - and β -cells are Controllers for blood glucose, but not for body temperature, whereas adipose tissue and liver are Plants for blood glucose, but not for blood calcium (where the relevant Plants are the kidney, intestine, and bone). Additionally, most tissues and organs perform many functions and can therefore act as Plants for multiple regulated variables, depending on the requirements of the organism: because skeletal muscle can both consume glucose and generate heat during shivering thermogenesis, it can act as a Plant for both blood glucose and body temperature. Thus, Controllers are characterized by the regulated variables they monitor, while Plants are characterized by the controlled variables (activities of the flows) associated with them.

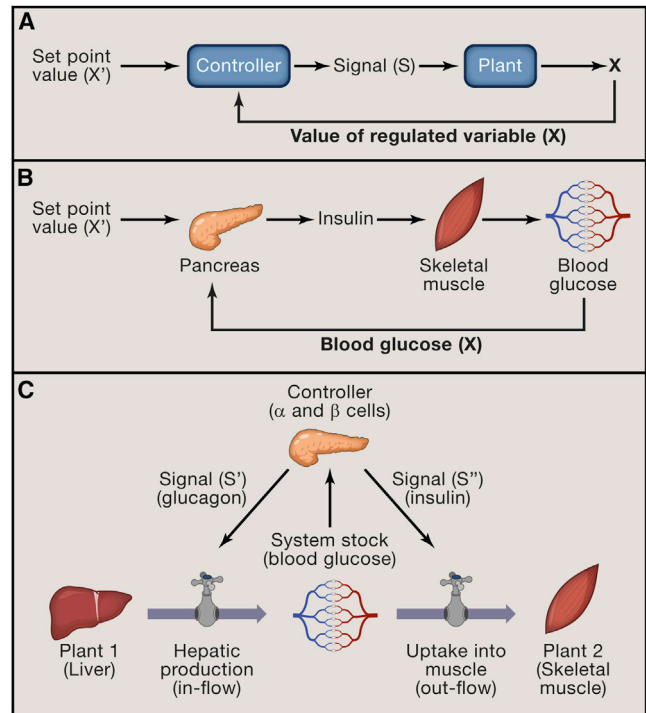


Figure 2. Homeostatic Control Circuit

(A) Basic homeostatic control circuits have two essential components: Controllers and Plants. Controllers monitor the value of regulated variable (X) and compare it to the reference value (X'). In response to deviation of X from X' , Controllers generate a signal (S) that acts on Plants. Plants are the effectors of the homeostatic systems that change the value of the regulated variable.

(B) A physiologic example of control circuit: pancreatic beta cells act as Controller, sensing elevated blood glucose and producing insulin (signal S) to increase glucose uptake into skeletal muscle (Plant). In the simplest model, the output of the Controller (signal S) is proportional to the deviation of regulated variable from the reference value, $|X - X'|$. The proportionality constant is referred to as the *gain*.

(C) Combining stock and flow modeling with the basic control circuit provides a more complete model of homeostasis. The Controller monitors the value of the Stock and produces signals that act on Plants. Such signals cause Plants to modulate the flows that contribute to the Stock. In this example, glucose sensing by the pancreas (Controller), induces glucagon or insulin secretion (Signals S' and S''), which act on liver and muscle (Plants), to control glucose production and uptake, respectively (flows) and stabilize blood glucose (Stock).

Fifty years after its inception, there is still disagreement over Hardy's concept of set point, which in his model was analogous to the *reference value* of engineered systems. Some argue that regulated variables can reach steady state or “settling point” without an external reference point (Wirtshafter and Davis, 1977). In stock and flow terms, the stock would not be regulated by comparison to a set point, but simply reach a passive “settling point” when in-flows and out-flows balance. In other words, one can think of set point as being either a predefined, or an emergent characteristic of a system. A full discussion of the strengths and limitations of these two models is beyond the scope of this article. However, the two models may not necessarily be mutually exclusive (Speakman et al., 2011). Regardless of whether a reference point is real or imaginary, the term set point, if nothing else, is a convenient shortcut by which to refer to the defended

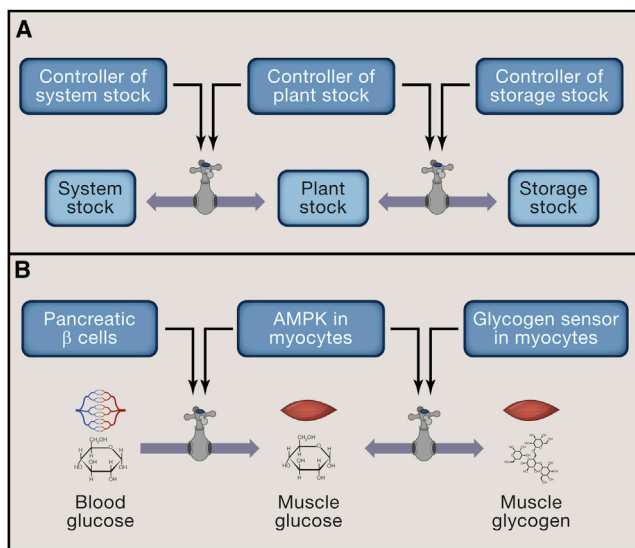


Figure 3. Homeostatic Units

(A) System stock, Plant stock and Storage stock each represent homeostatic units that are connected by flows. Each of the stocks is monitored by a specialized Controller, which regulates the flows into and out of the stock. Homeostatic system is thus hierarchically organized into “nested” homeostatic units.

(B) Physiologic example of nested homeostatic units: System stock (blood glucose) is monitored by System Controller (pancreatic β -cells), Plant stock (glucose in skeletal muscle) is monitored by Plant specific Controller (e.g., AMPK) and Storage stock (muscle glycogen) is presumably monitored by a glycogen sensor, which is currently unknown. Each of the Controllers regulates the flows into and out of the corresponding stock.

level of a regulated variable and will be used herein for simplicity. For the sake of this discussion, it should not be thought of as equivalent to the external reference value in engineered systems.

Homeostatic Units

Homeostasis has been studied primarily with regard to systemically regulated variables such as plasma glucose level and core body temperature. However, many of the same variables are also homeostatically maintained at the level of individual cells within tissues. Such variables are referred to as *System stocks* when they are maintained at the systemic level and *Plant stocks* when they are maintained at the level of individual Plants. Thus, while blood glucose (System stock) is maintained by insulin, glucagon, and catecholamines, glucose level in skeletal muscle (Plant stock) is simultaneously monitored by intracellular sensors and homeostatically maintained through regulated expression of glucose transporters and activity of metabolic pathways of glucose utilization (Herman and Kahn, 2006; Jensen et al., 2008). On the organismal level, pancreatic β -cells function as Controllers and skeletal muscle as Plants. Within individual myocytes, AMPK functions as a Controller (monitoring intracellular glucose level) and GLUT4 (a glucose transporter) functions as a Plant. The signal connecting Controllers to Plants in this case is the signaling pathway connecting AMPK to GLUT4 expression. Note that System stock and Plant stock are connected by a flow (e.g., glucose transport from blood into skeletal

muscle by GLUT4) (Figure 3). GLUT4 expression and glucose flow can be controlled by both the system level Controller (in this case, by insulin) and by the tissue level Controller (in this case, by AMPK). In exercising muscle, for example, glucose and ATP depletion leads to AMPK activation, prompting insulin-independent glucose uptake (a tissue-level control) even when insulin-stimulated uptake might be suppressed (a system-level control) (Herman and Kahn, 2006; Russell et al., 1999). Conversely, when skeletal muscle energy stores are high, insulin-dependent glucose uptake is inhibited, as illustrated by insulin resistance that can be caused by fatty acid accumulation in the muscle (Samuel and Shulman, 2012) or by activity of the hexosamine biosynthetic pathway (Ruan et al., 2013).

Some Plant stocks have a special property: glycogen in the liver and muscle, triglycerides in the adipose tissue, and calcium phosphate in the bone are examples of *Storage stocks*. They buffer regulated variables (blood glucose, fatty acids, and calcium) from the variations in dietary intake or expenditure. The System stocks (e.g., blood glucose), Plant stocks (muscle glucose) and Storage stocks (muscle glycogen) are connected by in- and out-flows (glucose transport, glycogenolysis, and glycogenesis), which are adjusted by hormones and neurotransmitters to maintain the System stock within a desired range (Figure 3). The relationship between regulated stocks and storage stocks is analogous to the relationship between pocket money and money in a bank account: they are connected by flows (deposits and withdrawals) and while the former is usually maintained within a relatively narrow range, the latter is not. Storage stocks exist for some regulated variables (glucose, fatty acids, vitamin A, calcium), but not for others (oxygen, sodium, potassium). Accordingly, the latter variables are more vulnerable to fluctuations in environmental availability.

As noted earlier, Plants are defined by the regulated variables they maintain. The notion of the Plant is only relevant with respect to a specific homeostatic circuit. When skeletal muscle is referred to as a Plant in glucose homeostasis, it is specifically its activities in glucose handling that are relevant. In that sense the terms “Plant” and “Tissue” are not equivalent. All tissues have their own homeostatic circuits that may or may not be related to their function as Plants or Controllers. Like any homeostatic systems, tissues have their own regulated and controlled variables. Oxygen and nutrient concentration, interstitial fluid volume, pH, osmolarity, cell number, and cellular composition are all examples of regulated variables of tissue homeostasis (Chovatiya and Medzhitov, 2014). Cell proliferation, apoptosis and migration, lymphatic drainage, and vascular permeability are examples of controlled variables. Typical Controllers include tissue resident macrophages, mast cells, and somatosensory neurons, all of which monitor various regulated variables of tissue homeostasis. Finally, many cells within tissues (including vascular and lymphatic endothelium, stromal, and parenchymal cells) can act as Plants, depending on the controlled variable (Chovatiya and Medzhitov, 2014).

As noted earlier, some regulated variables, for example, glucose, are homeostatically maintained as System stock (blood glucose), Plant stock (muscle glucose), and Storage stock (muscle glycogen). All three stocks are connected by flows. However, not all regulated variables are connected in this manner: for

example, protein concentration in a cell and in plasma are both regulated variables, but they are not connected by flows; collagen stiffness/elasticity is a regulated variable of tissue homeostasis, but it does not even have a counterpart at cellular or organismal levels. When a regulated variable is maintained by homeostatic circuits at multiple levels that are connected by flows, the result is interdependent, “nested” homeostatic units (Figure 3). This hierarchical organization of homeostasis provides buffering and flexibility in addressing systemic and tissue-specific physiologic needs and priorities.

Controllers as Sensors of Regulated Variables

Controllers play a key role in homeostasis by monitoring the values of the regulated variables. There are two methods used by Controllers to perform this function. Some Controllers monitor the values of regulated variables through a flow that samples the System stock. As an example, β -cells monitor blood glucose level by transporting glucose through GLUT2 transporter and converting it by glucokinase into glucose-6-phosphate (G6P) to initiate glycolysis (Olson and Pessin, 1996). ATP generated by glycolysis then inhibits the ATP-sensitive potassium channel resulting in plasma membrane depolarization, calcium influx, and insulin secretion (Newgard et al., 2002; Newgard and McGarry, 1995). The flow of glucose into β -cells has special features that enable glucose sensing: First, GLUT2 has a very high K_m for glucose (15–20 mM) and only transports glucose when its level in the blood is high (Burant and Bell, 1992). Similarly, glucokinase has a low affinity for glucose compared to other hexokinases (Matschinsky, 1996). These properties make the β -cell sensitive to high plasma glucose level. Second, the flows into Controllers are not subject to inhibition by negative feedback, unlike the flows into Plants. Thus, glucokinase, unlike hexokinases, is not inhibited by G6P (Matschinsky, 1996); otherwise the amount of ATP generated by glycolysis would not be proportional to the amount of glucose transported into the β -cells.

An alternative means by which to monitor the system stock is through dedicated receptors. For example, sensory neurons typically use various gated channels and other sensors to monitor temperature (e.g., TRMP8 and TRPV1), pH (ASICs), oxygen (pO_2 sensor in glomus cells of carotid body), and stretch sensors in baroreceptors (Krishtal, 2003; Montell, 2005; Prabhakar, 2000). Many metabolites, for example, fatty acids and ketones, can be monitored both directly by GPCRs (Briscoe et al., 2003; Oh et al., 2010) and through their flow into Controllers where they are metabolized.

Physiological Priorities

As Cannon aptly noted when selecting the prefix *homeo*, or similar, rather than *homo*, same (Cannon, 1929), homeostatic variables are not maintained at a constant level, but rather within a certain range of values. Some physiological variables (e.g., plasma glucose) are tolerated over a relatively wide dynamic range, while others must remain within a narrow range (e.g., plasma calcium). Moreover, the same regulated variable can have a different acceptable dynamic range in different tissues: for example, the brain has low tolerance to deviations in many physiologic variables (including oxygen, glucose, and temperature) while white adipose tissue is typically less demanding.

Thus, the most sensitive tissues both define the limits of homeostatic range for the corresponding regulated variables and tend to be better protected from the fluctuations in these variables. For example, the brain is relatively insulated from the normal variation of blood glucose levels (ranging between 4 mM and 7 mM) due to the neuronal expression of the high-affinity glucose transporter GLUT3, which has a low K_M for glucose (~ 1 mM) (Burant and Bell, 1992).

Homeostatic prioritization is also reflected in the contribution of the different Plants to the maintenance of the regulated variable. As eluded to earlier, a given regulated variable can be affected by multiple Plants. For example, blood glucose level can be affected by muscle, liver, adipose, kidney, and intestine through uptake, metabolism, and excretion. The relative contributions of different Plants to blood glucose level need to be coordinated to minimize fluctuation of the stock. Thus, increased glucose consumption by exercising skeletal muscle can be compensated for by decreased consumption by the adipose tissue and/or by increased gluconeogenesis by the liver. While all three Plants can affect the value of the regulated variable (in this case glucose), their relative contributions can change depending on their functional states and physiological priorities of the organism. The corollary to this feature is that increased flow burden is dynamically allocated between different Plants, which in turn necessitates communication between Plants to coordinate their contributions to systemic homeostasis, as we discuss next.

Homeostatic Control Signals

The classical view of homeostasis is that it is maintained by signals from the endocrine and autonomic nervous systems. Recent discoveries have extended this paradigm by demonstrating that signals produced by tissues and organs not historically thought of as endocrine organs—including adipose tissue, the intestine, the liver, the muscle, and the kidneys—also play critical roles in homeostatic control. Examples of these signals include the adipokines leptin (Friedman and Halaas, 1998), adiponectin (Yamauchi et al., 2001), and RBP4 (Yang et al., 2005); the hepatokine FGF21 (Fisher et al., 2011); the myokines IL-6 (Pedersen and Febbraio, 2012) and meteorin-like (Rao et al., 2014); and the gut hormones FGF15/19 (Potthoff et al., 2011), CCK (Gibbs et al., 1973), and GLP-1 (Holst, 2007). While the mechanisms of action of many of these signals are still being elucidated, one could argue that not all signals are equivalent in the type of information they communicate within a homeostatic circuit.

As discussed above, there are two types of variables in homeostasis: stocks and flows. The stocks can be further divided into System stocks (e.g., plasma glucose), Plant stocks (e.g., muscle glucose), and Storage stocks (e.g., muscle glycogen). We propose that each type of stock and flow is monitored and translated into a distinct class of homeostatic signals that reports on their value (Figure 4), giving rise to four classes of homeostatic signals:

- (1) Signals of the first class are produced by System Controllers and report on the value of the System stocks (Signal S_a in Figure 4). These are classical endocrine hormones

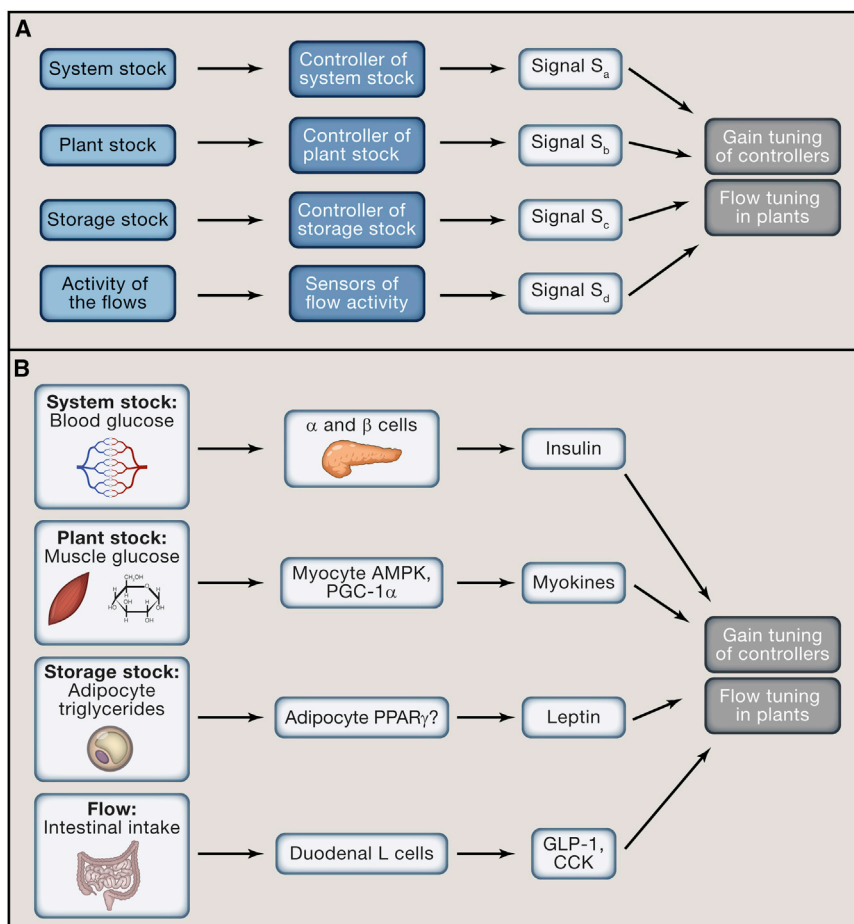


Figure 4. Four Classes of Signals Control Systemic Homeostasis

(A) Four classes of homeostatic signals report on values of four different types of variables: System stock (regulated variable), Plant stock, Storage stock and Flows. Each stock and the flows are monitored by dedicated Controllers and sensors. All four categories of homeostatic signals modulate gain tuning of Controllers and flow tuning in Plants. Signals that report on stocks operate in feed-back loops. Signals that report on flows operate in feed-forward loops.

(B) Signals reporting on the System stock (S_a) are classical endocrine hormones and efferents of the autonomic nervous system (e.g., insulin and glucagon). Signals reporting on Plant stocks (S_b) primarily operate in a cell or tissue autonomous manner (e.g., AMPK controlling GLUT4 expression), but may include signals acting systemically (e.g., AMPK controlling IL-6 expression in exercising muscle). Signals reporting on Storage stocks (S_c) indicate available resources (e.g., leptin reporting on fat stores). Finally, signals reporting on Flows (S_d) indicate anticipated changes in the System stock (e.g., GLP-1 reporting on incoming glucose). The examples are chosen to illustrate the point.

dietary iron uptake and prevent iron overload (Nemeth et al., 2004). Signals reporting on available glycogen stores are not known but are likely to exist. Signals of this class also participate in negative feedback circuits.

(4) Signals of the fourth class report the values of flows (Signal S_d in Figure 4). For example, the gut

and efferents of the autonomic nervous system that operate in negative feedback loops. Examples include insulin and glucagon reporting on plasma glucose level, or parathyroid hormone reporting on plasma calcium level.

- (2) Signals of the second class report the value of the Plant stocks (Signal S_b in Figure 4). Plant stocks are monitored by cell or tissue specific Controllers, such as AMPK, mTOR, HIF-1 α , stretch receptors and many others. These sensors generate negative feedback signals that control the flows into Plant stocks in a cell or tissue autonomous manner (such as the example of insulin-independent glucose uptake in exercising muscle, described above). Additionally, Plants produce signals that control the flows in a systemic manner. Signals of this category include various myokines, such as IL-6 and meteorin-like (Pedersen and Febbraio, 2012; Rao et al., 2014), which appear to report on fuel depletion in muscle.
- (3) Signals of the third class report the value of Storage stocks (Signal S_c in Figure 4). For example, leptin reports on the available fat storage in adipose tissue, and therefore controls food intake (caloric inflow) and energy expenditure (caloric outflow) (Friedman and Halaas, 1998). Hepcidin, similarly, reports on the storage stock of iron in the reticuloendothelial system in order to inhibit

hormone, GLP-1, reports on dietary glucose inflow, and therefore anticipates rising systemic glucose stock (which is itself reported by insulin) (Holst, 2007). CCK and NAPEs (N-Acylphosphatidylethanolamines) similarly report on dietary fat inflow and reduce appetite to suppress further inflow (Gibbs et al., 1973; Gillum et al., 2008). FGF21 is produced by hepatocytes during fasting (Badman et al., 2007; Inagaki et al., 2007) and potentially reports on flow of fatty acids from the adipocytes during lipolysis. FGF21 expression in the liver is induced by fatty acids through PPAR α (Potthoff et al., 2012). One might speculate that while PPAR γ sensing of fatty acids in adipose tissue is an indicator of the inflow into the fat storage stock (taking place during feeding-associated lipogenesis), PPAR α sensing of fatty acids in the liver is an indicator of the outflow from the storage stock (taking place during fasting-induced lipolysis). One important feature of signals that report on flows is that they typically operate in a feed-forward fashion. Because a change in a flow is predictive of the subsequent change in the stock, the signal reporting on an increased inflow, for example, would be expected to increase the outflow and inhibit other inflows of the same stock. This is in contrast to signals that report on

the System, Plant, and Storage stocks, which all operate in a *feedback* fashion to maintain the stock within an acceptable range.

Monitoring the flows enables the system to minimize time delays that are unavoidable in negative feedback systems. Reacting to changing flows elicits an anticipatory response that makes the homeostatic system more robust to environmental fluctuations and helps to prevent dramatic changes in the stock. For example, intestinal glucose in-flow reporting by GLP-1 helps to prevent dramatic postprandial glucose spikes that would be unavoidable if only stock (blood glucose) reporting by insulin were available. Not every flow in the system needs to be monitored and reported as a signal. Presumably, only the flows that have a major impact on the system's stock are monitored, particularly the flows that operate at the interface with the environment (for example, in the intestine, liver, kidney, lungs, and skin).

The four categories of signals outlined above are defined by the homeostatic variables they report on. The effects of homeostatic signals fall into three categories: First, homeostatic signals directly regulate the flows of the system: for example, insulin suppresses hepatic gluconeogenesis. Second, homeostatic signals can change the sensitivity of the flows to another homeostatic signal: for example, placental hormones and glucocorticoids reduce the sensitivity of target tissues to insulin. Third, homeostatic signals can change the gains of the Controllers. For example, GLP-1 increases and leptin decreases the gain of the pancreatic β -cells – they change the amount of insulin produced in response to a given level of blood glucose. Thus, in addition to adjusting the flows of Plants, homeostatic signals can change the gains of Controllers.

In summary, a complex array of signals reporting on available stocks and flows allows Controllers to coordinate multiple Plants toward regulation of a homeostatic variable, while simultaneously balancing the needs and capabilities of individual Plants. Thus, application of the “stock and flow” model provides a framework for functional classification of homeostatic signals and extends the traditional model of homeostasis, which is focused exclusively on Controller-to-Plant signals.

Adjustable Set Points and Homeostatic Adaptation

Homeostatic circuits can be broadly divided into two classes—those that have a single fixed set point and those with multiple or adjustable set points. The fixed set point circuits are characteristic of regulated variables that have a narrow dynamic range, such as arterial $[pO_2]$ or blood calcium concentration. Homeostatic systems with fixed set points are regulated solely by changing the flows, such as calcium resorption, excretion, storage, and utilization. The adaptability of systems with a single set point is limited by the homeostatic range of the regulated variable; when the regulated variable deviates beyond the acceptable range (for example in extreme environments when the buffering capacity of the system is overwhelmed), the system can undergo catastrophic pathological changes. The failure of one homeostatic circuit may lead to a disruption of other connected circuits, resulting in particularly dangerous scenarios of *cascading failures*, as seen, for example, in sepsis.

In some cases, the changing environment or physiologic demands cannot be accommodated by homeostatic circuits with a fixed set point. In these cases, adjustable set points can be employed to maintain regulated variables within different dynamic ranges and enable more efficient adaptation to varying demands. This ability to maintain conditions “at changing rather than similar levels or values” has been referred to as *rheostasis* (Mrosovsky, 1990).

There are several examples of homeostasis with variable set points. Among the most obvious is fever, where the set point for core body temperature rises and is maintained at a higher level (as opposed to hyperthermia, where homeostatic mechanisms are engaged to return the temperature to the default set point). An extreme example of set point change is seen during hibernation: normally, ground squirrels exhibit an average daily body temperature near 37°C. During hibernation, however, their temperature may fall below 0°C and metabolic rate is dramatically suppressed (Barnes, 1989). This extreme physiologic switch is thought to permit adaptation to conditions of food scarcity that would be incompatible with life if the squirrels maintained their normal metabolic and temperature set points. Similarly, in human pregnancy, many physiologic parameters such as blood pressure, blood glucose, total body water, and adiposity are dramatically altered in order to meet the needs of the fetus (King, 2000). These set point adjustments can occur even in a stable environment and reflect the adaptation to changing physiological priorities. Thus, a variety of environmental factors and changing physiological priorities, including seasonal and circadian changes, reproductive status (puberty and pregnancy), stress, nutrition, and infection, require homeostatic adaptations which in some cases appear to involve set point adjustments.

The change of the set points can occur in two different ways, depending on whether the set point-adjusting stimulus has to be continuously present to maintain a new set point value. The change of the body temperature set point during fever is induced by prostaglandin PGE₂, which acts on thermoregulatory hypothalamic neurons (Romanovsky et al., 2005). As soon as inflammation subsides (or PGE₂ production is blocked by COX2 inhibitors), the temperature set point changes back to the original value of 37°C. Thus, in this case, the continuous presence of PGE₂ is required to maintain the altered set point for body temperature. The implication of this is that although all set points are defended, not all set points are equally stable: 37°C is the *default set point* for human body temperature, whereas set points induced by fever are not. As soon as the inducing stimulus subsides or is blocked, the system switches back from the induced set point to the default set point. This design feature provides a failsafe to prevent permanent and pathological shifts in the set point by requiring persistent stimulation. In contrast, the set point for human body weight appears to be maintained at multiple *alternative stable states*. The homeostatic systems that have alternative stable states without a default set point are particularly vulnerable to dysregulation, as we discuss next.

Set Points and Diseases of Homeostasis

In contrast to circuits with fixed set points, which are generally robust to perturbations, homeostatic circuits with adjustable

set points are vulnerable to dysregulation precisely because they are designed to be adjustable. For example, the adjustable set point for body weight and adiposity allows for adaptation to times of food abundance or scarcity, as well as to the accumulation of fuel stores to feed a growing fetus. However, in the setting of the modern environment, adjustable set points may have contributed to the current obesity epidemic (Speakman et al., 2011; Woods and Ramsay, 2007). If body adiposity had a fixed set point value, obesity would be impossible except for purely genetic reasons. In fact, most tissues other than visceral fat, have a single set point value for their size control as a function of body size, which is why they are not subject to homeostatic dysregulation. Like adiposity, glucose, and lipid homeostasis are characterized by adjustable set points, while amino acid and purine/pyrimidine metabolism appear to have a single set point; accordingly, the former are vulnerable to homeostatic dysregulation while the latter are not.

One disease state particularly interesting from this perspective is insulin resistance. Insulin's best-known function is to stimulate glucose uptake by skeletal muscle and adipose tissue, thereby reducing glycaemia. However, it is now appreciated that insulin has myriad effects, orchestrating a coordinated anabolic effort by liver, skeletal muscle, and white adipose tissue to convert glucose and fatty acids into glycogen and triglycerides, respectively, to export these when necessary for storage in the appropriate organ, and to suppress the mobilization of stored fuels (Schenk et al., 2008; Shulman and Petersen, 2011). In addition, insulin induces a trophic response in many cell types that promotes protein synthesis, and consequently cellular and tissue growth (Shulman and Petersen, 2011). Interestingly, not all of these functions are reduced during the insulin resistant state (Brown and Goldstein, 2008), nor are all organs equally affected. Thus, insulin resistance is not equivalent to reducing the quantity of insulin in the blood, but rather is a method of physiologic set point adjustment that allows the organism to reallocate resources between different tissues.

Insulin sensitivity can be changed in many altered physiologic states. During pregnancy, critical illness, infection, and stress, insulin responsiveness is diminished, presumably to allocate resources toward a growing fetus, tissue repair, or the immune system, respectively (Odegaard and Chawla, 2013; Power and Schulkin, 2012; Watve and Yajnik, 2007). Conversely, insulin sensitivity is heightened during caloric restriction and weight loss, perhaps to increase anabolic efficiency.

Unfortunately, the adjustability of the insulin sensitivity set point also makes it vulnerable to disease. Insulin resistance is widely accepted as the pathological precursor for diabetes, a dangerous potential complication of obesity. Thus, the very mechanisms that evolved to make insulin receptor sensitivity adjustable also enable pathological insulin resistance. The same argument applies to other homeostatic systems with multiple set points that correspond to alternative stable states—they are vulnerable to dysregulation because they are designed to be adjustable.

As noted above, some homeostatic systems with multiple set points have a default set point value and any change of set point has to be actively maintained. Such systems, including control of body temperature, are generally less vulnerable to dysregulation because alternative set points are not stable.

Inflammation and Homeostatic Circuits

Inflammation is a protective response to extreme challenges to homeostasis, such as infection, tissue stress, and injury. Inflammatory signals—including cytokines, chemokines, biogenic amines, and eicosanoids, induce myriad changes in diverse biological processes, ranging from local vascular responses to alterations of body temperature. Despite this complexity and diversity of functions, all the activities of inflammatory signals can be described in terms of their effects on homeostatic circuits: First, inflammatory signals can directly stimulate or inhibit the flows of various homeostatic systems. For example, TNF and IL-1 β activate lipolysis, inhibit gluconeogenesis, and increase vascular permeability to fluids and solutes, while IL-6 changes hepatic protein synthesis (Medzhitov, 2008). Second, in addition to directly affecting the flows, inflammatory signals can change the sensitivity of the Plants to homeostatic signals. For example, TNF makes liver, fat, and skeletal muscle less sensitive to insulin (Hotamisligil et al., 1993; Weisberg et al., 2003). Third, inflammatory signals can change the gain of the Controllers. For example TNF and IL-1 β suppress expression of GLUT2 and glucokinase in pancreatic β -cells, thus making them less sensitive to the blood glucose level (Park et al., 1999). Consequently, β -cells produce less insulin given the same amount of plasma glucose—an example of *gain tuning* of the Controller. As discussed above, homeostatic signals also operate by directly regulating flows, by changing sensitivity of Plants to other homeostatic signals, and by gain-tuning of Controllers. Thus homeostatic and inflammatory signals employ identical methods to change the same homeostatic variables (Figure 5).

Importantly, the inflammatory mediators are both antagonistic to and dominant over homeostatic signals. They are antagonistic because normal homeostasis is often incompatible with the goals of the inflammatory response, and the former has to be temporarily disengaged. Inflammatory signals are dominant because they have higher physiological priority as they orchestrate the protective response to life threatening insults of infection and injury. Thus, homeostatic control of body temperature (thermogenesis or sweating) is normally induced by changes in ambient temperature. However, acute inflammation overrides this control by raising the set point of body temperature, thereby inducing thermogenesis and fever regardless of ambient temperature. Likewise, acute inflammation-induced anorexia suppresses caloric intake regardless of the adiposity, circulating nutrient concentrations, or body weight.

It is increasingly appreciated that chronic inflammation is an important component of numerous disease states including obesity, type 2 diabetes, atherosclerosis, asthma, and neurodegenerative diseases. One potential mechanism by which inflammation may initiate or perpetuate disease is through set point changes. In obesity, for example, macrophages and other cells of the immune system infiltrate adipose tissue in response to the increased burden of lipid accumulation and adipocyte stress (Hotamisligil and Erbay, 2008; Weisberg et al., 2003). These cells produce inflammatory cytokines that are capable of shifting homeostatic set points in states of chronic inflammation, just as they do in acute inflammatory states. The rationale for transiently adjusting the insulin responsiveness in acute inflammation is presumed to be in shifting nutrient allocation from tissues that

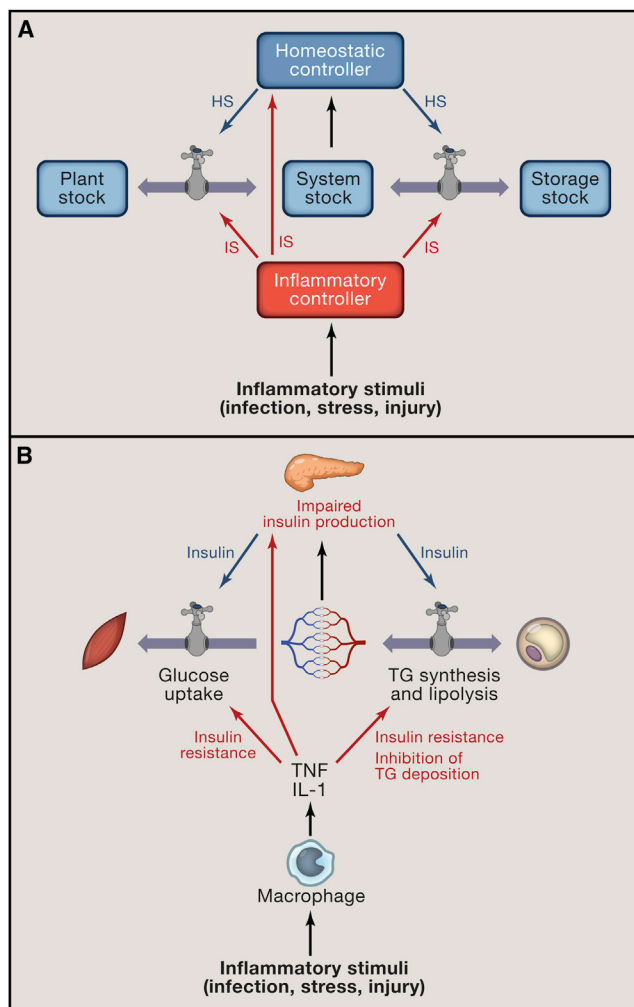


Figure 5. Inflammatory Signals and Homeostasis

(A) Inflammatory signals (IS) act through the same control points (Plants flows and Controller gains) as homeostatic signals (HS). To illustrate the parallels between homeostatic and inflammatory signals, the source of inflammatory signal is referred to as Inflammatory Controller (e.g., macrophage), by analogy to Homeostatic Controller (e.g., endocrine pancreas).

(B) Macrophages produce TNF and IL-1 which act on the same flows as insulin, but in opposite direction: TNF and IL-1 induce insulin resistance and suppress lipid storage in adipose tissue by inhibiting lipoprotein lipase. In addition, these cytokines induce gain tuning of the pancreatic β -cells to reduce the amount of insulin produced in response to a given level of blood glucose. This effect is achieved in part by suppressing glucose flow into β -cells.

have lower priority during infection (adipose and skeletal muscle) toward the higher priority immune defenses (Hotamisligil and Erbay, 2008). In obesity, chronic inflammation may contribute to the shift of insulin sensitivity to an alternative set point.

Inflammation is a protective response that is engaged to defend and restore physiological functions when homeostatic mechanisms are insufficient. The inflammatory response can only achieve this goal by overriding or suppressing incompatible homeostatic controls. However, in its attempts to restore homeostasis, inflammation may enforce and propagate homeostatic set point changes that are detrimental and can result in

chronic pathological states. This happens when a persistent change in the set point itself creates a problem sufficient to promote inflammation. For example, hyperglycemia can lead to glucose toxicity and tissue damage, which in turn can lead to secondary inflammation. Similarly, the abnormal accumulation of harmful lipid mediators (lipotoxicity) in adipocytes, liver, and muscle in obesity leads to cellular stress and tissue dysfunction, and consequently to inflammation (DeFronzo, 2010; Samuel and Shulman, 2012; Summers, 2006). Thus, a homeostatic perturbation initially induced by lipotoxicity may be further perpetuated by inflammation. In such scenarios, a vicious cycle can ensue that may explain the chronicity of some homeostatic diseases and their perpetuation by inflammation. Such a model is consistent with data demonstrating that inflammation is dispensable for the initial induction of insulin resistance, but contributes to maintaining and even worsening insulin resistance in states of chronic obesity (Oh et al., 2012).

Successful inflammatory response is followed by the resolution phase that restores homeostasis. However, because inflammation is induced by loss of homeostasis, but also intentionally disrupts incompatible homeostatic processes, the system has the potential to become locked in a state of a chronic inflammation that fails to resolve. The non-resolving inflammation may, in turn, account for the persistence of chronic diseases (Nathan and Ding, 2010; Serhan et al., 2007). It is therefore important to identify the mechanisms responsible for physiological shifts between alternative stable states of the homeostatic systems, as the same mechanisms could be employed therapeutically to reverse pathological states in chronic diseases of homeostasis.

Perspectives: Evolution, Adaptation, and Disease

The concept of adaptability as vulnerability is pervasive in many forms of phenotypic variation, be they reversible (body weight) or irreversible (body height), continuous (reaction norms) or discontinuous (polyphenisms). Traits that are discontinuous are expressed through one of several alternative developmental pathways, a phenomenon known as phenotypic plasticity (Dewitt et al., 1998; Feinberg, 2007; Stearns and Koella, 2008). Such plasticity can allow for different phenotypes in the same organism, and can therefore afford greater adaptability. The choice of a particular developmental pathway is dictated by anticipation of certain environments where these pathways and associated traits would provide greater adaptation. However, if the environment is not as anticipated and the phenotypic choice is irreversible, maladapted phenotypes susceptible to disease may result (Dewitt et al., 1998; Feinberg, 2007; Stearns and Koella, 2008). Consequently, the mechanisms that afford greater adaptability can also create vulnerability to diseases (Bateson et al., 2004). Thus, phenotypic plasticity can be thought of as a developmental equivalent of homeostasis with alternative stable states dictated by adjustable set points.

The homeostatic capacity of an organism determines its ability to adapt to varying environments. Homeostatic systems with fixed set points are inflexible but resistant to dysregulation. If their buffering capacity is overwhelmed, the consequences are likely to be catastrophic, acute, and transient, but rarely yielding chronic disease. Comparatively, homeostatic systems with adjustable set points provide a greater degree of adaptability,

but are vulnerable to dysregulation and disease when the set points of the system are changed inappropriately, as often happens during chronic inflammation. Thus, the flexibility and adjustment of physiological and developmental characteristics, while providing a benefit of more efficient adaptation, are also responsible for the diseases of homeostasis. Treatment and prevention of diseases of homeostasis therefore will require a better understanding of the mechanisms responsible for the switch between developmental trajectories and homeostatic set points.

Summary

Here, we present a framework that highlights the fundamental connections between homeostasis and inflammation. This framework is based on concepts previously developed in control theory and system dynamics theory. The key points of the framework are summarized below:

- Homeostasis maintains essential parameters of the system within acceptable range. These parameters are regulated variables or stocks of the system. The processes that change or maintain these parameters are known as flows. The activity of the flow is a parameter known as controlled variable.
- Homeostatic systems have two components: Controllers and Plants. Controllers monitor the stocks while Plants operate the flows.
- If the value of regulated variable (X) differs from the set point value (X'), Controllers produce signals (S) that act on Plants to change the relevant flows.
- Controller output is proportional to the error value $|X-X'|$. The coefficient of proportionality is a characteristic known as Controller's *gain*.
- Controllers can have a combination of different gains: *proportional gain* corresponds to the present error value, *integral gain* corresponds to the accumulated past error values, and *differential gain* corresponds to the anticipated future error value. The Controllers that have all three gains are known as PID (proportional, integral, differential) Controllers.
- The gain of Controller can be tuned to change the setting of the system. In PID Controllers different gains can be tuned independently of each other to optimize system's performance.
- Homeostatic systems can have a single fixed set point, or multiple adjustable set points. The former are inflexible but robust to dysregulation. The latter are more adaptable but vulnerable to dysregulation. Chronic homeostatic diseases can result when the system becomes locked in an alternative stable state.
- Plants have their own stocks. A special case of Plant stock is Storage stock. Storage stocks buffer the System stock from external fluctuations. System stock, Plant stock and Storage stock are connected by flows. Stocks connected by flows form *nested homeostatic units*, where each stock is regulated coordinately with other connected stocks.
- Homeostatic signals fall into four classes defined by the four types of homeostatic variables they report on: System stock, Plant stock, Storage stock and the flows. Each of these variables and the signals that report on them, provide different information about homeostatic system:
 - System stock—information about the present value of regulated variable and its deviation from set point. Reported by classical endocrine hormones and efferents of the autonomic nervous system.
 - Plant stock—information about the homeostatic capacity of individual Plants to maintain the System stock. Reported by non-endocrine tissue derived hormones.
 - Storage stock—information about the amount of resources available to the system. Some storage stocks may reflect the accumulated past deviations of System stock from set point. Reported by hormones produced by tissues that serve as depots for regulated variables.
 - Flows—information about the anticipated change in the System stock. Reported by hormones produced by tissues that operate flows with large impact on System stock.
- Homeostatic signals affect two types of variables: Plant flows and Controller's gains. In addition, the *sensitivity* of Controllers and Plants to homeostatic signals can also be regulated.
- Signals that report on Storage stock tune the *integral gain* of Controllers, whereas signals that report on flows tune the *differential gain* of Controllers.
- Inflammatory signals target the same control points as the homeostatic signals: these are Plant flows and Controller's gains. In addition to directly affecting these parameters, inflammatory signals can modulate the sensitivity of Controllers and Plants to homeostatic signals.
- Inflammatory response aims to restore homeostasis, but to achieve this goal it has to suppresses incompatible lower priority homeostatic processes. Therefore, inflammatory signals are antagonistic to the incompatible homeostatic signals.
- Inflammatory signals are dominant over homeostatic signals because they have higher priority. Physiological priorities determine the hierarchy of signals.
- The parallels between homeostatic and inflammatory signals suggest the evolutionary origin of inflammation as a control system that complements the homeostatic control when the latter is insufficient.
- Inflammation can change homeostatic settings of a system by changing Controller's gains and by overriding homeostatic signals. Inflammation commonly accompanies homeostatic diseases associated with set point changes.

ACKNOWLEDGMENTS

We thank members of the Medzhitov lab and Dr. Stephen Stearns for discussions and critical reading of the manuscript. The work in the Medzhitov lab is supported by the Howard Hughes Medical Institute, Blavatnik Family Foundation, Else Kröner-Fresenius-Stiftung award, and grants from the NIH (AI046688 AI089771, CA157461, DK071754). M.E.K. was supported by the NIH MSTP training grant (2T32GM07205).

REFERENCES

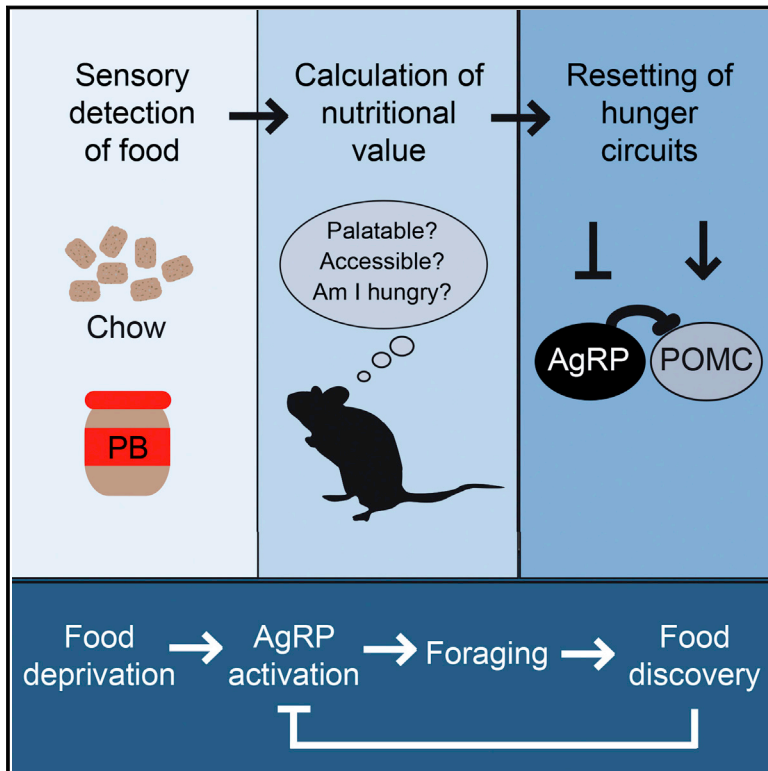
Åström, K.J., and Murray, R.M. (2008). Feedback systems: an introduction for scientists and engineers (Princeton: Princeton University Press).

- Badman, M.K., Pissios, P., Kennedy, A.R., Koukos, G., Flier, J.S., and Maratos-Flier, E. (2007). Hepatic fibroblast growth factor 21 is regulated by PPAR α and is a key mediator of hepatic lipid metabolism in ketotic states. *Cell Metab.* 5, 426–437.
- Barnes, B.M. (1989). Freeze avoidance in a mammal: body temperatures below 0 degree C in an Arctic hibernator. *Science* 244, 1593–1595.
- Bateson, P., Barker, D., Clutton-Brock, T., Deb, D., D'Udine, B., Foley, R.A., Gluckman, P., Godfrey, K., Kirkwood, T., Lahr, M.M., et al. (2004). Developmental plasticity and human health. *Nature* 430, 419–421.
- Bernard, C. (1878). *Leçons sur les phénomènes de la vie communs aux animaux et aux végétaux* (Paris: J. B. Baillière et fils).
- Briscoe, C.P., Tadayyon, M., Andrews, J.L., Benson, W.G., Chambers, J.K., Eilert, M.M., Ellis, C., Elshourbagy, N.A., Goetz, A.S., Minnick, D.T., et al. (2003). The orphan G protein-coupled receptor GPR40 is activated by medium and long chain fatty acids. *J. Biol. Chem.* 278, 11303–11311.
- Brown, M.S., and Goldstein, J.L. (2008). Selective versus total insulin resistance: a pathogenic paradox. *Cell Metab.* 7, 95–96.
- Burant, C.F., and Bell, G.I. (1992). Mammalian facilitative glucose transporters: evidence for similar substrate recognition sites in functionally monomeric proteins. *Biochemistry* 31, 10414–10420.
- Cabanac, M. (2006). Adjustable set point: to honor Harold T. Hammel. *J. Appl. Physiol.* 100, 1338–1346.
- Cannon, W.B. (1929). Organization for physiological homeostasis. *Physiol. Rev.* 9, 399–431.
- Chovatiya, R., and Medzhitov, R. (2014). Stress, inflammation, and defense of homeostasis. *Mol. Cell* 54, 281–288.
- DeFronzo, R.A. (2010). Insulin resistance, lipotoxicity, type 2 diabetes and atherosclerosis: the missing links. The Claude Bernard Lecture 2009. *Diabetologia* 53, 1270–1287.
- Dewitt, T.J., Sih, A., and Wilson, D.S. (1998). Costs and limits of phenotypic plasticity. *Trends Ecol. Evol.* 13, 77–81.
- Feinberg, A.P. (2007). Phenotypic plasticity and the epigenetics of human disease. *Nature* 447, 433–440.
- Fisher, F.M., Estall, J.L., Adams, A.C., Antonellis, P.J., Bina, H.A., Flier, J.S., Kharitonov, A., Spiegelman, B.M., and Maratos-Flier, E. (2011). Integrated regulation of hepatic metabolism by fibroblast growth factor 21 (FGF21) in vivo. *Endocrinology* 152, 2996–3004.
- Friedman, J.M., and Halaas, J.L. (1998). Leptin and the regulation of body weight in mammals. *Nature* 395, 763–770.
- Gibbs, J., Young, R.C., and Smith, G.P. (1973). Cholecystokinin decreases food intake in rats. *J. Comp. Physiol. Psychol.* 84, 488–495.
- Gillum, M.P., Zhang, D., Zhang, X.M., Erion, D.M., Jamison, R.A., Choi, C., Dong, J., Shanabrough, M., Duenas, H.R., Frederick, D.W., et al. (2008). N-acylphosphatidylethanolamine, a gut-derived circulating factor induced by fat ingestion, inhibits food intake. *Cell* 135, 813–824.
- Gluckman, P.D., Beedle, A., and Hanson, M.A. (2009). *Principles of evolutionary medicine* (Oxford, New York: Oxford University Press).
- Hammel, H.T. (1968). Regulation of internal body temperature. *Annu. Rev. Physiol.* 30, 641–710.
- Hardy, J.D. (1953–1954). Control of heat loss and heat production in physiologic temperature regulation. *Harvey Lect.* 49, 242–270.
- Herman, M.A., and Kahn, B.B. (2006). Glucose transport and sensing in the maintenance of glucose homeostasis and metabolic harmony. *J. Clin. Invest.* 116, 1767–1775.
- Holst, J.J. (2007). The physiology of glucagon-like peptide 1. *Physiol. Rev.* 87, 1409–1439.
- Hotamisligil, G.S., and Erbay, E. (2008). Nutrient sensing and inflammation in metabolic diseases. *Nat. Rev. Immunol.* 8, 923–934.
- Hotamisligil, G.S., Shargill, N.S., and Spiegelman, B.M. (1993). Adipose expression of tumor necrosis factor- α : direct role in obesity-linked insulin resistance. *Science* 259, 87–91.
- Inagaki, T., Dutchak, P., Zhao, G., Ding, X., Gautron, L., Parameswara, V., Li, Y., Goetz, R., Mohammadi, M., Esser, V., et al. (2007). Endocrine regulation of the fasting response by PPAR α -mediated induction of fibroblast growth factor 21. *Cell Metab.* 5, 415–425.
- Jensen, M.V., Joseph, J.W., Ronnebaum, S.M., Burgess, S.C., Sherry, A.D., and Newgard, C.B. (2008). Metabolic cycling in control of glucose-stimulated insulin secretion. *Am. J. Physiol. Endocrinol. Metab.* 295, E1287–E1297.
- King, J.C. (2000). Physiology of pregnancy and nutrient metabolism. *Am. J. Clin. Nutr.* 71, 1218S–1225S.
- Krishtal, O. (2003). The ASICs: signaling molecules? Modulators? *Trends Neurosci.* 26, 477–483.
- Matschinsky, F.M. (1996). Banting Lecture 1995. A lesson in metabolic regulation inspired by the glucokinase glucose sensor paradigm. *Diabetes* 45, 223–241.
- Medzhitov, R. (2008). Origin and physiological roles of inflammation. *Nature* 454, 428–435.
- Montell, C. (2005). The TRP superfamily of cation channels. *Sci. STKE* 2005, re3.
- Moran, T.H., and Schulkin, J. (2000). Curt Richter and regulatory physiology. *Am. J. Physiol. Regul. Integr. Comp. Physiol.* 279, R357–R363.
- Mrosovsky, N. (1990). *Rheostasis: the physiology of change* (New York: Oxford University Press).
- Nathan, C., and Ding, A. (2010). Nonresolving inflammation. *Cell* 140, 871–882.
- Nemeth, E., Tuttle, M.S., Powelson, J., Vaughn, M.B., Donovan, A., Ward, D.M., Ganz, T., and Kaplan, J. (2004). Hepcidin regulates cellular iron efflux by binding to ferroportin and inducing its internalization. *Science* 306, 2090–2093.
- Newgard, C.B., and McGarry, J.D. (1995). Metabolic coupling factors in pancreatic beta-cell signal transduction. *Annu. Rev. Biochem.* 64, 689–719.
- Newgard, C.B., Lu, D., Jensen, M.V., Schissler, J., Boucher, A., Burgess, S., and Sherry, A.D. (2002). Stimulus/secretion coupling factors in glucose-stimulated insulin secretion: insights gained from a multidisciplinary approach. *Diabetes* 51(3), S389–S393.
- Odegaard, J.I., and Chawla, A. (2013). Pleiotropic actions of insulin resistance and inflammation in metabolic homeostasis. *Science* 339, 172–177.
- Oh, D.Y., Talukdar, S., Bae, E.J., Imamura, T., Morinaga, H., Fan, W., Li, P., Lu, W.J., Watkins, S.M., and Olefsky, J.M. (2010). GPR120 is an omega-3 fatty acid receptor mediating potent anti-inflammatory and insulin-sensitizing effects. *Cell* 142, 687–698.
- Oh, D.Y., Morinaga, H., Talukdar, S., Bae, E.J., and Olefsky, J.M. (2012). Increased macrophage migration into adipose tissue in obese mice. *Diabetes* 61, 346–354.
- Olson, A.L., and Pessin, J.E. (1996). Structure, function, and regulation of the mammalian facilitative glucose transporter gene family. *Annu. Rev. Nutr.* 16, 235–256.
- Park, C., Kim, J.R., Shim, J.K., Kang, B.S., Park, Y.G., Nam, K.S., Lee, Y.C., and Kim, C.H. (1999). Inhibitory effects of streptozotocin, tumor necrosis factor- α , and interleukin-1 β on glucokinase activity in pancreatic islets and gene expression of GLUT2 and glucokinase. *Arch. Biochem. Biophys.* 362, 217–224.
- Pedersen, B.K., and Febbraio, M.A. (2012). Muscles, exercise and obesity: skeletal muscle as a secretory organ. *Nat. Rev. Endocrinol.* 8, 457–465.
- Potthoff, M.J., Boney-Montoya, J., Choi, M., He, T., Sunny, N.E., Satapati, S., Suino-Powell, K., Xu, H.E., Gerard, R.D., Finck, B.N., et al. (2011). FGF15/19 regulates hepatic glucose metabolism by inhibiting the CREB-PGC-1 α pathway. *Cell Metab.* 13, 729–738.
- Potthoff, M.J., Kliewer, S.A., and Mangelsdorf, D.J. (2012). Endocrine fibroblast growth factors 15/19 and 21: from feast to famine. *Genes Dev.* 26, 312–324.
- Power, M.L., and Schulkin, J. (2012). Maternal obesity, metabolic disease, and allostatic load. *Physiol. Behav.* 106, 22–28.

- Prabhakar, N.R. (2000). Oxygen sensing by the carotid body chemoreceptors. *J Appl Physiol.* 88(1985), 2287–2295.
- Rao, R.R., Long, J.Z., White, J.P., Svensson, K.J., Lou, J., Lokurkar, I., Jedrychowski, M.P., Ruas, J.L., Wrann, C.D., Lo, J.C., et al. (2014). Meteorin-like is a hormone that regulates immune-adipose interactions to increase beige fat thermogenesis. *Cell* 157, 1279–1291.
- Richter, C.P. (1943). Total self-regulatory functions in animals and human beings. *Harvey Lecture Series* 38, 63–103.
- Romanovsky, A.A., Almeida, M.C., Aronoff, D.M., Ivanov, A.I., Konsman, J.P., Steiner, A.A., and Turek, V.F. (2005). Fever and hypothermia in systemic inflammation: recent discoveries and revisions. *Frontiers in bioscience* 10, 2193–2216.
- Ruan, H.B., Singh, J.P., Li, M.D., Wu, J., and Yang, X. (2013). Cracking the O-GlcNAc code in metabolism. *Trends Endocrinol. Metab.* 24, 301–309.
- Russell, R.R., 3rd, Bergeron, R., Shulman, G.I., and Young, L.H. (1999). Translocation of myocardial GLUT-4 and increased glucose uptake through activation of AMPK by AICAR. *Am. J. Physiol.* 277, H643–H649.
- Samuel, V.T., and Shulman, G.I. (2012). Mechanisms for insulin resistance: common threads and missing links. *Cell* 148, 852–871.
- Schenk, S., Saberi, M., and Olefsky, J.M. (2008). Insulin sensitivity: modulation by nutrients and inflammation. *J. Clin. Invest.* 118, 2992–3002.
- Serhan, C.N., Brain, S.D., Buckley, C.D., Gilroy, D.W., Haslett, C., O'Neill, L.A., Perretti, M., Rossi, A.G., and Wallace, J.L. (2007). Resolution of inflammation: state of the art, definitions and terms. *FASEB journal* 21, 325–332.
- Shulman, G.I., and Petersen, K.F. (2011). Metabolism. In *Medical Physiology: A Cellular and Molecular Approach*, W.F. Boron and E.L. Boulpaep, eds. (Sunders).
- Speakman, J.R., Levitsky, D.A., Allison, D.B., Bray, M.S., de Castro, J.M., Clegg, D.J., Clapham, J.C., Dulloo, A.G., Gruer, L., Haw, S., et al. (2011). Set points, settling points and some alternative models: theoretical options to understand how genes and environments combine to regulate body adiposity. *Dis. Model. Mech.* 4, 733–745.
- Stearns, S.C., and Koella, J.C. (2008). *Evolution in health and disease*, Second Edition (Oxford, New York: Oxford University Press).
- Summers, S.A. (2006). Ceramides in insulin resistance and lipotoxicity. *Prog. Lipid Res.* 45, 42–72.
- Wavre, M.G., and Yajnik, C.S. (2007). Evolutionary origins of insulin resistance: a behavioral switch hypothesis. *BMC Evol. Biol.* 7, 61.
- Weisberg, S.P., McCann, D., Desai, M., Rosenbaum, M., Leibel, R.L., and Ferrante, A.W., Jr. (2003). Obesity is associated with macrophage accumulation in adipose tissue. *J. Clin. Invest.* 112, 1796–1808.
- Williams, G.C. (1957). Pleiotropy, Natural Selection, and the Evolution of Senescence. *Evolution* 11, 398–411.
- Wirtshafter, D., and Davis, J.D. (1977). Set points, settling points, and the control of body weight. *Physiol. Behav.* 19, 75–78.
- Woods, S.C., and Ramsay, D.S. (2007). Homeostasis: beyond Curt Richter. *Appetite* 49, 388–398.
- Yamauchi, T., Kamon, J., Waki, H., Terauchi, Y., Kubota, N., Hara, K., Mori, Y., Ide, T., Murakami, K., Tsuboyama-Kasaoka, N., et al. (2001). The fat-derived hormone adiponectin reverses insulin resistance associated with both lipodystrophy and obesity. *Nat. Med.* 7, 941–946.
- Yang, Q., Graham, T.E., Mody, N., Preitner, F., Peroni, O.D., Zabolotny, J.M., Kotani, K., Quadro, L., and Kahn, B.B. (2005). Serum retinol binding protein 4 contributes to insulin resistance in obesity and type 2 diabetes. *Nature* 436, 356–362.

Sensory Detection of Food Rapidly Modulates Arcuate Feeding Circuits

Graphical Abstract



Authors

Yiming Chen, Yen-Chu Lin, Tzu-Wei Kuo, Zachary A. Knight

Correspondence

zachary.knight@ucsf.edu

In Brief

Simply presenting food to a hungry mouse resets the activity of its AgRP and POMC neurons from a pattern associated with energy deficit to one associated with satiety, even if no food is consumed. The extent of the neuronal activity changes depends on the accessibility and palatability of the food.

Highlights

- Sensory detection of food rapidly inhibits AgRP and activates POMC neurons
- Rapid sensory feedback occurs before any food is consumed
- The magnitude of neuronal response depends on food palatability and nutritional state
- AgRP/POMC neurons may play a primary role in driving food discovery



Sensory Detection of Food Rapidly Modulates Arcuate Feeding Circuits

Yiming Chen,¹ Yen-Chu Lin,¹ Tzu-Wei Kuo,¹ and Zachary A. Knight^{1,*}

¹Department of Physiology, University of California, San Francisco, San Francisco, CA 94158, USA

*Correspondence: zachary.knight@ucsf.edu

<http://dx.doi.org/10.1016/j.cell.2015.01.033>

SUMMARY

Hunger is controlled by specialized neural circuits that translate homeostatic needs into motivated behaviors. These circuits are under chronic control by circulating signals of nutritional state, but their rapid dynamics on the timescale of behavior remain unknown. Here, we report optical recording of the natural activity of two key cell types that control food intake, AgRP and POMC neurons, in awake behaving mice. We find unexpectedly that the sensory detection of food is sufficient to rapidly reverse the activation state of these neurons induced by energy deficit. This rapid regulation is cell-type specific, modulated by food palatability and nutritional state, and occurs before any food is consumed. These data reveal that AgRP and POMC neurons receive real-time information about the availability of food in the external world, suggesting a primary role for these neurons in controlling appetitive behaviors such as foraging that promote the discovery of food.

INTRODUCTION

Food intake is controlled by evolutionarily hard-wired neural circuits that contain specialized neural cell types. Two cell types in the arcuate nucleus (ARC) of the hypothalamus are known to be particularly important for the control of feeding. These neurons are identified by expression of the neuropeptides Agouti-related Protein (AgRP) and Proopiomelanocortin (POMC) and have opposing functions. AgRP neurons are activated by energy deficit (Hahn et al., 1998) and promote food seeking and consumption. Optogenetic or chemogenetic activation of AgRP neurons induces voracious eating in sated mice (Aponte et al., 2011; Krashes et al., 2011), whereas inhibition or ablation of AgRP neurons results in aphagia (Gropp et al., 2005; Krashes et al., 2011; Luquet et al., 2005). These effects of AgRP neurons are mediated by release of GABA as well as two neuropeptides, AgRP and NPY, that stimulate food intake when delivered into the brain (Clark et al., 1985; Fan et al., 1997; Ollmann et al., 1997; Tong et al., 2008). POMC neurons by contrast are activated by energy surfeit and their activity inhibits food intake and promotes weight loss. These two cell types interact in part through a common set of downstream neural targets that express melanocortin receptors, which are activated by POMC and inhibited by AgRP (Fan

et al., 1997; Ollmann et al., 1997; Seeley et al., 1997). Thus, AgRP and POMC neurons are two intermingled, interacting neural cell types that have opposing roles in the control of feeding.

Despite intense investigation of these cells over the past 20 years, their activity dynamics during behavior remain unknown. This knowledge gap reflects the difficulty of recording cell-type-specific neural activity within heterogeneous deep brain structures such as the hypothalamus. As a result, our current understanding of the regulation of AgRP and POMC neurons is based on a combination of approaches that include in vitro electrophysiology, *c-fos* staining, pharmacology, and genetic manipulations. These pioneering studies have revealed a dominant role for circulating hormones and nutrients in the control of these cells (Williams and Elmquist, 2012). AgRP and POMC neurons are modulated by hormones such as ghrelin and leptin (Cowley et al., 2001, 2003; Nakazato et al., 2001; Pinto et al., 2004) as well as circulating nutrients (Blouet and Schwartz, 2010) in part via their metabolic effects on mitochondrial dynamics (Dietrich et al., 2013; Schneeberger et al., 2013). Together, these findings have led to a generally accepted model in which AgRP and POMC neurons function as interoceptors that monitor the concentration of hormones and nutrients in the blood and then gradually adjust their activity in parallel with changes in nutritional state. This model provides a compelling explanation for how nutritional changes can be translated into counterregulatory responses but leaves unanswered the question of whether these neurons are also subject to rapid regulation on the timescale of behavior.

AgRP and POMC neurons also receive abundant synaptic input which provides the potential for more rapid modulation. However, the function of this afferent input is not well understood. Fasting increases excitatory tone onto AgRP neurons (Liu et al., 2012; Yang et al., 2011), and one source of such excitatory input is neurons in the paraventricular hypothalamus (PVH) (Krashes et al., 2014). AgRP neurons also receive inhibitory input from the dorsomedial hypothalamus (DMH) among other sources (Krashes et al., 2014). POMC neurons by contrast receive inhibitory input from cells in the ARC, including neighboring AgRP neurons, as well as excitatory input from the ventromedial hypothalamus (VMH) and other regions (Cowley et al., 2001; Krashes et al., 2014; Pinto et al., 2004; Sternson et al., 2005; Vong et al., 2011). As these circuit connections have only recently been described, their regulation and function are not yet clear. An important open question regards the nature of the information that these presynaptic cells communicate to their AgRP and POMC targets.

In the present study, we have used an optical approach to record the natural activity of AgRP and POMC neurons in awake

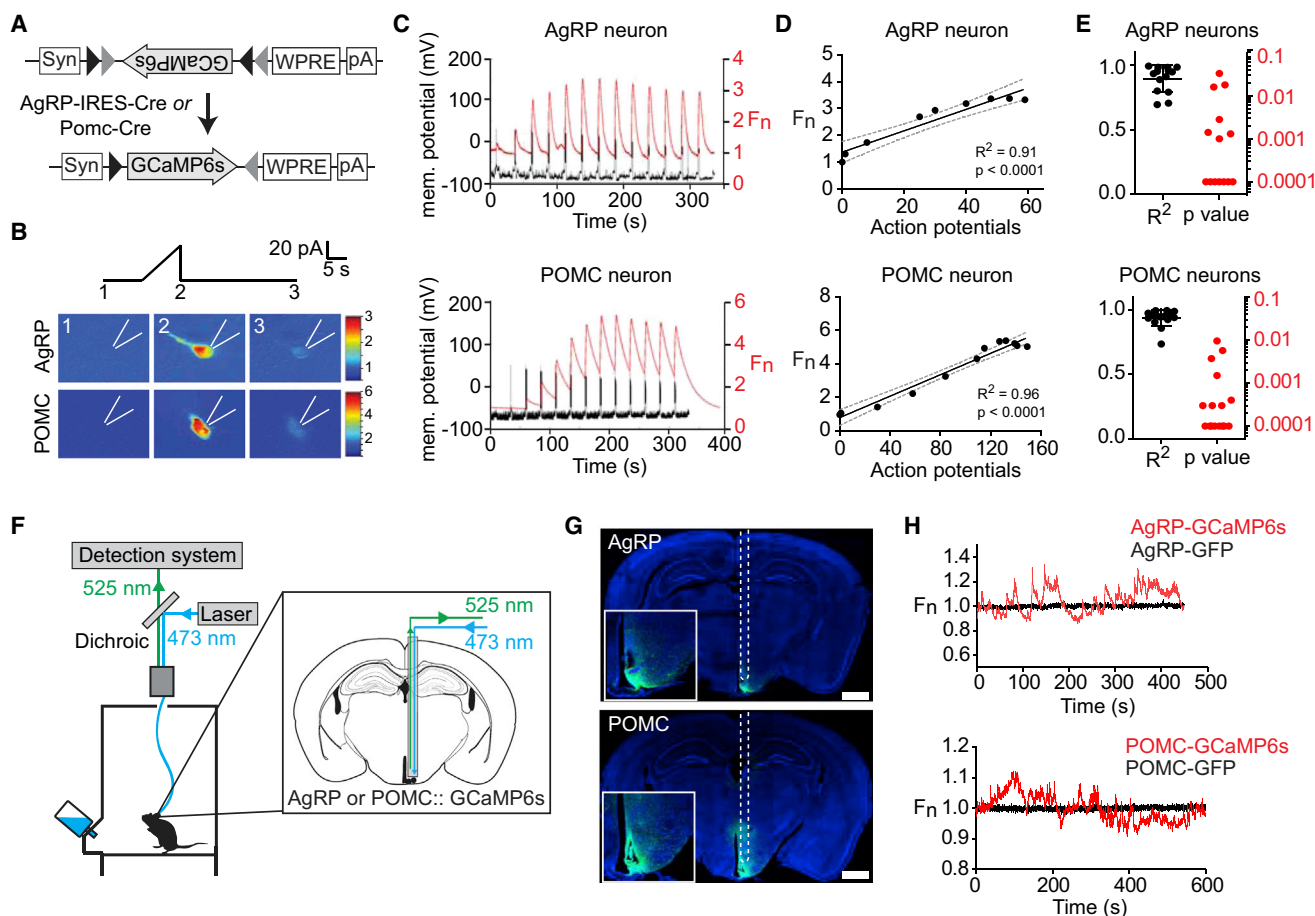


Figure 1. Optical Recording of AgRP and POMC Neuron Activity in Awake Behaving Mice

(A) FLEX AAV used to drive GCaMP6s expression.

(B) Response of AgRP and POMC neurons to current ramp. Scale bar represents GCaMP6s fluorescence normalized to 1.0 at start of the experiment (F_n).

(C) Membrane potential and GCaMP6s fluorescence in response to sequential 10 pA current steps of duration 2 s separated by 20 s.

(D) Relationship between action potential number and fluorescence for cells in (C).

(E) R^2 and p values for the linear regression of fluorescence versus action potential number for 16 POMC and 14 AgRP neurons.

(F) Schematic of the fiber photometry setup.

(G) Coronal section from AgRP and POMC mice showing path of optical fiber and injection site. Scale bar represents 1 mm.

(H) Fluorescence trace during cage exploration for mice expressing GCaMP6s or GFP in AgRP neurons or POMC neurons.

All error bars represent \pm SEM.

See also Figure S1.

behaving mice. These experiments have unexpectedly revealed that AgRP and POMC neurons are strongly regulated in vivo by the sensory detection of food. This rapid sensory regulation resets the activation state of these cells induced by food deprivation prior to the start of food consumption. This rapid regulation also contains information about the food's hedonic properties and depends on the animal's nutritional state. These findings reveal that AgRP and POMC neurons receive real-time information about the availability of food in the outside world, which they then use to anticipate the nutritional value of a forthcoming meal and adjust their activity in advance. This anticipatory regulation provides a mechanism to rapidly inhibit foraging upon food discovery, suggesting a primary role for these neurons in the regulation of appetitive behaviors in vivo.

RESULTS

Optical Recording of AgRP and POMC Neuron Activity in Awake Behaving Mice

In order to gain deeper insight into the regulation of AgRP and POMC neurons, we sought to record their natural activity during feeding behavior. To do this, we used fiber photometry (Cui et al., 2013; Gunaydin et al., 2014), an approach that employs a multimode optical fiber to record the total fluorescence from a population of neurons expressing a calcium reporter for neural activity (Figure 1F). By targeting the calcium reporter to a specific cell type, this method enables optical recording of the real-time activity of a molecularly defined population of neurons within a deep brain structure. The resulting trace

represents the integrated activity of the neurons defined by a genetic marker and anatomic location and therefore is particularly well-suited for use in the hypothalamus, which contains genetically separable populations of neurons with distinct functions.

We first confirmed that calcium signals from AgRP and POMC neurons correlate with changes in firing rate *ex vivo*. We targeted the sixth generation calcium reporter GCaMP6s (Chen et al., 2013) to AgRP and POMC neurons by stereotaxic injection of Cre-dependent AAVs into AgRP-IRES-Cre and POMC-Cre mice (Figure 1A). We then prepared acute brain slices for imaging, and fluorescent cells in the ARC were identified for whole-cell current clamp recordings. Activation by depolarizing current ramp (0–40 pA, 10 s) induced bursts in firing accompanied by increased GCaMP6s fluorescence (Figure 1B). To quantify the relationship between firing rate and fluorescence signal, we applied step currents (–20 pA to +120 pA, 10 pA increments), which resulted in progressive increases in spikes and fluorescence (Figure 1C). Quantification of this response revealed a linear correlation between action potential number and GCaMP6s signal (Figures 1D and 1E). Thus, GCaMP6s can report on activity dynamics in AgRP and POMC neurons as shown for other cell types (Chen et al., 2013).

To apply this approach *in vivo*, we injected AAVs expressing GCaMP6s into the ARC of the corresponding Cre mice and in the same surgery installed an optical fiber unilaterally above the ARC (Figure S1). After allowing 2 weeks for transgene expression, we connected mice to a photometry rig and recorded fluorescence from these cells as mice explored a feeding chamber without access to food. Baseline recordings from AgRP and POMC neurons showed dynamic fluctuations (~10%–20% $\Delta F/F$) that resembled bursts of synchronous activity observed in other cell types (Cui et al., 2013; Gunaydin et al., 2014) (Figure 1H). These dynamics were unrelated to mouse movement, unaffected by changes in ambient lighting, and absent from recordings from control mice expressing GFP in AgRP or POMC neurons (Figure 1H), indicating that they represent calcium-dependent GCaMP6s signals.

To test the sensitivity of this assay to detect changes in neural activity, we challenged mice with ghrelin, a hormone that activates AgRP neurons and inhibits POMC neurons (Cowley et al., 2003; Nakazato et al., 2001). Mice expressing GCaMP6s in either AgRP or POMC neurons were acclimated to a behavioral chamber, given an intraperitoneal injection of ghrelin, and then returned to the chamber. Ghrelin sharply increased calcium signals from AgRP neurons ($\Delta F/F = 71\% \pm 10\%$ at 5 min, $p < 0.001$ compared to vehicle) (Figures 2A and 2B; Movie S1). This increase began within seconds of injection (mean latency = 33 ± 7 s) and reached a plateau within 2 min ($\tau = 76 \pm 12$ s, where τ is the exponential time constant corresponding to the time after injection resulting in ~63.8% of the total change). In the absence of further intervention, this increase in AgRP activity was sustained for the duration of the recording ($\Delta F/F = 62\% \pm 10\%$ at 15 min) (Figure 2B). By contrast injection of vehicle (PBS) had no effect on the activity of AgRP neurons ($\Delta F/F = -3\% \pm 2\%$ at 5 min) (Figure 2B; Movie S1).

POMC neurons showed the opposite response, with ghrelin injection rapidly and potently inhibiting POMC activity ($\tau = 160 \pm 17$ s; $\Delta F/F = -49\% \pm 4\%$ at 15 min, $p = 0.001$ compared to vehicle) (Figures 2C and 2D; Movie S2). Interestingly, vehicle injection alone produced a small but reversible drop in POMC activity (Figure 2D; Movie S2). This transient decline in POMC activity was consistently observed following animal handling, suggesting that POMC but not AgRP neurons receive an inhibitory stress regulated input.

We next tested the effect of food on the response to ghrelin. Our prediction based on the known nutritional regulation of these cells was that food consumption would gradually inhibit AgRP neurons and activate POMC neurons as animals transitioned from hunger to satiety. To test this, we challenged mice with ghrelin and then 20 min later presented them with a pellet of chow. Unexpectedly, we found that food presentation alone rapidly reversed much of the effect of ghrelin treatment ($\Delta F/F = -29\% \pm 3\%$ at 2 min for AgRP neurons and $\Delta F/F = 80\% \pm 3\%$ at 2 min for POMC neurons) (Figure 2). This response began immediately upon placing food in the cage and was complete within seconds ($\tau = 12 \pm 2$ s for AgRP neurons; $\tau = 44 \pm 3$ s for POMC neurons). All animals tested showed this response to food presentation (traces for ten mice are shown in Figure 2E), suggesting that it represents a general mechanism that regulates the activity of these neurons *in vivo*.

Food Detection Reverses the Effects of Fasting on AgRP and POMC Activity

The regulation of AgRP and POMC neurons by sensory detection of food has not previously been described. To investigate this phenomenon under more physiologic conditions, we fasted mice overnight and then presented a pellet of chow. As observed for ghrelin-treated animals, food presentation to fasted mice strongly inhibited AgRP neurons ($\Delta F/F = -37\% \pm 4\%$, at 5 min, $p < 0.001$ compared to object) and activated POMC neurons ($\Delta F/F = 38\% \pm 5\%$ at 5 min, $p < 0.001$ compared to object) (Figure 3; Movies S3 and S4). These responses began the moment that food was presented and were rapidly complete ($\tau = 20 \pm 4$ s for AgRP neurons and $\tau = 42 \pm 18$ s for POMC neurons). To quantify the extent to which these changes required food consumption, we analyzed video data to estimate the moment at which the first bite of food was consumed in each trial and then aligned calcium traces to this event. This revealed that most of the activity changes in these neurons were already complete by the time food intake was initiated ($96\% \pm 6\%$ complete before feeding in AgRP neurons, $85\% \pm 5\%$ in POMC neurons) (Figures 3H and 3I). Thus, the response of AgRP and POMC neurons to food is triggered primarily by food detection rather food consumption. Of note, these stereotyped responses to food presentation were consistently observed in the first trial of each mouse (Figure 3G), indicating that this effect does not require prior training.

We investigated the determinants of this rapid response to food discovery. Presentation of an inedible object (a rubber stopper similar in size to a piece of chow) had little effect on the activity of AgRP neurons ($\Delta F/F = 4.9\% \pm 2.2\%$) and induced a small change in POMC neurons in the opposite direction of food ($\Delta F/F = -10\% \pm 2\%$). Thus, the response of these neurons to food

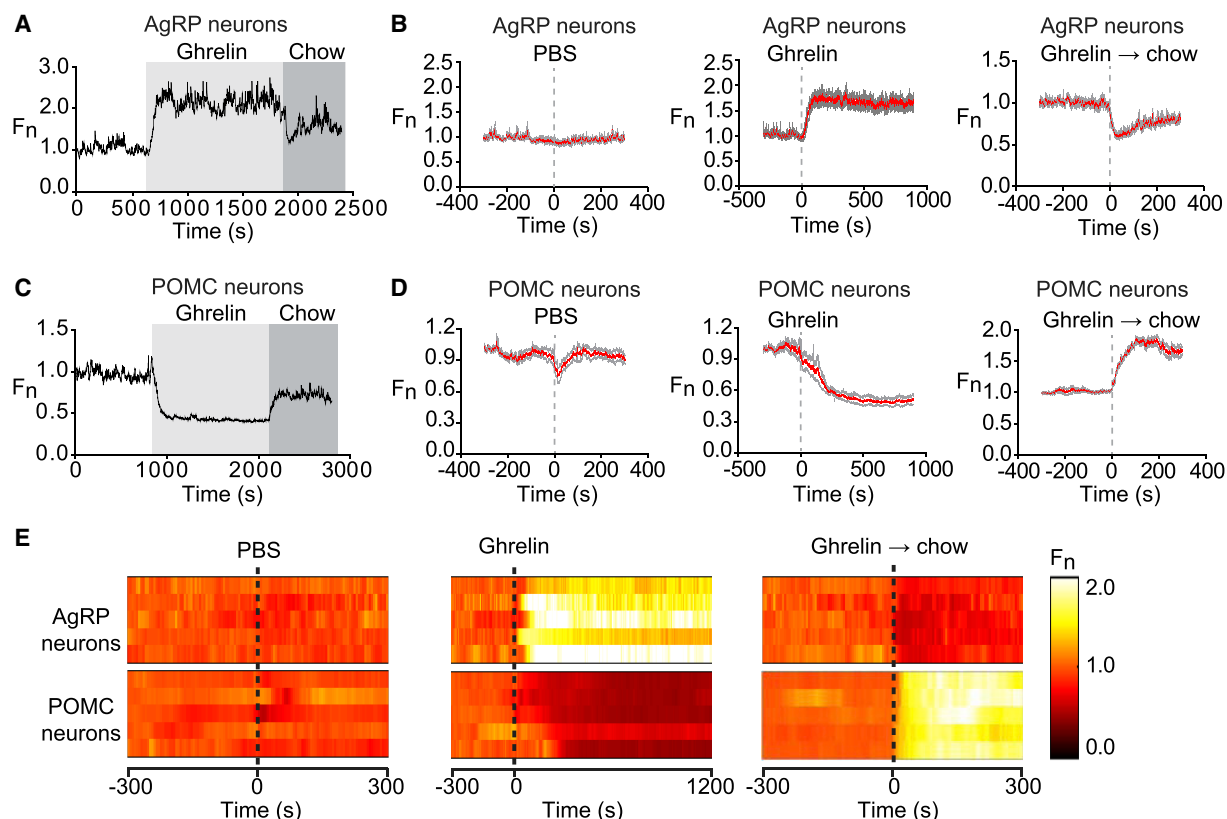


Figure 2. Ghrelin Rapidly Modulates AgRP and POMC Neurons

(A and C) Recordings from a mouse expressing GCaMP6s in AgRP or POMC neurons that was challenged with injection of ghrelin (light gray) followed by presentation of a pellet of chow (dark gray).

(B and D) Calcium signals from AgRP and POMC neurons aligned to the time of PBS or ghrelin injection, or chow presentation to ghrelin-treated mice. Red and gray indicate the mean response and SE (AgRP, $n = 7$; POMC, $n = 5$). In each trial fluorescence was normalized by assigning a value of 1.0 to the median value of data points within a 2-min window at -5 min before treatment.

(E) Peri-event plots showing the response from a single trial of five AgRP mice and five POMC mice.

All error bars represent \pm SEM.

See also [Movies S1](#) and [S2](#).

presentation is food-specific ([Figure 3](#); [Movies S3](#) and [S4](#)). The sensitivity of these cells to food presentation also depended on nutritional state, as AgRP neurons from ad-libitum-fed mice showed no response to food presentation ($\Delta F/F = -4.7\% \pm 1.0\%$, $p = 0.21$ compared to object) whereas POMC neurons from ad-libitum-fed mice showed a greatly diminished response ($\Delta F/F = 4.7\% \pm 2.4\%$, $p = 0.01$ compared to object) ([Figures 3E](#) and [3F](#)). Thus, conditions that reflect energy deficit, such as fasting or ghrelin treatment, potentiate the response of AgRP and POMC neurons to food detection.

Food Quality Influences the Magnitude of the Response

We considered the possibility that the response of AgRP and POMC neurons to food presentation depends on the food's hedonic properties. In this regard, sensory cues associated with palatable or energy dense foods trigger activation of brain regions involved in reward, but how this hedonic information is integrated with homeostatic signals remains poorly understood. To investigate this, we first measured the response to peanut butter, an energy dense food that mice will eat in preference to

chow and is considered rewarding. Mice were fasted overnight, acclimated to a behavioral chamber, and then presented with either pellet of chow or a dollop of peanut butter. Presentation of peanut butter strongly inhibited AgRP neurons ($\Delta F/F = -54\% \pm 6\%$ at 5 min) ([Figure 4A](#)) and activated POMC neurons ($\Delta F/F = 101\% \pm 31\%$ at 5 min) ([Figure 4C](#)). These responses began immediately upon food presentation ([Movies S5](#) and [S6](#)) and were complete in <1 min ($\tau = 23 \pm 6$ s for AgRP and $\tau = 29 \pm 6$ s for POMC). The responses to peanut butter were significantly larger than the responses to chow ([Figure 4E](#)) and indeed were comparable in magnitude (but opposite in sign) to the effect of injection with pharmacologic doses of ghrelin ([Figure 4F](#)), which to our knowledge is the strongest known stimulus that modulates these cells.

A defining feature of palatable foods is that animals will consume them in the absence of hunger because they are intrinsically rewarding (e.g., eating dessert after a meal). We therefore tested whether AgRP and POMC neurons from ad-libitum-fed mice, which show little or no response to chow ([Figure 3](#)), would nonetheless respond to the presentation of peanut butter. Indeed,

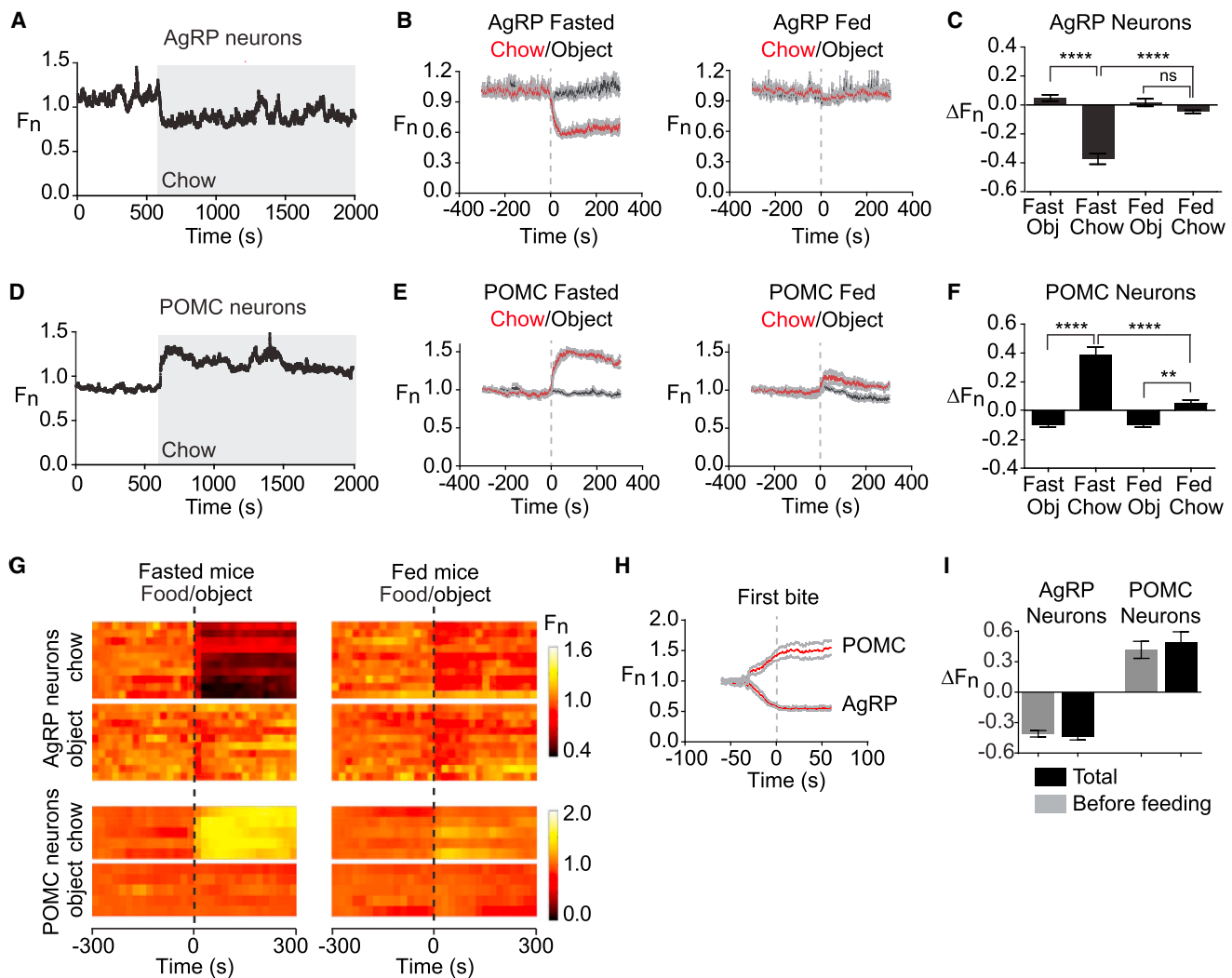


Figure 3. Sensory Detection of Food Rapidly Regulates AgRP and POMC Neurons

(A and D) Recordings from fasted mice expressing GCaMP6s in AgRP or POMC neurons presented with a pellet of chow (gray).

(B and E) Plots of calcium signals from AgRP and POMC neurons aligned to the time of presentation of a pellet of chow (red) or inedible object (black). Mice were either subjected to an overnight fast (left) or fed ad libitum (right) prior to experiment. Gray indicates SE (AgRP, $n = 10$; POMC, $n = 5$).

(C and F) Quantification of fluorescence changes 5 min after event, as indicated.

(G) Peri-event plots aligned to the time of event. Each row is a single trial of a different mouse.

(H) Calcium signals aligned to the initiation of feeding for AgRP and POMC neurons.

(I) Quantification of change in fluorescence that occurs before feeding is initiated versus the total change in the trial. * $p < 0.05$, ** $p < 0.01$, *** $p < 0.001$, **** $p < 0.0001$.

All error bars represent \pm SEM.

See also [Movies S3](#) and [S4](#).

we found that presentation of peanut butter to ad-libitum-fed mice strongly inhibited AgRP neurons ($\Delta F/F = -24\% \pm 4\%$, at 5 min, $p < 0.001$ compared to chow) and activated POMC neurons ($\Delta F/F = 55\% \pm 11\%$, at 5 min, $p = 0.14$ compared to chow) (Figures 4A and 4C). Thus, more palatable food can modulate these neurons even in the absence of signals of energy deficit.

To further probe this relationship, we tested whether the response of these neurons to different foods depended on the order in which they were presented. Mice were fasted overnight and then sequentially presented with an inedible object, peanut

butter, or chow in randomized order at 10-min intervals. We then calculated the change in activity that occurred following each of these presentations. This revealed that presentation of peanut butter could completely block the subsequent neural response to presentation of chow (Figures 4B and 4D). By contrast, presentation of chow had no effect on the response to peanut butter in POMC neurons (Figure 4D) and only partially diminished the response in AgRP neurons (Figure 4B). The asymmetry in the response to these two foods is consistent with their differential effects in fasted and fed mice.

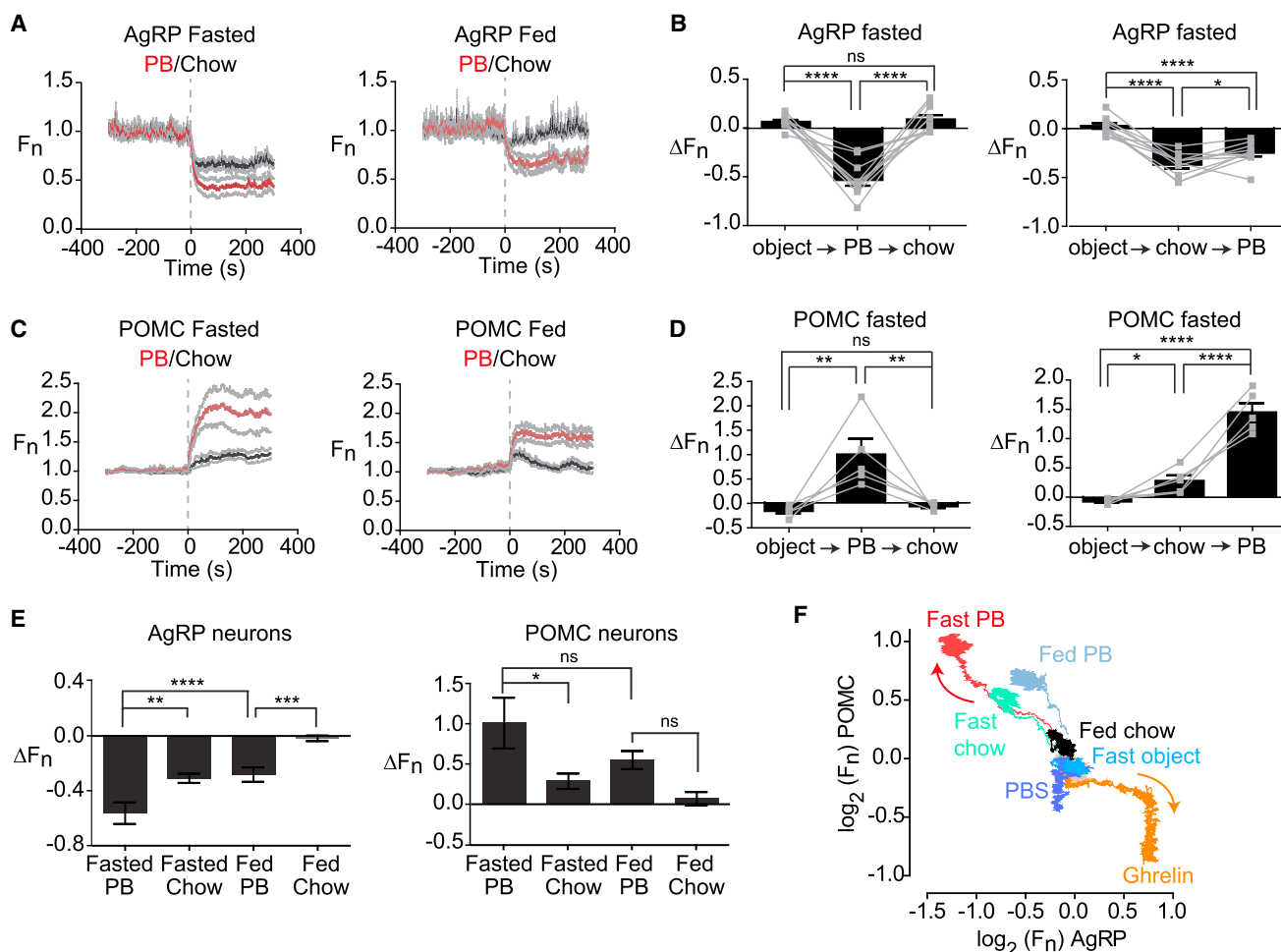


Figure 4. Food Palatability Determines the Magnitude of the Response to Food Detection

(A and C) Calcium signals from AgRP and POMC neurons in fasted and fed mice aligned to the time of presentation of peanut butter or chow.

(B and D) Fluorescence change of AgRP and POMC neurons upon sequential presentation of an inedible object, chow, and peanut butter in fasted mice.

(E) Quantification of responses of AgRP and POMC neurons 5 min after food presentation.

(F) Plot showing the response of AgRP and POMC neurons over 5 min to different foods and pharmacologic treatments in the context of varying nutritional states.

All traces start at the origin (0,0) and emanate outward. Arrows indicate the direction of movement.

All error bars represent \pm SEM.

See also Figure S2 and Movies S5 and S6.

To extend these findings we tested a chocolate, a second food that is commonly used in rodent studies of reward. We found that presentation of chocolate (Hershey Kiss) to fasted mice inhibited AgRP neurons to a greater extent than chow (Figure S2A). Like peanut butter, chocolate also elicited a response in AgRP neurons from ad-libitum-fed mice that are unresponsive to chow (Figure S2B). Sequential presentation experiments revealed that chocolate could block the neural response to subsequent presentation of chow, but not vice versa, similar to our observations with peanut butter (Figures S2D and S2E). Although chocolate was a novel food for these animals, we observed responses to chocolate presentation in the first trial, indicating mice could identify it as food without prior experience. However, the speed of the response to chocolate increased during subsequent tests, suggesting involvement of a learning process as well ($\tau = 40 \pm 8$ s

in trial 1 versus 17 ± 2 s in trial 4, $p < 0.01$) (Figure S2C). Collectively, these data show that the rapid sensory regulation of AgRP and POMC neurons contains information about the hedonic properties of the food that has been detected.

Food Accessibility Modulates the Response to Food Discovery

Most of the response of AgRP and POMC neurons to food presentation occurred before food intake was initiated (Figures 3H and 3I). We therefore wondered whether food consumption played any role in this response. To test this, mice were fasted overnight and then presented with peanut butter in a container that allowed the food to be seen and smelled but not consumed (Figure 5A). Presentation of this inaccessible peanut butter rapidly activated POMC neurons ($\Delta F/F = 43\% \pm 9\%$ after

2 min; $\tau = 31 \pm 8$ s) and inhibited AgRP neurons ($\Delta F/F = -39\% \pm 4\%$ after 2 min; $\tau = 21 \pm 4$ s) (Figures 5B and 5C). Similar responses were observed in mice pretreated with ghrelin (Figures S3A and S3B). These responses occurred as quickly as the response to accessible food, but were somewhat smaller in magnitude (Figures S3C and S3D), and the response of POMC neurons was less durable (Figures 5B and 5C). This indicates that food accessibility can modulate the strength of the response to food presentation.

To further dissect this effect, we tested whether an isolated sensory cue could modulate the activity of these two cell types. As mice rely heavily on the sense of smell, we tested whether the smell of peanut butter could elicit an activity change in AgRP and POMC neurons. Mice were fasted overnight and then exposed to peanut butter placed underneath the cage in a covered container so that it could be smelled but not seen or accessed (Figure 5D). We found that this “hidden peanut butter” rapidly modulated AgRP and POMC neurons in a way that resembled food presentation ($\Delta F/F = -12\% \pm 5\%$ after 1 min in AgRP neurons and $\Delta F/F = 17\% \pm 6\%$ after 1 min in POMC neurons) (Figures 5E and 5F). However, this effect was much smaller in magnitude and transient, with neural activity returning to baseline within 8 min ($\Delta F/F = 8.3\% \pm 4.5\%$ after 8 min in AgRP neurons and $\Delta F/F = -3.0\% \pm 4.0\%$ after 8 min in POMC neurons) (Figures 5F and S3). Together, these data suggest that food-associated sensory cues can modulate these two cell types, but that the magnitude and durability of this response depends on the extent to which these cues are interpreted as representing access to food.

Food Removal Reverses the Effects of Food Presentation

The response of AgRP and POMC neurons to food presentation is consistent with a model in which these neurons anticipate the change in their activity that will occur after food consumption and then enact this change in advance, taking into account factors such as the food's energy density, the food's accessibility, and the animal's nutritional state. A prediction of this model is that the response to food presentation should be reversed if the food is removed before it can be consumed. To test this, mice were fasted overnight, presented with accessible chow, and then the food was removed after either a 2-, 10-, or 30-min interval. As predicted, we found that food removal reversed the effects of food presentation, resulting activation of AgRP neurons, and inhibition of POMC neurons (Figures 5G and 5J; for clarity only data after 2 and 10 min removal are shown). The magnitude and kinetics of this reversal depended on the duration that mice were given food access. For example, mice given access to food for 30 min showed a smaller reversal of AgRP and POMC neuron activity following food removal than mice given access to food for 2 or 10 min (Figures 5H and 5K). Extended food access also slowed the response to food removal in AgRP but not POMC neurons (Figures 5I and 5L). These findings are consistent with food consumption during the feeding interval partially resetting the activation state of these neurons.

The response to food removal exhibited hysteresis, occurring ~10-fold more slowly than the initial response to food presentation (Figures 5I and 5L). This asymmetry was observed after only 2 min food access in both AgRP ($\tau = 15 \pm 1$ s versus 258 ± 26 s,

$p < 0.0001$) and POMC neurons ($\tau = 19 \pm 3$ s versus 269 ± 66 s, $p = 0.03$) and therefore was unlikely to be caused by the post-ingestive effects of food consumption. Rather, this suggests that the circuit interprets the sensory detection of food in such a way that food removal induces a more gradual change than food discovery.

Neural Dynamics within Feeding Bouts

We have focused on the initial response of AgRP and POMC neurons to food presentation, because this response is much larger than the fluctuations in the activity of these neurons that occur during feeding (Figures 3A and 3D). However, we considered the possibility that these smaller intrameal dynamics might also be correlated with components of behavior. To test this, we switched to a system in which mice were fed a liquid diet (vanilla Ensure) via a lickometer so that we could align individual feeding bouts to photometry data with millisecond precision.

Mice were transitioned from a solid to liquid diet over several days, then fasted overnight and tested in a 1-hr trial. Licks were aligned to photometry traces and individual feeding bouts defined as clusters of licks separated from their nearest neighbor by >20 s. This resulted in identification of an average of 17 ± 2 feeding bouts in each 1-hr trial, with each bout lasting an average of 17 ± 3 s and containing 53 ± 10 licks. The start of each bout in a representative trial is indicated by gray lines in Figures 6A and 6B.

We compared the average activity of these neurons during active feeding (intrabout) versus intermeal intervals (interbout), by calculating the difference in fluorescence between these stages (interbout – intrabout). This revealed that POMC neurons were more active during feeding whereas AgRP neurons were less active ($\Delta F_n = 0.042 \pm 0.011$ for AgRP versus $\Delta F_n = -0.029 \pm 0.004$ for POMC, $p = 0.001$) (Figure 6C). To investigate the dynamics underlying these differences, we aligned each feeding bout so that the start of the bout (first lick) corresponded to time zero and then analyzed a 10-s window flanking this moment. We found that AgRP and POMC neurons showed a consistent pattern of activity that predicted the onset of each meal. AgRP neurons declined in activity until the moment of the first lick and then their activity flattened (Figure 6D), whereas POMC neurons increased in activity prior to and throughout the start of feeding (Figure 6E). Cross-correlation analysis between AgRP and POMC showed that there was an inverse correlation between the activity of these two cell types that reached a peak at approximately time zero (Figure 6F). These effects were tightly linked to behavioral state, as they were robust to changes in the definition of a feeding bout (e.g., changes in the minimum intermeal interval) yet were completely absent when the data were re-analyzed using randomly generated feeding bouts (Figures 6D and 6E, black). Remarkably, these intrameal anticipatory changes in AgRP and POMC activity appear to recapitulate, on a smaller scale, the dramatic changes in activity that occur in these neurons in response to food presentation.

Dynamics of AgRP Projections to the PVH

AgRP neurons project broadly to brain regions involved in the control of food intake in a primarily one-to-one configuration (Betley et al., 2013). Optogenetic experiments have identified

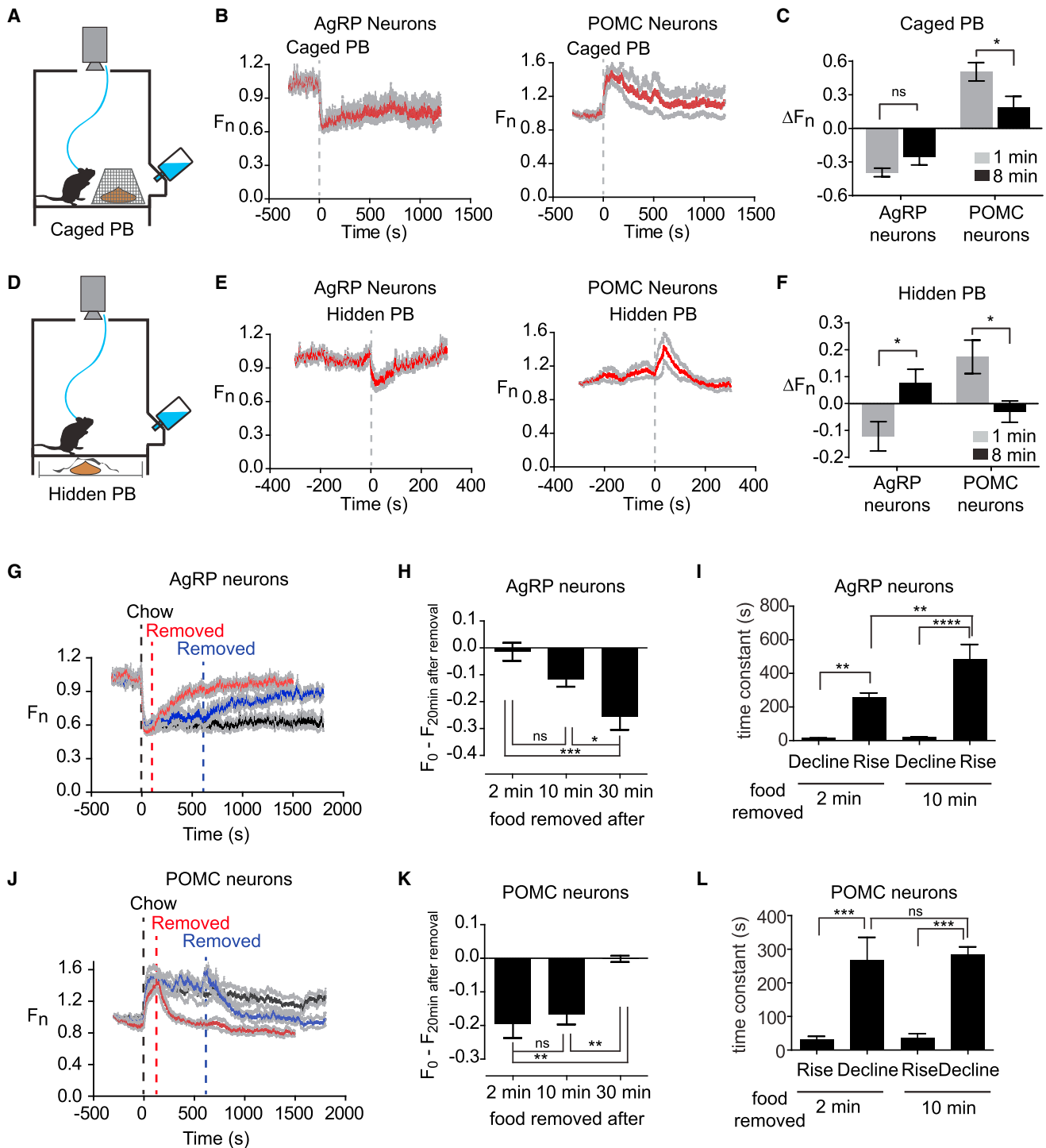


Figure 5. The Response to Food Detection Depends on Food Accessibility and Is Reversible

(A) Schematic of caged peanut butter.
 (B) Calcium signals aligned to the time of presentation of a caged peanut butter.
 (C) Change in fluorescence 1 and 8 min after caged peanut butter presentation.
 (D) Schematic of hidden peanut butter.
 (E) Calcium signals aligned to the time of presentation of hidden peanut butter.
 (F) Change in fluorescence 1 and 8 min after hidden peanut butter presentation.
 (G and J) Chow was presented at time 0, and then food was removed at 2 min (red), 10 min (blue) or not removed (black).

(legend continued on next page)

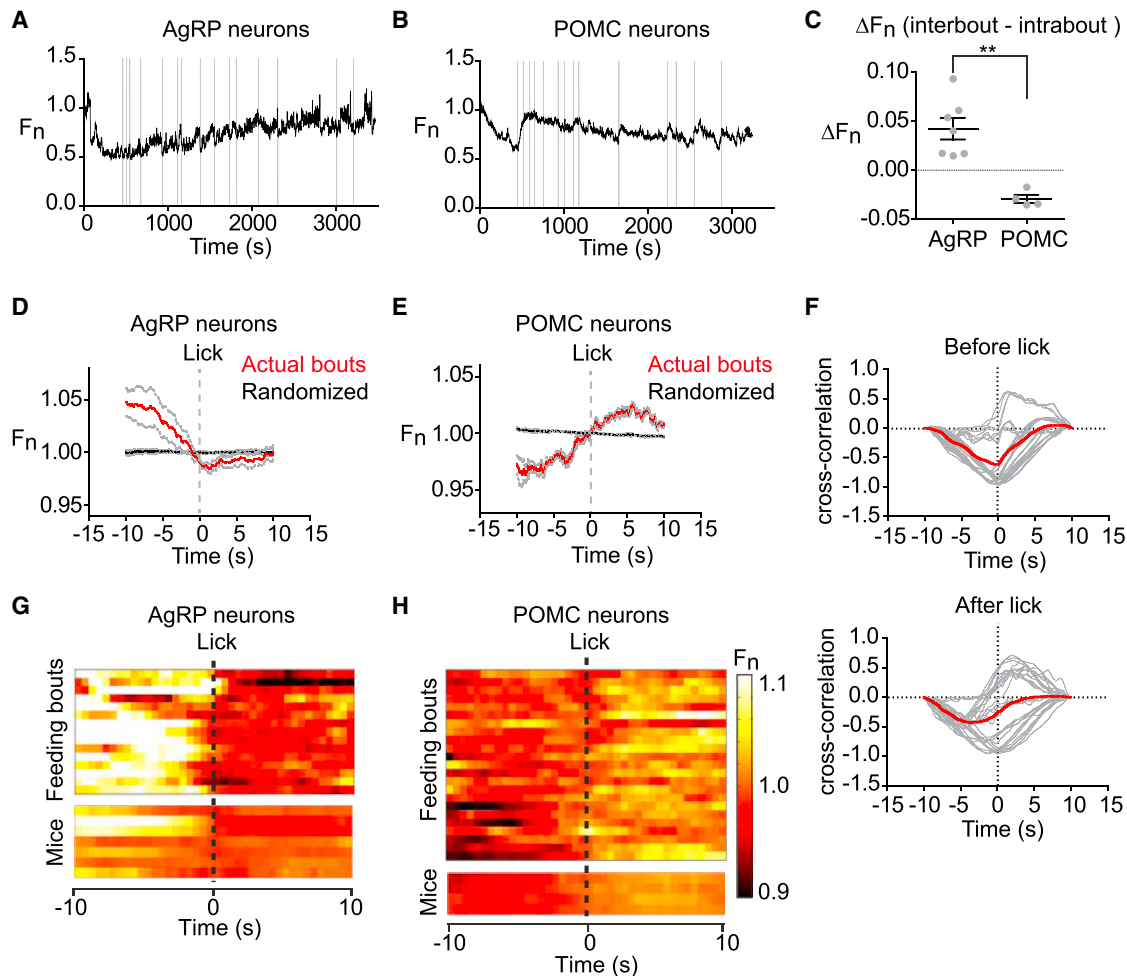


Figure 6. Intrameal Dynamics of AgRP and POMC Neurons

(A and B) Traces of AgRP and POMC activity in mice during consumption of a liquid diet. Licks that mark initiation of a feeding bout are shown in gray. (C) Difference in average fluorescence between periods of feeding (intrabout) and intermeal intervals (interbout) for each mouse. (D and E) Calcium signals from AgRP and POMC neurons aligned to the moment of the first lick that initiates a feeding bout. Data from actual feeding bouts shown in red; data from simulated randomly generated feeding bouts in black. (F) Cross-correlation plots showing the correlation between activity of AgRP and POMC neurons before and after licking. Red is mean, gray is 28 individual comparisons between AgRP ($n = 7$) and POMC ($n = 4$) mice. (G and H) Peri-event plots showing the activity of AgRP and POMC neurons aligned to the start of feeding bouts. The top plot shows all of the bouts for one trial of a mouse. The bottom plot shows the average response across all bouts for seven AgRP and four POMC mice. All error bars represent \pm SEM.

AgRP projections to the PVH as being particularly important for the control of feeding (Atasoy et al., 2012). As fiber photometry enables direct monitoring of axonal calcium transients (Gunaydin et al., 2014), we sought to record the activity of these key AgRP (ARC \rightarrow PVH) projections during behavior.

AAVs expressing Cre-dependent GCaMP6s were delivered to the ARC of AgRP-IRES-Cre mice and in the same surgery an

optical fiber was implanted ipsilaterally in the PVH (Figure 7A). Photometry recordings 4 weeks after surgery revealed spontaneous synchronous activity in these projections (Figure 7B) that resembled calcium dynamics observed in AgRP cell bodies (Figure 1H), albeit somewhat smaller in magnitude. Intraperitoneal injection of ghrelin, but not vehicle, induced a rapid increase in calcium signals in these projections ($\Delta F/F = 17\% \pm 5\%$ for

(H and K) Recovery in fluorescence 20 min after food removal for experiments in which food was removed after 2, 10, or 30 min.

(I and L) Time constant for the response to upon food presentation and food removal after 2 and 10 min.

All error bars represent \pm SEM.

See also Figure S3.

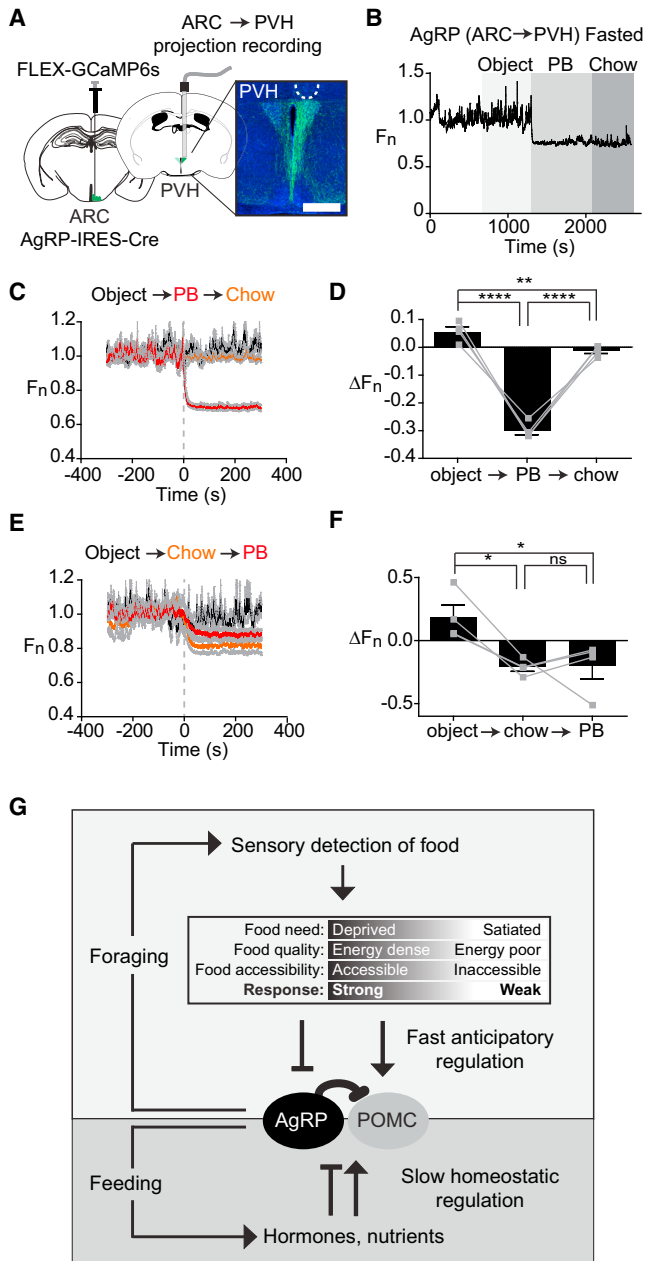


Figure 7. Natural Dynamics of AgRP Projections to the PVH

(A) Schematic showing infection of cell bodies in the ARC and installation of optical fiber in the PVH. Scale bar represents 0.5 mm.

(B) Recording from PVH of a fasted mouse presented sequentially with an inedible object, peanut butter, and chow.

(C and E) Calcium signals from PVH of mice presented sequentially with an inedible object, peanut butter, and chow.

(D and F) Quantification of calcium signals 5 min after event ($n = 4$ mice).

(G) Model for regulation of AgRP and POMC neurons by homeostatic and sensory information.

All error bars represent \pm SEM.

See also Figure S4.

ghrelin versus $-9\% \pm 3\%$ for PBS at 5 min, $p = 0.02$) (Figure S4), indicating that they are appropriately regulated by hormonal signals.

We next tested the effect of food presentation. Mice were fasted overnight and then presented with either an inedible object, chow, or peanut butter. Presentation of either chow or peanut butter rapidly and potently inhibited calcium dynamics in AgRP (ARC → PVH) projections ($\Delta F/F = -30\% \pm 2\%$ for peanut butter versus $-21\% \pm 3\%$ for chow at 5 min) whereas presentation of an inedible object had no effect (Figures 7C and 7E). Of note, peanut butter almost completely eliminated detectable synchronous activity in PVH axons (Figures 7B and 7C), suggesting that palatable food presentation is particularly potent in suppressing the activity of this pathway. Assays utilizing sequential food presentation revealed a pattern of responses in PVH projections that closely resembled responses observed in AgRP cell bodies (Figures 7D and 7F). Likewise, chow presentation partially reversed the activation of these PVH projections by ghrelin (Figure S4). Thus, the activity of AgRP (ARC → PVH) projections is regulated by ghrelin and food presentation in a way that mirrors the population response in the ARC.

DISCUSSION

It has been known for more than 75 years that the hypothalamus plays a critical role in the control of food intake (Hetherington and Ranson, 1939), yet the dynamics of the hypothalamic circuits that give rise to feeding behavior have remained a mystery. Here, we have used an optical approach to record the natural dynamics of the two most widely studied cell types that control feeding, AgRP and POMC neurons, in awake behaving mice. These experiments have revealed unexpectedly that these neurons are potently regulated by the sensory detection of food. This rapid regulation resets the activation state of AgRP and POMC neurons induced by orexigenic signals such as ghrelin or fasting. The magnitude and robustness of this response suggests that it is a primary mechanism that controls the activity of these neurons in vivo. The speed of this response suggests that it is likely mediated by neural input. The dependence on food palatability suggests that this response contains information about the food's hedonic properties or energy content, possibly through a learned association with smells or other sensory cues. Collectively, these findings reveal that AgRP and POMC neurons receive real-time information about the availability of food in the external world, which they then integrate with homeostatic signals arising from the body (Figure 7G). This demonstrates a more complex and dynamic role for these circuits in the control of feeding behavior than is currently appreciated.

Sensory Feedback Enables Rapid Inhibition of Appetitive Processes

The rapid sensory regulation of AgRP and POMC neurons is counterintuitive, since it appears to "short circuit" their well-established function as interoceptive sensors of nutritional state. In this model, energy deficit activates AgRP neurons and inhibits POMC neurons, thereby generating a motivational drive that promotes food intake and is only relieved when energy stores are replenished. An assumption of this model is that internal signals

generated during feeding (e.g., accumulation of circulating nutrients or hormones) are responsible for resetting the activation state of these neurons and thereby reducing the drive to eat.

Our data, by contrast, show that food detection alone rapidly resets the activity of these two cell types and that this resetting precedes the onset of actual food consumption. This is surprising in light of the fact that stimulation of AgRP neurons is sufficient to promote food intake (Aponte et al., 2011; Krashes et al., 2011). However, our data also show that if food is removed before it can be consumed, then these neurons revert to their activity level prior to food presentation (Figures 5G and 5J). We have likewise found that inaccessible food induces smaller and less durable changes in AgRP and POMC neuron activity (Figures 5C and 5F). Together, these findings suggest that food detection modulates AgRP and POMC neurons in a way that anticipates the change in their activity that will occur following food consumption, taking into account factors such as the food's energy density, perceived accessibility, and the nutritional state of the mouse (Figure 7G).

What is the purpose of this anticipatory regulation? We propose that it represents a mechanism to rapidly inhibit foraging and other appetitive behaviors once food has been discovered (Figure 7G). In this regard, activation of AgRP neurons induces not only food consumption but also motivational processes that drive food obtainment, including dramatic foraging behavior and a willingness to work for food (Atasoy et al., 2012; Krashes et al., 2011). These appetitive processes are blocked by food discovery as part of the natural transition from foraging to feeding, but the mechanisms by which this transition is regulated have not been described. Our data show that food discovery results in rapid feedback inhibition of AgRP neurons themselves, rather than some downstream circuit element, which provides a direct mechanism to inhibit foraging once food has been obtained. The fact that this feedback occurs at the level of AgRP neurons is surprising and suggests that the activity of these neurons is particularly important for generating the motivation to search for food relative to other aspects of feeding behavior.

Models for AgRP-Driven Food Consumption

The natural dynamics of AgRP neuron activity are consistent with a primary function for these neurons in regulating appetitive behaviors that promote food discovery. Yet multiple lines of evidence have suggested a role for these neurons in controlling food consumption as well. We discuss below two possible mechanisms by which AgRP neurons could drive food intake that are consistent with our data.

Subpopulations of AgRP Neurons with Specialized Functions

A limitation of fiber photometry is that it measures the average activity of a population of a neurons, which can mask heterogeneity in the responses of individual cells. AgRP neurons that project to different downstream targets differ in their ability to induce food intake and in their expression of the leptin receptor (Atasoy et al., 2012; Betley et al., 2013; Wu et al., 2012). It is therefore unlikely that all AgRP neurons show identical responses to stimuli such as hormone challenge or food presentation. One possibility is that a subset of AgRP neurons are activated, rather than inhibited, by food presentation, and this subpopulation of AgRP

neurons is responsible for driving food consumption. Testing this possibility will require measuring the single-cell dynamics of AgRP neurons during behavior, using approaches such as optogenetic phototagging combined with in vivo recording (Lima et al., 2009) or fluorescence microendoscopic imaging (Ziv et al., 2013).

While future experiments are likely to uncover additional heterogeneity in these cells, three observations argue against this heterogeneity being the primary explanation for how AgRP activity drives food consumption. First, the magnitude of the decrease in AgRP calcium dynamics that we observe following food presentation, particularly for palatable foods (Figure 4F), is inconsistent with a major subset of these neurons having the opposite regulation. Therefore, if some AgRP neurons are activated during feeding, they must represent a minority of the population. Second, our analysis of AgRP dynamics during individual feeding bouts reveals that AgRP activity declines immediately preceding meal initiation and then is relatively flat during the course of food intake (Figure 6D). These intrameal dynamics are not what would be predicted for a neuron whose activity directly drives food consumption. Third, and most importantly, we have shown that food presentation potentially inhibits AgRP projections to the PVH (Figure 7). Optogenetic experiments have strongly implicated these ARC → PVH projections in the control of food intake (Atasoy et al., 2012; Betley et al., 2013). The fact that these PVH projections show the same activity pattern as the population as a whole argues that projection-specific dynamics are unlikely to be the primary explanation for how these neurons can drive feeding.

Learning Mediated by AgRP Activity

An alternative possibility is that AgRP neurons drive food consumption indirectly via a learning process. In this regard, we have shown that the inhibition of AgRP activity following food discovery is contingent on subsequent food intake, since this inhibition is reversed if the food is removed before it can be consumed (Figure 5G). If AgRP activity has negative motivational valence (analogous to the unpleasant sensation of hunger), then this might enable animals to learn the consequences of failing to eat after obtaining food. In this model, food discovery would temporarily relieve the sensation of hunger, but animals would learn through experience that this sensation returns if the food is not consumed. Over time, this would result in appetitive and consummatory aspects of feeding becoming linked in sequence so that food discovery is always followed by food intake, even though AgRP activity itself would largely be extinguished before the onset of feeding. Alternative models based on negative reinforcement and learning are also conceivable, and untangling these possibilities will be an important area for future investigation.

Neural Input into AgRP and POMC Neurons Communicates the Discovery of Food

AgRP and POMC neurons receive abundant neural input, and indeed, the activation of AgRP neurons by fasting is mediated primarily by increased excitatory tone (Liu et al., 2012; Yang et al., 2011). Yet most studies of these cells have focused on the role of hormones and nutrients, and the role of this afferent neural input has remained unclear. Our data indicate that one

function of this neural input is to communicate to AgRP and POMC neurons the discovery of food. This is appealing because it demonstrates a function for this synaptic input that extends beyond merely serving as a redundant source of homeostatic information. The fact that the strength of this neural input varies depending on the hedonic properties of the detected food suggests that, at some level, the upstream circuit encodes an association between sensory information and the food's nutritional content (i.e., a "food memory"). Identification of the neural substrate of this association may provide an entry point into the study of the maladaptive associations between sensory cues and food that develop in some eating disorders. As several cell types that provide input into AgRP neurons have recently been identified (Krashes et al., 2014), it should be possible to elucidate this afferent pathway using modern circuit mapping techniques.

Information Processing by Arcuate Feeding Circuits

Feeding is influenced by diverse types of signals including sensory, hedonic, homeostatic, and visceral cues. A long-standing question has been whether there exists a site in the brain where the neural circuits that sense these signals converge, thereby enabling integration of this information into a single decision to eat or not to eat (Friedman, 2014). The arcuate nucleus in this model is traditionally viewed as a sensor for homeostatic cues, which it then relays to higher centers where more complex integration occurs. This viewpoint is encapsulated in the fact that AgRP and POMC neurons are often described as "first order" neurons, analogous to primary sensory transduction neurons such as rods and cones in the visual system.

A complication for this model as mentioned previously is that AgRP and POMC neurons are strongly regulated by neural input and therefore are not merely sensors of circulating nutritional signals. However, absent an understanding of the function of this afferent input, it has not been possible to assemble a complete picture of the role of these cells. The discovery that this input contains information about the sensory and hedonic properties of food reveals that these long-studied neurons themselves integrate multiple types of food-related information and indeed may represent a key convergence point in the feeding circuit. The further application of new methods for recording cell-type-specific neural activity is likely to provide additional insight into how this complex integration is achieved.

EXPERIMENTAL PROCEDURES

Experimental protocols were approved by the University of California, San Francisco IACUC following the NIH guidelines for the Care and Use of Laboratory Animals.

Stereotaxic Surgery

Recombinant AAV expressing GCaMP6s (AAV1.Syn.Flex.GCaMP6s) was purchased from the Penn Vector Core. AAV was stereotactically injected into the ARC of AgRP-IRES-Cre and POMC-Cre mice. In the same surgery, a photometry cannula was implanted unilaterally in either the ARC or PVH. Mice were allowed 2–4 weeks for viral expression and recovery from surgery before behavioral testing.

Slice Electrophysiology and Calcium Imaging

Acute hypothalamic slices were prepared from 8- to 15-week-old AgRP-IRES-Cre and POMC-Cre mice expressing AAV GCaMP6s for 2–4 weeks. Fluores-

cent cells in the ARC were identified for whole-cell patch clamp recordings, and cells were activated using step currents (10 pA, 2 s) from -20 pA to $+120$ pA or ramp currents (0–40 pA, 10 s) injected under current clamp mode. Calcium imaging was performed simultaneously using a digital CCD camera mounted on an Olympus BX51 microscope.

Immunohistochemistry

Mice were transcardially perfused with PBS followed by formalin. Brains were postfixed overnight in formalin and placed in 30% sucrose for 2 days. Free floating sections (40 μ m) were prepared with a cryostat, blocked (3% BSA, 2% NGS, and 0.1% Triton-X in PBS for 2 hr), and then incubated with primary antibody (chicken anti-GFP, Abcam, ab13970, 1:1,000) overnight at 4°C. Samples were washed, incubated with secondary antibody (goat anti-chicken Alexa 488 secondary antibody; Invitrogen, 1:500) for 2 hr at room temperature, mounted, and imaged.

Fiber Photometry

A rig for performing fiber photometry recordings was constructed following basic specifications previously described (Gunaydin et al., 2014). All experiments were performed in behavioral chambers (Coulbourn Instruments, Habitest Modular System) and video recorded using infrared cameras installed above each cage. Experiments were performed at the beginning of the dark cycle (CT12–CT14) to control for circadian factors and performed in a dark environment with illumination of red or infrared light. Mice were acclimated to the behavioral chamber for at least 15 min prior to the beginning of each testing session.

For hormone challenge, ghrelin (60 μ g/mouse) or vehicle (PBS) was delivered by intraperitoneal injection in a total volume of 200 μ l. For food presentation experiments, mice were exposed in their home cage prior to testing to both peanut butter and the rubber stopper in order to remove any effects of novelty. Mice were not exposed to chocolate prior to testing. Liquid diet experiments were performed using a behavioral chamber equipped with an optical lickometer (Coulbourn Instruments). Mice were habituated to a liquid diet (Ensure vanilla flavor) for 3 days prior to the experiment. Mice were then fasted overnight, acclimated to the behavioral chamber for 15 min, and then a bottle filled with liquid diet was plugged into the lickometer system and the trial was run for 1 hr. Photometry data were subjected to minimal processing consisting of only autofluorescence background subtraction and within trial fluorescence normalization.

Statistics

Values are reported as mean \pm SEM in the figures and text. *p* values for pairwise comparison were performed using a two-tailed Student's *t* test. *p* values for comparisons across multiple groups were corrected using the Holm-Sidak method in Prism. **p* < 0.05, ***p* < 0.01, ****p* < 0.001, *****p* < 0.0001.

See also [Extended Experimental Procedures](#).

SUPPLEMENTAL INFORMATION

Supplemental Information includes Extended Experimental Procedures, four figures, and six movies and can be found with this article online at <http://dx.doi.org/10.1016/j.cell.2015.01.033>.

AUTHOR CONTRIBUTIONS

Y.C. and Z.A.K. designed the experiments, analyzed the data, and wrote the paper. Y.C. built the photometry rig, wrote the programs for data analysis, and performed the photometry experiments. Y.L. assisted with PVH projection experiments and histology. T.K. and Y.L. performed slice physiology experiments.

ACKNOWLEDGMENTS

Z.A.K. is a New York Stem Cell Foundation-Robertson Investigator. This research was supported by the New York Stem Cell Foundation, the Rita Allen Foundation, the McKnight Foundation, the Alfred P. Sloan Foundation, a

NARSAD Young Investigator Grant from the Brain and Behavior Research Foundation, the Esther A. and Joseph Klingenstein Foundation, the Program for Breakthrough Biomedical Research, the UCSF Diabetes Center Obesity Pilot program (U01 DK089541) and NIH R00-DK083531 (Z.A.K.). We thank Jennifer Garrison, Nirao Shah, Kevan Shokat, and members of the Z.A.K. laboratory for comments on the manuscript and Anthony Lee and Scott Owen for technical advice on photometry.

Received: November 19, 2014

Revised: December 31, 2014

Accepted: January 16, 2015

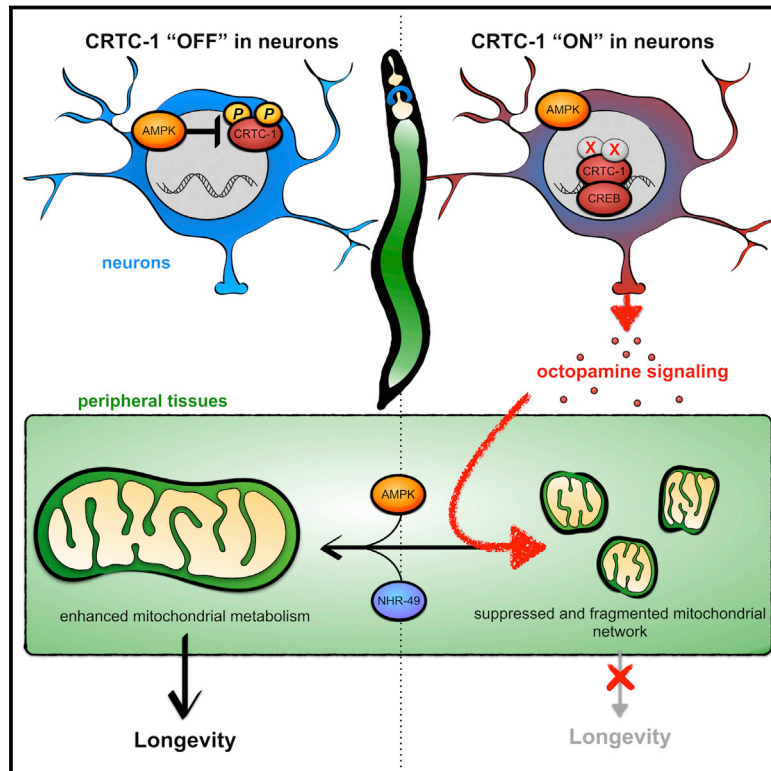
Published: February 19, 2015

REFERENCES

- Aponte, Y., Atasoy, D., and Sternson, S.M. (2011). AGRP neurons are sufficient to orchestrate feeding behavior rapidly and without training. *Nat. Neurosci.* **14**, 351–355.
- Atasoy, D., Betley, J.N., Su, H.H., and Sternson, S.M. (2012). Deconstruction of a neural circuit for hunger. *Nature* **488**, 172–177.
- Betley, J.N., Cao, Z.F., Ritola, K.D., and Sternson, S.M. (2013). Parallel, redundant circuit organization for homeostatic control of feeding behavior. *Cell* **155**, 1337–1350.
- Blouet, C., and Schwartz, G.J. (2010). Hypothalamic nutrient sensing in the control of energy homeostasis. *Behav. Brain Res.* **209**, 1–12.
- Chen, T.W., Wardill, T.J., Sun, Y., Pulver, S.R., Renninger, S.L., Baohan, A., Schreiter, E.R., Kerr, R.A., Orger, M.B., Jayaraman, V., et al. (2013). Ultrasensitive fluorescent proteins for imaging neuronal activity. *Nature* **499**, 295–300.
- Clark, J.T., Kalra, P.S., and Kalra, S.P. (1985). Neuropeptide Y stimulates feeding but inhibits sexual behavior in rats. *Endocrinology* **117**, 2435–2442.
- Cowley, M.A., Smart, J.L., Rubinstein, M., Cerdán, M.G., Diano, S., Horvath, T.L., Cone, R.D., and Low, M.J. (2001). Leptin activates anorexigenic POMC neurons through a neural network in the arcuate nucleus. *Nature* **411**, 480–484.
- Cowley, M.A., Smith, R.G., Diano, S., Tschöp, M., Pronchuk, N., Grove, K.L., Strasburger, C.J., Bidlingmaier, M., Esterman, M., Heiman, M.L., et al. (2003). The distribution and mechanism of action of ghrelin in the CNS demonstrates a novel hypothalamic circuit regulating energy homeostasis. *Neuron* **37**, 649–661.
- Cui, G., Jun, S.B., Jin, X., Pham, M.D., Vogel, S.S., Lovinger, D.M., and Costa, R.M. (2013). Concurrent activation of striatal direct and indirect pathways during action initiation. *Nature* **494**, 238–242.
- Dietrich, M.O., Liu, Z.W., and Horvath, T.L. (2013). Mitochondrial dynamics controlled by mitofusins regulate AgRP neuronal activity and diet-induced obesity. *Cell* **155**, 188–199.
- Fan, W., Boston, B.A., Kesterson, R.A., Hruby, V.J., and Cone, R.D. (1997). Role of melanocortinergic neurons in feeding and the agouti obesity syndrome. *Nature* **385**, 165–168.
- Friedman, J. (2014). 20 years of leptin: leptin at 20: an overview. *J. Endocrinol.* **223**, T1–T8.
- Gropp, E., Shanabrough, M., Borok, E., Xu, A.W., Janoschek, R., Buch, T., Plum, L., Balthasar, N., Hampel, B., Waisman, A., et al. (2005). Agouti-related peptide-expressing neurons are mandatory for feeding. *Nat. Neurosci.* **8**, 1289–1291.
- Gunaydin, L.A., Grosenick, L., Finkelstein, J.C., Kauvar, I.V., Fenno, L.E., Adhikari, A., Lammel, S., Mirzabekov, J.J., Airan, R.D., Zalocusky, K.A., et al. (2014). Natural neural projection dynamics underlying social behavior. *Cell* **157**, 1535–1551.
- Hahn, T.M., Breininger, J.F., Baskin, D.G., and Schwartz, M.W. (1998). Coexpression of AgRP and NPY in fasting-activated hypothalamic neurons. *Nat. Neurosci.* **1**, 271–272.
- Hetherington, A.W., and Ranson, S.W. (1939). Experimental hypothalamico-hypophyseal obesity in the rat. *Proc. Soc. Exp. Biol. Med.* **41**, 465–466.
- Krashes, M.J., Koda, S., Ye, C., Rogan, S.C., Adams, A.C., Cusher, D.S., Maratos-Flier, E., Roth, B.L., and Lowell, B.B. (2011). Rapid, reversible activation of AgRP neurons drives feeding behavior in mice. *J. Clin. Invest.* **121**, 1424–1428.
- Krashes, M.J., Shah, B.P., Madara, J.C., Olson, D.P., Strohlic, D.E., Garfield, A.S., Vong, L., Pei, H., Watabe-Uchida, M., Uchida, N., et al. (2014). An excitatory paraventricular nucleus to AgRP neuron circuit that drives hunger. *Nature* **507**, 238–242.
- Lima, S.Q., Hromádka, T., Znamenskiy, P., and Zador, A.M. (2009). PINP: a new method of tagging neuronal populations for identification during in vivo electrophysiological recording. *PLoS ONE* **4**, e6099.
- Liu, T., Kong, D., Shah, B.P., Ye, C., Koda, S., Saunders, A., Ding, J.B., Yang, Z., Sabatini, B.L., and Lowell, B.B. (2012). Fasting activation of AgRP neurons requires NMDA receptors and involves spinogenesis and increased excitatory tone. *Neuron* **73**, 511–522.
- Luquet, S., Perez, F.A., Hnasko, T.S., and Palmiter, R.D. (2005). NPY/AgRP neurons are essential for feeding in adult mice but can be ablated in neonates. *Science* **310**, 683–685.
- Nakazato, M., Murakami, N., Date, Y., Kojima, M., Matsuo, H., Kangawa, K., and Matsukura, S. (2001). A role for ghrelin in the central regulation of feeding. *Nature* **409**, 194–198.
- Olmann, M.M., Wilson, B.D., Yang, Y.K., Kerns, J.A., Chen, Y., Gantz, I., and Barsh, G.S. (1997). Antagonism of central melanocortin receptors in vitro and in vivo by agouti-related protein. *Science* **278**, 135–138.
- Pinto, S., Roseberry, A.G., Liu, H., Diano, S., Shanabrough, M., Cai, X., Friedman, J.M., and Horvath, T.L. (2004). Rapid rewiring of arcuate nucleus feeding circuits by leptin. *Science* **304**, 110–115.
- Schneeberger, M., Dietrich, M.O., Sebastián, D., Imbernón, M., Castaño, C., Garcia, A., Esteban, Y., Gonzalez-Franquesa, A., Rodríguez, I.C., Bortolozzi, A., et al. (2013). Mitofusin 2 in POMC neurons connects ER stress with leptin resistance and energy imbalance. *Cell* **155**, 172–187.
- Seeley, R.J., Yagaloff, K.A., Fisher, S.L., Burn, P., Thiele, T.E., van Dijk, G., Baskin, D.G., and Schwartz, M.W. (1997). Melanocortin receptors in leptin effects. *Nature* **390**, 349.
- Sternson, S.M., Shepherd, G.M., and Friedman, J.M. (2005). Topographic mapping of VMH → arcuate nucleus microcircuits and their reorganization by fasting. *Nat. Neurosci.* **8**, 1356–1363.
- Tong, Q., Ye, C.P., Jones, J.E., Elmquist, J.K., and Lowell, B.B. (2008). Synaptic release of GABA by AgRP neurons is required for normal regulation of energy balance. *Nat. Neurosci.* **11**, 998–1000.
- Vong, L., Ye, C., Yang, Z., Choi, B., Chua, S., Jr., and Lowell, B.B. (2011). Leptin action on GABAergic neurons prevents obesity and reduces inhibitory tone to POMC neurons. *Neuron* **71**, 142–154.
- Williams, K.W., and Elmquist, J.K. (2012). From neuroanatomy to behavior: central integration of peripheral signals regulating feeding behavior. *Nat. Neurosci.* **15**, 1350–1355.
- Wu, Q., Clark, M.S., and Palmiter, R.D. (2012). Deciphering a neuronal circuit that mediates appetite. *Nature* **483**, 594–597.
- Yang, Y., Atasoy, D., Su, H.H., and Sternson, S.M. (2011). Hunger states switch a flip-flop memory circuit via a synaptic AMPK-dependent positive feedback loop. *Cell* **146**, 992–1003.
- Ziv, Y., Burns, L.D., Cocker, E.D., Hamel, E.O., Ghosh, K.K., Kitch, L.J., El Gamal, A., and Schnitzer, M.J. (2013). Long-term dynamics of CA1 hippocampal place codes. *Nat. Neurosci.* **16**, 264–266.

Neuronal CRTC-1 Governs Systemic Mitochondrial Metabolism and Lifespan via a Catecholamine Signal

Graphical Abstract



Authors

Kristopher Burkewitz,
Ilanessa Morante, ..., Ana R. Grant,
William B. Mair

Correspondence

wmair@hsph.harvard.edu

In Brief

The energy sensor AMPK acts locally as well as cell nonautonomously to regulate longevity through neuronal CRTC-1-dependent remodeling of systemic mitochondrial metabolism.

Highlights

- CRTC-1 uncouples AMPK-mediated longevity from pleiotropic side effects
- AMPK promotes longevity via CRTC-1-dependent remodeling of mitochondrial metabolism
- Neuronal CRTC-1/CREB and NHR-49 antagonistically regulate longevity and metabolism
- Neuronal CRTC-1 regulates mitochondrial dynamics and lifespan via octopamine

Accession Numbers

GSE58931



Neuronal CRTC-1 Governs Systemic Mitochondrial Metabolism and Lifespan via a Catecholamine Signal

Kristopher Burkewitz,¹ Ianessa Morante,¹ Heather J.M. Weir,¹ Robin Yeo,¹ Yue Zhang,¹ Frank K. Huynh,² Olga R. Ilkayeva,² Matthew D. Hirschey,² Ana R. Grant,³ and William B. Mair^{1,*}

¹Department of Genetics and Complex Diseases, Harvard School of Public Health, 665 Huntington Avenue, Boston, MA 02115, USA

²Duke Molecular Physiology Institute, Duke University Medical Center, 300 North Duke Street, Durham, NC 27701, USA

³Department of Computational Medicine and Bioinformatics, University of Michigan Medical School, 100 Washtenaw Avenue, Ann Arbor, MI 48109, USA

*Correspondence: wmair@hsph.harvard.edu

<http://dx.doi.org/10.1016/j.cell.2015.02.004>

SUMMARY

Low energy states delay aging in multiple species, yet mechanisms coordinating energetics and longevity across tissues remain poorly defined. The conserved energy sensor AMP-activated protein kinase (AMPK) and its corresponding phosphatase calcineurin modulate longevity via the CREB regulated transcriptional coactivator (CRTC)-1 in *C. elegans*. We show that CRTC-1 specifically uncouples AMPK/calcineurin-mediated effects on lifespan from pleiotropic side effects by reprogramming mitochondrial and metabolic function. This pro-longevity metabolic state is regulated cell nonautonomously by CRTC-1 in the nervous system. Neuronal CRTC-1/CREB regulates peripheral metabolism antagonistically with the functional PPAR α ortholog, NHR-49, drives mitochondrial fragmentation in distal tissues, and suppresses the effects of AMPK on systemic mitochondrial metabolism and longevity via a cell-non-autonomous catecholamine signal. These results demonstrate that while both local and distal mechanisms combine to modulate aging, distal regulation overrides local contribution. Targeting central perception of energetic state is therefore a potential strategy to promote healthy aging.

INTRODUCTION

An organism's energy status is tightly coupled to its rate of aging, as low energy conditions increase longevity and disease resistance across the evolutionary spectrum (Burkewitz et al., 2014). Mechanisms that communicate energetic state between tissues to coordinate organismal health and longevity remain poorly understood, however, and must be defined in order to translate these effects to human therapeutics. AMP-activated protein kinase (AMPK) is a conserved energy sensor activated by increases in the AMP/ADP:ATP ratio, which signals low en-

ergy charge (Hardie et al., 2012). AMPK upregulates catabolic processes and shuts down energy-consuming processes to restore cellular energy homeostasis (Hardie et al., 2012). AMPK is also pro-longevity; activating AMPK in *C. elegans* and *Drosophila* increases healthy lifespan and mimics a low energy state in well-fed animals (Apfeld et al., 2004; Stenlesen et al., 2013). *C. elegans* lacking AMPK activity fail to respond to low energy conditions, such as dietary restriction, that extend wild-type lifespan (Burkewitz et al., 2014).

Both AMPK and its effects on aging are conserved across eukaryotes (Hardie et al., 2012). Metformin, an indirect AMPK agonist, promotes healthy aging in *C. elegans* (Onken and Driscoll, 2010) and mice (Martin-Montalvo et al., 2013). Deregulation of AMPK results in age-onset human pathologies including cancer and neurodegenerative diseases (Hardie et al., 2012). AMPK signaling therefore plays a critical role linking energetics to pathology, making it an attractive target to treat or prevent multiple age-related diseases.

AMPK has both cell-autonomous effects on energetics through direct phosphorylation of metabolic effectors (Hardie et al., 2012) and cell-nonautonomous effects via integration of hormonal and neuroendocrine signals (Dagon et al., 2012; Lerner et al., 2009; Minokoshi et al., 2004). The extent to which AMPK promotes longevity locally via regulation of metabolism or distally via a secondary signal remains unclear. Additionally, AMPK's pro-longevity effects may not be universal in all tissues, as AMPK activation in certain cell types appears to increase risk for some diseases, and pleiotropic effects of AMPK activation unrelated to aging have detrimental physiological consequences (Burkewitz et al., 2014). Identifying downstream targets and processes regulated by AMPK that specifically mediate its role in longevity would therefore enhance our capacity to harness the link between energetics and aging for treatment of age-related pathologies.

Previously, we identified the cyclic AMP-responsive element binding protein (CREB)-regulated transcriptional coactivator (CRTC)-1 as a critical longevity target of AMPK and calcineurin in *C. elegans* (Mair et al., 2011). AMPK and calcineurin antagonistically regulate CRTC-1 phosphorylation status, thereby modulating its activity and effect on aging. CRTCs are transcriptional coactivators first discovered in mammals for their ability to

bind CREB and regulate its transcriptional activity (Altarejos and Montminy, 2011). Mammals possess 3 CRTC family members that act in distinct tissues, including neurons (CRTC1/2), liver (CRTC2), and adipose tissue (CRTC3), and aberrant regulation of CRTCs is implicated in multiple chronic diseases, including obesity, metabolic disease, and neurodegeneration (Altarejos and Montminy, 2011). *C. elegans* possess a single, highly conserved CRTC family member, CRTC-1. AMPK phosphorylates CRTC-1 directly, promoting 14-3-3 binding, cytosolic sequestration and inactivation. Blocking phosphorylation of CRTC-1 at conserved AMPK target sites, serines 76 and 179, renders it refractory to AMPK regulation and constitutively nuclear. CRTC-1^{S76A,S179A} blocks lifespan extension by AMPK activation or inhibition of the corresponding phosphatase calcineurin (Mair et al., 2011).

In this study we demonstrate that CRTC-1 specifically mediates the longevity output of AMPK. We perform transcriptomic analysis to elucidate genes downstream of AMPK/CRTC-1 signaling, which couple specifically to lifespan regulation. Through this approach we identify coordination of mitochondrial metabolism by CRTC-1 and the nuclear hormone receptor NHR-49, a functional PPAR α ortholog (Van Gilst et al., 2005). Notably, we demonstrate that these opposing transcriptional effectors act in the nervous system to regulate both longevity and systemic changes in metabolic transcription. NHR-49 is required for AMPK/calcineurin-mediated longevity, and limiting NHR-49 function to neurons is sufficient to mediate both longevity and regulation of metabolic genes in peripheral tissues. In addition, we demonstrate that neuronal CRTC-1 modulates AMPK/calcineurin-mediated longevity cell nonautonomously via regulation of the neurotransmitter/hormone octopamine. Neuron-specific activation of CRTC-1, like *nhr-49* loss, suppresses AMPK/calcineurin-mediated longevity and upregulates expression of key enzymes involved in octopamine synthesis. Correspondingly, neuronal CRTC-1^{S76A,S179A} has no effect on longevity in mutants deficient in octopamine synthesis. Together these data challenge the current paradigm that AMPK, CRTC-1 and NHR-49 act cell autonomously to regulate metabolism and longevity, and instead highlight their distinct role in communicating perception of energy status in neurons to systemic regulation of metabolism and lifespan.

RESULTS

CRTC-1 Is Specific to AMPK Longevity

We generated a *C. elegans* transgenic strain expressing a truncated AMPK $\alpha 2$ catalytic subunit (AAK-2), which results in increased T172 phosphorylation and constitutively active (CA) AMPK (Mair et al., 2011). CA-AAK-2 increases *C. elegans* lifespan (Figure 1A), yet induces detrimental pleiotropic side effects including small body size and reduced reproductive capacity (Figures 1B and 1C). As shown previously, CRTC-1^{S76A,S179A} abolishes lifespan extension from AAK-2 activation (Figure 1D) without altering AMPK activity (Figure S1). In contrast to its role in longevity, CRTC-1^{S76A,S179A} does not suppress CA-AAK-2-mediated effects on growth (Figure 1E) or reproductive period (Figure 1F, Figure S1). The physiological effects of CRTC-1^{S76A,S179A} in CA-AAK-2 animals are therefore

specific to longevity and do not extend to non-aging-related traits.

Increased longevity is often coupled to increased stress resistance. To determine if this was the case for AMPK, we examined the effect of CA-AAK-2 on resistance to heat stress at 33°C. *C. elegans* lacking *aak-2* are sensitive to heat stress compared to wild-type (Apfeld et al., 2004). Conversely, activation of AMPK promotes heat resistance, as *C. elegans* expressing CA-AAK-2 show a 125% increase in median survival at 33°C compared to wild-type animals (Figure 1G; 27 and 12 hr, respectively). However, unlike its effect on AMPK longevity (Figure 1D), CRTC-1^{S76A,S179A} does not suppress heat resistance conferred by CA-AAK-2 (Figure 1H). Mechanisms that protect CA-AAK-2 animals from heat stress are thus separable from those which promote lifespan extension, and CRTC-1 represents a molecular switch that uncouples the longevity effects of AMPK from pleiotropy unrelated to aging (Figure 1I).

AMPK and CRTC-1 Coordinate Mitochondrial Metabolism to Regulate Longevity

We reasoned that CRTC-1 could be leveraged to identify the mechanisms by which AMPK increases lifespan. As CRTC-1^{S76A,S179A} suppresses only the longevity effects of AMPK activation, genes differentially expressed in CA-AAK-2 animals in a CRTC-1-dependent manner would be enriched for functions specific to AMPK-mediated longevity (Figure 1I). We defined CRTC-1-dependent genes as those differentially regulated in CA-AAK-2 (Figure 2A, yellow), or in CRTC-1^{S76A,S179A}; CA-AAK-2 double-transgenics (Figure 2A, red), but not in both (Figure 2A, orange).

We performed RNA-Seq analyses and identified 1,680 genes differentially expressed in worms with activated AAK-2, activated CRTC-1^{S76A,S179A}, or double-transgenics, relative to wild-type animals (Figures 2B, S2A, Table S2). AMPK induces small body size, reduced reproduction, and stress resistance independent of CRTC-1 (Figure 1), thus we predicted that AMPK-dependent/CRTC-1-independent genes (Figure 2B, orange region) would be associated with these phenotypes. Supporting this hypothesis, the gene ontology (GO) terms most enriched among those genes include processes involving germline differentiation, growth/development, and reproduction (Figure 2C, Table S3). Importantly, this tight association between phenotypes and functional enrichments within the transcriptomic changes validated our hypothesis that CRTC-1 could be used to filter out pleiotropic effects of AMPK activation unrelated to aging.

To identify processes specifically coupled to longevity, we focused on transcriptional changes induced by AMPK that are dependent on CRTC-1 activation status (Figure 2A). Of the 869 genes differentially expressed by AAK-2 activation in a CRTC-1-dependent manner, over 75% are differentially expressed when both AMPK and CRTC-1 are active (Figure 2B, red region). These genes are highly enriched for processes associated with metabolism, and more specifically, processes localized to mitochondria (Figure 2D, Table S3). We examined the directionality of CRTC-1-dependent gene expression changes, and found that suppression of AMPK longevity is associated with a broad down-regulation of mitochondrial metabolic processes (Figure 2D).

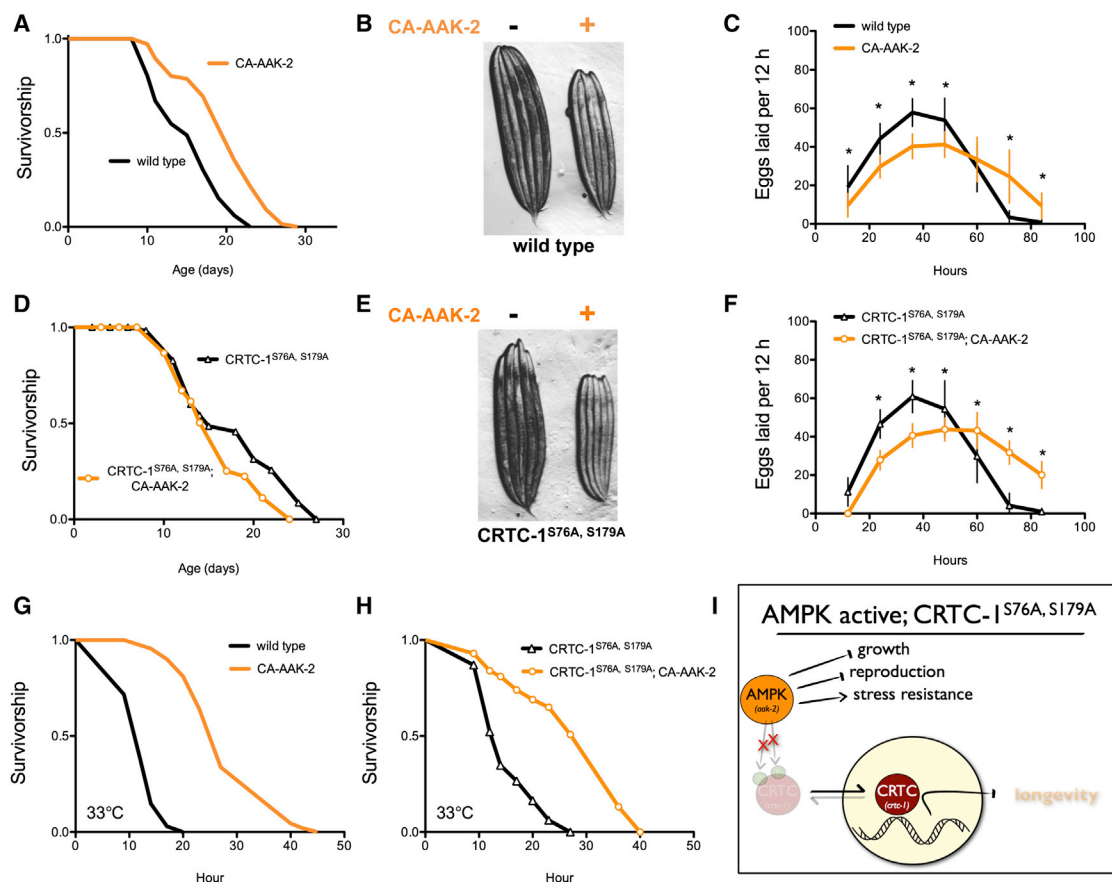


Figure 1. CRTC-1 Uncouples AMPK-Mediated Longevity from Other Pleiotropic Phenotypes

(A) AMPK activation (CA-AAK-2) extends lifespan in a wild-type *C. elegans* background. See Table S1 for lifespan statistics.

(B) CA-AAK-2 suppresses growth. Image of 5 wild-type (left) and 5 CA-AAK-2 (right) adult worms.

(C) Eggs laid per worm over successive 12 hr periods. Data are mean \pm SD for $n = 25$ –30 animals; * denotes $p < 10^{-4}$ via t test.

(D) CA-AAK-2 fails to promote longevity in a CRTC-1^{S76A, S179A} mutant background.

(E) CRTC-1^{S76A, S179A} does not suppress AMPK-mediated effects on growth.

(F) Eggs laid per worm over successive 12 hr periods (data are mean \pm SD for $n = 19$ –30 animals; * denotes $p < 10^{-4}$ via t test).

(G) and (H) Survival curves of AMPK and CRTC-1^{S76A, S179A} transgenic animals exposed to heat stress at 33°C. $n = 60$ –100 worms. $p < 10^{-5}$ via Log-rank (Mantel-Cox) analysis.

(I) CRTC-1 is a longevity-specific AMPK target that uncouples growth, reproduction, and stress resistance from lifespan extension.

To determine whether the transcriptional changes in metabolic genes ultimately alter metabolic function we performed metabolomic analyses. We measured organic acids, amino acids, and acylcarnitines, which represent metabolites of the major energy producing pathways, in CA-AAK-2 animals with and without CRTC-1^{S76A, S179A}. While there are few significant differences between CA-AAK-2 and CRTC-1^{S76A, S179A}, CA-AAK-2 in amino acids or acylcarnitines (Figures S2C and S2D, Table S4), the data show widespread differential regulation of TCA cycle intermediates (Figure 2E). Congruent with the changes observed at the transcriptional level, the TCA cycle intermediates exhibit a pattern consistent with altered mitochondrial metabolism being causal to AMPK/CRTC-1 regulation of longevity. Namely, TCA intermediates and associated organic acid levels are maintained or increased by AMPK activation, CRTC-1^{S76A, S179A} opposes these effects for several organic acids, including malate, citrate, and lactate (Figure 2E). These metabolomic data support a role

for AAK-2 and CRTC-1 in coordinating central metabolic processes and highlight a new role for CRTC-1 in mediating transcriptional links between AMPK status and mitochondrial metabolism. Although AMPK is a known sensor and regulator of mitochondrial function and biogenesis (Hardie et al., 2012), these data now specifically couple these processes to the role of AMPK in longevity assurance.

Transcriptional Regulation of Metabolism Is Required for AMPK and Calcineurin Longevity

To determine if the metabolic effects of CRTC-1 are causal to AMPK longevity, we searched for known alternative interventions that broadly regulate cellular metabolic processes to examine their effects on lifespan. Like AMPK, the nuclear hormone receptor and functional PPAR α ortholog, NHR-49, activates during low energy status such as fasting, and transcriptionally promotes genes required for mitochondrial function

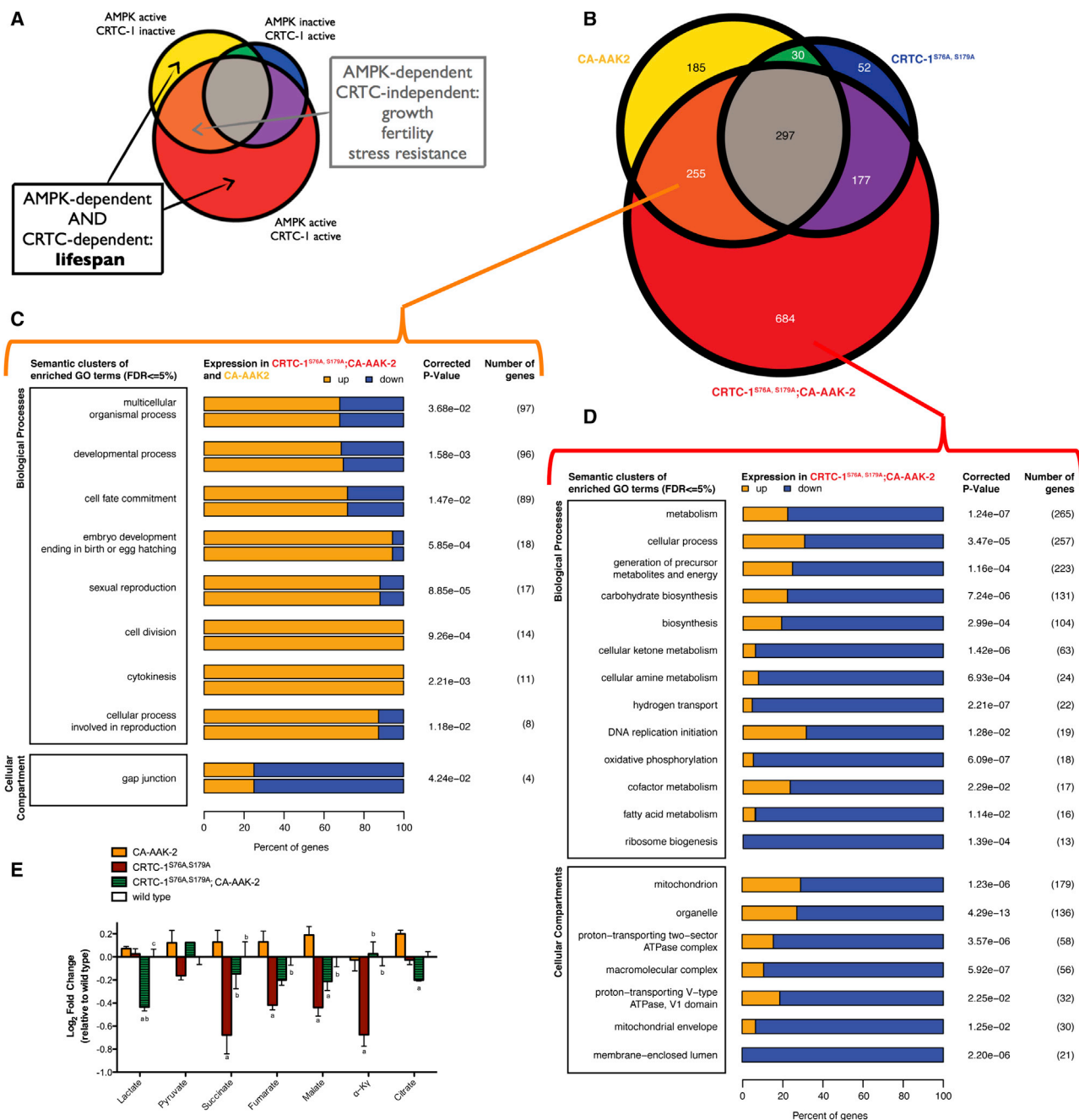


Figure 2. Leveraging CRTC-1 to Identify Longevity-Specific Processes Downstream of AMPK Reveals a Critical Role for Mitochondrial Metabolism

(A) Schematic Venn diagram illustrating how CRTC-1-specific gene expression filters AMPK-induced changes associated with longevity from those involved in other pleiotropic phenotypes.

(B) Venn diagram representing the number of differentially expressed (DE) genes identified through RNA-Seq analysis from each indicated genetic background relative to wild-type controls. See [Table S2](#) for complete list of DE genes.

(C and D) Clusters of enriched GO biological processes and cell compartments among the DE genes involved in CRTC-1-independent phenotypes (C, orange) or unique to the CRTC-1^{S76A, S179A}; CA-AAK-2 worms (D, red). Bars represent the percentage of genes within that category that are up- (orange) or downregulated (blue). The number of genes annotated within a cluster is tabulated, along with the smallest multiple-testing corrected p value for the observed enrichment attributed to a term within the cluster. See also [Figure S2](#) and [Table S3](#).

(E) Metabolomic analyses of transgenic strains to measure levels of organic acids (E), acylcarnitines, and amino acids ([Figure S2](#)). Two-way ANOVAs were performed with a Sidak multiple comparisons test after metabolite levels were normalized to total protein. Data are mean ± SEM of n = 2-5 replicates per metabolite in each group. ^ap ≤ 0.05 versus CA-AAK2, ^bp ≤ 0.05 versus CRTC-1^{S76A, S179A}, ^cp ≤ 0.05 versus CRTC-1^{S76A, S179A}; CA-AAK-2. See also [Table S4](#).

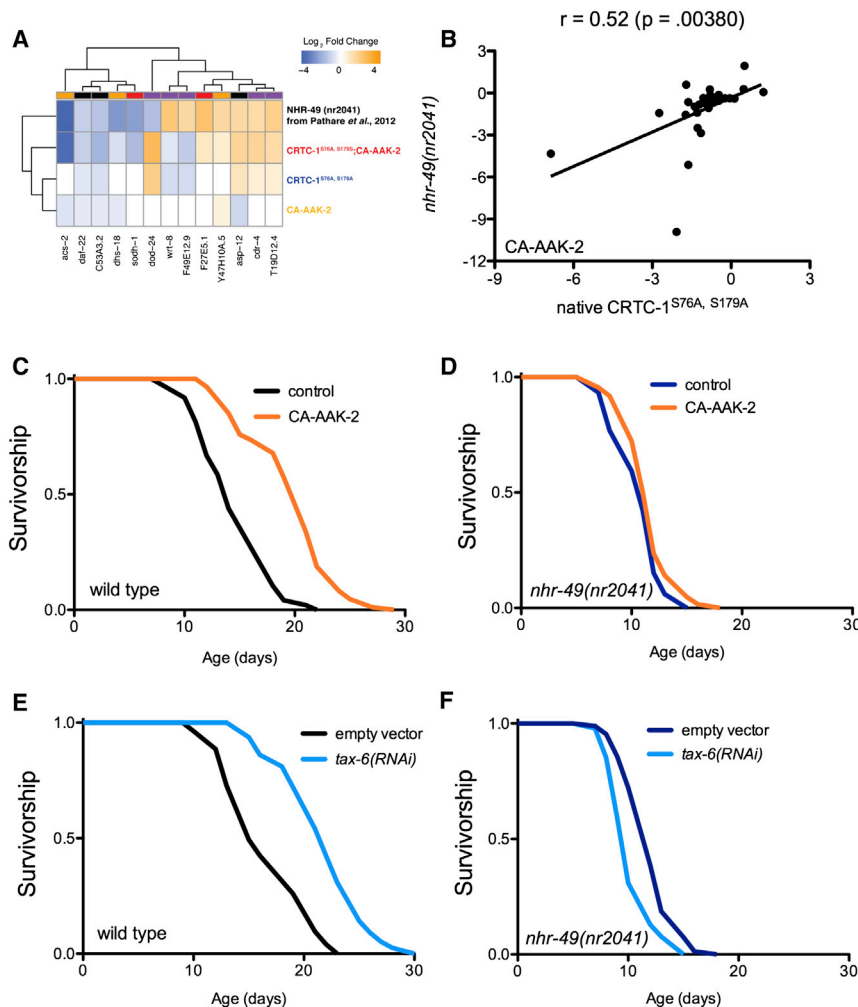


Figure 3. NHR-49 Is Required for AMPK- and Calcineurin-Mediated Longevity

(A) Heat map of genes differentially expressed in CRT-1^{S76A,S179A}, CA-AAK-2 and *nhr-49(nr2041)* worms, demonstrating significant overlap in gene expression patterns. See also Table S5.

(B) Mean mRNA expression levels (average log₂ of fold change relative to wild-type worms) of 29 metabolic genes. In a CA-AAK-2 background, native CRT-1^{S76A,S179A} (*crtc-1* promoter) correlates with whole-organism loss of NHR-49 (Pearson correlation coefficient, *r*), validating the comparison made in (A). Note *r* = 0.66; *p* ≤ 0.0001 after 10% winsorization of strong outliers. See Table S6.

(C) and (D) CA-AAK-2 extends lifespan in a wild-type background (C), but not in the absence of NHR-49 function (D). See Table S1 for lifespan statistics.

(E) and (F) *tax-6* RNAi extends lifespan in a wild-type background (E), but not in the absence of NHR-49 function (F). The genetic background in B–F is noted next to the origin.

(Pathare et al., 2012). We compared genes differentially expressed in CRT-1^{S76A,S179A}, CA-AAK-2 transgenic animals with genes previously reported to be differentially expressed in nematodes lacking functional *nhr-49* (Pathare et al., 2012). Of the 47 NHR-49-dependent genes identified by Pathare et al., we observe 30% overlap ($\chi^2 = 13.45$, *p* = 10^{−5}), suggesting that NHR-49 and CRT-1 coordinately regulate shared metabolic targets (Figure 3A; Table S5). We selected a candidate list of 29 metabolic genes, including genes regulated by CRT-1 from our RNA-Seq dataset and by NHR-49 from previously published data (Table S6), and validated the high degree of correlation between CRT-1 activation and NHR-49 loss of function in a CA-AAK-2 background relative to wild-type (Figure 3B; *p* < 0.01). When AMPK is activated, loss of *nhr-49* mirrors activation of CRT-1 to promote a transcriptional reprogramming of metabolic genes.

If transcriptional regulation of metabolism by CRT-1 is causal to AMPK lifespan extension, we hypothesized that AMPK should also fail to promote longevity in *nhr-49* mutants, since they recapitulate similar transcriptional changes in metabolic processes. In support of this hypothesis, an *nhr-49(nr2041)* deletion allele

suppresses lifespan extension via CA-AAK-2 (Figures 3C and 3D). Our previous work established that AMPK and calcineurin mediate longevity through a shared signaling pathway that converges on CRT-1. Calcineurin, a protein phosphatase, directly opposes AMPK by dephosphorylating and activating CRT-1. RNAi-mediated knockdown of *tax-6*, the catalytic subunit of calcineurin, mimics AMPK activation by increasing *C. elegans* lifespan in a CRT-1-dependent manner (Mair et al., 2011) and additionally activates expression of the NHR-49-dependent target, *acs-2* (Figure S3). Strikingly, *tax-6* RNAi also requires intact NHR-49 function to promote longevity (Figures 3E and 3F). These results suggest that AMPK/calcineurin signaling promotes a shift in metabolic programs by orchestrating the activity of opposing transcriptional effectors, CRT-1 and NHR-49, and that this metabolic switch is required for longevity.

CRTC-1 Acts through CREB in Neurons to Mediate Longevity

Both *aak-2* and *nhr-49* are expressed ubiquitously (Mair et al., 2011; Van Gilst et al., 2005) and are believed to function as cell-autonomous regulators of metabolism. In contrast, *crtc-1* expression is limited to the intestine and neurons in *C. elegans* (Mair et al., 2011). We reasoned that CRT-1 may directly regulate transcription of genes involved in metabolism in the intestine, one of the major organs of cellular metabolic activity and fat storage in *C. elegans*, and that this effect may be sufficient to systemically modulate longevity. To test this hypothesis, we expressed CRT-1^{S76A,S179A} from the *ges-1* promoter, limiting its expression to intestinal cells. Surprisingly, intestinal expression of CRT-1^{S76A,S179A} has no effect on *tax-6* RNAi-mediated

longevity (Figures 4A and 4B). Ruling out the intestine as the site of action, we examined the role of neuronal CRTC-1 in AMPK/calci- neurin-mediated longevity. Expressing CRTC-1^{S76A,S179A} from the pan-neuronal *rab-3* promoter (Figure 4C, inset) fully sup- presses lifespan extension by both *tax-6* RNAi (Figure 4C) and AAK-2 activation (Figures 4D and 4E). Upon finding that selective CRTC-1 activation in neurons is sufficient for its effects on life- span, we asked whether activating AMPK in select tissues is also sufficient to promote longevity. We expressed CA-AAK-2 from pan-neuronal, muscle, and intestinal-specific promoters. AMPK activation is not sufficient for longevity in any of the individ- ual tissues tested (Figure S4A), suggesting this longevity mecha- nism in *C. elegans* requires local AMPK-mediated programming of mitochondrial function in multiple tissues. Taken together these results indicate that CRTC-1 activity in neurons cell nonau- tonomously modulates AMPK/calci- neurin-mediated longevity. Moreover, signals downstream of neuronal CRTC-1 dominantly override the effects AMPK exerts locally in peripheral tissues.

CRTCs lack DNA-binding activity and depend on partner tran- scription factors for recruitment to DNA in order to stimulate gene transcription (Altarejos and Montminy, 2011). Though first identi- fied as CREB modulators, CRTCs also bind and regulate other bZIP transcription factor family members. To determine whether the effects of neuronal CRTC-1 on aging occur via CREB, we tested whether CREB was necessary for longevity suppression by CRTC-1^{S76A,S179A}. In animals lacking CRH-1, the *C. elegans* CREB ortholog, CRTC-1^{S76A,S179A} expressed under its endoge- nous promoter no longer suppressed CA-AAK-2-mediated longevity (Figures 4F and 4G). Additionally, neuronal expression of CRTC-1^{S76A,S179A} in *crh-1* null animals had no effect on life- span extension by *tax-6* RNAi (Figures 4H and 4I). Lifespan extension via AMPK/calci- neurin therefore requires inhibition of the CRTC-1/CRH-1 transcriptional complex in neurons.

Neuronal CRTC-1 Cell Nonautonomously Regulates Metabolic Genes

Since CRTC-1 regulates longevity through a systemic metabolic program (Figure 2) and neuron-limited CRTC-1 activation is suf- ficient to suppress longevity, we sought to determine if neuronal CRTC-1 is sufficient to produce the lifespan-related effects on metabolic transcription. Analyzing the same panel of 29 meta- bolic genes used previously (Figure 3B), we found that limiting CRTC-1^{S76A,S179A} expression to neurons recapitulates the ef- fects on peripheral metabolic genes seen in animals expressing CRTC-1^{S76A,S179A} from its native promoter (Figure 4J; $p < 0.0001$). Therefore, similarly to lifespan, CRTC-1 regulates meta- bolism cell nonautonomously from neurons. Finally, we deter- mined that neuron-specific activation of CRTC-1 mimics genetic deletion of *nhr-49* regarding peripheral expression of genes involved in cellular metabolism (Figure 4K; $p < 0.01$). Despite the presence of CA-AAK-2 in every background, AAK-2 acti- vated animals alone exhibit no correlation in gene expression with any of the double transgenics, indicating these transcrip- tional effects are all attributable to NHR-49 and CRTC-1 (Figures S4B–S4D; $p > 0.05$). Taken together, the striking overlap between gene expression profiles (Figure 4L; Table S6) reveals an antagonistic relationship between metabolic programs regu- lated by NHR-49 and neuronal CRTC-1.

NHR-49 Regulates Metabolism and Lifespan Cell Nonautonomously

NHR-49 has previously been characterized as a functional ortho- log of mammalian PPAR α , as *nhr-49* mutants fail to activate mitochondrial fatty acid oxidation (FAO) genes during starvation (Van Gilst et al., 2005). However, whether this effect is cell auton- omous is unknown, as the NHR-49 DNA-binding motif has not been determined and direct targets of NHR-49 remain elusive. To determine whether NHR-49 can mediate lifespan and meta- bolism cell nonautonomously, we selectively restored NHR-49 function to neurons in an *nhr-49* null background by driving expression with the *rab-3* promoter. As previously described, *C. elegans* subjected to 24 hr of fasting show strong upregulation of a key gene involved in beta-oxidation, acyl-CoA synthetase (ACS)-2, which is dependent on *nhr-49* (Figure 5A). Supporting a role for NHR-49 beyond cell-autonomous regulation of meta- bolic gene expression, neuronal rescue of NHR-49 is sufficient to restore both basal *acs-2* expression (Figure 5A) and the induc- tion of *acs-2* by fasting (Figure 5B). Since mRNA measurements were obtained using whole-animal preparations, we generated animals expressing GFP under control of the *acs-2* promoter to examine tissue-specific induction. Fasting for 24 hr induces expression of GFP in multiple tissues, including pharynx, mus- cle, and intestine (Figure 5C). This induction is abrogated by loss of *nhr-49* (Figure 5D). Remarkably, neuronal expression of *nhr-49* is sufficient to restore induction of *acs-2* in both neurons and distal tissues, including muscle and intestine, but not pharynx (Figure 5E).

Induction of *acs-2* expression in multiple tissues lacking NHR-49 suggests alternative transcription factors might respond to signals downstream of neuronal CRTC-1. To identify transcriptional regulators in this pathway, we revisited our RNA- Seq dataset and performed Hypergeometric Optimization of Motif EnRichment (HOMER) analysis of the ‘CRTC-1-dependent genes’ (Figure 2B, red section). We identified a motif with consensus TGATAACG or CGTTATCA enriched in the putative promoter regions of genes downstream of AMPK/CRTC-1 ($p = 1e-25$, found in 38% of targets versus 21% of background) (Figure S5A). The motif strongly resembles the GATA-like DAE (DAF-16 Associated Element), recently identified as the binding site for PQM-1 (Tepper et al., 2013). modENCODE ChIP-seq data also suggests that both DAF-16 and PQM-1 bind the *acs-2* promoter directly. To determine whether DAF-16 can regulate expression of *acs-2*, we examined the effect of fasting on our *acs-2::GFP* reporter under control conditions, and in animals subjected to RNAi for *daf-16*, along with two other transcription factors known to mediate DR longevity, *skn-1* and *pha-4*. While inhibition of *skn-1* and *pha-4* does not alter induction of *acs-2* by fasting, *daf-16* RNAi significantly suppresses *acs-2* induction (Figures S5B and S5C). These data therefore suggest that DAF- 16 and/or PQM-1 might be acting downstream of the neuronal CRTC-1 signal to modulate metabolic gene expression.

Given the ability of NHR-49 to cell nonautonomously regulate metabolic genes, we next asked whether, like CRTC-1, NHR-49 mediates longevity through its effects in neurons. Restoring NHR-49 function in neurons exclusively was sufficient to restore lifespan extension via both *tax-6* RNAi (Figures 5F–5H) and AMPK activation (Figures 5I–5K) in *nhr-49* deletion mutants.

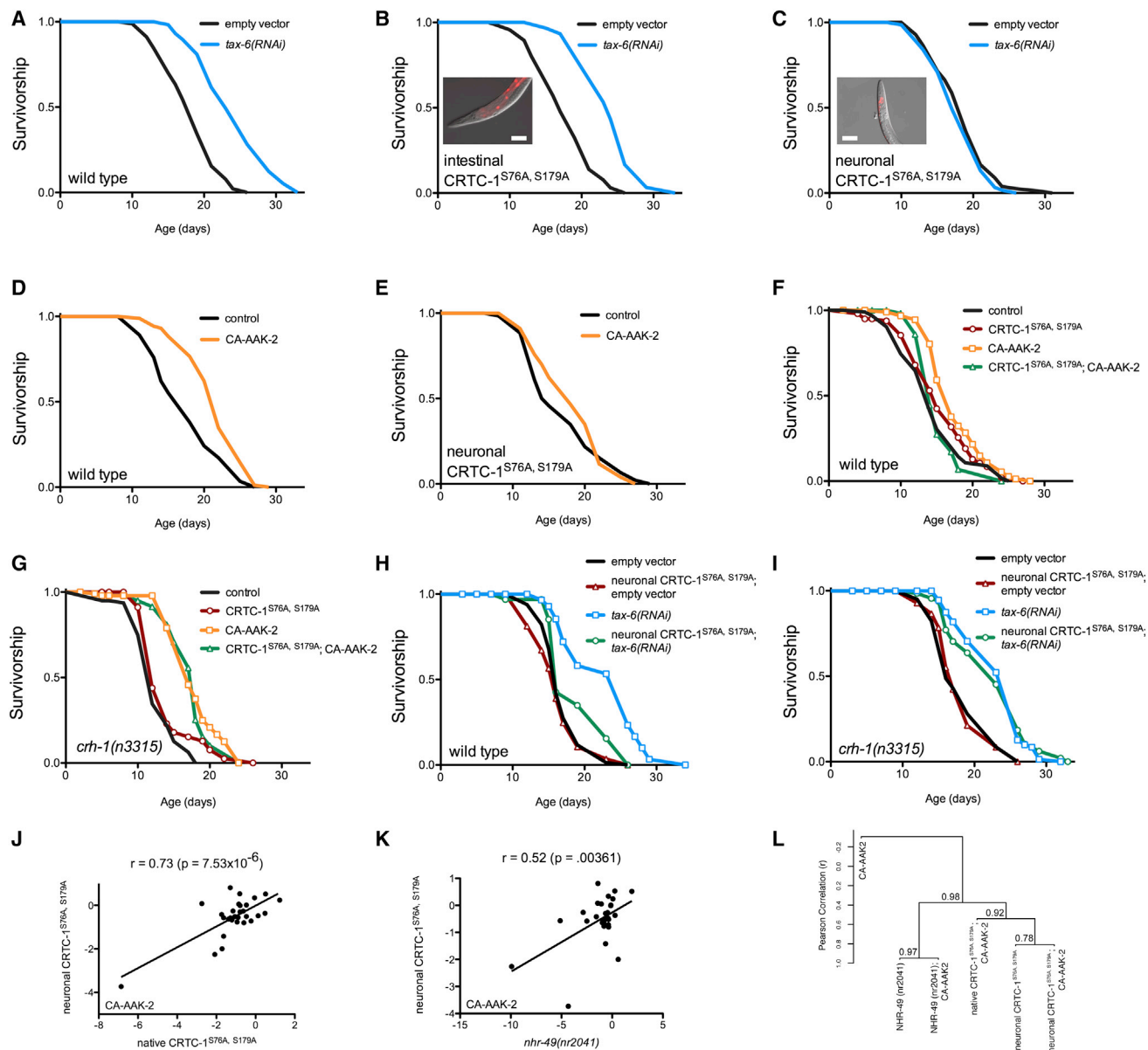


Figure 4. Neuronal CRTC-1/CRH-1 Activation Suppresses Longevity Downstream of AMPK and Calcineurin Signaling and Cell Non-autonomously Regulates Metabolic Transcription

(A) *tax-6* RNAi increases longevity. See Table S1 for lifespan statistics. The genetic background in A – I is noted next to the origin.

(B) Intestine-specific CRTC-1^{S76A, S179A} (*ges-1* promoter) fails to suppress *tax-6* RNAi longevity. Inset: image of intestine-specific tdTOMATO-tagged CRTC-1^{S76A, S179A}; scale bar, 100 μ m.

(C) Neuronal-specific (*rab-3* promoter) CRTC-1^{S76A, S179A} fully suppresses *tax-6* RNAi-mediated longevity. Inset: image of neuron-specific tdTOMATO-tagged CRTC-1^{S76A, S179A}; scale bar, 100 μ m.

(D and E) CA-AAK-2 extends lifespan in a wild-type background (D), but neuronal CRTC-1^{S76A, S179A} suppresses AMPK-mediated longevity (E).

(F and G) CA-AAK-2 extends lifespan and this effect is blocked by expressing CRTC-1^{S76A, S179A} from its native promoter (F). In *crh-1* null mutants, CRTC-1 activation fails to suppress AMPK-mediated longevity (G).

(H and I) Neuron-specific activation of CRTC-1^{S76A, S179A} suppresses longevity mediated by *tax-6* RNAi (H), but neuronal CRTC-1^{S76A, S179A} requires intact *crh-1* function to mediate its effects on aging (I).

(J and K) Expression levels of 29 metabolic genes in CA-AAK-2 animals reveal that the effects of neuron-specific CRTC-1^{S76A, S179A} correlate strongly with expression of CRTC-1^{S76A, S179A} from its native promoter (J); and neuron-specific CRTC-1^{S76A, S179A} activation correlates with the transcriptional effects of loss of NHR-49 function (K). r and p values were derived by Pearson correlation. See also Table S6.

(L) Dendrogram summarizing similarities in metabolic gene expression between AMPK, CRTC-1 and NHR-49 mutants. Strains were clustered by their pair-wise Pearson correlations using Ward's minimum variance method. Vertical heights of branches indicate the degree of correlation (r ; y axis). Multiscale bootstrap resampling p values on each branch were calculated via pvclust R package [http://www.sigmath.es.osaka-u.ac.jp/shimo-lab/prog/pvclust/].

However, unlike the effects of CRTC-1 on AMPK/calcieneurin-mediated longevity, which is specific to neurons, the role of NHR-49 is more complex, as intestinal rescue can also partially reverse suppression of *tax-6* RNAi lifespan in *nhr-49* deletion mutants and is sufficient to restore *acs-2* induction exclusively in intestinal cells (Figures S6A and S6B). Additionally, while *nhr-49* overexpression in intestine does not affect *C. elegans* longevity, overexpression of *nhr-49* in neurons is sufficient to extend lifespan, further highlighting tissue-specific functions (Figures S6C and S6D).

Neuronal CRTC-1 Cell Nonautonomously Regulates Mitochondrial Dynamics

Recent studies of mitochondrial dynamics suggest that remodeling of the mitochondrial network itself may impact metabolic function (Liesa and Shirihai, 2013), and loss of NHR-49 has been shown to disrupt mitochondrial morphology and function (Pathare et al., 2012). Given that neuronal CRTC-1 and NHR-49 antagonistically regulate AMPK/calcieneurin-mediated longevity and metabolic processes, we explored whether changes in mitochondrial architecture were involved in the metabolic reprogramming and longevity by AMPK/CRTC-1. To observe the mitochondrial network directly in distinct tissues, we employed nematodes expressing mRFP targeted to the outer mitochondrial membrane via fusion to TOM20. Typically, the mitochondria of muscle cells of young (day 1) adult worms are fused and tubular, running parallel among the myofilaments (Figure 6A). Activation of CRTC-1 exclusively in neurons of young adult worms, however, results in significant fragmentation of the mitochondrial network in muscle cells, demonstrating a cell-nonautonomous role for CRTC-1 in regulating mitochondrial dynamics (Figure 6B). This effect is consistent with the opposing transcriptional effects of NHR-49 and neuronal CRTC-1, as loss of *nhr-49* also causes mitochondrial fragmentation and altered morphology (Figures 6C–6E). To quantify the degree of fragmentation in these animals, we determined the ratio of mitochondrial area to perimeter in muscle cells of neuronal CRTC-1^{S76A,S179A} mutants and found a 56% reduction relative to control animals (Figure 6F; $p < 0.0001$). The area of muscle cells occupied by mitochondria was also decreased 30% upon neuronal CRTC-1 activation (Figure 6G; $p < 0.0001$), supporting CRTC-1-mediated suppression of mitochondrial function observed at the transcriptional and metabolomic levels (Figure 2).

CRTC-1 Mediates Lifespan via a Catecholamine Signal

Having determined neuronal CRTC-1 mediates longevity and mitochondrial function cell nonautonomously, we reasoned it might regulate a signal that relays energy status from neurons to coordinate aging and metabolism in peripheral tissues. Monoamine signals, e.g., dopamine and serotonin, act in nutrient-sensing pathways to regulate behavioral and peripheral metabolic changes conserved from nematodes to humans (Ashrafi, 2007). We therefore examined whether monoamine signaling might provide a potential mechanism by which neuronal CRTC-1 could regulate longevity and mitochondrial dynamics. Monoamines are secreted via exocytosis in dense core vesicles (DCVs), which in *C. elegans* requires the Ca^{2+} -dependent activator protein for secretion (CAPS), UNC-31 (Grishanin et al.,

2004). Null mutation of *unc-31* suppresses *acs-2* expression, as determined by our *acs-2P::GFP* reporter strain and qRT-PCR (Figures S7A–S7C), suggesting secreted signals within DCVs may mediate distal metabolic gene regulation.

In our RNA-Seq analysis we identified multiple enzymes involved in the synthesis of biogenic amines that were differentially mediated by AMPK and CRTC-1 (Figure 7A). We further examined the genes involved in monoamine synthesis by qRT-PCR and identified a catecholamine biosynthetic enzyme, tyramine beta-hydroxylase (TBH)-1, among the genes regulated by CRTC-1 that couples to AMPK longevity (Table S2). Downregulation of *tbh-1* expression by AMPK activation is attenuated by CRTC-1^{S76A,S179A} (Figure 7B). Acting in a pathway with tyrosine decarboxylase (TDC)-1, TBH-1 catalyzes the synthesis of octopamine, which functions as the invertebrate noradrenaline equivalent (Figure 7C). Analysis of the *tdc-1* and *tbh-1* promoters revealed putative cAMP response elements (not shown), suggesting that CRTC-1/CRH-1 may directly regulate transcription of these genes. As previously reported, expressing GFP downstream of the *tbh-1* promoter results in expression exclusively in two octopaminergic RIC neurons (Alkema et al., 2005), notably CRTC-1 also localizes to RIC neurons (Figure 7D) and thus may be capable of directly regulating octopamine signaling. We therefore hypothesized that octopamine may play a role in intercellular AMPK/CRTC-1 longevity signaling.

If octopamine mediates neuronal CRTC-1 signaling to other tissues, we reasoned it might be sufficient to generate the mitochondrial and metabolic phenotypes observed upon neuronal CRTC-1 activation. To test this hypothesis, we cultured nematodes expressing the mitoRFP reporter in the presence of exogenous octopamine. Strikingly, octopamine treatment elicits a similar degree of mitochondrial fragmentation in *C. elegans* muscle to that observed when CRTC-1 is activated neuronally, further suggesting that octopamine signaling may mediate CRTC-1 regulation of metabolism to peripheral tissues (Figures 7E–7G). In direct support of octopamine as a relay signal, *tax-6* RNAi increases expression of *acs-2*, but this effect is blunted in animals lacking TDC-1 or TBH-1 (Figure S7D).

To define the functional requirement of octopamine signaling in the modulation of aging by the AMPK/CRTC-1/NHR-49 pathway, we tested whether the suppression of longevity by neuronal CRTC-1^{S76A,S179A} or *nhr-49* deletion required either TDC-1 or TBH-1. As shown previously, AMPK activation robustly increases lifespan of wild-type animals and this effect is suppressed in worms expressing neuronal CRTC-1^{S76A,S179A} (Figure 7H) or *nhr-49(nr2041)* (Table S1). While suppression of lifespan by *nhr-49* deletion is independent of octopamine signaling (Figures S7E and S7F), the ability of neuronal CRTC-1^{S76A,S179A} to suppress longevity is completely abolished in animals harboring null mutations in either *tdc-1* (Figure 7I) or *tbh-1* (Figure 7J), both of which lack octopamine (Alkema et al., 2005). Confirming these findings, neuronal CRTC-1^{S76A,S179A} suppresses longevity mediated by *tax-6* RNAi (Figure 7K), and this suppression requires TDC-1 (Figure 7L) and TBH-1 (Figure 7M) function. The ability of CRTC-1 to regulate aging in *C. elegans* therefore requires functional octopamine signaling. Together these results suggest that neuronal CRTC-1 modulates AMPK/calcieneurin-mediated longevity and metabolism via an

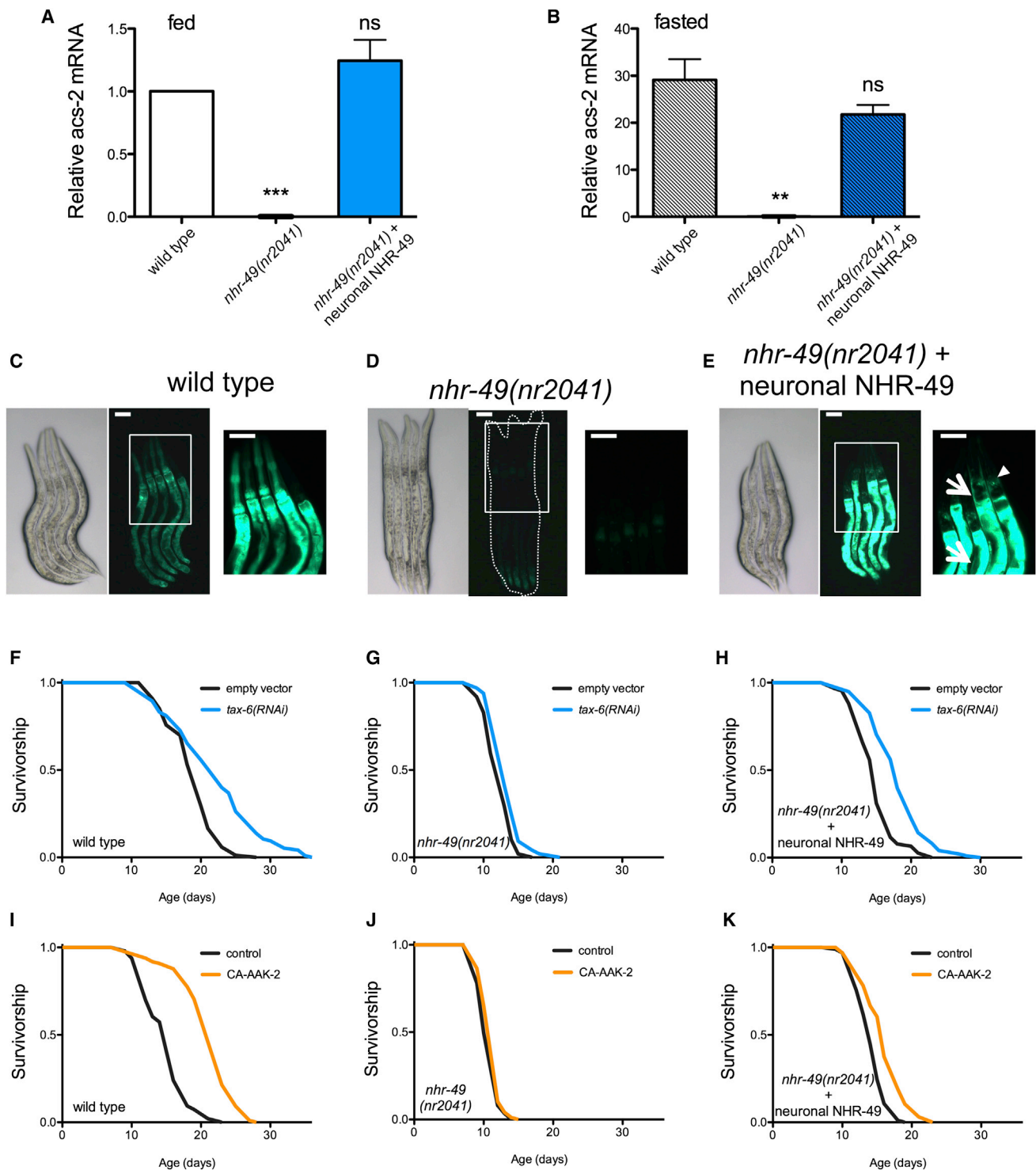


Figure 5. NHR-49 Regulates Mitochondrial Metabolism and Longevity Cell Nonautonomously from Neurons

(A) and (B) Analysis of *acs-2* transcript levels by RT-PCR in L4/young adult worms fed (A) and fasted 16 hr (B). Data are mean \pm SEM of 3-4 independent experiments. By 1-sample (A) or 2-sample (B) t test relative to fed wild-type animals, *** denotes $p < 0.001$; ** = $p < 0.01$; ns = $p > 0.05$.

(C-E) Brightfield (left) and fluorescence (middle and right) imaging of L4-stage 16 hr fasted worms expressing GFP driven by the *acs-2* promoter. (C) Fasting activates the *acs-2* promoter ubiquitously in *C. elegans* (middle), and higher magnification reveals strongest expression in the intestine and pharynx (right).

(legend continued on next page)

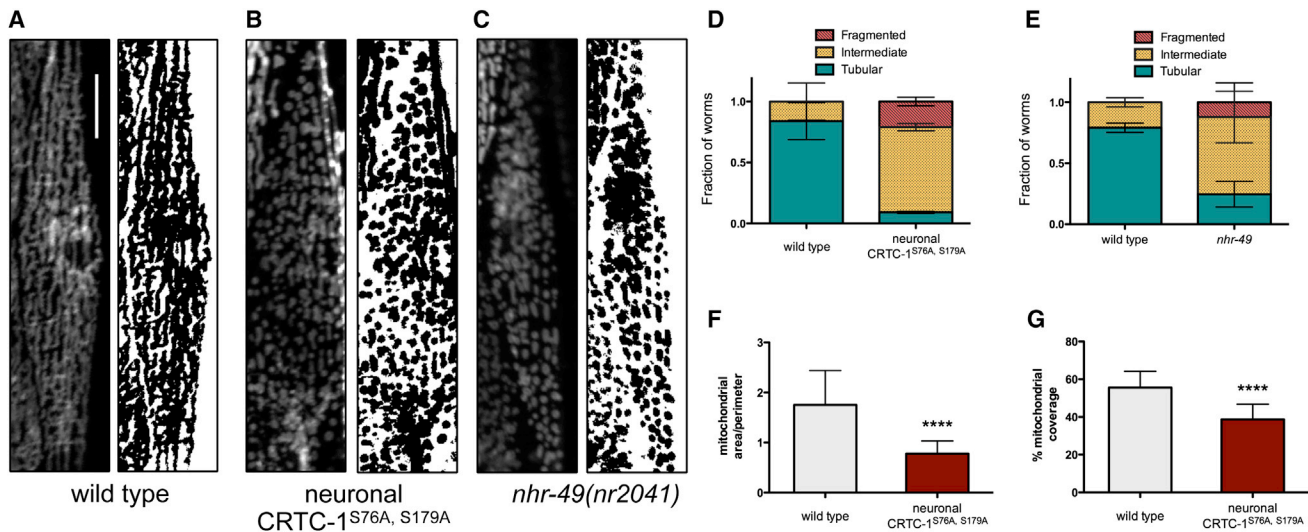


Figure 6. Neuronal CRTC-1 and NHR-49 Regulation of Mitochondrial Dynamics Mirrors Their Respective Roles in Longevity

(A–C) Fluorescence imaging (left) and binary representations (right) of mitochondrial networks in body wall muscle cells of day 1 adult worms. Neuronal CRTC-1^{S76A, S179A} (B) and *nhr-49* loss-of-function (C) induce fragmentation of the mitochondrial network in muscle cells relative to wild-type (A). Scale bars represent 20 μm.

(D and E) Quantification of neuronal CRTC-1^{S76A, S179A} (D) and *nhr-49* loss-of-function (E) dependent mitochondrial fragmentation in a population of worms demonstrates loss of tubular morphology (mean ± SD of n = 3 groups of 10–17 worms; p = 0.001 by t test).

(F) Quantification of the ratio between mitochondrial area and perimeter (Mean ± SD from muscle cells of 32 worms; p < 0.0001 by t test).

(G) Neuronal CRTC-1^{S76A, S179A} activation decreases the area of muscle cells occupied by mitochondria (Mean ± SD from muscle cells of 32 worms; p < 0.0001 by t test).

octopamine signal. Moreover, this cell-nonautonomous signal is dominant over the cell-autonomous effects of AMPK in peripheral tissues (Figure S7G).

DISCUSSION

These data challenge current thinking regarding strategies to translate the link between energetics and longevity for therapeutics; perception and cell-nonautonomous communication of energy status in neurons can override direct activation of pro-longevity factors in distal tissues and might therefore be targeted for healthy aging. Although AMPK and PPARs are both targeted peripherally to promote metabolic homeostasis in humans (Hardie et al., 2012; Wahli and Michalik, 2012), both can affect metabolism cell nonautonomously from the CNS (Bantubungi et al., 2012; Kocalis et al., 2012; Minokoshi et al., 2004). To date, the relative contributions of these local and distal effects to healthy aging have not been explored. Here, we demonstrate a cell-nonautonomous role these metabolic regulators play in coordinating energetics and longevity via effects on neuronal catecholamine signaling. AMPK locally and cell autonomously promotes remodeling of mitochondrial metabolic networks to increase longevity; however, AMPK must also inactivate CRTC-1-dependent transcription in neurons to systemically and cell nonautonomously

generate a permissive transcriptional landscape for its local metabolic programming. Critically, these cell-nonautonomous signals dominantly impact longevity, irrespective of AMPK activation and energetic state in receiving cells. Intriguingly, both neuronal activation of CRTC-1 and octopamine supplementation promote mitochondrial network fragmentation, suggesting dynamics of the mitochondrial network can be shaped from a distance and are critical for the ability of AMPK to promote longevity. However, this study also raises key questions going forward, including the sufficiency of the neuronal signal for longevity assurance, and how these mechanisms might translate to mammalian systems and therapeutics designed to promote metabolic homeostasis. Specifically, perhaps treatments targeting peripheral metabolic effectors to promote healthy aging will have reduced efficacy if cell-nonautonomous CNS signals remain discordant.

Although AMPK, PPARs, and CRTCs are key peripheral metabolic regulators, all have emerging roles in neuroendocrine control of organismal metabolism that may become dysfunctional with age or obesity. Early studies of CRTCs focused on regulation of glucose metabolism in the mammalian liver, but there are three CRTC family members in mammals, two of which are expressed in the nervous system. Though less studied, recently elucidated roles of neuronal CRTCs include regulating

(D) *nhr-49* mutants fail to activate *acs-2*. (E) Neuron-limited rescue of NHR-49 restores *acs-2* levels in neurons (arrowhead) and peripheral tissues (arrows). Boxes outline areas magnified in the right panels. Scale bars represent 50 μm.

(F–I) Survival analysis demonstrating that *tax-6* RNAi (F) and CA-AAK-2 (I) extend lifespan in wild-type worms, but not worms lacking *nhr-49* (G, J). Restoring NHR-49 function selectively to neurons via the *rab-3* promoter rescues *tax-6* RNAi- (H) and CA-AAK-2-mediated longevity (K). Common genetic backgrounds are indicated next to the origin. See also Figure S5 and Table S1 for lifespan statistics.

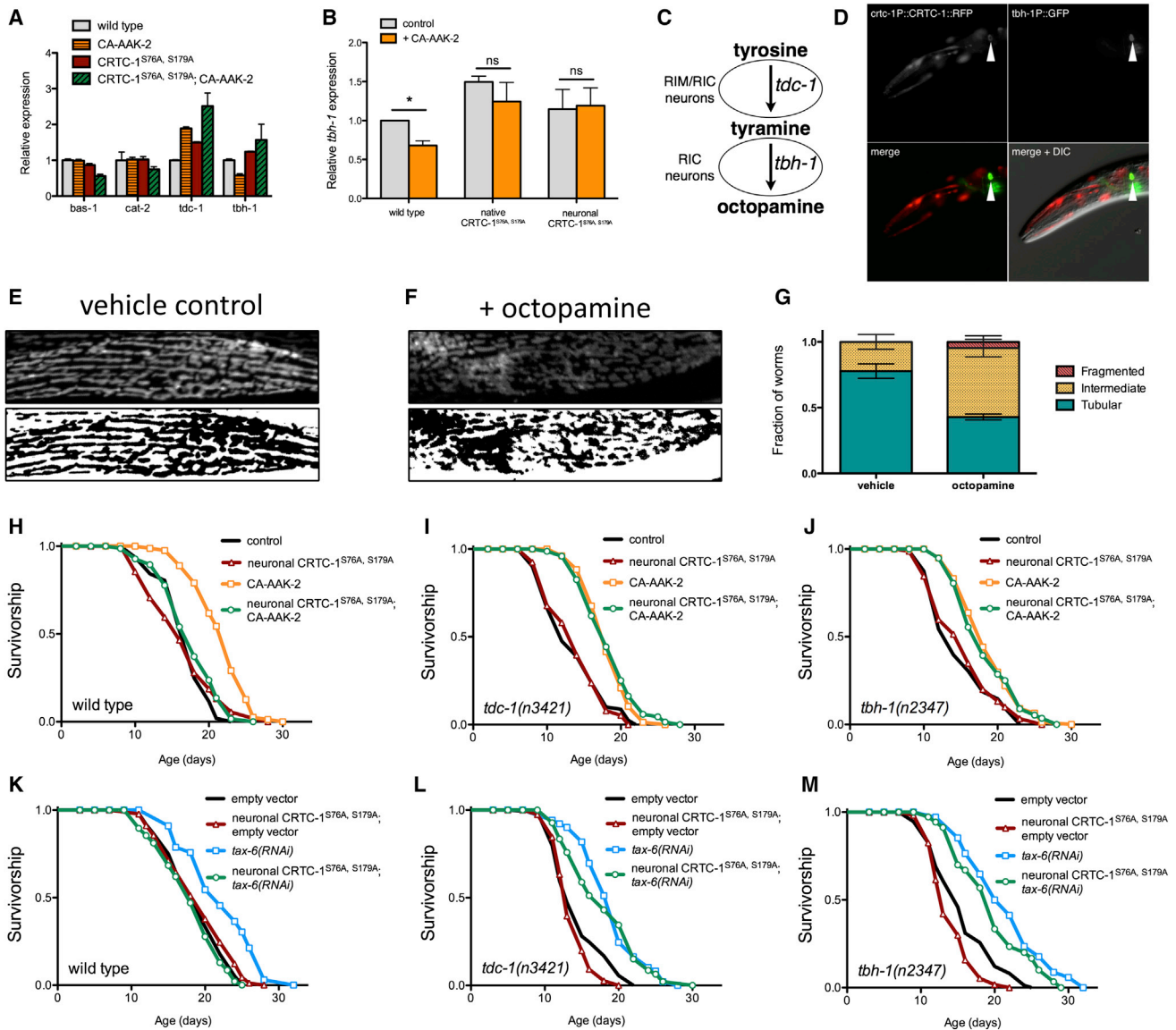


Figure 7. Neuronal CRTC-1 Regulates Longevity and Mitochondrial Function Cell Nonautonomously through Catecholamine Signaling

(A) Normalized read counts for enzymes involved in synthesis of biogenic amines from the RNA-Seq analysis (see also Table S2).

(B) qRT-PCR validating AMPK/CRTC-1 regulation of *tbh-1* transcript levels (Mean \pm SEM of mRNA levels extracted from 2–4 samples of 50–100 animals; * denotes $p < 0.05$ by t test).

(C) The biosynthetic pathway of octopamine.

(D) Fluorescence imaging of a worm co-expressing CRTC-1::tdTOMATO from the native *crtc-1* promoter (top left) and GFP driven by the *tbh-1* promoter reveals CRTC-1 expression in octopaminergic RIC neurons.

(E and F) Fluorescence imaging (top) and binary representations (bottom) of the mitochondrial network in muscle cells of animals vehicle-treated (water) or grown on media with 5 mM octopamine (F).

(G) Classifying worms by their mitochondrial morphology reveals a 45% decline in the fraction of worms with tubular mitochondria treated with octopamine versus control ($p < 0.001$ by t test; mean \pm SD of $n = 3$ samples of 11–19 worms).

(H–M) Survival curves demonstrating that neuron-specific activation of CRTC-1^{S76A, S179A} suppresses both AMPK- (H) and calcineurin-mediated (K) lifespan extension. However, neuronal CRTC-1^{S76A, S179A} has no effect on AMPK or calcineurin-mediated longevity in animals lacking functional *tdc-1* (I, L) or *tbh-1* (J, M). Genetic backgrounds are noted next to the origin. See Table S1 for lifespan statistics.

expression of peptide signals and metabolic homeostasis in the periphery. Deletion of CRTC1, which is expressed primarily in the brain in mammals, results in hyperphagia and obesity in mice (Altarejos et al., 2008; Breuillaud et al., 2009). More recently,

knockout of TRPV1 pain receptors was shown to both promote metabolic fitness and extend lifespan through effects in mouse sensory neurons (Riera et al., 2014). Interestingly, TRPV1 mutant mice exhibit nuclear exclusion of CRTC1 and reduced

expression of a neuropeptide important for regulating glucose homeostasis. Although the requirement of neuronal CRT1 inhibition for the longevity effects associated with TRPV1 loss of function in mice remains untested, our results point to a potentially conserved, neuronally mediated mechanism by which CRTCs regulate systemic metabolic homeostasis and impact the aging process in worms and mice.

AMPK cell autonomously regulates numerous physiological processes known to play roles in aging, including autophagy, protein synthesis, mitochondrial biogenesis, and both lipid and glucose metabolism (Burkewitz et al., 2014). Our data indicate mitochondrial metabolism is causally associated with AMPK longevity. Moreover, they suggest that AMPK regulation of both longevity and metabolism can be divided into two components: acute remodeling of metabolic pathways through direct regulation of enzymatic activity, and long-term remodeling of cell function via transcriptional reprogramming. Surprisingly, the transcriptional effects of AMPK are induced via cell-nonautonomous signals that override local enzymatic effects; CRT1 transcription in neurons suppresses lifespan despite AMPK being constitutively active in all tissues. Cunningham et al. (2014) recently identified a cell-nonautonomous role for neuronal AMPK in modulating peripheral lipid storage in nematodes, which supports cell-nonautonomous effects of AMPK/CRTC on metabolism. The role of AMPK in the central regulation of peripheral metabolism is conserved in mammals; AMPK integrates hormonal signals in the hypothalamus to control energy homeostasis, satiety, and metabolism (Minokoshi et al., 2004). Further, in response to changes in glucose levels, AMPK regulates CRT2 activity in the murine hypothalamus to modulate insulin signaling via IRS2 (Lerner et al., 2009). Communication between central and peripheral AMPK activity and its effect on metabolic homeostasis and aging in other organisms will be an exciting area for future research. While expressing truncated CA-AAK-2 in individual tissues of *C. elegans* in our study failed to promote longevity, work in *Drosophila* has shown that overexpressing wild-type AMPK in muscle or fat body (Stenesen et al., 2013) or activated AMPK mutants in brain or gut (Ulgherait et al., 2014) is sufficient to extend lifespan. Differential effects seen in *C. elegans* and *Drosophila* may be due to methods employed to generate tissue-specific strains. Moving forward, more work is needed to better elucidate how tissue-specific roles of AMPK coordinate to control longevity across different model systems.

Like AMPK and CRTCs, PPAR family transcription factors are best known for their primarily cell-autonomous roles in regulating metabolism, including lipid uptake, storage, and oxidation. Here, we demonstrate that the proposed worm PPAR α , NHR-49, acts antagonistically to CRT1/CREB, regulating the shift in metabolic and mitochondrial programming, and that neuronal *nhr-49* is sufficient for AMPK-mediated longevity (Figure 5). Notably, novel PPAR functions in the mammalian brain have also begun to emerge. The thiazolidinedione (TZD) class of anti-diabetic drugs is associated with weight gain, and two complementary studies identified brain PPAR γ as the critical mediator of TZD-induced effects on food intake, thermogenic energy expenditure, and peripheral glucose metabolism (Lu et al., 2011; Ryan et al., 2011). In addition, PPAR α null mice show increases in glucose turnover,

body weight, and adipogenesis that are not rescued by restoring hepatic PPAR α function. Pharmacologically activating PPAR α in the brain of these mice, however, decreases glucose usage in peripheral tissues (Knauf et al., 2006). How PPARs and NHR-49 function in neurons to systemically regulate metabolic homeostasis with age remains unknown and is an important scope for future work.

An exciting key finding of this study is the novel role of octopamine, the invertebrate equivalent to the catecholamine (nor)adrenaline, as a signal communicating energetic state between neuronal AMPK/CRTC-1 and the periphery to modulate longevity (Figure 7). Interestingly, there is precedent for both AMPK and CRTCs in the regulation of analogous bioamine pathways in mammals. In mice, AMPK α 2 suppresses sympathetic catecholamine release (Violet et al., 2003), while CRT1 enhances monoamine signaling in the prefrontal cortex (Violet et al., 2003). However, it remains unclear whether octopamine is acting as a neurotransmitter or a neuroendocrine signal to mediate longevity in *C. elegans*. Octopamine and 5-HT were recently shown to act through a positive regulatory loop in neurons to promote release of an unidentified endocrine factor capable of activating the nuclear hormone NHR-76 to regulate lipid oxidation in the *C. elegans* intestine (Noble et al., 2013). That at least 2 nuclear hormone receptors (NHR-49 and NHR-76) act downstream of octopamine suggests that perhaps octopamine regulates the release of a lipophilic hormone. Alternatively, given our finding that DAF-16/FOXO may be involved in metabolic transcription downstream of neuronal CRT1, octopamine may regulate the secretion of specific insulin-like peptides. Beyond serving as a signaling molecule between neurons, octopamine could also act as an endocrine molecule itself. *C. elegans* possesses three putative octopamine receptors, *ser-3*, *ser-6*, and *oct-1*, whose expression outside the nervous system has not been extensively examined. Interestingly, a small-molecule screen for drugs capable of extending *C. elegans* lifespan identified a molecule that was shown to be an antagonist of the SER-3 receptor (Petrascheck et al., 2007). Future studies characterizing the respective roles of each octopamine receptor will be enlightening in understanding how octopamine elicits metabolic and longevity-related responses in the periphery.

Although our studies point toward remodeling of mitochondrial metabolism as being required for AMPK longevity, they do not preclude a role for other cellular processes. AMPK and CRTCs are known regulators of autophagy (Egan et al., 2011; Seok et al., 2014), and autophagy is required for lifespan extension by AMPK activation in *Drosophila* (Ulgherait et al., 2014) and calcineurin inhibition in *C. elegans* (Dwivedi et al., 2009). Highlighting the role of inter-tissue communication in AMPK longevity, tissue-specific activation of AMPK in the fly promotes systemic tissue homeostasis via the autophagic effector, Atg1, which subsequently and cell nonautonomously promotes activation of autophagy in other tissues (Ulgherait et al., 2014). DAF-16/FOXO is a known regulator of autophagy and is directly regulated by both AMPK and calcineurin and required for their effects on longevity (Greer et al., 2007; Tao et al., 2013). We saw enrichment of the DAE element in genes downregulated when both AMPK and CRT1 were active, suggesting CRT1 might

remotely regulate DAF-16/FOXO activity and/or activate its transacting antagonist PQM-1 (Tepper et al., 2013). Understanding how neuronal CRTC-1 interacts with DAF-16 and/or PQM-1 and if they function intra- or intercellularly to modulate AMPK/calcineurin-mediated longevity will be informative.

In summary this study highlights “mito-centric” metabolism as the critical target of AMPK/CRTC-mediated effects on aging, and establishes that neurons are the causal and crucial site for CRTC-1-dependent regulation of longevity. Though both sensory perception of nutrient availability in neurons (Petrascheck et al., 2007) and organismal energy status (Burkewitz et al., 2014) are known to modulate aging, our data suggest an emerging paradigm: the optimal pro-longevity intervention requires coordination of energy perception in the neurons with accurately executed metabolic programs in peripheral tissues. Indeed, we show here that the pro-longevity, AMPK-mediated metabolic program in peripheral tissues is overridden when the regulatory link between AMPK and CRTC-1 is broken exclusively in neurons, completely suppressing all gains in longevity for the organism. If neuronal energy-sensing mechanisms are dominant, as our data indicate, selectively targeting central sensors and regulators of energy homeostasis may be sufficient to generate a peripheral metabolic program that promotes healthier aging.

EXPERIMENTAL PROCEDURES

Additional details are provided in the [Extended Experimental Procedures](#).

Lifespans

Lifespan experiments were performed on standard nematode growth media (NGM) at 20°C. Worms were synchronized by timed egg lays using gravid adults. When the progeny reached adulthood (~72 hr), 100 worms were transferred to fresh plates at 10–25 worms per plate and this was considered time = 0. Worms were transferred to fresh bacterial lawns every other day until the first deaths (10–14 days). Survival was scored every 1–2 days and a worm was deemed dead when unresponsive to 3 taps on the head and tail. Worms were censored due to contamination on the plate, leaving the NGM, eggs hatching inside the adult or loss of vulval integrity during reproduction. Only in the lifespans noted (TABLE S1), 5-Fluoro-2'-deoxyuridine (FUDR) was added to media to prevent excessive censoring. FUDR (100 µl; 1 mg ml⁻¹) was added 24 hr before picking worms to the plate on the first day of adulthood, and worms were transferred off FUDR-containing plates once reproduction had ceased (7 day), after which the assays continued normally.

RNA Sequencing

The experiment was performed with three biological replicates. Eggs were synchronized to L1 larvae overnight in M9 and 1,000 larvae were grown to L4 on NGM seeded with OP50-1 *E. coli*. Animals were collected and washed with M9 media to remove bacteria. Worms were then snap frozen in liquid nitrogen. RNA was extracted by five freeze/thaw cycles in Qiazol then purified by RNeasy mini kit (QIAGEN). RNA quality was checked using an Agilent Technologies 2100 Bioanalyzer. All samples had an RNA integrity number of 10. cDNA libraries were prepared from 4 µg of total RNA using the TruSeq RNA Sample Preparation v2 kit (Illumina). See [Extended Experimental Procedures](#) for more details of the data analysis.

Metabolomics

Synchronized L1 larvae were grown to L4 on NGM/OP50-1 before being washed off plates with M9, resuspended in 0.6% formic acid, snap-frozen, and thawed immediately before lysis by sonication. Aliquots were taken for total protein quantification, then an equal volume of acetonitrile was added to reach a final concentration of 0.3% formic acid and 50% acetonitrile. Samples

were then subject to metabolomic analysis as detailed in [Extended Experimental Procedures](#).

Mitochondrial Analysis

Mitochondria were analyzed in muscle cells from ≥ 10 d1 adult worms per genotype. Qualitative assessment of mitochondrial morphology was made by scoring worms based on three categories: tubular (interconnected mitochondrial network), intermediate (combination of interconnected network and isolated smaller mitochondria) or fragmented (mostly fragmented mitochondria). Quantitative assessments of percent mitochondrial coverage of the cell and mitochondrial area/perimeter ratio were made by measuring >30 muscle cells per genotype using a macro for ImageJ, as previously described (Dagda et al., 2009).

ACCESSION NUMBERS

The GEO accession number for the RNA-seq dataset in this paper is GSE58931.

SUPPLEMENTAL INFORMATION

Supplemental Information includes Extended Experimental Procedures, seven figures, and seven tables and can be found with this article online at <http://dx.doi.org/10.1016/j.cell.2015.02.004>.

ACKNOWLEDGMENTS

Funding support was provided by the Ellison Medical Foundation (WBM and MDH) the NIH [1R01AG044346 (WBM), U54CA155626 (WBM), 1R01AG045351 (MDH), 1F32AG044944 (KB)], and the American Diabetes Association/Canadian Diabetes Association PF-3-13-4342 (FH). We thank the *Caenorhabditis* Genetic Center for providing several strains, Mark Alkema for the *crh-1(n3315)* mutant, and Sean Curran/Paul Sternberg for the mitochondrial marker strain. We also thank Tinatini Tavhelidse and Ana Paula Morales Allende for preliminary contributions to the project.

Received: June 30, 2014

Revised: November 21, 2014

Accepted: January 28, 2015

Published: February 26, 2015

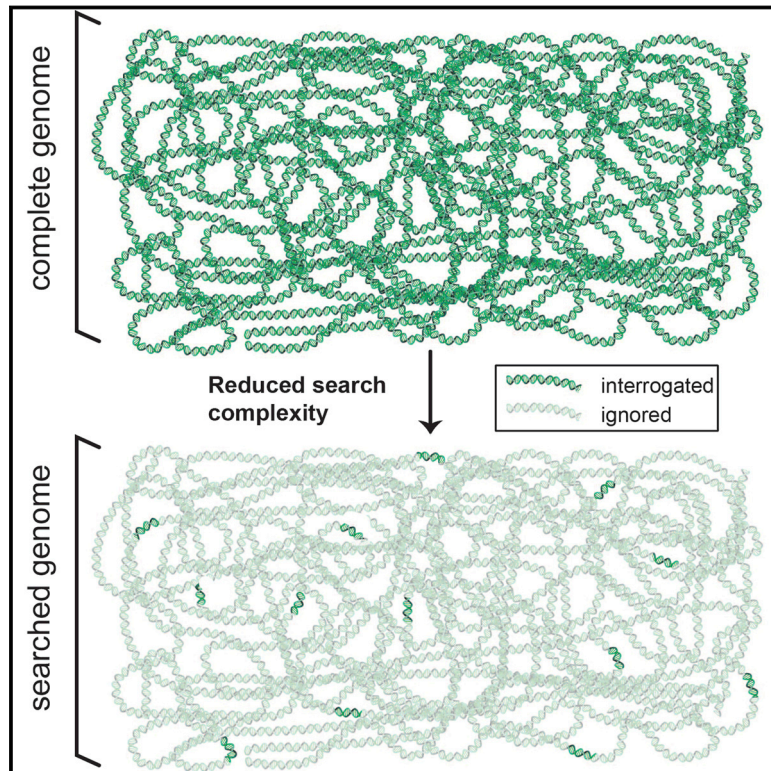
REFERENCES

- Alkema, M.J., Hunter-Ensor, M., Ringstad, N., and Horvitz, H.R. (2005). Tyramine Functions independently of octopamine in the *Caenorhabditis elegans* nervous system. *Neuron* 46, 247–260.
- Altarejos, J.Y., and Montminy, M. (2011). CREB and the CRTC co-activators: sensors for hormonal and metabolic signals. *Nat. Rev. Mol. Cell Biol.* 12, 141–151.
- Altarejos, J.Y., Goebel, N., Konkright, M.D., Inoue, H., Xie, J., Arias, C.M., Sawchenko, P.E., and Montminy, M. (2008). The Creb1 coactivator Crtc1 is required for energy balance and fertility. *Nat. Med.* 14, 1112–1117.
- Apfeld, J., O'Connor, G., McDonagh, T., DiStefano, P.S., and Curtis, R. (2004). The AMP-activated protein kinase AAK-2 links energy levels and insulin-like signals to lifespan in *C. elegans*. *Genes Dev.* 18, 3004–3009.
- Ashrafi, K. (2007). Obesity and the regulation of fat metabolism. *WormBook*, 1–20.
- Bantubungi, K., Prawitt, J., and Staels, B. (2012). Control of metabolism by nutrient-regulated nuclear receptors acting in the brain. *J. Steroid Biochem. Mol. Biol.* 130, 126–137.
- Breuillaud, L., Halfon, O., Magistretti, P.J., Pralong, F.P., and Cardinaux, J.R. (2009). Mouse fertility is not dependent on the CREB coactivator Crtc1. *Nat. Med.* 15, 989–990, author reply 991.
- Burkewitz, K., Zhang, Y., and Mair, W.B. (2014). AMPK at the nexus of energetics and aging. *Cell Metab.* 20, 10–25.

- Cunningham, K.A., Bouagnon, A.D., Barros, A.G., Lin, L., Malard, L., Romano-Silva, M.A., and Ashrafi, K. (2014). Loss of a neural AMP-activated kinase mimics the effects of elevated serotonin on fat, movement, and hormonal secretions. *PLoS Genet.* 10, e1004394.
- Dagda, R.K., Cherra, S.J., 3rd, Kulich, S.M., Tandon, A., Park, D., and Chu, C.T. (2009). Loss of PINK1 function promotes mitophagy through effects on oxidative stress and mitochondrial fission. *J. Biol. Chem.* 284, 13843–13855.
- Dagon, Y., Hur, E., Zheng, B., Wellenstein, K., Cantley, L.C., and Kahn, B.B. (2012). p70S6 kinase phosphorylates AMPK on serine 491 to mediate leptin's effect on food intake. *Cell Metab.* 16, 104–112.
- Dwivedi, M., Song, H.O., and Ahnn, J. (2009). Autophagy genes mediate the effect of calcineurin on life span in *C. elegans*. *Autophagy* 5, 604–607.
- Egan, D.F., Shackelford, D.B., Mihaylova, M.M., Gelino, S., Kohnz, R.A., Mair, W., Vasquez, D.S., Joshi, A., Gwinn, D.M., Taylor, R., et al. (2011). Phosphorylation of ULK1 (hATG1) by AMP-activated protein kinase connects energy sensing to mitophagy. *Science* 331, 456–461.
- Greer, E.L., Dowlatabadi, D., Banko, M.R., Villen, J., Hoang, K., Blanchard, D., Gygi, S.P., and Brunet, A. (2007). An AMPK-FOXO pathway mediates longevity induced by a novel method of dietary restriction in *C. elegans*. *Curr. Biol.* 17, 1646–1656.
- Grishanin, R.N., Kowalchuk, J.A., Klenchin, V.A., Ann, K., Earles, C.A., Chapman, E.R., Gerona, R.R., and Martin, T.F. (2004). CAPS acts at a pre-fusion step in dense-core vesicle exocytosis as a PIP2 binding protein. *Neuron* 43, 551–562.
- Hardie, D.G., Ross, F.A., and Hawley, S.A. (2012). AMPK: a nutrient and energy sensor that maintains energy homeostasis. *Nat. Rev. Mol. Cell Biol.* 13, 251–262.
- Knauf, C., Rieusset, J., Foretz, M., Cani, P.D., Uldry, M., Hosokawa, M., Martinez, E., Bringart, M., Waget, A., Kersten, S., et al. (2006). Peroxisome proliferator-activated receptor- α -null mice have increased white adipose tissue glucose utilization, GLUT4, and fat mass: Role in liver and brain. *Endocrinology* 147, 4067–4078.
- Kocalis, H.E., Turney, M.K., Printz, R.L., Laryea, G.N., Muglia, L.J., Davies, S.S., Stanwood, G.D., McGuinness, O.P., and Niswender, K.D. (2012). Neuron-specific deletion of peroxisome proliferator-activated receptor delta (PPAR δ) in mice leads to increased susceptibility to diet-induced obesity. *PLoS ONE* 7, e42981.
- Lerner, R.G., Depatie, C., Rutter, G.A., Screatton, R.A., and Balthasar, N. (2009). A role for the CREB co-activator CRTC2 in the hypothalamic mechanisms linking glucose sensing with gene regulation. *EMBO Rep.* 10, 1175–1181.
- Liesa, M., and Shirihai, O.S. (2013). Mitochondrial dynamics in the regulation of nutrient utilization and energy expenditure. *Cell Metab.* 17, 491–506.
- Lu, M., Sarruf, D.A., Talukdar, S., Sharma, S., Li, P., Bandyopadhyay, G., Nalbandian, S., Fan, W., Gayen, J.R., Mahata, S.K., et al. (2011). Brain PPAR- γ promotes obesity and is required for the insulin-sensitizing effect of thiazolidinediones. *Nat. Med.* 17, 618–622.
- Mair, W., Morantte, I., Rodrigues, A.P., Manning, G., Montminy, M., Shaw, R.J., and Dillin, A. (2011). Lifespan extension induced by AMPK and calcineurin is mediated by CRTC-1 and CREB. *Nature* 470, 404–408.
- Martin-Montalvo, A., Mercken, E.M., Mitchell, S.J., Palacios, H.H., Mote, P.L., Scheibye-Knudsen, M., Gomes, A.P., Ward, T.M., Minor, R.K., Blouin, M.J., et al. (2013). Metformin improves healthspan and lifespan in mice. *Nat. Commun.* 4, 2192.
- Minokoshi, Y., Alquier, T., Furukawa, N., Kim, Y.B., Lee, A., Xue, B., Mu, J., Foufelle, F., Ferré, P., Birnbaum, M.J., et al. (2004). AMP-kinase regulates food intake by responding to hormonal and nutrient signals in the hypothalamus. *Nature* 428, 569–574.
- Noble, T., Stieglitz, J., and Srinivasan, S. (2013). An integrated serotonin and octopamine neuronal circuit directs the release of an endocrine signal to control *C. elegans* body fat. *Cell Metab.* 18, 672–684.
- Onken, B., and Driscoll, M. (2010). Metformin induces a dietary restriction-like state and the oxidative stress response to extend *C. elegans* Healthspan via AMPK, LKB1, and SKN-1. *PLoS ONE* 5, e8758.
- Pathare, P.P., Lin, A., Bornfeldt, K.E., Taubert, S., and Van Gilst, M.R. (2012). Coordinate regulation of lipid metabolism by novel nuclear receptor partnerships. *PLoS Genet.* 8, e1002645.
- Petrasccheck, M., Ye, X., and Buck, L.B. (2007). An antidepressant that extends lifespan in adult *Caenorhabditis elegans*. *Nature* 450, 553–556.
- Riera, C.E., Huisin, M.O., Follett, P., Leblanc, M., Halloran, J., Van Andel, R., de Magalhães Filho, C.D., Merkwirth, C., and Dillin, A. (2014). TRPV1 pain receptors regulate longevity and metabolism by neuropeptide signaling. *Cell* 157, 1023–1036.
- Ryan, K.K., Li, B., Grayson, B.E., Matter, E.K., Woods, S.C., and Seeley, R.J. (2011). A role for central nervous system PPAR- γ in the regulation of energy balance. *Nat. Med.* 17, 623–626.
- Seok, S., Fu, T., Choi, S.E., Li, Y., Zhu, R., Kumar, S., Sun, X., Yoon, G., Kang, Y., Zhong, W., et al. (2014). Transcriptional regulation of autophagy by an FXR-CREB axis. *Nature* 516, 108–111.
- Stenesen, D., Suh, J.M., Seo, J., Yu, K., Lee, K.S., Kim, J.S., Min, K.J., and Graff, J.M. (2013). Adenosine nucleotide biosynthesis and AMPK regulate adult life span and mediate the longevity benefit of caloric restriction in flies. *Cell Metab.* 17, 101–112.
- Tao, L., Xie, Q., Ding, Y.H., Li, S.T., Peng, S., Zhang, Y.P., Tan, D., Yuan, Z., and Dong, M.Q. (2013). CAMKII and Calcineurin regulate the lifespan of *Caenorhabditis elegans* through the FOXO transcription factor DAF-16. *eLife* 2, e00518.
- Tepper, R.G., Ashraf, J., Kaletsky, R., Kleemann, G., Murphy, C.T., and Bussemaker, H.J. (2013). PQM-1 complements DAF-16 as a key transcriptional regulator of DAF-2-mediated development and longevity. *Cell* 154, 676–690.
- Ulgherait, M., Rana, A., Rera, M., Graniel, J., and Walker, D.W. (2014). AMPK modulates tissue and organismal aging in a non-cell-autonomous manner. *Cell Rep.* 8, 1767–1780.
- Van Gilst, M.R., Hadjivassiliou, H., Jolly, A., and Yamamoto, K.R. (2005). Nuclear hormone receptor NHR-49 controls fat consumption and fatty acid composition in *C. elegans*. *PLoS Biol.* 3, e53.
- Viollet, B., Andreelli, F., Jørgensen, S.B., Perrin, C., Geloën, A., Flamez, D., Mu, J., Lenzner, C., Baud, O., Bannoun, M., et al. (2003). The AMP-activated protein kinase α 2 catalytic subunit controls whole-body insulin sensitivity. *J. Clin. Invest.* 111, 91–98.
- Wahli, W., and Michalik, L. (2012). PPARs at the crossroads of lipid signaling and inflammation. *Trends Endocrinol. Metab.* 23, 351–363.

DNA Sequence Alignment by Microhomology Sampling during Homologous Recombination

Graphical Abstract



Authors

Zhi Qi, Sy Redding, ..., Patrick Sung, Eric C. Greene

Correspondence

ecg2108@columbia.edu

In Brief

Single-molecule imaging with ssDNA curtains reveals how the Rad51/RecA family of DNA recombinases make use of short tracts of microhomology to interrogate and align homologous DNA sequences.

Highlights

- Single-molecule imaging reveals how Rad51 presynaptic complexes interrogate dsDNA
- Rad51 quickly samples and rejects any DNA lacking 8-nt tracts of microhomology
- Rad51 stably captures DNA harboring 8 nt of microhomology
- Subsequent strand invasion occurs in precise 3-nt steps



DNA Sequence Alignment by Microhomology Sampling during Homologous Recombination

Zhi Qi,¹ Sy Redding,² Ja Yil Lee,¹ Bryan Gibb,¹ YoungHo Kwon,^{3,5} Hengyao Niu,^{3,5} William A. Gaines,³ Patrick Sung,³ and Eric C. Greene^{1,4,*}

¹Department of Biochemistry and Molecular Biophysics, Columbia University, 650 West 168th Street, New York, NY 10032, USA

²Department of Chemistry, Columbia University, 650 West 168th Street, New York, NY 10032, USA

³Department of Molecular Biophysics and Biochemistry, Yale University School of Medicine, 333 Cedar Street, New Haven, CT 06520, USA

⁴Howard Hughes Medical Institute, Columbia University, 650 West 168th Street, New York, NY 10032, USA

⁵Present address: Molecular and Cellular Biochemistry Department, Indiana University, 212 South Hawthorne Drive, Bloomington, IN 47405, USA

*Correspondence: ecg2108@columbia.edu
<http://dx.doi.org/10.1016/j.cell.2015.01.029>

SUMMARY

Homologous recombination (HR) mediates the exchange of genetic information between sister or homologous chromatids. During HR, members of the RecA/Rad51 family of recombinases must somehow search through vast quantities of DNA sequence to align and pair single-strand DNA (ssDNA) with a homologous double-strand DNA (dsDNA) template. Here, we use single-molecule imaging to visualize Rad51 as it aligns and pairs homologous DNA sequences in real time. We show that Rad51 uses a length-based recognition mechanism while interrogating dsDNA, enabling robust kinetic selection of 8-nucleotide (nt) tracts of microhomology, which kinetically confines the search to sites with a high probability of being a homologous target. Successful pairing with a ninth nucleotide coincides with an additional reduction in binding free energy, and subsequent strand exchange occurs in precise 3-nt steps, reflecting the base triplet organization of the presynaptic complex. These findings provide crucial new insights into the physical and evolutionary underpinnings of DNA recombination.

INTRODUCTION

Homologous recombination (HR) is ubiquitous among all three kingdoms of life and serves as a driving force in evolution. HR is a major pathway for repairing DNA double-strand breaks (DSBs) and single-strand DNA (ssDNA) gaps and plays essential roles in repairing stalled or collapsed replication forks (Heyer et al., 2010; San Filippo et al., 2008). HR provides an alternative pathway for telomere maintenance (Eckert-Boulet and Lisby, 2010), can lead to the duplication of long regions of chromosomes (Smith et al., 2007), and some organisms utilize HR as the sole means of initiating DNA replication (Hawkins et al., 2013). HR also generates genetic diversity and ensures proper

chromosome segregation during meiosis (Neale and Keeney, 2006) and is a major source of phenotypic variation in many organisms (Fraser et al., 2007; Hastings et al., 2009). In humans, aberrant HR underlies chromosomal rearrangements often associated with cancers, cancer prone syndromes, and numerous genetic diseases (Heyer et al., 2010; San Filippo et al., 2008).

DSB repair in *Saccharomyces cerevisiae* has long served as paradigm for studying HR (Heyer et al., 2010; San Filippo et al., 2008). The DNA ends present at DSBs are first processed by 5' → 3' strand resection, yielding 3' ssDNA overhangs whose production coincides with the binding of replication protein A (RPA). RPA is then replaced by Rad51 or the meiosis-specific recombinase Dmc1, which is thought to have arisen by a gene duplication event early in the evolutionary history of eukaryotes (Lin et al., 2006). Rad51 and Dmc1 are both closely related to *Escherichia coli* RecA. These proteins are DNA-dependent ATPases that form right-handed helical filaments on ssDNA, and the resulting presynaptic complexes (PCs) display a striking degree of conservation from bacteriophage to humans (Bianco et al., 1998). Structural studies have revealed that the presynaptic ssDNA is organized into base triplets that are maintained in near B-form conformation, but there is a 7.8 Å rise between adjacent triplets causing an overall extension of the ssDNA (Chen et al., 2008). Single-molecule force measurements suggest that this ssDNA extension may promote release of nonhomologous double-strand (dsDNA) and facilitate strand exchange with homologous dsDNA (Danilowicz et al., 2014). Many proteins participate in HR, including those encoded by the conserved RAD52 epistasis group of genes (Heyer et al., 2010; San Filippo et al., 2008). Despite these layers of complexity, Rad51, like other members of the Rad51/RecA family, can promote strand invasion in the absence of other proteins, implying that more specialized accessory factors augment the basal recombinase activities without conferring new catalytic properties.

Rad51/RecA recombinases must align ssDNA with a homologous duplex elsewhere in the genome. This process is referred to as the “homology search” and it is conceptually similar to target searches conducted by all other site-specific

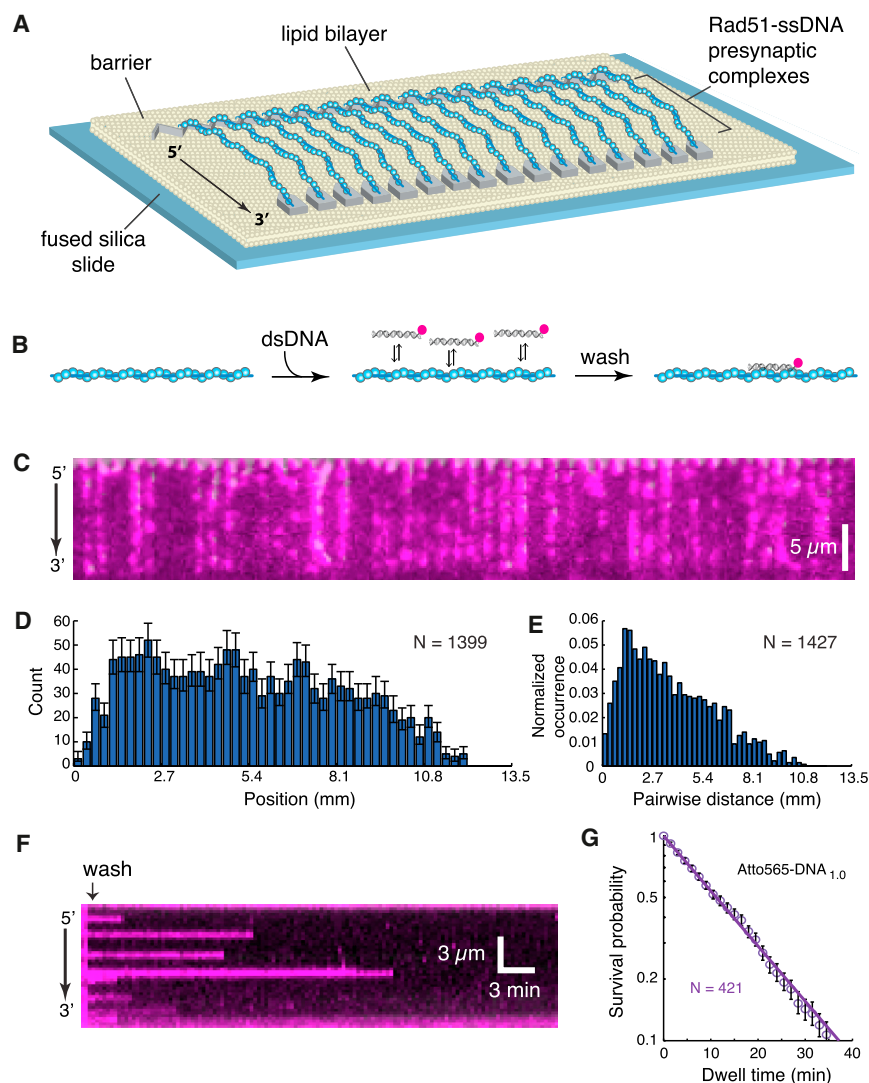


Figure 1. Visualizing dsDNA Capture by Rad51

(A) Schematic of Rad51-ssDNA curtains. (B) Strategy for detecting binding of Atto565-labeled dsDNA to the PCs. (C) Wide-field image of Rad51 PCs bound to Atto565-DNA_{1.0}. (D and E) Binding site distribution (D) and pair-wise distance distribution (E) of Atto565-DNA_{1.0}. (F) Kymograph showing dissociation Atto565-DNA_{1.0} from a single Rad51 PC; 100-msec frames were collected at 20-s intervals. (G) Dissociation kinetics of Atto565-DNA_{1.0}. Unless otherwise stated, error bars for all binding site distributions and survival probability plots represent 70% confidence intervals obtained through bootstrap analysis. See also [Figures S1, S2, S3, S4, and S6](#).

align homologous DNA sequences are broadly conserved among the Rad51/RecA family members. This mechanism can drastically reduce the amount time necessary to align homologous dsDNA sequences.

RESULTS

Assembly of Rad51 Presynaptic Complexes

We used ssDNA curtains and total internal reflection fluorescence microscopy (TIRFM) to visualize Rad51 PCs ([Gibb et al., 2014a](#)). The ssDNA was generated using M13mp18 (7,249-nt) as a template for rolling circle replication ([Figures 1A and S1](#)) and then anchored to a lipid bilayer within a microfluidic chamber through a biotin-streptavidin linkage and

DNA-binding proteins ([Barzel and Kupiec, 2008; Renkawitz et al., 2014; von Hippel and Berg, 1989](#)). The principles that govern sequence alignment during HR remain poorly understood because the corresponding intermediates are transient and asynchronous ([Barzel and Kupiec, 2008; Renkawitz et al., 2014](#)). What features are the recombinases searching for within dsDNA? How do they distinguish between nonhomologous and homologous sequences? Over what length scales do they test for homology? What distinguishes search intermediates from the commitment to strand exchange? These questions all pertain to the overarching issue of how homology is efficiently located given the vast sequence space encoded by the genome ([Neale and Keeney, 2006](#)). We sought to address these questions by visualizing the homology search at the single-molecule level. Our results lead to a model in which 8-nt microhomology motifs serve as the fundamental units of molecular recognition by *S. cerevisiae* Rad51, and this initial event is distinct from subsequent strand invasion. We show that the physical principles underlying the ability of Rad51 to search for and

aligned along chromium (Cr) barriers by application of hydrodynamic force. The ssDNA unravels when incubated with RPA-eGFP, and the downstream ends of the RPA-ssDNA are anchored to exposed Cr pedestals. Addition of wild-type *S. cerevisiae* Rad51 led to efficient, ATP-dependent PC assembly ([Figures S1 and S2](#)).

Nonhomologous dsDNA Capture by Rad51

Rad51/RecA recombinases must interrogate nonhomologous dsDNA while attempting to locate and align homologous sequences. We mimicked this process by testing the ability of the Rad51 PCs to interact with nonhomologous 70-base pair (bp) dsDNA oligonucleotides ([Figure 1B](#)). To visualize dsDNA binding, we injected Atto565-labeled dsDNA into the sample chamber; for brevity we designated this substrate Atto565-DNA_{1.0}. Following a brief incubation, unbound dsDNA was flushed away and the remaining molecules were visualized by TIRFM. These experiments revealed Atto565-DNA_{1.0} bound to the PCs with no evident site preference within our resolution

limits (Figures 1C–1E), and most of the bound dsDNA (78.4%) exhibited single-step photo-bleaching (not shown). Controls with RPA-ssDNA (minus Rad51) confirmed that dsDNA capture was Rad51-dependent (Figure S3A). In addition, the PCs rapidly disassembled when ATP was replaced with ADP (Figure S2), and the bound dsDNA was also quickly released when reactions were chased with ADP, indicating that dsDNA retention required the continued presence of Rad51 (Figures S3B–S3D). Kinetic measurements yielded a dissociation rate (k_{off}) of $0.062 \pm 0.001 \text{ min}^{-1}$ for Atto565-DNA_{1,0}, corresponding to a lifetime of $\sim 16 \text{ min}$ (Figures 1F and 1G). This was an extraordinarily stable interaction for a seemingly nonhomologous dsDNA, and such long-lived intermediates would appear incompatible with an efficient search mechanism. We next sought to understand the physical basis for these long lifetimes.

Substrate Length Does Not Impact dsDNA Retention

If nonhomologous dsDNA capture primarily involved nonspecific electrostatic contacts with the phosphate backbone, then the lifetime of the bound intermediates should vary with dsDNA length. We tested this possibility with 35-bp and 18-bp dsDNA substrates. Surprisingly, the truncated substrates bound tightly to the PCs, although more substrate and longer incubation times were required for initial engagement (Figure S4). We conclude that substrate length had a modest impact on initial association with the PC, but did not affect retention of the captured dsDNA, suggesting that the observed intermediates were not maintained primarily through nonspecific contacts with dsDNA phosphate backbone.

Microhomology Contributes to dsDNA Capture

We next asked whether sequence microhomology might contribute to dsDNA capture. Analysis of DNA_{1,0} revealed many short tracts of microhomology complementary to sequences scattered throughout the M13mp18 ssDNA, including 12 regions with ≥ 8 -nts of microhomology (Figures 2A and 2B). Previous reports suggested that *E. coli* RecA can pair DNA substrates perhaps as short as 8-nt in length (De Vlamincq et al., 2012; Hsieh et al., 1992; Xiao et al., 2006). Based on this knowledge, we designed a new substrate (Atto565-DNA_{2,0}), which retained identical sequence composition as DNA_{1,0}, but lacked microhomology ≥ 8 -nt in length (Figures 2D and 2E). We readily detected capture of Atto565-DNA_{1,0} (Figure 2C), however, we were unable to detect stable capture of Atto565-DNA_{2,0} under identical conditions (Figure 2F), despite the fact that this substrate contains numerous tracts of microhomology ≤ 7 -nt in length (Figure 2D).

Stable dsDNA Capture Requires 8-nt Tracts of Microhomology

Our results imply that dsDNA capture involves 8-nt or longer tracts of microhomology. This hypothesis predicts that a single 8-nt tract of microhomology added to an otherwise nonhomologous dsDNA should confer stable association with the PC. We tested this prediction with a series of substrates bearing precisely 8-nt of microhomology (Figure 3A). Remarkably, addition of a single 8-nt tract of microhomology was sufficient to

confer stable binding of a nonhomologous dsDNA to the PC, and similar results were obtained for 8-nt microhomology motifs at different locations (Figures 3A–3E). The binding site distributions and the pairwise distance distributions of Atto565-dsDNA_{2,1} revealed a $2.6 \pm 0.2 \mu\text{m}$ periodicity, consistent with the expectation that the dsDNA was captured at a single position on M13mp18, and this conclusion was supported by analysis of a substrate targeted to an alternative location (Figures 1D, 1E, 3F, 3G, and S5).

The requirement for microhomology suggested that captured intermediates were retained through Watson-Crick pairing. This hypothesis predicts that the binding lifetime should scale with melting temperature (T_m), which was confirmed using substrates bearing 8-nt tracts of microhomology of varying AT-content (Figure 3H). Moreover, the change in free energy ($\Delta\Delta G^\ddagger$) scaled with hydrogen bonding potential, with each hydrogen bond contributing $\sim 0.14 k_B T$ to the binding of the 8-nt motif. The modest contribution to overall stability for each hydrogen bond was consistent with the requirement that the homology search be driven by thermal fluctuations and supports the notion that stretch-induced disruption of base stacking destabilizes the Watson-Crick base pairs relative to B-DNA (Chen et al., 2008).

We also tested how microhomology length influenced dsDNA capture (Figure 3I). We were unable to detect any stable binding intermediates when the 8-nt tract of microhomology was decreased to 7-nt (Atto565-DNA_{2,6}), in agreement with the conclusion that 8-nts of microhomology was necessary for stable dsDNA capture (Figure 3I and see below). In contrast, increasing the 8-nt tract of microhomology to 9-nt reduced the dissociation rate, and additional length increases resulted in step-wise reductions in the dissociation rates in precise 3-nt increments (Figure 3I and see below). The microhomology requirement, the periodic binding patterns, and the influence of AT-content and microhomology length all suggested that the bound intermediates were maintained through Watson-Crick interactions.

Transient dsDNA Sampling by Rad51

Rad51 did not stably capture dsDNA lacking 8-nt tracts of microhomology, but it must be transiently sampling these molecules. Even microhomology-bearing dsDNA must in most instances be transiently sampled, because the vast majority of bimolecular encounters will occur at nonhomologous sites. Therefore, the 70-bp substrates used in our assays offered the unique potential for exploring how Rad51 samples and rejects dsDNA while searching for homology. We detected these transient intermediates by visualizing reactions in real time at 60-ms resolution (Figures 4A–4D). Remarkably, the survival probabilities of substrates lacking ≥ 8 -nt of microhomology (Atto565-DNA_{2,0}) did not decay exponentially, but rather scaled as a power-law, with 50% of the molecules dissociating within 0.54 s (Figure 4E), even though this substrate harbors numerous ≤ 7 -nt tracts of microhomology (Figure 2D). Power-law dependence was also observed over short time regimes for a substrate bearing a single 8-nt tract of microhomology (Atto565-DNA_{2,1}), whereas the lifetimes were limited by photo-bleaching at longer time scales, as expected (Figure 4E).

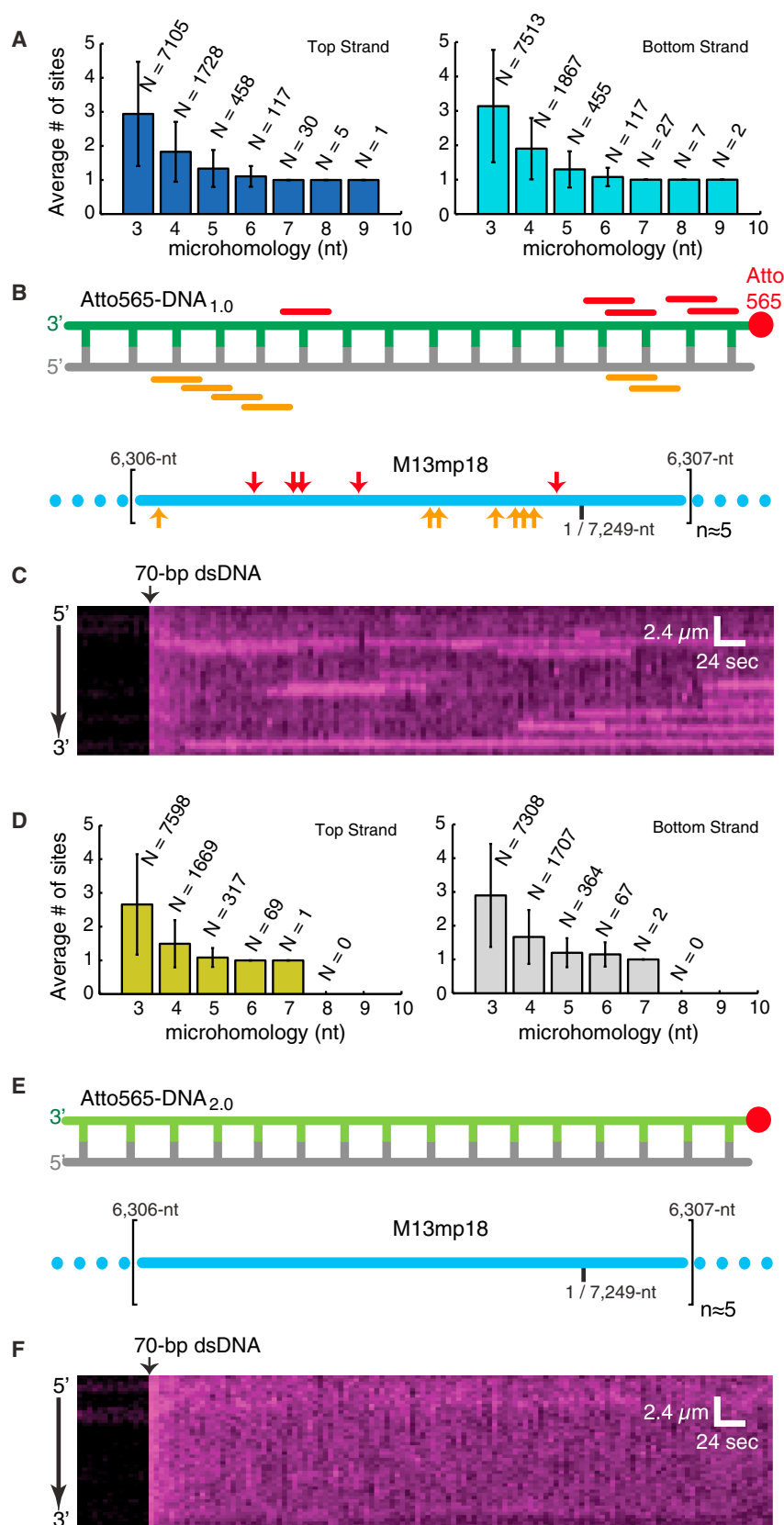


Figure 2. Stable Capture of Nonhomologous dsDNA

(A) Analysis showing the total number (N) and the average number (\pm SD) for the given length of microhomology within each occupied 70-nt window along M13mp18; additional details are presented as [Supplemental Information](#).

(B) Positions of microhomology (≥ 8 -nt) within Atto565-DNA_{1.0} (color-coded bars indicate relative positions of microhomology within the dsDNA) and the schematic illustration showing the corresponding locations (indicated with color-coded arrow-heads) of the tracts of microhomology along a single unit length M13mp18 ssDNA substrate (lower panel). Illustrations are not to scale.

(C) Kymograph showing binding of Atto565-DNA_{1.0} to a single Rad51 PC; 100-ms frames were collected at 5-s intervals.

(D and E) Analysis (D) and schematic (E) of a re-designed 70-bp dsDNA (Atto565-DNA_{2.0}) lacking 8-nt tracts of microhomology. Error bars represent SD.

(F) Kymograph showing Atto565-DNA_{2.0} incubated with a single PC; data were collected as in (C). See also [Figure S6](#).

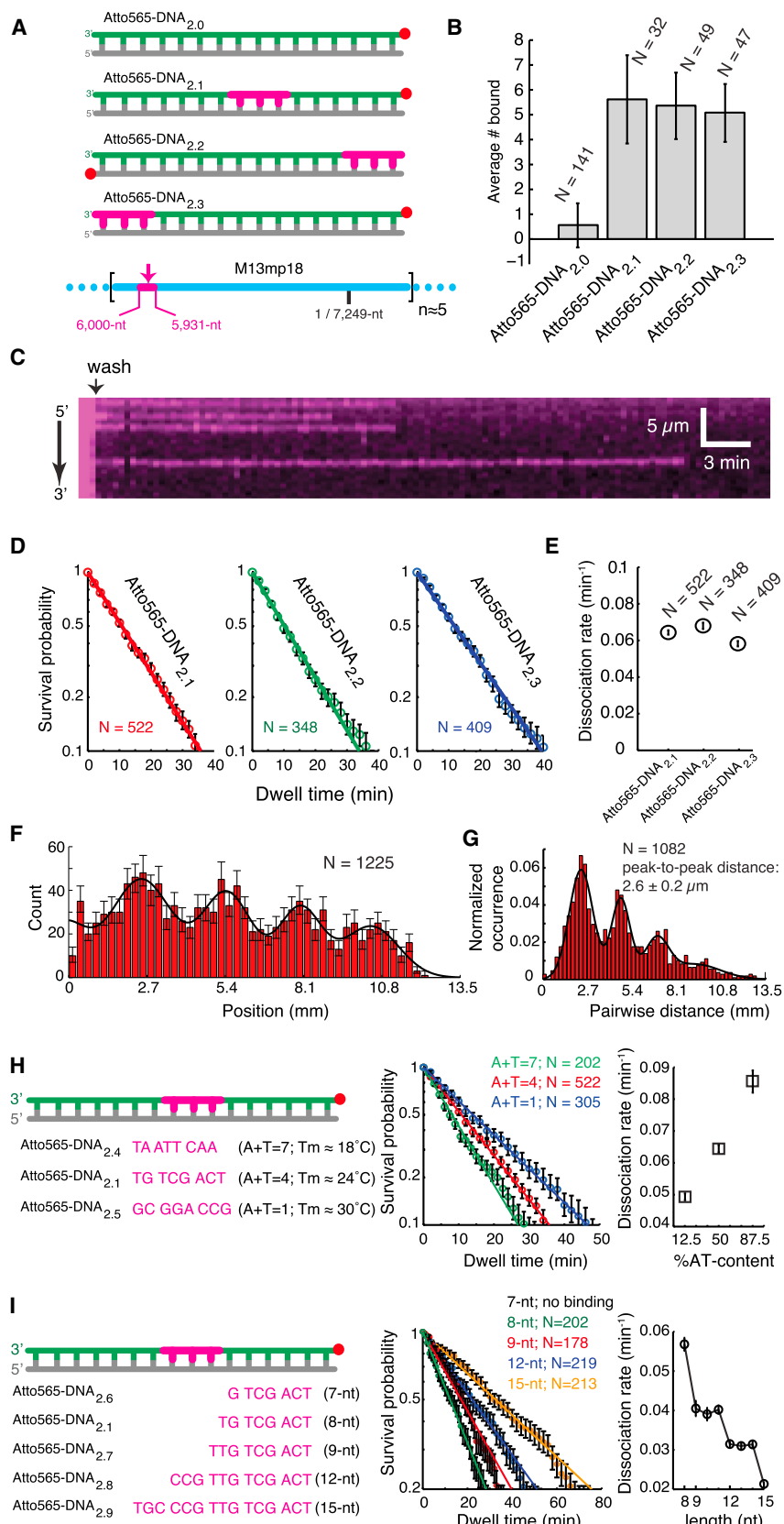


Figure 3. 8-nt Tracts of Microhomology Are Sufficient for dsDNA Capture

(A) Substrates bearing a single 8-nt tract of microhomology (highlighted in magenta) at different positions within the 70-bp dsDNA.

(B) Average number of Atto565-dsDNA bound per PC. N corresponds to the number of PCs counted. Error bars represent SD.

(C) Kymograph showing an example of Atto565-DNA_{2.1} dissociating from a PC.

(D and E) Survival probability plots (D) and dissociation rates (E) for each substrate.

(F and G) Binding distribution (F) and pairwise distance distribution (G) for Atto565-DNA_{2.1}.

(H) Design, survival probability plots, and dissociation rates for DNA substrates bearing a single 8-nt tract of microhomology with varying AT-content.

(I) Design, survival probability plots, and dissociation rates for substrates bearing 8- to 15-nts of microhomology; sequences and survival probability curves for the 10-nt, 11-nt, 13-nt, and 14-nt substrates are omitted for clarity. There was no detectable binding activity for Atto565-DNA_{2.6} in these assays. In (D)–(I), N corresponds to the number of Atto565-DNA molecules measured. Error bars represent SD.

See also Figure S5.

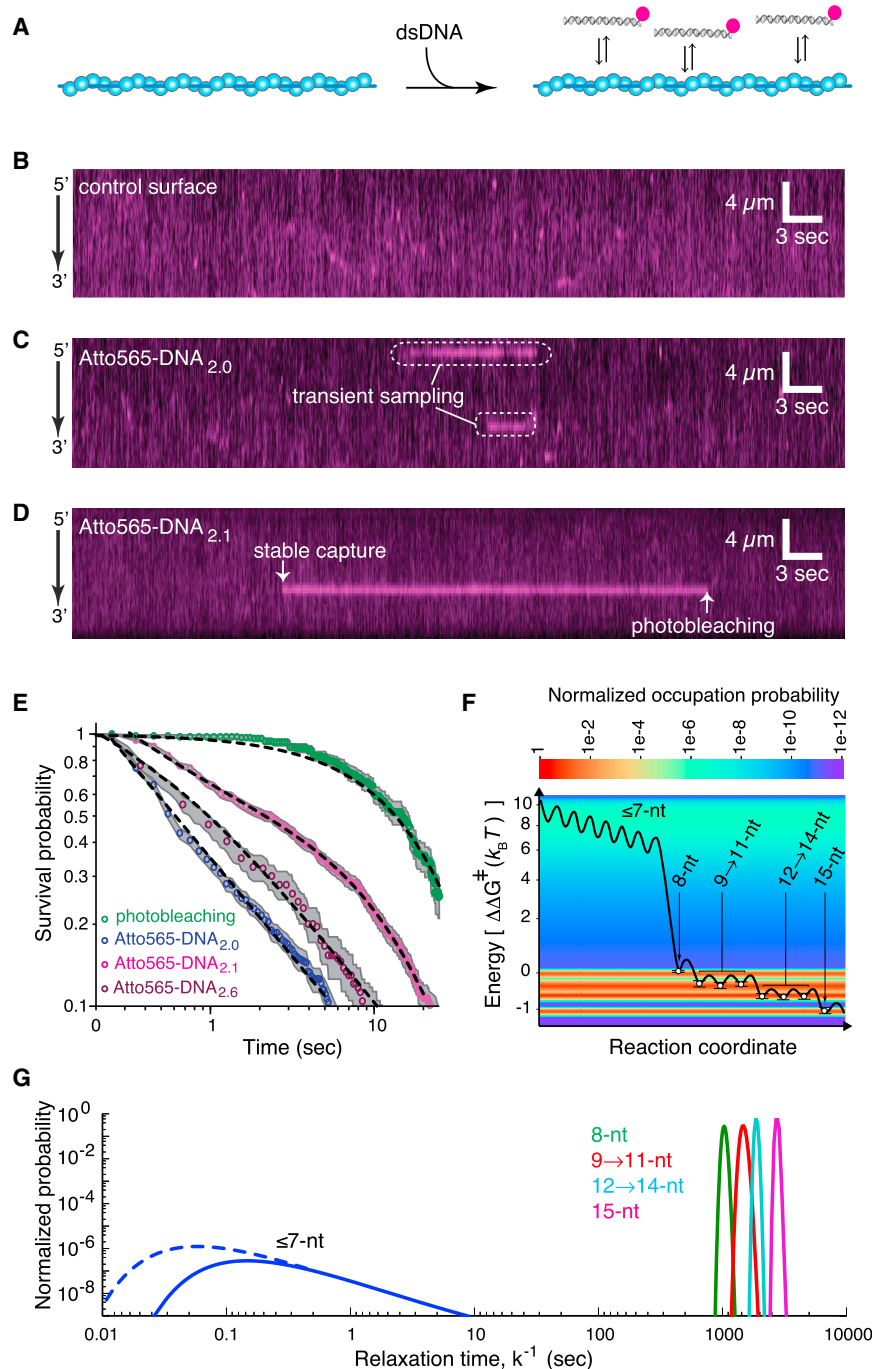


Figure 4. Transient Sampling dsDNA Lacking Microhomology

(A) Strategy for visualizing dsDNA sampling at 60-ms resolution.

(B–D) Kymographs showing (B) Atto565-DNA_{1.0} in the absence of the PC (control surface), and Rad51 PCs sampling (C) Atto565-DNA_{2.0} or (D) Atto565-DNA_{2.1}.

(E) Log-log plot revealing the power-law dependence of the transient search intermediates. Dashed lines represent a single exponential fit to the photo-bleaching data, power-law fits for Atto565-DNA_{2.0} and Atto565-DNA_{2.6}, and combination of a power-law and single exponential fit for Atto565-DNA_{2.1}.

(F) Energy landscape describing dsDNA sampling and strand invasion by Rad51. The heat map and open circles (\pm SD) represent calculated values for normalized occupation probability and $\Delta\Delta G^\ddagger$ values based on experimental data, respectively. The black line is a representation of the landscape and the heights of the energy barriers between states is for illustrative purposes only. Additional details are presented in the main text and [Supplemental Information](#).

(G) Distribution of kinetic rates for dsDNA sampling and capture by Rad51. Solid lines represent experimental data and the dashed line reflects intermediates that are sampled too rapidly to be detected.

See also [Figure S6](#).

pathway, as revealed by its characteristic power-law dependence, but only substrates bearing 8-nts of microhomology transitioned into the long-lived state.

A crucial implication of this power-law behavior is that the transient sampling events cannot be ascribed to a single conformational state that can be assigned a unique dissociation rate constant, but rather reflects the existence of a highly diverse ensemble of states with a correspondingly broad distribution of dissociation rates (Austin et al., 1975; Frauenfelder et al., 1991). The physical basis for this power-law dependence is readily understood given the vast number of potential intermediates. If one assumes recognition involving 8-nt sequence motifs, then a 70-bp dsDNA can be mis-

We next conducted real-time measurements with Atto565-DNA_{2.6}, which differs from Atto565-DNA_{2.1} by just a single nucleotide ([Figure 3I](#); [Supplemental Information](#)); as indicated above, this single nucleotide change reduces the 8-nt tract of microhomology to 7-nt and abolishes stable capture of this substrate by Rad51. Instead, Atto565-DNA_{2.6} exhibits power-law distributed dissociation kinetics with 50% of the molecules dissociating within 0.82 s ([Figure 4E](#)). These findings indicate that all the dsDNA substrates were initially sampled through the same

aligned with a total of 453,652 distinct sites on M13mp18, each of which can give rise to energetically distinct states based on differences in sequence composition. Power-law distributed dissociation kinetics are also consistent with recent molecular dynamics simulations, which suggest a large number of intermediates as RecA probes sequences for homology (M. Prentiss, personal communication). These considerations highlight the tremendous challenge faced during the homology search, even within our simplified experimental system.

Energy Landscape for dsDNA Sampling and Strand Invasion

Our data provide a free energy landscape describing dsDNA sampling and strand invasion by Rad51 (Figure 4F; Supplemental Information). The initial search process is characterized by transient intermediates that encompass a broad distribution of energetic states, which could reflect thousands of distinct complexes as Rad51 interrogates different sequences for homology (Figures 4F and 4G). Recognition of an 8-nt tract of microhomology results in an $\sim 8.2 k_B T$ drop in free energy ($\Delta\Delta G^\ddagger$) and gives rise to a ≥ 4 order-of-magnitude decrease in dissociation kinetics, providing a robust length-based mechanism for kinetically discriminating against sequences that are unlikely to be fully homologous (Figures 4F and 4G). This length-based microhomology recognition event is the single largest change in the energy landscape and most likely reflects a conformational transition within the Rad51-ssDNA-dsDNA ternary complex—the exact nature of which remains to be explored. The finding that recognition of an 8-nt tract (as opposed to either 6- or 9-nt) coincided with the largest drop in free energy was not anticipated given that ssDNA within the PC is organized into base triplets (Chen et al., 2008). Following microhomology capture, Rad51 can probe the flanking the DNA for additional homology while attempting strand invasion. Pairing with a ninth nt results in an additional $\sim 0.4 k_B T$ reduction in free energy, revealing that incorporation of the ninth nt enabled more stable engagement of the third base triplet. All subsequent reductions in free energy occurred in precise 3-nt increments, suggesting that the ssDNA bound by Rad51 was organized into base triplets, as observed for *E. coli* RecA (Chen et al., 2008), and the quantized reductions in binding energy were the functional consequence of this triplet organization. Together, these findings also indicate that capture of the first 8-nt tract of microhomology is mechanistically distinct from the subsequent reactions involved in strand invasion, suggesting that recognition of the ninth nt demarks the beginning of actual strand exchange, allowing subsequent reactions to take place in 3-nt steps.

Sliding or Intersegmental Transfer Do Not Contribute to Microhomology Capture

Prior smFRET measurements suggested that 1D sliding might contribute to DNA alignment by RecA over short distances (Ragunathan et al., 2012). However, in agreement with prior biochemical studies (Adzuma, 1998), our data revealed no evidence of 1D sliding for Rad51, although we do not rule out the possibility that sliding might take place over short distances (≤ 270 -nm). Other studies have shown that sequence alignment by RecA involves intersegmental transfer (Forget and Kowalczykowski, 2012). We found no evidence that the 70-bp dsDNA molecules moved by intersegmental transfer (Figure S6); however, these results do not argue against intersegmental transfer as a crucial component of the Rad51 homology search (see below), rather, our findings are as anticipated for a search entity engaging a single unit-length binding element.

Facilitated Exchange Promotes Turnover of dsDNA Bound to the Presynaptic Complex

Strand invasion in *S. cerevisiae* can be detected within ~ 10 –60 min of DSB formation, so the search for homology must

be completed within this time window. However, 8-nts is insufficient to define a sequence as statistically unique within the *S. cerevisiae* genome, and it is difficult to envision how recombination could be executed on a relevant timescale if the PC became kinetically trapped every time it encountered a ≥ 8 -nt tract of microhomology. This implies the existence of unknown mechanisms for disrupting these intermediates.

One possibility is that specific enzymes might disrupt intermediates involving short microhomology motifs; there are numerous helicases/translocases with the potential to fulfill such a role (e.g., Mph1, Srs2, Sgs1, Rdh54, and/or Rad54) (Heyer et al., 2010; Renkawitz et al., 2014; San Filippo et al., 2008). We do not exclude the possibility that these or other proteins may contribute to the homology search, perhaps by promoting the turnover of Rad51 bound to incorrect 8-nt tracts of microhomology—future work will be necessary to test this hypothesis. However, Rad51, like many other Rad51/RecA family members, can catalyze strand exchange *in vitro* with no need for these accessory factors despite the potential for sequence misalignment at any of the hundreds of 8-nt microhomology motifs present in the plasmids typically used for these assays, underscoring that the ability to search for homology is an intrinsic property of Rad51/RecA proteins. Therefore we asked whether a more fundamental mechanism(s) might promote dissolution of microhomology-bound intermediates. It has recently been recognized that facilitated exchange can contribute to disruption of protein-nucleic acid interactions (Gibb et al., 2014a; Graham et al., 2011; Sing et al., 2014) and may be a general but underappreciated phenomenon that influences macromolecular interactions under crowded physiological settings. Facilitated exchange reflects the existence of microscopically dissociated intermediates, which only undergo macroscopic dissociation when competing interactions arise from other molecules in the local environment. These concepts are readily extended to reactions involving the PC.

We considered the possibility that dissolution of intermediates arising from captured microhomology might be promoted by facilitated exchange with other dsDNA molecules. The hypothesis that DNA might disrupt search intermediates is intriguing given the high concentration of DNA within the nucleus and the potential ubiquity of such a mechanism. To test this hypothesis, we asked whether dsDNA bound to the PCs was released more rapidly into free solution when challenged with free competitor dsDNA. For this, Atto565-DNA_{1.0} was pre-bound to the PCs, and the reactions were chased with unlabeled competitor (DNA_{1.0}; Figure 5A). Remarkably, the competitor chase accelerated macroscopic dissociation of Atto565-DNA_{1.0} by up to ~ 3 -fold (Figures 5B–5E). We conclude that free dsDNA can accelerate turnover of dsDNA bound to the PCs consistent with a mechanism involving facilitated exchange.

Sequence and Length Requirements for Facilitated Exchange

PCs capture dsDNA through 8-nt tracts of microhomology, implying that facilitated exchange might involve overlapping tracts of microhomology. If correct, then facilitated exchange should only occur with competitor substrates bearing identical 8-nt tracts of microhomology. Indeed, reactions with two

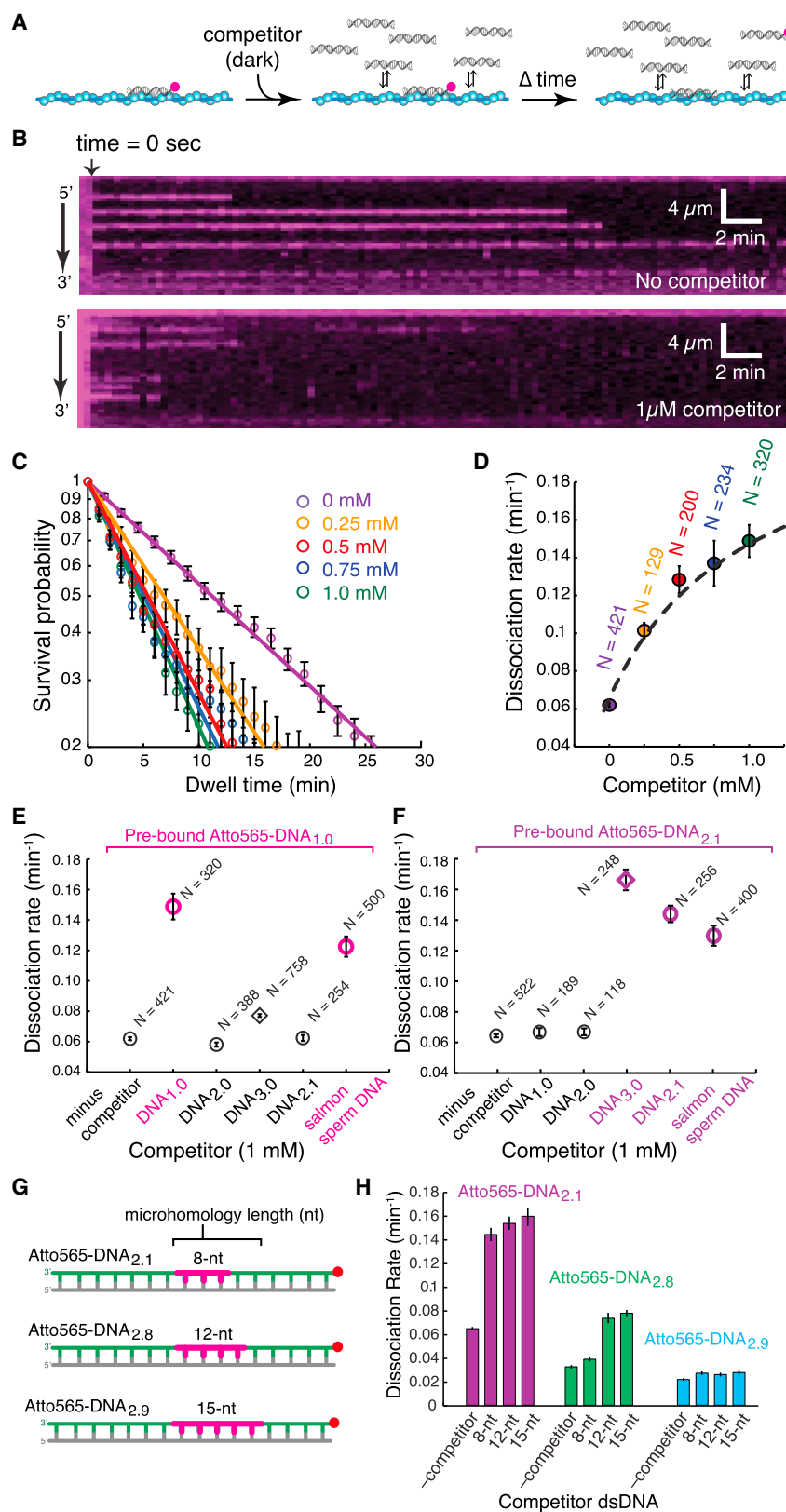


Figure 5. Facilitated Exchange of Captured Intermediates

(A) Strategy for quantifying dsDNA dissociation after injection of unlabeled competing DNA.

(B) Kymographs showing the dissociation of Atto565-DNA_{1.0} from the Rad51 PC in the absence (upper panel) and presence (lower panel) of unlabeled competitor DNA_{1.0}.

(C and D) Dwell time analysis of dissociation kinetics (C) and dissociation rates (D) for Atto565-DNA_{1.0} when chased with varying concentrations of dark DNA_{1.0}. The dissociation rates as a function of dark competitor are fit to a Hill-type curve with an intercept conveying the reaction in the absence of competitor. N corresponds to the number of Atto565-DNA molecules measured. Error bars represent SD.

(E and F) Dissociation rates for Atto565-DNA_{1.0} (E) and Atto565-DNA_{2.1} (F) when challenged with different competitor substrates (1 μ M each), as indicated; like colors correspond to competitors bearing overlapping tracts of microhomology, competitors lacking overlapping microhomology are shown in black. N corresponds to the number of Atto565-DNA molecules measured. Error bars represent SD.

(G and H) Schematic (G) and corresponding (H) data for substrates used to test the influence of microhomology length and alignment on facilitated exchange.

different Atto565-labeled substrates and series of competitors confirmed that facilitated exchange required overlapping tracts of microhomology (Figures 5E and 5F), and exchange was abolished if the competing microhomology was shifted by even a single nucleotide in either direction (not shown).

We next tested how facilitated exchange was influenced by microhomology length. The increased stability of substrates bearing longer tracts of microhomology (see Figure 3I) was reflected in the finding that shorter tracts of microhomology were more readily exchanged with longer tracts, whereas longer tracts of microhomology were more resistant to exchange with shorter tracts (Figures 5G and 5H). Moreover, a 15-nt tract of microhomology was sufficient to render a bound substrate completely resistant to facilitated exchange. Together, these results demonstrate that facilitated exchange requires overlapping microhomology, indicate that once the PC has engaged a particular dsDNA it ignores substrates lacking overlapping microhomology, and suggest that facilitated exchange can lead to preferential association with longer microhomology motifs. These results also imply the existence of a length-based threshold of ~15-nts as perhaps demarking the commitment to strand exchange; reversibility at this stage of the reaction would likely require accessory proteins dedicated to dissolution of aberrant strand exchange intermediates (Heyer et al., 2010; San Filippo et al., 2008).

In addition to facilitated exchange, Atto565-labeled substrates bearing an 8-nt microhomology motif were also displaced from the PC when challenged with a fully homologous 70-bp substrate (DNA_{3,0}), but only if the homologous substrate overlapped in sequence with the bound dsDNA (Figures 5E and 5F). This finding implies that the initiation of strand exchange with a homologous substrate anywhere along the PC would be sufficient to drive disruption of captured 8-nt tracts of microhomology located at adjacent positions along the PC, ensuring that strand invasion could progress unimpeded once homology was correctly identified.

Joint Molecules Made with Fully Homologous dsDNA Resist Disruption

The results presented above lead to four predictions for reactions involving homologous substrates: (1) initial sampling of the homologous substrate should exhibit power-law dependence over short time regimes, (2) a homologous substrate should bind to all locations bearing ≥ 8 -nt of microhomology, (3) a captured homologous substrate should exhibit two categories of lifetimes corresponding to those molecules bound to microhomology motifs and those that are bound to the full region of homology, and (4) the captured intermediates should be differentially affected when chased with competitor dsDNA. We tested these predictions using a homologous 70-bp substrate (Atto565-DNA_{3,0}); analysis of this substrate revealed ≥ 8 -nt tracts of microhomology at 19 distinct sites on M13mp18 ssDNA (Figure 6A). As anticipated, the initial sampling intermediates exhibited characteristic power-law behavior, reflecting the existence of a diverse ensemble of transient complexes (Figures 6B and 6C). Once captured, lifetime analysis of the bound dsDNA revealed the existence of two spatially distinct populations: shorter-lived intermediates and longer-lived intermediates that

displayed a periodic binding distribution as expected for the unique 70-nt region of homology (Figures 6C and 6D). As predicted, only the shorter-lived intermediates were disrupted when challenged with competing dsDNA, whereas the longer-lived complexes were resistant to facilitated exchange (Figures 6E and 6F). We conclude that Rad51 utilizes a length-based microhomology recognition mechanism even when presented with a fully homologous substrate and that products generated through strand invasion of the homologous substrate were highly stable.

Model for DNA Sequence Alignment during HR

Our results are unified in a model for how Rad51 aligns DNA sequences during HR (Figure 7A). For clarity, Figure 7A depicts a single interacting unit; we anticipate multiple unit-length interactions will occur throughout the PC, as expected for intersegmental transfer (Forget and Kowalczykowski, 2012). We propose that Rad51 samples dsDNA in 8-nt increments and quickly rejects any sequences lacking 8-nt tracts of contiguous microhomology. This stage of the reaction is characterized by a complex energetic landscape as Rad51 quickly explores a vast amount of sequence space. The presence of an 8-nt tract of microhomology allows dsDNA to be captured through Watson-Crick pairing, enabling Rad51 to probe the flanking duplex for additional complementarity while attempting more extensive strand exchange. If pairing with a ninth nt is successful, then the resulting intermediates are rendered more stable by virtue of more extensive Watson-Crick pairing in precise 3-nt increments, eventually crossing a threshold (~15-nt) beyond which they are much less susceptible to either spontaneous dissociation or facilitated exchange. In contrast, if further strand invasion fails, then any search intermediates bound to incorrect 8-nt tracts of microhomology can be disrupted by either spontaneous dissociation or facilitated exchange, or successful capture of full homology anywhere along the length of the PC will also disrupt any existing search intermediates allowing unimpeded strand exchange.

This model hints at a deeper understanding for how *E. coli* RecA might search for homology—RecA can capture as little as 8-nt of homology (Hsieh et al., 1992), and re-evaluation of the 1,762-nt ssDNA and 48,502-bp dsDNA sequences used to substantiate the RecA intersegmental transfer mechanism reveals a total of 2,089 tracts of 8-nt microhomology (Forget and Kowalczykowski, 2012). We suggest that RecA may establish numerous points of contact with dsDNA through these short tracts of microhomology.

A Conserved Search Mechanism for the Rad51/RecA Recombinases

The salient feature of our model for the homology search is that it minimizes nonproductive interactions with short (≤ 7 -nt) dsDNA sequences that have little chance of being the homologous target. This assertion is based upon two key features of *S. cerevisiae* Rad51: (1) rapid sampling and rejection of dsDNA lacking microhomology motifs through a mechanism characterized by its distinctive power-law dependence, and (2) length-specific kinetic selection of microhomology tracts (Figure 7A). We next asked whether human Rad51 (hRad51), *S. cerevisiae* Dmc1, and *E. coli* RecA behaved similarly. Remarkably, all three

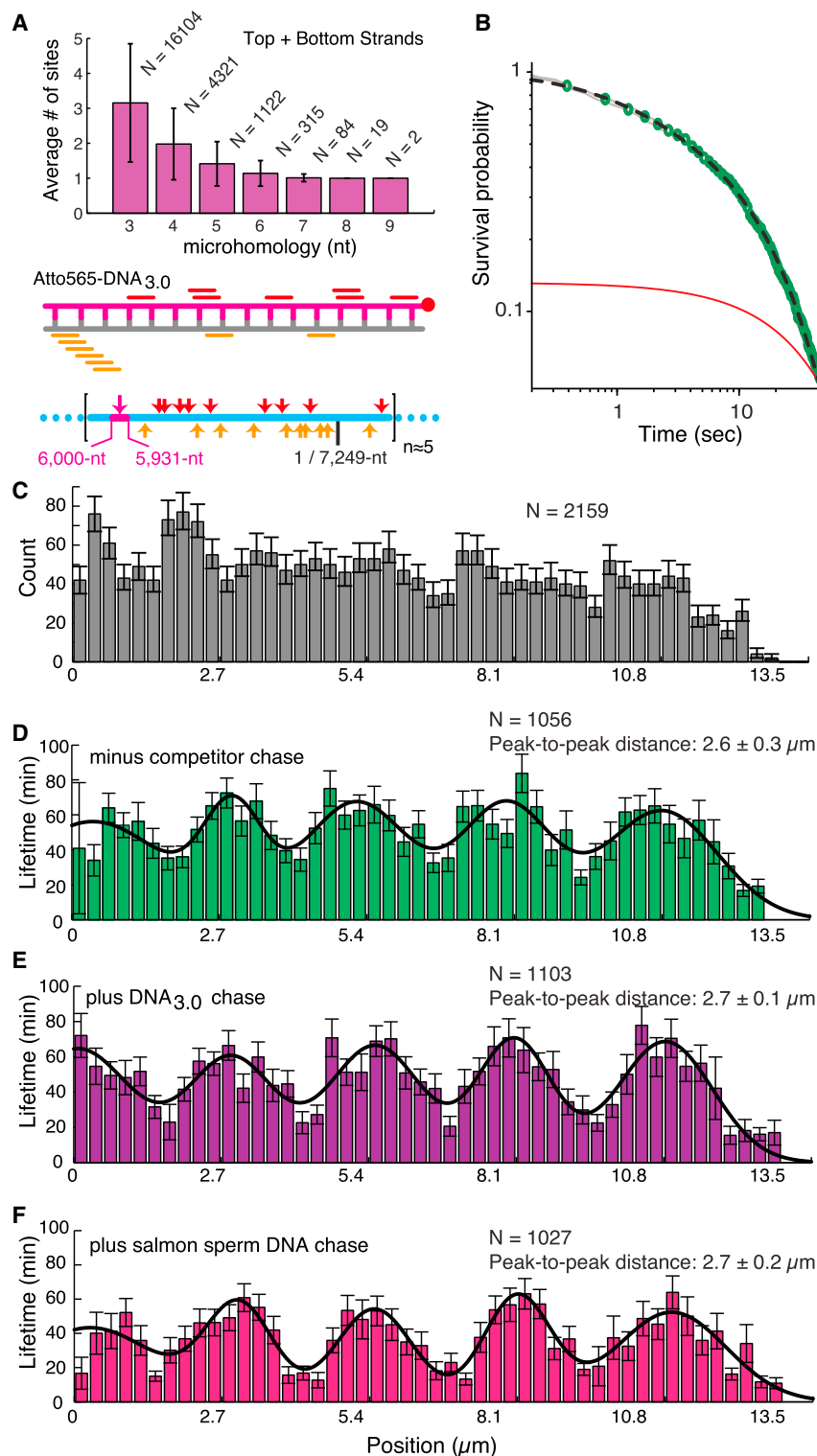


Figure 6. Sampling and Capture of a Fully Homologous Substrate

(A) Microhomology analysis and schematic of the 70-bp homologous dsDNA substrate (Atto565-DNA_{3,0}) highlighting the ≥ 8 -nt tracts of microhomology complementary to the M13mp18 ssDNA substrate.

(B) Power-law dependence of search intermediates observed with DNA_{3,0}. The dashed black line shows combination of a power-law and single exponential fit (to account for photo-bleaching) to the data, and the red line presents an exponential fit to the data for comparison.

(C) Observed binding distribution of Atto565-DNA_{3,0} at time zero.

(D) Lifetime distribution of Atto565-DNA_{3,0} in the absence of competitor dsDNA challenge.

(E and F) Lifetime distribution of Atto565-DNA_{3,0} when challenged with either (E) 1 μM DNA_{3,0} or (F) 1 μM salmon sperm DNA. N corresponds to the number of Atto565-DNA molecules measured. Error bars represent SEM.

three proteins preferentially captured substrates harboring 8-nts of microhomology (Figure 7C). These results revealed that recognition of an 8-nt microhomology motif coincided with ~ 6.1 , ~ 6.5 , and $\sim 6.2 k_B T$ ($\Delta\Delta G^\ddagger$) reductions in the free energy landscapes for hRad51, ScDmc1, and RecA, respectively, reflecting the drastic differences in affinity for dsDNA with and without an 8-nt tract of microhomology. These findings suggest that the ability to interrogate dsDNA through a mechanism involving length-specific microhomology recognition emerged early in the evolutionary history of the RAD51/recA gene family.

DISCUSSION

The genetic transactions that take place during HR are governed by the physicochemical properties of the macromolecules that promote these reactions, and a full appreciation for the elegance of DNA recombination requires a detailed understanding of the underlying mechanistic principles. Our work suggests that length-specific kinetic selection of 8-nt microhomology motifs underlies the intrinsic ability of the Rad51/RecA recombinases to efficiently align homologous sequences and mechanistically distinguishes this process from the 3-nt steps that take place during strand exchange.

proteins displayed power-law behavior while transiently sampling dsDNA that lacked 8-nt microhomology motifs, with 50% of the sampling events occurring within 3.5 s, 1.1 s, and 2.5 s for hRad51, ScDmc1, and RecA, respectively (Figure 7B). All

The use of microhomology motifs as recognition elements has crucial implications for understanding how DNA sequences are aligned during HR.

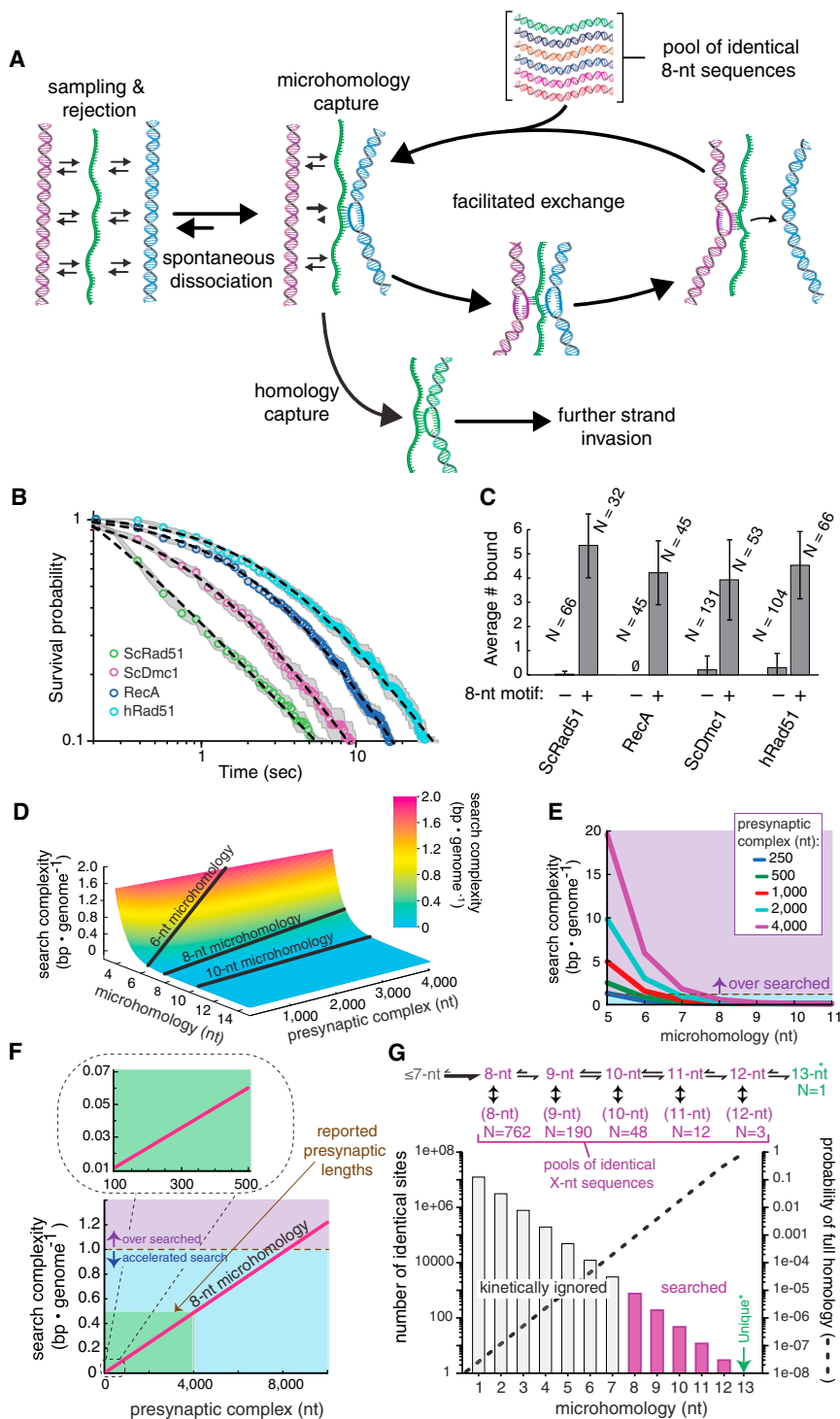


Figure 7. A Conserved Homology Search Mechanism

(A) Model depicting a homology search mechanism involving rapid sampling and rejection of DNA lacking microhomology, followed by eventual capture of an 8-nt tract of microhomology and facilitated exchange allowing for an iterative search through sequence space. Additional details are presented in the main text.

(B and C) Plots showing power-law behavior during dsDNA sampling (B) and microhomology-dependent binding (C) for *E. coli* RecA, hRad51, and *S. cerevisiae* Dmc1. Data presented for ScRad51 are reproduced from Figures 3B and 4E for comparison. The plus and minus 8-nt motif designations in (C) correspond to Atto565-DNA_{2.1} and Atto565-DNA_{2.0}, respectively, and N corresponds to the number of PCs counted. Error bars represent SD.

(D) Surface plot showing how search complexity varies with PC length and the length of microhomology necessary for dsDNA interrogation.

(E) Variation in search complexity for search models employing different lengths of microhomology, as indicated.

(F) Relationship between search complexity and PC length for recognition involving 8-nt of microhomology. The green shaded region encompasses length estimates for *S. cerevisiae* PCs.

(G) Fraction of the *S. cerevisiae* genome that can be kinetically ignored when employing a length-dependent search mechanism based on recognition of 8-nt motifs.

See also Figure S7.

align two homologous sequences can be quantitatively described as search complexity, which reflects the number of sites a searching entity must visit within the genome while attempting to locate a unique sequence (Figure 7A). A full treatment of search complexity is presented as Supplemental Information; here, we highlight key concepts and their relevance to HR. In brief, search complexity can be defined as:

$$\text{complexity (bp} \cdot \text{genome}^{-1}) = \frac{2n}{l} (o - n + 1) \times (l - n + 1) \left(\frac{1}{4}\right)^n$$

where n is the length of microhomology used during the search, l is the length of the genome, and o is PC length. Any value

for search complexity $\geq 1.0 \text{ bp} \times \text{genome}^{-1}$ indicates that the PC will on average sample more than a genome equivalent's worth of sites before locating homology; e.g., for an organism with a $1 \times 10^6 \text{ bp}$ genome, a search complexity of $1 \text{ bp} \times \text{genome}^{-1}$ indicates that the PC would on average need to sample the equivalent of 100% of the genome (i.e., $1 \times 10^6 \text{ bp}$) before

Microhomology Recognition Minimizes Search Complexity

The advantages of a length-based microhomology recognition can be illustrated by considering its influence on the amount of sequence space that must be interrogated during the homology search. The information that must be processed in order to

locating homology. Values $<1.0 \text{ bp} \times \text{genome}^{-1}$ reflect a search that is accelerated relative to genome size; e.g., search complexity of $0.1 \text{ bp} \times \text{genome}^{-1}$ indicates that only one-tenth of the genome would need to be sampled to locate homology.

The benefits of microhomology recognition can now be explored by considering the impact on search complexity (Figures 7D–7G). The most important revelation from this analysis is that search complexity decreases exponentially with the minimal length of microhomology necessary for dsDNA recognition. The source of this exponential dependence is evident given that for any genome short sequences will always have many exact matches, while longer sequences will always have fewer exact matches. For example, any defined 3-nt motif occurs on average once every 639-bp, and there would be $\sim 377,229$ such sequences in the *S. cerevisiae* genome (Figure S7A). In contrast, 8-nt motifs will on average occur just once every 65,536-bp, and there would only be ~ 762 identical 8-nt motifs in the yeast genome (corresponding to an in vivo concentration of $\sim 0.3 \mu\text{M}$ for any given 8-mer). As a consequence, a search utilizing an 8-nt motif would only need to interrogate just $\sim 0.01\%$ of the genome to locate the homologous target, and the vast majority of the genome could be kinetically ignored. Indeed, a homology search involving length-specific recognition of 8-nt motifs, while kinetically minimizing interactions with shorter sequence motifs, would effectively eliminate $\geq 99.9\%$ of the genome for species ranging from *E. coli* to humans.

Genetic and physical measures of the ssDNA overhangs generated during DSB repair suggest that *S. cerevisiae* PCs are ~ 100 – $4,000$ nt in length (Chung et al., 2010; Jinks-Robertson et al., 1993), and it is informative to consider how search complexity varies within this length regime. For a search utilizing 8-nt tracts of microhomology, a 100-nt PC would only need to process information content corresponding to $1/100^{\text{th}}$ of the genome (Figure 7F, inset), a 4,000-nt PC would only need to sample one-half of the genome (Figure 7F), and search complexity would not enter the over searched regime until PC length exceeded $\sim 8,000$ -nt (Figure 7F). In contrast, if one assumes a model without microhomology recognition (i.e., $n = 1$), then PCs ranging from 100– $4,000$ -nt in length might have to process information equivalent to 2,500%–100,000% of the genome. These considerations illustrate how simply subdividing the search into length-based microhomology recognition elements can drastically reduce the time necessary to align homologous sequences.

Physiological Implications for HR and DSB Repair

Our reductionist treatment of search complexity excludes potential effects of accessory factors, chromatin structural proteins, chromosome organization, etc. Interpretation of our results within the context of these physiological realities leads to several important insights and predictions. First, end resection, PC assembly, and the homology search are often presented as distinct stages of DSB repair. However, there is no reason to believe that these reactions are completely uncoupled, and the relative timing of these events dictates how much information must be processed during the homology search. Our results predict a substantial benefit to beginning the homology search as soon as possible after initiating DSB resection (Figure 7G).

Second, for mechanisms involving length-dependent microhomology recognition, the fractional reduction in search complexity is the same regardless of genome size. Although longer recognition motifs offer the potential for further reductions in search complexity, this would compromise reversibility because of the greater enthalpic penalty incurred for disruption of a larger binding surface, which could ultimately lead to misalignment of DNA sequences trapped in local minima. Moreover, assuming a randomized nucleotide distribution, the length required to statistically define a given sequence as unique does not vary drastically across species. For instance, average lengths of just ~ 12 , ~ 13 , and ~ 17 nucleotides are sufficient to uniquely define most sequences within the *E. coli*, *S. cerevisiae*, and human genomes, respectively (Figure S7B). These considerations imply that there may be little or no evolutionary pressure to utilize longer tracts of microhomology to compensate for variations in genome size. Notably, real genomes contain repetitive sequences and other regions of low sequence complexity (e.g., rDNA and tRNA genes, transposons, centromeres, telomeres, etc.), and such regions would require longer sequences to define “uniqueness,” or else may suffer from a greater potential for misalignment during HR. Interestingly, recombination within these regions is often suppressed and/or otherwise tightly regulated (Eckert-Boulet and Lisby, 2009, 2010; Pan et al., 2011; Sasaki et al., 2010), perhaps reflecting in part the unique challenges faced by the recombination machinery in these regions of low sequence complexity.

Third, PC organization affects the amount of information that must be processed during the homology search. The preceding discussion assumes a contiguous PC consisting of all possible overlapping 8-nt units (Figure S7C). However, search complexity declines by an entire order of magnitude if the PC is segregated into non-overlapping 8-nt sections, and intermediate subdivisions are similarly beneficial (Figures S7C–S7E). It is not known whether PCs in vivo are comprised of uninterrupted Rad51/RecA filaments, or whether they contain protein-free gaps and/or other physical discontinuities (e.g., other HR proteins). Our results suggest some proteins could promote HR by segregating Rad51/RecA filaments into non-overlapping functional units.

Fourth, once the PC has engaged a particular 8-nt tract of microhomology it can undergo exchange with other regions of dsDNA bearing the same microhomology, but resists exchange with unrelated sequences. Moreover, shorter tracts of microhomology are more readily exchanged with longer tracts, reflecting the higher stability of intermediates held together by longer tracts of Watson-Crick pairing. Preferential exchange with longer tracts of microhomology may yield a hierarchy of increasingly stable intermediates, which might in turn funnel the PC through progressively smaller pools of sequences leading to the homologous target (Figure 7G).

Fifth, compartmentalization of the search through either spatial organization or steric occlusion will decrease search complexity linearly with respect to the amount of sequence accessible for interrogation. Benefits are readily envisaged if homologous chromosomes are physically juxtaposed, as anticipated for sister chromatids immediately following DNA replication, and accumulating evidence suggests that homologous sequences also have a greater probability of being juxtaposed

at other points in the cell cycle (Barzel and Kupiec, 2008; Gladyshev and Kleckner, 2014; Weiner and Kleckner, 1994). Similarly, restricting search intermediates to the linker DNA between nucleosomes could reduce search complexity by ~75% based on nucleosome occupancy of the *S. cerevisiae* genome.

Reduction of Dimensionality versus Reduction of Search Complexity

Target search studies have historically centered upon whether the path-to-target involves 3D diffusion (i.e., “jumping”), or pathways that accelerate the search through reduction of dimensionality (i.e., facilitated diffusion), such as 1D diffusion (i.e., sliding or “hopping”), or intersegmental transfer (von Hippel and Berg, 1989). Our results now highlight reduction of search complexity as an efficient means of accelerating target searches. Rad51 accomplishes this by first looking for a small portion of its target before testing the flanking DNA for homology. The difference in stability for substrates bearing ≤ 7 -nt versus ≥ 8 -nt of microhomology minimizes off-target interactions, ensuring that Rad51 spends most of the search interrogating sequences that already have a high probability of being a homologous target (Figure 7G). This mechanism is strikingly similar to the strategy employed by the Cas9 CRISPR RNA-guided endonuclease (Sternberg et al., 2014). Cas9 search intermediates are restricted to a trinucleotide sequence called the protospacer adjacent motif (PAM). Cas9 kinetically ignores non-PAM sequences, but binds transiently to PAMs (5'-NGG-3'), allowing it to test the flanking dsDNA for complementarity to the guide RNA. This simple mechanism allows Cas9 to kinetically ignore ~90% of the λ phage genome, ensuring that the search is focused on sequences that have a high probability of being the correct target (Sternberg et al., 2014). Rad51 and Cas9 are unrelated, yet they share extraordinarily similar search strategies—the only difference is that Cas9 looks for a fixed 3-nt motif, whereas Rad51 looks for variable 8-nt motifs. We suggest that similar mechanisms involving the initial recognition of short sequence motifs representing just a small portion of a complete binding site may be a broadly utilized strategy for DNA-binding proteins to minimize search complexity while searching within genomes for particular targets.

CONCLUSIONS

Our work supports a model in which short tracts of microhomology represent the fundamental functional units of dsDNA recognition during HR, yielding insights into how Rad51/RecA recombinases align homologous sequences. The emergent concepts may be broadly applicable.

EXPERIMENTAL PROCEDURES

S. cerevisiae RPA-eGFP and *S. cerevisiae* Rad51 were expressed and purified as previously described (Gibb et al., 2014a). Single-stranded DNA substrates were prepared by rolling circle replication using $\phi 29$ DNA polymerase and a 5' biotinylated primer annealed to a circular M13mp18 ssDNA template (Gibb et al., 2012). Fused silica slides were patterned by e-beam lithography and lipid bilayers were prepared with 91.5% DOPC, 0.5% biotinylated-DPPE, and 8% mPEG 550-DOPE (Avanti Polar Lipids) (Greene et al., 2010). Experiments were performed using a prism-type TIRFM equipped with 488-nm and 561-nm lasers (Coherent) and two iXon EMCCDs (Andor Technology). Videos were collected

with NIS Elements AR (Nikon), data were quantitated using NIH Image J, and all survival probability curves were corrected for photo-bleaching.

All ScRad51 experiments were conducted at 30°C in HR buffer containing 30 mM Tris-acetate (pH 7.5), 20 mM Mg-acetate, 50 mM KCl, 1 mM DTT, 0.2 mg/ml BSA, plus 2.5 mM ATP (Sugiyama et al., 1997). Presynaptic complexes were assembled by incubating RPA-eGFP bound ssDNA curtains with 2 μ M ScRad51 in HR buffer for 15 min at 30°C. Free ScRad51 was then flushed from the sample chamber using HR buffer plus 2.5 mM ATP. Presynaptic complex assembly was confirmed by visual inspection of the ssDNA before, during, and after the ScRad51 injection.

DNA binding was measured by injecting Atto565-dsDNA (10 nM) into the sample chambers. Reactions were then incubated for 10 min in the absence of buffer flow, and free dsDNA was quickly flushed away. For reactions containing competitor dsDNA, the competitor was included at the indicated concentration in the buffer used to flush the sample chamber. Data were obtained by acquiring single 100-ms frames at either 20-s, 30-s, 40-s, or 60-s intervals, and the laser was shuttered between each acquired image to minimize photo-bleaching. Kymographs were generated from the resulting videos. The average number of bound dsDNA molecules, binding distributions and survival probabilities were all determined from analysis of the kymographs.

Transient dsDNA sampling at higher temporal resolution was measured by injecting Atto565-tagged dsDNA substrate (10 nM), buffer flow was then terminated and data were acquired using a 60-ms exposure time and continuous laser illumination in the absence of shuttering. The resulting data was analyzed based on the corresponding kymographs, as previously described (Sternberg et al., 2014).

Reaction conditions for *E. coli* RecA, *S. cerevisiae* Dmc1, and human Rad51 are presented in the Extended Experimental Procedures. Search complexity calculations presented in Figure 7 are described in the Extended Experimental Procedures.

SUPPLEMENTAL INFORMATION

Supplemental Information includes Extended Experimental Procedures and seven figures and can be found with this article online at <http://dx.doi.org/10.1016/j.cell.2015.01.029>.

AUTHOR CONTRIBUTIONS

Z.Q. designed and conducted the single-molecule experiments and data analysis. S.R. conducted all theoretical calculations and assisted in data analysis and experimental design. J.Y.L. assisted with single-molecule experiments, data analysis, and experimental design. B.G. expressed and purified human and yeast RPA and assisted with Rad51 characterization. Y.K., H.N., and W.G. purified yeast and human Rad51 and yeast Dmc1. E.C.G. supervised the project and wrote the manuscript with input from all co-authors.

ACKNOWLEDGMENTS

We thank Lorraine Symington, Max Gottesman, Jonathan Dworkin, Hannah Klein, Rodney Rothstein, and members of the E.C.G. and P.S. laboratories for comments on the manuscript. We are grateful to Mara Prentiss for sharing results prior to publication, and Mauro Modesti for providing GFP-tagged hRPA expression constructs. This research was funded by NIH grants GM074739 (E.C.G.), RO1ES007061 (P.S.), and CA146940 (E.C.G. and P.S.), and by NSF grant MCB-1154511 (E.C.G.). E.C.G. is an HHMI Early Career Scientist.

Received: September 26, 2014

Revised: November 18, 2014

Accepted: January 9, 2015

Published: February 12, 2015

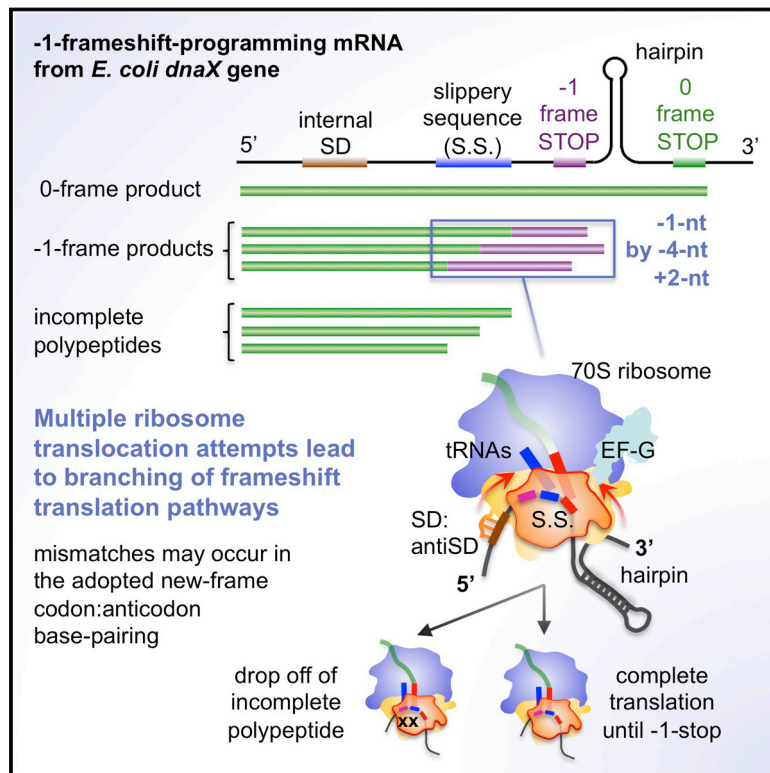
REFERENCES

Adzuma, K. (1998). No sliding during homology search by RecA protein. *J. Biol. Chem.* 273, 31565–31573.

- Austin, R.H., Beeson, K.W., Eisenstein, L., Frauenfelder, H., and Gunsalus, I.C. (1975). Dynamics of ligand binding to myoglobin. *Biochemistry* 14, 5355–5373.
- Barzel, A., and Kupiec, M. (2008). Finding a match: how do homologous sequences get together for recombination? *Nat. Rev. Genet.* 9, 27–37.
- Bianco, P.R., Tracy, R.B., and Kowalczykowski, S.C. (1998). DNA strand exchange proteins: a biochemical and physical comparison. *Front. Biosci.* 3, D570–D603.
- Chen, Z., Yang, H., and Pavletich, N.P. (2008). Mechanism of homologous recombination from the RecA-ssDNA/dsDNA structures. *Nature* 453, 489–494.
- Chung, W.H., Zhu, Z., Papusha, A., Malkova, A., and Ira, G. (2010). Defective resection at DNA double-strand breaks leads to de novo telomere formation and enhances gene targeting. *PLoS Genet.* 6, e1000948.
- Danilowicz, C., Peacock-Villada, A., Vlassakis, J., Facon, A., Feinstein, E., Kleckner, N., and Prentiss, M. (2014). The differential extension in dsDNA bound to Rad51 filaments may play important roles in homology recognition and strand exchange. *Nucleic Acids Res.* 42, 526–533.
- De Vlaminc, I., van Loenhout, M.T., Zweifel, L., den Blanken, J., Hoening, K., Hage, S., Kerssemakers, J., and Dekker, C. (2012). Mechanism of homology recognition in DNA recombination from dual-molecule experiments. *Mol. Cell* 46, 616–624.
- Eckert-Boulet, N., and Lisby, M. (2009). Regulation of rDNA stability by sumoylation. *DNA Repair (Amst.)* 8, 507–516.
- Eckert-Boulet, N., and Lisby, M. (2010). Regulation of homologous recombination at telomeres in budding yeast. *FEBS Lett.* 584, 3696–3702.
- Forget, A.L., and Kowalczykowski, S.C. (2012). Single-molecule imaging of DNA pairing by RecA reveals a three-dimensional homology search. *Nature* 482, 423–427.
- Fraser, C., Hanage, W.P., and Spratt, B.G. (2007). Recombination and the nature of bacterial speciation. *Science* 315, 476–480.
- Frauenfelder, H., Sligar, S.G., and Wolynes, P.G. (1991). The energy landscapes and motions of proteins. *Science* 254, 1598–1603.
- Gibb, B., Silverstein, T.D., Finkelstein, I.J., and Greene, E.C. (2012). Single-stranded DNA curtains for real-time single-molecule visualization of protein-nucleic acid interactions. *Anal. Chem.* 84, 7607–7612.
- Gibb, B., Ye, L.F., Gergoudis, S.C., Kwon, Y., Niu, H., Sung, P., and Greene, E.C. (2014a). Concentration-dependent exchange of replication protein A on single-stranded DNA revealed by single-molecule imaging. *PLoS ONE* 9, e87922.
- Gladyshev, E., and Kleckner, N. (2014). Direct recognition of homology between double helices of DNA in *Neurospora crassa*. *Nat. Commun.* 5, 3509.
- Graham, J.S., Johnson, R.C., and Marko, J.F. (2011). Concentration-dependent exchange accelerates turnover of proteins bound to double-stranded DNA. *Nucleic Acids Res.* 39, 2249–2259.
- Greene, E.C., Wind, S., Fazio, T., Gorman, J., and Visnapuu, M.L. (2010). DNA curtains for high-throughput single-molecule optical imaging. *Methods Enzymol.* 472, 293–315.
- Hastings, P.J., Lupski, J.R., Rosenberg, S.M., and Ira, G. (2009). Mechanisms of change in gene copy number. *Nat. Rev. Genet.* 10, 551–564.
- Hawkins, M., Malla, S., Blythe, M.J., Nieduszynski, C.A., and Allers, T. (2013). Accelerated growth in the absence of DNA replication origins. *Nature* 503, 544–547.
- Heyer, W.D., Ehmsen, K.T., and Liu, J. (2010). Regulation of homologous recombination in eukaryotes. *Annu. Rev. Genet.* 44, 113–139.
- Hsieh, P., Camerini-Otero, C.S., and Camerini-Otero, R.D. (1992). The synapsis event in the homologous pairing of DNAs: RecA recognizes and pairs less than one helical repeat of DNA. *Proc. Natl. Acad. Sci. USA* 89, 6492–6496.
- Jinks-Robertson, S., Michelitch, M., and Ramcharan, S. (1993). Substrate length requirements for efficient mitotic recombination in *Saccharomyces cerevisiae*. *Mol. Cell. Biol.* 13, 3937–3950.
- Lin, Z., Kong, H., Nei, M., and Ma, H. (2006). Origins and evolution of the recA/RAD51 gene family: evidence for ancient gene duplication and endosymbiotic gene transfer. *Proc. Natl. Acad. Sci. USA* 103, 10328–10333.
- Neale, M.J., and Keeney, S. (2006). Clarifying the mechanics of DNA strand exchange in meiotic recombination. *Nature* 442, 153–158.
- Pan, J., Sasaki, M., Kniewel, R., Murakami, H., Blitzblau, H.G., Tischfield, S.E., Zhu, X., Neale, M.J., Jasin, M., Socci, N.D., et al. (2011). A hierarchical combination of factors shapes the genome-wide topography of yeast meiotic recombination initiation. *Cell* 144, 719–731.
- Ragunathan, K., Liu, C., and Ha, T. (2012). RecA filament sliding on DNA facilitates homology search. *eLife* 1, e00067.
- Renkawitz, J., Lademann, C.A., and Jentsch, S. (2014). Mechanisms and principles of homology search during recombination. *Nat. Rev. Mol. Cell Biol.* 15, 369–383.
- San Filippo, J., Sung, P., and Klein, H. (2008). Mechanism of eukaryotic homologous recombination. *Annu. Rev. Biochem.* 77, 229–257.
- Sasaki, M., Lange, J., and Keeney, S. (2010). Genome destabilization by homologous recombination in the germ line. *Nat. Rev. Mol. Cell Biol.* 11, 182–195.
- Sing, C.E., Olvera de la Cruz, M., and Marko, J.F. (2014). Multiple-binding-site mechanism explains concentration-dependent unbinding rates of DNA-binding proteins. *Nucleic Acids Res.* 42, 3783–3791.
- Smith, C.E., Llorente, B., and Symington, L.S. (2007). Template switching during break-induced replication. *Nature* 447, 102–105.
- Sternberg, S.H., Redding, S., Jinek, M., Greene, E.C., and Doudna, J.A. (2014). DNA interrogation by the CRISPR RNA-guided endonuclease Cas9. *Nature* 507, 62–67.
- Sugiyama, T., Zaitseva, E.M., and Kowalczykowski, S.C. (1997). A single-stranded DNA-binding protein is needed for efficient presynaptic complex formation by the *Saccharomyces cerevisiae* Rad51 protein. *J. Biol. Chem.* 272, 7940–7945.
- von Hippel, P.H., and Berg, O.G. (1989). Facilitated target location in biological systems. *J. Biol. Chem.* 264, 675–678.
- Weiner, B.M., and Kleckner, N. (1994). Chromosome pairing via multiple interstitial interactions before and during meiosis in yeast. *Cell* 77, 977–991.
- Xiao, J., Lee, A.M., and Singleton, S.F. (2006). Direct evaluation of a kinetic model for RecA-mediated DNA-strand exchange: the importance of nucleic acid dynamics and entropy during homologous genetic recombination. *ChemBioChem* 7, 1265–1278.

Ribosome Excursions during mRNA Translocation Mediate Broad Branching of Frameshift Pathways

Graphical Abstract



Authors

Shannon Yan, Jin-Der Wen, Carlos Bustamante, Ignacio Tinoco

Correspondence

intinoco@lbl.gov

In Brief

Programmed frameshifting allows the translation of alternative protein products from a single transcript. To achieve this, *E. coli* ribosomes undergo several translocation excursions to shift reading frames and access a range of codon positions.

Highlights

- Ribosome translocation excursions occur before adopting a frame to resume translation
- Ribosomes achieve –1, –4, and +2 nt slips to enter the –1 frame on the mRNA
- Ribosomes frameshift not from one specific codon but from a range of codon positions
- The presence of incomplete translation products underscores fidelity maintenance



Ribosome Excursions during mRNA Translocation Mediate Broad Branching of Frameshift Pathways

Shannon Yan,¹ Jin-Der Wen,² Carlos Bustamante,^{1,3,4,5,6,7,8} and Ignacio Tinoco, Jr.^{1,*}

¹Department of Chemistry, University of California, Berkeley, Berkeley, CA 94720, USA

²Institute of Molecular and Cellular Biology, National Taiwan University, Taipei 10617, Taiwan

³Jason L. Choy Laboratory of Single-Molecule Biophysics, University of California, Berkeley, Berkeley, CA 94720, USA

⁴QB3 Institute, University of California, Berkeley, Berkeley, CA 94720, USA

⁵Department of Molecular and Cell Biology, University of California, Berkeley, Berkeley, CA 94720, USA

⁶Department of Physics, University of California, Berkeley, Berkeley, CA 94720, USA

⁷Howard Hughes Medical Institute, University of California, Berkeley, Berkeley, CA 94720, USA

⁸Kavli Energy NanoSciences Institute, Berkeley, CA 94720, USA

*Correspondence: intinoco@lbl.gov

<http://dx.doi.org/10.1016/j.cell.2015.02.003>

SUMMARY

Programmed ribosomal frameshifting produces alternative proteins from a single transcript. -1 frameshifting occurs on *Escherichia coli*'s *dnaX* mRNA containing a slippery sequence AAAAAAG and peripheral mRNA structural barriers. Here, we reveal hidden aspects of the frameshifting process, including its exact location on the mRNA and its timing within the translocation cycle. Mass spectrometry of translated products shows that ribosomes enter the -1 frame from not one specific codon but various codons along the slippery sequence and slip by not just -1 but also -4 or $+2$ nucleotides. Single-ribosome translation trajectories detect distinctive codon-scale fluctuations in ribosome-mRNA displacement across the slippery sequence, representing multiple ribosomal translocation attempts during frameshifting. Flanking mRNA structural barriers mechanically stimulate the ribosome to undergo back-and-forth translocation excursions, broadly exploring reading frames. Both experiments reveal aborted translation around mutant slippery sequences, indicating that subsequent fidelity checks on newly adopted codon position base pairings lead to either resumed translation or early termination.

INTRODUCTION

During translation, the ribosome successively reads three nucleotides—one codon—at a time to produce the protein encoded in the messenger RNA (mRNA). This process involves base pairing each codon with the anticodon of the cognate aminoacylated transfer RNA (aa-tRNA). As a result, each mRNA sequence specifies one unique polypeptide translated from start to stop codon in the so-called 0 frame. Crystals of such ribosomes in the de-

coding mode—complexed with mRNA and two tRNAs—have provided a detailed structural basis for reading frame maintenance (Jenner et al., 2010; Schmeing and Ramakrishnan, 2009; Selmer et al., 2006; Stahl et al., 2002; Yusupov et al., 2001). Specifically, the mRNA wrapping around the neck of the ribosome small subunit is kinked into segments, with the three consecutive codons positioned in the exit- (E), peptidyl- (P), and aminoacyl- (A) codon:anticodon binding sites. The anticodon stem loop and the aminoacyl-acceptor end of each tRNA are accommodated on the small (30S) and large (50S) subunits, respectively, corresponding to the classical-state P/P- and A/A-tRNAs (capital letters denote sites on 30S/50S). After peptidyl-transfer between the tRNAs, the ribosome facilitates the two tRNAs to adopt hybrid states in which the anticodons remain in the 30S P and A sites, but the acceptor ends have advanced to the E and P sites on the 50S, denoted as P/E- and A/P-tRNAs (Bretscher, 1968; Moazed and Noller, 1989a). Upon binding elongation factor EF-G in the A site, the ribosome can proceed to translocate one codon forward (Rodnina and Wintermeyer, 2011; Savelsbergh et al., 2003). The strict reading frame configuration and the segregation of decoding and translocation help keep the translation accurate with an error rate of less than 0.1% (Drummond and Wilke, 2009).

However, ribosomes can be programmed to frameshift—accessing either of the two out-of-frames (-1 or $+1$ frame), thereby expanding gene coding capacity on a single transcript (Farabaugh, 1996). Such a mechanism is essential to the virulence of compact genomic systems such as HIV-1, where successive frameshifts occur on the mRNA to produce a retroviral polyprotein (Jacks et al., 1988).

Here, we investigate frameshift-programming mRNAs derived from the *Escherichia coli dnaX* gene. Its -1 frameshift efficiency in vivo reaches 80%, yielding a 4:1 product ratio between the γ subunit and the τ subunit of DNA polymerase III (Tsuchihashi and Brown, 1992). Such translation regulation is achieved by three sequence elements in the mRNA: a heptanucleotide slippery sequence AAAAAAG that is flanked by an internal Shine-Dalgarno sequence located 10 nucleotides (nt) upstream and an 11 base pair (bp) hairpin 6 nt downstream (Figure 1A). It has

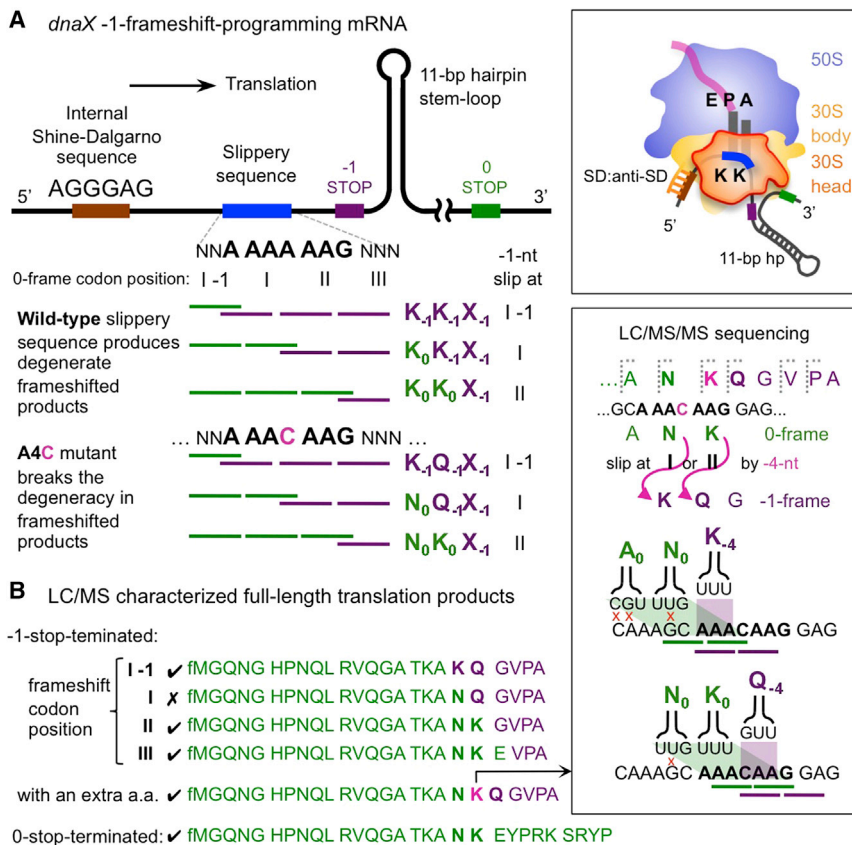


Figure 1. Resolving Ribosomal Frame-shifting Codon Positions on *dnaX*-Derived mRNAs

(A) Three mRNA sequence elements program the -1 nt ribosomal frameshift: a slippery sequence, AAAAAAG (region in blue), an internal Shine-Dalgarno sequence (region in brown), and a downstream hairpin. The cartoon shows the position of these elements on the mRNA relative to the ribosome. Exact frameshift codon positions are indistinguishable due to the identical product sequence. A single mutation A4C in the slippery sequence (I and II denotes the two 0 frame codons) differentiates possible frameshift positions.

(B) Various -1-stop-terminated products (sequences ended in purple) from the A4C mutant, detected by LC/MS, show that ribosomes frameshift from different codons around the slippery sequence, including positions I-1, II, and III. One major frameshifted product, sequenced by LC/MS/MS, bears an extra amino acid in the slippery sequence region (Figure S1D and Table S2); thus, the ribosome has slipped by -4 nt to enter the -1 frame. Two degenerate frameshift pathways exist to translate such a product (right box): -4 slip at codon position I or II (green-shaded rhombus area); the latter imposes fewer codon:anticodon base pair mismatches (red crosses).

long been thought that, while the ribosome decodes the 0 frame codons in the slippery sequence (A₃AAA₃AAG), the peripheral base-pairing structures on the mRNA serve as barriers to impede normal translation and promote backward frameshifting by 1 nt (Figure 1A) (Gesteland and Atkins, 1996). Specifically, the upstream Shine-Dalgarno sequence hybridizes with the complementary anti-Shine-Dalgarno sequence at the 3' end of 16S ribosomal RNA (rRNA), thus forming a flexible yet mRNA-anchoring mini-helix (Jenner et al., 2007; Kaminishi et al., 2007; Korostelev et al., 2007; Yusupova et al., 2006). Downstream, the base-pairing junction of the hairpin acts as a roadblock situated at the mRNA entry site on the ribosome—a single-strand-permitting channel formed by three ribosomal proteins: S3 on the 30S head and S4 and S5 from the 30S body (Yusupova et al., 2001).

Recently, perturbed ribosome translation dynamics on the slippery sequence has been confirmed and visualized in single-molecule fluorescence resonance energy transfer (FRET) experiments (Chen et al., 2014; Kim et al., 2014). However, exact details on how the programmed mRNA elements act on the ribosome to induce frameshifting dynamics remain unclear (Tinoco et al., 2013). For example, from which 0 frame codon does the ribosome frameshift? In which sub-step within the translation cycle does the frameshift take place? How does the frameshift-programming mRNA break the regular ribosome translation stepping—3 nt per codon—to promote efficient and apparently precise frameshifting? Answering these questions requires looking beyond ribosome conformational

dynamics; we thus sought to examine the ribosome translation dynamics on the mRNA and to characterize the synthesized polypeptides.

Here, we use mass spectrometry (MS) to analyze the products of translation along *dnaX*-derived mRNAs containing wild-type or mutant slippery sequences. These analyses reveal that the ribosome can access a broad range of frameshift pathways by shifting from different codon positions and using various slipping sizes. We complement these studies by acquiring single-ribosome translation trajectories using optical tweezers (Wen et al., 2008) to follow in real-time the ribosome dynamics that accompanies the exploration of alternative frameshift pathways. These trajectories display distinctive fluctuations—larger than 1 nt—in mRNA displacement during translocation as the ribosome attempts to overcome the mRNA structural barriers flanking the slippery sequence. We found that, after this dynamic exploration, the ribosome may frameshift, but it is sensitive to mismatches that result from the pairing between the frameshifted codons and anticodons. These mismatches likely trigger a fidelity check mechanism that results in the ribosome either to continue translation in a new frame or to prematurely abort translation.

RESULTS

Frameshifts Occur at Various Codon Positions

Ribosomes are thought to backshift on the mRNA slippery sequence—AAAAAAG for the *dnaX* gene—and translate to the -1 stop codon (Figure 1A) (Farabaugh, 1996). This conjecture is based on the fact that, here, both the 0 frame (A₃AAA₃AAG)

and -1 frame (AAA₀AAA₀G) encode identical amino acids: a pair of lysines. Hence, a -1 nt slippage in this region involves minimal base-pairing difference between the lysine codons, AAA and AAG, and the UUU anticodon used in *E. coli* (Tsuchihashi and Brown, 1992). Note, however, that the resultant tandem lysines incorporated in the frameshifted product preclude identifying from the polypeptide sequence where exactly the 0 frame ends. As shown in Figure 1A, on the *dnaX* slippery sequence, there are three possible decoding routes, all translating the same amino acids but via a -1 frameshift at different codon positions. To differentiate those potential decoding routes, we introduced a slippery sequence variant: A₀AAC₀AAG, which retains $\sim 5\%$ frameshift efficiency in vivo (Tsuchihashi and Brown, 1992). The single mutation of the fourth adenine to a cytosine lifts the encoding degeneracy and yields different amino acid compositions depending on the last-read 0 frame codon position (Figure 1A, A4C mutant; the two 0 frame codons in the slippery sequence are denoted as positions I and II). Like the original *dnaX* mRNA, the mRNA variant contains an upstream internal Shine-Dalgarno sequence and a downstream 25 bp duplex equivalently 6 nt downstream from the slippery sequence (Figure S1A); we denote this design as the “25 bp” mRNA construct. To generate samples for frameshifting analysis, in-vitro-transcribed and gel-purified mRNAs, together with *E. coli* 70S ribosomes, were added to a reconstituted translation mixture (PURExpress Δ Ribosome kit, NEB) (Ohashi et al., 2010). The in vitro translation products were then collected and examined using liquid chromatography/mass spectrometry (LC/MS) intact polypeptide detection (Extended Experimental Procedures).

In addition to the non-frameshifted, 0-stop-terminated polypeptide (Figure 1B, bottom-most sequence in green), multiple frameshifted products terminating at the -1 stop were identified (Figure 1B; the last green-colored residue of each sequence shows the last read 0 frame codon from which the ribosome frameshifts). We found that ribosomes take two of the three possible -1 -frameshift-decoding routes (at codon position I-I and II), respectively incorporating K₋₁Q₋₁ or N₀K₀ from the slippery sequence (subscripts denote the frame); or they switch to the -1 frame after the slippery sequence at codon position III (Figure 1B, fourth sequence from the top). The frameshifted polypeptide via slipping at codon position I was, however, not observed (Figure S1B). Whereas a recent search for -1 -frameshifted products was limited to two codon positions on the slippery sequence of HIV-1 (Liao et al., 2011), here we observed that frameshifts in fact emerge from at least three positions.

We explored two more mRNA templates, bearing either the original frameshift-promoting slippery sequence, AAAAAAG (wild-type/25 bp; $\sim 80\%$ frameshift efficiency in vivo) or a frameshift-attenuating variant, AAAAGAG (A5G/25 bp; $\sim 0\%$ frameshift efficiency in vivo) (Tsuchihashi and Brown, 1992). In all templates examined, independently of the frameshift efficiencies attained, the ribosome undergoes -1 frameshifts from a broad range of codon positions spanning regions before, within, and beyond the slippery sequence (Table S1).

Ribosomes Frameshift via Various Slip Sizes

Intriguingly, one polypeptide ~ 100 Da heavier than the other identified -1 -frameshifted products was consistently detected

in the mass spectrum ($n = 5$) as a major species translated from the A4C mutant mRNA (Figure 2A, top box, largest red bar: $\sim 74\%$ of all -1 -stop-terminated products detected). To determine the sequence of this unexpected product, we employed tandem mass spectrometry (LC/MS/MS) to select and fragment the polypeptide (Figure 1B, right box; Table S2). We found that not two but three amino acids were incorporated along the slippery sequence for this unusual -1 -stop-terminated frameshifted product. To translate an extra amino acid while switching to the -1 frame, the ribosome must slip by -4 nt during frameshifting.

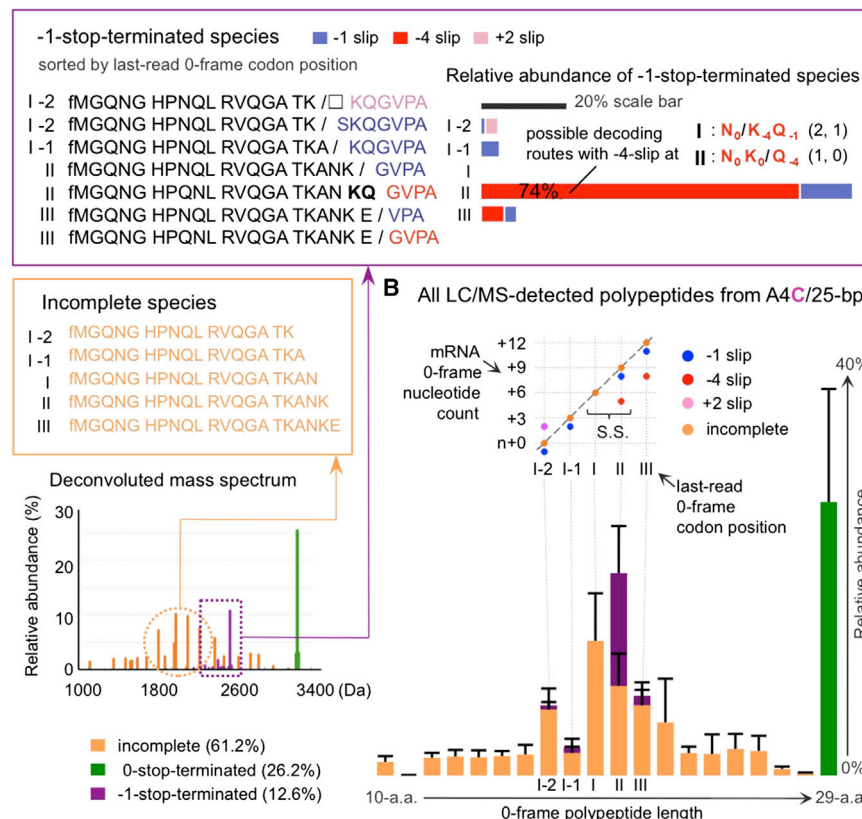
The resolved three amino acids, NKQ, can be translated via two possible decoding routes: a -4 slip either at codon position I or at position II on the slippery sequence (Figure 1B, right box). In the first route, the 0 frame ends at asparagine to yield N₀K₋₁Q₋₁; thus, the last two 0-frame-specified tRNAs carrying the alanine and asparagine—after backshifting on the mRNA by 4 nt—would encounter three mismatches (red crosses). In contrast, the second route would cause only one mismatch for the tRNA^{Asn}, suggesting that this route involving a -4 slip from codon position II could be the more productive frameshift pathway.

For the other two templates (wild-type/25 bp and A5G/25 bp), several, though less abundant, frameshifted products bearing an extra amino acid were also detected (Figure S2A and Table S1; relative abundance $\sim 5\%$ and $\sim 3\%$ of overall -1 -stop-terminated products). These species point to the general capability of the ribosome to conduct -4 nt slips on -1 -frameshift-programming mRNAs. The presence of -4 slip products led us to expand the search for alternative slipping sizes entering the -1 frame (our template design is capable of detecting only slips into the -1 frame and thus precludes readout of potential $+1$ frameshifting; see Figure S1A). We found that ribosomes also take $+2$ slips and terminate at the -1 stop, producing frameshifted polypeptides one amino acid short (Figure 2A top box, sequences ended in pink; relative abundance $\sim 3\%$ for A4C).

The Figure 2A top box summarizes the relative abundance of all -1 -stop-terminated products detected by LC/MS for the A4C mutant template (wild-type and A5G are in Table S1; see Extended Experimental Procedures for explanation of abundance measurements). These findings show that ribosomes slip by -1 , -4 , or $+2$ nt at various codon positions around the slippery sequence region, producing a collection of -1 -stop-terminated products. While an earlier work reported that specific slipping sizes, e.g., -2 , -1 , $+2$, $+5$, and $+6$ nt, can be individually programmed by different mRNA templates (Weiss et al., 1987), our study shows that various slipping sizes take place on a single naturally occurring template. Note that the MS-resolved frameshifted polypeptides reported here would have appeared as a single protein band on electrophoresis gels, therefore being indistinguishable in earlier studies (Tsuchihashi and Brown, 1992).

The -1 -stop- and 0-stop-terminated full-length products, however, only account for a fraction of the polypeptides found in the mass spectrum, e.g., $\sim 39\%$ of the total intensity of all species detected from the A4C template (Figure 2A). We found the rest to be incomplete polypeptides ended at 0 frame codon positions around the slippery sequence and particularly

A LC/MS-detected polypeptides translated from A4C/25-bp mRNA construct



B All LC/MS-detected polypeptides from A4C/25-bp

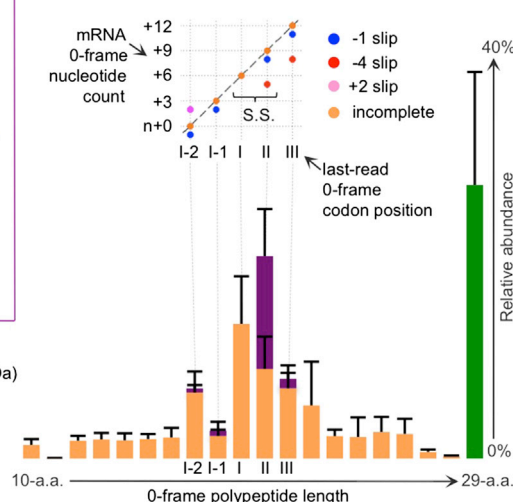


Figure 2. In Addition to Various Stop-Codon-Terminated Polypeptides, Frame-shift-Programming mRNAs Produce Incomplete Species

(A) A4C slippery sequence variant (construct with a downstream 25 bp duplex) as an example: LC/MS detected a broad collection of -1-stop-terminated products frameshifted from codon positions around the slippery sequence; the top bar graph shows their relative abundance (x axis). These frameshifted species were translated via -1 slips (blue), -4 slips (red), and +2-slips (pink); the latter two lead to polypeptides one amino acid longer or shorter (Figure S2). When degenerate decoding routes exist (as those shown in Figure 1B right box; numbers of base-pair mismatches for the last two 0 frame tRNAs are tabulated here in parenthesis; every non-Watson-Crick base-pair scores a 1), we assigned the given product to frameshift codon positions with fewer mismatches. Incomplete polypeptides ended with 0 frame amino acids along the slippery sequence were also found (sequences in orange; orange peaks in the mass spectrum; Table S1).

(B) Bottom bar graph: relative abundance (y axis) of detected species in the MS spectrum; species are organized based on their last 0 frame amino acid incorporated, i.e. 0 frame polypeptide length (x axis). Error bar represents SD. A 2D diagram, focusing on codon positions around the slippery sequence (SS) region, displays from where (x axis) the ribosome frameshifts or leaves behind incomplete species. With the y axis listing the mRNA nucleotide counts in reference to the 0 frame, incomplete species (orange dots) lie along the diagonal line; the frame-shifted products—as located by the first nucleotide read in the -1 frame on the mRNA—distribute above and below the diagonal line.

accumulating at positions where the ribosome tends to frame-shift (Figure 2A, left orange box). We hence sorted full-length and incomplete species by their last-incorporated 0 frame amino acids and rearranged the purely mass-based LC/MS spectrum into a bar graph ordered by 0 frame polypeptide length (i.e., x axis of the bottom graph in Figure 2B); the bar heights depict the relative abundance of products detected (SDs from multiple measurements shown as error bars).

To provide a comprehensive view for the various ribosomal frameshifting translation events observed around the slippery sequence region, we construct a 2D diagram (Figure 2B, top) to visualize from which 0 frame codon and to which -1 frame codon the ribosome slips. Specifically, the x axis marks the last-read 0-frame codon position along the mRNA, whereas the y axis—counting mRNA nucleotides in the 0 frame by multiples of 3—indicates the first nucleotide read in the -1 frame. Therefore, incomplete species (orange dots) drop off along the diagonal, whereas -1-stop-terminated products frameshifted via plus slips (pink dots) and minus slips (blue and red dots) distribute above and below.

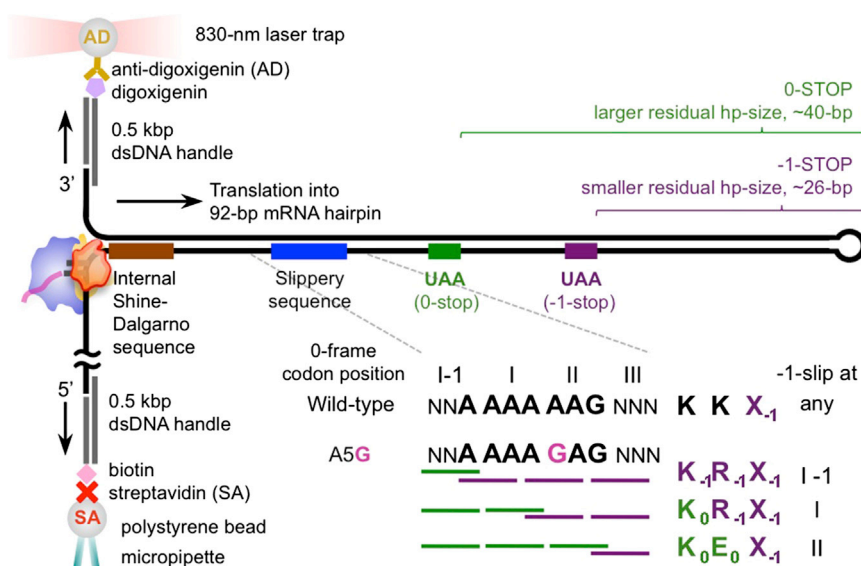
Ribosomes Make Distinctive Translocation Attempts

Having detected such diverse frameshift pathways via translation product analysis, we sought to unravel the molecular mech-

anisms that give rise to the broad range of ribosomal slippage observed. Specifically, how does the ribosome switch the mRNA reading frame—i.e., allowing the tRNAs to slip and to simultaneously base pair across adjacent codons that are spatially kinked into nucleotide triplets by the intercalating 16S rRNA residues inside the 30S decoding groove (Yusupova et al., 2001)? This issue can be addressed by determining when—and how—within one translation cycle the ribosome frameshifts. To this end, we employed a real-time in vitro mRNA hairpin unwinding assay. Using optical tweezers we monitored codon-by-codon translation by a single ribosome along the entire frameshift-programming mRNA template embedded inside a 92-bp-long hairpin (Figures 3 and S3A) (Qu et al., 2011; Wen et al., 2008).

Here, an mRNA hairpin molecule—bound with a single ribosome—is tethered through its two ends and held under tension by the optical tweezers (Figure 3). As the ribosome gradually translates the mRNA, it must unzip the hairpin by 3 bp per codon. As a result, the tether end-to-end distance extends by 6 nt (i.e., the gridline spacing: ~2.65 nm/codon on the left y axis in Figures 4A and 5A trajectory plots), thus reporting the translocation movement of the ribosome from one codon to the next. As seen from the trajectory, translation occurs in alternating phases of translocations and dwells (seen as vertical extensions and

Real-time single-ribosome translation – mRNA hairpin unwinding assay



horizontal segments). During each dwell, the ribosome decodes the A site codon and catalyzes peptidyl-transfer between the P- and A-tRNAs (Rodnina et al., 2005; Wohlgemuth et al., 2008). The ribosome subsequently binds the GTPase EF-G, partially displacing the P- and A-tRNAs into the 50S E and P sites, and proceeds with mRNA forward translocation, which requires unzipping the transcript downstream (Qu et al., 2011; Rodnina and Wintermeyer, 2011; Savelsbergh et al., 2003; Wen et al., 2008). To confirm whether the ribosome terminated at the 0 or -1 frame stop, after translation ceased, we applied force to unfold the remaining mRNA hairpin. Because the two stop codons result in different untranslated residual hairpin sizes—as measured by the mRNA extension gained from unfolding—we could verify where the ribosome ended in each trajectory (shown schematically in Figure S3B).

An ~55 bp hairpin remains ahead as the ribosome resides on the slippery sequence (Figure S3A) downstream from the internal Shine-Dalgarno sequence (with the first codon, i.e., position I, of the slippery sequence in the P site) (Qu et al., 2011). We chose a “55 bp construct” for the tweezer experiments instead of the previously discussed 25 bp construct because the longer—and thus more stable—hairpin allows more accurate measurements of the termination codon positions. Both frame-shift-promoting (wild-type/55 bp) and frameshift-attenuating (A5G/55 bp) slippery sequence variants were translated on the tweezers. The frameshift efficiencies for these two templates were 77% and 57%, respectively, showing a trend similar to that observed in vivo (Table 1) (Tsuchihashi and Brown, 1992).

Significantly, ~90% of the trajectories exhibit distinct fluctuations in mRNA extension specifically around the slippery sequence region (orange-shaded area in Figures 4A and 5A; trajectories recorded at 1 kHz and displayed at 20 Hz). These unique signals manifest back-and-forth movements of the ribosome on the mRNA ≥ 1 codon on average, distinctively above the noise level, and are not observed elsewhere in the trajectory

Figure 3. Probing Ribosomal Frameshifting Translation Translocation Dynamics Using Optical Tweezers

A single-ribosome translation progression is reported by the stepwise unwinding of a 92 bp mRNA hairpin held on the optical tweezers (see also Experimental Procedures); 3 bp are unzipped per codon translocated at the hairpin junction, thus reflecting displacements between the ribosome and mRNA. When the first 0 frame codon in the slippery sequence (codon position I) resides in the ribosome 30S P site, a 55 bp hairpin remains downstream. Hairpin portions not unwound by the ribosome were measured at the end of experiments; if the ribosome terminates at the -1 stop, it leaves a smaller residual hairpin, as compared to that for the 0 stop termination (Figure S3B). Both the wild-type slippery sequence and the frame-shift-attenuating A5G mutant were examined.

(Figures 4A and 5A zoom-ins, a range of fluctuation amplitudes appear within each trace; Figure 4B table; more examples in Figure S4B).

These fluctuations are noticeably different from the noisy sections recorded when the ribosome nears the end of the hairpin, where the tethered mRNA has mostly unwound into single strands and inevitably become much more elastic (the increase in noise is illustrated in Figure S4A and is corroborated by frequency analysis in Figure S4D). These large displacement fluctuations between the ribosome and the mRNA around the slippery sequence indicate that multiple mRNA translocation attempts occur at this region and that large slipping sizes such as -4 nt are indeed attainable. Interestingly, we find that fluctuations appear regardless of whether the ribosome ultimately frameshifts or not (Figure 4B table); also, they consistently occur even when the sequence is not slippery, e.g., on the A5G mutant mRNA (Figure 5A; Figure 4B table for lifetimes) whose frameshifting efficiency is reduced. Just as the slippery sequence is not the cause of fluctuations, neither is the hairpin; even though a hairpin barrier always remains in front of the ribosome throughout the entire trajectory, we detect these fluctuations only at the region downstream from the internal Shine-Dalgarno sequence. Thus, these observations indicate that a combination of flanking structural barriers—the upstream Shine-Dalgarno:anti-Shine-Dalgarno mini-helix and the downstream hairpin junction—suffice to induce distinctive fluctuating ribosome translocation dynamics as the ribosome translates the region between the barriers. The barrier-induced, multiple translocation ribosomal excursions directly observed here have been indirectly detected in single-molecule fluorescence experiments (Chen et al., 2014; Kim et al., 2014).

To probe the nature of these large and persistent fluctuations, we characterized their dynamics. The average excursion lifetimes—i.e., the time between a backward shift and a forward motion (Figures 4A and 5A, zoom-ins)—is ~0.5 s, independent of slippery sequence variant and frameshifting outcome (Figure 4B table). The distribution of the pooled excursion lifetimes is not a single exponential, indicating that more than one rate-limiting

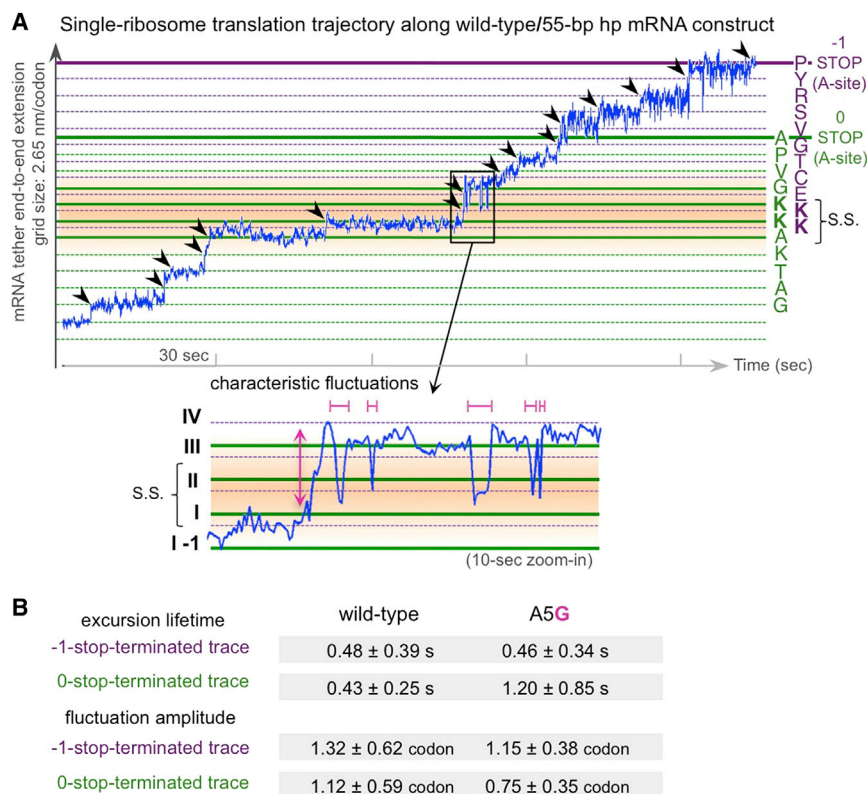


Table 1. Apparent Frameshift Efficiency and Overall Frameshift Slipping Attempts

		Wild-Type		A4C		A5G	
In Vivo Translation Protein Gel Resolved							
		11 bp hp		11 bp hp		11 bp hp	
Frameshift efficiency	$\frac{(-1 \text{ stop})}{(-1 \text{ stop} + 0 \text{ stop})}$	80%		5%		0%	
In Vitro Translation LC/MS-Detected (n ≥ 3)							
		25 bp	55 bp hp	25 bp	55 bp hp	25 bp	55 bp hp
Frameshift efficiency	$\frac{(-1 \text{ stop})}{(-1 \text{ stop} + 0 \text{ stop})}$	99%	99%	33%	66%	9%	35%
Overall slipping attempts	$\frac{(-1 \text{ stop} + \text{drop} - \text{off})}{(-1 \text{ stop} + \text{drop} - \text{off} + 0 \text{ stop})}$	99%	99%	65%	87%	39%	66%
Most probable drop-off codon position			I, II (21%, 29%)		I (34%)		II (58%)
In Vitro Translation, Single-Ribosome Translation Trajectories							
			55 bp hp			55 bp hp	
			n = 134			n = 216	
Frameshift efficiency	$\frac{(-1 \text{ stop})}{(-1 \text{ stop} + 0 \text{ stop})}$	77%			57%		
Overall slipping attempts	$\frac{(-1 \text{ stop} + \text{aborted})}{(-1 \text{ stop} + \text{aborted} + 0 \text{ stop})}$	83%			69%		
Most probable aborted codon position			I, II (30%, 40%)			II (58%)	

In addition to the conventionally defined frameshift efficiency—accounting only the -1 -stop and 0 -stop-terminated products (gray rows 1 [Tsuchihashi and Brown, 1992], 2, and 5), the overall slipping attempts made by the ribosome are estimated by including the incomplete, i.e., drop-off, species or, equivalently, the prematurely stalled and aborted translation trajectories (gray rows 3 and 6). For the two template variants examined (wild-type and A5G), the most probable aborted codon positions are consistent with the most probable drop-off codon positions resolved by LC/MS. Some differences in frameshift efficiency are seen between in vivo and in vitro translation conditions, which we attribute to known differences in overall translation rates.

incomplete species—is taken into account. Specifically, the locations around the slippery sequence that were frequently visited by the fluctuating ribosome—thus transiently establishing alternative codon:anticodon base pairing—are also the places where the higher populated frameshift translation products are found (Figure 5, red arrow).

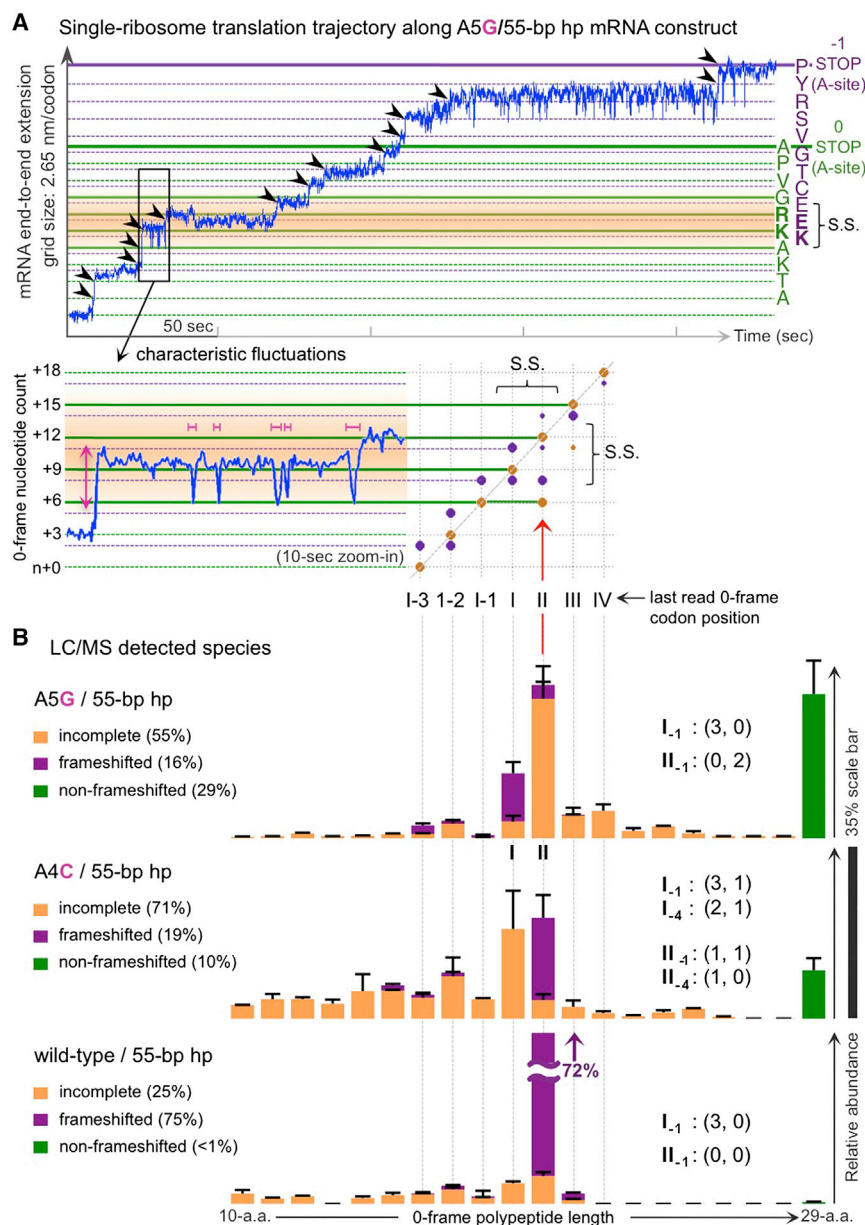
Altogether, our findings portray a dynamic frameshifting scheme via alternative reading frame sampling, which is accessed upon multiple mRNA translocation attempts by the ribosome. Because these distinctive translocation excursions are seen only when translating between mRNA structural barriers, the energetic cost of breaking codon:anticodon base pairs to frameshift is likely partially balanced by the energy liberated at the peripheral base-pairing interactions. It is conceivable that multiple EF-G binding events (Chen et al., 2014) may also play a role in driving the excursions. Furthermore, such a broad browsing range is presumably permitted by the swiveling and rotating 30S head when the ribosome is in the translocating mode—as suggested by the fluctuation frequency analysis described above. Indeed, structure studies have shown that, first, head tilting rearranges the mRNA binding groove on the 30S neck by disengaging the 16S rRNA residues that intercalate on the mRNA (Pulk and Cate, 2013; Schuwirth et al., 2005; Tourigny et al., 2013; Zhou et al., 2013); this process should ease the spatial restriction that prevents the tRNAs from base pairing across adjacent codons in the out-of-frame manner. Second, 30S head rotation is coupled with mRNA forward translocation

(Dunkle et al., 2011; Ermolenko and Noller, 2011; Gao et al., 2009; Guo and Noller, 2012; Ramrath et al., 2012, 2013; Ratje et al., 2010; Zhang et al., 2009; Zhou et al., 2012); thus, the 30S head is likely the agent for achieving large mRNA displacements that facilitate ribosomal frameshifting. A similar mechanism was proposed in recent kinetic studies, where—averaging over an ensemble and presumably over multiple translocation attempts—prolonged 30S head rotation was observed on a frame-shift-programming mRNA (Caliskan et al., 2014). Our results hence illustrate a mechanism by which the 30S head rotation is perturbed by the flanking mechanical barrier elements, leading to multiple translocation attempts that enable frameshifting.

Not Every Frameshift Attempt Succeeds

Although the distinctive translocation excursions observed in the single-ribosome translation trajectories occur at the slippery sequence region, they are independent of the detailed content encoded in that sequence. Hence, we wondered how the overall distribution of frameshift translation products varies as the ribosome translates different templates.

For all template variants examined (the “55 bp” mRNA construct series; Figure 5B, bar graphs), as noted before, incomplete species (ended with 0 frame amino acids before reaching the 0 stop; orange bars) accumulate at codon positions along the slippery sequence where the ribosome frequently frameshifts. When the slippery sequence becomes “less slippery,” i.e., more likely to cause codon:anticodon base-pair mismatches



upon a slip, the incomplete species also become more populated (Figure 5B; 55%, 71%, and 25% for A5G, A4C, and wild-type, respectively). The equivalents of these aborted translation products were also observed among the single-ribosome translation trajectories: some of the ribosomes aborted translation midway and prematurely stalled around the slippery sequence. Based on the residual hairpin sizes measured upon ribosome stalling (Figure S3B; position resolution: ± 0.8 nm $\sim 1/3$ codon), we found that the most probable aborted codon positions for each slippery sequence variant agree with the most abundant drop-off species detected by MS (Table 1). The presence of prematurely stalled ribosomes and aborted polypeptides indicate that not every frameshift attempt succeeds in resuming translation. Accordingly, our data suggest that, while translocation

Figure 5. Connecting Frameshift Translation Dynamics and Product Distribution

(A) The ≥ 1 codon translocation fluctuations (black-squared section on the blue trace; expanded underneath) persist in translation trajectory along the frameshift-attenuating A5G mutant, occurring around the slippery sequence (orange-shaded area). Meanwhile, LC/MS detected a wide range of frameshift translation species produced from the same A5G/55-bp construct, including frameshifted and incomplete species (purple and orange dots in 2D diagram; x axis showing last read 0 frame codons, y axis marking first read nucleotides in the -1 frame, relative to those counted in the 0 frame; Figure S5B). The accumulation of frameshifted and incomplete species at codon position II (the column of purple and orange dots indicated by red arrow) coincide with the locations on the mRNA slippery sequence region that were frequently explored by the back-and-forth fluctuating ribosome, as revealed by the trajectory zoom-in section.

(B) Relative abundances of LC/MS-detected translation products from the 55 bp mRNA constructs—each for the A5G, A4C, and wild-type slippery sequence variants representing low, medium, and high frameshift efficiency—are shown in bar graphs (error bar represents SD). Products are sorted by their last 0 frame amino acids incorporated along the mRNA (x axis: increasing 0 frame polypeptide length), and their abundances (Table S1) are plotted along the y axis. Less efficient slippery sequence variants produce higher amount of incomplete species, particularly at codon positions I and II, from where most frameshifted species were also translated (purple bars). Numbers of base-pair mismatches for the frameshifted E- and P-tRNAs are tabulated in parenthesis for frameshift pathways at codon position I and II, via -1 or -4 slips (in subscripts). We count 1 for every non-Watson-Crick interaction.

excursions induced around the slippery sequence cause the ribosome to slip out of the 0 frame, if no compatible codon:anticodon base pairing is found, the ribosomes stall and fail to incorporate the

next amino acid, leading to the generation of incomplete 0 frame polypeptides.

To learn why some frameshift attempts fail, we compared the relative abundances of incomplete species to their frameshifted, -1 -stop-terminated counterparts. For the A4C mutant (Figure 5B, middle bar graph), $\sim 87\%$ of the -1 -stop-terminated products (purple bars) come from codon position II, via -1 and -4 slips. However, a comparable amount of incomplete polypeptides (orange bars)—and no frameshifted products—was detected at codon position I. Such biases over particular frameshift pathways can be explained by the number of codon:anticodon base-pair mismatches encountered by the two tRNAs on a translocating ribosome. Here, we use a dyad notation: (x, y) to annotate the number of

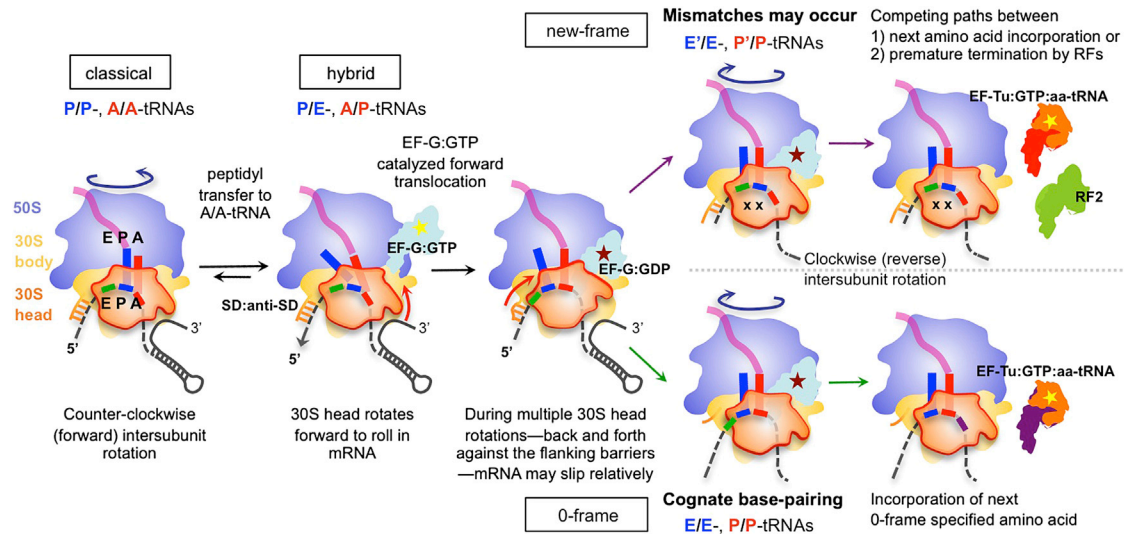


Figure 6. During mRNA Translocation: A Dynamic Scheme for Versatile Ribosomal Frameshifting

Left: after the polypeptide chain (magenta curvy line) transfers from the P- to A-tRNA (blue and red vertical sticks), the elongation factor G (EF-G:GTP; complex in cyan and yellow star) catalyzes the P/E-, A/P-tRNAs translocation on the ribosome, along with mRNA (gray dashed line) forward translocation by one codon. This mRNA movement is brought by 30S head forward rotation (dark orange counter-clockwise arrow), displacing the E, P, and A site codons (in green, blue, and red) to the left (gray downward arrow). To reset the ribosome for next round of translation, the head rotates back (middle cartoon; dark orange clockwise arrow). Multiple 30S head rotation—thus back-and-forth mRNA displacement—may be taken to achieve translocation between flanking mRNA structural barriers, e.g., Shine-Dalgarno:anti-Shine-Dalgarno mini-helix and downstream hairpin, hence permitting the tRNAs to base pair in alternative frames around the slippery sequence. When a new frame is adopted (top row)—at times with mismatches (black crosses)—both the new-frame specified aminoacyl-tRNA (delivered as EF-Tu:GTP:aa-tRNA; in orange, yellow star, and red) and the release factors (e.g., RF2, in green) can compete to bind with the mismatch-encountering, frameshifted ribosome. In the latter case, the ribosome ceases translation and releases an incomplete polypeptide.

mismatches at the two frameshifted tRNAs, in the E and P sites respectively, before the subsequent -1 frame aa-tRNA; every non-canonical base pairing is given a score of 1, and G:U wobbles are allowed only at the third nucleotide position. Specifically, both -1 and -4 slips at codon position II result in fewer mismatches for the two tRNAs, as compared to those at codon position I (Figure 5B, middle bar graph, numbers of mismatches tabulated). Therefore, due to better alternative base-pairing options, codon position II on the A4C mutant becomes the productive frameshift pathway. This analysis indicates that, once the ribosome has attempted to frameshift, the nucleotide composition along the slippery sequence dictates the outcome. Whereas the accumulation of incomplete species reveals the frequent slippages attempted at codon position I, the specific A4C mutation rendered those events unsuccessful. Consequently, the overall frameshift attempts on a given mRNA template should be estimated by including the amount of both frameshifted products and incomplete species (Table 1).

In comparison to A4C, the A5G mutant promoted -1 frameshift predominately at codon position I, whereas codon position II was a minor pathway (Figure 5B, top bar graph). The former slipping route leads to mismatches (tabulated in the graph) only at the first tRNA, which moves to the E site on the ribosome after translocation. In contrast, in the latter route, enduring only a P site mismatch, $\sim 90\%$ of the ribosomes ceased translation (top bar graph position II). Thus, P site mismatches appear to incur a higher penalty against continuing translation.

The correlation between the production of incomplete polypeptides and the occurrence of codon:anticodon mismatches is consistent with a retrospective fidelity check discovered in *E. coli* (Zaher and Green, 2009). After an amino acid mis-incorporation, the 30S subunit can recognize base-pair mismatches in its P and E sites as translation errors. The authors showed that post-translocation ribosomes—particularly with P site mismatches—prematurely terminate translation by recruiting a release factor protein, e.g., RF2, into its A site, in competition with the A site codon specified aa-tRNA. Upon termination, incomplete polypeptides are released as premature drop offs from the ribosomes. The correspondence between this retrospective quality control and our observations of prematurely aborted polypeptides, in the presence of both RF1 and RF2, indicate that a similar fidelity control operates during frameshifting along the slippery sequence.

By integrating all of our findings presented here with the current understanding of the bacterial ribosome translation mechanism, we arrive at the dynamic frameshifting scheme illustrated in Figure 6. In response to the flanking mRNA structural barriers acting as mechanical restoring devices, the ribosome stochastically makes multiple translocation attempts—i.e., excursions—promoted by the back-and-forth rotation of its 30S head. As each attempt has some probability of success, the succeeding translation may resume in a different frame, thereby mediating a widely branching set of translation pathways along the slippery sequence. The dynamic excursions observed in the single-ribosome translation trajectories not only corroborate the perturbed

ribosome translocation revealed by ensemble kinetic studies (Caliskan et al., 2014) but also further refine their frameshifting model by showing that the barrier-hindered ribosome makes, in fact, multiple attempts to translocate through the frameshift-programming sequence region. We see no evidence for frameshifting pathways via schemes other than translocation excursions. Hence, although our data cannot rule out models in which A site tRNA accommodation can also mediate frameshifting (Chen et al., 2014), we adopt the simpler translocation-mediated pathway branching mechanism.

DISCUSSION

Versatile Pathway Branching Regulates Frameshifting

Previous studies have indicated that ribosomes are able to frameshift despite the creation of mismatches that would normally be perceived as translation errors (Atkins and Björk, 2009; Farabaugh, 1996; Harger et al., 2002; Tsuchihashi and Brown, 1992). It is known that translation accuracy is primarily monitored and verified at steps prior to the irreversible peptidyl transfer, ensuring proper charging and specific acceptance of the cognate aa-tRNA into the A site on the ribosome (Gromadski and Rodnina, 2004; Guth and Francklyn, 2007). In the frameshifting scheme presented here, the potential conflict between frameshifting and fidelity is alleviated along the mRNA translocation step. Any mismatches upon codon:anticodon re-pairing during reading frame sampling would occur after the peptide bond formation (Figure 6) and, thus, it is not susceptible to the fidelity controls governing proper mRNA decoding.

Instead, the retrospective fidelity check by the post-translocation ribosome very likely becomes the critical quality control in programmed frameshifting—a context that showcases its biological significance. This fidelity check subjects the mismatch-encountering ribosome to two competing routes—depending on the number and site of mismatches created upon a slip, the ribosome can either stop synthesis by recruiting a release factor or proceed to the next round of amino acid incorporation in the new reading frame. Therefore, regardless of how the surrounding mRNA structural barriers may kinetically trap the ribosome and effectively promote frameshifting, only a fraction of ribosome slipping attempts during the dynamic translocation excursions succeeds to yield full-length frameshifted products. While mutant slippery sequences render a random slipping attempt risky, the *dnaX* slippery sequence—having evolved to offer optimal thermodynamic stability for alternative base pairing—facilitates passing the fidelity check.

Our observations illustrate the indispensable role played by the slippery sequence—as well as adjacent codon positions before and after it—to assure high efficiency of “programmed” frameshifting. We can begin to parameterize and predict the apparent slipperiness of a given frameshift-programming mRNA by considering: (1) for each 0 frame codon within the sequence region flanked by the upstream and downstream barriers, how many alternative cognate and near-cognate base-pairing positions—i.e., slipping routes—exist in the out-of-frames; (2) for each of the slipping routes, how feasible is the required slipping size, given that it must be attained by ribosome 30S head rotation during mRNA translocation. Pro-

grammed mRNAs with greater totals of alternative codon:anticodon base-pairing options, weighted by the ease of the required slipping sizes, should exhibit greater frameshift efficiencies.

The fraction of completed frameshifted products—that as found here, can differ in length by a few amino acid residues—however, only reports half of the story for programmed frameshifting. The missing half is the previously unrecognized prematurely terminated polypeptides, whose significance is twofold. First, they likely reflect the retrospective fidelity control used by the ribosome; second, they represent the relics of unsuccessful slipping attempts induced by the surrounding secondary structures. Intriguingly, ribosome stalling and premature termination, as the aftermath of unsuccessful slipping attempts, have recently been shown to serve as characteristics of frameshift translation, which eukaryotic systems recognize to degrade exogenous programming mRNAs (Belew et al., 2014). Therefore, these impeded slipping attempts—ultimately leading to the “off-pathway” incomplete translation products—may have profound implications for the regulation both of translation and of mRNA abundance inside cells.

The overall frameshift attempts—composed of both the completed and the heretofore hidden aborted species—hence are the genuine measure for the frameshift-promoting strength of a programmed mRNA. In turn, this strength is determined by the mechanical properties of the mRNA structures that flank the slippery sequence and that interfere with the normal translation cycle. In this work, we have utilized these mechanical properties as a probe in situ: when the ribosome translates between the structural barriers, its intrinsic translocation dynamics are uniquely amplified, permitting a ribosomal slip and possibly engaging the retrospective fidelity check. Using optical tweezers, we have captured the underlying dynamics of frameshifting translation in real time, providing a glimpse of an unexpectedly versatile translation scheme.

EXPERIMENTAL PROCEDURES

In vitro translation was performed using either the PURExpress Δ Ribosome kit (NEB) to synthesize polypeptide samples in large scale and analyze by MS or a custom-made reconstituted reaction mixture for real-time single-ribosome translation in the optical tweezer experiments. The same preparations of purified *E. coli* MRE600 ribosomes and mRNA constructs were used in both experiments.

Exact composition and protocols of the PURExpress system have been documented previously (Ohashi et al., 2010; see also [Extended Experimental Procedures](#)). All LC/MS experiments were performed on an LTQ Orbitrap XL mass spectrometer (Thermo Scientific) connected with an Agilent 1200 nano-flow HPLC system by means of nanoelectrospray. MS full scans were acquired in the Orbitrap analyzer (using internal lock mass recalibration in real time), whereas tandem mass spectra were recorded in the linear ion trap. Each translation product was identified within 10 ppm deviation in mass (Da)—and with verification of its unique isotope pattern originated from specific amino acid composition.

Reconstituted reaction mixtures for tweezer experiments include elongation factors (EF-G and EF-Tu), release factors (RF1 and RF2), GTP, etc., along with selectively charged aminoacyl-tRNAs to fuel translation inside a micro-fluidic chamber. We first tether one ribosome-mRNA complex (single ribosome initiated and halted on the long mRNA hairpin construct)—via a pair of terminal-modified dsDNA handles—between two 2.1 μ m, surface-modified polystyrene beads in the tweezers setup (Figure 3A). Before beginning translation, we register the starting position of the ribosome on the mRNA based on the

downstream hairpin size measured; this measurement is done by applying force to unfold and refold the hairpin. Upon flowing the above mixture into the chamber while holding the mRNA tether at constant force, we commence recording stepwise hairpin unwinding that reports single-ribosome translation in real time. After the course of translation, we again measure the residual hairpin to verify the ribosome termination position. Detailed protocols for protein factor and material preparations, ribosome-mRNA complex formations, configurations of the single-trap optical miniTweezers (S.B. Smith, TweezerLAB), step-by-step instrumental operations, and single-ribosome translation trajectory data analysis have been described in the literature and our previous studies (Dinçbas-Renqvist et al., 2000; Qu et al., 2011; Wen et al., 2008; see also Extended Experimental Procedures).

SUPPLEMENTAL INFORMATION

Supplemental Information includes Extended Experimental Procedures, five figures, and two tables and can be found with this article online at <http://dx.doi.org/10.1016/j.cell.2015.02.003>.

AUTHOR CONTRIBUTIONS

S.Y. and J.-D.W. designed the experiments and prepared the materials, S.Y. performed the experiments and analyzed the data, and all authors wrote the paper.

ACKNOWLEDGMENTS

We thank Dr. S.B. Smith for help with the optical tweezers instrument, Dr. T. Iavarone (QB3/Chemistry Mass Spectrometry Facility) for assistance on MS data collection and analysis, Dr. L. Lancaster and Prof. H. Noller for expertise in sample preparations, Dr. C.L. Hetherington for comments on the manuscript, and members of the Tinoco and Bustamante labs for discussions. This work was supported by grants from the National Institutes of Health (GM10840 to I.T.).

Received: October 2, 2014

Revised: December 1, 2014

Accepted: January 28, 2015

Published: February 19, 2015

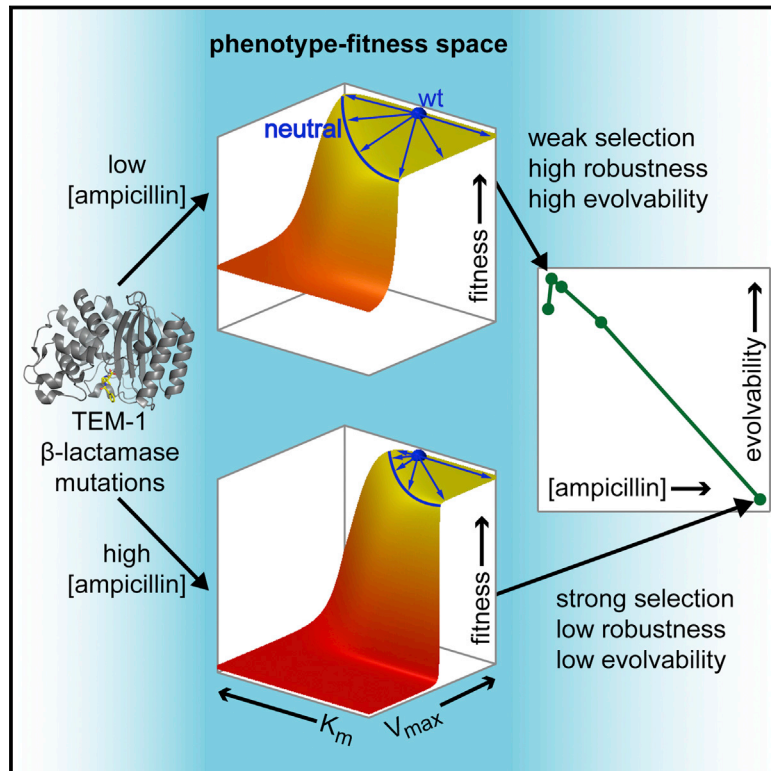
REFERENCES

- Atkins, J.F., and Björk, G.R. (2009). A gripping tale of ribosomal frameshifting: extragenic suppressors of frameshift mutations spotlight P-site realignment. *Microbiol. Mol. Biol. Rev.* 73, 178–210.
- Belew, A.T., Meskauskas, A., Musalgaonkar, S., Advani, V.M., Sulima, S.O., Kasprzak, W.K., Shapiro, B.A., and Dinman, J.D. (2014). Ribosomal frameshifting in the CCR5 mRNA is regulated by miRNAs and the NMD pathway. *Nature* 512, 265–269.
- Bretscher, M.S. (1968). Translocation in protein synthesis: a hybrid structure model. *Nature* 218, 675–677.
- Caliskan, N., Katunin, V.I., Belardinelli, R., Peske, F., and Rodnina, M.V. (2014). Programmed -1 frameshifting by kinetic partitioning during impeded translocation. *Cell* 157, 1619–1631.
- Chen, J., Petrov, A., Johansson, M., Tsai, A., O'Leary, S.E., and Puglisi, J.D. (2014). Dynamic pathways of -1 translational frameshifting. *Nature* 512, 328–332.
- Dinçbas-Renqvist, V., Engström, A., Mora, L., Heurgué-Hamard, V., Buckingham, R., and Ehrenberg, M. (2000). A post-translational modification in the GGQ motif of RF2 from *Escherichia coli* stimulates termination of translation. *EMBO J.* 19, 6900–6907.
- Drummond, D.A., and Wilke, C.O. (2009). The evolutionary consequences of erroneous protein synthesis. *Nat. Rev. Genet.* 10, 715–724.
- Dunkle, J.A., Wang, L., Feldman, M.B., Pulk, A., Chen, V.B., Kapral, G.J., Noeske, J., Richardson, J.S., Blanchard, S.C., and Cate, J.H. (2011). Structures of the bacterial ribosome in classical and hybrid states of tRNA binding. *Science* 332, 981–984.
- Ermolenko, D.N., and Noller, H.F. (2011). mRNA translocation occurs during the second step of ribosomal intersubunit rotation. *Nat. Struct. Mol. Biol.* 18, 457–462.
- Farabaugh, P.J. (1996). Programmed translational frameshifting. *Microbiol. Rev.* 60, 103–134.
- Gao, Y.G., Selmer, M., Dunham, C.M., Weixlbaumer, A., Kelley, A.C., and Ramakrishnan, V. (2009). The structure of the ribosome with elongation factor G trapped in the posttranslocational state. *Science* 326, 694–699.
- Gesteland, R.F., and Atkins, J.F. (1996). Recoding: dynamic reprogramming of translation. *Annu. Rev. Biochem.* 65, 741–768.
- Gromadski, K.B., and Rodnina, M.V. (2004). Kinetic determinants of high-fidelity tRNA discrimination on the ribosome. *Mol. Cell* 13, 191–200.
- Guo, Z., and Noller, H.F. (2012). Rotation of the head of the 30S ribosomal subunit during mRNA translocation. *Proc. Natl. Acad. Sci. USA* 109, 20391–20394.
- Guth, E.C., and Francklyn, C.S. (2007). Kinetic discrimination of tRNA identity by the conserved motif 2 loop of a class II aminoacyl-tRNA synthetase. *Mol. Cell* 25, 531–542.
- Harger, J.W., Meskauskas, A., and Dinman, J.D. (2002). An “integrated model” of programmed ribosomal frameshifting. *Trends Biochem. Sci.* 27, 448–454.
- Jacks, T., Power, M.D., Masiarz, F.R., Luciw, P.A., Barr, P.J., and Varmus, H.E. (1988). Characterization of ribosomal frameshifting in HIV-1 gag-pol expression. *Nature* 331, 280–283.
- Jenner, L., Rees, B., Yusupov, M., and Yusupova, G. (2007). Messenger RNA conformations in the ribosomal E site revealed by X-ray crystallography. *EMBO Rep.* 8, 846–850.
- Jenner, L.B., Demeshkina, N., Yusupova, G., and Yusupov, M. (2010). Structural aspects of messenger RNA reading frame maintenance by the ribosome. *Nat. Struct. Mol. Biol.* 17, 555–560.
- Kaminishi, T., Wilson, D.N., Takemoto, C., Harms, J.M., Kawazoe, M., Schlutzen, F., Hanawa-Suetsugu, K., Shirouzu, M., Fucini, P., and Yokoyama, S. (2007). A snapshot of the 30S ribosomal subunit capturing mRNA via the Shine-Dalgarno interaction. *Structure* 15, 289–297.
- Kim, H.K., Liu, F., Fei, J., Bustamante, C., Gonzalez, R.L., Jr., and Tinoco, I., Jr. (2014). A frameshifting stimulatory stem loop destabilizes the hybrid state and impedes ribosomal translocation. *Proc. Natl. Acad. Sci. USA* 111, 5538–5543.
- Korostelev, A., Trakhanov, S., Asahara, H., Laurberg, M., Lancaster, L., and Noller, H.F. (2007). Interactions and dynamics of the Shine Dalgarno helix in the 70S ribosome. *Proc. Natl. Acad. Sci. USA* 104, 16840–16843.
- Liao, P.Y., Choi, Y.S., Dinman, J.D., and Lee, K.H. (2011). The many paths to frameshifting: kinetic modelling and analysis of the effects of different elongation steps on programmed -1 ribosomal frameshifting. *Nucleic Acids Res.* 39, 300–312.
- Moazed, D., and Noller, H.F. (1989a). Intermediate states in the movement of transfer RNA in the ribosome. *Nature* 342, 142–148.
- Moffitt, J.R., Chemla, Y.R., and Bustamante, C. (2010). Mechanistic constraints from the substrate concentration dependence of enzymatic fluctuations. *Proc. Natl. Acad. Sci. USA* 107, 15739–15744.
- Ohashi, H., Kanamori, T., Shimizu, Y., and Ueda, T. (2010). A highly controllable reconstituted cell-free system—a breakthrough in protein synthesis research. *Curr. Pharm. Biotechnol.* 11, 267–271.
- Pulk, A., and Cate, J.H. (2013). Control of ribosomal subunit rotation by elongation factor G. *Science* 340, 1235970.
- Qu, X., Wen, J.D., Lancaster, L., Noller, H.F., Bustamante, C., and Tinoco, I., Jr. (2011). The ribosome uses two active mechanisms to unwind messenger RNA during translation. *Nature* 475, 118–121.
- Ramrath, D.J.F., Yamamoto, H., Rother, K., Wittek, D., Pech, M., Mielke, T., Loeke, J., Scheerer, P., Ivanov, P., Teraoka, Y., et al. (2012). The complex of tmRNA-SmpB and EF-G on translocating ribosomes. *Nature* 485, 526–529.
- Ramrath, D.J., Lancaster, L., Sprink, T., Mielke, T., Loeke, J., Noller, H.F., and Spahn, C.M. (2013). Visualization of two transfer RNAs trapped in transit during

- elongation factor G-mediated translocation. *Proc. Natl. Acad. Sci. USA* **110**, 20964–20969.
- Ratje, A.H., Loerke, J., Mikolajka, A., Br  nner, M., Hildebrand, P.W., Starosta, A.L., D  nh  fer, A., Connell, S.R., Fucini, P., Mielke, T., et al. (2010). Head swivel on the ribosome facilitates translocation by means of intra-subunit tRNA hybrid sites. *Nature* **468**, 713–716.
- Rodnina, M.V., and Wintermeyer, W. (2011). The ribosome as a molecular machine: the mechanism of tRNA-mRNA movement in translocation. *Biochem. Soc. Trans.* **39**, 658–662.
- Rodnina, M.V., Gromadski, K.B., Kothe, U., and Wieden, H.J. (2005). Recognition and selection of tRNA in translation. *FEBS Lett.* **579**, 938–942.
- Savelsbergh, A., Katunin, V.I., Mohr, D., Peske, F., Rodnina, M.V., and Wintermeyer, W. (2003). An elongation factor G-induced ribosome rearrangement precedes tRNA-mRNA translocation. *Mol. Cell* **11**, 1517–1523.
- Schmeing, T.M., and Ramakrishnan, V. (2009). What recent ribosome structures have revealed about the mechanism of translation. *Nature* **461**, 1234–1242.
- Schuwirth, B.S., Borovinskaya, M.A., Hau, C.W., Zhang, W., Vila-Sanjurjo, A., Holton, J.M., and Cate, J.H. (2005). Structures of the bacterial ribosome at 3.5 Å resolution. *Science* **310**, 827–834.
- Selmer, M., Dunham, C.M., Murphy, F.V., 4th, Weixlbaumer, A., Petry, S., Kelley, A.C., Weir, J.R., and Ramakrishnan, V. (2006). Structure of the 70S ribosome complexed with mRNA and tRNA. *Science* **313**, 1935–1942.
- Stahl, G., McCarty, G.P., and Farabaugh, P.J. (2002). Ribosome structure: revisiting the connection between translational accuracy and unconventional decoding. *Trends Biochem. Sci.* **27**, 178–183.
- Tinoco, I., Jr., Kim, H.K., and Yan, S. (2013). Frameshifting dynamics. *Biopolymers* **99**, 1147–1166.
- Tourigny, D.S., Fern  ndez, I.S., Kelley, A.C., and Ramakrishnan, V. (2013). Elongation factor G bound to the ribosome in an intermediate state of translocation. *Science* **340**, 1235490.
- Tsuchihashi, Z., and Brown, P.O. (1992). Sequence requirements for efficient translational frameshifting in the *Escherichia coli* dnaX gene and the role of an unstable interaction between tRNA(Lys) and an AAG lysine codon. *Genes Dev.* **6**, 511–519.
- Weiss, R.B., Dunn, D.M., Atkins, J.F., and Gesteland, R.F. (1987). Slippery runs, shifty stops, backward steps, and forward hops: -2, -1, +1, +2, +5, and +6 ribosomal frameshifting. *Cold Spring Harb. Symp. Quant. Biol.* **52**, 687–693.
- Wen, J.D., Lancaster, L., Hodges, C., Zeri, A.C., Yoshimura, S.H., Noller, H.F., Bustamante, C., and Tinoco, I. (2008). Following translation by single ribosomes one codon at a time. *Nature* **452**, 598–603.
- Wohlgemuth, I., Brenner, S., Beringer, M., and Rodnina, M.V. (2008). Modulation of the rate of peptidyl transfer on the ribosome by the nature of substrates. *J. Biol. Chem.* **283**, 32229–32235.
- Yusupov, M.M., Yusupova, G.Z., Baucom, A., Lieberman, K., Earnest, T.N., Cate, J.H., and Noller, H.F. (2001). Crystal structure of the ribosome at 5.5 Å resolution. *Science* **292**, 883–896.
- Yusupova, G.Z., Yusupov, M.M., Cate, J.H., and Noller, H.F. (2001). The path of messenger RNA through the ribosome. *Cell* **106**, 233–241.
- Yusupova, G., Jenner, L., Rees, B., Moras, D., and Yusupov, M. (2006). Structural basis for messenger RNA movement on the ribosome. *Nature* **444**, 391–394.
- Zaher, H.S., and Green, R. (2009). Quality control by the ribosome following peptide bond formation. *Nature* **457**, 161–166.
- Zhang, W., Dunkle, J.A., and Cate, J.H. (2009). Structures of the ribosome in intermediate states of ratcheting. *Science* **325**, 1014–1017.
- Zhou, J., Lancaster, L., Trakhanov, S., and Noller, H.F. (2012). Crystal structure of release factor RF3 trapped in the GTP state on a rotated conformation of the ribosome. *RNA* **18**, 230–240.
- Zhou, J., Lancaster, L., Donohue, J.P., and Noller, H.F. (2013). Crystal structures of EF-G-ribosome complexes trapped in intermediate states of translocation. *Science* **340**, 1236086.

Evolvability as a Function of Purifying Selection in TEM-1 β -Lactamase

Graphical Abstract



Authors

Michael A. Stiffler, Doeke R. Hekstra, Rama Ranganathan

Correspondence

rama.ranganathan@utsouthwestern.edu

In Brief

The origins of evolvability are examined systematically by analyzing single amino acid mutants in an enzyme under selection for a wild-type function (ampicillin resistance) and for a new function (cefotaxime resistance). The findings indicate that fluctuating environments might select for enzymes with excess activity relative to the strength of selection.

Highlights

- A study of how enzyme robustness and evolvability depend on selection strength.
- Fitness effects of all single amino acid mutations for wild-type and new function.
- Adaptation to new function is enhanced in a weak selection environment.
- A spatially distributed pattern of adaptive mutations in the protein structure.



Evolvability as a Function of Purifying Selection in TEM-1 β -Lactamase

Michael A. Stiffler,¹ Doeke R. Hekstra,¹ and Rama Ranganathan^{1,2,*}

¹Green Center for Systems Biology

²Department of Pharmacology

University of Texas Southwestern Medical Center, Dallas, TX 75390-9050, USA

*Correspondence: rama.ranganathan@utsouthwestern.edu

<http://dx.doi.org/10.1016/j.cell.2015.01.035>

SUMMARY

Evolvability—the capacity to generate beneficial heritable variation—is a central property of biological systems. However, its origins and modulation by environmental factors have not been examined systematically. Here, we analyze the fitness effects of all single mutations in TEM-1 β -lactamase (4,997 variants) under selection for the wild-type function (ampicillin resistance) and for a new function (cefotaxime resistance). Tolerance to mutation in this enzyme is bimodal and dependent on the strength of purifying selection in vivo, a result that derives from a steep non-linear ampicillin-dependent relationship between biochemical activity and fitness. Interestingly, cefotaxime resistance emerges from mutations that are neutral at low levels of ampicillin but deleterious at high levels; thus the capacity to evolve new function also depends on the strength of selection. The key property controlling evolvability is an excess of enzymatic activity relative to the strength of selection, suggesting that fluctuating environments might select for high-activity enzymes.

INTRODUCTION

Biological systems are often regarded as remarkably tolerant of genetic perturbations. Mutational robustness has been observed at nearly all levels of biological organization, from protein structure and function (McLaughlin et al., 2012; Rennell et al., 1991; Suckow et al., 1996) to metabolic flux (Kacser and Burns, 1981) to regulation of gene expression (Wagner, 2005a) to development (Waddington, 1942, 1953). Because processes that buffer the effects of genetic variation inevitably have consequences for evolutionary outcomes, an understanding of both the causes and consequences of robustness is of central importance to biology (de Visser et al., 2003; Masel and Siegal, 2009; Wagner, 2005a). For example, recent studies (Draghi et al., 2010; Hayden et al., 2011; Payne and Wagner, 2014; Wagner, 2008) show that robustness can facilitate the adaptation of biological systems to environmental change—a property sometimes called “evolvability” (Kirschner and Gerhart, 1998). Besides being essential to basic evolutionary theory, understanding robustness

may also be important in the engineering of useful proteins that are more resilient to the effects of random mutations and for understanding the emergence of mutations that impact human health.

Due to their importance in defining phenotypes at the cellular and organismal level, and the ease with which large numbers of mutations can be introduced and assessed, proteins represent ideal model systems for studying robustness and evolvability. The tolerance of many proteins to mutations has been assessed in a number of important studies with high-throughput site-directed and random mutagenesis (Fowler et al., 2010; Guo et al., 2004; Huang et al., 1996; Jacquier et al., 2013; Loeb et al., 1989; McLaughlin et al., 2012; Melnikov et al., 2014; Rennell et al., 1991; Suckow et al., 1996). Overall, these studies suggest that the function of proteins is insensitive to the vast majority of amino acid changes (Bowie et al., 1990). By contrast, it is generally accepted that many missense mutations have measurable biophysical effects (e.g., on protein stability), supporting a view that most mutations are not neutral at the biochemical level (DePristo et al., 2005; Tokuriki and Tawfik, 2009). One possible explanation for this discrepancy is that robustness and evolvability are characteristics that ultimately refer to organismal fitness, a property that is difficult to assess and whose relationship to biochemical parameters of a protein could be complex and is generally unknown. Indeed, many comprehensive studies of mutational tolerance in proteins have assessed biochemical traits (e.g., protein-binding affinity; Fowler et al., 2010; McLaughlin et al., 2012) or other phenotypes (e.g., minimal inhibitory concentration of antibiotic, MIC; Firnberg et al., 2014; Jacquier et al., 2013); although much has been learned from these studies, the relationships between these properties and fitness are less clear.

More fundamentally, it is logical that the relationship between organismal fitness and biochemical parameters might vary significantly with the strength of selective pressure acting on the protein. If so, then robustness and evolvability must not be considered as absolute, invariant features of proteins but instead as properties that depend on environmental or experimental conditions that control purifying selection. To examine these ideas rigorously, we require (1) a quantitative mapping of the relationship between in vivo fitness and in vitro biochemistry in an appropriate model system, (2) a study of how both mutational sensitivity to existing function and the capacity to evolve new function depend upon selection pressure, and (3) a mechanistic principle for how these characteristics emerge from the properties of extant proteins.

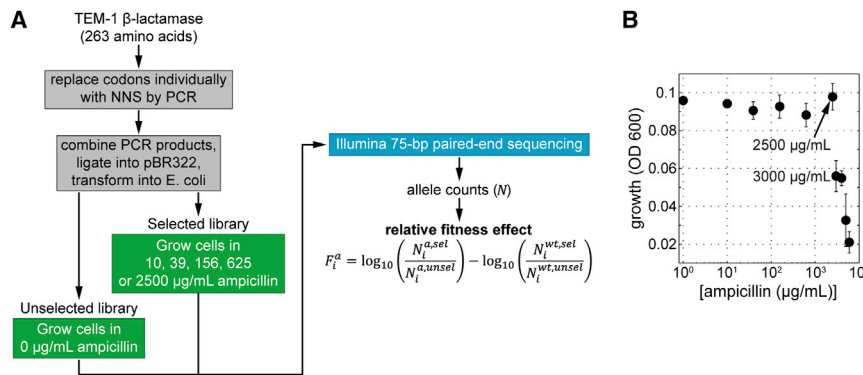


Figure 1. Experimental Scheme

(A) Strategy for comprehensive assessment of the fitness effects of mutations in TEM-1 (Experimental Procedures and Extended Experimental Procedures). Each codon corresponding to the 263 amino acid positions of the mature TEM-1 protein was individually mutated to NNS (where N is a mixture of all four nucleotide bases, and S a mixture of C and G) using PCR. PCR products were combined in equimolar ratios, cloned into the pBR322 plasmid, and transformed into *E. coli*. The resulting whole-gene saturation mutagenesis library was then selected in ampicillin at either 0 μg/ml (unselected library) or various concentrations (selected library). Illumina 75 bp paired-end sequencing was used to obtain allele counts N for

each amino acid mutation a at every position i and under each selection condition; relative fitness effect F_i^a is assessed as the logarithmic increase in allele counts in the selected library versus the unselected library, relative to the wild-type allele.

(B) Results of growth assays ($n = 3$) for *E. coli* cells harboring wild-type TEM-1 under selection at various concentrations of ampicillin, indicating that growth is unaffected at ampicillin concentrations $\leq 2,500$ μg/ml (Extended Experimental Procedures). See also Figure S1.

The problem of how robustness and evolvability are conditional on selection strength can be investigated in proteins conferring antibiotic resistance by comprehensive experimental assessment of the fitness effects of mutations as a function of antibiotic concentration. Here, we focus on a powerful model system for protein evolution studies, TEM-1 β -lactamase (Bershtein et al., 2006; Salverda et al., 2010; Weinreich et al., 2006). TEM-1 is an enzyme that hydrolyzes penicillin-class β -lactam antibiotics (e.g., ampicillin); the ability of bacteria to survive and reproduce (i.e., fitness) in the presence of these antibiotics relies solely on TEM-1 activity (Matagne et al., 1998; Medeiros, 1997). Using an application of deep sequencing (Fowler et al., 2010; McLaughlin et al., 2012), we determined the effects on organismal fitness of all single amino acid mutations in TEM-1 (4,997 mutations) under selection for ampicillin resistance (the wild-type function) and for resistance to cefotaxime (a new function). By assessing fitness under increasing concentration of ampicillin, we demonstrate that robustness indeed depends strongly and inversely on the strength of purifying selection. The pattern of mutational sensitivity is hierarchically organized in the atomic structure, building out from the active site as a function of ampicillin concentration in physically contiguous but anisotropic amino acid networks. Furthermore, we find that in TEM-1, evolvability is facilitated by robustness and therefore is also dependent on the strength of selection; mutations conferring cefotaxime resistance are predominantly neutral under selection at low to moderate ampicillin concentrations yet deleterious to fitness under high concentration. To mechanistically understand these properties, we propose a simple kinetic model that describes the fitness effects of all mutations in our study as a function of ampicillin concentration and intracellular β -lactamase activity. This model shows that, mechanistically, robustness and evolvability can be understood to arise from an excess of intracellular enzymatic activity relative to the strength of selection, a finding that suggests a role for fluctuating environments in the evolution of high-activity enzymes.

RESULTS

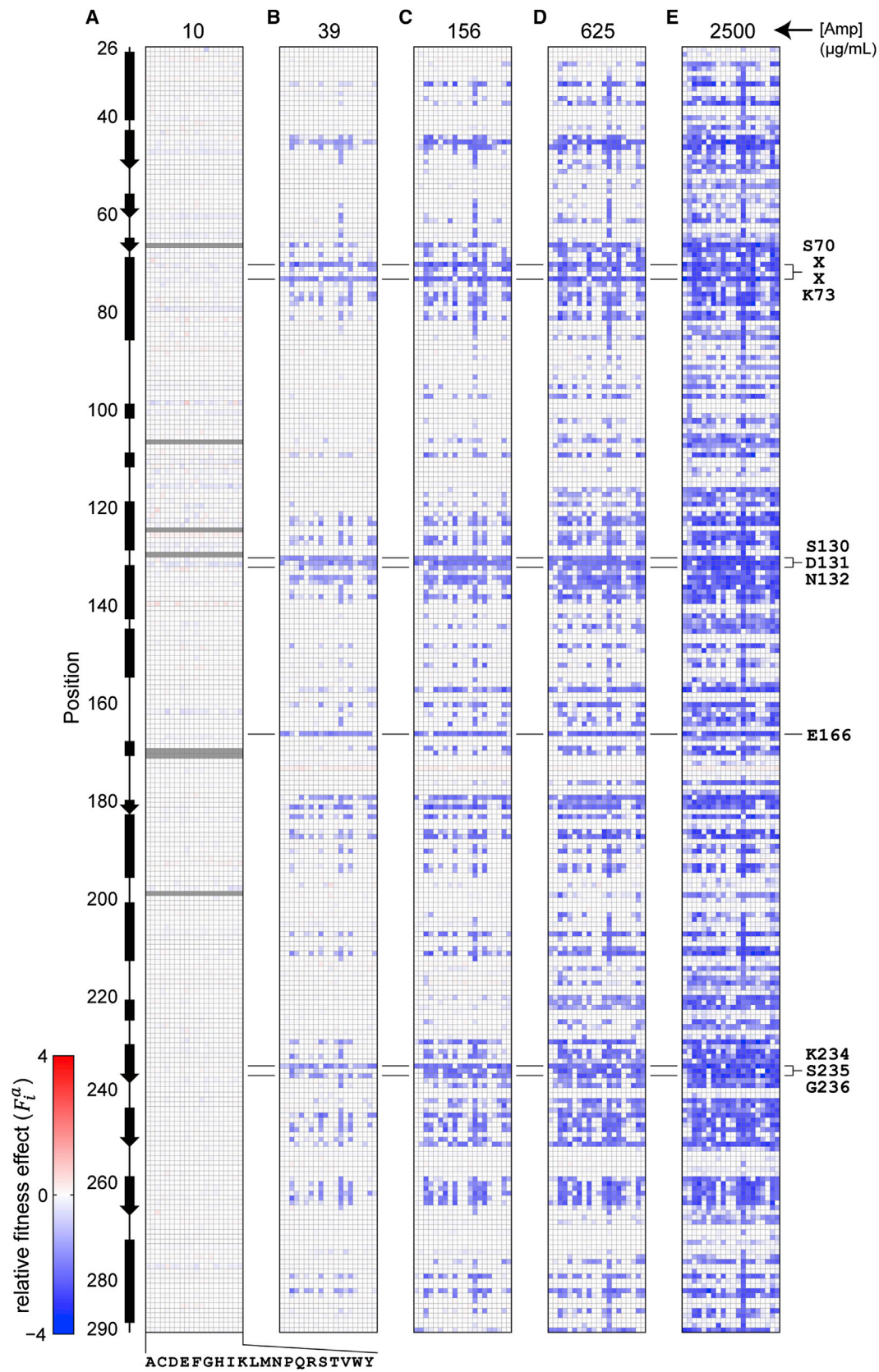
Whole-Genes Saturation Mutagenesis and Fitness under Ampicillin Selection

We used site-directed mutagenesis to create a whole-gene saturation mutagenesis library comprising all 19 possible single-site amino acid point mutations at every position in the mature form of TEM-1 β -lactamase (4,997 amino acid mutations total; Experimental Procedures and Extended Experimental Procedures; Figure 1A). To assess the effects of selection strength on robustness, the library was transformed into *E. coli* and selected at several concentrations of ampicillin ranging from zero to a concentration just below that at which cells encoding even wild-type TEM-1 decline considerably in fitness (2500 μg/ml ampicillin; Extended Experimental Procedures; Figure 1B).

Illumina 75 bp paired-end sequencing was used to obtain counts for each mutant allele after selection at each ampicillin concentration; an average of 1,000 counts per amino acid mutation was obtained under conditions of no selection (0 μg/ml ampicillin; Figure S1A). The relative fitness F_i^a of each amino acid mutation a at each position i is assessed as the logarithm of the allele counts in the selected population ($N_i^{a,sel}$) versus the unselected population (0 μg/ml ampicillin, $N_i^{a,unsel}$), relative to the wild-type allele:

$$F_i^a = \log_{10} \left[\frac{N_i^{a,sel}}{N_i^{a,unsel}} \right] - \log_{10} \left[\frac{N_i^{wt,sel}}{N_i^{wt,unsel}} \right]. \quad (1)$$

Mutations that show no fitness effect have values of F_i^a close to that of wild-type ($F_i^a \approx 0$), and those with an increase or decrease in fitness relative to wild-type have a positive or negative value of F_i^a , respectively, in proportion to their effect. The values of F_i^a are generally reproducible over two independent trials ($r^2 = 0.91$ at 2500 μg/ml ampicillin; Figure S1B), and effects due to codon bias under ampicillin selection appear to be small ($r^2 = 0.96$ for relative fitness between all synonymous mutations at 2500 μg/ml ampicillin; Figure S1C). Examination of the distribution of F_i^a for all mutations under no selection (0 μg/ml ampicillin) provides a



(legend on next page)

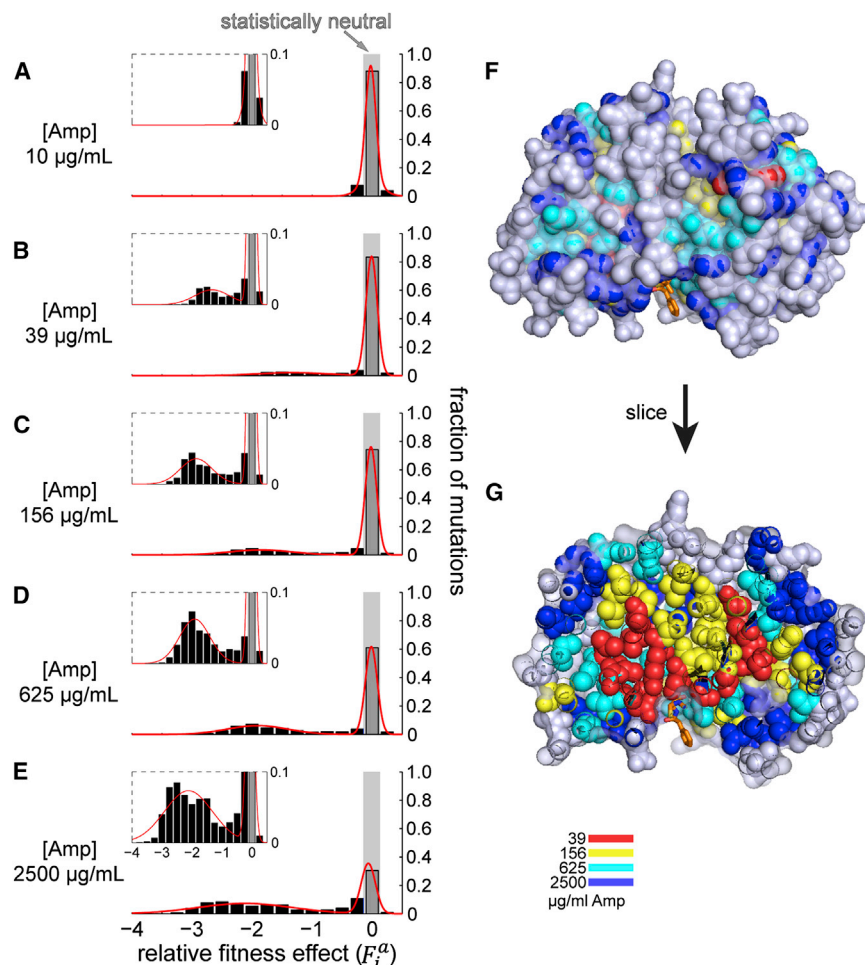


Figure 3. Distribution of Fitness Effects

(A–E) Histograms of F_i^a values show that the distribution of the fitness effects (DFE) is bimodal and depends on the strength of purifying selection: (A) 10, (B) 39, (C) 156, (D) 625, and (E) 2,500 $\mu\text{g}/\text{mL}$ ampicillin. Red lines are heuristic fits to a bi-Gaussian function. The range of F_i^a that corresponds to a statistically neutral fitness effect is indicated in gray. Insets show DFEs enlarged over the range 0–0.1.

(F and G) The pattern of mutational sensitivity involves spatially heterogeneous yet physically connected networks of residues, building out from the active site and core as the strength of purifying selection is increased. Shown are (F) surface and (G) slice representations of the pattern of sensitivity to single-site amino acid point mutations at each ampicillin concentration mapped onto the structure of TEM-1 (PDB: 1FQG). Colored spheres indicate residues with a significant positional fitness effect (see Figure S2); different colors indicate results at each ampicillin concentration. Co-crystallized β -lactam (penicillin G) is shown as yellow stick bonds. See also Figure S2 and Table S2.

subset of more moderately conserved positions distributed within the protein core (Figures 3F and 3G). As the ampicillin concentration used for selection is further increased, the overall fitness cost of mutations dramatically increases—both in the number of mutations that show a fitness effect and in the degree of their effect relative to wild-type (Figures 2C–2E and 3C–3E). To some extent, these results seem obvious; it is reasonable to expect that the fitness cost of mutations in an enzyme will depend on the strength of purifying selection for its function. In contrast, no single mutations at any concentration significantly increase fitness, indicating that TEM-1 occupies a local peak in its genotype-fitness landscape under the conditions of these experiments.

More interestingly, the distribution of the fitness effects of mutations (DFE) is decidedly bimodal, with one mode corresponding to mutations with significant deleterious effects on fitness, and the other mode comprising those with neutral or nearly neutral fitness effects (Figures 3A–3E and Table S2). The strength of ampicillin selection controls the fraction of mutations in these two modes; increasing antibiotic concentration causes the relative proportion of mutations in the mode with deleterious mutations to increase and in the mode with neutral/nearly neutral

basis for defining cutoffs for F_i^a corresponding to statistically neutral effects on fitness (mean \pm two SD in F_i^a ; Figure S1D).

Robustness Is Conditional on the Strength of Purifying Selection

Figure 2 shows the fitness effect of all single amino acid mutations in TEM-1 at all ampicillin concentrations examined (10, 39, 156, 625, and 2500 $\mu\text{g}/\text{mL}$; see also Table S1). Under weak selection at a low ampicillin concentration (39 $\mu\text{g}/\text{mL}$; no selection was observed at 10 $\mu\text{g}/\text{mL}$; Figures 2A and 3A), the vast majority of mutations are statistically neutral ($F_i^a \approx 0$), and only a small fraction of mutations significantly affect fitness (Figures 2B and 3B). These include highly conserved positions within the active site (S70, K73, S130, D131, N132, K234, and G236; numbering according to Ambler; Ambler et al., 1991) but also a

Figure 2. Fitness Effects of All Single Amino Acid Mutations in TEM-1 under Increasing Ampicillin Selection

Shown are the data matrices containing the relative fitness effect for every amino acid mutation at every position in TEM-1 under selection with ampicillin at (A) 10, (B) 39, (C) 156, (D) 625, or (E) 2,500 $\mu\text{g}/\text{mL}$. Rows within each matrix depict positions along the primary sequence of TEM-1, and columns indicate a mutation to one of the 20 amino acids (in alphabetical order by one-letter code indicated at bottom of A). Relative fitness effect is depicted colorimetrically with blue representing a deleterious fitness effect, red a positive fitness effect, and white no fitness effect relative to wild-type. Positions for which no data were obtained at 10 $\mu\text{g}/\text{mL}$ ampicillin are colored gray. The secondary structure of the wild-type sequence is indicated to left of (A). Several highly conserved motifs within the active site (S70-X-X-K73, S130-D131-N132, E166, and K234-S235-G236) are indicated to the right of (E). See also Table S1.

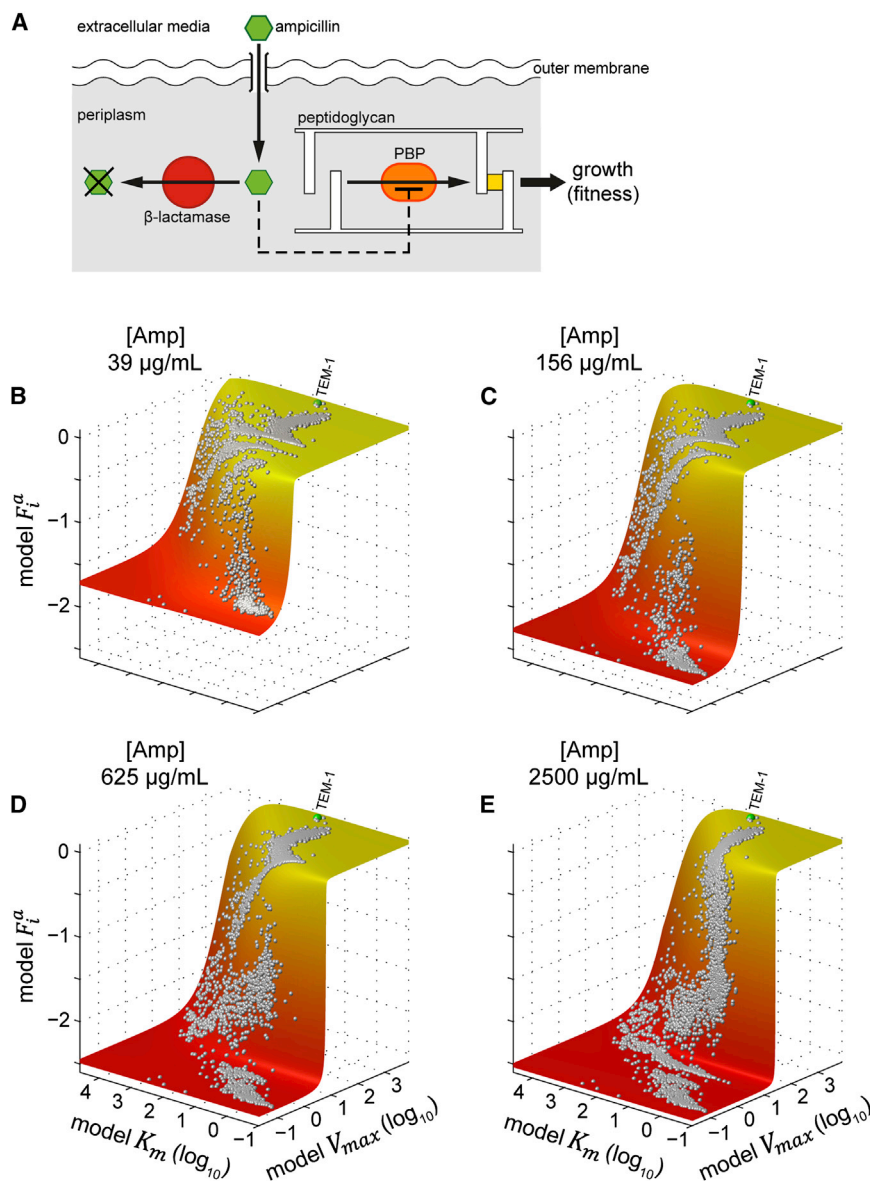


Figure 4. A Phenotype-Fitness Landscape for TEM-1

(A) Overview of the kinetic model describing fitness as a function of ampicillin concentration and intracellular β -lactamase activity (Experimental Procedures and Extended Experimental Procedures). The periplasmic concentration of ampicillin (green) is determined by the rate of passive diffusion across the outer membrane and the rate of inactivation (hydrolysis, denoted by X) by β -lactamase (red). Growth (i.e., fitness) is proportional to the rate of peptidoglycan strand-joining (yellow) by PBPs (orange); PBP activity, and thus fitness, is inhibited (dashed line) by unhydrolyzed ampicillin in the periplasm.

(B–E) Surface representation of the model revealing a non-linear relationship between phenotype (intracellular β -lactamase activity: K_m and V_{max}) and fitness marked by a plateau at neutrality ($F_i^a \approx 0$) that is dependent on the strength of selection: (B) 39, (C) 156, (D) 625, and (E) 2,500 $\mu\text{g/ml}$ ampicillin. Model estimated values of kinetic parameters and fitness for wild-type TEM-1 (green sphere) and all 4,997 single mutations (silver spheres) are shown.

See also Figure S3 and Table S3.

mutations to decrease. In addition, to different extents, both modes shift toward a greater average fitness cost as a function of ampicillin concentration (Table S2). Thus, these data (Figures 2 and 3) reveal that robustness in TEM-1 is strongly dependent on the strength of selection—under weak selection, TEM-1 is more robust as most mutations are neutral or nearly neutral in their fitness effects. But as selection is increased, robustness concomitantly decreases as more and more mutations become deleterious to fitness.

Mapping of the data onto an atomic structure of TEM-1 reveals a spatially anisotropic pattern of amino acid contributions to organismal fitness (Figures 3F and 3G). Here, we describe the average fitness cost of all mutations at each position ($\langle F_i^a \rangle_a$) at each ampicillin concentration; for comparison, positions sensitive to mutation are defined based on the distribution of $\langle F_i^a \rangle_a$ under selection at 2500 $\mu\text{g/ml}$ ampicillin (Figure S2). Under weak

selection (39 $\mu\text{g/ml}$ ampicillin), mutation-sensitive positions comprise a physically contiguous but anisotropic network of residues buried within the protein core and extending out from the active site. As the level of selective pressure is increased, this main “functional core” acquires successive shells of mutation-sensitive residues that grow outward until nearly the whole protein core shows some degree of fitness cost upon mutation. Nevertheless, the heterogeneity in positional contribution to fitness persists even at the highest levels of ampicillin; the most mutationally sensitive positions at 2500 $\mu\text{g/ml}$ ampicillin are similar to

the functional core defined at 39 $\mu\text{g/ml}$ ampicillin (Figure 7, compare panels D and F).

Robustness as an Excess of Intracellular Enzymatic Activity Relative to the Strength of Purifying Selection

To study the mechanistic basis for both the dependency of robustness on selection strength and the bimodality of the DFE, we developed a simple kinetic model describing relative fitness as a function of ampicillin concentration and intracellular β -lactamase activity (Figure 4A, Experimental Procedures, and Extended Experimental Procedures). In this model, organismal fitness is proportional to the flux of peptidoglycan substrate through DD-carboxypeptidases and other penicillin-binding proteins (PBPs) involved in cell-wall biogenesis, with ampicillin acting as a competitive inhibitor of this process. The periplasmic concentration of ampicillin is dynamically set by the balance of

intracellular β -lactamase activity and passive diffusion of ampicillin across the outer membrane (Zimmermann and Rosselet, 1977). We determined values for the free parameters of our model by globally fitting the experimental data obtained for all 4,997 mutations (Extended Experimental Procedures and Table S3). The free parameters uniquely converge, and the model fits the data well with an overall $r^2 = 0.98$.

The main result of our model is the finding of a non-linear phenotype-fitness relationship in which fitness saturates at different levels of enzyme activity as a function of the concentration of applied ampicillin (Figures 4B–4E). The non-linearity arises from two sources: the steady state achieved between diffusion and hydrolysis of ampicillin and the competitive inhibition of the PBPs. This result provides a simple explanation for both the dependence of mutational robustness on selection strength and the bimodal nature of the DFE. In the model, enzyme activity of every mutant is defined by two parameters, the maximum intracellular rate of ampicillin hydrolysis (V_{\max}) and the concentration of ampicillin that produces half-maximal rate (K_m). Due to the high overall activity of TEM-1 for ampicillin, the wild-type enzyme resides well within the saturated regime (plateau) of the fitness-activity relationship. Mutational robustness emerges as a consequence because within the saturated region, changes in enzyme activity due to mutation have negligible effects on fitness (de Visser et al., 2003; Hartl et al., 1985; Kacser and Burns, 1981; Wagner, 2005a). The model is also consistent with the dependence of robustness on the strength of selection because fitness saturates at increasingly higher levels of activity as the ampicillin concentration increases (Figures 4B–4E, S3A, and S3B). That is, robustness collapses steadily with increasing selection pressure because the fitness-activity relationship depends on the steady-state levels of ampicillin in the periplasm. Finally, the bimodal nature of the fitness effects of mutations can be understood as a direct consequence of the steep non-linearity relating enzyme activity to fitness. For example, mutational variation in enzyme activity has basically two outcomes: to stay in front of the non-linearity and have a relatively negligible effect on fitness, or to cross the non-linearity “threshold” and display a profound effect on fitness (see Figures S3C–S3G for a simulation). Further contribution could come from inherent non-linearities in the effects of mutations on TEM-1 activity, but the model shows that such is not required for bimodality in the DFE. In short, the model shows that robustness and its dependency on the strength of selection arise from the high intracellular activity of TEM-1 and the ampicillin-dependent non-linear saturation relationship between enzyme activity and fitness.

A general model for mutational robustness in proteins has been previously proposed based on the thermodynamic stability of proteins. The idea is that the “extra” stability beyond that required to asymptotically populate the native state provides a thermodynamic basis for robustness by buffering the slightly destabilizing effects of most mutations (Bloom et al., 2005; Tokuriki and Tawfik, 2009; Wylie and Shakhnovich, 2011). We note that our conclusions are not inconsistent with this view; the overall rate of ampicillin hydrolysis in vivo is a combination of both the fraction of natively folded β -lactamase protein and the specific activity of the native state, and mutations could influence either

or both properties. More generally, we propose that robustness comes from an excess of intracellular enzymatic activity relative to the fitness threshold present at a particular strength of selection—a description that combines the probability of native-state folding with the biochemical parameters controlling catalytic power and accounts for the dependency of robustness on the strength of selection.

Evolvability and Fitness under Cefotaxime Selection

Robustness implies invariance of organismal fitness upon mutation, which at first glance suggests that robust biological systems should have a decreased ability to evolve new phenotypes, or decreased evolvability. On the other hand, mutations that are neutral with regard to the current or wild-type function might be able to promote new functions; indeed, such “conditional neutrality,” whether with respect to genetic background or environmental factors, has been suggested to facilitate evolvability by permitting the accumulation of mutations that could be useful upon changes in selective pressure (de Visser et al., 2003; Kirschner and Gerhart, 1998, 2005; Masel and Trotter, 2010; Wagner, 2005a, b). To assess the relationship between robustness and evolvability in TEM-1, we performed selection on our whole-gene saturation mutagenesis library in the presence of a different β -lactam drug, cefotaxime. Cefotaxime is a poor substrate for TEM-1, with an approximately 1000-fold decrease in k_{cat}/K_m for cefotaxime versus ampicillin ($\approx 10^4$ versus $\approx 10^7$ M $^{-1}$ s $^{-1}$, respectively). As such, TEM-1 imparts no significant fitness advantage; the minimal inhibitory concentration (MIC) of cefotaxime for *E. coli* cells encoding wild-type TEM-1 is essentially unchanged from that of cells without β -lactamase (0.0625 μ g/ml) (Hall, 2002). However, single amino acid changes in TEM-1 are known to increase resistance to cefotaxime both in nature and in the laboratory (Matagne et al., 1998; Salverda et al., 2010). Selection was performed at 0.15 μ g/ml cefotaxime (approximately double the MIC for TEM-1), and the fitness of each mutation relative to wild-type TEM-1 determined as described above.

Figure 5 shows the fitness effect of all single mutations under cefotaxime selection, and Figure S4 shows the corresponding DFE (see also Table S4). In contrast to the results obtained under ampicillin selection, no mutations show a significant fitness decrease relative to wild-type TEM-1, a result that simply reflects the already poor activity of TEM-1 on cefotaxime. However, a small number of mutations (106 total, or 2%) act to increase fitness; among these we observe alleles previously reported to impart an extended-spectrum phenotype in both TEM-1 and/or its homolog SHV-1 in clinical isolates (E104K, R164H, R164S, D179G, D179N, G238A, G238S) (Matagne et al., 1998; Salverda et al., 2010) and error-prone PCR libraries (Bershtein and Tawfik, 2008; Schenk et al., 2012).

Robustness and Adaptation in TEM-1

A comparison of the relative fitness effects obtained for each mutation at each ampicillin concentration versus their respective effects under cefotaxime selection reveals how the robustness of TEM-1 under ampicillin selection (the current or wild-type function) relates to its evolvability toward cefotaxime resistance (a new function) (Figures 6A–6D). Under weak selection for ampicillin resistance (e.g., 39 μ g/ml ampicillin, Figure 6A), nearly all

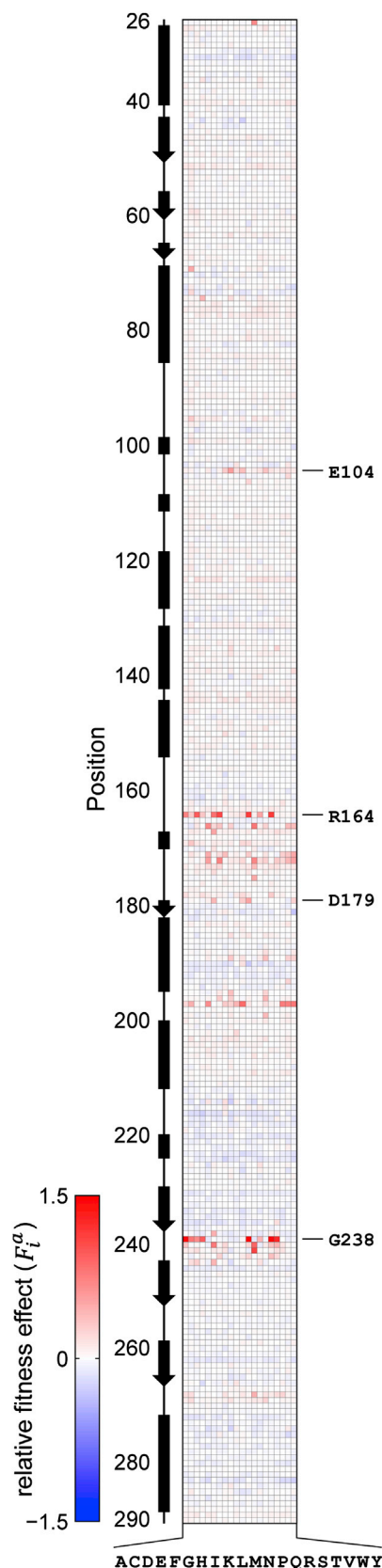


Figure 5. Fitness Effects of All Single Amino Acid Mutations in TEM-1 under Cefotaxime Selection

Shown is the data matrix depicting F_i^a for each amino acid mutation at each position in TEM-1 under selection with the non-optimal TEM-1 substrate cefotaxime at 0.15 $\mu\text{g/ml}$. Labels and coloring are as in Figure 2. Several positions previously reported to confer increased cefotaxime resistance upon mutation in TEM-1 or its homolog SHV-1 are indicated at right (E104, R164, D179, and G238). See also Figure S4 and Table S4.

mutations conferring significant cefotaxime resistance are statistically neutral in their fitness effect in ampicillin; this includes all the above-stated mutations found in clinical isolates. These mutations are said to be conditionally neutral with respect to the environment (as their phenotypes depend on the condition of selection) and have been linked to the rate of evolution of new phenotypes (Draghi et al., 2011; Wagner, 2005b). However, under selection at increasing ampicillin concentration, mutations conferring cefotaxime resistance have progressively deleterious fitness effects in ampicillin; for example, the mutations R164H, R164S, D179G, D179N, and G238S, which are neutral at 39 $\mu\text{g/ml}$ ampicillin, now have significant deleterious fitness effects at 2,500 $\mu\text{g/ml}$ ampicillin (Figure 6D). That is, the neutrality of these mutations is itself conditional on the strength of selection, present at low levels of ampicillin and diminishing at higher levels. Thus, for TEM-1, more useful genetic variation (mutations conferring cefotaxime resistance) is proportionately available when robustness is high (weak ampicillin selection) than when robustness is low (strong ampicillin selection; Figure 6E).

To test this in an independent experiment, we created a library of TEM-1 variants by error-prone PCR (average of 1 ± 1 mutations per gene, Extended Experimental Procedures), transformed into *E. coli*, and screened for growth of the population on cefotaxime (0.2 $\mu\text{g/ml}$) either with prior selection (Figures 6F, S5A, and S5B) or with co-selection (Figures S5C and S5D) on varying doses of ampicillin (Extended Experimental Procedures). The data show that in fact, the growth of the population of TEM-1 variants on cefotaxime is a function of ampicillin exposure and very nearly reflects the fraction of mutations that confer cefotaxime resistance but are statistically neutral for ampicillin in the comprehensive single-mutation library (Figure 6E). We conclude that in TEM-1, robustness enhances evolvability by permitting environmentally conditional neutral mutations that can confer cefotaxime resistance.

The Spatial Distribution of Cefotaxime Adaptation in TEM-1

Mutations conferring initial cefotaxime resistance are distributed broadly throughout the tertiary structure of TEM-1 and include residues both in the core and on the surface of the protein (residues in dark gray, Figure 7). However, there is an interesting and physically informative pattern to the organization of these mutations. Few cefotaxime-adaptive mutations are directly within the functional core defined by residues with significant fitness effects at 39 $\mu\text{g/ml}$ ampicillin (residues in red, Figures 3G, 7A, and 7D), consistent with the finding that they are largely neutral in fitness effect under weak ampicillin selection (Figure 6A). But remarkably, the mutations conferring cefotaxime resistance are organized into sparse, physically connected networks of amino acids that connect a subset of surface positions to the functional

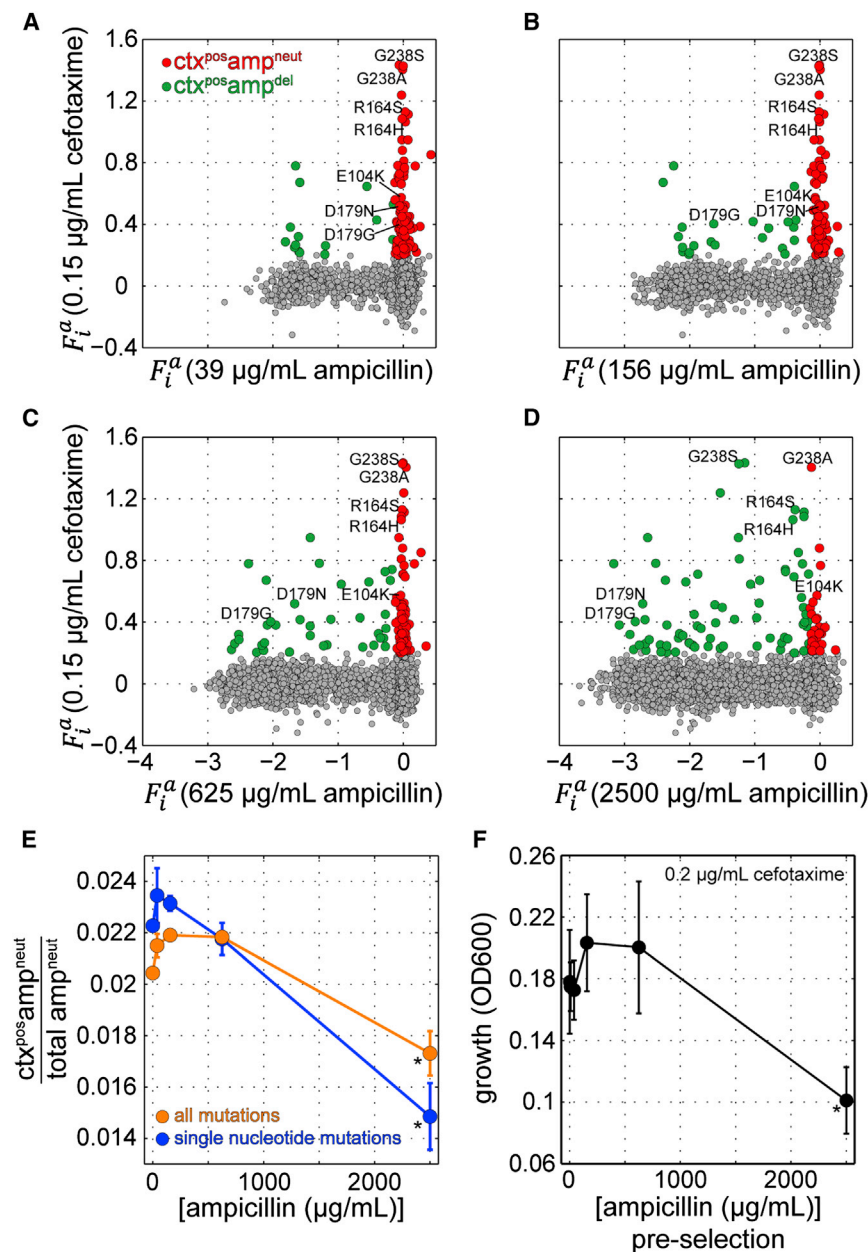


Figure 6. Robustness and Evolvability of TEM-1

(A–D) Comparison of F_i^a values for all mutations under ampicillin (x axis) versus cefotaxime selection (0.15 $\mu\text{g/mL}$; y axis) shows that most mutations conferring significant cefotaxime resistance are statistically neutral in fitness effect at a low ampicillin concentration but deleterious at the highest ampicillin concentration. Mutations that confer cefotaxime resistance and are either statistically neutral ($\text{ctx}^{\text{pos}}\text{amp}^{\text{neut}}$) or deleterious ($\text{ctx}^{\text{pos}}\text{amp}^{\text{del}}$) in fitness effect under selection at the indicated ampicillin concentration are colored red and green, respectively: (A) 39, (B) 156, (C) 625, and (D) 2,500 $\mu\text{g/mL}$ ampicillin. Several mutations previously reported to impart an “extended-spectrum” phenotype in both TEM-1 and/or its homolog SHV-1 in clinical isolates are indicated.

(E) A comparison of the fraction of statistically neutral mutations that confer cefotaxime resistance at each ampicillin concentration as determined from the whole-genome saturation mutagenesis data. Results are shown as the mean and SD from two independent ampicillin selection experiments for all mutations (orange) or those obtainable by single-nucleotide mutation from TEM-1 (blue).

(F) Results of growth experiments ($n = 6$) in which an error-prone PCR library of TEM-1 was subjected to pre-selection at several concentrations of ampicillin followed by cefotaxime selection (Extended Experimental Procedures). In (E) and (F), asterisks denote that results at 2,500 $\mu\text{g/mL}$ ampicillin are significantly different from those at all other ampicillin concentrations (one-way ANOVA and post-hoc Tukey test, $p < 0.05$). See also Figure S5.

core (Figure 7D). The physical interpretation of such “pathways” of amino acid connectivity remain to be established but suggest the possibility that these represent anisotropic collective modes in the protein structure that functionally connect a small set of surface sites to the protein active site (Lee et al., 2008; Reynolds et al., 2011). This architecture makes it so that about 50% of cefotaxime-adaptive single mutations (53/106 total) occur at surface positions far from the active site. The effect of selection under high levels of ampicillin is to reduce the set of mutations available for conferring cefotaxime resistance by reducing the likelihood of those that occur within the protein core and near to the active site (Figures 6D, 7B, 7C, 7E, and 7F). Nevertheless, the distributed architecture of adaptive mutations is such that

some surface positions (e.g., E104, T195, E197, E240) still maintain the capacity for initiation of cefotaxime resistance while remaining neutral over the full range of ampicillin concentrations examined here.

DISCUSSION

In summary, these results show that both the robustness and evolvability of TEM-1

are not invariant properties of the protein but instead are dependent on the strength of purifying selective pressure applied. At low doses of ampicillin, the high activity of TEM-1 and the non-linear dependence of fitness on enzyme activity render many mutations statistically neutral in their fitness effects under moderate selection conditions. Under these conditions, we find that the constraints on fitness are loaded in a small, physically connected network of residues in the TEM-1 tertiary structure—a functional core—that is built around and extending from the active site. Interestingly, a small fraction of positions showing neutral variation display the capacity to confer increased resistance to a new β -lactam drug, cefotaxime, upon single amino acid mutation. These positions comprise contiguous amino acid networks

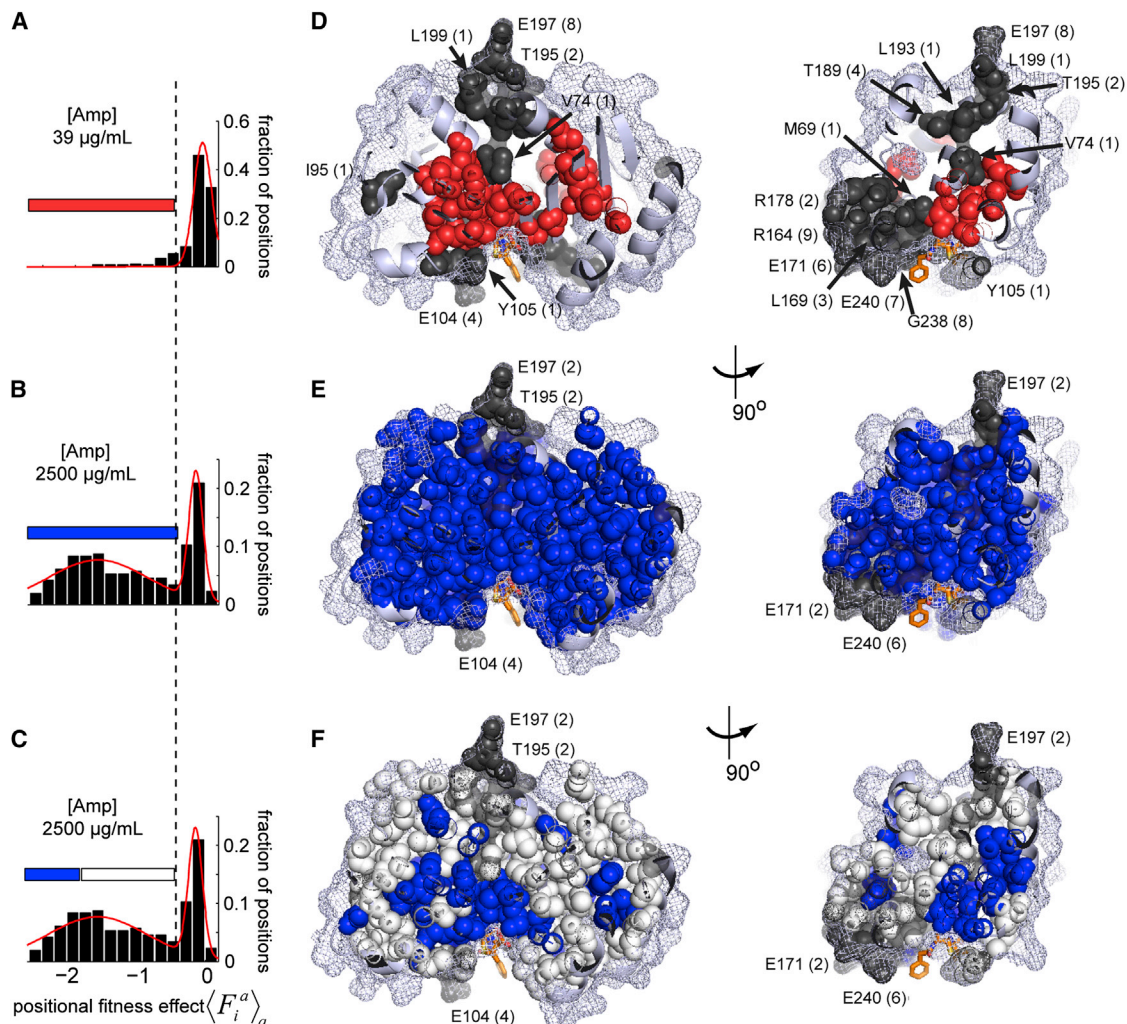


Figure 7. Structural Relationship of Robustness and Evolvability

(A–C) Shown are histograms of the average fitness effects of mutations at each position $\langle F_i^a \rangle_a$ under selection at (A) 39 $\mu\text{g}/\text{mL}$ and (B and C) 2,500 $\mu\text{g}/\text{mL}$ ampicillin (see Figure S2). Red lines are fits to a double Gaussian function. The dashed line indicates a $\langle F_i^a \rangle_a$ cutoff for positions with significant mutational sensitivity (see Figure S2), whereas colored bars indicate the range of $\langle F_i^a \rangle_a$ for positions shown on structures in panels to the right (note the lower range in C).

(D–F) The spatial pattern of adaptability toward cefotaxime (dark gray spheres) in the context of mutational sensitivity under ampicillin selection at (D) 39 $\mu\text{g}/\text{mL}$ (red spheres) or (E and F) 2,500 $\mu\text{g}/\text{mL}$ (blue or white/blue spheres); shown are slices through the core of the TEM-1 protein, and the surface of TEM-1 is in mesh. The number of adaptive mutations per position is in parentheses (note that not all positions conferring cefotaxime resistance are labeled). The data show that adaptation to cefotaxime resistance in TEM-1 arises from different physically contiguous networks of residues that connect specific distal sites to the core catalytic and structural residues defined by mutational sensitivity at low levels of ampicillin selection (red, D). At high levels of ampicillin (B and E), most core positions display a significant fitness cost upon mutation, reducing the number of cefotaxime-adaptive but ampicillin-neutral mutations. The pattern of mutational sensitivity remains heterogeneous even at high ampicillin levels (C and F), with positions showing the largest fitness cost similar to those with a significant fitness cost at low ampicillin (compare D and F).

that extend from the functional core to connect the active site to a number of distantly positioned surface positions at which cefotaxime resistance can be acquired. The robustness of TEM-1, however, collapses at high levels of ampicillin, as more and more mutations are drawn into the regime where they affect organismal fitness. With the loss of robustness, the capacity for adaptation to cefotaxime is also much reduced as many adaptive mutations that were neutral at low ampicillin concentration now have a significant impact on fitness. It is important to note that these data address only the initial single mutation step toward

the evolution of new function and with only two substrates; it will be interesting to examine how paths of higher-order mutations and robustness and evolvability under different β -lactam selection regimes are related to the functional and adaptive architecture of TEM-1 described by the global saturation mutagenesis data presented here.

The key property underlying both robustness and evolvability of TEM-1 is the high activity of the enzyme *in vivo*—the enzyme sits far along the saturated region in the activity-fitness relationship (Figure 4). In much the same way that an excess of

thermodynamic stability has been associated with enhanced protein robustness and evolvability (Bloom et al., 2006; Bloom et al., 2005; Tokuriki and Tawfik, 2009), our results here make the more general point that an excess of activity in vivo (from high catalytic activity or in vivo enzyme concentration, or both) may underlie both of these properties.

Importantly, these findings suggest new testable hypotheses for how enzymes like TEM-1 could be selected to have such high enzymatic activity. TEM-1 is an example of a so-called perfect enzyme, catalyzing the hydrolysis of penicillin-class antibiotics near the diffusion-controlled limit (Matagne et al., 1998). Why should it be so highly active if organismal fitness can saturate at much lower levels of activity? One obvious hypothesis is simply that TEM-1 may have evolved a high activity phenotype because of direct selection under periods of high concentrations of penicillin class β -lactam compounds (e.g., ampicillin) or under conditions of high mutation rate (Wilke et al., 2001). However, the finding that cefotaxime resistance in TEM-1 predominantly emerges from mutations that are neutral under ampicillin selection at low to moderate doses suggests that high activity could also result indirectly due to selection for evolvability. In this scenario, ancestral TEM-1 also randomly encountered other non-optimal β -lactams (e.g., cephalosporins). Such conditions would favor evolvable variants, those by mutation capable of conferring resistance to non-optimal β -lactams while still maintaining high fitness in the presence of ampicillin. Given that the data show that high in vivo enzyme activity underlies robustness, and robustness in turn promotes new activities through harboring conditionally neutral mutations, it thus follows that an enzyme with high activity would be evolutionarily favored under fluctuations in the distribution of β -lactam substrates. Thus, mechanisms that promote evolvability could be selected as a result of their success under historical environmental fluctuations (Kirschner and Gerhart, 1998, 2005). Future work will experimentally address the notion that the history of environmental fluctuations fundamentally defines the robustness and evolvability of natural proteins.

EXPERIMENTAL PROCEDURES

Whole-Genome Saturation Mutagenesis Library Construction

A comprehensive whole-genome saturation mutagenesis library was constructed by an overlap extension PCR mutagenesis technique (Higuchi et al., 1988; McLaughlin et al., 2012). To permit full coverage of the *bla*_{TEM-1} coding region (789 bp) with 80 base paired-end reads by Illumina sequencing, we split the sequence into ten subgroups (amino acid positions 26–51, 52–78, 79–104, 105–132, 133–156, 157–183, 184–209, 210–236, 237–264, and 265–290). The mutagenesis PCR products for the positions of each subgroup were mixed in equimolar ratios and ligated as a single library. Each subgroup was independently subject to selection in antibiotic and sample preparation for Illumina sequencing. A detailed description of the cloning procedure is provided in the Extended Experimental Procedures.

Antibiotic Selection

All selection experiments for the whole-genome saturation mutagenesis library were performed in *E. coli* MegaX DH10B T1 (Invitrogen). Selection was performed in 96-well deep-well plate format at 37°C in Luria-Bertani broth (Fisher Scientific) containing 12 μ g/ml tetracycline hydrochloride (Sigma). Wells contained either 0, 10, 39, 156, 625, or 2,500 μ g/ml of ampicillin or 0.15 μ g/ml cefotaxime at 25-fold concentration. The duration of growth (~2 hr) was chosen to obtain significant selection while maintaining sufficient population size

(~10⁶ cells) relative to the library diversity and avoiding stationary growth. Details are provided in the Extended Experimental Procedures.

Illumina Sequencing

Samples for Illumina sequencing were prepared by PCR from libraries after antibiotic selection as previously described (McLaughlin et al., 2012). Addition of adaptor sequences for Illumina sequencing was performed in two rounds: the first round amplifies the mutated region of TEM-1, adds the annealing site for the Illumina paired-end sequencing primer, and incorporates a 4 bp barcode to indicate the concentration of antibiotic. The second round adds the remainder of the sequencing primer annealing site along with the annealing site for the Illumina flow cell. Primer sequences are available upon request. Illumina sequencing and determination of allele counts were performed as previously described (McLaughlin et al., 2012). Sequencing was performed at the UT Southwestern Genomics Core on an Illumina Genome Analyzer IIx using a version 4 paired-end PE-75 flow cell. Sequences from the Illumina base-caller were imported into CLC Genomics Workbench and trimmed for size and quality using a cutoff of 0.01 for the modified Mott algorithm. Custom scripts written in MATLAB were used to count the number of each allele under each selection condition and to determine relative fitness values. MATLAB scripts are available upon request.

Mechanistic Model

A detailed description of the model describing relative fitness as a function of intracellular β -lactamase activity and ampicillin concentration is provided in the Extended Experimental Procedures. β -lactam antibiotics inhibit bacterial growth through competitive inhibition of DD-carboxypeptidases and other PBPs involved in synthesis of the peptidoglycan layer of bacterial cell walls. In the model, relative fitness (F_i^a) is proportional to the difference in PBP activity in the presence of mutant versus wild-type TEM-1. PBP activity is described according to Michaelis-Menten kinetics, modified to include competitive inhibition by ampicillin. The periplasmic concentration of ampicillin is determined by the equilibrium between the flux of antibiotic across the outer membrane and its rate of hydrolysis (inactivation) by β -lactamase (Zimmermann and Rosselet, 1977). We determined values for the free parameters of our model (total of 9,998 free parameters for 29,849 data points) by fitting the experimental data obtained for all 4,997 mutations using a Monte Carlo simulated annealing (MCSA) procedure; the model fits the data well with an overall $r^2 = 0.9767$.

SUPPLEMENTAL INFORMATION

Supplemental Information includes Extended Experimental Procedures, five figures, and four tables and can be found with this article online at <http://dx.doi.org/10.1016/j.cell.2015.01.035>.

AUTHOR CONTRIBUTIONS

M.A.S. and R.R. developed the research plan and experimental strategy. M.A.S. performed all experiments. M.A.S. and D.R.H. developed the kinetic model. M.A.S., D.R.H., and R.R. interpreted the data and wrote the paper.

ACKNOWLEDGMENTS

We thank F.J. Poelwijk, V. Salinas, V. Krishna, K.A. Reynolds, and S.J. Helms for assistance with the kinetic model, processing of Illumina data, and/or critical reading of the manuscript. We also thank C. Liang and the UT Southwestern Genomics Core for assistance with Illumina sequencing. R.R. acknowledges support from the National Institutes of Health (R01EY018720-05), the Robert A. Welch Foundation (I-1366), and the Green Center for Systems Biology.

Received: July 9, 2014

Revised: October 30, 2014

Accepted: January 17, 2015

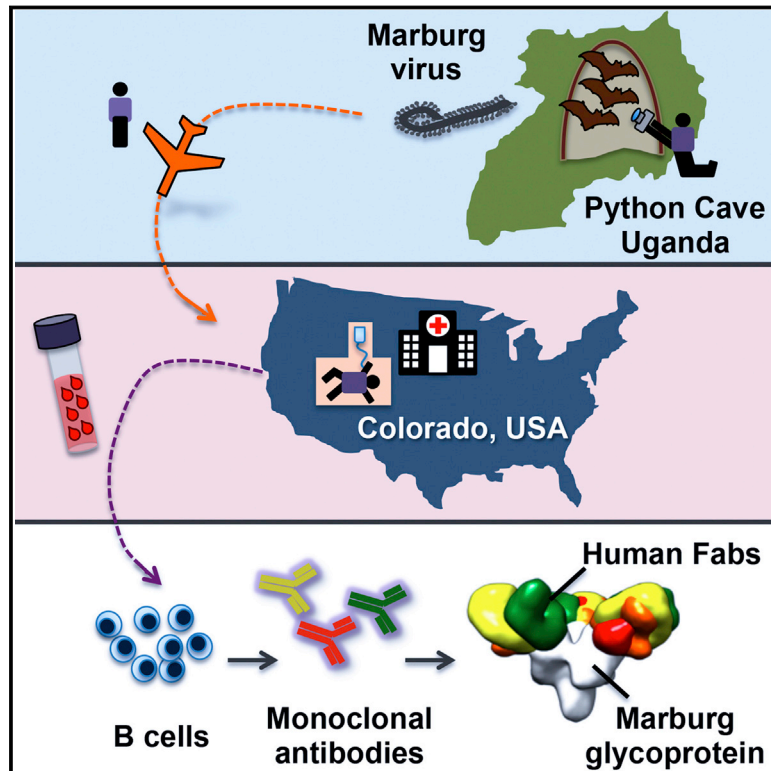
Published: February 26, 2015

REFERENCES

- Ambler, R.P., Coulson, A.F., Frère, J.M., Ghuysen, J.M., Joris, B., Forsman, M., Levesque, R.C., Tiraby, G., and Waley, S.G. (1991). A standard numbering scheme for the class A beta-lactamases. *Biochem. J.* 276, 269–270.
- Bershtein, S., and Tawfik, D.S. (2008). Ohno's model revisited: measuring the frequency of potentially adaptive mutations under various mutational drifts. *Mol. Biol. Evol.* 25, 2311–2318.
- Bershtein, S., Segal, M., Bekerman, R., Tokuriki, N., and Tawfik, D.S. (2006). Robustness-epistasis link shapes the fitness landscape of a randomly drifting protein. *Nature* 444, 929–932.
- Bloom, J.D., Silberg, J.J., Wilke, C.O., Drummond, D.A., Adami, C., and Arnold, F.H. (2005). Thermodynamic prediction of protein neutrality. *Proc. Natl. Acad. Sci. USA* 102, 606–611.
- Bloom, J.D., Labthavikul, S.T., Otey, C.R., and Arnold, F.H. (2006). Protein stability promotes evolvability. *Proc. Natl. Acad. Sci. USA* 103, 5869–5874.
- Bowie, J.U., Reidhaar-Olson, J.F., Lim, W.A., and Sauer, R.T. (1990). Deciphering the message in protein sequences: tolerance to amino acid substitutions. *Science* 247, 1306–1310.
- de Visser, J.A., Hermisson, J., Wagner, G.P., Ancel Meyers, L., Bagheri-Chaichian, H., Blanchard, J.L., Chao, L., Cheverud, J.M., Elena, S.F., Fontana, W., et al. (2003). Perspective: Evolution and detection of genetic robustness. *Evolution* 57, 1959–1972.
- DePristo, M.A., Weinreich, D.M., and Hartl, D.L. (2005). Missense meanderings in sequence space: a biophysical view of protein evolution. *Nat. Rev. Genet.* 6, 678–687.
- Draghi, J.A., Parsons, T.L., Wagner, G.P., and Plotkin, J.B. (2010). Mutational robustness can facilitate adaptation. *Nature* 463, 353–355.
- Draghi, J.A., Parsons, T.L., and Plotkin, J.B. (2011). Epistasis increases the rate of conditionally neutral substitution in an adapting population. *Genetics* 187, 1139–1152.
- Fimberg, E., Labonte, J.W., Gray, J.J., and Ostermeier, M. (2014). A comprehensive, high-resolution map of a gene's fitness landscape. *Mol. Biol. Evol.* 31, 1581–1592.
- Fowler, D.M., Araya, C.L., Fleishman, S.J., Kellogg, E.H., Stephany, J.J., Baker, D., and Fields, S. (2010). High-resolution mapping of protein sequence-function relationships. *Nat. Methods* 7, 741–746.
- Guo, H.H., Choe, J., and Loeb, L.A. (2004). Protein tolerance to random amino acid change. *Proc. Natl. Acad. Sci. USA* 101, 9205–9210.
- Hall, B.G. (2002). Predicting evolution by in vitro evolution requires determining evolutionary pathways. *Antimicrob. Agents Chemother.* 46, 3035–3038.
- Hartl, D.L., Dykhuizen, D.E., and Dean, A.M. (1985). Limits of adaptation: the evolution of selective neutrality. *Genetics* 111, 655–674.
- Hayden, E.J., Ferrada, E., and Wagner, A. (2011). Cryptic genetic variation promotes rapid evolutionary adaptation in an RNA enzyme. *Nature* 474, 92–95.
- Higuchi, R., Krummel, B., and Saiki, R.K. (1988). A general method of in vitro preparation and specific mutagenesis of DNA fragments: study of protein and DNA interactions. *Nucleic Acids Res.* 16, 7351–7367.
- Huang, W., Petrosino, J., Hirsch, M., Shenkin, P.S., and Palzkill, T. (1996). Amino acid sequence determinants of beta-lactamase structure and activity. *J. Mol. Biol.* 258, 688–703.
- Jacquier, H., Birgy, A., Le Nagard, H., Mechulam, Y., Schmitt, E., Glodt, J., Bercot, B., Petit, E., Poulain, J., Barnaud, G., et al. (2013). Capturing the mutational landscape of the beta-lactamase TEM-1. *Proc. Natl. Acad. Sci. USA* 110, 13067–13072.
- Kacser, H., and Burns, J.A. (1981). The molecular basis of dominance. *Genetics* 97, 639–666.
- Kirschner, M., and Gerhart, J. (1998). Evolvability. *Proc. Natl. Acad. Sci. USA* 95, 8420–8427.
- Kirschner, M., and Gerhart, J. (2005). *The Plausibility of Life* (New Haven, CT: Yale University Press).
- Lee, J., Natarajan, M., Nashine, V.C., Socolich, M., Vo, T., Russ, W.P., Benkovic, S.J., and Ranganathan, R. (2008). Surface sites for engineering allosteric control in proteins. *Science* 322, 438–442.
- Loeb, D.D., Swannstrom, R., Everitt, L., Manchester, M., Stamper, S.E., and Hutchison, C.A., 3rd. (1989). Complete mutagenesis of the HIV-1 protease. *Nature* 340, 397–400.
- Masel, J., and Siegal, M.L. (2009). Robustness: mechanisms and consequences. *Trends Genet.* 25, 395–403.
- Masel, J., and Trotter, M.V. (2010). Robustness and evolvability. *Trends Genet.* 26, 406–414.
- Matagne, A., Lamotte-Brasseur, J., and Frère, J.M. (1998). Catalytic properties of class A beta-lactamases: efficiency and diversity. *Biochem. J.* 330, 581–598.
- McLaughlin, R.N., Jr., Poelwijk, F.J., Raman, A., Gosal, W.S., and Ranganathan, R. (2012). The spatial architecture of protein function and adaptation. *Nature* 491, 138–142.
- Medeiros, A.A. (1997). Evolution and dissemination of beta-lactamases accelerated by generations of beta-lactam antibiotics. *Clin. Infect. Dis.* 24 (Suppl 1), S19–S45.
- Melnikov, A., Rogov, P., Wang, L., Gnirke, A., and Mikkelsen, T.S. (2014). Comprehensive mutational scanning of a kinase in vivo reveals substrate-dependent fitness landscapes. *Nucleic Acids Res.* 42, e112.
- Payne, J.L., and Wagner, A. (2014). The robustness and evolvability of transcription factor binding sites. *Science* 343, 875–877.
- Rennell, D., Bouvier, S.E., Hardy, L.W., and Poteete, A.R. (1991). Systematic mutation of bacteriophage T4 lysozyme. *J. Mol. Biol.* 222, 67–88.
- Reynolds, K.A., McLaughlin, R.N., and Ranganathan, R. (2011). Hot spots for allosteric regulation on protein surfaces. *Cell* 147, 1564–1575.
- Salverda, M.L., De Visser, J.A., and Barlow, M. (2010). Natural evolution of TEM-1 β -lactamase: experimental reconstruction and clinical relevance. *FEMS Microbiol. Rev.* 34, 1015–1036.
- Schenk, M.F., Szendro, I.G., Krug, J., and de Visser, J.A. (2012). Quantifying the adaptive potential of an antibiotic resistance enzyme. *PLoS Genet.* 8, e1002783.
- Suckow, J., Markiewicz, P., Kleina, L.G., Miller, J., Kisters-Woike, B., and Müller-Hill, B. (1996). Genetic studies of the Lac repressor. XV: 4000 single amino acid substitutions and analysis of the resulting phenotypes on the basis of the protein structure. *J. Mol. Biol.* 261, 509–523.
- Tokuriki, N., and Tawfik, D.S. (2009). Stability effects of mutations and protein evolvability. *Curr. Opin. Struct. Biol.* 19, 596–604.
- Waddington, C.H. (1942). Canalization of development and the inheritance of acquired characters. *Nature* 150, 563–565.
- Waddington, C.H. (1953). Genetic assimilation of an acquired character. *Evolution* 7, 118–126.
- Wagner, A. (2005a). *Robustness and Evolvability in Living Systems* (New Jersey: Princeton University Press).
- Wagner, A. (2005b). Robustness, evolvability, and neutrality. *FEBS Lett.* 579, 1772–1778.
- Wagner, A. (2008). Robustness and evolvability: a paradox resolved. *Proc. Biol. Sci.* 275, 91–100.
- Weinreich, D.M., Delaney, N.F., DePristo, M.A., and Hartl, D.L. (2006). Darwinian evolution can follow only very few mutational paths to fitter proteins. *Science* 312, 111–114.
- Wilke, C.O., Wang, J.L., Ofria, C., Lenski, R.E., and Adami, C. (2001). Evolution of digital organisms at high mutation rates leads to survival of the flattest. *Nature* 412, 331–333.
- Wylie, C.S., and Shakhnovich, E.I. (2011). A biophysical protein folding model accounts for most mutational fitness effects in viruses. *Proc. Natl. Acad. Sci. USA* 108, 9916–9921.
- Zimmermann, W., and Rosselet, A. (1977). Function of the outer membrane of *Escherichia coli* as a permeability barrier to beta-lactam antibiotics. *Antimicrob. Agents Chemother.* 12, 368–372.

Mechanism of Human Antibody-Mediated Neutralization of Marburg Virus

Graphical Abstract



Authors

Andrew I. Flyak, Philipp A. Illykh, ..., Alexander Bukreyev, James E. Crowe, Jr.

Correspondence

james.crowe@vanderbilt.edu

In Brief

The characterization of Marburg-specific antibodies in several patients who survived the infection reveals a common binding site in the viral glycoprotein and a mechanism for filovirus inhibition.

Highlights

- Marburg virus survivor-neutralizing antibodies bind to a single antigenic site
- Several of the survivors' antibodies also bind to Ebola virus glycoprotein
- All antibodies identified bind at the predicted region of the receptor-binding site
- Binding to receptor-binding site is a new mechanism of filovirus inhibition



Mechanism of Human Antibody-Mediated Neutralization of Marburg Virus

Andrew I. Flyak,¹ Philipp A. Illykh,^{5,6} Charles D. Murin,^{7,8} Tania Garron,^{5,6} Xiaoli Shen,^{5,6} Marnie L. Fusco,⁸ Takao Hashiguchi,^{8,11} Zachary A. Bornholdt,⁸ James C. Slaughter,^{3,4} Gopal Sapparapu,³ Curtis Klages,^{5,6} Thomas G. Ksiazek,^{5,6} Andrew B. Ward,⁷ Erica Ollmann Saphire,^{8,9} Alexander Bukreyev,^{5,6,10} and James E. Crowe, Jr.^{1,2,3,10,*}

¹Department of Pathology, Microbiology, and Immunology, Vanderbilt University, Nashville, TN 37232, USA

²Department of Pediatrics, Vanderbilt University, Nashville, TN 37232, USA

³Vanderbilt Vaccine Center, Vanderbilt University, Nashville, TN 37232, USA

⁴Department of Biostatistics, Vanderbilt University, Nashville, TN 37232, USA

⁵Department of Pathology, University of Texas Medical Branch, Galveston, TX 77555, USA

⁶Galveston National Laboratory, Galveston, TX 77550, USA

⁷Department of Integrative Structural and Computational Biology, The Scripps Research Institute, La Jolla, CA 92037, USA

⁸Department of Immunology and Microbial Science, The Scripps Research Institute, La Jolla, CA 92037, USA

⁹The Skaggs Institute for Chemical Biology, The Scripps Research Institute, La Jolla, CA 92037, USA

¹⁰Co-senior author

¹¹Present address: Faculty of Medicine, Department of Virology, Kyushu University, Fukuoka 812-8582, Japan

*Correspondence: james.crowe@vanderbilt.edu

<http://dx.doi.org/10.1016/j.cell.2015.01.031>

SUMMARY

The mechanisms by which neutralizing antibodies inhibit Marburg virus (MARV) are not known. We isolated a panel of neutralizing antibodies from a human MARV survivor that bind to MARV glycoprotein (GP) and compete for binding to a single major antigenic site. Remarkably, several of the antibodies also bind to Ebola virus (EBOV) GP. Single-particle EM structures of antibody-GP complexes reveal that all of the neutralizing antibodies bind to MARV GP at or near the predicted region of the receptor-binding site. The presence of the glycan cap or mucin-like domain blocks binding of neutralizing antibodies to EBOV GP, but not to MARV GP. The data suggest that MARV-neutralizing antibodies inhibit virus by binding to infectious virions at the exposed MARV receptor-binding site, revealing a mechanism of filovirus inhibition.

INTRODUCTION

Marburg virus (MARV) and Ebola virus (EBOV), which are members of the family *Filoviridae*, infect humans and non-human primates, causing a hemorrhagic fever with mortality rates up to 90% (Brauburger et al., 2012). There have been a dozen outbreaks of Marburg virus infection in humans reported to date, including the most recent report from Uganda of a 30-year-old male health worker who died in September 2014 (WHO, 2014a). As of January 7, 2015, there have been in excess of 20,000 confirmed, probable, and suspected cases of Ebola virus disease (EVD) in the current EBOV outbreak in nine affected countries (Guinea, Liberia, Mali, Nigeria, Senegal, Sierra Leone,

Spain, the United Kingdom, and the United States of America), with more than 8,000 deaths (WHO, 2014b).

There is no licensed treatment or vaccine for filovirus infection. Recently, several studies showed that filovirus glycoprotein (GP)-specific neutralizing antibodies (nAbs) can reduce mortality following experimental inoculation of animals with a lethal dose of EBOV (Dye et al., 2012; Marzi et al., 2012; Olinger et al., 2012; Qiu et al., 2012, 2014; Pettitt et al., 2013) or MARV (Dye et al., 2012). The primary target of these nAbs, the filovirus surface GP, is a trimer composed of three heavily glycosylated GP1-GP2 heterodimers (Figure S1). The GP1 subunit can be divided further into base, head, glycan cap, and mucin-like domains (Lee et al., 2008). During viral entry, the mucin-like domain and glycan cap mediate binding to multiple host attachment factors present on the cell membrane. After the virus enters the host cell by macropinocytosis (Nanbo et al., 2010; Saeed et al., 2010), the GP is cleaved by host proteases that remove approximately 80% of the mass of the GP1 subunit, including the mucin-like domain and glycan cap (Chandran et al., 2005; Dube et al., 2009). After cleavage of GP in the endosome, the receptor-binding sites on GP become exposed, and the GP1 head then is able to bind to its receptor, Niemann-Pick C1 (NPC1) protein (Carette et al., 2011; Chandran et al., 2005; Côté et al., 2011). Subsequent conformational changes in GP facilitate fusion between viral and endosomal membranes.

The dense clustering of glycans on the glycan cap and mucin-like domain likely shield much of the surface of EBOV GP from humoral immune surveillance, leaving only a few sites on the EBOV GP protein at which nAbs could bind without interference by glycans (Cook and Lee, 2013). Most of our knowledge about humoral response against filovirus infections has come from studies of murine Abs that recognize EBOV GP. From those studies, we learned that mouse nAbs preferentially target peptides exposed in upper, heavily glycosylated domains or lower areas (the GP1 base), where rearrangements occur that drive

fusion of viral and host membranes (Saphire, 2013). Abs have not been identified that target protein features of the GP1 head sub-domain, where the receptor-binding site to NPC1 protein is located. Ab KZ52, the only reported human EBOV GP-specific mAb, was obtained from a phage display library that was constructed from bone marrow RNA obtained from a survivor (Maruyama et al., 1999). KZ52 binds a site at the base of the GP and neutralizes EBOV, most likely by inhibiting the conformational changes required for fusion of viral and endosomal membranes (Lee et al., 2008). Some murine Abs also have been reported to bind to the base region of Ebola virus GPs (Dias et al., 2011; Murin et al., 2014). In contrast, very little is known about the mechanisms by which Abs neutralize MARV. Two murine Abs that bound the mucin-like domain of MARV GP reduced MARV budding from infected cells in culture but failed to neutralize virus directly (Kajihara et al., 2012). Polyclonal MARV-specific Abs were shown to protect non-human primates when administrated passively after challenge (Dye et al., 2012). The epitopes recognized by such polyclonal nAbs, and the mechanism of neutralization by which these Abs act, are unknown. In this study, we isolated a large panel of human nAbs from B cells of a human survivor of severe MARV infection and used these Abs to define the molecular basis of MARV neutralization by human Abs. The results show that MARV nAbs recognize the NPC1 receptor-binding domain of MARV GP and, in some cases, also recognize conserved structural features in the equivalent receptor-binding domain on EBOV GP.

RESULTS

Isolation of Monoclonal Antibodies

We tested plasma of a MARV survivor previously infected in Uganda for the 50% neutralization activity against the Uganda strain of MARV and found a serum-neutralizing titer of 1:1,010. To generate human hybridoma cell lines secreting mAbs to MARV, we screened supernatants from EBV-transformed B cell lines derived from the survivor for binding to several recombinant forms of MARV GP or to irradiated cell lysates prepared from MARV-infected cell cultures. We fused transformed cells from B cell lines producing MARV-reactive Abs to the MARV antigens with myeloma cells and generated 51 cloned hybridomas secreting MARV-specific human mAbs. Thirty-nine of these mAbs were specific to the MARV GP, while 12 bound to infected-cell lysate, but not to GP; these latter mAbs were shown in secondary screens to bind to MARV internal proteins (NP, VP35, or VP40; data not shown). Analysis of the Ab heavy- and light-chain variable domain sequences revealed that all MARV-specific mAbs were encoded by unique Ab genes.

Neutralization Activity

To evaluate the inhibitory activity of the mAbs, we first performed *in vitro* neutralization studies using a chimeric vesicular stomatitis virus with MARV GP from Uganda strain on its surface (vesicular stomatitis virus/Marburg glycoprotein recombinant VSV/GP-Uganda). Eighteen of the 39 MARV GP-specific mAbs exhibited neutralization activity against VSV/GP-Uganda (Figures 1A and 1C; Figures S2 and S4). Of those 18 nAbs, 9 displayed strong ($IC_{50} < 10 \mu\text{g/ml}$), 8 nAbs displayed moderate (IC_{50} : 10–

99 $\mu\text{g/ml}$), and one displayed weak (IC_{50} : 100–1,000 $\mu\text{g/ml}$) neutralizing activity against VSV/GP-Uganda. We also tested the neutralization potency of all nAbs that bound to MARV GP in a plaque reduction assay using live MARV-Uganda virus. Of 18 Abs that neutralized VSV/GP-Uganda, 11 Abs exhibited neutralizing activity against MARV-Uganda (Figures 1A and 1C; Figures S3 and S4). These data suggest that VSV/GP, often used to study neutralizing potency of Abs because of its BSL-2 containment level, is more susceptible to Ab-mediated neutralization than live MARV. This difference is likely explained by the significantly lower copy number of MARV GP molecules that incorporate into VSV particles compared with the large number of GP molecules on the surface of filovirus filaments (Beniac et al., 2012; Thomas et al., 1985). Comparison of MARV-neutralizing and non-neutralizing antibodies at concentration up to 1.6 mg/ml revealed dose-dependent activity of those mAbs that neutralized. The neutralization activity of nAbs was not enhanced by the presence of complement (data not shown). As expected, we did not detect neutralizing activity for any of the 12 Abs specific to MARV NP, VP35, or VP40 proteins.

Recognition of Varying Forms of GP

To characterize the binding of isolated Abs to recombinant MARV GPs, we performed binding assays using either a recombinant MARV GP ectodomain containing the mucin-like domain (MARV GP) or a recombinant GP lacking residues 257–425 of the mucin-like domain (MARV GP Δ muc). Based on OD_{405} values at the highest Ab concentration tested (E_{max}) and 50% effective concentration (EC_{50}), we divided the MARV-GP-specific Abs into four major groups, based on binding phenotype (designated binding groups 1, 2, 3A, and 3B; Figures 1B and S5). Binding group 1 mAbs had an E_{max} to GP < 2 (i.e., these mAbs never exhibited a maximal binding level to MARV GP); binding group 2 mAbs had an E_{max} to GP > 2 , with EC_{50} for GP $< EC_{50}$ for GP Δ muc (i.e., these mAbs bound to the mucin-like domain or glycan cap); and binding group 3 had an E_{max} to GP > 2 , with EC_{50} for GP $\approx EC_{50}$ for GP Δ muc (i.e., these mAbs bound equally well to full-length and mucin-deleted forms of GP), with the group 3A mAbs having an EC_{50} for GP $< 0.5 \mu\text{g/ml}$ and the group 3B mAbs having an EC_{50} for GP $> 0.5 \mu\text{g/ml}$ (suggesting that, as a class, the group 3B mAbs possess a lower steady-state K_D of binding to GP than did group 3A mAbs).

Abs that lacked neutralization activity against VSV/GP-Uganda or MARV-Uganda fell principally into binding groups 1, 2, and 3A. Interestingly, all VSV/GP-Uganda nAbs displayed a unique binding pattern and segregated into binding group 3B (Figure 1C). It was interesting that while both mAbs from groups 3A and 3B bound equally well to the full-length MARV GP and to the GP Δ muc, EC_{50} values for nAbs from binding group 3B were higher than those for non-neutralizing Abs from group 3A.

Competition-Binding Studies

To determine whether mAbs from distinct binding groups targeted different antigenic regions on the MARV GP surface, we performed a competition-binding assay using a real-time biosensor. We tested 18 MARV nAbs from binding group 3B, 4 Abs from binding group 3A, and 1 Ab from binding group 2 in a tandem blocking assay in which biotinylated GP Δ muc was

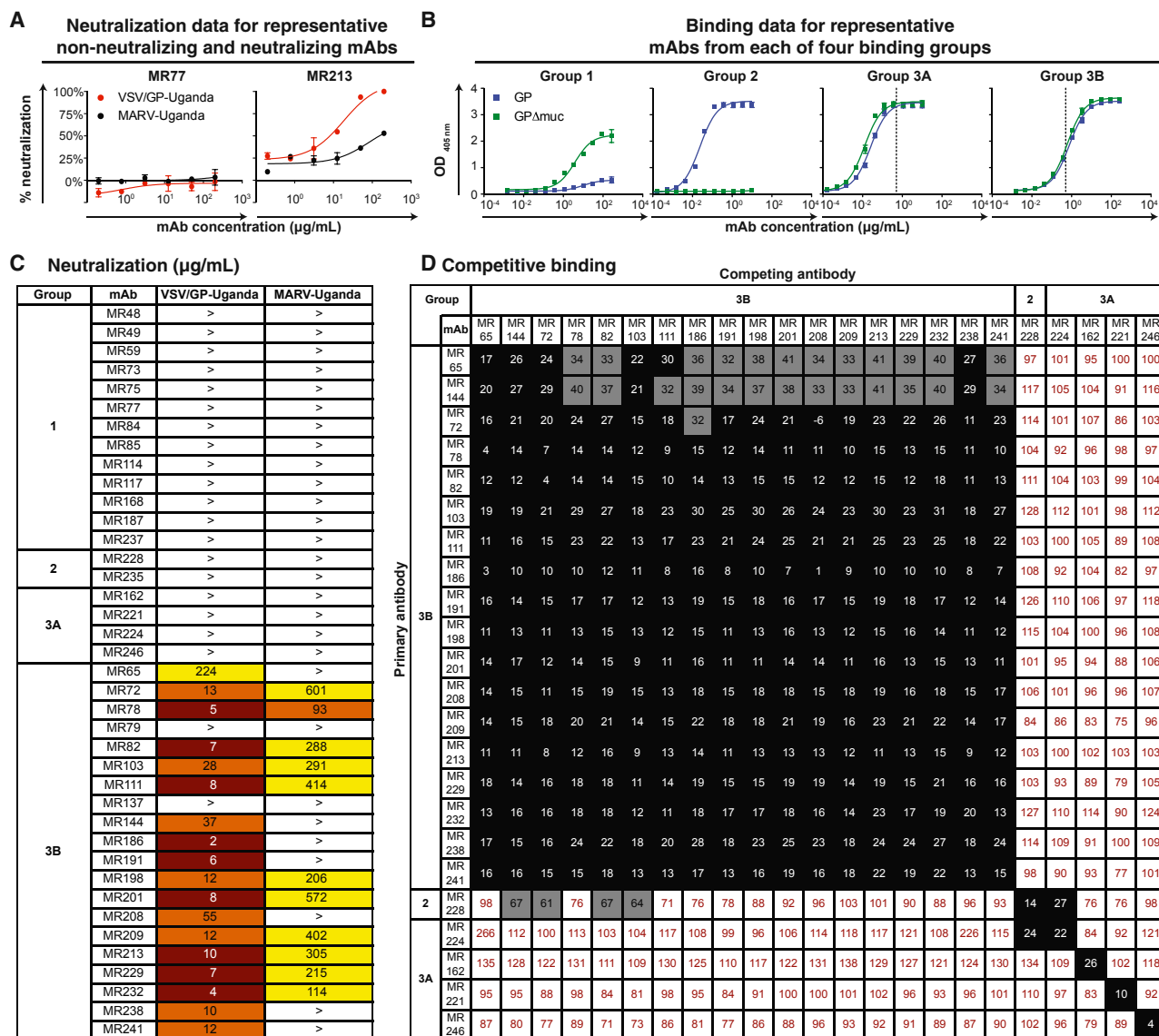


Figure 1. MARV-Neutralizing mAbs Display a Unique Binding Pattern and Target a Distinct Antigenic Region on the GP Surface

(A) Neutralization activity of MR77 (non-neutralizing antibody) or MR213 (neutralizing antibody) against VSV/GP-Uganda (red circles) or MARV-Uganda (black circles). Error bars represent the SE of the experiment performed in triplicate.

(B) Binding of representative mAbs from four distinct binding groups to the MARV GP (blue squares) or MARV GPΔmuc (green squares). A dotted line indicates 0.5 µg/ml threshold for categorizing group 3 antibodies as possessing low (3A) or high (3B) EC₅₀ values.

(C) Heatmap showing the neutralization potency of MARV GP-specific mAbs against VSV/GP-Uganda or MARV-Uganda. The IC₅₀ value for each virus-mAb combination is shown, with dark red, orange, yellow, or white shading indicating high, intermediate, low, or no potency, respectively. IC₅₀ values greater than 1,000 µg/ml are indicated by >. Neutralization assays were performed in triplicate.

(D) Data from competition binding assays using mAbs from binding groups 2, 3A, or 3B. Numbers indicate the percent binding of the competing mAb in the presence of the first mAb, compared to binding of competing mAb alone. MAb was judged to compete for the same site if maximum binding of the competing mAb was reduced to <30% of its un-competed binding (black boxes with white numbers). MAb was considered non-competing if maximum binding of the competing mAb was >70% of its un-competed binding (white boxes with red numbers). Gray boxes with black numbers indicate an intermediate phenotype (between 30 and 70% of un-competed binding).

See also Figures S2, S3, S4, and S5.

attached to a streptavidin biosensor. Abs from group 1 and the two non-neutralizing Abs from binding group 3B did not bind to biotinylated GPΔmuc in the competition assay and were excluded from the analysis. While non-neutralizing Abs from

binding groups 2 and 3A did not prevent binding of the binding group 3B nAbs to GPΔmuc, all nAbs blocked binding of each of the other nAbs to the antigen and segregated into a single competition-binding group (Figure 1D). These data suggested

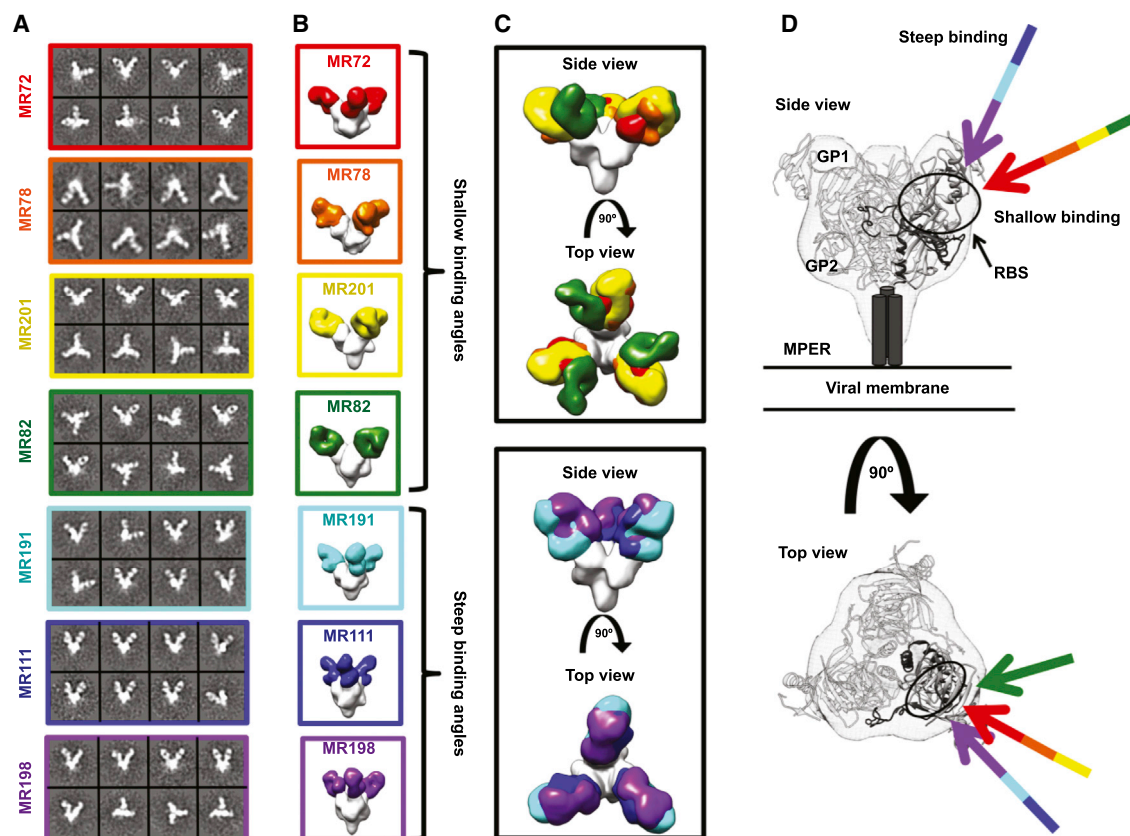


Figure 2. Neutralizing Antibodies from a Human Survivor of MARV Bind to the Receptor-Binding Site of GP at Two Distinct Angles of Approach

(A) Representative reference-free 2D class averages of the MARV GPΔMuc:MR Fab complexes.

(B) EM reconstructions of seven Fab fragments of neutralizing antibodies bound to MARV GPΔmuc (side views). All seven antibodies target a similar epitope on the top of GP.

(C) These antibodies can be subdivided based on their angles of approach: (1) those that bind toward the top and side of GP1 at a shallow angle relative to the central 3-fold axis (MR72 in red, MR78 in orange, MR201 in yellow, or MR82 in green) and (2) those that bind at a steeper angle toward the top of GP1 (MR191 in cyan, MR111 in blue, or MR198 in purple).

(D) The crystal structure of EBOV GPΔMuc (GP1 in white and GP2 in dark gray) is modeled into the MARV GP density (mesh), and the angles of approach of the neutralizing antibodies are indicated with arrows, colored as in (B). The footprint of the antibodies is indicated by a black circle targeting residues in the putative receptor-binding site (RBS) through a variety of approach angles.

See also Figure S1.

that all of the nAbs target a single major antigenic region on the MARV GP surface.

Electron Microscopy Studies of Antigen-Antibody Complexes

To determine the location of the antigenic region targeted by MARV nAbs, we performed negative stain single-particle electron microscopy (EM) studies using complexes of GPΔmuc with Fab fragments of seven nAbs from Binding Group 3B. The EM reconstructions clearly showed that Fab fragments for all seven nAbs bind at the top of the GP in or near the NPC1 protein receptor-binding site (Figures 2A and 2B). The binding pattern of these Abs could be divided further into two major groups based on their relative angle of approach to the GP head domain. MAbs MR72, MR78, MR201, and MR82 bound toward the top and side of GP1 at a shallow angle relative to the central 3-fold axis, while

mAbs MR191, MR111, and MR198 bound at a steeper angle toward the top of GP1 (Figures 2C and 2D). When we compared IC_{50} values for nAbs that bound in the two binding poses, we did not detect a significant difference in neutralization potency based on the angle of approach (Figure 1C).

Antibody Neutralization Escape Mutant Viruses

As an additional strategy to determine residues on MARV GP involved in binding to nAbs, we generated VSV/GP-Uganda variant viruses that escaped neutralization, and then we determined the sequence of the GP of those mAb escape viruses. Vero E6 cells were inoculated with VSV/GP-Uganda in the presence of MR72 or MR78 nAbs. Two escape mutant viruses were isolated: virus variant VSV/GP-72.5 contained three missense mutations in the MARV GP gene (N129S in the putative NPC1 receptor-binding site, S220P in the glycan cap and P455L in the

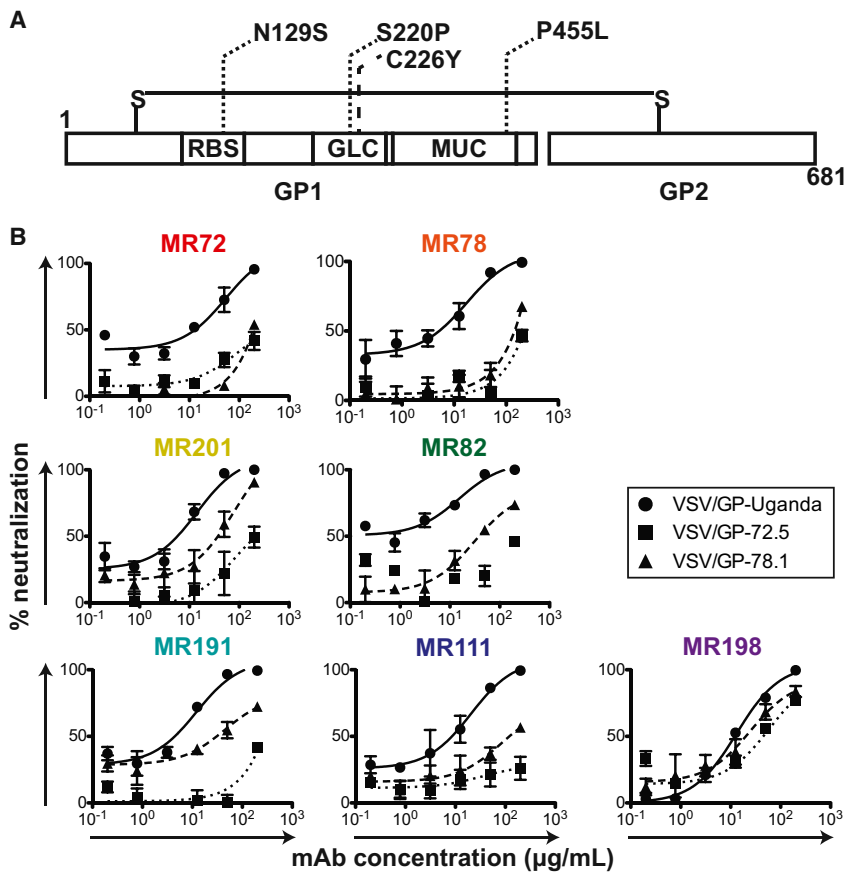


Figure 3. Generation of Escape Mutants for MARV-Neutralizing Antibodies

(A) VSV-MARV-72.5 (dotted lines) or VSV-MARV-78.1 (dashed line) escape mutations mapped onto the domain schematic of MARV GP. RBS, receptor binding site; GLC, glycan cap; MUC, mucin-like domain.

(B) Neutralization activity of antibodies from binding group 3B against wild-type VSV/GP-Uganda (circles, straight curves), VSV/GP-72.5 (squares, dotted curves), or VSV/GP-78.1 (triangles, dashed curves) escape mutant viruses.

mucin-like domain), and virus variant VSV/GP-78.1 possessed missense mutation C226Y in the glycan cap (Figure 3A). Consistent with the EM data, six out of seven nAbs tested displayed a higher level of neutralization activity against the wild-type VSV/GP-Uganda than to the VSV/GP-72.5 or VSV/GP-78.1 escape mutant viruses, suggesting these nAbs recognize MARV GP in a similar fashion (Figure 3B). MAb MR198 exhibited equal neutralization potency against wild-type VSV/GP-Uganda or the two escape mutant viruses (Figure 3B). As all nAbs segregated into one competition group (Figure 1D), bound the MARV GP at the NPC1 receptor-binding site (Figures 2A–2D), and displayed a similar profile of neutralization of escape mutant viruses (Figure 3B), we propose that blocking of MARV GP binding to NPC1 is the principal mechanism of MARV neutralization by these naturally occurring human Abs. This model is supported by the data in the accompanying paper by Hashiguchi et al. (2015; this issue of *Cell*) showing that MR78 inhibits binding of NPC1 domain C to MARV GP.

Cross-Reactive Binding of MARV Antibodies with EBOV GP

It is surprising that human MARV nAbs recognize the putative NPC1 protein receptor-binding site on GP, since previous studies suggested that the NPC1 protein receptor-binding site on EBOV GP may be obscured from Ab binding by the presence of the highly glycosylated glycan cap and mucin-like domain

(Lee et al., 2008). To determine whether the MARV nAbs we isolated also could bind in a cross-reactive manner to the EBOV GP receptor-binding site, we performed ELISA using three recombinant forms of MARV and EBOV GPs: full-length GP ectodomain containing the glycan cap and mucin-like domain (designated MARV or EBOV GP), ectodomains lacking residues 257–425 (MARV) or 314–462 (EBOV) of the mucin-like domain (designated MARV or EBOV GP Δ muc), and cleaved GP ectodomains enzymatically treated to remove the mucin-like domain and glycan cap (designated MARV or EBOV GPcl). Three of the MARV nAbs, designated MR78, MR111, and MR191, recognized the EBOV GPcl that lacked

In Vivo Testing

We tested the in vivo protective activity of the mAbs in a murine model using mouse-adapted MARV strain Ci67 (Warfield et al., 2007, 2009). Inoculation of mice with MARV Ci67 causes clinical disease and, in a proportion of animals, causes lethal disease, although typically less than 100% lethality in mice (Warren et al., 2014). We selected four of the mAbs among those with the lowest in vitro neutralization IC_{50} values: MR72, MR82, MR213, and MR232. The IC_{50} values in neutralization assays with MARV Uganda or mouse-adapted MARV strain Ci67 were comparable (within 2-fold). Seven-week-old BALB/c mice were

A Binding ($\mu\text{g/mL}$)

mAb	MARV			EBOV		
	GP	GP Δmuc	GPcl	GP	GP Δmuc	GPcl
MR65	8.3	7.5	5.0	>	>	>
MR72	3.0	4.7	0.8	6.1	2.1	<0.1
MR78	1.4	2.3	1.1	>	>	107.4
MR82	1.0	1.5	0.5	>	>	>
MR103	8.8	14.2	4.8	>	>	>
MR111	2.5	4.3	1.5	>	>	21.5
MR144	8.1	8.0	3.3	>	>	>
MR186	1.3	0.9	0.5	>	>	>
MR191	2.5	5.1	1.4	>	>	<0.1
MR198	1.4	1.4	0.8	>	>	>
MR201	1.5	1.9	0.5	>	>	>
MR208	5.6	7.3	2.8	>	>	>
MR209	4.0	5.4	2.0	>	>	>
MR213	2.8	3.6	1.1	>	>	>
MR229	1.8	2.9	1.2	>	>	>
MR232	2.0	1.3	0.5	>	>	>
MR238	6.8	11.7	4.9	>	>	>
MR241	2.2	4.0	1.2	>	>	>

B Neutralization ($\mu\text{g/mL}$)

mAb	MARV						EBOV	
	VSV/GP-Musoke	VSV/GP-Uganda	MARV-Musoke	MARV-Uganda	MARV-Angola	MARV-Ravn	VSV/GP-EBOV	EBOV
MR65	31.0	224	>	>	214	>	>	>
MR72	3.6	13.4	>	601	>	368	>	>
MR78	3.8	4.5	>	93	>	286	>	>
MR82	1.8	7.4	234	288	184	185	>	>
MR103	16.5	27.5	>	291	>	>	>	>
MR111	12.2	7.9	370	414	>	444	>	>
MR144	43.1	37.3	900	>	>	354	>	>
MR186	1.5	1.5	24	>	97	64	>	>
MR191	5.5	6.2	441	>	413	>	>	>
MR198	2.7	11.6	290	206	128	30	>	>
MR201	6.6	8.0	343	572	358	832	>	>
MR208	13.8	54.9	896	>	>	106	>	>
MR209	4.2	12.2	577	402	>	93	>	>
MR213	7.6	9.7	>	305	207	121	>	>
MR229	5.1	7.3	103	215	110	59	>	>
MR232	3.9	4.0	>	114	103	127	>	>
MR238	11.9	10.2	264	>	416	>	>	>
MR241	2.7	11.9	376	>	162	>	>	>

Figure 4. Breadth of Binding or Neutralization of Human MARV-Specific mAbs for Diverse Filoviruses

(A) A heatmap showing the binding in ELISA of neutralizing mAbs from binding group 3B to the MARV and EBOV GPs. EC_{50} value for each antigen-mAb combination is shown, with dark red shading indicating lower EC_{50} values and orange or yellow shading indicating intermediate or higher EC_{50} values. EC_{50} values greater than 1,000 $\mu\text{g/mL}$ are indicated by >.

(B) A heatmap showing the neutralization breadth of mAbs from binding group 3B. The IC_{50} value for each virus-mAb combination is shown, with dark red shading indicating increased potency and orange or yellow shading indicating intermediate or low potency. IC_{50} values greater than 1,000 $\mu\text{g/mL}$ are indicated by >. Neutralization assays were performed in triplicate.

injected with 100 μg of antibody by the IP route and challenged with 1,000 plaque-forming unit (PFU) of Ci67. Twenty-four hours later, antibody treatment was repeated. By day 6, all five control (untreated) mice developed progressive loss of weight and symptoms of the disease, including dyspnea, recumbency, and unresponsiveness, and on days 8 and 9, two animals were found dead and one animal was found moribund and euthanized. The remaining two animals demonstrated recovery by day 11. In contrast, all animals treated with any antibody survived and did not display the elevation of the disease score, with the exception of two animals treated with MR72, which showed a transient marginal loss of weight and increase of the disease score on days 6–9, which did not exceed 1 (Figure 5). The observed level of protection was remarkable given the relatively modest in-vitro-neutralizing potency of the antibodies.

DISCUSSION

There is an obvious urgent need for prophylactic and therapeutic interventions for filovirus infections given the recurrence of MARV outbreaks, including that in Uganda in October 2014 and a massive outbreak of EBOV infections in West Africa in 2014. There is very little information about the structural determinants of neutralization on which to base the rational selection of antibodies, and for MARV there have been no reported human nAbs.

This study reveals that naturally occurring human MARV nAbs isolated from the B cells of a recovered donor principally target the MARV NPC1 protein receptor-binding site, suggesting that a major mechanism of MARV neutralization could be inhibition of binding to receptor. Remarkably, some of the isolated anti-

bodies also bound to the EBOV GP. This mechanism of MARV neutralization was unexpected, because previous studies with EBOV showed that the putative receptor-binding domain on GP is obscured on the surface of virions by the presence of the glycan cap and mucin-like domain, only becoming exposed following cleavage by cathepsin in the endosome. These studies suggest that the configuration of the MARV GP differs significantly from that of EBOV GP because the receptor-binding domain must be accessible for immune recognition on MARV GP. Indeed, determination of the structure of the MARV GP and structural analysis of the interaction of mAb MR78 with MARV and EBOV GP molecules shows this to be the case (see Hashiguchi et al., 2015).

The information obtained from these studies can be used to inform development of new therapeutics and structure-based vaccine designs against filoviruses. Furthermore, as these nAbs are fully human and exhibit inhibitory activity, they might be useful as a component of a prophylactic or therapeutic approach for filovirus infection and disease. The challenge studies using a murine model here show clear evidence of in vivo activity and suggest additional preclinical studies in other species, such as guinea pigs and macaques, are warranted. Their ability to bind a broad range of MARV isolates indicates they may offer detection of or efficacy against new viral strains yet to emerge. Although some of these mAbs bind to certain forms of EBOV GP, these antibodies are not likely to be effective against natural Ebola infection because the EBOV receptor-binding site is obscured on the viral surface. However, such mAbs might neutralize EBOV if they could be delivered to the endosome, where the EBOV receptor-binding site is exposed following GP cleavage.

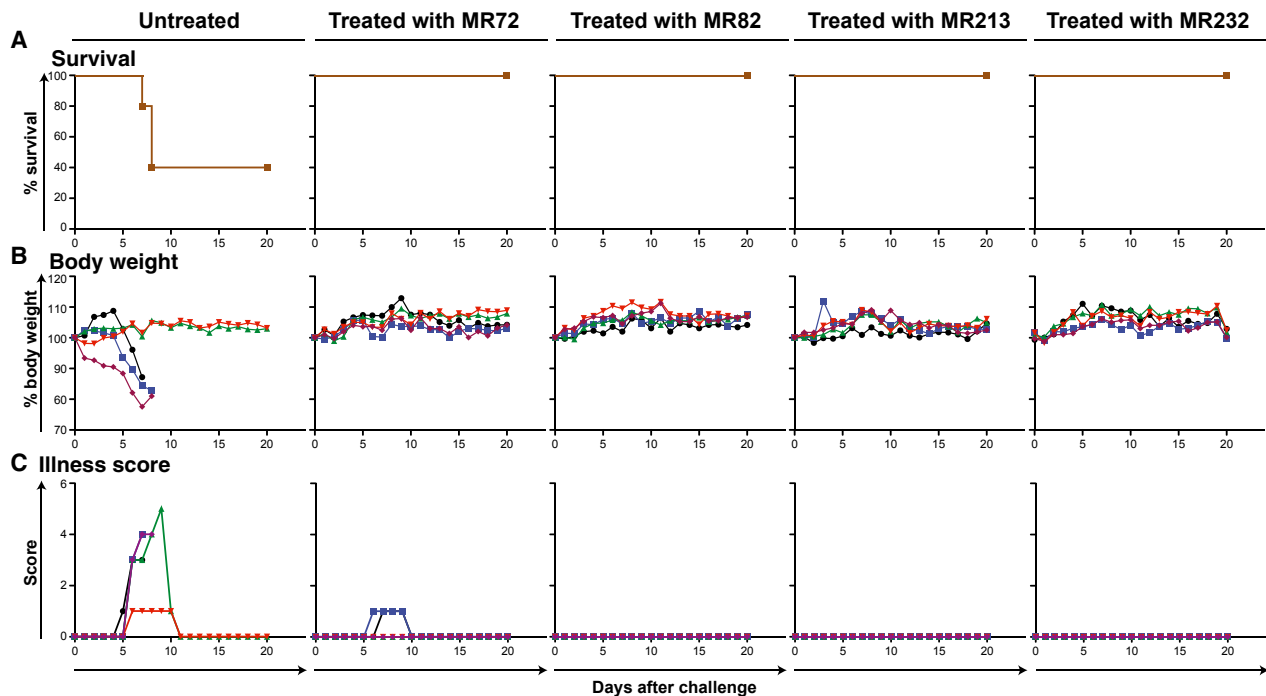


Figure 5. Survival and Clinical Overview of Mice Treated with MARV mAbs

(A–C) Groups of mice at five animals per group were injected with individual mAbs by the intraperitoneal route twice: 1 hr prior and 24 hr after MARV challenge at 100 μ g per treatment. Untreated animals served as controls. (A) Kaplan-Meier survival curves. (B) Body weight. (C) Illness score.

EXPERIMENTAL PROCEDURES

Donor

The donor was an otherwise healthy adult woman who contracted Marburg virus (MARV) infection in 2008 following exposure to fruit bats in the Python Cave in Queen Elizabeth National Park, Uganda. The donor's clinical course was documented previously (CDC, 2009). Peripheral blood from the donor was obtained in 2012, four years after the illness, following informed consent. The study was approved by the Vanderbilt University Institutional Review Board.

Viruses

MARV strain 200702854 Uganda (MARV-Uganda) was isolated originally from a subject designated "patient A" during the outbreak in Uganda in 2007 (CDC, 2009; Townner et al., 2009) and underwent four passages in Vero E6 cells. MARV strain Musoke (MARV-Musoke) was isolated during the outbreak in Kenya in 1980 (Smith et al., 1982) and passaged five times in Vero E6 cells. MARV strain 200501379 Angola (MARV-Angola) was isolated during the outbreak in Angola in 2005 (Townner et al., 2006) and passaged three times in Vero E6 cells. MARV Ravn virus (Ravn) was isolated from a patient in 1987 in Kenya (Johnson et al., 1996) and passaged four times in Vero E6 cells. All strains of MARV were obtained originally from the Special Pathogens Branch, U.S. Centers for Disease Control (CDC), and deposited at the World Reference Center of Emerging Viruses and Arboviruses (WRCEVA) housed at UTMB. The recombinant Ebola Zaire strain Mayinga (EBOV) expressing eGFP was generated in our laboratory by reverse genetics (Lubaki et al., 2013; Townner et al., 2005) from plasmids provided by the Special Pathogens Branch at CDC and passaged three times in Vero E6 cells. For analysis of antibody binding by ELISA, viruses were gamma-irradiated with the dose of 5×10^6 rad. The recombinant VSV in which the VSV/GP protein was replaced with that of MARV strain Musoke (VSV/GP-Musoke) or EBOV strain Mayinga (Garbutt et al., 2004) were provided by Dr. Thomas Geisbert (UTMB) and Dr. Heinz Feldmann (NIH), respectively; a similar virus with GP from MARV (strain

200702854 Uganda) was constructed as described below. All work with EBOV and MARV was performed within the Galveston National Laboratory BSL-4 laboratories.

We used a mouse-adapted strain of MARV for testing the effect of mAbs in vivo. The mouse-adapted Ci67 strain of Marburg virus (Warfield et al., 2007) was provided by Dr. Sina Bavari (U.S. Army Medical Research Institute of Infectious Diseases) and amplified by a single passage in Vero-E6 cells.

Generation of a Chimeric Strain of VSV in which VSV G Protein Was Replaced with the GP Protein of MARV Strain Uganda

The plasmid pVSV-XN2 carrying cDNA of the full-length VSV anti-genome sequence and the support plasmids pBS-N, pBS-L, and pBS-P encoding the internal VSV proteins under control of the T7 promoter were kindly provided by Dr. John Rose (Yale University). The plasmid pC-T7, encoding the T7 polymerase, was kindly provided by Dr. Yoshihiro Kawaoka (University of Wisconsin). For generation of the VSV/GP-Uganda construct, Vero E6 cell monolayers were inoculated with MARV strain 200702854, and total cellular RNA was isolated and reverse transcribed. MARV GP open reading frame (ORF) was PCR amplified from cDNA using forward primer 5'-CATGTACG ACGCGTCAACATGAGGACTA-3' and reverse primer 5'-TCTAGCAGCTC GAGCTATCCAATATATTTAGTAAAGATACGACAA-3' (MluI and XhoI endonuclease sites are underlined, respectively; the start and end of MARV GP ORF direct and complementary sequences are italicized, respectively). To replace VSV G with MARV GP, the resulting PCR product was cloned into pVSV-XN2 using the unique MluI and XhoI endonuclease sites located between the VSV G gene-start and gene-end signals and flanking its ORF, resulting in the plasmid pVSV/GP-Uganda. To recover the recombinant virus, 1×10^6 BSR-T7 cells, kindly provided by Dr. Ursula Buchholz (U.S. National Institute of Allergy and Infectious Diseases), were transfected with the following plasmids: pVSV/GP-Uganda, 5 μ g, pBS-N, 1.5 μ g, pBS-P, 2.5 μ g, pBS-L, 1 μ g, and pC-T7, 5 μ g. After 48 hr, transfected BSR-T7 cells were collected with a cell scraper and transferred, along with the supernates, to Vero E6 cell monolayers for amplification of the recovered VSV/GP-Uganda.

Generation of Human Hybridomas Secreting Monoclonal Antibodies

Peripheral blood mononuclear cells (PBMCs) from the donor were isolated with Ficoll-Histopaque by density gradient centrifugation. The cells were cryopreserved immediately and stored in the vapor phase of liquid nitrogen until use. Previously cryopreserved samples were thawed, and ten million PBMCs were plated into 384-well plates (Nunc #164688) using 17 μ l of cell culture medium (ClonaCell-HY Medium A, StemCell Technologies, #03801), 8 μ g/ml of the TLR agonist CpG (phosphorothioate-modified oligodeoxynucleotide ZOEZOEZZZZZOEZOEZZZT, Invitrogen), 3 μ g/ml of the Chk2 inhibitor (Sigma #C3742), 1 μ g/ml of cyclosporine A (Sigma #C1832), and 4.5 ml of clarified supernate from cultures of B95.8 cells (ATCC VR-1492) containing Epstein-Barr virus (EBV). After 7 days, cells from each 384-well culture plate were expanded into four 96-well culture plates (Falcon #353072) using cell culture medium containing 8 μ g/ml CpG, 3 μ g/ml Chk2i, and ten million irradiated heterologous human PBMCs (Nashville Red Cross) and incubated for an additional 4 days. Plates were screened for MARV antigen-specific antibody-secreting cell lines using ELISAs. Cells from wells with supernates reacting in a MARV antigen ELISA were fused with HMM2.5 myeloma cells using an established electrofusion technique (Yu et al., 2008). After fusion, hybridomas were resuspended in medium containing 100 μ M hypoxanthine, 0.4 μ M aminopterin, 16 μ M thymidine (HAT Media Supplement, Sigma #HO262), and 7 μ g/ml ouabain (Sigma #O3125) and incubated for 18 days before screening hybridomas for antibody production by ELISA.

Human mAb and Fab Production and Purification

After fusion with HMM2.5 myeloma cells, hybridomas producing MARV-specific antibodies were cloned biologically by two rounds of limiting dilution and by single-cell fluorescence-activated cell sorting. After cloning, hybridomas were expanded in post-fusion medium (ClonaCell-HY Medium E, STEMCELL Technologies #03805) until 50% confluent in 75-cm² flasks (Corning #430641). For antibody production, cells from one 75-cm² flask were collected with a cell scraper and expanded to four 225-cm² flasks (Corning #431082) in serum-free medium (Hybridoma-SFM, GIBCO #12045-076). After 21 days, supernates were clarified by centrifugation and sterile filtered using 0.2- μ m pore size filter devices. HiTrap Protein G or HiTrap MabSelectSure columns (GE Healthcare Life Sciences #17040501 and #11003494, respectively) were used to purify antibodies from filtered supernates. Fab fragments were generated by papain digestion (Pierce Fab Preparation Kit, Thermo Scientific #44985) and purified by chromatography using a two-column system in which the first column contained protein G resin (GE Healthcare Life Sciences #29048581) and the second column contained either anti-kappa or anti-lambda antibody light chain resins (GE Healthcare Life Sciences #17545811 and #17548211, respectively).

Expression and Purification of MARV and EBOV GPs

Angola strain MARV GP ectodomains, containing the mucin-like domain (MARV GP) or lacking residues 257–425 of the mucin-like domain (MARV GP Δ muc), were used to screen supernates of transformed B cells and human hybridomas separately. Recombinant proteins for Ravn strain cleaved GP, EBOV Mayinga strain GP, EBOV Mayinga strain GP Δ muc, and EBOV Mayinga strain cleaved GP were designed and expressed similarly. Large-scale production of recombinant GP or GP Δ muc was performed by transfection of *Drosophila* Schneider 2 (S2) cells with modified pMTpuro vectors, followed by stable selection of transfected cells with 6 μ g/ml puromycin. Secreted GP ectodomain expression was induced with 0.5 mM CuSO₄ for 4 days. Proteins were engineered with a modified double strep tag at the C terminus (enterokinase cleavage site followed by a strep tag/linker/strep tag) to facilitate purification using Strep-Tactin resin (QIAGEN #2-1201). Proteins were purified further by Superdex 200 size-exclusion chromatography in 10 mM Tris and 150 mM NaCl (pH 7.5) (1 \times TBS).

Lysates of MARV-Infected Cells

Lysates were prepared as previously described (Ksiazek et al., 1999). Briefly, Vero E6 cell monolayers in 850 cm² roller bottles were inoculated with approximately 10⁶ PFU MARV or EBOV and incubated at 37°C until partial destruction of monolayer occurred (approximately 9–10 days). Cell monolayers were detached using 3-mm glass beads, and cell suspensions were centrifuged at

16,000 \times g for 10 min at 4°C. Supernates were discarded; cell pellets were resuspended in 10 \times excess of borate buffer saline (10 mM Na₂B₄O₇ and 150 mM NaCl [pH 9.0]) and centrifuged at 16,000 \times g for 10 min at 4°C. Supernates were discarded; cell pellets were resuspended in cold 1% Triton X-100 (Fisher Scientific) in borate buffer saline, vortexed, and gamma-irradiated on dry ice at 5 \times 10⁶ rad. The lysates were sonicated with a 600 W Tekmar Sonic Disruptor TM600 (Tekmar) using a cuphorn sonicator at maximum power setting and 50% duty cycle for 10 min and centrifuged at 16,000 \times g, and the supernates were aliquoted.

Screening ELISA

ELISA plates were coated with lysates of MARV-infected cells (diluted 1:1,000 in Dulbecco's PBS [DPBS]) or recombinant MARV GP or MARV GP Δ muc proteins (20 μ g in 10 ml DPBS per plate) and incubated at 4°C overnight. Plates were blocked with 100 μ l of blocking solution/well for 1 hr. Blocking solution consisted of 10 g powdered milk, 10 ml of goat serum, 100 ml of 10 \times DPBS, and 0.5 ml of Tween-20 mixed to a 1 l final volume with distilled water. The presence of antibodies bound to the GP was determined using goat anti-human immunoglobulin G (IgG) horseradish peroxidase-conjugated secondary antibodies (Southern Biotech #2040-05, 1:4,000 dilution) and 1-Step Ultra TMB-ELISA substrate (Thermo Scientific #34029), with optical density read at 450 nm after stopping the reaction with 1M HCl.

Half-Maximal Effective Concentration Binding Analysis

MARV or EBOV GPs, MARV or EBOV GP Δ muc, or Ravn or EBOV cathepsin-cleaved GPs were coated onto 384-well plates (Thermo Scientific Nunc #265203) in DPBS at 2 μ g/ml overnight, then antigen was removed, and plates were blocked with blocking solution made as above. Antibodies were applied to the plates at a concentration range of 1.5 μ g/ml to 270 ng/ml (binding groups #1, #2, and 3A) and 0.1 μ g/ml to 10 ng/ml (binding group #3B) using 3-fold serial dilutions. The presence of antibodies bound to the GP was determined using goat anti-human IgG alkaline phosphatase conjugate (Meridian Life Science #W99008A, 1:4,000 dilution) and p-nitrophenol phosphate substrate tablets (Sigma #S0942), with optical density read at 405 nm after 120 min. A non-linear regression analysis was performed on the resulting curves using Prism (v. 5) (GraphPad) to calculate EC₅₀ values.

MARV and EBOV Neutralization Experiments

Dilutions of mAbs in triplicate were mixed with 150 PFU of MARV or EBOV expressing eGFP in MEM containing 10% fetal bovine serum (FBS) (HyClone) and 50 μ g/ml gentamicin (Cellgro #30-005-CR) with or without 5% guinea pig complement (MP Biomedicals #642836) in a total volume of 0.1 ml and incubated for 1 hr at 37°C for virus neutralization. Following neutralization, virus-antibody mixtures were placed on monolayers of Vero E6 cells in 24-well plates, incubated for 1 hr at 37°C for virus adsorption, and overlaid with MEM containing 2% FBS and 0.8% methylcellulose (Sigma-Aldrich #M0512). After incubation for 5 days, medium was removed, cells were fixed with 10% formalin (Fisher Scientific #245-684), and plates were sealed in plastic bags and incubated for 24 hr at room temperature. Sealed plates were taken out of the BSL-4 laboratory according to approved SOPs, and monolayers were washed three times with PBS. Viral plaques were immunostained with the serum of rabbits that had been hyperimmunized with MARV, or with a mAb against EBOV, clone 15H10 (BEI Resources #NR-12184). Alternatively, following virus adsorption, monolayers were covered with MEM containing 10% FBS and 1.6% tragacanth (Sigma-Aldrich #G1128). After incubation for 14 days, medium was removed, cells were fixed with 10% formalin, and plates were sealed in plastic bags, incubated for 24 hr at room temperature, and taken out of the BSL-4 laboratory as above. Fixed monolayers were stained with 10% formalin containing 0.25% crystal violet (Fisher Scientific #C581-100), and plaques were counted.

VSV-MARV and VSV-EBOV Neutralization Tests

Neutralization assays were performed in triplicate, as described above for MARV and EBOV. Following neutralization, virus-antibody mixtures were placed on monolayers of Vero E6 cells in duplicate, incubated for 1 hr at 37°C for virus adsorption, and overlaid with MEM containing 2% FBS containing 0.9% methylcellulose. After incubation for 3 days, medium was

removed, monolayers were fixed and stained with 10% formalin containing 0.25% crystal violet, and plaques were counted.

Generation and Sequencing of VSV/GP-Uganda Escape Mutants

Vero E6 cell monolayers with 2-fold dilutions of mAbs (12.5–200 $\mu\text{g/ml}$) added to the medium were inoculated with 200 PFU of recombinant VSV/GP-Uganda and incubated at 37°C for 2–4 days. To determine which samples contained live virus, supernates were collected, virus was titrated in Vero E6 cell monolayers under methylcellulose overlay, monolayers were incubated at 37°C for 3–4 days, and plaques were counted. Supernates with the highest concentrations of mAbs, which were found to contain live virus by plaque titration, were incubated in presence of serially diluted mAbs, followed by titration of virus as above. The procedure was performed a total of three times. Escape mutant viruses harvested after the third passage were cloned biologically by plaque purification. For biological cloning, Vero E6 cell monolayers in 24-well plates were inoculated with dilutions of the escape mutant viruses in the presence of the corresponding mAbs (200 $\mu\text{g/ml}$ of MR72 or 100 $\mu\text{g/ml}$ of MR78) and covered with 0.7% low melting temperature SeaPlaque agarose (Lonza #50100). Monolayers were incubated at 37°C for 6 days; plaques were visualized with 0.01% neutral red aqueous solution (Electron Microscopy Sciences), picked, resuspended in medium, and transferred to Vero E6 cell monolayers in 24-well plates in the presence of the corresponding mAbs (200 $\mu\text{g/ml}$ of MR72 or 100 $\mu\text{g/ml}$ of MR78) for virus propagation. In 2–5 days, based on the extent of CPE observed, virus was harvested, and cells were dissolved in Trizol reagent (Life Technologies 315596018). Total cellular RNA was extracted, reverse transcribed, and amplified by PCR with the primers described above for generation of a chimeric strain of VSV. Two overlapping fragments covering MARV GP ORF were PCR amplified from cDNA using forward primer 5'-CATGTACGACGCGTCAACATGAGGACTA-3' and reverse primer 5'-ACTAAGCCCTGCTGCCAGGT-3' or forward primer 5'-ACAACAATGTACCGAGGCAA-3' and reverse primer 5'-TCTAGCAGCTCGAGCTATCCAATATATTAGTAAAGATACGACAA-3', and the nucleotide sequences of the GP ORFs were determined using standard procedures.

Analysis of Growth Kinetics of VSV/GP-Uganda Escape Mutant Viruses

Vero E6 cell monolayers in 24-well plates were inoculated in triplicate with VSV/GP-Uganda escape mutants or non-mutated virus at an MOI of 0.0025 PFU/cell in the presence of varying concentrations of the corresponding mAbs. Aliquots of medium were collected every 12 hr and frozen for titration at a later time. Titration of virus in aliquots was performed as above, without adding antibodies to the culture medium.

Biolayer Interferometry Competition Binding Assay

Biotinylated GP or GP Δ muc (EZ-link Micro NHS-PEG₄-Biotinylation Kit, Thermo Scientific #21955) (1 $\mu\text{g/ml}$) was immobilized onto streptavidin-coated biosensor tips (ForteBio #18-5019) for 2 min. After measuring the baseline signal in kinetics buffer (KB; 1× PBS, 0.01% BSA, and 0.002% Tween 20) for 2 min, biosensor tips were immersed into the wells containing primary antibody at a concentration of 100 $\mu\text{g/ml}$ for 10 min. Biosensors then were immersed into wells containing competing mAbs at a concentration of 100 $\mu\text{g/ml}$ for 5 min. The percent binding of the competing mAb in the presence of the first mAb was determined by comparing the maximal signal of competing mAb applied after the first mAb complex to the maximal signal of competing mAb alone. MABs were judged to compete for binding to the same site if maximum binding of the competing mAb was reduced to <30% of its un-competed binding. MABs were considered non-competing if maximum binding of the competing mAb was >70% of its un-competed binding. A level of 30%–70% of its un-competed binding was considered intermediate competition.

Sequence Analysis of Antibody Variable Region Genes

Total cellular RNA was extracted from clonal hybridomas that produced MARV antibodies, and RT-PCR reaction was performed using mixtures of primers designed to amplify all heavy-chain or light-chain antibody variable regions. The generated PCR products were purified and cloned into the pJET 1.2 plasmid vector (Thermo Scientific, #K1231) for sequence analysis. The nucleotide se-

quences of plasmid DNAs were determined using an ABI3700 automated DNA sequencer. Heavy-chain or light-chain antibody variable region sequences were analyzed using the IMGT/V-Quest program (Brochet et al., 2008; Giudicelli et al., 2011). The analysis involved the identification of germline genes that were used for antibody production, location of complementary determining regions (CDRs), and framework regions (FRs), as well as the number and location of somatic mutations that occurred during affinity maturation.

Statistical Analysis

EC₅₀ values for neutralization were determined by finding the concentration of mAb at which a 50% reduction in plaque counts occurred after incubation of virus with neutralizing antibody. A logistic curve was fit to the data using the count as the outcome and the log-concentration as the predictor variable. The results of the model then were transformed back to the concentration scale. Results are presented as the concentration at the dilution that achieves a 50% reduction from challenge control with accompanying 95% confidence intervals. Each antibody was treated as a distinct analysis in a Bayesian non-linear regression model.

Sample Preparation for EM Studies

A Ravn strain MARV GP mucin-deleted construct (GP Δ muc) was produced by stable cell line expression in *Drosophila* S2 cells, as described above. Human Fab proteins for MARV-specific antibodies were generated as described above. Fabs were added in molar excess to GP Δ muc and allowed to incubate overnight at 4°C. Complexes then were purified by Superdex 200 size-exclusion chromatography in TBS.

Electron Microscopy and Sample Preparation

A 4 μl aliquot of each complex that had been diluted to a concentration of ~ 0.03 $\mu\text{g/ml}$ with TBS buffer was placed for 15 s onto carbon-coated 400 Cu mesh grids that had been plasma cleaned for 20 s (Gatan), blotted off on the edge of the grid, and then immediately stained for 30 s with 4 μl of 2% uranyl formate. The stain was blotted off on the edge of the grid, and the grid was allowed to dry. Data were automatically collected with Legion (Carragher et al., 2000; Potter et al., 1999; Suloway et al., 2005) using a FEI Tecnai F20 electron microscope operating at 120 keV with an electron dose of 30 e⁻/Å² and a magnification of 52,000× that resulted in a pixel size of 2.65 Å at the specimen plane when collected with Tietz CMOS 4k × 4k CCD camera. Particle orientations appeared to be generally isotropic, and images were acquired at a constant defocus value of -1.0 μm at 0° stage tilt.

Image Processing of Protein Complexes

Particles were picked automatically using DoG Picker (34) and placed into a particle stack using the Appion software (Lander et al., 2009). Reference-free 2D class averages were generated with the Xmipp clustering 2D alignment software (van Heel et al., 1996) and sorted into an initial 300 classes. Non-GP particles were removed, and the stack was further subclassified into classes with ~ 100 particles per class in order to generate the final particle stack used for the reconstruction. Various numbers of class averages were chosen to create initial models using EMAN2 common lines software (Tang et al., 2007). A model that best matched its projected classes was then used for refinement against the raw particle stack, imposing C3 symmetry, and the reconstruction was generated with ten rounds of refinement and increasingly smaller angular sampling rates with EMAN2 (Tang et al., 2007). All model fitting and manipulation was completed using UCSF Chimera (Pettersen et al., 2004).

In Vivo Testing

The animal protocol for testing of mAbs in mice was approved by the Institutional Animal Care and Use Committee of the University of Texas Medical Branch at Galveston. Seven-week-old BALB/c mice (Harlan) were placed in the ABSL-4 facility of the Galveston National Laboratory. Groups of mice at five animals per group were injected with individual mAbs by the intraperitoneal route twice: 1 hr prior and 24 hr after MARV challenge, using 100 μg per treatment. Untreated animals served as controls. For the challenge, mice were injected with 1,000 PFU of the mouse-adapted MARV strain Ci67 by the intraperitoneal route. Animals were weighed and monitored daily over the 3-week period after challenge. Once animals were symptomatic, they

were examined twice per day. The disease was scored using the following parameters: dyspnea (possible scores 0–5), recumbency (0–9), unresponsiveness (0–5), and bleeding/hemorrhage (0–5); the individual scores for each animal were summarized.

ACCESSION NUMBERS

EM reconstructions have been deposited in the Electron Microscopy Data Bank under the accession codes EMD-6232 through 6238.

SUPPLEMENTAL INFORMATION

Supplemental Information includes five figures and can be found with this article online at <http://dx.doi.org/10.1016/j.cell.2015.01.031>.

AUTHOR CONTRIBUTIONS

A.I.F., P.A.I., and C.D.M. planned, performed, and analyzed experiments and wrote the paper. T.G., X.S., C.K., M.L.F., T.H., Z.A.B., and G.S. performed and analyzed experiments. J.C.S. performed statistical analysis. T.G.K. and A.B.W. planned and analyzed experiments. E.O.S., A.B., and J.E.C. planned and analyzed experiments and wrote the paper.

ACKNOWLEDGMENTS

This project received support from the Defense Threat Reduction Agency (HDTRA1-13-1-0034) (to J.E.C.) and the U.S. NIH (1U19AI109711 to J.E.C. and A.B.; U19AI109762 to E.O.S. and A.B.W.; R01AI089498 and U01AI082156 to E.O.S.). E.O.S. is an Investigator in the Pathogenesis of Infectious Disease of the Burroughs Wellcome Fund. The project was supported by the NCRR (UL1 RR024975-01) and is now at the National Center for Advancing Translational Sciences (UL1 TR000445-06). T.H. received support from MEXT and JSPS Postdoctoral Fellowships for Research Abroad and a Research Fellowship of The Uehara Memorial Foundation. The content of this paper is solely the responsibility of the authors and does not necessarily represent the official views of the NIH. We thank Dr. Eugene Agapov (Washington University in St. Louis) for useful suggestions concerning the generation of VSV/GP-Uganda escape mutants. We thank the donor, Dr. Norman Fujit (Wheat Ridge, Colorado), and the Vanderbilt Clinical Trials Center for help in sample acquisition. We thank Frances Smith-House, Gloria Fritz, Vidisha Singh, and Leland Brown for excellent technical support and Dr. Scott A. Smith for thoughtful comments and discussions. Flow cytometry experiments were performed in the VMC Flow Cytometry Shared Resource and supported by NIH grants (P30 CA68485 and DK058404). The EM work was conducted at the National Resource for Automated Molecular Microscopy at The Scripps Research Institute, which is supported by the Biomedical Technology Research Center program (GM103310) of the National Institute of General Medical Sciences.

Received: October 18, 2014

Revised: January 9, 2015

Accepted: January 14, 2015

Published: February 26, 2015

REFERENCES

Beniac, D.R., Melito, P.L., Devarenes, S.L., Hiebert, S.L., Rabb, M.J., Lamboo, L.L., Jones, S.M., and Booth, T.F. (2012). The organisation of Ebola virus reveals a capacity for extensive, modular polyploidy. *PLoS ONE* 7, e29608.

Brauburger, K., Hume, A.J., Mühlberger, E., and Olejnik, J. (2012). Forty-five years of Marburg virus research. *Viruses* 4, 1878–1927.

Brochet, X., Lefranc, M.P., and Giudicelli, V. (2008). IMGT/V-QUEST: the highly customized and integrated system for IG and TR standardized V-J and V-D-J sequence analysis. *Nucleic Acids Res.* 36, W503–W508.

Carette, J.E., Raaben, M., Wong, A.C., Herbert, A.S., Obernosterer, G., Mulherkar, N., Kuehne, A.I., Kranzusch, P.J., Griffin, A.M., Ruthel, G., et al.

(2011). Ebola virus entry requires the cholesterol transporter Niemann-Pick C1. *Nature* 477, 340–343.

Carragher, B., Kisseberth, N., Kriegman, D., Milligan, R.A., Potter, C.S., Pulkas, J., and Reilein, A. (2000). Leginon: an automated system for acquisition of images from vitreous ice specimens. *J. Struct. Biol.* 132, 33–45.

Centers for Disease Control and Prevention (CDC) (2009). Imported case of Marburg hemorrhagic fever - Colorado, 2008. *MMWR Morb. Mortal. Wkly. Rep.* 58, 1377–1381.

Chandran, K., Sullivan, N.J., Felbor, U., Whelan, S.P., and Cunningham, J.M. (2005). Endosomal proteolysis of the Ebola virus glycoprotein is necessary for infection. *Science* 308, 1643–1645.

Cook, J.D., and Lee, J.E. (2013). The secret life of viral entry glycoproteins: moonlighting in immune evasion. *PLoS Pathog.* 9, e1003258.

Côté, M., Misasi, J., Ren, T., Bruchez, A., Lee, K., Filone, C.M., Hensley, L., Li, Q., Ory, D., Chandran, K., and Cunningham, J. (2011). Small molecule inhibitors reveal Niemann-Pick C1 is essential for Ebola virus infection. *Nature* 477, 344–348.

Dias, J.M., Kuehne, A.I., Abelson, D.M., Bale, S., Wong, A.C., Halfmann, P., Muhammad, M.A., Fusco, M.L., Zak, S.E., Kang, E., et al. (2011). A shared structural solution for neutralizing ebolaviruses. *Nat. Struct. Mol. Biol.* 18, 1424–1427.

Dube, D., Brecher, M.B., Delos, S.E., Rose, S.C., Park, E.W., Schornberg, K.L., Kuhn, J.H., and White, J.M. (2009). The primed ebolavirus glycoprotein (19-kilodalton GP1,2): sequence and residues critical for host cell binding. *J. Virol.* 83, 2883–2891.

Dye, J.M., Herbert, A.S., Kuehne, A.I., Barth, J.F., Muhammad, M.A., Zak, S.E., Ortiz, R.A., Prugar, L.I., and Pratt, W.D. (2012). Postexposure antibody prophylaxis protects nonhuman primates from filovirus disease. *Proc. Natl. Acad. Sci. USA* 109, 5034–5039.

Garbutt, M., Liebscher, R., Wahl-Jensen, V., Jones, S., Möller, P., Wagner, R., Volchkov, V., Klenk, H.D., Feldmann, H., and Ströher, U. (2004). Properties of replication-competent vesicular stomatitis virus vectors expressing glycoproteins of filoviruses and arenaviruses. *J. Virol.* 78, 5458–5465.

Giudicelli, V., Brochet, X., and Lefranc, M.P. (2011). IMGT/V-QUEST: IMGT standardized analysis of the immunoglobulin (IG) and T cell receptor (TR) nucleotide sequences. *Cold Spring Harb Protoc* 2011, 695–715.

Hashiguchi, T., Fusco, M.L., Bornholdt, Z.A., Lee, J.E., Flyak, A.I., Matsuoka, R., Kohda, D., Yanagi, Y., Hammel, M., Crowe, J.E., Jr., and Saphire, E.O. (2015). Structural basis for Marburg virus neutralization by a cross-reactive human antibody. *Cell* 160, this issue, 904–912.

Johnson, E.D., Johnson, B.K., Silverstein, D., Tukei, P., Geisbert, T.W., Sanchez, A.N., and Jahrling, P.B. (1996). Characterization of a new Marburg virus isolated from a 1987 fatal case in Kenya. *Arch. Virol. Suppl.* 11, 101–114.

Kajihara, M., Marzi, A., Nakayama, E., Noda, T., Kuroda, M., Manzoor, R., Matsuno, K., Feldmann, H., Yoshida, R., Kawaoka, Y., and Takada, A. (2012). Inhibition of Marburg virus budding by nonneutralizing antibodies to the envelope glycoprotein. *J. Virol.* 86, 13467–13474.

Ksiazek, T.G., West, C.P., Rollin, P.E., Jahrling, P.B., and Peters, C.J. (1999). ELISA for the detection of antibodies to Ebola viruses. *J. Infect. Dis.* 179 (Suppl 1), S192–S198.

Lander, G.C., Stagg, S.M., Voss, N.R., Cheng, A., Fellmann, D., Pulkas, J., Yoshioka, C., Irving, C., Mulder, A., Lau, P.W., et al. (2009). Appion: an integrated, database-driven pipeline to facilitate EM image processing. *J. Struct. Biol.* 166, 95–102.

Lee, J.E., Fusco, M.L., Hessel, A.J., Oswald, W.B., Burton, D.R., and Saphire, E.O. (2008). Structure of the Ebola virus glycoprotein bound to an antibody from a human survivor. *Nature* 454, 177–182.

Lubaki, N.M., Ilinykh, P., Pietzsch, C., Tigabu, B., Freiberg, A.N., Koup, R.A., and Bukreyev, A. (2013). The lack of maturation of Ebola virus-infected dendritic cells results from the cooperative effect of at least two viral domains. *J. Virol.* 87, 7471–7485.

Maruyama, T., Rodriguez, L.L., Jahrling, P.B., Sanchez, A., Khan, A.S., Nichol, S.T., Peters, C.J., Parren, P.W., and Burton, D.R. (1999). Ebola virus can be

effectively neutralized by antibody produced in natural human infection. *J. Virol.* 73, 6024–6030.

Marzi, A., Yoshida, R., Miyamoto, H., Ishijima, M., Suzuki, Y., Higuchi, M., Matsuyama, Y., Igarashi, M., Nakayama, E., Kuroda, M., et al. (2012). Protective efficacy of neutralizing monoclonal antibodies in a nonhuman primate model of Ebola hemorrhagic fever. *PLoS ONE* 7, e36192.

Murin, C.D., Fusco, M.L., Bornholdt, Z.A., Qiu, X., Olinger, G.G., Zeitlin, L., Kobinger, G.P., Ward, A.B., and Saphire, E.O. (2014). Structures of protective antibodies reveal sites of vulnerability on Ebola virus. *Proc. Natl. Acad. Sci. USA* 111, 17182–17187.

Nanbo, A., Imai, M., Watanabe, S., Noda, T., Takahashi, K., Neumann, G., Halfmann, P., and Kawaoka, Y. (2010). Ebolavirus is internalized into host cells via macropinocytosis in a viral glycoprotein-dependent manner. *PLoS Pathog.* 6, e1001121.

Olinger, G.G., Jr., Pettitt, J., Kim, D., Working, C., Bohorov, O., Bratcher, B., Hiatt, E., Hume, S.D., Johnson, A.K., Morton, J., et al. (2012). Delayed treatment of Ebola virus infection with plant-derived monoclonal antibodies provides protection in rhesus macaques. *Proc. Natl. Acad. Sci. USA* 109, 18030–18035.

Pettersen, E.F., Goddard, T.D., Huang, C.C., Couch, G.S., Greenblatt, D.M., Meng, E.C., and Ferrin, T.E. (2004). UCSF Chimera—a visualization system for exploratory research and analysis. *J. Comput. Chem.* 25, 1605–1612.

Pettitt, J., Zeitlin, L., Kim, D.H., Working, C., Johnson, J.C., Bohorov, O., Bratcher, B., Hiatt, E., Hume, S.D., Johnson, A.K., et al. (2013). Therapeutic intervention of Ebola virus infection in rhesus macaques with the MB-003 monoclonal antibody cocktail. *Sci. Transl. Med* 5, 199ra113.

Potter, C.S., Chu, H., Frey, B., Green, C., Kisseberth, N., Madden, T.J., Miller, K.L., Nahrstedt, K., Pulokas, J., Reilein, A., et al. (1999). Legimon: a system for fully automated acquisition of 1000 electron micrographs a day. *Ultramicroscopy* 77, 153–161.

Qiu, X., Audet, J., Wong, G., Pillet, S., Bello, A., Cabral, T., Strong, J.E., Plummer, F., Corbett, C.R., Alimonti, J.B., et al. (2012). Successful treatment of Ebola virus-infected cynomolgus macaques with monoclonal antibodies. *Sci. Trans. Med* 4, 138ra181–138ra181.

Qiu, X., Wong, G., Audet, J., Bello, A., Fernando, L., Alimonti, J.B., Fausther-Bovendo, H., Wei, H., Aviles, J., Hiatt, E., et al. (2014). Reversion of advanced Ebola virus disease in nonhuman primates with ZMapp. *Nature* 514, 47–53.

Saeed, M.F., Kolokoltsov, A.A., Albrecht, T., and Davey, R.A. (2010). Cellular entry of ebola virus involves uptake by a macropinocytosis-like mechanism and subsequent trafficking through early and late endosomes. *PLoS Pathog.* 6, e1001110.

Saphire, E.O. (2013). An update on the use of antibodies against the filoviruses. *Immunotherapy* 5, 1221–1233.

Smith, D.H., Johnson, B.K., Isaacson, M., Swanapoel, R., Johnson, K.M., Killey, M., Bagshawe, A., Siongok, T., and Keruga, W.K. (1982). Marburg-virus disease in Kenya. *Lancet* 1, 816–820.

Suloway, C., Pulokas, J., Fellmann, D., Cheng, A., Guerra, F., Quispe, J., Stagg, S., Potter, C.S., and Carragher, B. (2005). Automated molecular microscopy: the new Legimon system. *J. Struct. Biol.* 151, 41–60.

Tang, G., Peng, L., Baldwin, P.R., Mann, D.S., Jiang, W., Rees, I., and Ludtke, S.J. (2007). EMAN2: an extensible image processing suite for electron microscopy. *J. Struct. Biol.* 157, 38–46.

Thomas, D., Newcomb, W.W., Brown, J.C., Wall, J.S., Hainfeld, J.F., Trus, B.L., and Steven, A.C. (1985). Mass and molecular composition of vesicular stomatitis virus: a scanning transmission electron microscopy analysis. *J. Virol.* 54, 598–607.

Towner, J.S., Paragas, J., Dover, J.E., Gupta, M., Goldsmith, C.S., Huggins, J.W., and Nichol, S.T. (2005). Generation of eGFP expressing recombinant Zaire ebolavirus for analysis of early pathogenesis events and high-throughput antiviral drug screening. *Virology* 332, 20–27.

Towner, J.S., Khristova, M.L., Sealy, T.K., Vincent, M.J., Erickson, B.R., Bawiec, D.A., Hartman, A.L., Comer, J.A., Zaki, S.R., Ströher, U., et al. (2006). Marburgvirus genomics and association with a large hemorrhagic fever outbreak in Angola. *J. Virol.* 80, 6497–6516.

Towner, J.S., Amman, B.R., Sealy, T.K., Carroll, S.A.R., Comer, J.A., Kemp, A., Swanepoel, R., Paddock, C.D., Balinandi, S., Khristova, M.L., et al. (2009). Isolation of genetically diverse Marburg viruses from Egyptian fruit bats. *PLoS Pathog.* 5, e1000536.

van Heel, M., Harauz, G., Orlova, E.V., Schmidt, R., and Schatz, M. (1996). A new generation of the IMAGIC image processing system. *J. Struct. Biol.* 116, 17–24.

Warfield, K.L., Alves, D.A., Bradfute, S.B., Reed, D.K., VanTongeren, S., Kalina, W.V., Olinger, G.G., and Bavari, S. (2007). Development of a model for marburgvirus based on severe-combined immunodeficiency mice. *Virol. J.* 4, 108.

Warfield, K.L., Bradfute, S.B., Wells, J., Lofts, L., Cooper, M.T., Alves, D.A., Reed, D.K., VanTongeren, S.A., Mech, C.A., and Bavari, S. (2009). Development and characterization of a mouse model for Marburg hemorrhagic fever. *J. Virol.* 83, 6404–6415.

Warren, T.K., Wells, J., Panchal, R.G., Stuthman, K.S., Garza, N.L., Van Tongeren, S.A., Dong, L., Retterer, C.J., Eaton, B.P., Pegoraro, G., et al. (2014). Protection against filovirus diseases by a novel broad-spectrum nucleoside analogue BCX4430. *Nature* 508, 402–405.

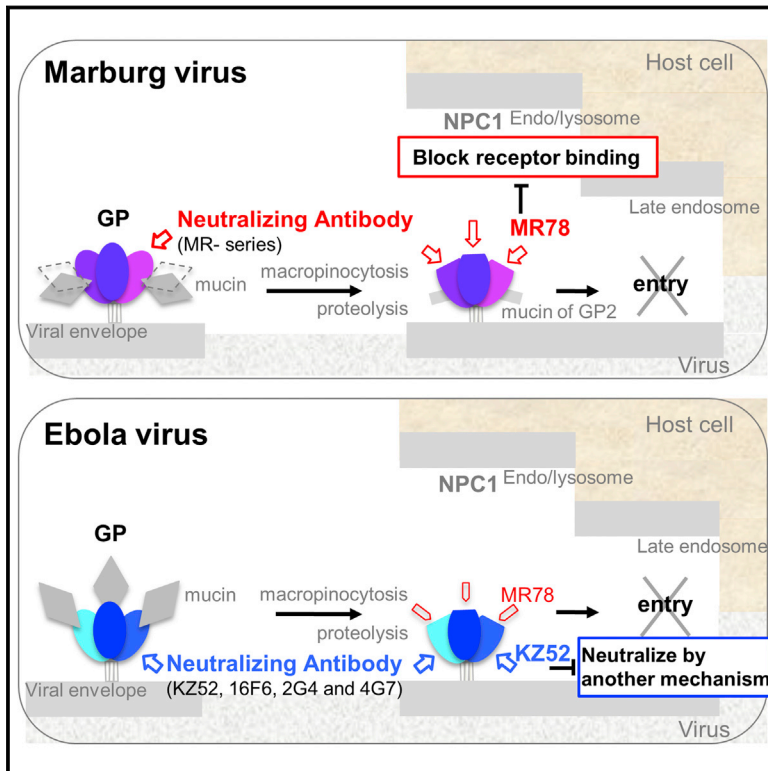
World Health Organization (2014a). Ebola situation report. W.H.O. Global Alert and Response. January 2015. <http://www.who.int/csr/disease/ebola/situation-reports/en/?m=20150121>.

World Health Organization (2014b). Marburg virus disease - Uganda. W.H.O. Global Alert and Response. October 2014. <http://www.who.int/csr/don/10-october-2014-marburg/en/>.

Yu, X., McGraw, P.A., House, F.S., and Crowe, J.E., Jr. (2008). An optimized electrofusion-based protocol for generating virus-specific human monoclonal antibodies. *J. Immunol. Methods* 336, 142–151.

Structural Basis for Marburg Virus Neutralization by a Cross-Reactive Human Antibody

Graphical Abstract



Authors

Takao Hashiguchi, Marnie L. Fusco, ..., James E. Crowe, Jr., Erica Ollmann Saphire

Correspondence

erica@scripps.edu

In Brief

The structures of Marburg virus glycoprotein in complex with a cross-reactive human antibody, as well as of the Ebola virus glycoprotein bound to the same antibody, reveal that there is a conserved epitope among filoviruses that overlaps with the putative receptor-binding site. These studies provide a map by which therapy with cross-reactive antibodies and inhibitors of entry could be developed.

Highlights

- Structure of the Marburg virus GP bound by MR78, a cross-reactive human antibody
- The epitope is conserved among filoviruses and is the likely receptor-binding site
- The antibody-GP interaction mimics that made by the Ebola virus glycan cap
- Mucin domain structure may cause mAbs to react to Ebola and Marburg differently

Accession Numbers

3X2D



Structural Basis for Marburg Virus Neutralization by a Cross-Reactive Human Antibody

Takao Hashiguchi,^{1,2} Marnie L. Fusco,¹ Zachary A. Bornholdt,¹ Jeffrey E. Lee,^{1,3} Andrew I. Flyak,⁴ Rei Matsuoka,⁵ Daisuke Kohda,⁵ Yusuke Yanagi,² Michal Hammel,⁶ James E. Crowe, Jr.,^{4,7} and Erica Ollmann Saphire^{1,8,*}

¹Department of Immunology and Microbial Science, The Scripps Research Institute, La Jolla, CA 92037, USA

²Department of Virology, Faculty of Medicine, Kyushu University, Fukuoka, 812-8582, Japan

³Current address: Department of Laboratory Medicine and Pathobiology, University of Toronto, Toronto, ON M5S 1A1, Canada

⁴Department of Pathology, Microbiology, and Immunology, Vanderbilt University, Nashville, TN 37232, USA

⁵Division of Structural Biology, Medical Institute of Bioregulation, Kyushu University, Fukuoka, 812-8582, Japan

⁶Life Sciences Division, Lawrence Berkeley National Laboratory, Berkeley, CA 94720 USA

⁷Vanderbilt Vaccine Center, Vanderbilt University, Nashville, TN 37232, USA

⁸The Skaggs Institute for Chemical Biology, The Scripps Research Institute, La Jolla, CA 92037, USA

*Correspondence: erica@scripps.edu

<http://dx.doi.org/10.1016/j.cell.2015.01.041>

SUMMARY

The filoviruses, including Marburg and Ebola, express a single glycoprotein on their surface, termed GP, which is responsible for attachment and entry of target cells. Filovirus GPs differ by up to 70% in protein sequence, and no antibodies are yet described that cross-react among them. Here, we present the 3.6 Å crystal structure of Marburg virus GP in complex with a cross-reactive antibody from a human survivor, and a lower resolution structure of the antibody bound to Ebola virus GP. The antibody, MR78, recognizes a GP1 epitope conserved across the filovirus family, which likely represents the binding site of their NPC1 receptor. Indeed, MR78 blocks binding of the essential NPC1 domain C. These structures and additional small-angle X-ray scattering of mucin-containing MARV and EBOV GPs suggest why such antibodies were not previously elicited in studies of Ebola virus, and provide critical templates for development of immunotherapeutics and inhibitors of entry.

INTRODUCTION

The filovirus family includes Marburg virus and five ebolaviruses (Ebola, Sudan, Reston, Bundibugyo, and Tai Forest viruses), most of which cause highly lethal hemorrhagic fever and multiple outbreaks among humans. Among the filoviruses, Marburg virus was the first to be identified when it sickened laboratory workers in Europe in 1967 (Malherbe and Strickland-Cholmley, 1968; Siebert et al., 1968). Marburg virus has since re-emerged multiple times, with modern strains conferring greater lethality (~90%) (Geisbert et al., 2007; Towner et al., 2006). Sudan virus has caused at least six outbreaks between 1976 and 2013 (Albariño et al., 2013; Bowen et al., 1977; Sanchez and Rollin, 2005; Shoemaker et al., 2012), Bundibugyo virus emerged in 2007 (Towner

et al., 2008; Wamala et al., 2010) and again in 2012 (Albariño et al., 2013), and Reston virus was found to infect ranches of swine being raised for human consumption in Asia in 2009 and 2011 (Barrette et al., 2009; Pan et al., 2014; Sayama et al., 2012). Ebola virus is typically found in Central Africa, but re-emerged in Western Africa in 2014 to cause an outbreak unprecedented in magnitude and geographic spread (WHO Ebola Response Team, 2014). During this outbreak, an experimental Ebola virus-specific monoclonal antibody (mAb) cocktail (Qiu et al., 2014) was used compassionately in several patients. No such treatment yet exists that could be used against Marburg virus or the other four ebolaviruses.

Filoviruses express a single protein on their envelope surface, a glycoprotein termed GP, which is responsible for attachment to, and entry of, host cells (Sanchez et al., 1996). GP forms a trimer on the viral surface. In the trimer, each monomer is comprised of GP1 and GP2 subunits that are anchored together by a GP1-GP2 disulfide bond (Volchkov et al., 1998). GP1 contains a receptor-binding core topped by a glycan cap and a heavily glycosylated mucin-like domain (Lee et al., 2008), while GP2 contains two heptad repeats and a transmembrane domain. Filoviruses initially enter cells via macropinocytosis (Aleksandrowicz et al., 2011; Nanbo et al., 2010; Saeed et al., 2010; Mulherkar et al., 2011). Once in the endosome, the viral surface GP is cleaved by host cathepsins. Cleavage removes the mucin-like domains and glycan cap (Chandran et al., 2005; Schornberg et al., 2006; Hood et al., 2010; Marzi et al., 2012a; Brecher et al., 2012) and renders GP competent to bind the Niemann Pick C1 (NPC1) receptor (Carette et al., 2011; Côté et al., 2011). Interestingly, Ebola virus entry requires cleavage by cathepsin B (Chandran et al., 2005; Martinez et al., 2010; Schornberg et al., 2006), while Marburg virus entry is independent of cathepsin B (Gnirss et al., 2012; Misasi et al., 2012). The reasons underlying these differences are unknown. After enzymatic cleavage and receptor binding, the GP2 subunit unwinds from its GP1 clamp and rearranges irreversibly into a six-helix bundle (Malashkevich et al., 1999; Weissenhorn et al., 1998a; Weissenhorn et al., 1998b) to drive fusion of virus and host membranes.

Antibody therapies recently have demonstrated effective post-exposure protection against filoviruses in animal models (Dye et al., 2012; Marzi et al., 2012b; Olinger et al., 2012; Pettitt et al., 2013; Qiu et al., 2012; Qiu et al., 2014). MAbs can be produced on large scale and offer more reproducible effects than polyclonal sera from survivors. However, most mAbs available only recognize Ebola virus. Very few are yet described against Marburg virus, and no antibodies are yet described that cross-react among the filoviruses. Indeed, Marburg and Ebola GP are 72% different in protein sequence, and the filoviruses are thought to be antigenically distinct. Further, there is no structure available for the unique Marburg virus GP, by which we may interpret differences in requirements for viral entry, or develop immunotherapeutics or inhibitors of entry.

Here, we report the crystal structure of the trimeric, receptor-competent form of Marburg virus GP in complex with a neutralizing antibody, termed MR78, that was identified in a recent human survivor of Marburg virus infection (Flyak et al., 2015). Atypically, MR78 cross-reacts to cleaved Ebola virus GP. An additional structure of MR78 in complex with Ebola virus GP illustrates the basis of the cross-reactivity: the antibody binds a hydrophobic “trough” at the top of GP1, the sequence and structure of which are conserved across the filoviruses. We propose that this trough is the binding site of the critical domain C of the NPC1 receptor. Indeed, MR78 blocks binding of domain C to Marburg GP. Further, the extended third complementarity-determining region of the heavy chain (CDR H3) of MR78 mimics the glycan cap that shields this site on Ebola virus prior to entry and may mimic the receptor itself. These crystal structures plus additional biophysical analysis of complete, mucin-containing Ebola and Marburg GP ectodomains reveal that the receptor-binding site is masked on the surface of Ebola virus but more exposed on the surface of Marburg virus. These findings may explain why a cross-reactive antibody such as MR78 has not been identified in studies of Ebola virus.

RESULTS

Structure Determination

Trimeric GP ectodomains for Marburg virus (MARV; strain Ravn) or Ebola virus (EBOV, also known as Ebola Zaire; strain Mayinga) were expressed in *Drosophila* S2 cells, with or without their mucin-like domains (GP and GP Δ muc, respectively). MARV and EBOV GP Δ muc were further proteolyzed by trypsin or thermolysin, respectively, to produce cleaved GP (GPcl) resembling the version of GP competent for receptor binding in the endosome (Figure S1A). Three hundred versions of MARV GP were engineered and complexed with 22 different mAbs in order to find a crystallizable combination. Hundreds of crystals of the final MARV GPcl-MR78 combination were grown and screened for X-ray diffraction: just one crystal yielded suitable diffraction.

Diffraction to 3.6 Å resolution was obtained from a single crystal of the MARV GPcl-Fab MR78 complex. The structure was determined by molecular replacement using EBOV GP and Fab KZ52 (Lee et al., 2008) as search models and was refined to R_{work} of 24.7 % and R_{free} of 27.9 % (Table S1). Four GP-Fab complexes are contained in the asymmetric unit: one complete

trimer and one other monomer, which forms its biologically relevant trimer around a crystallographic 3-fold axis.

Differences in GP Structure between EBOV and MARV

Although the overall organization is similar between Marburg and Ebola GPs (1.8 Å rmsd among 212 C α atoms) (Figures 1A and 1B), several structural differences exist that may explain their differing requirements for cellular entry. The first difference is that the intra-GP1 disulfide bond formed by C121 and C147 in ebolavirus GP structures (Ebola [Lee et al., 2008] and Sudan [Bale et al., 2012; Dias et al., 2011]) does not exist in MARV. In MARV, the two cysteines are replaced instead with L105 and H131 (Figure 1C and Figure S1B). As a result, the equivalent polypeptides, which form the crest of the receptor-binding subunit, differ in structure and flexibility. In the ebolaviruses, the polypeptide bearing C147 (residues 145 to 150) turns inward, toward the trimer center to disulfide bond to C121. In MARV, the equivalent polypeptide (residues 129 to 134) turns outward into solvent, away from the trimer center.

A second difference between MARV and the ebolaviruses lies at the base of the cathepsin cleavage loop. In MARV, these residues (172–180) form a clear α 2 helix (α 2), which packs against the outside of the GP2 fusion loop, interacting with both the N- and C-terminal strands of the fusion loop (Figure 1D). In ebolaviruses, the equivalent residues predict to form a loop rather than a helix and are disordered (Bale et al., 2012; Dias et al., 2011; Lee et al., 2008). In MARV GP, the peptide connecting this α 2 helix to β 14 in the glycan cap would necessarily and immediately cover the both N- and C-terminal arms of the GP2 fusion loop, and if uncleaved, would hinder the conformational changes of fusion. Structural differences in α 2 of MARV may prevent effective processing by cathepsin B.

The third difference in the MARV GP structure lies at the N terminus, in the base of the β sheet that forms the GP1 spool, about which the metastable GP2 subunit is wound. In EBOV, the base of the spool connects to the anchoring GP1-GP2 disulfide bond by a short stretch of polypeptide that intimately interacts with GP2. This short connecting polypeptide contains an N-linked glycan at Asn40, and also contains residue Asp47, which renders EBOV dependent on cathepsin B for entry (Misasi et al., 2012). In EBOV entry, cathepsin B removes an additional and critical 1 kDa of mass from GP beyond that removed by cathepsin L, but the site and consequences of that extra cleavage event are not yet known. We propose that if cathepsin B cleaves this connecting loop, EBOV GP2 would be freed from the constraints of the disulfide bond and better able to undergo the conformational rearrangements of fusion. Our crystal structure reveals that MARV, which is cathepsin B-independent, is structured differently from EBOV at the same site. In MARV, the base of the GP1 spool is more mobile and is shifted toward the center of the trimer, inside of the fusion loop. Further, unlike in ebolaviruses (Dias et al., 2011; Bale et al., 2012), the polypeptide connection to the MARV GP1-GP2 disulfide could not be visualized and the N-linked glycan is absent. The nearest glycan is instead attached to residue 171 on the MARV GP1 β sheet itself (Figure 1E). These differences in sequence, glycosylation, mobility, and conformation likely allow MARV to be cleaved by other enzymes and render MARV cathepsin B-independent.

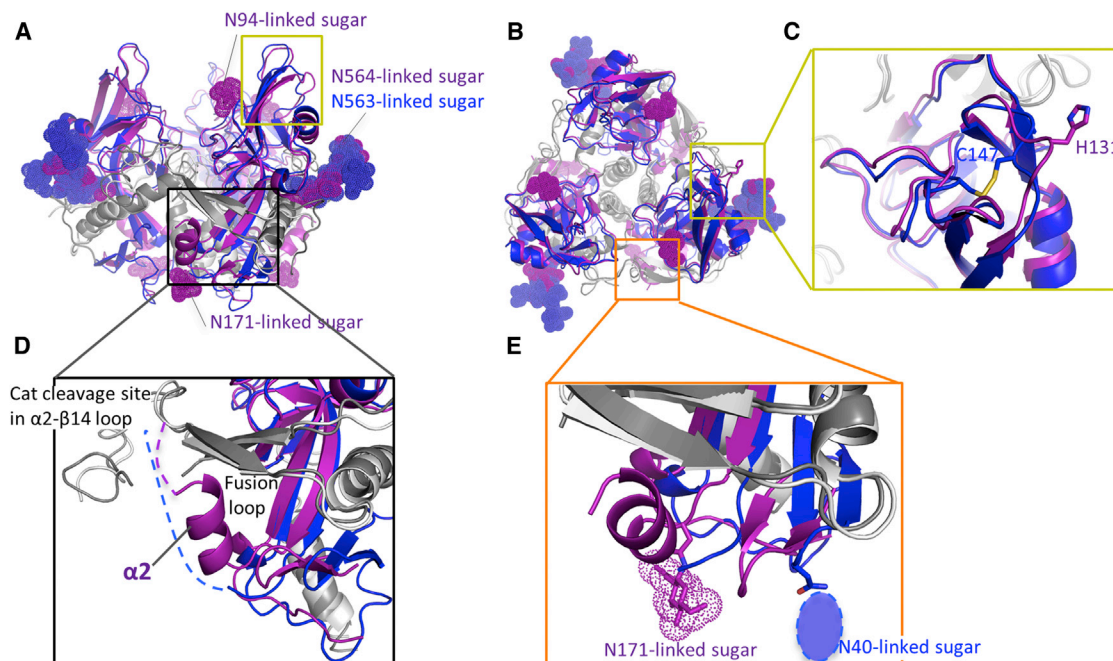


Figure 1. Structure of Marburg Virus GP

(A) Crystal structure of MARV GPcl (GP1, purple and GP2, dark gray) superimposed with the equivalent structure of EBOV (PDB ID, 3CSY; GP1, blue; and GP2, light gray). The glycan cap of EBOV GP is deleted for clarity. The yellow box outlines the MR78 epitope and putative receptor-binding site. The black box outlines the interaction site of the MARV-specific helix $\alpha 2$ of GP1 (purple) with the fusion loop of GP2 (dark gray). The visible N-linked sugars on MARV and EBOV GPcl crystal structures are shown as dot models. MARV GPcl bears glycans at positions N94 and N171, which are not glycosylated in EBOV. See also [Figure S1](#).

(B) Top view of GP.

(C) MARV GP lacks the intra-GP1 disulfide bond of EBOV. C147 of EBOV (blue) is replaced by H131 in MARV (purple), and the corresponding polypeptide traces outward from the trimer center. The orange box outlines the glycan attachment sites at the base of each GP.

(D) Residues 172–180 of MARV form an α helix ($\alpha 2$) that packs against both N- and C-terminal arms of the fusion loop. In ebolaviruses, the equivalent residues are predicted to form a loop rather than a helix and are disordered in crystal structures.

(E) At the base of GP, MARV bears a glycan attached to N171 while EBOV bears a glycan attached to N40 (drawn as an oval as it was not included in the EBOV crystal structure).

Overall Organization of the MARV or EBOV GPcl Bound to Fab MR78

The crystal structure of MARV GPcl in complex with the Fab fragment of MR78 indicates that MR78 binds the membrane-distal head of GP1 ([Figure 2A](#)). We determined an additional, low-resolution structure of EBOV GPcl bound to both MR78 and KZ52. The ternary EBOV complex, determined by molecular replacement, demonstrates that the MR78 antibody recognizes a similar site on both MARV and EBOV ([Figures 2B](#), [S2](#), and [Table S1](#)). MR78 binds into a highly conserved hydrophobic trough revealed at the top of the EBOV GP1 core, after removal of the glycan cap by proteolytic cleavage in the endosome. Although MARV and EBOV diverge significantly in sequence overall, residues contained in this site, the MR78 epitope, are 85% similar between the viruses ([Figures 3A](#) and [S1B](#)).

Likely Receptor-Binding Site

The location and structural conservation of this site suggest that it could be the binding site of the NPC1 receptor, used by all known filoviruses ([Carette et al., 2011](#); [Côté et al., 2011](#); [Miller et al., 2012](#); [Ng et al., 2014](#)). Indeed, in ELISA, MR78 inhibits binding of NPC1 domain C to MARV GP ([Figure S3A](#)). This

site, at the apex of cleaved GP1, resembles an ocean wave morphology, with a lower trough beneath a rising crest. The trough is hydrophobic and is formed by $\alpha 1$, $\beta 4$ and the loop that connects them (residues 63–74 in MARV). It is 22 Å wide and 8 Å deep at F72. The crest is hydrophilic, includes charged residues previously identified as essential for virus entry ([Dube et al., 2009](#); [Manicassamy et al., 2005](#); [Manicassamy et al., 2007](#)), and is formed by strands $\beta 7$, $\beta 9$ and their connecting loops (residues 92–106 and 120–134 in MARV). The 120–134 loop contains H131, which replaces the cysteine and the intra-GP1 disulfide bond of EBOV ([Figure 3B](#)).

Here, we show by ELISA that a Q128S and N129S double mutant in MARV GP abrogates binding to NPC1 domain C ([Figure S4A](#)). Q128 and N129 are at the tip of the crest and could make direct hydrophilic interaction with NPC1. The trough itself is formed by hydrophobic side chains, such as F72 (equivalent to F88 in EBOV). Also forming the trough are the main chains of hydrophilic residues; these polar side chains reach away from the trough into the trimer to make key stabilizing contacts to GP2. Two examples are R73 and K79, previously shown to be essential for MARV infectivity ([Manicassamy et al., 2007](#)). In the crystal structure, R73 makes multiple hydrogen bonds to the fusion loop

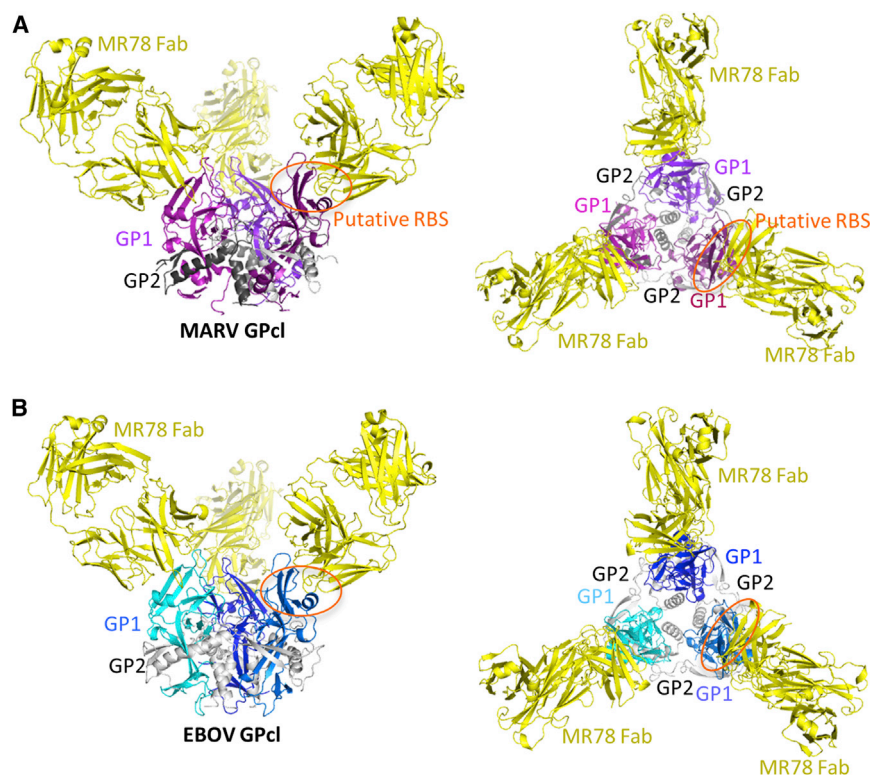


Figure 2. MR78 Binds Both MARV and EBOV GP1 at the Apex of GP1

(A) 3.6 Å crystal structure of MARV GP1 in complex with Fab MR78. Each GP1 is colored a different shade of purple, GP2 is gray, and the MR78 Fab is in yellow. (B) 8 Å structure of EBOV GP1 in complex with Fab MR78, determined by molecular replacement and rigid body refinement. Each EBOV GP1 is colored a different shade of blue and GP2 is gray. See also Figure S2. Fab MR78 (yellow) binds the apex of GP1 of both viruses.

of the neighboring protomer in the trimer (Figure S4B) and likely plays a key role in maintaining the prefusion structure or transmitting a conformational change to the fusion loop after receptor binding. K79 interacts with the main chain of residues 574–577 of GP2 (Figure S4C), residues that connect the separated helical segments of the first heptad repeat. We propose that binding of NPC1 domain C involves contact with the hydrophilic crest and hydrophobic trough, and that binding in the trough may transmit conformational changes to GP2 via R73 and K79 (equivalent to R89 and K95 in EBOV). Although MR78 binds both MARV and EBOV GP1, it only outcompetes NPC1 domain C for binding of MARV GP1 (Figure S3B). MR78 may have lower affinity for EBOV GP1 than MARV GP1 or domain C may bind the GPs slightly differently.

GP-MR78 Interactions

The interaction surface between the MR78 antibody and MARV GP buries 976 Å² of molecular surface and is primarily hydrophobic. Contact is mediated by both the heavy and light chains, but the primary region of interaction is the 17-residue CDR H3 (Figures 3C and S3CD), which penetrates the hydrophobic trough in MARV GP1. In this interaction, F111.2 and Y112.2 of the CDR H3 interact with P63, S67, W70, F72, I95 and I125 of MARV GP (IMGT numbering, Figure 4A).

Notably, these interactions are similar to those made by the Ebola virus glycan cap, which occupies this site prior to enzymatic cleavage in the endosome. In Ebola virus, the equivalent interactions are made by F225 and Y232 of the EBOV glycan cap interacting with P80, T83, W86, F88, L111 and V141 on EBOV GP (Figure 4B). Similarity may even extend to the key domain C

of the NPC1 receptor itself, as domain C contains similar Phenylalanine and Tyrosine residues that are essential for binding GP (Ndundo and Chandran, personal communication). Further, F72 in MARV, which is equivalent to F88 in EBOV, interacts with CDR H3 in the bottom of the trough. Both F72 of MARV and F88 of EBOV are critical for attachment and entry (Martinez et al., 2013; Mpanju et al., 2006) and may interact directly with essential hydrophobic residues of domain C. The binding mode of MR78 is reminiscent of anti-influenza virus human mAbs in which long CDR H3s similarly reach into the conserved receptor-binding site (Barbey-Martin et al., 2002; Bizebard et al., 1995; Hong et al., 2013; Lee et al., 2014; Schmidt et al., 2013; Whittle et al., 2011; Xu et al., 2013). In many cases those influenza mAbs also use Phe or Tyr aromatic residues to interact with an aromatic residue in the viral receptor binding domain, suggesting that the favorable energetics and intermolecular interactions of common aromatic molecules may constitute a canonical mode of binding of antiviral antibodies to recessed receptor-binding sites.

Although the MR78 epitope is largely conserved in sequence and structure between MARV and EBOV, it differs in its exposure at different stages of virus entry. MR78 binds MARV GP equally well whether MARV GP is in its uncleaved, viral-surface form or its cleaved, endosomal form. In contrast, MR78 does not bind uncleaved EBOV GP. It only binds the endosomal, cleaved form from which the glycan cap has been removed. Together, these results suggest that in EBOV, the glycan cap effectively blocks the MR78 epitope and putative receptor-binding site on the (uncleaved) viral surface, but that in MARV, the epitope and at least part of the receptor-binding site is fully exposed on the viral surface. Better exposure of this site may explain why antibodies against the putative receptor-binding site were elicited by MARV infection (see companion paper by Flyak et al., 2015), but seem to be more rarely elicited and have not yet been described against EBOV.

Differences in Mucin-Like Domains between MARV and EBOV, and Possible Effect on Antibody Reactivity

In addition to a glycan cap, the GP spike on the viral surface includes three heavily glycosylated mucin-like domains that are ~75 kDa each in mass and are predicted to have little secondary

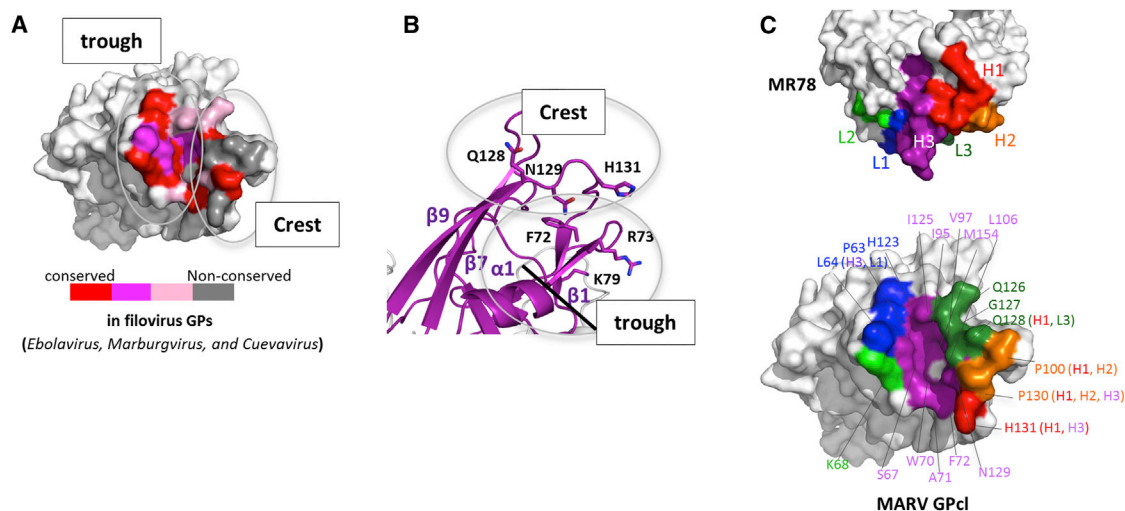


Figure 3. MR78 Recognizes a Conserved Epitope at the Apex of Cleaved GP1

(A) Conservation of the MR78 epitope among filovirus GPs, mapped onto one monomer of MARV GP1. Sequence alignment was performed in *ebolavirus* (*Ebola*, *Sudan*, *Reston*, *Tai Forest*, *Bundibugyo*), *marburgvirus* (*Musoke*, *Angola*, *Popp*, *Ci67*, *DRC1999*, *Ravn*), and *cuevavirus* (*Lloviu*) genuses. Residues identical across the filoviruses are colored red; residues that possess strong similarity, magenta; weak similarity, pink; no similarity, gray.

(B) The apex of cleaved MARV GP1, where Fab MR78 binds, forms a wave crest-and-trough morphology (magenta). The hydrophilic crest and the hydrophobic trough each contain residues previously shown to be critical for virus entry (Dube et al., 2009; Manicassamy et al., 2005; Manicassamy et al., 2007; Mpanju et al., 2006). The diagonal black line indicates the base of the trough. See also Figure S4.

(C) Surface representation of the interface between one monomer of MARV GP1 (bottom) and Fab MR78 (top). CDR H1 is colored red; CDR H2, orange; CDR H3, purple; CDR L1, blue; CDR L2, green; CDR L3, forest green. The footprint on MARV GP1 is colored according to the CDR that mediates the contact. GP residues contacted by MR78 are indicated and colored according to the CDR that mediates the contact (CDR names in parentheses).

structure. All mucin-containing GPs thus far have been refractory to crystallization. In order to visualize the native glycoprotein ectodomain and position of the mucin-like domain relative to the receptor-binding core, we turned to Small-Angle X-ray Scattering (SAXS) in solution. SAXS data collected for mucin-containing EBOV or MARV GP trimers indicate that the mucin-like domains of both viruses are large and extend outward from the GP core. The radius of gyration, R_G , for mucin-deleted and mucin-containing MARV GPs are 50 and 72 Å, respectively, and maximum dimension, D_{max} , for mucin-deleted and mucin-containing GPs are 160 and 250 Å, respectively, indicating that the mucin-like domain of MARV widens the molecule up to 90 Å (Figures 5A and S5). The mucin-like domains of MARV are a bit larger than those of EBOV (67 Å R_G and 225 Å D_{max} for mucin-containing EBOV GP), consistent with their greater volume determined by SAXS (Figure S5C) and mass noted by SDS-PAGE (Figure S5D). The mucin-like domains of EBOV appear to project more upward (consistent with EM tomography [Tran et al., 2014]), while those of MARV appear to project less upward, more equatorially, and to cover the sides of the GP trimer (Figures 5A and 5B). Although the mucin-like domains are likely flexible (see Porod-Debye coefficient P in Figure S5C), an equatorial, rather than upward projection is consistent with attachment points of the mucin-like domain to both GP1 and GP2 in MARV. In EBOV, a different position of the furin cleavage site results in all of mucin-like domain being attached to GP1. The MARV GP2 portion of the mucin-like domain, residues 436–509, is attached to residue 510 on the side of the MARV GP trimer, but is flexible and disordered.

A differing position of the mucin-like domains between MARV and EBOV would leave different surfaces exposed for immune recognition. The equatorial projection of the MARV mucin-like domain, for example, would leave the expected receptor-binding site at the top more accessible on MARV than EBOV, and further supports the notion that antibodies against the expected receptor-binding site would be more likely to be elicited using marburgvirus antigens than ebolavirus antigens. The accompanying paper (Flyak et al., 2015) and other immunization studies (Qiu et al., 2011; Wilson et al., 2000) support this notion.

In contrast, on EBOV, the upward projection of the mucin-like domains and the absence of mucin attached to EBOV GP2 would leave the EBOV base more exposed for antibody surveillance, compared to that of MARV. Indeed, in the accompanying paper by Flyak et al., none of the 18 neutralizing antibodies raised against MARV appear to bind the base of the MARV GP, while multiple neutralizing antibodies elicited by ebolaviruses are known to bind, or thought to bind, to the base of ebolavirus GP (Dias et al., 2011; Lee et al., 2008; Qiu et al., 2012; Murin et al., 2014) (Figure 5C).

DISCUSSION

In summary, the crystal structures and accompanying experiments indicate that MR78 binds a conserved site on the apex of GP1 that is available on the surface of MARV GP, but masked on EBOV GP prior to enzymatic cleavage. The epitope of MR78 likely overlaps with the receptor-binding site, and hydrophobic contacts made by CDR H3 to the hydrophobic trough may mimic

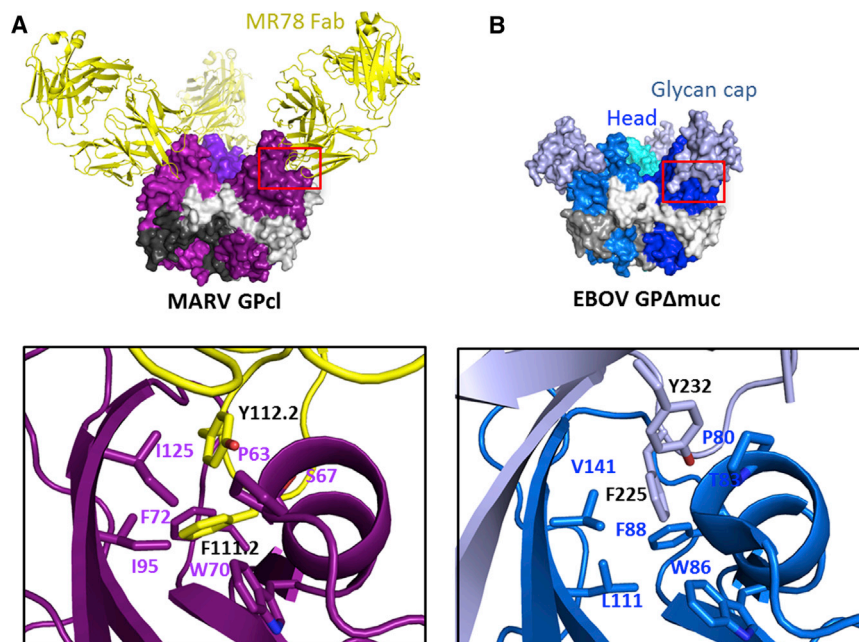


Figure 4. Similarity in Recognition of the Putative Receptor-Binding Site by MR78 and the Ebola Virus Glycan Cap

(A) The CDR H3 of MR78 (yellow) reaches into the hydrophobic trough of GP1 (purple). F111.2 and Y112.2 of CDR H3 interact with P63, S67, W70, F72, I95, and I125 of MARV GP.

(B) Similar residues of the EBOV glycan cap (light blue) bind into this trough on the surface of EBOV GP (blue), prior to enzymatic cleavage. Here, F225 and Y232 of the glycan cap interact with P80, T83, W86, F88, L111, and V141 in the trough (PDB ID: 3CSY).

Preparation and Crystallization of GP-Antibody Complexes

To mimic endosomal protease cleavage and produce MARV GPcl, MARV GPΔmuc was incubated with 0.01 mg trypsin at 37°C for 1 hr in 20 mM TBS [pH 8.0], 100 mM NaCl. The reaction was stopped using 0.5 mM 4-(2-Aminoethyl) benzene-sulfonyl fluoride hydrochloride (AEBSF), and the protein was purified by S200 SEC. EBOV GPcl was produced by incubating EBOV GPΔmuc with 0.02 mg thermolysin overnight at room temperature in 20 mM TBS [pH 7.5], 100 mM NaCl, 1 mM CaCl₂, and purified by S200 SEC.

those of the as-yet-unvisualized NPC1 domain C. MR78 does not neutralize authentic EBOV, likely because its epitope is masked on the EBOV surface by the mucin-like domain and glycan cap on the virus surface. MR78 does, however, neutralize authentic MARV (Flyak et al., 2015) and could be a valuable monoclonal antibody therapeutic against this extremely lethal virus. Importantly, no mAb therapeutic yet exists against MARV, and few mAbs are yet known against MARV from which such a therapeutic could be developed. The crystal structure of MARV GP presented here, and the highly conserved MR78 epitope, provide strategies for immunotherapy and templates for development of potentially broad-spectrum inhibitors of filovirus entry.

EXPERIMENTAL PROCEDURES

Construction, Expression, and Purification of MARV/EBOV GP

DNA encoding the MARV GPΔmuc ectodomain (residues 1–636 with a mucin deletion of residues 257–425), point mutants of MARV GPΔmuc and the EBOV GPΔmuc ectodomain (residues 1–637 with a mucin deletion of residues 314–462) were amplified by PCR using codon-optimized and whole-gene synthesized MARV or EBOV GPs as templates. Four point mutations in MARV GPΔmuc, F438L, W439A, F445G, and F447N, on GP2, located around the furin cleavage site were found to improve the efficiency of furin cleavage. GP constructs were cloned into a derivative of the expression vector pMT. This derivative vector contains the puromycin resistant gene and a C-terminal double-strep tag sequence. Expression plasmids were transfected using Effectin (QIAGEN) into 80% confluent *Drosophila* Schneider S2 cells. The cells were first cultured in complete Schneider's medium supplemented with 10% (v/v) FCS (LONZA), and were adapted to Insect Xpress medium by progressively modifying the Schneider/Insect Xpress medium ratio with 6.0 μg/ml puromycin. Large-scale expression of the MARV/EBOV GPΔmuc was performed using stable S2 cell lines in 2 l Erlenmeyer flask at 27.0°C, induced with 0.5 mM CuSO₄. Supernatants containing the expressed proteins were harvested 4 days after induction, and mixed with the Strep-Tactin affinity column binding buffer (100 mM Tris-HCl, 150 mM NaCl, 1 mM EDTA, 15 μg/ml Avidin [pH8.0]). The proteins were purified via Strep-Tactin affinity, followed by Superdex 200GL 10/300 (GE Healthcare Life Sciences) size-exclusion chromatography (S200 SEC).

Hybridoma cells expressing the human MR78 antibody were generated from peripheral blood mononuclear cells (PBMCs) from a donor, who contracted MARV infection in the Python Cave in Queen Elizabeth National Park, Uganda in 2008 (see Flyak et al., 2015). MR78 was expressed in serum-free medium (Hybridoma-SFM, GIBCO), and culture supernatants were centrifuged, sterile-filtered, and purified over HiTrap Protein G columns (GE Healthcare Life Sciences). Fab fragments were generated by standard papain digestion, with released Fc and undigested IgG removed by Protein A chromatography, and remaining Fab fragments further purified by MonoQ ion-exchange chromatography. For crystallization, purified MARV GPcl was mixed with excess Fab MR78 for 2 days at 4°C. Complexes were separated from unbound Fab via S200 SEC. Crystals were grown by hanging-drop vapor diffusion at 20°C using 0.8 μl protein (13.0 mg ml⁻¹, in 20 mM Tris-HCl [pH 8.0], 100 mM NaCl) and 0.8 μl of mother liquor (100 mM NaCl, 50 mM MES [pH 6.5], 13 % PEG 4000, 0.5 % ethyl acetate). These crystals were cryoprotected with 25% glycerol plus mother liquor before flash cooling in liquid nitrogen. One crystal diffracted to a resolution of 3.6 Å. EBOV GPcl was complexed with Fabs KZ52 and MR78 and crystallized using hanging-drop vapor diffusion at 20°C with 1.0 μl of protein (6 mg/ml, 150 mM NaCl, 10 mM Tris [pH 7.5]) and 1.0 μl of mother liquor (100 mM NaAcetate [pH 4.6], 200 mM NH₄SO₄, 10% PEG 3350, 2% PEG 400). The crystals were then cryoprotected by washing in 100 mM NaAcetate [pH 4.6], 200 mM NH₄SO₄, 12% PEG 3350, 10% PEG 400, 10% ethylene glycol. Only diffraction to 8 Å was obtained, but this data permitted molecular replacement using Phaser (McCoy et al., 2007) and EBOV GP and KZ52 (Lee et al., 2008) as search models.

ACCESSION NUMBERS

Coordinates and structure factors have been deposited into the Protein Data Bank under the accession code 3X2D.

SUPPLEMENTAL INFORMATION

Supplemental Information includes Extended Experimental Procedures, five figures, and one table and can be found with this article online at <http://dx.doi.org/10.1016/j.cell.2015.01.041>.

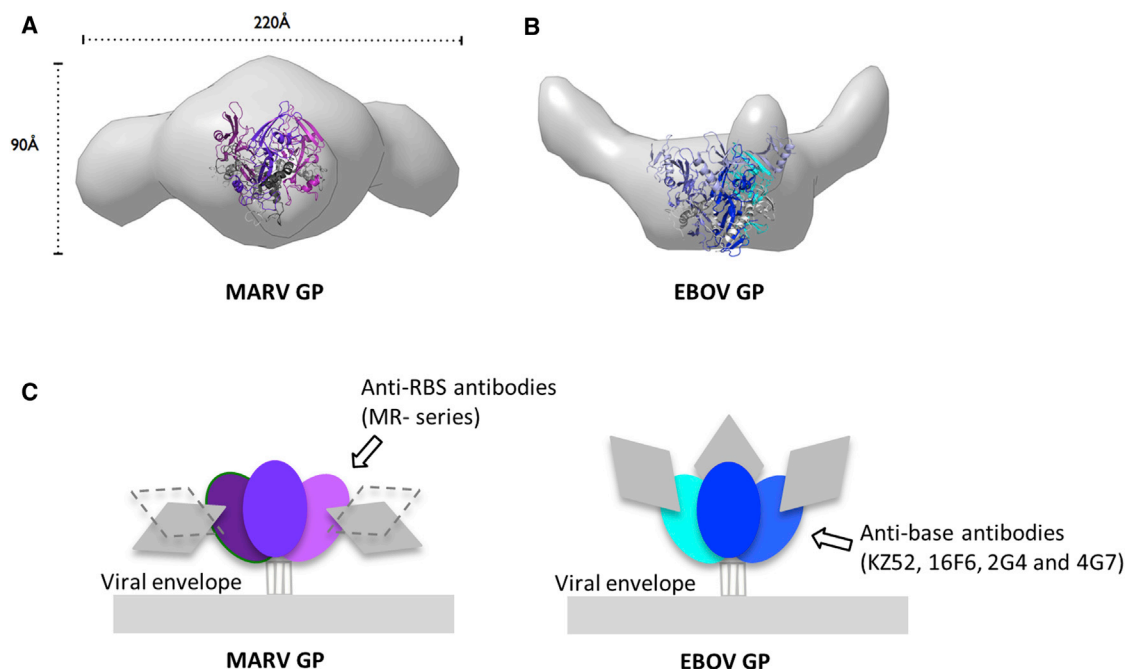


Figure 5. MARV and EBOV Present Different Surfaces for Antibody Recognition

(A and B) Molecular envelopes of mucin-containing MARV and EBOV GP ectodomains determined by SAXS. Rendered Gaussian distributions of molecular envelopes are illustrated in light gray, with ribbon models of the crystallized MARV GP1 and EBOV GP Δ muc trimers to scale and overlaid for comparison. The trimers are illustrated as ribbons. Note that the glycan cap was removed from MARV GP used in crystallization in order to improve diffraction but was contained in the complete MARV GP used for SAXS. The glycan cap did not inhibit diffraction of EBOV GP and is included in the EBOV GP crystal structure. MARV GP1 is colored in purple (GP1) and gray (GP2). EBOV GP Δ muc is colored blue (GP1), white blue (GP1 glycan cap), and gray (GP2). MARV GP is drawn in two possible orientations because definitive placement of polypeptide is challenging at this resolution. In either orientation however, the mucin-like domains of MARV project sideways, equatorially or downward from the core of GP. In MARV, the mucin-like domain is attached to both GP1 and GP2. By contrast, in EBOV, the mucin-like domain is attached solely to GP1, there is no anchor at the base. Both these SAXS experiments and previous electron tomography (Tran et al., 2014) agree on the upward projection of the mucin-like domains in EBOV. See also Figure S5.

(C) Differing positions of the mucin-like domains between MARV and EBOV may lead to elicitation of different types of antibodies. The lower position and GP2 anchor of the mucin-like domain of MARV may better mask the base of GP but expose its upper surfaces, allowing antibodies like mAb MR78 to be elicited. The upward projection of the EBOV mucin-like domain and absence of any GP2 anchor, appear to better mask upper surfaces, but expose the base, allowing antibodies such as KZ52 (Lee et al., 2008), 2G4, 4G7 (Murin et al., 2014), and 16F6 (directed against Sudan ebolavirus [Dias et al., 2011; Bale et al., 2012]) to be elicited.

AUTHOR CONTRIBUTIONS

Experiments were conceived by E.O.S. with T.H., M.L.F., J.E.L., and Z.A.B. All structural and biochemical work was performed by T.H., M.L.F., Z.A.B., J.E.L., A.I.F. and analyzed by T.H., M.L.F., Z.A.B., J.E.L., A.I.F., R.M., D.K., Y.Y., M.H., J.E.C., and E.O.S. The manuscript was written by E.O.S. and T.H. All authors contributed to editing the manuscript and support the conclusions.

ACKNOWLEDGMENTS

We would like to thank Dr. Adrianna P.P. Zhang (TSRI) for help with data collection, Dr. Sebastien Igonet (TSRI and Calixar) for assistance with S2 cell expression, Dr. Kartik Chandran (Albert Einstein College of Medicine), C. Daniel Murin, and Dr. Andrew Ward (TSRI) for valuable discussions, and the beamline staff of Photon Factory (Tsukuba, Japan) for technical help during data collection. We thank NIAID CETR U19 AI109762 (E.O.S.), R01 AI089498, and R21AI069347 (E.O.S.); Defense Threat Reduction Agency grant HDTRA1-13-1-0034; NIAID grant U19 AI109711 (J.E.C.); MEXT KAKENHI grant numbers 26713018 (T.H.) and 24115005 (Y.Y.); MEXT Platform for Drug Discovery Informatics and Structural Life Science (T.H.), JSPS Postdoctoral Fellowships (DC2 [R.M.], Research Abroad [T.H.]); a Research Fellowship of The Uehara Memorial Foundation (T.H.); an Investi-

gators in the Pathogenesis of Infectious Disease award from the Burroughs Wellcome Fund (E.O.S.); and an NIH grant MINOS GM105404 (M.H.) for support. SIBYLS beamline efforts to combine SAXS and crystallography at the Advanced Light Source of Lawrence Berkeley National Laboratory are supported in part by US DOE program Integrated Diffraction Analysis Technologies (IDAT). This is manuscript # 28060 from The Scripps Research Institute.

Received: October 18, 2014

Revised: January 8, 2015

Accepted: January 27, 2015

Published: February 26, 2015

REFERENCES

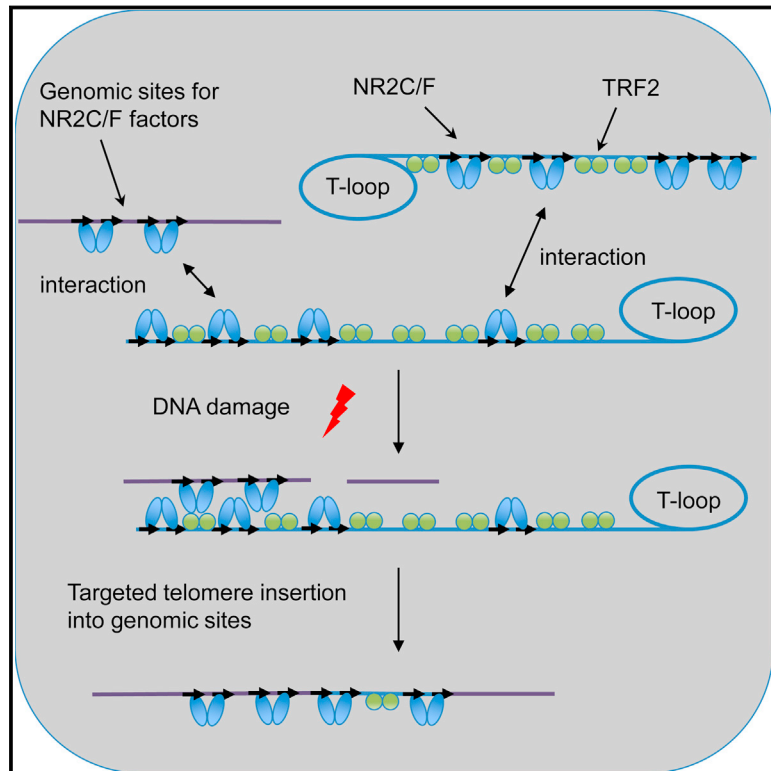
- Albariño, C.G., Shoemaker, T., Khristova, M.L., Wamala, J.F., Muyembe, J.J., Balinandi, S., Tumusiime, A., Campbell, S., Cannon, D., Gibbons, A., et al. (2013). Genomic analysis of filoviruses associated with four viral hemorrhagic fever outbreaks in Uganda and the Democratic Republic of the Congo in 2012. *Virology* 442, 97–100.
- Aleksandrowicz, P., Marzi, A., Biedenkopf, N., Beimforde, N., Becker, S., Hoenen, T., Feldmann, H., and Schnitzler, H.J. (2011). Ebola virus enters host cells

- by macropinocytosis and clathrin-mediated endocytosis. *J. Infect. Dis.* 204 (3), S957–S967.
- Bale, S., Dias, J.M., Fusco, M.L., Hashiguchi, T., Wong, A.C., Liu, T., Keuhne, A.I., Li, S., Woods, V.L., Jr., Chandran, K., et al. (2012). Structural basis for differential neutralization of ebolaviruses. *Viruses* 4, 447–470.
- Barbey-Martin, C., Gigant, B., Bizebard, T., Calder, L.J., Wharton, S.A., Skehel, J.J., and Knossow, M. (2002). An antibody that prevents the hemagglutinin low pH fusogenic transition. *Virology* 294, 70–74.
- Barrette, R.W., Metwally, S.A., Rowland, J.M., Xu, L., Zaki, S.R., Nichol, S.T., Rollin, P.E., Towner, J.S., Shieh, W.J., Batten, B., et al. (2009). Discovery of swine as a host for the Reston ebolavirus. *Science* 325, 204–206.
- Bizebard, T., Gigant, B., Rigolet, P., Rasmussen, B., Diat, O., Bösecke, P., Wharton, S.A., Skehel, J.J., and Knossow, M. (1995). Structure of influenza virus haemagglutinin complexed with a neutralizing antibody. *Nature* 376, 92–94.
- Bowen, E.T., Lloyd, G., Harris, W.J., Platt, G.S., Baskerville, A., and Vella, E.E. (1977). Viral haemorrhagic fever in southern Sudan and northern Zaire. Preliminary studies on the aetiological agent. *Lancet* 1, 571–573.
- Brecher, M., Schornberg, K.L., Delos, S.E., Fusco, M.L., Saphire, E.O., and White, J.M. (2012). Cathepsin cleavage potentiates the Ebola virus glycoprotein to undergo a subsequent fusion-relevant conformational change. *J. Virol.* 86, 364–372.
- Carette, J.E., Raaben, M., Wong, A.C., Herbert, A.S., Obernosterer, G., Mulherkar, N., Kuehne, A.I., Kranzusch, P.J., Griffin, A.M., Ruthel, G., et al. (2011). Ebola virus entry requires the cholesterol transporter Niemann-Pick C1. *Nature* 477, 340–343.
- Chandran, K., Sullivan, N.J., Felbor, U., Whelan, S.P., and Cunningham, J.M. (2005). Endosomal proteolysis of the Ebola virus glycoprotein is necessary for infection. *Science* 308, 1643–1645.
- Côté, M., Misasi, J., Ren, T., Bruchez, A., Lee, K., Filone, C.M., Hensley, L., Li, Q., Ory, D., Chandran, K., and Cunningham, J. (2011). Small molecule inhibitors reveal Niemann-Pick C1 is essential for Ebola virus infection. *Nature* 477, 344–348.
- Dias, J.M., Kuehne, A.I., Abelson, D.M., Bale, S., Wong, A.C., Halfmann, P., Muhammad, M.A., Fusco, M.L., Zak, S.E., Kang, E., et al. (2011). A shared structural solution for neutralizing ebolaviruses. *Nat. Struct. Mol. Biol.* 18, 1424–1427.
- Dube, D., Brecher, M.B., Delos, S.E., Rose, S.C., Park, E.W., Schornberg, K.L., Kuhn, J.H., and White, J.M. (2009). The primed ebolavirus glycoprotein (19-kilodalton GP1,2): sequence and residues critical for host cell binding. *J. Virol.* 83, 2883–2891.
- Dye, J.M., Herbert, A.S., Kuehne, A.I., Barth, J.F., Muhammad, M.A., Zak, S.E., Ortiz, R.A., Prugar, L.I., and Pratt, W.D. (2012). Postexposure antibody prophylaxis protects nonhuman primates from filovirus disease. *Proc. Natl. Acad. Sci. USA* 109, 5034–5039.
- Flyak, A.I., Ilinykh, P.A., Murin, C.D., Garron, T., Shen, X., Fusco, M.L., Hashiguchi, T., Bornholdt, Z.A., Slaughter, J.C., Sapparapu, G., et al. (2015). Mechanism of Human Antibody-Mediated Neutralization of Marburg virus. *Cell* 160, this issue, 893–903.
- Geisbert, T.W., Daddario-DiCaprio, K.M., Geisbert, J.B., Young, H.A., Formenty, P., Fritz, E.A., Larsen, T., and Hensley, L.E. (2007). Marburg virus Angola infection of rhesus macaques: pathogenesis and treatment with recombinant nematode anticoagulant protein c2. *J. Infect. Dis.* 196 (2), S372–S381.
- Gnirss, K., Kühl, A., Karsten, C., Glowacka, I., Bertram, S., Kaup, F., Hofmann, H., and Pöhlmann, S. (2012). Cathepsins B and L activate Ebola but not Marburg virus glycoproteins for efficient entry into cell lines and macrophages independent of TMPRSS2 expression. *Virology* 424, 3–10.
- Hong, M., Lee, P.S., Hoffman, R.M., Zhu, X., Krause, J.C., Laursen, N.S., Yoon, S.I., Song, L., Tussey, L., Crowe, J.E., Jr., et al. (2013). Antibody recognition of the pandemic H1N1 Influenza virus hemagglutinin receptor binding site. *J. Virol.* 87, 12471–12480.
- Hood, C.L., Abraham, J., Boyington, J.C., Leung, K., Kwong, P.D., and Nabel, G.J. (2010). Biochemical and structural characterization of cathepsin L-processed Ebola virus glycoprotein: implications for viral entry and immunogenicity. *J. Virol.* 84, 2972–2982.
- Lee, J.E., Fusco, M.L., Hessel, A.J., Oswald, W.B., Burton, D.R., and Saphire, E.O. (2008). Structure of the Ebola virus glycoprotein bound to an antibody from a human survivor. *Nature* 454, 177–182.
- Lee, P.S., Ohshima, N., Stanfield, R.L., Yu, W., Iba, Y., Okuno, Y., Kurosawa, Y., and Wilson, I.A. (2014). Receptor mimicry by antibody F045-092 facilitates universal binding to the H3 subtype of influenza virus. *Nat. Commun.* 5, 3614.
- Malashkevich, V.N., Schneider, B.J., McNally, M.L., Milhollen, M.A., Pang, J.X., and Kim, P.S. (1999). Core structure of the envelope glycoprotein GP2 from Ebola virus at 1.9-Å resolution. *Proc. Natl. Acad. Sci. USA* 96, 2662–2667.
- Malherbe, H., and Strickland-Cholmley, M. (1968). Human disease from monkeys (Marburg virus). *Lancet* 1, 1434.
- Manicassamy, B., Wang, J., Jiang, H., and Rong, L. (2005). Comprehensive analysis of ebola virus GP1 in viral entry. *J. Virol.* 79, 4793–4805.
- Manicassamy, B., Wang, J., Rumschlag, E., Tymen, S., Volchkova, V., Volchkov, V., and Rong, L. (2007). Characterization of Marburg virus glycoprotein in viral entry. *Virology* 358, 79–88.
- Martinez, O., Johnson, J., Manicassamy, B., Rong, L., Olinger, G.G., Hensley, L.E., and Basler, C.F. (2010). Zaire Ebola virus entry into human dendritic cells is insensitive to cathepsin L inhibition. *Cell. Microbiol.* 12, 148–157.
- Martinez, O., Ndungo, E., Tantral, L., Miller, E.H., Leung, L.W., Chandran, K., and Basler, C.F. (2013). A mutation in the Ebola virus envelope glycoprotein restricts viral entry in a host species- and cell-type-specific manner. *J. Virol.* 87, 3324–3334.
- Marzi, A., Reinheckel, T., and Feldmann, H. (2012a). Cathepsin B & L are not required for ebola virus replication. *PLoS Negl. Trop. Dis.* 6, e1923.
- Marzi, A., Yoshida, R., Miyamoto, H., Ishijima, M., Suzuki, Y., Higuchi, M., Matsuyama, Y., Igarashi, M., Nakayama, E., Kuroda, M., et al. (2012b). Protective efficacy of neutralizing monoclonal antibodies in a nonhuman primate model of Ebola hemorrhagic fever. *PLoS ONE* 7, e36192.
- McCoy, A.J., Grosse-Kunstleve, R.W., Adams, P.D., Winn, M.D., Storoni, L.C., and Read, R.J. (2007). Phaser crystallographic software. *J. Appl. Cryst.* 40, 658–674.
- Miller, E.H., Obernosterer, G., Raaben, M., Herbert, A.S., Deffieu, M.S., Krishnan, A., Ndungo, E., Sandesara, R.G., Carette, J.E., Kuehne, A.I., et al. (2012). Ebola virus entry requires the host-programmed recognition of an intracellular receptor. *EMBO J.* 31, 1947–1960.
- Misasi, J., Chandran, K., Yang, J.Y., Considine, B., Filone, C.M., Côté, M., Sullivan, N., Fabozzi, G., Hensley, L., and Cunningham, J. (2012). Filoviruses require endosomal cysteine proteases for entry but exhibit distinct protease preferences. *J. Virol.* 86, 3284–3292.
- Mpanju, O.M., Towner, J.S., Dover, J.E., Nichol, S.T., and Wilson, C.A. (2006). Identification of two amino acid residues on Ebola virus glycoprotein 1 critical for cell entry. *Virus Res.* 121, 205–214.
- Mulherkar, N., Raaben, M., de la Torre, J., Whelan, S., and Chandran, K. (2011). The Ebola virus glycoprotein mediates entry via a non-classical dynamin-dependent macropinocytic pathway. *Virology* 418, 72–83.
- Murin, C.D., Fusco, M.L., Bornholdt, Z.A., Qiu, X., Olinger, G.G., Zeitlin, L., Koberinger, G.P., Ward, A.B., and Saphire, E.O. (2014). Structures of protective antibodies reveal sites of vulnerability on Ebola virus. *Proc. Natl. Acad. Sci. USA* 111, 17182–17187.
- Nanbo, A., Imai, M., Watanabe, S., Noda, T., Takahashi, K., Neumann, G., Halfmann, P., and Kawaoka, Y. (2010). Ebolavirus is internalized into host cells via macropinocytosis in a viral glycoprotein-dependent manner. *PLoS Pathog.* 6, e1001121.
- Ng, M., Ndungo, E., Jangra, R.K., Cai, Y., Postnikova, E., Radoshitzky, S.R., Dye, J.M., Ramirez de Arellano, E., Negrode, A., Palacios, G., et al. (2014). Cell entry by a novel European filovirus requires host endosomal cysteine proteases and Niemann-Pick C1. *Virology* 468–470, 637–646.

- Olinger, G.G., Jr., Pettitt, J., Kim, D., Working, C., Bohorov, O., Bratcher, B., Hiatt, E., Hume, S.D., Johnson, A.K., Morton, J., et al. (2012). Delayed treatment of Ebola virus infection with plant-derived monoclonal antibodies provides protection in rhesus macaques. *Proc. Natl. Acad. Sci. USA* *109*, 18030–18035.
- Pan, Y., Zhang, W., Cui, L., Hua, X., Wang, M., and Zeng, Q. (2014). Reston virus in domestic pigs in China. *Arch. Virol.* *159*, 1129–1132.
- Pettitt, J., Zeitlin, L., Kim do, H., Working, C., Johnson, J.C., Bohorov, O., Bratcher, B., Hiatt, E., Hume, S.D., Johnson, A.K., et al. (2013). Therapeutic intervention of Ebola virus infection in rhesus macaques with the MB-003 monoclonal antibody cocktail. *Sci. Transl. Med.* *5*, 199ra113.
- Pflugrath, J.W. (1999). The finer things in X-ray diffraction data collection. *Acta Crystallogr. D Biol. Crystallogr.* *55*, 1718–1725.
- Qiu, X., Alimonti, J.B., Melito, P.L., Fernando, L., Ströher, U., and Jones, S.M. (2011). Characterization of Zaire ebolavirus glycoprotein-specific monoclonal antibodies. *Clin. Immunol.* *141*, 218–227.
- Qiu, X., Audet, J., Wong, G., Pillet, S., Bello, A., Cabral, T., Strong, J.E., Plummer, F., Corbett, C.R., Alimonti, J.B., et al. (2012). Successful treatment of ebola virus-infected cynomolgus macaques with monoclonal antibodies. *Sci. Transl. Med.* *4*, 138ra181.
- Qiu, X., Wong, G., Audet, J., Bello, A., Fernando, L., Alimonti, J.B., Fausther-Bovendo, H., Wei, H., Aviles, J., Hiatt, E., et al. (2014). Reversion of advanced Ebola virus disease in nonhuman primates with ZMapp. *Nature* *514*, 47–53.
- Saeed, M.F., Kolokoltsov, A.A., Albrecht, T., and Davey, R.A. (2010). Cellular entry of ebola virus involves uptake by a macropinocytosis-like mechanism and subsequent trafficking through early and late endosomes. *PLoS Pathog.* *6*, e1001110.
- Sanchez, A., and Rollin, P.E. (2005). Complete genome sequence of an Ebola virus (Sudan species) responsible for a 2000 outbreak of human disease in Uganda. *Virus Res.* *113*, 16–25.
- Sanchez, A., Trappier, S.G., Mahy, B.W., Peters, C.J., and Nichol, S.T. (1996). The virion glycoproteins of Ebola viruses are encoded in two reading frames and are expressed through transcriptional editing. *Proc. Natl. Acad. Sci. USA* *93*, 3602–3607.
- Sayama, Y., Demetria, C., Saito, M., Azul, R.R., Taniguchi, S., Fukushi, S., Yoshikawa, T., Iizuka, I., Mizutani, T., Kurane, I., et al. (2012). A seroepidemiologic study of Reston ebolavirus in swine in the Philippines. *BMC Vet. Res.* *8*, 82.
- Schmidt, A.G., Xu, H., Khan, A.R., O'Donnell, T., Khurana, S., King, L.R., Manischewitz, J., Golding, H., Suphaphiphat, P., Carfi, A., et al. (2013). Pre-configuration of the antigen-binding site during affinity maturation of a broadly neutralizing influenza virus antibody. *Proc. Natl. Acad. Sci. USA* *110*, 264–269.
- Schornberg, K., Matsuyama, S., Kabsch, K., Delos, S., Bouton, A., and White, J. (2006). Role of endosomal cathepsins in entry mediated by the Ebola virus glycoprotein. *J. Virol.* *80*, 4174–4178.
- Shoemaker, T., MacNeil, A., Balinandi, S., Campbell, S., Wamala, J.F., McMullan, L.K., Downing, R., Lutwama, J., Mbidde, E., Ströher, U., et al. (2012). Re-emerging Sudan Ebola virus disease in Uganda, 2011. *Emerg. Infect. Dis.* *18*, 1480–1483.
- Siegert, R., Shu, H.L., and Slenczka, W. (1968). [Isolation and identification of the “Marburg virus”]. *Dtsch. Med. Wochenschr.* *93*, 604–612.
- Towner, J.S., Khristova, M.L., Sealy, T.K., Vincent, M.J., Erickson, B.R., Bawiec, D.A., Hartman, A.L., Comer, J.A., Zaki, S.R., Ströher, U., et al. (2006). Marburgvirus genomics and association with a large hemorrhagic fever outbreak in Angola. *J. Virol.* *80*, 6497–6516.
- Towner, J.S., Sealy, T.K., Khristova, M.L., Albariño, C.G., Conlan, S., Reeder, S.A., Quan, P.L., Lipkin, W.I., Downing, R., Tappero, J.W., et al. (2008). Newly discovered ebola virus associated with hemorrhagic fever outbreak in Uganda. *PLoS Pathog.* *4*, e1000212.
- Tran, E.E., Simmons, J.A., Bartesaghi, A., Shoemaker, C.J., Nelson, E., White, J.M., and Subramaniam, S. (2014). Spatial localization of the Ebola virus glycoprotein mucin-like domain determined by cryo-electron tomography. *J. Virol.* *88*, 10958–10962.
- Volchkov, V.E., Feldmann, H., Volchkova, V.A., and Klenk, H.D. (1998). Processing of the Ebola virus glycoprotein by the proprotein convertase furin. *Proc. Natl. Acad. Sci. USA* *95*, 5762–5767.
- Wamala, J.F., Lukwago, L., Malimbo, M., Nguku, P., Yoti, Z., Musenero, M., Amone, J., Mbabazi, W., Nanyunja, M., Zaramba, S., et al. (2010). Ebola hemorrhagic fever associated with novel virus strain, Uganda, 2007–2008. *Emerg. Infect. Dis.* *16*, 1087–1092.
- Weissenhorn, W., Calder, L.J., Wharton, S.A., Skehel, J.J., and Wiley, D.C. (1998a). The central structural feature of the membrane fusion protein subunit from the Ebola virus glycoprotein is a long triple-stranded coiled coil. *Proc. Natl. Acad. Sci. USA* *95*, 6032–6036.
- Weissenhorn, W., Carfi, A., Lee, K.H., Skehel, J.J., and Wiley, D.C. (1998b). Crystal structure of the Ebola virus membrane fusion subunit, GP2, from the envelope glycoprotein ectodomain. *Mol. Cell* *2*, 605–616.
- Whittle, J.R., Zhang, R., Khurana, S., King, L.R., Manischewitz, J., Golding, H., Dormitzer, P.R., Haynes, B.F., Walter, E.B., Moody, M.A., et al. (2011). Broadly neutralizing human antibody that recognizes the receptor-binding pocket of influenza virus hemagglutinin. *Proc. Natl. Acad. Sci. USA* *108*, 14216–14221.
- WHO Ebola Response Team (2014). Ebola Virus Disease in West Africa - The First 9 Months of the Epidemic and Forward Projections. *N. Engl. J. Med.* *371*, 1481–1495.
- Wilson, J.A., Hevey, M., Bakken, R., Guest, S., Bray, M., Schmaljohn, A.L., and Hart, M.K. (2000). Epitopes involved in antibody-mediated protection from Ebola virus. *Science* *287*, 1664–1666.
- Xu, R., Krause, J.C., McBride, R., Paulson, J.C., Crowe, J.E., Jr., and Wilson, I.A. (2013). A recurring motif for antibody recognition of the receptor-binding site of influenza hemagglutinin. *Nat. Struct. Mol. Biol.* *20*, 363–370.

Nuclear-Receptor-Mediated Telomere Insertion Leads to Genome Instability in ALT Cancers

Graphical Abstract



Authors

Paulina Marzec, Claudia Armenise, ..., Frédéric Chibon, Jérôme Déjardin

Correspondence

jerome.dejardin@igh.cnrs.fr

In Brief

GGGTCA variant repeats accumulate on ALT telomeres and lead to the aberrant recruitment of NR2C/F nuclear receptors. These receptors can then bridge to their native binding sites within chromatin and drive the inclusion of telomeric sequences within the genome, creating sites prone to breakage and translocations.

Highlights

- NR2C/F orphan nuclear receptors bind to ALT telomeres at GGGTCA direct repeats
- NR2C/F factors bridge their target loci, clustering and relocalizing ALT telomeres
- Telomeric sequences are inserted in ALT genomes in an NR2C/F-dependent manner
- Telomere insertion destabilizes ALT genomes and contributes to complex rearrangements



Nuclear-Receptor-Mediated Telomere Insertion Leads to Genome Instability in ALT Cancers

Paulina Marzec,¹ Claudia Armenise,¹ Gaëlle Pérot,^{2,3} Fani-Marlen Roumelioti,⁴ Eugenia Basyuk,⁵ Sarantis Gagos,⁴ Frédéric Chibon,^{2,3} and Jérôme Déjardin^{1,*}

¹INSERM AVENIR Team, Institute of Human Genetics, CNRS UPR 1142, 141 rue de la Cardonille, 34396 Montpellier, France

²Translational Research, Department of Biopathology, Institut Bergonié, 229 cours de l'Argonne, 33076 Bordeaux, France

³INSERM U916, 229 cours de l'Argonne, 33076 Bordeaux, France

⁴Laboratory of Genetics and Gene Therapy, Center of Basic Research II, Biomedical Research Foundation of the Academy of Athens, 11527 Athens, Greece

⁵Institut de Génétique Moléculaire de Montpellier, CNRS-UMR5535, 1919 route de Mende, 34293 Montpellier Cedex 5, France

*Correspondence: jerome.dejardin@igh.cnrs.fr

<http://dx.doi.org/10.1016/j.cell.2015.01.044>

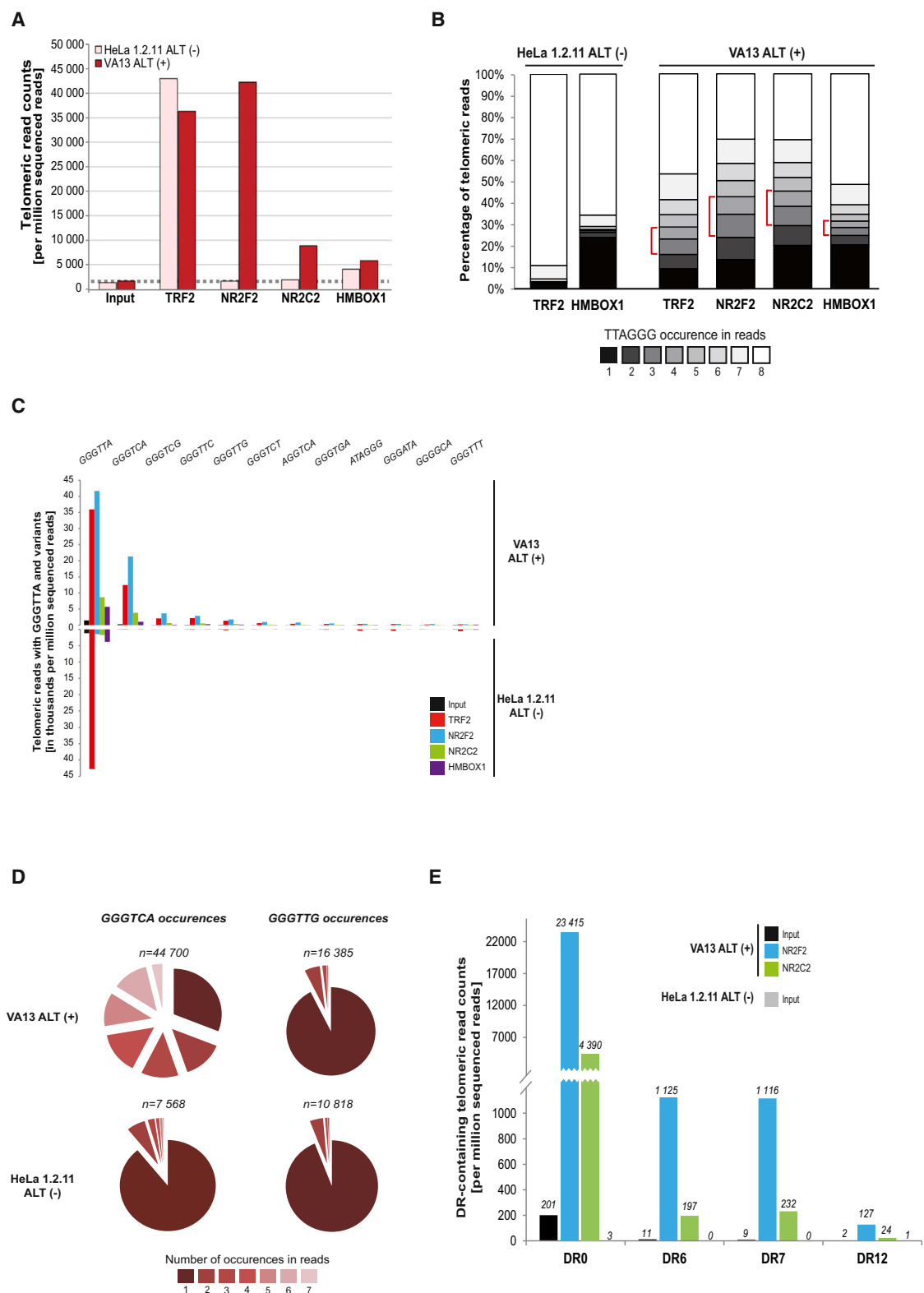
SUMMARY

The breakage-fusion-bridge cycle is a classical mechanism of telomere-driven genome instability in which dysfunctional telomeres are fused to other chromosomal extremities, creating dicentric chromosomes that eventually break at mitosis. Here, we uncover a distinct pathway of telomere-driven genome instability, specifically occurring in cells that maintain telomeres with the alternative lengthening of telomeres mechanism. We show that, in these cells, telomeric DNA is added to multiple discrete sites throughout the genome, corresponding to regions regulated by NR2C/F transcription factors. These proteins drive local telomere DNA addition by recruiting telomeric chromatin. This mechanism, which we name targeted telomere insertion (TTI), generates potential common fragile sites that destabilize the genome. We propose that TTI driven by NR2C/F proteins contributes to the formation of complex karyotypes in ALT tumors.

INTRODUCTION

Cancer is characterized by genomic alterations that lead to oncogene activation and/or tumor suppressor loss. These changes accumulate during tumor development and can be detected as translocations, amplifications, or deletions of chromosomal segments. Another major characteristic of cancer cells is their unlimited proliferative potential. This feature is dependent on the activation of a telomere maintenance mechanism upon exit from crisis (Hanahan and Weinberg, 2011). During cell crisis, genome instability and telomere dysfunction have been primarily linked through the classical mechanism of breakage-fusion-bridge cycle (BFB) first described by Barbara McClintock (McClintock, 1941). In this chain of events, unprotected or broken telomeres can fuse to another chromosomal extremity via non-homologous end joining. Fusions create di-centric chromosomes that eventually break at random positions during

mitosis, generating deletions and amplifications of chromosomal segments and more unprotected chromosome ends (Murnane, 2012). This cycle persists until chromosomal extremities get stabilized by telomere addition via telomerase activation. In human, telomerase is activated in the majority of cancers. However, in a subset of tumors, mostly sarcomas, telomeres are maintained by a recombination/amplification mechanism termed alternative lengthening of telomeres (ALT) (Bryan et al., 1997). These tumors typically harbor highly heterogeneous and complex karyotypes (Taylor et al., 2011). The lack of apparent specific translocations makes it challenging to identify the mechanism driving tumorigenesis in these cancers. Efforts to characterize these tumors are thus currently limited to identifying specific gene expression signatures (Chibon et al., 2010). Similarly, the mechanism underlying ALT activation and maintenance in these tumors is unknown. Because tumors in which telomerase is inhibited can activate ALT in mouse models (Hu et al., 2012), it is critical to dissect this pathway to design efficient anti-cancer therapies targeting telomere maintenance. We previously showed that orphan nuclear receptors of the NR2C/F classes (TR2, TR4, COUP-TF1, COUP-TF2, and EAR2), which belong to the nuclear hormone receptor (NHR) family of transcription factors, are aberrantly associated with telomeres in a prototypic ALT(+) cell line (Déjardin and Kingston, 2009). This finding was unexpected, as transcription factors usually associate with gene regulatory regions, and telomeres do not contain classical genes. Here, we address the biological relevance of this finding. We identify a critical role for these proteins in the ALT process and in active destabilization of the genome. We dissect the mechanism leading to their aberrant recruitment to telomeres, and we show that these proteins have a major architectural role: NR2C/F proteins can bridge together bound loci in the nuclear space. By promoting spatial proximity, NR2C/F proteins favor the telomere-telomere recombination necessary for ALT maintenance. Surprisingly, NR2C/F-driven spatial proximity also induces the tethering of telomeric chromatin to hundreds of regular NR2C/F-binding sites throughout the genome. This abnormal organization triggers the insertion of telomeric material to these sites, and this process depends on NR2C/F proteins. Insertions of telomeric DNA throughout the genome lead to the creation of potential common fragile sites that are known to be prone to breakage



and translocations. Because this mechanism of telomere-driven genome instability is fundamentally distinct from the BFB cycles and occurs as the consequence of the activation of a telomere maintenance mechanism, we name it targeted telomere insertions (TTI). In line with the role played by NR2C/F factors in TTI, we show that these proteins associate with telomeres in primary ALT tumors in situ and that this association correlates with the extent of karyotype rearrangements. Therefore, NR2C/F have a critical role in ALT and in the activation of TTI. We propose that this mechanism of telomere-driven genome instability induces heterogeneous genomes and contributes to the generation of complex karyotypes in ALT sarcomas (Taylor et al., 2011).

RESULTS

NR2C/F Factors Bind to Direct Repeats of a Variant Telomeric Motif

To get insights into the significance of NR2C/F binding to telomeres, we first examined how these factors are recruited. A mutant NR2C2 protein with point mutations disrupting DNA binding (Tanabe et al., 2007) fails to accumulate at telomeres (Figures S1A and S1B), suggesting that NR2C/F directly bind to DNA. NHR usually associate with DNA as dimers by binding to a composite sequence made of two half-sites (the 5'-A/GGGTCA-3' motif). Depending on the mutual orientation and spacing of these half-motifs, the full binding site varies extensively (Sandelin and Wasserman, 2005). Since the NHR half-site is related to the canonical telomere basic repeat unit 5'-GGGTCA-3', we hypothesized that NR2C/F could be recruited to ALT telomeres through binding to an iteration of the naturally occurring variant 5'-GGGTCA-3' (Allshire et al., 1989). We thus analyzed by chromatin immunoprecipitation (ChIP) combined with high-throughput sequencing the DNA sequences associated with NR2C2 and NR2F2, those associated with the canonical telomere-binding protein TRF2 (de Lange, 2005), and with HMBOX1, another DNA-binding protein that we previously identified at telomeres regardless of the maintenance mechanism (Déjardin and Kingston, 2009). This analysis was performed in both ALT(+) and in ALT(−) cell lines (WI-38 VA13 2RA and HeLa 1.2.11 cells, respectively) using validated antibodies (Figures S2A, S4A, and S7A). While TRF2 and HMBOX1 are enriched at both types of telomeres, NR2C2/F2 proteins bind only to ALT(+) telomeres (Figures 1A and S2A), consistent with our original findings (Déjardin and Kingston, 2009). Even when overexpressed, these factors cannot be detected at ALT(−) telomeres (Figure S1D), ruling out an effect due to differences in the expres-

sion level. To further characterize the binding mode of these factors, immunoprecipitated sequences were categorized according to their content in the canonical telomere motif GGGTCA (from one to eight occurrences in each 50-nt-long sequencing read). The canonical telomere motif has a similar distribution in the TRF2 and HMBOX1 libraries, implying similar binding specificity in both cell types (Figure 1B). In these libraries, the majority of enriched reads contains seven or eight occurrences of the canonical motif, suggesting that TRF2 and HMBOX1 bind to the canonical telomere sequence in vivo, as expected (Bilaud et al., 1997; Broccoli et al., 1997; Kappei et al., 2013). In contrast, reads associated with NR2C2/F2 showed a different distribution of GGGTCA occurrences, indicating a distinct binding specificity (Figure 1B). To characterize the motifs that allow specific NR2C2/F2 binding, we analyzed these reads further (red brackets in Figure 1B) and found that, among all possible sequences, the GGGTCA motif was specifically enriched in NR2C2/F2 reads (Figure 1C). This is in agreement with the classical sequence-specific binding mode for NHR and our original hypothesis (Benoit et al., 2006; Déjardin and Kingston, 2009; Conomos et al., 2012). Although less frequent (by ~6-fold), the GGGTCA motif is also present in ALT(−) telomeres, indicating that the simple presence of the motif is not sufficient to promote NR2C/F recruitment. Thus, we analyzed the occurrence of the NHR motif in telomeric reads. GGGTCA is essentially found as a multimer in ALT(+) sequences and as a monomer in ALT(−) reads (Figure 1D), suggesting that NR2C/F cannot be recruited to single GGGTCA motif at telomeres. Since these data suggest a classical binding mode for NR2C/F factors, we searched for the full binding sites for these proteins. We identified the direct repeats DR0, DR6, and DR7 (two half-sites in the same orientation and separated by 0, 6, or 7 nucleotides) as the major NR2C/F-binding sites at telomeres (Figure 1E), and these sites are, at least for DR0, ~80-fold enriched in ALT(+) compared to ALT(−) telomeric DNA. Therefore, NR2C/F recruitment is promoted by the presence of DR0, 6, and 7 motifs specifically in ALT telomeres.

The Telomere Protein TRF2 Binds to Hundreds of NR2C/F Regions throughout the Genome of ALT Cells

The aberrant recruitment of NR2C/F factors could suggest that telomeres potentially act as “molecular sinks” for these transcription factors in ALT cells. Titration could impinge on the binding and the regulation of NR2C/F targets, which would indirectly control ALT and/or tumorigenesis (Safe et al., 2014). Therefore, we analyzed the genome-wide binding profile of NR2C2 and

(B) TTAGGG content of telomeric reads in IPs from ALT(−) (left) and ALT(+) (right) cells. Histograms display for each library the percentages of telomeric reads containing one to eight TTAGGG occurrences. Red brackets highlight subsets of telomeric reads containing three or four TTAGGG occurrences that are strongly enriched in ALT(+) libraries.

(C) Percentage of telomeric reads containing the indicated repeat variant in ALT(+) and ALT(−) libraries prepared from input DNA, TRF2, NR2F/C, and HMBOX1 IPs. Variant repeats were identified within telomeric reads that contained three or four TTAGGG occurrences and were sorted based on their relative amount in telomeric reads from ALT(+) NR2C/F libraries.

(D) Pie charts showing that GGGTCA multimerization is specific for ALT(+) telomeres. The charts display the number of telomeric reads containing one to seven GGGTCA (left) or NHR unrelated variant “GGGTTG” (right) occurrences (n indicates the number of telomeric reads containing the GGGTCA or GGGTTG variants in ALT(+) and ALT(−) input libraries). GGGTTG is used as a control to show that multimerization is specific for the GGGTCA motif.

(E) Normalized number of telomeric reads containing GGGTCA DR0, DR6, DR7, and DR12 in libraries prepared from ALT(−) input and ALT(+) input and orphan receptors NR2F/C IPs.

See also Figures S1 and S2.

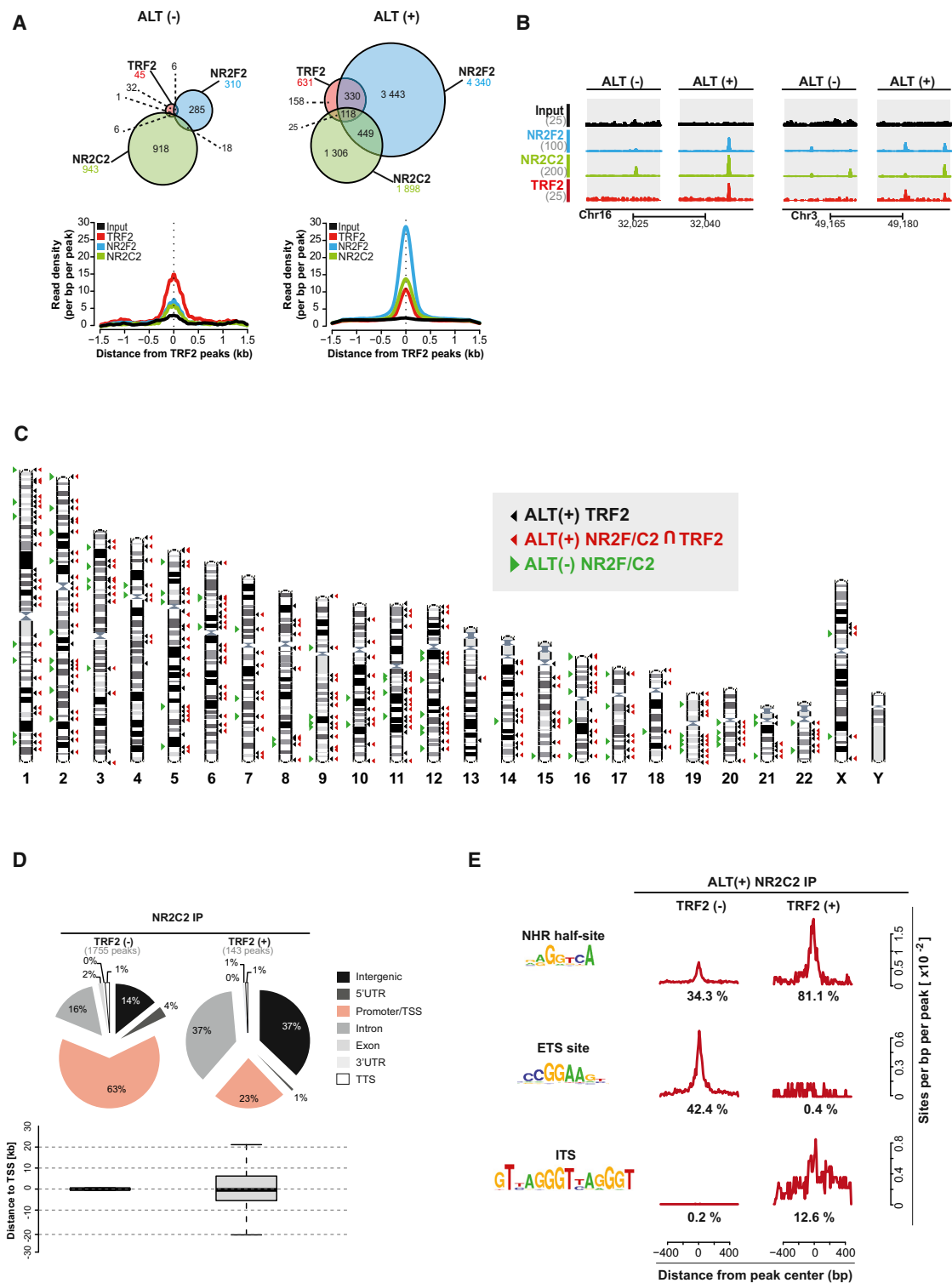


Figure 2. TRF2 Binds to Hundreds of Loci throughout the Genome in ALT Cells

(A) Overlap between TRF2- and NR2F/C-binding sites genome wide. (Top) Venn diagrams displaying peak overlap (values indicate the number of peaks). (Bottom) Average read densities in NR2F/C libraries relative to the TRF2 peaks.

(B) Density profiles of input, TRF2, and NR2F/C reads in two representative loci in ALT(-) and ALT(+). TRF2 is only bound in ALT(+).

(C) Chromosomal locations of ALT(+) TRF2 peaks, ALT(+) NR2F/C peaks overlapping with TRF2 peaks, and ALT(-)NR2C/F peaks.

(legend continued on next page)

NR2F2 and concluded that ALT(+) telomeres do not titrate these transcription factors since we identify more binding regions in ALT(+) than in ALT(−) genomes (Figure 2A). We also analyzed the genomic distribution of TRF2, as it supposedly binds not only to telomeres, but also to rare interstitial telomeric sequences (ITS) (Simonet et al., 2011). ITS contain a various number of iterations of the GGGTTA motif explaining TRF2 recruitment and are well-characterized common fragile sites (CFS) (Bosco and de Lange, 2012). Surprisingly in ALT(+) cells, we identified several hundreds of TRF2-binding sites (Figure 2A) that are not mapping to known ITS. However, most of these sites (75%) overlap with binding sites for NR2C2/F2 proteins (Figures 2A and 2B). Importantly, none of these regions were bound by TRF2 in ALT(−) cells, pointing to an ALT-specific binding mode for TRF2 (Figure 2B). In contrast, in ALT(−) cells, TRF2 binds only to 45 regions, 20 of which corresponded to known ITS often located in subtelomeric regions (Simonet et al., 2011) (Figures 2A–2C). Interestingly, when we looked at the position of these sites with respect to genes, we found that the NR2C2 regions that also recruit TRF2 have a broad distribution and are usually located far from gene promoters (Figure 2D). In contrast, the TRF2-negative NR2C2 regions are principally located at gene transcription start sites. Moreover, the sequence content of these two populations is different. The classical promoter-bound NR2C2 regions are enriched in the expected motifs, in particular the ETS binding sequence (O’Geen et al., 2010) (Figure 2E). On the other hand, the non-genic NR2C2 regions bound by TRF2 lack the ETS motif but are highly enriched in the GGGTCA motif (81% reads). Remarkably, most of these sites (~87%) also lack the canonical telomere sequence, excluding a classical DNA-mediated recruitment mechanism for TRF2. Thus, our data point to an unusual recruitment mode for TRF2 throughout the genome of ALT cells.

NR2C/F Proteins Induce Spatial Proximity of Their Binding Loci

A simple interaction between TRF2 and NR2C2/F2 only in ALT(+) cells is unlikely because a large number of NR2C2/F2 sites remain TRF2 free. Moreover, we failed to detect any interaction between TRF2 and NR2C/F proteins by coimmunoprecipitation (data not shown). Additionally, the absence of telomeric motifs at NR2C2/F2 sites likely excludes a direct TRF2 recruitment. Thus, we hypothesized that physical interactions between ALT telomeric material and endogenous NR2C/F-binding sites occur via NR2C/F proteins (Figure 3A). Accordingly, NR2C/F proteins would bridge ALT telomeres and extra-chromosomal telomeric material generated by the recombination process (Cesare and Griffith, 2004) together and to endogenous NR2C/F regions. By carrying over telomeric material, TRF2 is most probably cross-linked by formaldehyde “in *trans*” at endogenous NR2C/F regions, resulting in the appearance of enrichment peaks for TRF2 throughout the ALT genome at NR2C/F binding regions.

The same bridging feature would explain why telomeres extensively interact with each other in ALT cells. Classical methods to measure locus interactions like chromosome conformation capture (Dekker et al., 2002) are challenging for repetitive sequences like telomeres. Thus, to test telomere bridging by these factors, we used super-resolution three-dimensional structured illumination microscopy (3D-SIM), which improves spatial resolution by a factor of eight (Gustafsson et al., 2008). We expressed the DNA-binding mutant NR2C2 protein in the SaOS-2 ALT cell line. This mutant acts as a dominant-negative for endogenous NR2C2 (Tanabe et al., 2007), stripping it off telomeres (Figure S1C). In SaOS-2 cells, NR2C2 is the only orphan nuclear receptor bound to telomeres, suggesting that no other NHR could compensate for NR2C2 loss. The expression of this mutant disrupts telomere-telomere interactions, as shown by super-resolution microscopy (Figure 3B). The number of telomeric clusters is reduced, and this is accompanied by an increase in the number of single detectable telomere signals (Figures 3B–3E, S3A, and S3B). On the other hand, expression of the mutant form of NR2C2 in *HeLa* 1.2.11 ALT(−) line has no effect on telomere number (Figure S4C). Similar results were obtained upon simultaneously knocking down NR2C1, NR2C2, and NR2F2 (NR2C/F) proteins in the W38-VA13 ALT cell line (Figures S4A and S4B). Next, to evaluate bridging between telomeric material and non-telomeric NR2C/F regions, we developed an independent assay. In this approach, the sub-nuclear localization of a fluorescent plasmid DNA harboring NR2C/F DR0-binding sites can be tracked (Figure S3C). If our bridging hypothesis is valid, this plasmid should be targeted to ALT(+) telomeres, which concentrate NR2C/F proteins. In contrast, this plasmid should not co-localize with ALT(−) telomeres, which are devoid of NR2C/F factors. Indeed, despite the formation of large cytoplasmic aggregates in transfected cells, which were unavoidable, the plasmid is efficiently targeted to ALT(+), but not to ALT(−) telomeres (Figure S3C), whereas the control plasmid, not containing NR2C/F binding motifs, does not accumulate at telomeres. Moreover, this recruitment is NR2C/F dependent, as it disappears upon NR2C/F depletion by RNAi. Next, we measured whether NR2C/F tethering to a *LacO* transgenic locus non-homologous to telomeric sequences is sufficient to drive the proximity of that locus to ALT telomeres. We used a transgenic U2-OS ALT cell line containing a single *LacO* array (Robinett et al., 1996), in which we expressed a NR2C2-LacI fusion protein, able to bind to the *LacO* array in the absence of NHR binding motif. Tethering NR2C2-LacI to *LacO* leads to the extensive co-localization of the array to telomeric clusters (85% co-localization, Figure 3F), consistent with the bridging feature of this factor. Unexpectedly, this also leads to the appearance of multiple *LacO* signals co-localized with telomeric signals (82% of cells were showing, on average, ten independent *LacO* foci), suggesting a dramatic instability of the *LacO* array upon interaction with ALT telomeres. Neither the tethering of GFP alone nor the

(D) Distribution of NR2C2 peaks overlapping (+) or not (−) with TRF2 peaks in ALT(+) cells. (Top) Pie charts displaying categories according to the nearest transcriptional start site (promoter, TSS). (Bottom) Boxplots showing the distribution of NR2C2 peaks to the nearest TSS.

(E) Overrepresented motifs in NR2C2 peaks overlapping (+) or not (−) with TRF2 peaks in ALT(+) cells (red curves display the average location of the motif around central peak positions, and values indicate the percentage of peaks containing the motif). See also Figures S1 and S2.

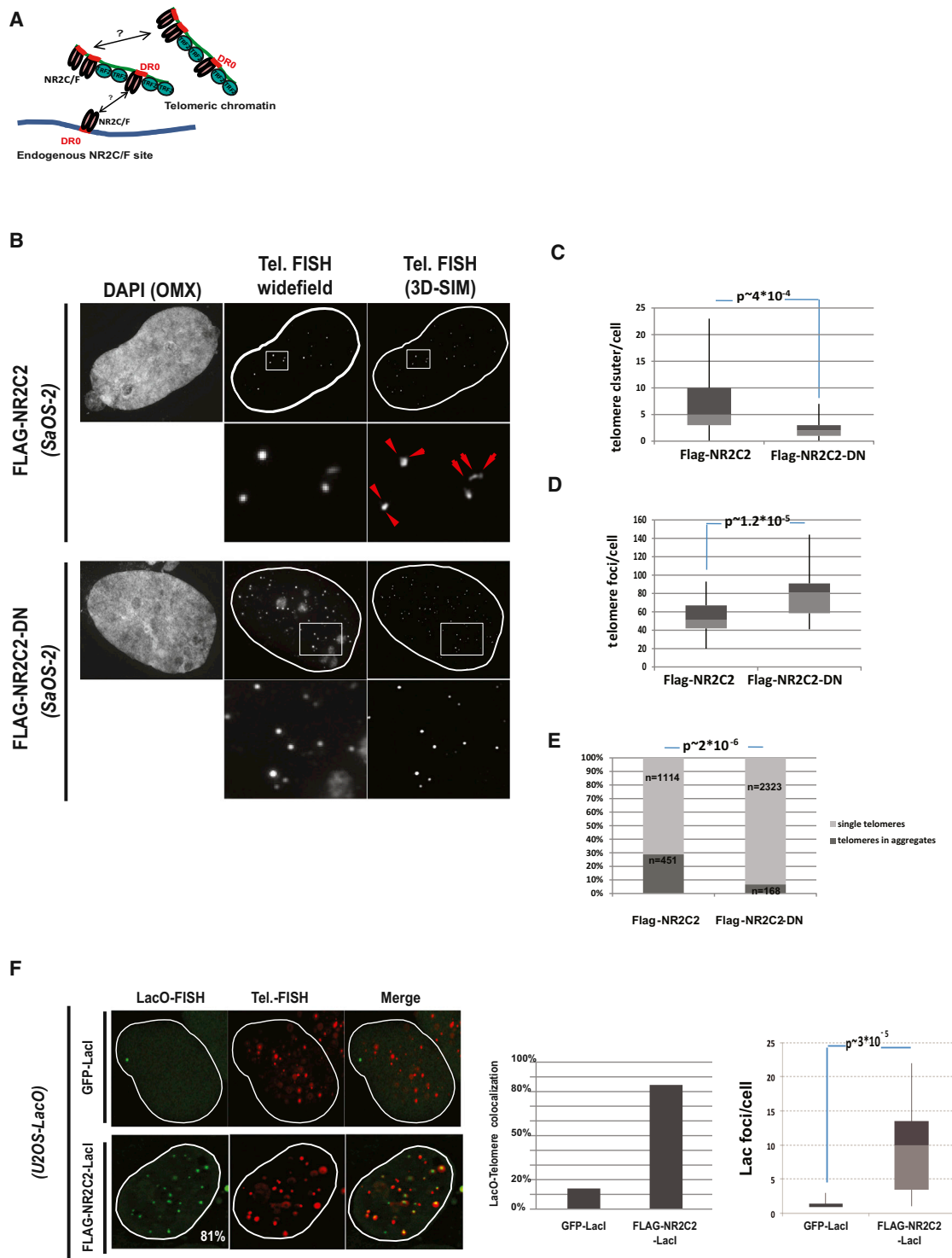


Figure 3. Locus Proximity Induced by NR2C/F Proteins

(A) Model of NR2C/F-induced proximity of telomeric and genomic sites. The same model applies to the telomere/telomere proximity necessary for recombination in ALT.

(B) Telomere FISH showing “de-clustering” of telomeres (visible by 3D-SIM super resolution microscopy) and increased number of telomeric foci upon NR2C2-DN expression in SaOS-2 cells, suggesting that telomere/telomere interactions are dissociated. The arrowheads indicate single telomeric foci within clusters. Clusters were defined as single signals in the wide field mode, which could be resolved as at least two individual signals in super-resolution mode. Right panels

(legend continued on next page)

tethering of NR2C2-LacI in a transgenic *HeLa* ALT(–) cell line harboring a single *LacO* array leads to its telomeric re-localization, or an amplification of *LacO* (Figures 3F and S3D). Altogether, our data demonstrate that NR2C/F binding is necessary for telomere-telomere proximity and for bridging bound loci to telomeres in the nuclear space. The amplification of *LacO* in the NR2C2 tethering experiment also suggests that bridging to ALT telomeres likely induces instability of the co-localized locus.

Telomere DNA Insertions at NR2C/F Regions in the Genome of ALT Cells

Physical interactions between translocating loci is a major requirement for chromosomal translocations. In fact, translocations are primarily driven by the spatial organization of chromosomes in the nucleus (Misteli and Soutoglou, 2009). Chromosomal architecture must be highly perturbed in ALT cells because ALT genomes show complex chromosome rearrangements with multiple heterogeneous translocations (Guillou and Aurias, 2010; Jain et al., 2010; Lovejoy et al., 2012). Since NR2C/F proteins can drive the physical interaction of bound loci and their apparent instability, we asked whether this feature could trigger instability at endogenous NR2C/F loci. We hypothesized that the genomic NR2C/F-binding sites interacting with telomeric material could also be sites of telomere sequence insertion. Telomeric DNA insertions at discrete genomic sites should yield composite sequencing reads that fail to be aligned to the reference genome. Thus, we focused our analysis on sequencing reads that had mismatches. In both ALT(+) and ALT(–) cell lines, ~90% of the input libraries contain perfectly mappable reads, suggesting comparably high sequencing quality (Figure S2B). Likewise, reads mapping to repeated DNA are of comparably high quality (~88% aligned perfectly). However, while telomere reads from ALT(–) cells are also of high quality, telomere reads from ALT(+) cells are more degenerated and ~25% cannot be aligned without allowing mismatches (Figure S2B). To characterize this telomere specific discrepancy, we analyzed TRF2 libraries in both ALT(+) and ALT(–) cells and examined the sequence organization of the reads that could not be aligned to the reference genome. This showed that, among all possible random hexamers in rearranged sequences, there is a striking bias for the canonical GGGTTA and the variant GGGTCA motifs in ALT(+) samples (Figure 4A). This indicates that, specifically in ALT cells, reads containing these motifs are prone to rearrangements, regardless of their location in the genome. We extended this analysis to NR2C2, NR2F2, and HMBOX1 libraries. Reads in the NR2C2 and NR2F2 libraries are even more degenerated than in the TRF2 and HMBOX1 libraries (Figures S2C and S2D), suggesting that NHR binding re-

gions are intrinsically more unstable. To get insights into the nature of these rearranged sequences, we analyzed their content in details using the strategy depicted in Figure 4B. Strikingly, these rearranged sequences are composed of a part mapping to unique genome regions and aberrant random additions of GGGTCA and/or GGGTTA sequences (Figure 4B, bottom), suggesting that they can result from insertions of telomeric DNA. These insertions do not occur at a precise position but are always located close to (<30 nt) DR0 motifs. The systematic presence of DR0 motifs in the non-rearranged portion of these reads points to the involvement of NR2C/F proteins in targeting the local rearrangement between ALT telomeric DNA and endogenous NR2C/F-binding sites. The few ALT(–) sequences that could not be mapped to the genome contain mostly single-nucleotide changes with no motif addition, suggesting that they did not arise from telomeric DNA insertion. In ALT cells, the rearranged reads map to 23 distinct genomic regions of which 19 (~82%) corresponded to TRF2-positive NR2C/F peaks (Figure S6D). This indicates that only a small subset (19/473, ~4%) of NR2C/F regions able to recruit telomeric material are in fact loci for targeted telomeric insertions (TTI) in ALT cells.

NR2C/F-Driven Telomeric DNA Insertions at DNA Double-Stranded Breaks Are Involved in Chromosomal Translocations in ALT Cells

Artificial insertion of telomeric DNA inside genomes creates ITS, and this has been shown to promote chromosome rearrangements (Kilburn et al., 2001). Because ITS are potential common fragile sites (Bosco and de Lange, 2012), addition of telomeric DNA throughout the genome by TTI can be viewed as a source of genome instability. As TTI parallels ALT, it must be an ongoing mechanism in proliferating cells. To demonstrate that TTI is an active process in ALT cells, we tried to provoke telomere sequence addition throughout the genome. To this aim, we induced DNA double-strand breaks (DSB) by drug treatments or γ irradiation and looked for telomere insertions at these sites by scoring the number of ITS signals on metaphase chromosome spreads. Detectable ITS are more frequent in untreated ALT(+) than ALT(–) chromosomes (~5-fold), in line with our sequencing data showing enrichment in telomeric sequences at genomic sites in ALT(+) cells (Figure 5A). Upon DSB induction, they double in ALT(+). No change was observed in ALT(–) chromosomes, suggesting that breaks are normally repaired without telomeric sequences added in this cell line (Murnane, 2012). In ALT cells, ~30% of both pre-existing and newly formed ITS sites are also bound by NR2C2 and 39% by TRF1, indicating their telomeric origin (Figures 5B and 5C). Consistent with previous data (Bosco and de Lange, 2012), these sites are potentially

show the boxplot quantification of this effect. Top and bottom boxes show the first and third quartile around the mean. p values are from a two-sided Student's t test.

(C) Loss of telomere clustering upon NR2C2 DN expression (aggregate).

(D) Increase in detectable single telomere number.

(E) Distribution of telomeres as individual or clustered signals as measured by super-resolution microscopy. p value from a two-sided Student's t test.

(F) (Left) FISH in U2-OS cells harboring the *LacO* transgenic array. Cells were transfected either with GFP-LacI (top) or Flag-NR2C2-LacI (bottom). (Middle) Chart displaying the co-localization of *LacO* with telomere signals. (Right) Chart measuring the extent of *LacO* signal amplification as counted by the number of individual Lac signals in transfected cells. Right panel shows the boxplot quantification of this effect. Top and bottom boxes show the first and third quartiles around the mean. p values are from a two-sided Student's t test.

See also Figures S3 and S4.

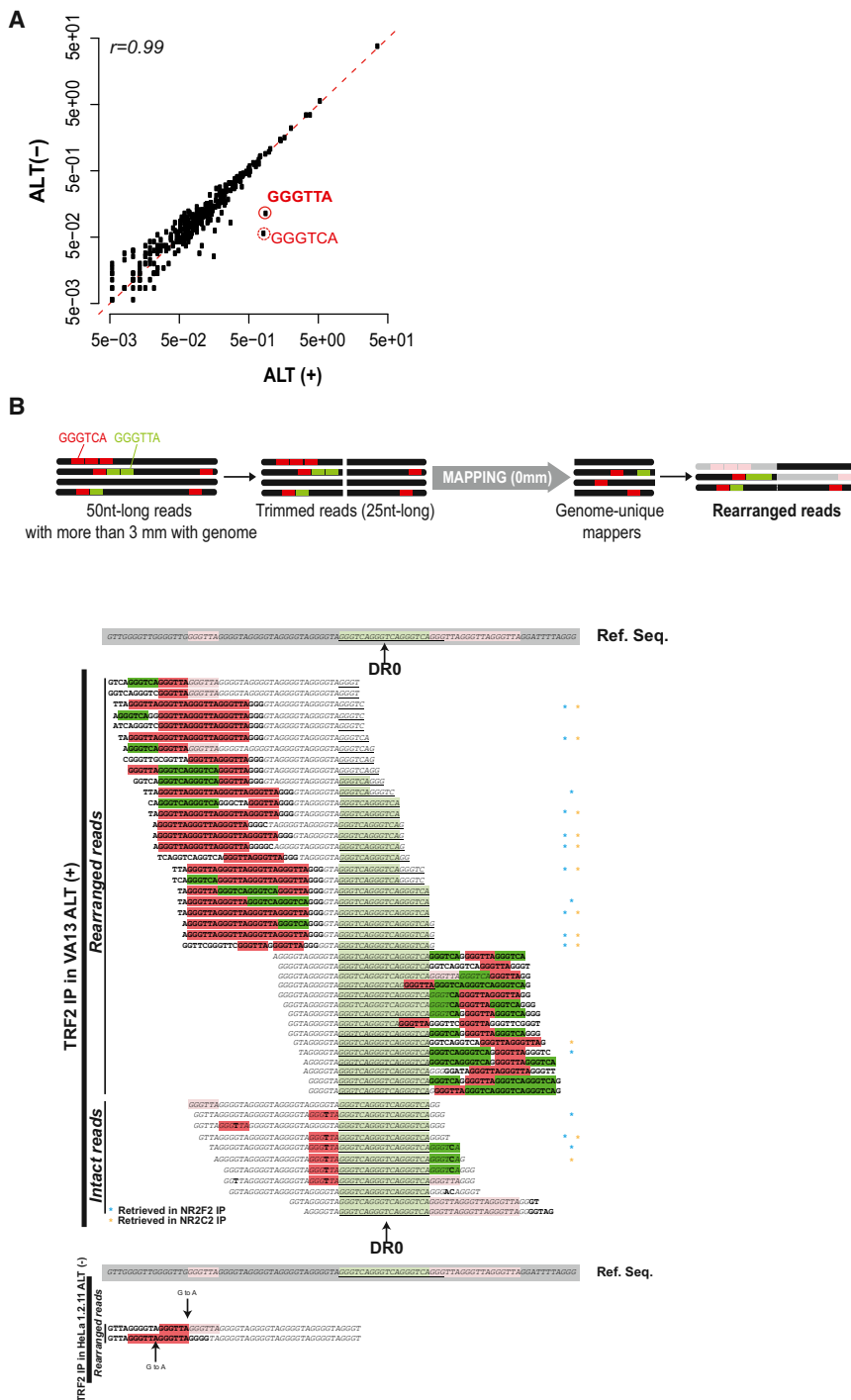


Figure 4. Degenerated Sequencing Reads in ALT Cells Contain Telomeric Motifs

(A) Plot showing the frequency of degenerated reads (≥ 3 mismatches) containing different hexamers in ALT(-) and ALT(+) TRF2 IPs. Each dot represents a different hexamer. Circled in red: hexamers that are abundant in ALT(+), but not in ALT(-).

(B) (Top) Flowchart displays the strategy to identify "rearranged reads" (see Experimental Procedures). Briefly, non-mappable 50-nt-long reads were split in two 25-nt-long "trimmed" reads that were then individually mapped onto the genome. Non-mappable reads with at least one "trimmed" read that mapped uniquely were considered as "rearranged." (Bottom) Representative examples of rearranged and intact reads mapping near a putative OR-binding site (DR0 underlined) of the Chr2 fusion ITS (reference genome sequence from the hg18 assembly on the top) retrieved from the TRF2 IP library in ALT (+) (top) and ALT(-) (bottom) cells. Bold letters highlight mismatched nucleotides relative to the reference sequence, and italic letters perfectly mapped nucleotides. Red and green boxes highlight GGGTTA and GGGTCA repeats, respectively, found in the reference genomic sequence (light color) or only in the rearranged reads (dark). Asterisks highlight rearranged reads identified also in the NR2F/C2 libraries. In the ALT(-) panel, the arrows indicate single-nucleotide substitutions.

DSB induction (up to 30% of fused chromosomes). This also suggests the involvement of NR2C/F proteins in preventing chromosomal fusions, a necessary condition for the maintenance of telomeric integrity in ALT cells. Similar results were also obtained in another ALT(+) cell line and with another DNA-damaging agent (Figure S5B), demonstrating that telomere sequence addition to broken chromosomal sites is common in ALT. Moreover, because NR2C/F depletion has no major effect on TRF1 and TRF2 levels (Figure S4A), this effect is unlikely due to a shelterin defect but suggests a protective role for NR2C/F factors on ALT telomeres. Since internal telomeric DNA has the inherent potential to form common fragile sites (CFS) in the human genome (Bosco and de Lange, 2012) and telomeres are fragile sites (Sfeir

et al., 2009), we reasoned that TTI should have the potential to form translocations. Such translocations could leave telomeric DNA between two chromosomal segments. DSB induced by γ irradiation in the VA13 cell line resulted in 88 unique random break points on 693 analyzed chromosomes. 33% (29) of scored translocations have detectable telomeric signals at the translocation points between segments from distinct chromosomes,

fragile sites, as we observed increased breakage upon combined TRF1 knockdown and aphidicolin treatments (Figure S5A). TTI is NR2C/F dependent because no new ITS formed upon NR2C1, NR2C2, and NR2F2 silencing (Figure 5C). Moreover, NR2C/F-silenced cells have a significantly higher number of chromosomal fusions (arrowheads in Figure 5D), mostly without detectable telomeric signal. These fusions greatly increase upon

as measured by SKY-FISH and telomere FISH on metaphase spreads (Figures 5E and S6 and Table S1). Out of these 29 events, 13 do not involve terminal fusions, suggesting that TTI occurs frequently (~15% of scored translocations) when cells are challenged. Thus, telomeric DNA likely participates in chromosomal translocations in ALT cells.

Binding of NR2C/F Proteins to Telomeres Is a Hallmark of ALT in Tumors and Correlates with the Extent of Genome Rearrangements

To directly explore the link between NR2C/F association to telomeres, genome instability, and cancer in humans, we checked whether these proteins can also be found on telomeres in human primary tumors. We analyzed 180 primary sarcomas from the “complexity index in sarcoma” (CINSARC) signature collection (Chibon et al., 2010) by immunofluorescence and FISH on tissue microarrays (see Table S2 for tumors data). ALT nuclei contain structures called ALT-associated pro-myelocytic leukemia bodies (APB), in which the telomeric DNA is abnormally associated with the PML protein. The presence of APB is a diagnostic marker of ALT (Henson et al., 2005). Accordingly, we scored 54.4% primary tumors analyzed as ALT(+) because these tumors have detectable APB. This is in line with the average ALT occurrence in sarcomas (Henson and Reddel, 2010), validating our approach. The vast majority of ALT(+) tumors (~79%) also show telomeric accumulation of NR2F2 or NR2C2 (Figures 6A and 6B). We also analyzed healthy tissue sections surrounding 12 distinct tumors, and none (0/12) show NR2C2/F2 telomeric accumulation (Figure S7 and Table S3). Thus, NR2C/F telomeric accumulations are cancer specific and do not predate tumor development. Importantly, the extent of NR2C/F association to telomeres correlates with the tumor grade (25% in grades 1 and 2, versus 61% in grade 3) (Figure 6C). As tumor grade is a strong indicator of genome complexity in sarcomas (Chibon et al., 2010), increased telomeric accumulation of NR2C/F proteins mirrors increased genome rearrangements. This suggests the involvement of NR2C/F proteins in generating complex karyotypes in human sarcomas.

DISCUSSION

Telomeres are important protective chromosomal structures that safeguard the genome. When telomeres are deprotected, classical BFB cycles ensue and lead to genome alterations. These alterations include deletions and amplifications of chromosomal segments typically observed in tumors (Figure 7A). The BFB cycles, although probably arising as a consequence of the initial loss of important genome surveillance mechanisms, favor the acquisition of oncogenic mutations or accelerate the loss of surveillance pathways that characterize transformed cells (Artandi et al., 2000). Importantly, BFB cycles are stopped when broken chromosomal extremities are healed by the addition of telomeres. Chromosomal healing is usually achieved by the reactivation of telomerase, which is involved in the creation of functional telomeres. Therefore, it is thought that the acquisition of telomere maintenance by telomerase reactivation stabilizes the transformed genome

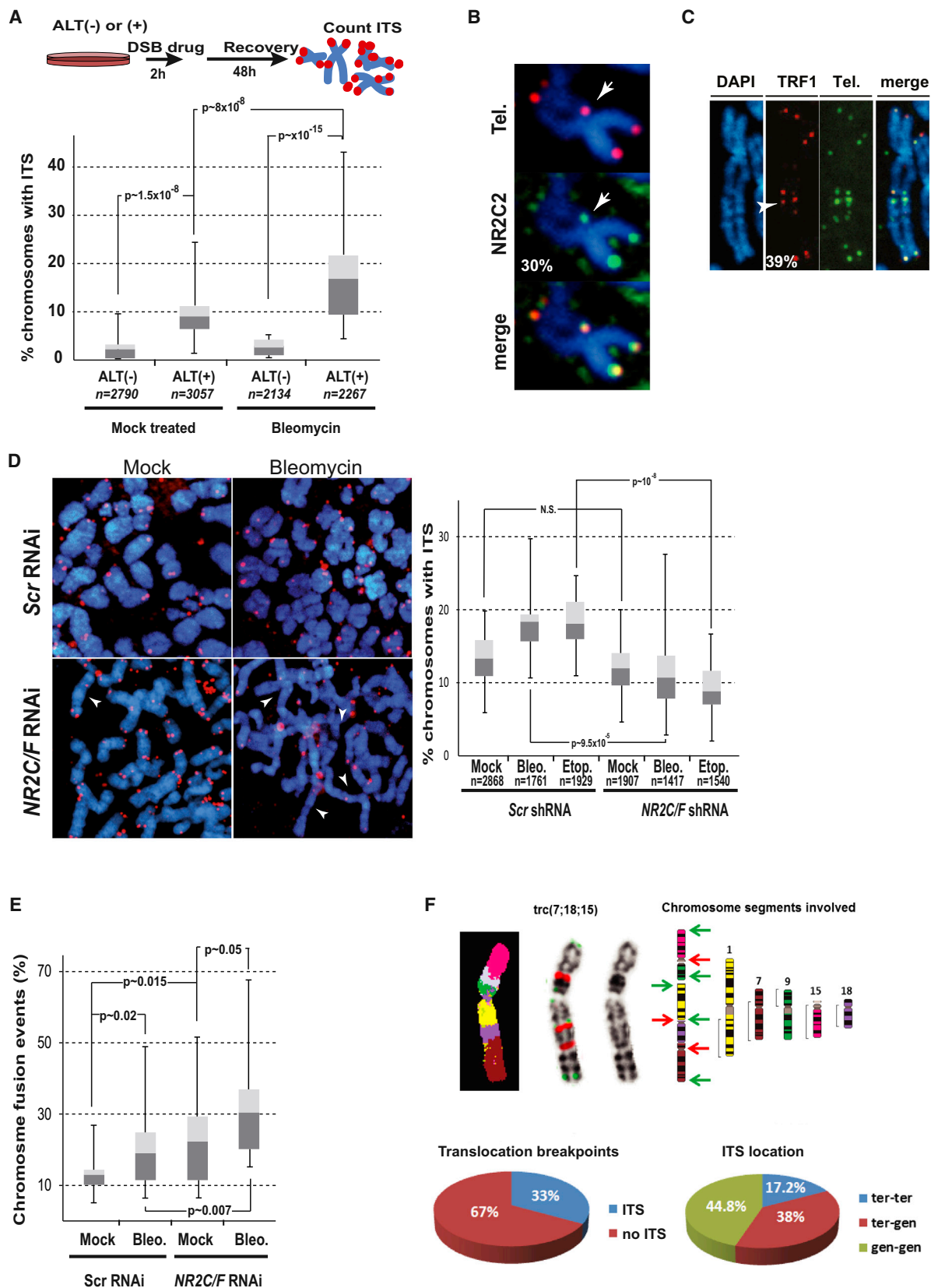
and favors an unlimited proliferation of selected transformed cells. Here, we describe another mechanism of telomere-driven genome instability that actually occurs as a consequence of the activation of aberrant telomere maintenance (Figure 7B). In contrast to the genome stabilization conferred by telomerase, we show that ALT activation also directly destabilizes the genome, using an unexpected mechanism that we name targeted telomere insertion (TTI). We propose that TTI contributes to the complex karyotypes found in tumors or cell lines in which ALT is activated.

NR2C/F-Mediated Long-Distance Interactions

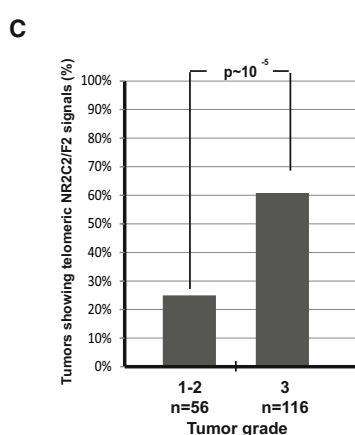
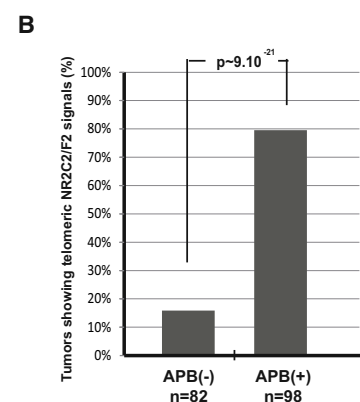
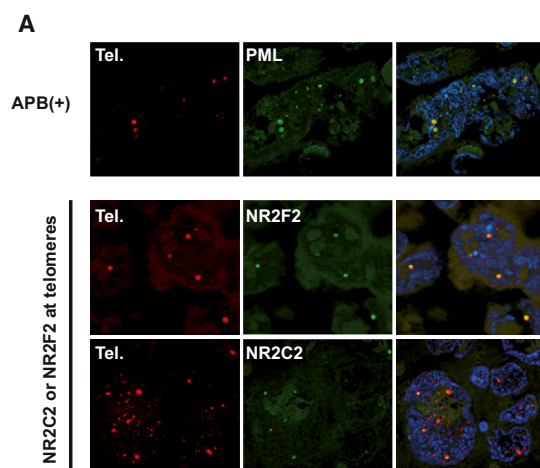
The massive recruitment of orphan nuclear receptors at telomeres in most ALT tumors or cell lines underlies a requirement to maintain a critical function. Consistently, loss of these proteins leads to defective telomere maintenance (Conomos et al., 2012; Déjardin and Kingston, 2009) and chromosomal fusions (Figure 5D). We found no evidence for a role of NR2C/F proteins in transcribing telomeres (data not shown), but we show here that this function is structural. By inducing the proximity of their binding loci, NR2C/F proteins promote physical interactions of telomeric material, a necessary requirement for recombination. An unexpected consequence of this bridging ability is that telomeric material is also able to physically interact with non-telomeric NR2C2/F2-binding sites throughout chromosomes. This represents a further confirmation that bridging is a major feature of NR2C/F proteins. Intriguingly, not all NR2C/F genomic sites have this ability. Telomere-genome interactions usually occur at NR2C/F regions located at a distance from genes, while promoters bound by NR2C/F do not seem to be involved. We believe that the regions able to contact telomeres might be enhancers because these elements are known to interact at long distance and organize local chromosomal architecture (Smallwood and Ren, 2013). How would regions bound by the same transcription factors be located in close physical proximity? We can think of at least two possibilities: either these proteins bind to a shared machinery/structure available in limiting amounts, or these factors have the ability to engage into homotypic interactions. In line with this, RXR proteins, which belong to the NR2B family of NHR, have been shown to be able to oligomerize *in vitro* (Chen and Privalsky, 1995). The biological significance of such architectural ability is not totally clear, but the clustering of co-regulated regions (presumably bound by the same factors) is a recurrent feature. A benefit of clustering/compartmentalizing nuclear transactions is to increase the local concentration of reactive species to ensure the robustness of biological processes (Déjardin, 2012).

Targeted Telomere Insertions: Implications for Genome Stability

Another NHR, the androgen receptor (AR), was shown to drive the proximity of a subset of its target genes upon hormone induction (Lin et al., 2009; Mani et al., 2009). Combined with genotoxic stress, proximity is required to promote cancer-specific translocations. We show here that the bridging function conferred upon NR2C/F binding drives telomere sequence additions throughout the genome upon genotoxic stress. Thus,



(legend on next page)



we believe that, in cancer cells, the bridging ability of transcription factors, ordinarily used to modulate gene expression, is frequently diverted to trigger chromosomal translocations. In contrast to the well-defined translocation that AR controls in prostate cancer, TTI yields heterogeneous rearrangements. We think that TTI contributes to the appearance and maintenance of complex mutator phenotypes at least at two levels: (1) the ongoing insertions of telomeric DNA at regulatory re-

a subset of complex chromosomal rearrangements in these cancers.

EXPERIMENTAL PROCEDURES

Cell Culture

The U2-OS, WI-38 VA13 2RA (VA13 throughout the text), and Saos-2 cell lines were obtained from ATCC. The HeLa 1.2.11 cell line was kindly provided by

Figure 6. Telomeric NR2C/F Correlate with Sarcoma Grades

(A) Most APB-positive sarcoma samples show NR2C/F localization at telomeres. Immunofluorescence (IF)/telomere FISH in grade 2 leiomyosarcoma biopsies. (Top) APB scoring by co-localization of the FISH signal (red) to PML bodies (green). (Bottom) Localization of NR2C2 or NR2F2 (green) at telomeres (red) in the same tumors. (B) Frequency of telomeric NR2C/F in APB(+) and in APB(-) tumors based on the IF/FISH analysis. p value from a two-sided t test. (C) The frequency of NR2C2/F(+) telomeres increases with the tumor grade. See [Extended Experimental Procedures](#) for staining procedures. See also [Figure S7](#) and [Tables S2](#) and [S3](#).

gions probably directly affect neighboring gene regulation, and (2) inserted telomeric DNA, which was shown to be prone to breakage, can contribute to elevated genomic instability. Our sequencing analysis could not allow us to measure the size of inserted telomeric DNA, but the detection of newly formed ITS by FISH ([Figure 5C](#)) suggests that these additions could extend to several kilobase pairs. Sarcomas in which ALT is active have been shown to systematically harbor complex karyotypes with non-specific translocations ([Montgomery et al., 2004](#); [Scheel et al., 2001](#)). Although we cannot exclude that other mechanisms could be involved, we propose that TTI contributes to generating

Figure 5. Translocation Breakpoints Contain ITS in ALT Cells

(A) (Top) Outline of the ITS induction assay; (bottom) boxplot showing the percentage of chromosomes with ITS signals in different conditions. Top and bottom boxes show the first and third quartiles around the mean. p values are from a two-sided Student's t test. (B) IF/FISH showing localization of NR2C2 (green) to a DSB-induced ITS signal (red) on a metaphase chromosome (VA13 cells). (C) IF/FISH showing localization of TRF1 (red) to a DSB-induced ITS signal (green) on a metaphase chromosome (VA13 cells). (D) (Left) Telomeric FISH on chromosome spreads of Scr RNAi and triple knockdown VA13 cells after DSB drug treatment (bleomycin) showing chromosome fusions (arrows); mock, no treatment. (Right) Boxplot displaying induction of ITS sites in Scr RNAi and in triple of NR2C1, NR2C2, and NR2F2 knocked down VA13 cells, treated or not with a DSB inducing drug. Top and bottom boxes show the first and third quartiles around the mean. p values are from a two-sided Student's t test. (E) Boxplot quantification of the fusion events. Top and bottom boxes show the first and third quartiles around the mean. p values are from a two-sided Student's t test. (F) (Upper-left) SKY-FISH combined with telomere (green) and centromere (red) FISH showing interstitial telomeric signals at the translocation points between chromosomes 1, 7, 9, 15, and 18 in the ALT+ VA13 cell line. (Upper-right) Graphical representation of the rearranged chromosome. (Bottom) Distribution of translocation events with or without ITS sites upon γ irradiation. ter-ter, telomere-telomere translocations; ter-Cen, telomere-centromere translocations; gen-gen, telomere-genome translocations.

See also [Figures S5](#) and [S6](#) and [Table S1](#).

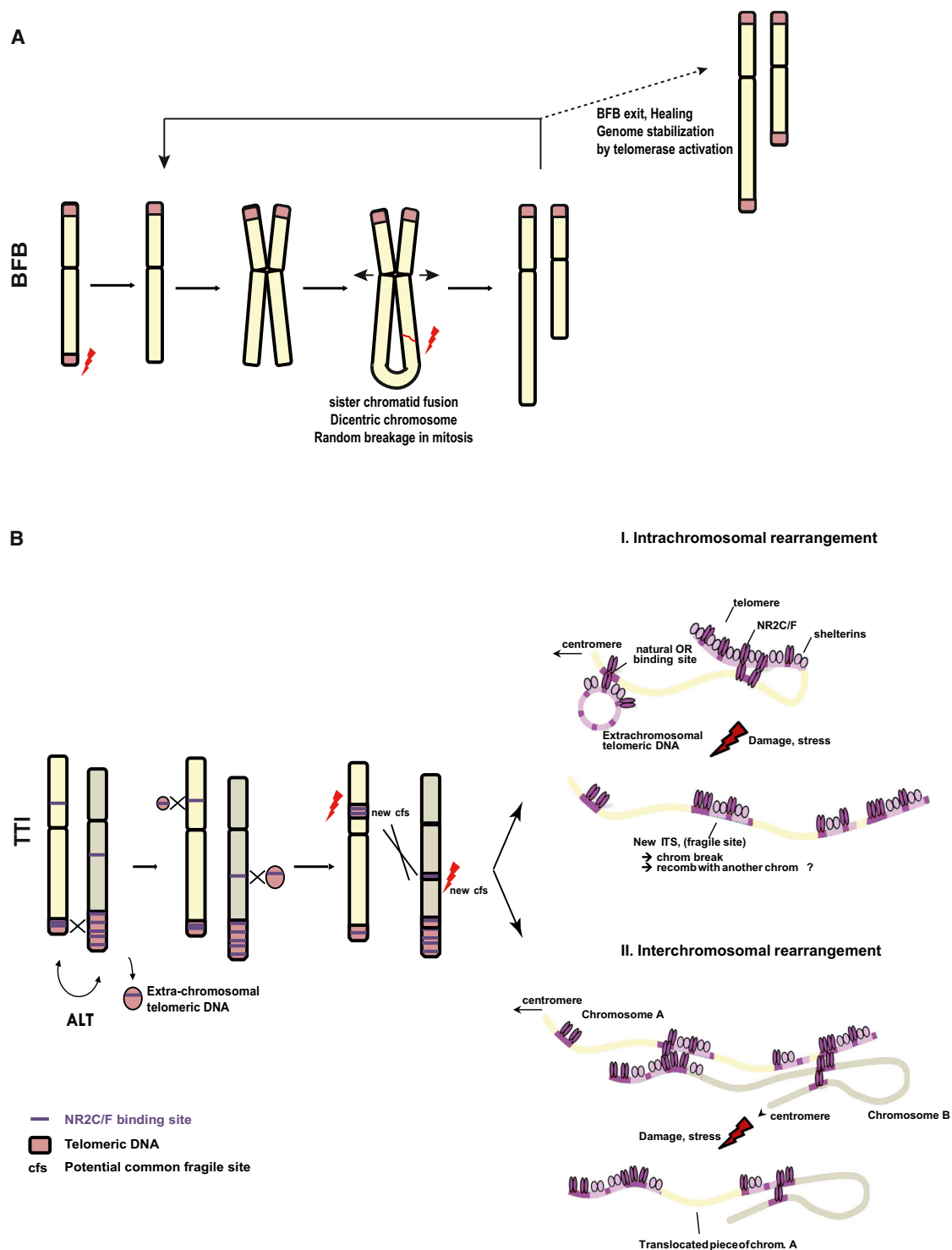


Figure 7. Comparison of TTI with BFB

(A) Outline of the BFB cycles. Instability is stopped by the acquisition of telomerase. (B) Outline of the TTI. Instability is further enhanced by ALT. Insertions of telomeric DNA lead to the creation of potential fragile sites at endogenous NR2C/F binding regions. Two possible outcomes are highlighted upon breakage of these sites, intra- or inter-chromosomal rearrangements.

Titia de Lange. All were cultured in DMEM Glutamax (Life Technologies) supplemented with 10% FBS (Eurobio). *U2-OS* and *HeLa* cell lines, harboring single genomic insertions of the *LacO* array, were cultured with hygromycin B.

Cell Immunofluorescence

Staining was performed as described before (Déjardin and Kingston, 2009), using the following antibodies: anti-TRF2 (Abcam [13579]); anti-PML (Santa Cruz Biotechnology [sc-5621/sc-966]); anti-NR2C2 (PPMX [PP-H0107B-00]); anti-HMBOX1 (Abcam [ab97643]); anti-NR2F2 (Abcam [ab50487]), anti-Flag (Sigma [F7425]). Secondary antibodies: Jackson ImmunoResearch (anti-rabbit DyLight 488 [711-485-152]; anti-mouse DyLight 488 [715-485-150]; anti-mouse DyLight549 [715-505-150]; anti-rabbit DyLight 549 [711-505-152]; anti-mouse DyLight649 [715-495-150]; anti-rabbit DyLight 549 [711-495-152]).

IF/FISH and FISH

After incubation with secondary antibodies, cells were cross-linked at 37°C in 3.6% formaldehyde for 20 min and then incubated at 75°C in 2×SSC for 1 hr and in 0.1M NaOH for 10 min and rinsed with 2×SSC. Then, cells were dehydrated by successive 75% and 100% ethanol baths and air dried. Slides were incubated at 82°C with a telomeric-C PNA probe coupled with FAM or Cy3 (Panagene [F1001/F1002]) for 2 min and then at 37°C for 12 hr. The probe was diluted in hybridization buffer (10% dextran sulfate, 50% deionized formamide, 2×SSC) to the final concentration of 50 mM. Then, cells were washed with 2×SSC at 42°C for 20 min. Finally, slides were mounted in ProlongGold (Life Technologies).

Structural-Illumination-Based Super-Resolution Microscopy and Telomere Clustering

Telomeres were labeled with a PNA probe using the FISH protocol described above. Full z stacks were acquired for each nucleus using the 100× objective. Telomeric signals were counted on Z projections of nuclei. If more than one telomeric signal could be distinguished within a telomeric focus, then such focus was scored as a telomeric cluster.

Targeting *LacO* to Telomeres

Cells were transfected either with GFP-LacI or with GFP-LacI and Flag-NR2C2-LacI, and the array was visualized either with the GFP or by *LacO*-specific FISH. Transfections were performed using the AMAXA nucleofactor device using nucleofector reagent from Mirus according to manufacturers' instructions. Quantification of *LacO* localization to telomeres was performed 48 hr after transfection.

Transfections and Constructs

We performed triple NR2C/F knockdown because neither single nor double knockdowns had a strong impact on ALT telomeres, probably because of redundant function (Déjardin and Kingston, 2009). The triple knockdown was performed with Stealth RNAi (Life Technologies) using Lipofectamine RNAiMAX (Life Technologies). The oligonucleotides were transfected twice within 48 hr. RNAi oligonucleotides used in the experiment were: siRNA negative control Med GC, NR2F2 [NR2F2MSS235955], NR2C1 [NR2C1HSS110947], and NR2C2 [NR2C2HSS110950]. Flag-NR2C2 and Flag-NR2C2-DN were kindly provided by Osamu Tanabe. Constructs were transfected using the AMAXA Cell Line Nucleofector Kit R (VA13 cells) or Kit V (Saos-2 cells) according to the manufacturer's instructions.

ITS Induction

Asynchronously growing cells were incubated with bleomycin (Calbiochem, 30 mU/ml) or etoposide (Sigma, 10 μM). After 2 hr, the drug-containing medium was replaced with fresh medium, and colcemid was added 43 hr after drug release to prepare chromosome spreads. We quantified the interstitial telomeric FISH signal on single and (rare) fused chromosomes. In triple *Nr2c/f* knockdown, because of the high frequency of chromosomal fusions, we quantified the interstitial telomeric FISH signal only from single (not fused) chromosomes to avoid counting fused chromosomes with residual telomere signal as ITS.

Aphidicolin Treatment and TRF1 Knockdown

Cells were treated with low doses (0.3 μM) of Aphidicolin for 24 hr. Aphidicolin was added 24 hr after a second TRF1 RNAi transfection (two RNAi transfections within 48 hr). After 20 hr of Aphidicolin treatment, colcemid was added to medium to induce mitotic arrest. RNAi used for TRF1 knockdown was purchased from Dharmacon (SmartPool RNAi).

Western Blotting

Nuclear extracts from transfected cells were run on 12% Bis-Tris gels (Life Technologies [NP0341]) and transferred to PVDF membranes using a liquid transfer system for 2 hr at 300 mA. The membrane was blocked for 30 min at room temperature in 1× PBS containing 5% milk and then incubated with primary antibodies diluted 1/1,000 in the same buffer for 2 hr at room temperature, washed twice for 15 min in PBS-0.05% Tween 20, and incubated for 1 hr with secondary antibodies diluted 1/5,000 in 5% milk-PBS which was followed by two washes in PBS-0.05% Tween 20. Antibodies: αFlag (Sigma [F7425]), αNR2C2 (PPMX [PP-H0107B-00]), αHMBOX1 (Abcam [ab97643]), αTRF2 (Abcam [ab13579]), αTRF1 (Abcam [ab10579]), αNR2F2 (Abcam [ab50487]), αNR2C1 (Santa Cruz [sc-9087]), αPCNA (Santa Cruz [sc-25280]), anti-rabbit-HRP (Sigma [A0545]), anti-mouse-HRP (Sigma [A4416]).

ChIP Sequencing

Cells growing in monolayer were cross-linked in 1% formaldehyde/PBS for 10 min, washed twice in PBS, and scraped in PBS/0.05% Tween. Then cells were pelleted, washed in PBS, and incubated at 4°C in lysis buffer 1 for 10 min, then at room temperature in lysis buffer 2 for 10 min, dounced with a tight pestle, centrifuged, resuspended in lysis buffer 3 (1 ml/IP for ~2 × 10⁷ cells) and sonicated (12 pulses of 70% power, 15" ON, 45" OFF using a Misonix sonicator) to obtain chromatin fragments of 200 bp. Subsequently, chromatin was pre-cleared at 4°C with 10 μl/ml BSA-blocked Dynabeads (Life Technologies, a mix 1:1 of protein A and protein G beads) for 30 min and incubated at 4°C with 5 μg antibody/IP overnight. Chromatin was then incubated with magnetic beads at 4°C for 2 hr. Beads were washed five times with RIPA and once in TE with 50 mM NaCl. Chromatin was eluted from the beads by incubating in elution buffer with shaking for 30 min. Cross-linking was removed by overnight incubation at 65°C. After RNaseA and proteinase K treatments, the DNA was extracted with phenol:chloroform and ethanol precipitation. Isolated DNA was resuspended in water. ChIP experiments were performed four to six times independently for each antibody. Libraries were cloned and sequenced by Fasteris SA (Switzerland) using the Illumina strategy (HiSeq2000, single-end).

Antibodies

anti-TRF2 (SantaCruz Biotechnology, sc-9143); anti-NR2C2-PPMX (PP-H0107B-00); anti-HMBOX1 (Abcam, ab97643); anti-NR2F2 (Abcam, ab50487).

Buffers Composition

Buffers used for ChIP have been described previously (Lee et al., 2006).

Bioinformatic Analysis

Bioinformatic analysis is described in the [Extended Experimental Procedures](#).

SUPPLEMENTAL INFORMATION

Supplemental information includes Extended Experimental Procedures, seven figures, and three tables and can be found with this article online at <http://dx.doi.org/10.1016/j.cell.2015.01.044>.

ACKNOWLEDGMENTS

We would like to thank Jan Karlseder and Cyril Ribeyre for critical reading of the manuscript and members of the Déjardin lab for stimulating discussions, Osamu Tanabe for the gift of the NR2C2 constructs, and Evi Soutoglou for the gift of the *HeLa LacO* transgenic line. Work in J.D.'s lab is funded by the European Research Council (StG#242934) and INSERM Avenir. P.M. is funded by the Association pour la Recherche contre le Cancer.

Received: December 19, 2013

Revised: November 18, 2014

Accepted: January 27, 2015

Published: February 26, 2015

REFERENCES

- Allshire, R.C., Dempster, M., and Hastie, N.D. (1989). Human telomeres contain at least three types of G-rich repeat distributed non-randomly. *Nucleic Acids Res.* 17, 4611–4627.
- Artandi, S.E., Chang, S., Lee, S.L., Alson, S., Gottlieb, G.J., Chin, L., and DePinho, R.A. (2000). Telomere dysfunction promotes non-reciprocal translocations and epithelial cancers in mice. *Nature* 406, 641–645.
- Benoit, G., Cooney, A., Giguere, V., Ingraham, H., Lazar, M., Muscat, G., Perlmann, T., Renaud, J.P., Schwabe, J., Sladek, F., et al. (2006). International Union of Pharmacology. LXVI. Orphan nuclear receptors. *Pharmacol. Rev.* 58, 798–836.
- Bilaud, T., Brun, C., Ancelin, K., Koering, C.E., Laroche, T., and Gilson, E. (1997). Telomeric localization of TRF2, a novel human telobox protein. *Nat. Genet.* 17, 236–239.
- Bosco, N., and de Lange, T. (2012). A TRF1-controlled common fragile site containing interstitial telomeric sequences. *Chromosoma* 121, 465–474.
- Broccoli, D., Smogorzewska, A., Chong, L., and de Lange, T. (1997). Human telomeres contain two distinct Myb-related proteins, TRF1 and TRF2. *Nat. Genet.* 17, 231–235.
- Bryan, T.M., Englezou, A., Dalla-Pozza, L., Dunham, M.A., and Reddel, R.R. (1997). Evidence for an alternative mechanism for maintaining telomere length in human tumors and tumor-derived cell lines. *Nat. Med.* 3, 1271–1274.
- Cesare, A.J., and Griffith, J.D. (2004). Telomeric DNA in ALT cells is characterized by free telomeric circles and heterogeneous t-loops. *Mol. Cell. Biol.* 24, 9948–9957.
- Chen, H., and Privalsky, M.L. (1995). Cooperative formation of high-order oligomers by retinoid X receptors: an unexpected mode of DNA recognition. *Proc. Natl. Acad. Sci. USA* 92, 422–426.
- Chibon, F., Lagarde, P., Salas, S., Pérot, G., Brouste, V., Tirode, F., Lucchesi, C., de Reynies, A., Kauffmann, A., Bui, B., et al. (2010). Validated prediction of clinical outcome in sarcomas and multiple types of cancer on the basis of a gene expression signature related to genome complexity. *Nat. Med.* 16, 781–787.
- Conomos, D., Stutz, M.D., Hills, M., Neumann, A.A., Bryan, T.M., Reddel, R.R., and Pickett, H.A. (2012). Variant repeats are interspersed throughout the telomeres and recruit nuclear receptors in ALT cells. *J. Cell Biol.* 199, 893–906.
- de Lange, T. (2005). Shelterin: the protein complex that shapes and safeguards human telomeres. *Genes Dev.* 19, 2100–2110.
- Déjardin, J. (2012). How chromatin prevents genomic rearrangements: locus colocalization induced by transcription factor binding. *BioEssays* 34, 90–93.
- Déjardin, J., and Kingston, R.E. (2009). Purification of proteins associated with specific genomic loci. *Cell* 136, 175–186.
- Dekker, J., Rippe, K., Dekker, M., and Kleckner, N. (2002). Capturing chromosome conformation. *Science* 295, 1306–1311.
- Guillou, L., and Aurias, A. (2010). Soft tissue sarcomas with complex genomic profiles. *Virchows Arch.* 456, 201–217.
- Gustafsson, M.G., Shao, L., Carlton, P.M., Wang, C.J., Golubovskaya, I.N., Cande, W.Z., Agard, D.A., and Sedat, J.W. (2008). Three-dimensional resolution doubling in wide-field fluorescence microscopy by structured illumination. *Biophys. J.* 94, 4957–4970.
- Hanahan, D., and Weinberg, R.A. (2011). Hallmarks of cancer: the next generation. *Cell* 144, 646–674.
- Henson, J.D., and Reddel, R.R. (2010). Assaying and investigating Alternative Lengthening of Telomeres activity in human cells and cancers. *FEBS Lett.* 584, 3800–3811.
- Henson, J.D., Hannay, J.A., McCarthy, S.W., Royds, J.A., Yeager, T.R., Robinson, R.A., Wharton, S.B., Jellinek, D.A., Arbuckle, S.M., Yoo, J., et al. (2005). A robust assay for alternative lengthening of telomeres in tumors shows the significance of alternative lengthening of telomeres in sarcomas and astrocytomas. *Clin. Cancer Res.* 11, 217–225.
- Hu, J., Hwang, S.S., Liesa, M., Gan, B., Sahin, E., Jaskelioff, M., Ding, Z., Ying, H., Boutin, A.T., Zhang, H., et al. (2012). Antitelomerase therapy provokes ALT and mitochondrial adaptive mechanisms in cancer. *Cell* 148, 651–663.
- Jain, S., Xu, R., Prieto, V.G., and Lee, P. (2010). Molecular classification of soft tissue sarcomas and its clinical applications. *Int. J. Clin. Exp. Pathol.* 3, 416–428.
- Kappei, D., Butter, F., Benda, C., Scheibe, M., Drašković, I., Stevense, M., Novo, C.L., Basquin, C., Araki, M., Araki, K., et al. (2013). HOT1 is a mammalian direct telomere repeat-binding protein contributing to telomerase recruitment. *EMBO J.* 32, 1681–1701.
- Kilburn, A.E., Shea, M.J., Sargent, R.G., and Wilson, J.H. (2001). Insertion of a telomere repeat sequence into a mammalian gene causes chromosome instability. *Mol. Cell. Biol.* 21, 126–135.
- Lee, T.I., Johnstone, S.E., and Young, R.A. (2006). Chromatin immunoprecipitation and microarray-based analysis of protein location. *Nat. Protoc.* 1, 729–748.
- Lin, C., Yang, L., Tanasa, B., Hutt, K., Ju, B.G., Ohgi, K., Zhang, J., Rose, D.W., Fu, X.D., Glass, C.K., and Rosenfeld, M.G. (2009). Nuclear receptor-induced chromosomal proximity and DNA breaks underlie specific translocations in cancer. *Cell* 139, 1069–1083.
- Lovejoy, C.A., Li, W., Reisenweber, S., Thongthip, S., Bruno, J., de Lange, T., De, S., Petrini, J.H., Sung, P.A., Jasin, M., et al.; ALT Starr Cancer Consortium (2012). Loss of ATRX, genome instability, and an altered DNA damage response are hallmarks of the alternative lengthening of telomeres pathway. *PLoS Genet.* 8, e1002772.
- Mani, R.S., Tomlins, S.A., Callahan, K., Ghosh, A., Nyati, M.K., Varambally, S., Palanisamy, N., and Chinnaiyan, A.M. (2009). Induced chromosomal proximity and gene fusions in prostate cancer. *Science* 326, 1230.
- McClintock, B. (1941). The Stability of Broken Ends of Chromosomes in Zea Mays. *Genetics* 26, 234–282.
- Misteli, T., and Soutoglou, E. (2009). The emerging role of nuclear architecture in DNA repair and genome maintenance. *Nat. Rev. Mol. Cell Biol.* 10, 243–254.
- Montgomery, E., Argani, P., Hicks, J.L., DeMarzo, A.M., and Meeker, A.K. (2004). Telomere lengths of translocation-associated and nontranslocation-associated sarcomas differ dramatically. *Am. J. Pathol.* 164, 1523–1529.
- Murnane, J.P. (2012). Telomere dysfunction and chromosome instability. *Mutat. Res.* 730, 28–36.
- O'Geen, H., Lin, Y.H., Xu, X., Echipare, L., Komashko, V.M., He, D., Fietze, S., Tanabe, O., Shi, L., Sartor, M.A., et al. (2010). Genome-wide binding of the orphan nuclear receptor TR4 suggests its general role in fundamental biological processes. *BMC Genomics* 11, 689.
- Robinett, C.C., Straight, A., Li, G., Wilhelm, C., Sudlow, G., Murray, A., and Belmont, A.S. (1996). In vivo localization of DNA sequences and visualization of large-scale chromatin organization using lac operator/repressor recognition. *J. Cell Biol.* 135, 1685–1700.
- Safe, S., Jin, U.H., Hedrick, E., Reeder, A., and Lee, S.O. (2014). Minireview: role of orphan nuclear receptors in cancer and potential as drug targets. *Mol. Endocrinol.* 28, 157–172.
- Sandelin, A., and Wasserman, W.W. (2005). Prediction of nuclear hormone receptor response elements. *Mol. Endocrinol.* 19, 595–606.
- Scheel, C., Schaefer, K.L., Jauch, A., Keller, M., Wai, D., Brinkschmidt, C., van Valen, F., Boecker, W., Dockhorn-Dworniczak, B., and Poremba, C. (2001). Alternative lengthening of telomeres is associated with chromosomal instability in osteosarcomas. *Oncogene* 20, 3835–3844.
- Sfeir, A., Kosiyaatrakul, S.T., Hockemeyer, D., MacRae, S.L., Karlseder, J., Schildkraut, C.L., and de Lange, T. (2009). Mammalian telomeres resemble fragile sites and require TRF1 for efficient replication. *Cell* 138, 90–103.

Simonet, T., Zaragosi, L.E., Philippe, C., Lebrigand, K., Schouteden, C., Augereau, A., Bauwens, S., Ye, J., Santagostino, M., Giulotto, E., et al. (2011). The human TTAGGG repeat factors 1 and 2 bind to a subset of interstitial telomeric sequences and satellite repeats. *Cell Res.* 21, 1028–1038.

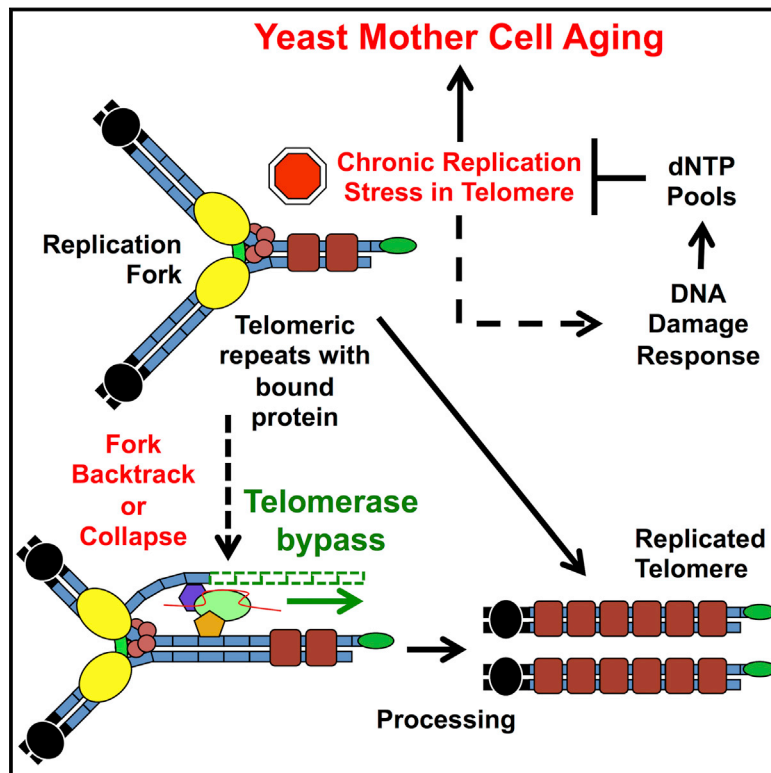
Smallwood, A., and Ren, B. (2013). Genome organization and long-range regulation of gene expression by enhancers. *Curr. Opin. Cell Biol.* 25, 387–394.

Tanabe, O., McPhee, D., Kobayashi, S., Shen, Y., Brandt, W., Jiang, X., Campbell, A.D., Chen, Y.T., Chang, C., Yamamoto, M., et al. (2007). Embryonic and fetal beta-globin gene repression by the orphan nuclear receptors, TR2 and TR4. *EMBO J.* 26, 2295–2306.

Taylor, B.S., Barretina, J., Maki, R.G., Antonescu, C.R., Singer, S., and Ladanyi, M. (2011). Advances in sarcoma genomics and new therapeutic targets. *Nat. Rev. Cancer* 11, 541–557.

Early Telomerase Inactivation Accelerates Aging Independently of Telomere Length

Graphical Abstract



Authors

Zhengwei Xie, Kyle A. Jay, ..., Hao Li, Elizabeth H. Blackburn

Correspondence

haoli@genome.ucsf.edu (H.L.),
elizabeth.blackburn@ucsf.edu (E.H.B.)

In Brief

Telomerase is required for telomere maintenance and protection. Here, early telomerase inactivation leads to accelerated aging through a mechanism independent from senescence caused by telomere shortening.

Highlights

- Early after telomerase inactivation (ETI) mother cell aging is accelerated in yeast
- Accelerated aging occurs before critical telomere shortness-induced senescence
- ETI mother cells show heterogeneous cell cycles that track with lifespan reduction
- ETI acceleration of mother cell aging results from transient DNA damage response



Early Telomerase Inactivation Accelerates Aging Independently of Telomere Length

Zhengwei Xie,^{1,2,3,4} Kyle A. Jay,^{2,4} Dana L. Smith,² Yi Zhang,^{1,2,3} Zairan Liu,^{1,2,3} Jiashun Zheng,^{2,3} Ruilin Tian,¹ Hao Li,^{2,3,*} and Elizabeth H. Blackburn^{2,*}

¹Center for Quantitative Biology, School of Physics and The Peking-Tsinghua Center for Life Sciences, Peking University, Beijing 100871, China

²Department of Biochemistry and Biophysics, University of California, San Francisco, San Francisco, CA 94158, USA

³California Institute for Quantitative Biosciences, University of California, San Francisco, San Francisco, CA 94158, USA

⁴Co-first author

*Correspondence: haoli@genome.ucsf.edu (H.L.), elizabeth.blackburn@ucsf.edu (E.H.B.)

<http://dx.doi.org/10.1016/j.cell.2015.02.002>

SUMMARY

Telomerase is required for long-term telomere maintenance and protection. Using single budding yeast mother cell analyses we found that, even early after telomerase inactivation (ETI), yeast mother cells show transient DNA damage response (DDR) episodes, stochastically altered cell-cycle dynamics, and accelerated mother cell aging. The acceleration of ETI mother cell aging was not explained by increased reactive oxygen species (ROS), Sir protein perturbation, or deprotected telomeres. ETI phenotypes occurred well before the population senescence caused late after telomerase inactivation (LTI). They were morphologically distinct from LTI senescence, were genetically uncoupled from telomere length, and were rescued by elevating dNTP pools. Our combined genetic and single-cell analyses show that, well before critical telomere shortening, telomerase is continuously required to respond to transient DNA replication stress in mother cells and that a lack of telomerase accelerates otherwise normal aging.

INTRODUCTION

Telomeres, protective DNA-protein complexes at the ends of eukaryotic chromosomes, buffer against the loss of sequence during DNA replication and distinguish normal chromosome ends from potentially dangerous double-strand breaks. Telomeres are composed of sequence-specific DNA binding proteins bound to highly repetitive DNA sequences and are increasingly recognized as genomic regions prone to replication stress (Miller et al., 2006; Sfeir et al., 2009; Drosopoulos et al., 2012). Without the telomeric DNA-elongating enzyme telomerase, progressive telomere shortening eventually causes the collapse of the protective DNA-protein complex (deprotection), but this occurs only after many cell divisions, late after telomerase inactivation (LTI). In LTI cells, telomere deprotection shares many properties with classic DNA damage (Nautiyal et al., 2002; d'Adda di Faga-

gna et al., 2003) and induces a DNA damage response (DDR) and a permanent G2/M cell-cycle arrest (senescence).

Previously, responses to telomerase deletion have generally been reported only after a significant delay (in *S. cerevisiae*, after ~50–80 divisions). Thus, it was thought that cells sense altered telomere properties that signal senescence only when telomeres become critically short and deprotected. Hence, responses and phenotypes of cells early after telomerase inactivation (ETI) have not been extensively investigated. However, it was previously shown that, in ETI cells, very short telomeres appear at low frequencies that fuse to an induced double-strand break (DSB) ($\sim 10^{-4}$ to 10^{-3}). These rare fusions became molecularly detectable when telomerase was inactivated by either deletion of the telomerase RNA template *TLC1* (*tlc1Δ*) or by replacing the reverse transcriptase subunit, *EST2*, with the mutant *est2-D530A*, which assembles a telomerase ribonucleoprotein enzyme complex lacking telomeric DNA polymerization activity (Chan and Blackburn, 2003; Lingner et al., 1997). These fusogenic telomeres arose in ETI cells well before any signs of bulk population senescence and even if the telomeres had been pre-lengthened. Therefore, even the short-term absence of telomerase activity causes cells to experience a low but detectable genomic instability.

In a process distinct from the permanent bulk population cell-cycle arrest resulting from critically short telomeres in senescent LTI cells, an individual wild-type (WT) yeast mother cell will cease divisions after it has produced ~25 daughter cells. As of yet, there has been very little evidence suggesting interaction between the pathways that regulate these two kinds of aging, hereafter referred to as “LTI senescence” and “mother cell aging/lifespan,” respectively. Despite the identification of multiple genes that regulate mother cells lifespans (Bishop and Guarente, 2007; Johnson et al., 1999; Kaeberlein, 2010), the mechanisms causing mother cell aging of even WT yeast remain poorly understood.

Here, we report experiments employing single cell methodologies, supporting a model in which budding yeast mother cells lacking telomerase activity are less able to resolve replication stress inherent to telomeres. These cells show induction of a signaling pathway indicative of transient DNA replication stress, altered cell-cycle dynamics even in young mother cells, and accelerated aging (reduced lifespan), independently of telomere length. Our results demonstrate that this occurs well before the

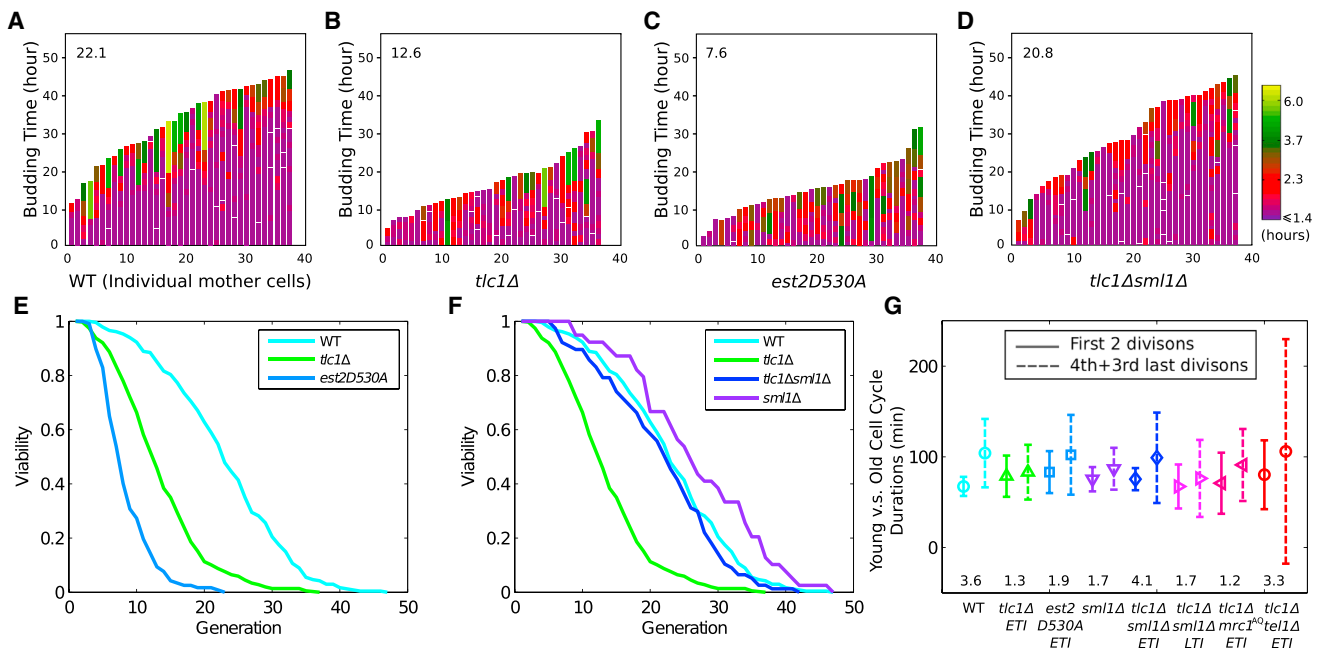


Figure 1. ETI Mother Cells Show a Non-Progressive Cell-Cycle Length Phenotype and Reduced Lifespan that is Rescued by SML1 Deletion (A–D) Mother cell budding profiles for (A) WT, (B) *tlc1Δ*, (C) *est2-D530A*, and (D) *tlc1Δsml1Δ*, showing cell-cycle durations and heterogeneity (see exponential color scale; cell cycles with durations 1.4 hr or less were colored in purple). The x axis displays individual mother cells shown as vertical bars, with budding events indicated as horizontal white divisions. Mean lifespan for each genotype is presented in the upper-left corner of the plot. (E) ETI mother cells showed reduced replicative lifespans compared to WT cells (number of cells [n]: *tlc1Δ*, 354; *est2-D530A*, 117; WT, 234. p value for difference between *tlc1Δ* and WT < 1e-37). (F) Deletion of *SML1* restores lifespan of ETI mother cells to WT levels (n: *tlc1Δsml1Δ*, 77; *sml1Δ*, 39). (G) The heterogeneity of cell-cycle lengths in ETI cells did not progressively worsen relative to WT as mother cells aged. Fold increase in cell-cycle variability from first and second to third and fourth last cell cycles compared for each genotype (shown below each set). The variance of first and second cell cycles of *tlc1Δ* and *est2530A* is significantly greater than that of WT (F test; $p < 1e-16$ and $1e-13$, respectively). Error bars indicate SD. See also Figures S1 and S2.

onset of LTI senescence and that the accelerated aging of ETI mother cells resembles the normal mother cell aging process.

RESULTS

Mother Cells Lacking Active Telomerase Show Increased Heterogeneity of Cell-Cycle Durations and Reduced Lifespans

We analyzed the properties of individual haploid ETI mother cells, well before any signs of cellular LTI senescence, freshly isolated from sporulation of heterozygous telomerase-competent diploids. Following genotyping, cells were taken from logarithmically growing cell cultures (~25–30 generations after telomerase loss), in which the overwhelming majority of cells were robustly growing newborn or very young mother cells. These cells were placed in a microfluidic device, and the budding cycles and lifespans of individual mother cells were continuously monitored for 2 days by repeated microscopic imaging (Xie et al., 2012; Zhang et al., 2012).

First, even the youngest ETI mother cells (*tlc1Δ* or *est2-D530A*) immediately showed higher frequencies of stochastically longer and more heterogeneous cell-cycle durations than WT (Figures 1A–1C; note especially between times 0 to 5 hr, as marked on Y axes). As the durations of the last two budding cycles were

highly heterogeneous in both WT and ETI mothers, they were discarded from all cell-cycle duration analyses discussed here. This cell-cycle heterogeneity was consistent with observations of bulk ETI population budding kinetics, as manifested by cells lingering in the large-budded state (G2/M), enriched for cells with short spindles and unsegregated chromosomes (Figures S1A–S1C). Second, we analyzed the mother cell aging of individual ETI cells and found that the lack of telomerase activity reduced ETI mother cell lifespan. Mean budding lifespan for *tlc1Δ* was 12.6 (7 replicates) and 7.6 generations for *est2-D530A* (3 replicates), compared to 22.1 for WT mother cells (Figures 1A–1C and 1E). Furthermore, the catalytically inactive telomerase *est2-D530A* point mutant showed even longer cell-cycle durations than *tlc1Δ* ETI mother cells, and the lifespan reduction was even more severe. Hence, lack of telomerase enzymatic activity, rather than the absence of an assembled telomerase ribonucleoprotein complex, causes increased cell-cycle heterogeneity and faster mother cell aging.

Heterogeneous Cell Cycles Do Not Progressively Worsen with Shortening Telomeres

If the extended, heterogeneous cell-cycle lengths of ETI mother cells were due solely to telomere shortening, we would have expected the phenotype to worsen progressively with each

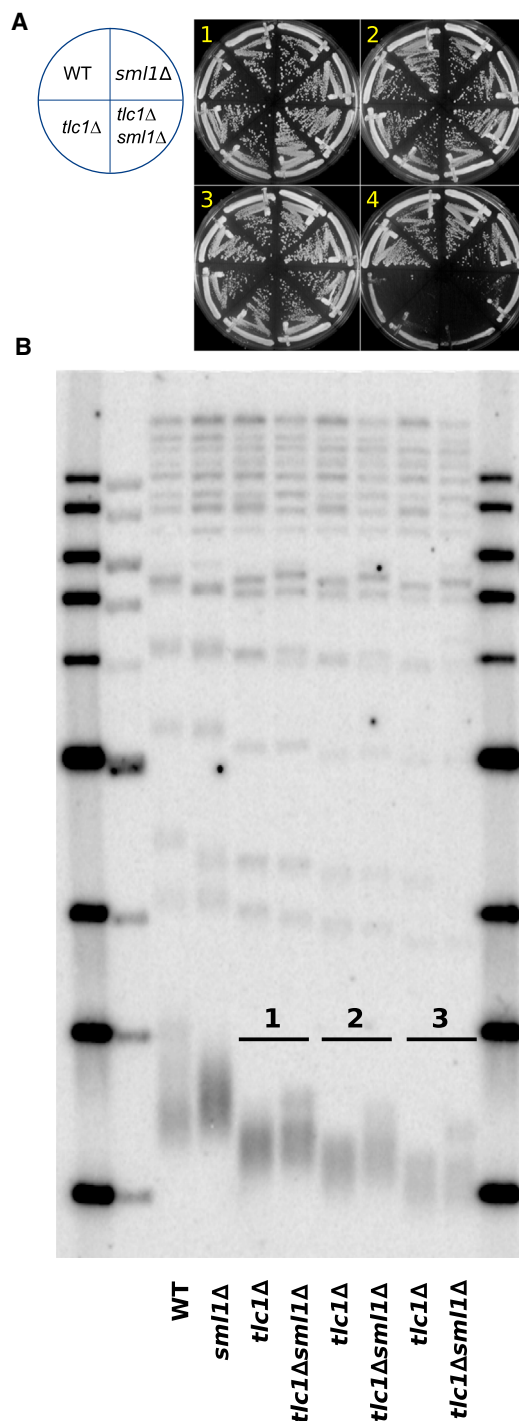


Figure 2. SML1 Deletion Rescues Mother Cell Lifespan of ETI Cells Independently of Telomere Length

(A) *SML1* deletion had no significant effect on the rate of bulk population senescence in ETI cells passaged on solid media to induce LTI-senescence. (B) Southern blot analysis of telomeric DNA restriction fragment lengths of cells taken from serial streaks shown in (A), using TG₍₁₋₃₎ repeat telomeric probe. ETI (*tlc1Δ*) and ETI *sml1Δ* (*tlc1Δ sml1Δ*) displayed similar rates of telomere shortening, and the lower end of the telomere length distributions were similar. See also Figure S3.

successive cell division. However, this was not the case. First, as individual mother cells progressed from being very young to old, ETI mother cells did not show any significant progressive increase in mean duration or heterogeneity of mother cell-cycle lengths relative to WT (Figure 1G). Second, during the individual ETI mother cell lineages, a young mother cell whose initial cell cycle was long had no greater probability of having subsequent longer cell cycles or a shorter lifespan than one with an initial short cell cycle (Figure S2), supporting a stochastic and episodic, rather than progressive, nature of the occurrence of longer cell cycles. These highly stochastic episodes of cell-cycle heterogeneity and lack of any progressive worsening of this phenotype as ETI mother cells aged are not the predicted result of progressive telomere shortening.

SML1 Deletion Rescues Mother Cell Lifespan of ETI Cells Independently of Telomere Length

Because we observed an extended G2/M phase in bulk population analyses (Figure S1), which is often the result of DDR activation, we determined whether mutations affecting the DDR affected the above ETI phenotypes. Responses to various forms of DNA damage, including that sensed at critically short telomeres in LTI senescence, involve a cascade of phosphorylation events, with early upstream steps occurring at the source of DNA damage through PIKK family member kinases Mec1 (*ATR*) and/or Tel1 (*ATM*). Strains lacking only Mec1 are inviable, but this *mec1Δ* lethality can be rescued by deletion of *SML1* (Zhao et al., 1998). Sml1 inhibits ribonucleotide reductase (RNR), which catalyzes the rate-limiting step in dNTP production (Reichard, 1988). Deletion of Sml1 increases RNR activity and elevates dNTP pools, obviating the need for certain DDR components under healthy growing conditions, and can be protective against some forms of DNA damage (Andreson et al., 2010; Jossen and Bermejo, 2013). Strikingly, deletion of *SML1* in ETI *tlc1Δ* strains efficiently rescued the ETI-induced heterogeneity of budding cycle durations (Figure 1D) as well as the shortening of mother cell lifespan (Figure 1F). However, *SML1* deletion alone produced no change in the rates of bulk telomere shortening in ETI cells, nor in the subsequent onset of LTI senescence (Figures 2 and S3). We also confirmed that the deletion of *SML1* alone caused no significant effect on mother cell lifespans and telomere length compared to WT (Figures 1F and S4B). Hence, the dramatic rescue of ETI cell-cycle heterogeneity and accelerated mother cell aging by *SML1* deletion cannot be explained by increased telomere length or by slower rates of telomere shortening.

ETI Mother Cells Age with Terminal Cellular and Mitochondrial Morphologies Distinct from LTI Senescence but Similar to Those of Normal Mother Cell Aging

We tested further whether budding cessation due to mother cell aging in ETI or WT cells was distinguishable from the G2/M arrest caused by LTI senescence by examining cell and mitochondrial morphology at the end of the lifespans (terminal morphology). Typical WT mother cell aging produces terminal cells that are mostly small budded with minimal or no mitochondrial fluorescence signal from a mitochondrially localized GFP (mtGFP)

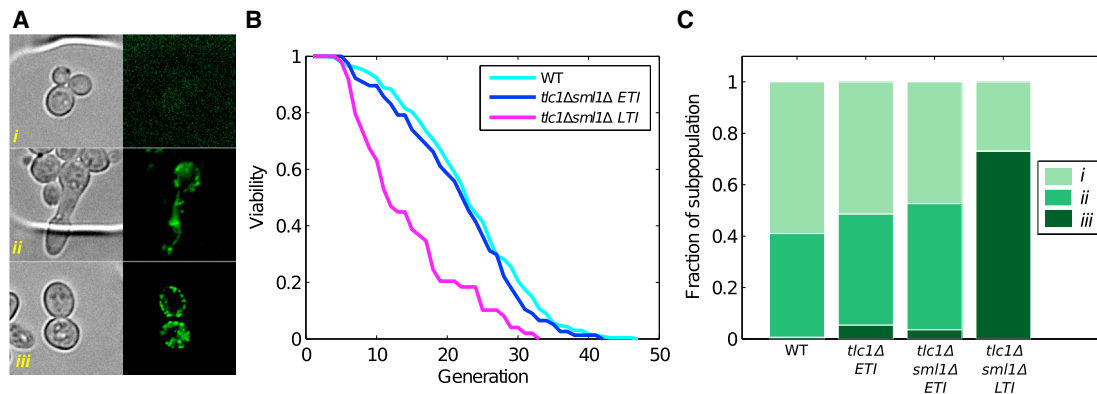


Figure 3. ETI Mother Cells Age with Terminal Cellular and Mitochondrial Morphologies Distinct from LTI Senescence but Similar to Those of Normal Mother Cell Aging

(A) Three possible terminal death morphologies were observed in WT, ETI, and/or LTI (see text for definition) mother cells: small budded (type i), elongated (type ii), and a G2/M large-budded (“dumbbell” shape) (type iii). Mitochondrial volume was measured using mitochondrially localized GFP (mtGFP). (B) ETI and LTI populations of *tlc1Δsml1Δ* cells were prepared to distinguish cell death from normal mother cell aging and LTI senescence. *tlc1Δsml1Δ* LTI (n = 49) strains senesced and showed reduced lifespan, as expected. (C) ETI cells terminally arrest in a manner similar to WT mother cells and distinct from LTI senescence. Most of the cells in ETI *tlc1Δ* and ETI *tlc1Δsml1Δ* show type i or type ii death morphologies (> 95%), similar to terminal WT mother cells. In LTI cells, a major fraction (~70%) displayed type iii morphology (p < 1e-4 compared to ETI *tlc1Δsml1Δ* by Fisher’s exact test), indicative of senescence induced by critically short telomeres.

(Figure 3Ai) and a smaller population of elongated cells with brighter mitochondrial fluorescence (Figure 3Aii). In contrast, cells terminally arrested due to LTI senescence accumulate with a swollen, large-budded (“dumbbell”) morphology and with mitochondrial fluorescence that gradually forms very bright dots (Figure 3Aiii) (Nautiyal et al., 2002). We created and analyzed two populations of *tlc1Δsml1Δ* cells. The first population was isolated as soon as possible after genotyping (ETI) and was enriched for mother cells that would reach their aging limit prior to LTI senescence. The second population was passaged for approximately ten additional generations prior to microfluidics analysis, thus enriching for cells that would undergo LTI senescence (critically short telomeres) before the mother cells reached their aging limit (Figure 3B). Terminally aged ETI *tlc1Δ* and ETI *tlc1Δsml1Δ* mother cells accumulated mostly in two dominant terminal morphologies, which resembled the two dominant WT terminal morphology phenotypes (Xie et al., 2012) and only very rarely in the dumbbell morphology (Figures 3A and 3C). In contrast, in terminal LTI *tlc1Δsml1Δ* mother cells, terminal dumbbell morphologies became the major type observed, indicating that a large proportion of the population had entered LTI senescence (Figures 3Aiii and 3C). These results support terminal cellular and mitochondrial morphology as an accurate distinction between LTI senescence and normal mother cell aging and provide further evidence that ETI mother cells cease divisions as a result of mother cell aging rather than LTI senescence.

Mutation of Specific DDR Components Exacerbates ETI Cell-Cycle and Lifespan Phenotypes

We investigated other proteins previously implicated in yeast telomere maintenance and in the DDR for effects on mother cell aging. Maintenance of yeast telomeres at normal length requires DDR kinases Mec1 and Tel1 (Sabourin and Zakian,

2008; Takata et al., 2004) and the replication stress-specific DDR adaptor protein Mrc1 (Grandin et al., 2005). First, we found that cell-cycle heterogeneity and mother cell lifespan were similar in WT, *tel1Δ*, and *mec1Δsml1Δ* strains (Figures 1A, 4A, 4C, S4C, and S5A). Because *tel1Δ* in haploid cells reduces telomerase action on telomeres, telomeres decline to a short length that is then stably maintained (Greenwell et al., 1995; Lustig and Petes, 1986). The *tel1Δ* cells used here were isolated immediately after sporulation of heterozygous parent diploids and analyzed when telomeres were still shortening from near-WT lengths. Therefore, having telomeres that are shortening but eventually stably maintained is not alone sufficient to alter cell-cycle duration and lifespan.

Next, we examined how mutations of Mec1 and Tel1 affect the ETI phenotypes. Because *sml1Δ*, as shown above, efficiently rescues the accelerated aging of ETI mother cells, it is difficult to determine whether Mec1 has a role in this process, due to the necessity of deleting *SML1* for viability in *mec1Δ* strains. However, ETI *tlc1Δtel1Δ* double-mutant mother cells had even greater cell-cycle heterogeneity and shorter budding lifespan (mean 9.8 generations, 2 replicates) than control ETI *tlc1Δ* single-mutant mother cells (Figures 1B, 4B, and 4D). As shown previously, freshly isolated ETI haploid cells that are also mutated for Tel1 or Mec1 (*tlc1Δmec1Δsml1Δ* or *tlc1Δtel1Δ*) have a rate of initial telomere shortening and progression to LTI population senescence similar to *tlc1Δ* single mutants (Chan and Blackburn, 2003) (Figures 4E and 4F). Hence, the exacerbation of the ETI cell-cycle heterogeneity and lifespan reduction phenotypes caused by lack of Tel1 is not explained by faster telomere shortening or accelerated population senescence.

Because *sml1Δ* rescues the cell-cycle and lifespan phenotypes of *tlc1Δ* mother cells and is known to facilitate DNA replication by increasing nucleotide levels (Chabes et al., 2003), we suspected that ETI cells may be more vulnerable to telomeric

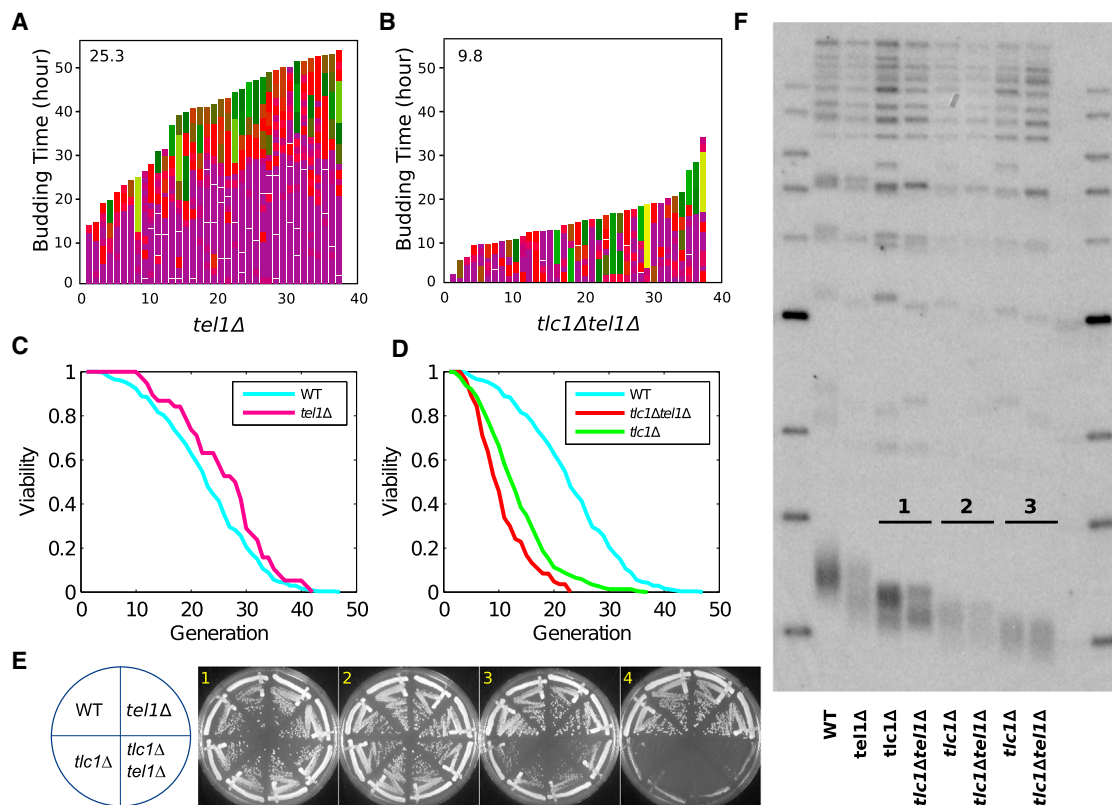


Figure 4. TEL1 Deletion Exacerbates ETI Cell Cycle and Lifespan Phenotypes, but Not Senescence or Telomere-Shortening Rates

(A and B) Mother cell budding profiles for *tel1Δ* (A) and *tlc1Δ tel1Δ* (B).

(C) *tel1Δ* ($n = 38$) strain lifespan does not differ from WT.

(D) *tlc1Δtel1Δ* ($n = 83$) mutation worsens the lifespan reduction caused by ETI mutations in mother cells ($p < 1e-4$, compared with *tlc1Δ* alone).

(E) ETI and ETI *tel1Δ* mutants displayed similar rates of senescence when passaged on solid media.

(F) Southern blot analysis of telomeric DNA restriction fragment lengths of cells taken from plates after serial streaks shown in (E).

See also Figures S4 and S5.

DNA replication stress. Therefore, we mutated the DDR adaptor protein Mrc1, which is required specifically for the DNA replication stress checkpoint (Alcasabas et al., 2001; Osborn and Elledge, 2003) and has a minor role in telomere length maintenance (Tsoulou and Lydall, 2007). Mutation of 17 potential PIKK family kinase consensus phosphorylation sites on Mrc1 (*mrc1^{AQ}*) allows full cell viability but disables the DNA replication stress response (Osborn and Elledge, 2003). Despite the lack of any mother cell lifespan or cell-cycle effect of *mrc1^{AQ}* alone (Figures 5A and 5C), *tlc1Δmrc1^{AQ}* double-mutant ETI mother cells showed even greater cell-cycle length heterogeneity than the *tlc1Δ* single-mutant ETI cells (Figure 5B). Consistent results were also seen in the G2/M durations in bulk populations (Figure S1D), and mean lifespan was markedly reduced to 8.8 generations (2 replicates), compared with 12.6 generations for the control *tlc1Δ* ETI strains (Figures 1B and 5D). These effects were not explainable by reduced telomere length or accelerated senescence, as the *mrc1^{AQ}* mutant allele produced stable telomeres only slightly shorter than WT and had no effect on the kinetics of telomere shortening or bulk population senescence (Figures 5E and 5F). We also tested the epistasis relationship of *tel1Δ* and *mrc1^{AQ}* in the ETI context. ETI triple-mutant *tlc1Δ tel1Δ*

mrc1^{AQ} cells showed the same lifespan shortening as the double ETI mutants (Figure S5B). We conclude that *Tel1* and *Mrc1* checkpoint functions act in the same pathway and that lack of either one acts synthetically with the ETI mother cell phenotypes.

In the DDR cascade, downstream of Tel1 or Mec1, the DDR adaptor protein Rad9 can act semi-redundantly with the adaptor protein Mrc1. Mrc1 is specifically involved in the replication stress response while Rad9 is mostly important for responding to DNA breaks and other DNA damage. In contrast to *tlc1Δmrc1^{AQ}* ETI cells, *tlc1Δrad9Δ* ETI mother cell-cycle durations and lifespans were not significantly different from *tlc1Δ* ETI cells, consistent with bulk population analyses (Figure S1 and data not shown). The ETI *tlc1Δ rad9Δ* mother cells had a mean lifespan of 16.5 generations (2 replicates), while the control *tlc1Δ* strain had a mean lifespan of 13.7 generations (Figure S5C). Thus, *rad9Δ* did not significantly affect the accelerated aging phenotypes of ETI mother cells. These results confirmed the specificity of the Mrc1 checkpoint function in the ETI mother cell phenotypes and indicate the involvement of a DNA replication stress response, rather than a response to other forms of DNA damage, which requires Rad9. In summary, disrupting the DDR via *tel1Δ* or *mrc1^{AQ}* mutations, but not by *mec1Δsmf1Δ*

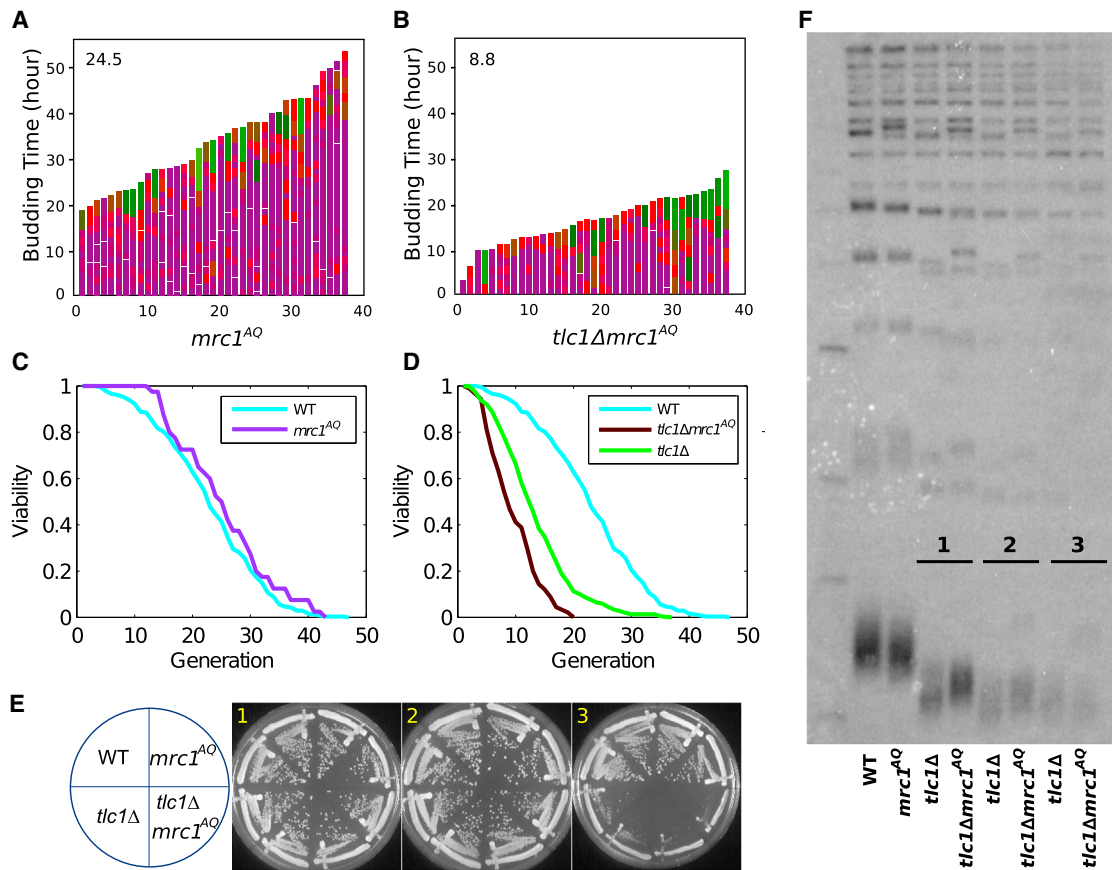


Figure 5. *MRC1* Mutation Exacerbates ETI Cell Cycle and Lifespan Phenotypes, but not Senescence or Telomere-Shortening Rates

(A and B) Mother cell budding profiles for *mrc1^{AQ}* (A) and *tlc1Δ mrc1^{AQ}* (B).
 (C) *mrc1^{AQ}* ($n = 40$) strain lifespan does not differ from WT.
 (D) *tlc1Δ mrc1^{AQ}* ($n = 90$) mutation worsens the lifespan reduction caused by ETI mutations in mother cells ($p < 2e-7$, compared with *tlc1Δ*).
 (E) ETI and ETI *mrc1^{AQ}* mutants displayed similar rates of senescence when passaged on solid media.
 (F) Southern blot analysis of telomeric DNA restriction fragment lengths of cells taken from plates after serial streaks shown in (E).
 See also Figures S4 and S5.

or *rad9Δ*, strongly exacerbated the cell-cycle abnormalities and acceleration of mother cell aging in ETI cells, independently of telomere length and without accelerating LTI senescence.

ETI Mother Cell Phenotypes Are Not Caused by Deprotected Telomeres

Previous results showed that short, fusogenic telomeres occur spontaneously at very low frequencies in ETI cells (Chan and Blackburn, 2003). These fusogenic telomeres derive from rare individual deprotected telomeres and can be detected by PCR assays upon their fusion to an induced DNA double-stranded break. We tested whether the amount of such fusogenic telomeres correlated with the severity of our ETI mother cell phenotypes using the same system (Chan and Blackburn, 2003) for semiquantitative PCR analyses. In agreement with the published work, we found that single-mutant ETI (*tlc1Δ*) and *tel1Δ* strains each showed detectable but low amounts of fusions resulting from a deprotected telomere fusing to an induced DSB and that *tlc1Δ tel1Δ* strains showed a synergistic increase (Figures

6A and 6B). However, in *tlc1Δ mrc1^{AQ}* ETI cells (Figure 6A), the *mrc1^{AQ}* mutation produced no further significant increase over a *tlc1Δ* single mutant. Furthermore, *smi1Δ* did not reduce (and possibly increased) the number of fusogenic telomeres detected (Figures 6A and 6B). This complete non-concordance in these various ETI genotypes with the phenotypes we have observed here in ETI mother cells argues strongly against deprotected telomeres as a cause for the exacerbated cell-cycle heterogeneity and accelerated mother cell aging.

Further evidence that ETI phenotypes are not caused by deprotected telomeres, which induce a robust DDR (Nautiyal et al., 2002; d'Adda di Fagagna et al., 2003), came from comparing the genetic dependencies of ETI cell phenotypes versus DNA damage sensitivity. As previously reported, *mec1Δ smi1Δ* and *rad9Δ* mutations made cells highly sensitive to treatment with various classic DNA damaging agents (HU, UV, phleomycin, or MMS) (Figure S4D). This is in dramatic contrast to the experiments described above, in which *mec1Δ smi1Δ* and *rad9Δ* did not exacerbate the ETI phenotypes.

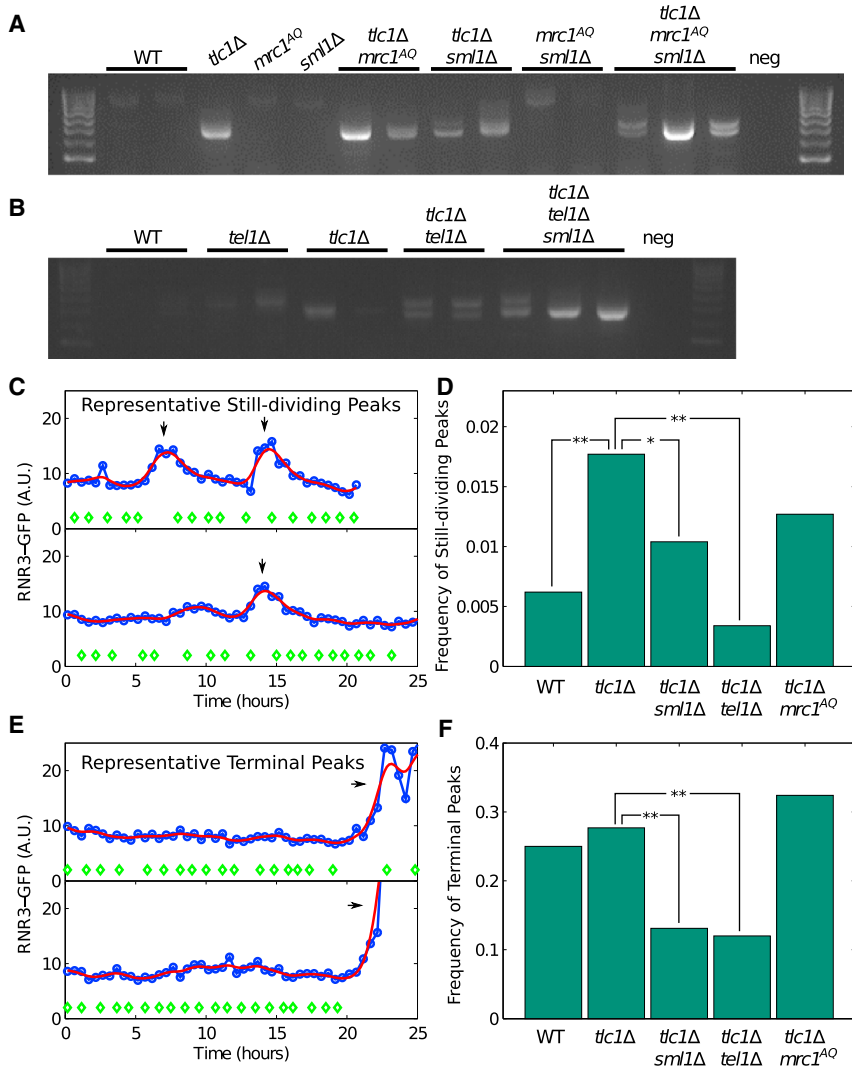


Figure 6. Genotype Dependence of Telomere Fusions and Transient DNA Damage Response Episodes in Mother Cells

(A) Semiquantitative PCR of DNA species resulting from the fusion of a deprotected telomere with an induced double-strand break in genetic backgrounds containing *ETI* and *mrc1^{ΔQ}* mutant combinations.

(B) Same as in (A) but with genetic backgrounds containing *ETI* and *tel1Δ* mutations.

(C) Two representative profiles of RNR3-GFP peaks occurring in still-dividing individual mother cells. Cell divisions (green diamonds) and RNR3-GFP reporter levels (blue circles) were plotted throughout an individual mother cell's lifespan. Spline fitting is shown as red lines.

(D) Frequencies of RNR3-GFP induction peaks in still-dividing cells such as those shown in (C). **p* < 0.01 and ***p* < 0.001 by Fisher's exact test are indicated.

(E) Two representative mother cell profiles shown, as in (C), with cells displaying terminal RNR3-GFP induction peaks.

(F) Frequencies of RNR3-GFP induction peaks in terminal mother cells, such as those shown in (E). See also Figure S6.

Hence, the genotype dependencies of ETI mother cell phenotypes are quite distinct from the dependencies of responses to classic DNA-damaging agents.

Altered Recombination Levels Are Not Responsible for ETI Mother Cell Phenotypes

Recombination is another process that has been implicated in maintaining yeast telomeres and occurs when telomeres lose protection, such as in LTI cells (McEachern and Blackburn, 1996; Basenko et al., 2011). Following the onset of LTI senescence, Rad52-dependent recombination at telomeres allows a small fraction ($\sim 10^{-4}$) of senescing LTI yeast cells to survive and continue dividing (Lundblad and Blackburn, 1993). Also, DNA replication stress can be relieved by mechanisms involving recombination. We therefore asked whether recombination plays any role in the ETI accelerated mother cell-cycle kinetics and aging response. Deletion of *RAD52* alone causes no changes in telomere length maintenance, and telomeres in *tlc1Δrad52Δ* strains shorten no faster than with *tlc1Δ* alone

13.2 (Figure S6A). Hence, lack of Rad52 function appears to act additively to the effect of *TLC1* deletion. This epistasis relationship indicates that absence of telomerase activity and of Rad52 each causes acceleration of mother cell aging but by two distinct mechanisms.

ETI Phenotypes Are Not Caused By Relocalization of Sir Proteins

Another pathway previously implicated in yeast mother cell aging involves changes in Sir protein concentration and localization. For example, Sir2 overexpression has been shown to increase mother cell lifespan (Kaeberlein et al., 1999). However, several lines of evidence argue that Sir2 sequestration in ETI cells does not explain their accelerated aging. First, all of our ETI strains mated normally, implying that the mating type loci were still silenced and arguing against a large relocalization of Sir proteins. Second, localized puncta of Sir3-GFP, indicative of telomere-bound Sir complex proteins (Martin et al., 1999), were not significantly different between ETI and WT mother cells

(Figure S6B). Third, although a single induced unrepairable DNA break has been reported to cause Rad9-dependent delocalization of Sir2 from telomeres (Martin et al., 1999; Mills et al., 1999), as described above, *rad9Δ* neither exacerbated nor significantly rescued the accelerated aging in ETI mother cells. Together, these findings indicate that altered sequestration of the Sir complex is not the mechanism causing the accelerated aging of ETI cells.

Lifespan Reduction of ETI Mother Cells Is Not Caused by Increased Reactive Oxygen Species

We re-examined the previously described transcriptional profile data sets (Nautiyal et al., 2002; Table S2, passage 1) of ETI *tlc1Δ* cells. In an unbiased approach, we compared the large available number of yeast gene expression profiles, measured under different environmental conditions and genetic backgrounds (Edgar et al., 2002), to that of ETI cells (Tables S3, S4, S5). The top hit (Pearson correlation = 0.495, $p < 1e-254$) was treatment with diamide, a thiol-oxidizing agent that causes oxidative stress. Because intracellular ROS have long been theorized to play a role in aging and ROS levels can be elevated as a result of DNA damage (Rowe et al., 2008; Salmon et al., 2004), we tested whether oxidative stress caused the ETI mother cell phenotypes.

We assessed oxidative stress in ETI cells by quantifying ROS levels in our strains. If the accelerated aging of ETI cells is caused by higher intracellular ROS levels, it would be predicted that ETI *tlc1Δ* mother cells would have higher ROS than WT and that ETI *tlc1Δ sml1Δ* cells would have lower ROS levels than ETI single *tlc1Δ* mutants. However, ETI cells did not have significantly higher levels of ROS than WT (Figure S6C). Furthermore, *sml1Δ* and *tlc1Δ sml1Δ* strains showed even higher levels of ROS, the opposite effect from that predicted if ETI causes faster aging of cells via higher intracellular ROS level. We also tested the effects of anti-oxidants by treatment with N-Acetyl-L-Cysteine (NAC). However, NAC equally and only modestly lengthened mother cell lifespans of both ETI and WT mother cells (Figure S6D). Hence, we conclude that, even though the transcriptional profile changes in ETI cells include features of an oxidative stress response, increased ROS levels and oxidative stress are not a primary cause of accelerated mother cell aging elicited by ETI.

ETI Cells Show Transient RNR3 Upregulation during Mother Cell Divisions

Given the connections between DNA damage and cell-cycle regulation, we turned to a more detailed analysis to establish whether DDR signaling was induced in ETI mother cells. Notably, phosphorylation of DDR components such as Rad53 and Mrc1 is only detectable in LTI cells and not in ETI cells (Grandin et al., 2005) (Figure S4A). Therefore, we employed a more sensitive single-cell monitoring method to detect evidence for DDR signaling. We examined DDR activation during mother cell aging using a GFP-tagged allele of *RNR3*, a gene that is strongly induced as a downstream component of the DDR. We monitored GFP intensity during mother cell lifespan assays and quantified RNR3-GFP peaks (at least 1.3-fold above background) using strains containing *RNR3-GFP* and all relevant combinations of *tlc1Δ*, *sml1Δ*, *mrc1^{AQ}*, and *tel1Δ* mutations. Peaks were classified as occurring before the last two cell divisions or during/after the

last two divisions, referred to here as “still-dividing” and “terminal” peaks, respectively (Figures 6C and 6E). Terminal peaks were scored as peaks per mother cell, and still-dividing peaks were scored as peaks per cell cycle as mother cells underwent a different average number of cycles depending on genotype (Figures 6D and 6F). In WT mother cells (two replicates), a transient RNR3-GFP peak appeared at a low frequency during the cell cycles of still-dividing mother cells (0.0062, 95% confidence limits 0.0031–0.0111; $n = 11$ events in 1,766 cell cycles) and terminal peaks occurred in 25.0% of mother cells (24/96 cells, 95% confidence limits 0.1736–0.3456). In contrast, in *tlc1Δ* ETI mother cell lineages (three replicates), RNR3-GFP peaks occurred at significantly greater frequency in still-dividing mother cells (0.0177, 95% confidence limits 0.0123–0.0252; $n = 30$ events out of 1,696 cell cycles, $p < 0.0025$ compared with WT), and in 27.7% of terminal mother cells (44/159 cells, 95% confidence limits 0.213–0.351). Hence, in still-dividing mother cells, ETI elicits an increased number of transient episodes of DDR signaling.

Notably, relative to *tlc1Δ* single mutants, RNR3-GFP peaks in *tlc1Δ sml1Δ* ETI mother cells (three replicates) were significantly diminished in frequency in the still-dividing mother cells (0.0104, 95% confidence limits 0.0071–0.0152; $n = 27$ events in 2,587 cell cycles, $p < 0.05$ compared with *tlc1Δ*), and terminal peaks occurred in only 13.1% of mother cells (22/168 cells, 95% confidence limits 0.087–0.191, $p < 0.01$ compared with *tlc1Δ*). This result is explainable, as *sml1Δ* raises nucleotide pools, making replication fork stalling less likely to occur (Andreson et al., 2010; Jossen and Bermejo, 2013) and hence reducing the possibility of eliciting a DNA replication stress response.

ETI *tlc1Δ tel1Δ* mother cells (two replicates) showed fewer RNR3 peaks than WT (or *tlc1Δ* ETI) in still-dividing cells (0.006, 95% confidence limits 0.0034–0.0124; $n = 10$ events in 1,505 cell cycles, $p < 0.006$ compared with *tlc1Δ*), and peaks occurred in 12.0% of terminal mother cells (15/125 cells, 95% confidence limits 0.0730–0.1897, $p < 0.009$ compared with *tlc1Δ*). This finding indicates that abrogating Tel1 greatly exacerbated the ETI mother cell aging phenotypes (Figures 4B and 4D) while reducing RNR3 induction events. We propose that the optimal response to the replication stress in *tlc1Δ* ETI cells requires Tel1 checkpoint function to activate DDR signaling, monitored here as downstream RNR3 induction.

Interestingly, the *tlc1Δ mrc1^{AQ}* ETI mother cells showed significantly more RNR3 peaks than WT cells in both still-dividing (0.0193, 95% confidence limits 0.0127–0.0289; $n = 23$ events in 1,192 cell cycles) and terminal mothers (32.4%, 35/108 cells, 95% confidence limits 0.243–0.417) and also trends to more RNR3 peaks than *tlc1Δ* (three replicates). Because the *mrc1^{AQ}* mutation exacerbates the ETI cell-cycle duration and lifespan reduction phenotypes, this finding indicates that telomeric replication stress requires Mrc1 checkpoint function in order to elicit an appropriate response in the absence of telomerase, but not for induction of the RNR3 reporter.

As the Rad9 adaptor protein is semi-redundant with Mrc1 in the DDR cascade, we investigated whether Rad9 is required for induction of RNR3 in the absence of Mrc1 checkpoint function. However, when combined with the *tlc1Δ* mutation, the *mrc1^{AQ} rad9Δ* double mutation induced rapid lethality of the

bulk ETI cell population, precluding mother cell analyses. Remarkably, this loss of viability in *tlc1Δmrc1^{AQ}rad9Δ* cells was also completely rescued by *sm1Δ* (data not shown). We conclude that, if ETI mother cells lack either Tel1 or Mrc1 checkpoint function, the response to, or repair of, telomeric DNA replication stress-induced damage is compromised.

The Degree of Heterogeneity of Cell-Cycle Durations and Mitochondrial Changes in Young ETI Mother Cells Each Quantitatively Predict Lifespan

Strikingly, for each mother cell genotype described above, the frequency and degree of lengthened cell cycles in young mother cells predicted the degree of reduction in mean lifespan (Figures S7A and S7B). Furthermore, for both WT and ETI mother cells, the extent of the mitochondrial fluorescence quantified at a given early time point in the budding lineage (4 hr) predicted the lifespan of that particular mother cell (Figures S7C and S7D). The finding that these relationships held across multiple genotypes suggests that responses that occur in even the youngest mother cells are caused by the same problem that eventually regulates the lifespan of the cell.

DISCUSSION

Here, we have shown that lack of active telomerase affects yeast mother cells much earlier than expected, well before any effect on cells that can be attributed to critical telomere shortness. Notably, early telomerase inactivation in yeast mother cells caused increased heterogeneity of the cell cycle and accelerated aging. These phenotypes were rescued by increasing nucleotide pool levels and were sensitive to inactivation of specific DDR components. By several criteria, the ETI mother cell aging phenotype is consistent with an acceleration of normal mother cell aging processes and not senescence caused by loss of telomere protective function. These criteria included terminal cell and mitochondrial morphologies that were characteristic of aging WT mother cells and distinct from those in senescent cells.

Previously, it was thought that telomeres had to become critically short in order to elicit a cellular DDR. In contrast, our results suggest that, independent of critical telomere shortness, ETI cells initiate signaling that accelerates an otherwise normal mother cell aging pathway. In the ETI setting, across multiple genotypes, the premature onset of mother cell aging is anticipated by the frequency and severity of stochastically slower cell-cycling events occurring in even young mother cells. In addition, we have shown that it is a lack of telomerase activity, rather than the lack of an assembled telomerase complex, that is the proximate cause of the response. Therefore, the action of telomerase on telomeres appears to be the most likely molecular property whose alteration causes these effects in ETI cells.

Our combined findings provide evidence for the model shown in Figure 7. In this model, during mother cell divisions in ETI cells, lack of telomerase activity may eliminate a potential bypass mechanism for replication stress in the telomere. This causes transient episodes of a much milder DDR than the robust and sustained DDR elicited by critically short telomeres (Nautiyal et al., 2002; d'Adda di Fagagna et al., 2003). We propose that deletion of *Sml1*, via its known phenotype of increasing dNTP

levels, alleviates this replication stress at an upstream level, preventing DNA damage signaling. This explains why *Sml1* deletion suppressed both the transient DDR signaling and the accelerated aging in ETI mother cells. We propose that such replication stress arises often in telomeres and is sensed by Tel1, which is required to cause the observed transient rises in RNR3 levels in ETI cells. This response promotes either repair or tolerance of the replication stress that allows ETI cells to bypass it and enter the next cell cycle. In ETI cells lacking the checkpoint functions of Tel1 or Mrc1 (*tlc1Δtel1Δ* or *tlc1Δmrc1^{AQ}*), cells cannot activate the appropriate response to this replication stress, thus exacerbating the ETI phenotypes. Without Mrc1 checkpoint function, compensation by the semi-redundant adaptor Rad9 occurs to some degree, but the telomeric replication stress is not fully resolved and further damage can ensue. However, in the absence of telomerase, even a fully functional DDR is not sufficient to fully alleviate telomeric replication stress and prevent accelerated mother cell aging.

We determined that neither ROS, recombination, deprotected (fusogenic) telomeres, redistribution of SIR protein complexes, nor a DDR similar to that in response to classic DNA damaging agents can account for the accelerated mother cell aging of ETI cells. Deletion of *SML1* rescued the cell cycle, lifespan, and DDR (RNR3) induction phenotypes in dividing ETI mother cells and is known to suppress replication fork stalling (Anderson et al., 2010; Jossen and Bermejo, 2013). The majority of mutant phenotypes known to be suppressed by *sm1Δ* are related to DNA replication, including replication fork progression. This suggests that suppression by *sm1Δ* is very specific and occurs through elevated nucleotide pools via the release of inhibition of the RNR complex. Furthermore, the transcriptional profile of ETI *tlc1Δ* cells indicates that they upregulate *RNR2*, *3*, and *4* gene expression (Nautiyal et al., 2002) (Table S2). Taken together with previous findings, our results suggest that the higher nucleotide pools in *sm1Δ* cells prevent telomeric replication stress from occurring, thus suppressing the ETI phenotype by preventing any need for DDR activation or telomerase intervention.

Telomerase is predicted to be recruited to backtracked replication forks resulting from stalling, which has been proposed to occur at measurable frequencies in telomeric DNA (Miller et al., 2006; Drosopoulos et al., 2012). Such backtracked forks will expose single-stranded leading-strand TG₍₁₋₃₎ repeat sequence DNA, which is the substrate for telomerase elongation. Also, telomerase could aid in the repair of a broken telomeric fork generated when a stalled replisome collapses (Chang et al., 2009). The resulting shortened telomere is a known preferred telomerase substrate (Miller et al., 2006). Other known interactions between DNA polymerase and telomerase actively engaged on telomeres may normally be required to optimize fork movement or fork restarting in telomeres. For example, the telomere-binding Cdc13-Stn1-Ten1 complex interacts via its Cdc13 subunit with a subunit of the telomerase complex (Est1) and also interacts (via Stn1) with a subunit of DNA polymerase alpha (Grossi et al., 2004).

The causal mechanism underlying mother cell aging remains unknown even for WT yeast despite extensive identification of genetic and environmental modifiers of this process. Our findings indicate that telomerase functionality is required throughout

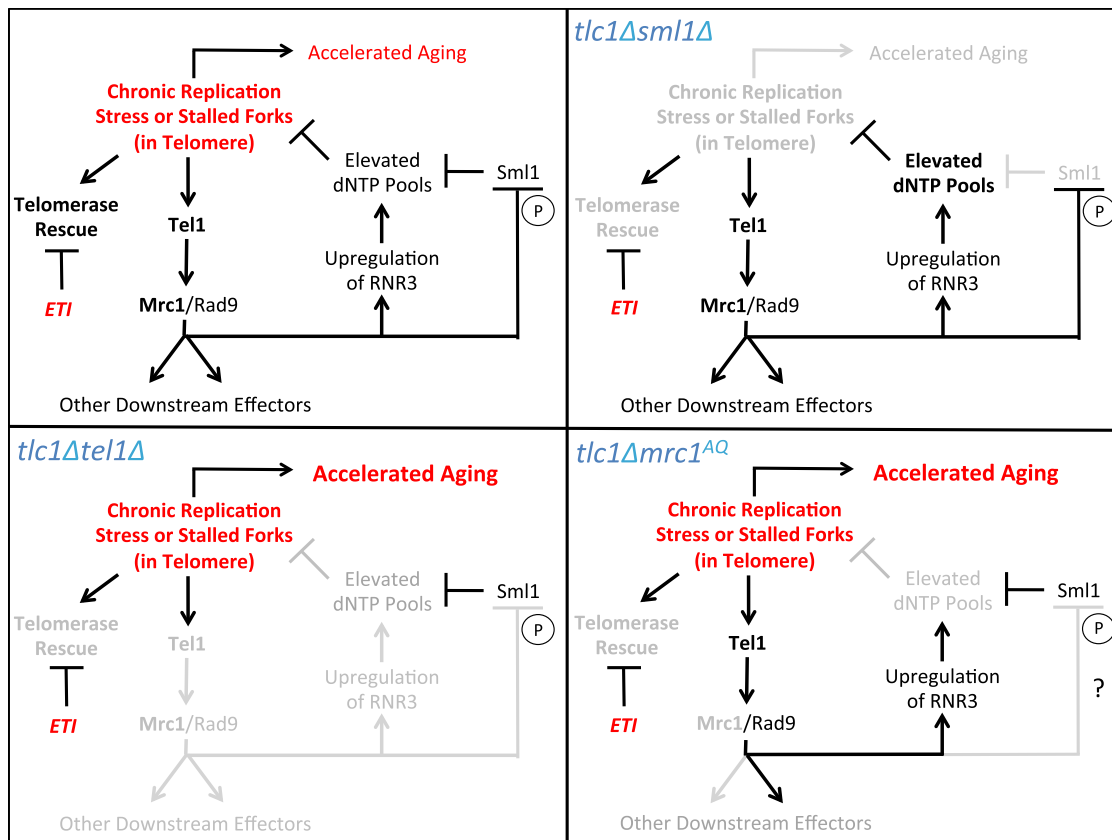


Figure 7. Proposed Model

(Upper-left) Proposed signaling interactions that regulate aging in response to telomeric DNA stress. Deleterious effects shown in red. (Upper-right) In ETI cells lacking Sml1 (*tlc1Δsml1Δ*), telomerase cannot alleviate replication stress. However, due to elevated dNTP levels, replication stress is prevented and aging is not accelerated. Eliminated or reduced signaling is shown in gray. (Lower-left) In ETI cells lacking Tel1 (*tlc1Δtel1Δ*), as well as lacking telomerase rescue, the DDR response is unavailable to alleviate replication stress, as indicated by the elimination of RNR3 signaling, and ETI-accelerated aging is exacerbated. (Lower-right) In ETI cells lacking Mrc1 function (*tlc1Δmrc1^{AQ}*), telomerase rescue is unavailable and the DDR response to telomeric replication stress is partially hindered. Rad9 is able to partially compensate and induce RNR3 induction, but other downstream DDR targets cannot be induced, thus exacerbating the ETI-accelerated aging. See also Figure S7.

the divisions of yeast mother cells in a more continuous mode than previously thought. The findings reported here indicate that telomerase activity is required to alleviate normal telomeric replication stress and allow mother cell aging to occur with wild-type kinetics. In addition, mutations known to inhibit telomerase activity or telomere maintenance have been implicated in the premature onset of diseases of aging and reduced lifespan in humans and mice (Codd et al., 2013, Armanios and Blackburn, 2012), and replication stress has been shown to induce aging in mouse cells (Flach et al., 2014). Therefore, this early requirement for active telomerase in preventing premature mother cell aging in yeast suggests a new possibility: that loss of telomerase activity may have telomere-length-independent consequences that accelerate aging and cause aging-related diseases in other eukaryotes.

EXPERIMENTAL PROCEDURES

See Extended Experimental Procedures for supplemental experiments: bulk population budding and chromosome segregation kinetics, NAC treatment, and ROS straining.

Yeast Strain Construction

All strains used in this study are listed in Table S1. Plasmid and oligo sequences are available upon request. Complete disruption of ORFs was carried out using PCR-mediated gene disruption (Rose et al., 1990). *mrc1^{AQ}* mutant strains were made either via a loop-in, loop-out of a plasmid containing the mutant, followed by PCR verification, or via plasmid transformation of the mutant into an *mrc1Δ* strain.

Growth of Mutants for Monitoring Early Loss of Telomerase

ETI cells were produced by two methods: by sporulation of diploid heterozygote strains (*tlc1Δ/TLC1*, *est2-D530A/EST2*) or by loss of a covering plasmid in a haploid telomerase-deficient background strain struck on solid media. Colonies underwent 2 days of growth at 30°C, were genotyped, and were grown overnight (five to ten generations) in YPD prior to experimentation.

Microfluidics Technique Analyses of Mother Cells

Mother cells were monitored for 2 days by repeated microscopic imaging as described (Xie et al., 2012; Zhang et al., 2012). Microposts contained within the microfluidic device were used to clamp mother cells in place while daughter cells were washed away by hydrodynamically controlled flow of the surrounding liquid medium. Cell-cycle durations analyzed here excluded the first cycle observed and the terminal two divisions.

Southern Blotting Analysis of Telomere Length

Genomic DNA was prepared from cells from serial streaks on solid media after the indicated number of passages. Genomic DNA was then digested with XhoI and run on 0.8% agarose gels. DNA was transferred from the gels to Hybond N+ membranes and probed with $\gamma^{32}\text{P}$ end-labeled WT telomeric repeat oligonucleotide (TGTGGTGTGGTGGTGGTGGT) as described previously (Rose et al., 1990; Sambrook and Russel, 2001) and visualized using a phosphorimager.

Mitochondrial and SIR3 Quantification

Cells containing mito-tagged (mt)GFP were placed on a microfluidics chip as described above. Images were taken every 2 hr, and mtGFP intensity was measured relative to WT to determine volume of mitochondria. For Sir3-GFP foci, 11 images were taken for the Z stack and projected to a single image using the maximum value of the column, and the fluorescence intensity of the foci was measured using customized software Cellseg 5.4.

Statistical Analysis

Lifespans were compared using the Wilcoxon rank-sum test. Significance for the variation of cell-cycle length was determined by F tests. We used Fisher's exact test to determine the significance of frequency of RNR3 peaks in different genotypes.

Quantification of RNR3 Peaks

Fluorescence was measured every 30 min during lifespan tracking. Frequency of RNR3 peaks (at least 1.3-fold over background) for "still-dividing" mother cells was calculated as the number of peaks divided by all cell cycles occurring within that genotype and for, "terminal" mother cells, as the percentage of mother cell lifespans that contained a peak during or after the last two divisions.

SUPPLEMENTAL INFORMATION

Supplemental Information includes Extended Experimental Procedures, five tables, and seven figures and can be found with this article online at <http://dx.doi.org/10.1016/j.cell.2015.02.002>.

AUTHOR CONTRIBUTIONS

Z.X. performed the microfluidic lifespan assays, cell counting and scoring, image segmentation, and fluorescence quantification. K.A.J. performed strain constructions, sample genotyping, bulk population studies, telomere length (Southern blot) experiments, and PCR-based telomere deprotection assays. D.L.S. performed strain constructions, cell-cycle and budding analyses, and DNA damage assays. E.H.B., Z.X., and H. L. analyzed the statistics. Y.Z. performed the Rad52 mutant lifespan assays. Z.L. synthesized the mtGFP plasmids. J.Z. and H.L. performed the bioinformatics analyses. R.T. aided in strain preparation. E.H.B., H.L., K.A.J., and Z.X. conceived the plans, interpreted and analyzed the data, and wrote the paper.

ACKNOWLEDGMENTS

This work was supported by NIH grant GM26259 to E.H.B. and NIH grants (GM070808 and AG043080) and a Packard Fellowship in Science and Engineering to H.L. and by the NIH Center for Systems and Synthetic Biology (P50 GM081879). Z.X. thanks the Postdoctoral Fellowship from PKU-THU Center for Life Science and Special Financial Grant from the China Postdoctoral Science Foundation.

Received: February 14, 2014

Revised: October 20, 2014

Accepted: January 28, 2015

Published: February 26, 2015

REFERENCES

Alcasabas, A.A., Osborn, A.J., Bachant, J., Hu, F., Werler, P.J.H., Bousset, K., Furuya, K., Diffley, J.F.X., Carr, A.M., and Elledge, S.J. (2001). Mrc1 trans-

duces signals of DNA replication stress to activate Rad53. *Nat. Cell Biol.* 3, 958–965.

Andreson, B.L., Gupta, A., Georgieva, B.P., and Rothstein, R. (2010). The ribonucleotide reductase inhibitor, Sml1, is sequentially phosphorylated, ubiquitinated and degraded in response to DNA damage. *Nucleic Acids Res.* 38, 6490–6501.

Armanios, M., and Blackburn, E.H. (2012). The telomere syndromes. *Nat. Rev. Genet.* 13, 693–704.

Basenko, E., Topcu, Z., and McEachern, M.J. (2011). Recombination can either help maintain very short telomeres or generate longer telomeres in yeast cells with weak telomerase activity. *Eukaryot. Cell* 10, 1131–1142.

Bishop, N.A., and Guarente, L. (2007). Genetic links between diet and lifespan: shared mechanisms from yeast to humans. *Nat. Rev. Genet.* 8, 835–844.

Chabes, A., Georgieva, B., Domkin, V., Zhao, X., Rothstein, R., and Thelander, L. (2003). Survival of DNA damage in yeast directly depends on increased dNTP levels allowed by relaxed feedback inhibition of ribonucleotide reductase. *Cell* 112, 391–401.

Chan, S.W., and Blackburn, E.H. (2003). Telomerase and ATM/Tel1p protect telomeres from nonhomologous end joining. *Mol. Cell* 11, 1379–1387.

Chang, M., Luke, B., Kraft, C., Li, Z., Peter, M., Lingner, J., and Rothstein, R. (2009). Telomerase is essential to alleviate pif1-induced replication stress at telomeres. *Genetics* 183, 779–791.

Codd, V., Nelson, C.P., Albrecht, E., Mangino, M., Deelen, J., Buxton, J.L., Hottenga, J.J., Fischer, K., Esko, T., Surakka, I., et al. (2013). Identification of seven loci affecting mean telomere length and their association with disease. *Nat. Genet.* 45, 422–427, e1–e2.

d'Adda di Fagagna, F., Reaper, P.M., Clay-Farrace, L., Fiegler, H., Carr, P., Von Zglinicki, T., Saretzki, G., Carter, N.P., and Jackson, S.P. (2003). A DNA damage checkpoint response in telomere-initiated senescence. *Nature* 426, 194–198.

Drosopoulos, W.C., Kosiyatrakul, S.T., Yan, Z., Calderano, S.G., and Schildkraut, C.L. (2012). Human telomeres replicate using chromosome-specific, rather than universal, replication programs. *J. Cell Biol.* 197, 253–266.

Edgar, R., Domrachev, M., and Lash, A.E. (2002). Gene Expression Omnibus: NCBI gene expression and hybridization array data repository. *Nucleic Acids Res.* 30, 207–210.

Flach, J., Bakker, S.T., Mohrin, M., Conroy, P.C., Pietras, E.M., Reynaud, D., Alvarez, S., Diolaiti, M.E., Ugarte, F., Forsberg, E.C., et al. (2014). Replication stress is a potent driver of functional decline in ageing haematopoietic stem cells. *Nature* 512, 198–202.

Grandin, N., Bailly, A., and Charbonneau, M. (2005). Activation of Mrc1, a mediator of the replication checkpoint, by telomere erosion. *Biol. Cell* 97, 799–814.

Greenwell, P.W., Kronmal, S.L., Porter, S.E., Gassenhuber, J., Obermaier, B., and Petes, T.D. (1995). TEL1, a gene involved in controlling telomere length in *S. cerevisiae*, is homologous to the human ataxia telangiectasia gene. *Cell* 82, 823–829.

Grossi, S., Puglisi, A., Dmitriev, P.V., Lopes, M., and Shore, D. (2004). Pol12, the B subunit of DNA polymerase α , functions in both telomere capping and length regulation. *Genes Dev.* 18, 992–1006.

Johnson, F.B., Sinclair, D.A., and Guarente, L. (1999). Molecular biology of aging. *Cell* 96, 291–302.

Jossen, R., and Bermejo, R. (2013). The DNA damage checkpoint response to replication stress: A Game of Forks. *Front. Genet.* 4, 26.

Kaeberlein, M. (2010). Lessons on longevity from budding yeast. *Nature* 464, 513–519.

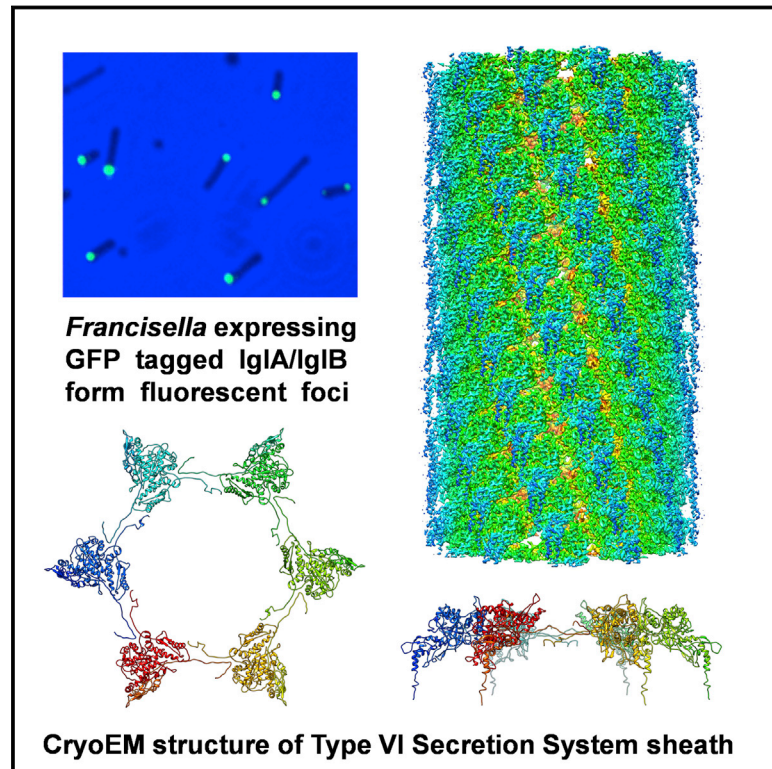
Kaeberlein, M., McVey, M., and Guarente, L. (1999). The SIR2/3/4 complex and SIR2 alone promote longevity in *Saccharomyces cerevisiae* by two different mechanisms. *Genes Dev.* 13, 2570–2580.

Lingner, J., Hughes, T.R., Shevchenko, A., Mann, M., Lundblad, V., and Cech, T.R. (1997). Reverse transcriptase motifs in the catalytic subunit of telomerase. *Science* 276, 561–567.

- Lundblad, V., and Blackburn, E.H. (1993). An alternative pathway for yeast telomere maintenance rescues est1- senescence. *Cell* 73, 347–360.
- Lustig, A.J., and Petes, T.D. (1986). Identification of yeast mutants with altered telomere structure. *Proc. Natl. Acad. Sci. USA* 83, 1398–1402.
- Martin, S.G., Laroche, T., Suka, N., Grunstein, M., and Gasser, S.M. (1999). Relocalization of telomeric Ku and SIR proteins in response to DNA strand breaks in yeast. *Cell* 97, 621–633.
- McEachern, M.J., and Blackburn, E.H. (1996). Cap-prevented recombination between terminal telomeric repeat arrays (telomere CPR) maintains telomeres in *Kluyveromyces lactis* lacking telomerase. *Genes Dev.* 10, 1822–1834.
- Miller, K.M., Rog, O., and Cooper, J.P. (2006). Semi-conservative DNA replication through telomeres requires Taz1. *Nature* 440, 824–828.
- Mills, K.D., Sinclair, D.A., and Guarente, L. (1999). MEC1-dependent redistribution of the Sir3 silencing protein from telomeres to DNA double-strand breaks. *Cell* 97, 609–620.
- Nautiyal, S., DeRisi, J.L., and Blackburn, E.H. (2002). The genome-wide expression response to telomerase deletion in *Saccharomyces cerevisiae*. *Proc. Natl. Acad. Sci. USA* 99, 9316–9321.
- Osborn, A.J., and Elledge, S.J. (2003). Mrc1 is a replication fork component whose phosphorylation in response to DNA replication stress activates Rad53. *Genes Dev.* 17, 1755–1767.
- Park, P.U., Defossez, P.-A., and Guarente, L. (1999). Effects of mutations in DNA repair genes on formation of ribosomal DNA circles and life span in *Saccharomyces cerevisiae*. *Mol. Cell. Biol.* 19, 3848–3856.
- Reichard, P. (1988). Interactions between deoxyribonucleotide and DNA synthesis. *Annu. Rev. Biochem.* 57, 349–374.
- Rowe, L.A., Degtyareva, N., and Doetsch, P.W. (2008). DNA damage-induced reactive oxygen species (ROS) stress response in *Saccharomyces cerevisiae*. *Free Radic. Biol. Med.* 45, 1167–1177.
- Sabourin, M., and Zakian, V.A. (2008). ATM-like kinases and regulation of telomerase: lessons from yeast and mammals. *Trends Cell Biol.* 18, 337–346.
- Salmon, T.B., Evert, B.A., Song, B., and Doetsch, P.W. (2004). Biological consequences of oxidative stress-induced DNA damage in *Saccharomyces cerevisiae*. *Nucleic Acids Res.* 32, 3712–3723.
- Sfeir, A., Kosiyatrakul, S.T., Hockemeyer, D., MacRae, S.L., Karlseder, J., Schildkraut, C.L., and de Lange, T. (2009). Mammalian telomeres resemble fragile sites and require TRF1 for efficient replication. *Cell* 138, 90–103.
- Takata, H., Kanoh, Y., Gunge, N., Shirahige, K., and Matsuura, A. (2004). Reciprocal association of the budding yeast ATM-related proteins Tel1 and Mec1 with telomeres in vivo. *Mol. Cell* 14, 515–522.
- Tsolou, A., and Lydall, D. (2007). Mrc1 protects uncapped budding yeast telomeres from exonuclease EXO1. *DNA Repair (Amst.)* 6, 1607–1617.
- Xie, Z., Zhang, Y., Zou, K., Brandman, O., Luo, C., Ouyang, Q., and Li, H. (2012). Molecular phenotyping of aging in single yeast cells using a novel microfluidic device. *Aging Cell* 11, 599–606.
- Zhang, Y., Luo, C., Zou, K., Xie, Z., Brandman, O., Ouyang, Q., and Li, H. (2012). Single cell analysis of yeast replicative aging using a new generation of microfluidic device. *PLoS ONE* 7, e48275.
- Zhao, X., Muller, E.G., and Rothstein, R. (1998). A suppressor of two essential checkpoint genes identifies a novel protein that negatively affects dNTP pools. *Mol. Cell* 2, 329–340.

Atomic Structure of T6SS Reveals Interlaced Array Essential to Function

Graphical Abstract



Authors

Daniel L. Clemens, Peng Ge, ..., Marcus A. Horwitz, Z. Hong Zhou

Correspondence

mhorwitz@mednet.ucla.edu (M.A.H.), hong.zhou@ucla.edu (Z.H.Z.)

In Brief

An atomic structure of the *Francisella novicida* type VI secretion system sheath, determined by cryoelectron microscopy, reveals a mesh-like architecture that is required for functional translocation of secreted proteins.

Highlights

- Specific environmental stimuli trigger *Francisella* T6SS assembly and secretion
- Atomic structure of T6SS sheath provides targets for mutagenesis and drug design
- Two-dimensional interlacing of T6SS sheath proteins is essential to its function
- Lack of ClpV and different sheath structure support an alternative functional state

Accession Numbers

3J90



Atomic Structure of T6SS Reveals Interlaced Array Essential to Function

Daniel L. Clemens,^{1,4} Peng Ge,^{2,3,4} Bai-Yu Lee,¹ Marcus A. Horwitz,^{1,2,*} and Z. Hong Zhou^{2,3,*}

¹Department of Medicine, University of California, Los Angeles, Los Angeles, CA 90095, USA

²Department of Microbiology, Immunology and Molecular Genetics

³The California NanoSystems Institute

University of California, Los Angeles, Los Angeles, CA 90095, USA

⁴Co-first author

*Correspondence: mhorwitz@mednet.ucla.edu (M.A.H.), hong.zhou@ucla.edu (Z.H.Z.)

<http://dx.doi.org/10.1016/j.cell.2015.02.005>

SUMMARY

Type VI secretion systems (T6SSs) are newly identified contractile nanomachines that translocate effector proteins across bacterial membranes. The *Francisella* pathogenicity island, required for bacterial phagosome escape, intracellular replication, and virulence, was presumed to encode a T6SS-like apparatus. Here, we experimentally confirm the identity of this T6SS and, by cryo electron microscopy (cryoEM), show the structure of its post-contraction sheath at 3.7 Å resolution. We demonstrate the assembly of this T6SS by IgIA/IgIB and secretion of its putative effector proteins in response to environmental stimuli. The sheath has a quaternary structure with handedness opposite that of contracted sheath of T4 phage tail and is organized in an interlaced two-dimensional array by means of β sheet augmentation. By structure-based mutagenesis, we show that this interlacing is essential to secretion, phagosomal escape, and intracellular replication. Our atomic model of the T6SS will facilitate design of drugs targeting this highly prevalent secretion apparatus.

INTRODUCTION

The type VI secretion system (T6SS) is a recently discovered (Bladergroen et al., 2003; Pukatzki et al., 2006; Silverman et al., 2012) and characterized (Basler et al., 2012, 2013; Ho et al., 2013; Kube et al., 2014) member of secretion systems of Gram-negative bacteria (Tseng et al., 2009). T6SSs are critical to the virulence of many important human pathogens, including *Vibrio cholerae*, *Salmonella enterica*, *Escherichia coli*, *Burkholderia pseudomallei*, and *Pseudomonas aeruginosa*. It delivers its protein effector into its prey cell by a contractile ejection apparatus similar to T4-like bacteriophage tails (Ak-syuk et al., 2009), R-type pyocins (Nakayama et al., 2000), and many other contractile nanomachines (Leiman and

Shneider, 2012), although T6SSs are several times longer than the other apparatuses (Ho et al., 2014). The T6SS is composed of a sheath and a tube anchored to the bacterial envelope by a baseplate (Ho et al., 2014) (Figure 1A). Instead of a single sheath protein in phage tails and pyocins, the T6SS sheath is composed of two proteins, VipA/VipB in *Vibrio*, which are orthologs of IgIA/IgIB of *F. tularensis* (Bröms et al., 2009; de Bruin et al., 2007). The contraction of the sheath drives the tube across its target membrane (Ho et al., 2014; Hood et al., 2010) (Figure 1B). However, the atomic structure of the T6SS and molecular interactions required for secretion are not known. Although the structure of *Vibrio* VipA/VipB outer sheath has recently been shown at 6 Å resolution (Kube et al., 2014), that structure is insufficient to guide drug design and mutagenesis studies.

Francisella tularensis subsp. *tularensis* is a Gram-negative bacterium that causes a zoonotic infection, tularemia, in animals and humans (Ellis et al., 2002). By the airborne route, a few organisms can cause lethal pneumonia in humans; hence, *F. tularensis* is a potential agent of bioterrorism and classified as a Tier 1 Select Agent. *F. tularensis* and the highly related *F. tularensis* subsp. *novicida* are facultative intracellular pathogens that replicate within macrophages. After uptake by macrophages via looping phagocytosis (Clemens et al., 2005, 2012), the bacteria initially reside within a fibrillar-coated membrane-bound phagosome that resists fusion with lysosomes and exhibits limited acquisition of lysosomal markers; however, the bacteria subsequently disrupt their phagosomal membrane and replicate extensively in the host cell cytosol (Chong and Celli, 2010; Clemens and Horwitz, 2007; Clemens et al., 2004). *F. novicida* has considerable homology with *F. tularensis*, but it has only a single copy of the *Francisella* Pathogenicity Island (FPI), and it is of low virulence for humans; it thus serves as a more practicable subspecies for study.

Here, we show that the FPI of *F. novicida* encodes a T6SS, and, by cryo electron microscopy (cryoEM), that the two proteins of its sheath, IgIA and IgIB, are interdigitated into a single fold similar to that of the phage sheath. CryoEM reconstruction at 3.7 Å reveals that β sheet augmentation interlaces the two-dimensional array of the sheath, and structure-based mutagenesis demonstrates that this interlacing is essential to secretion.

RESULTS

Environmental Stimuli Trigger Assembly of *F. novicida* T6SS and Secretion of Effector Proteins

To facilitate structural and functional studies of the FPI-encoded T6SS-like apparatus, we engineered *F. novicida* to express IgIA-GFP fusion protein in lieu of IgIA from its chromosome (Fn-IgIA-GFP). These bacteria show only a weak diffuse fluorescence when grown in standard liquid culture medium. However, within 15 min of uptake by macrophages, 10% of the bacteria exhibit intensely fluorescent foci (Figures 1C and 1E), and this percentage increases to ~70% by 1 day after uptake, by which time the bacteria have proliferated extensively in the macrophage cytosol (Figures 1D–1F). We used a split-GFP system (Cabantous and Waldo, 2006), with domains 1–10 of GFP fused to the C terminus of IgIA and domain 11 of GFP fused to the N terminus of IgIB (IgIA-GFP1-10 and IgIB-GFP11) to test the interaction of IgIA and IgIB in formation of fluorescent foci. These bacteria are not fluorescent when grown in broth culture but exhibit intense GFP fluorescent foci after uptake and replication within macrophages (Figures 1G and 1H). In contrast, *F. novicida* expressing IgIA-GFP1-10/SodB-GFP11 (Figure 1I) and *F. novicida* expressing IgIA-GFP1-10 without a GFP11 partner (Figure 1J) do not form green fluorescent structures, despite their capacity to replicate extensively within macrophages (Figure 1K). Western blotting confirmed expression pattern of IgIA/B-split GFP constructs (Figure 1L).

Because FPI mutants are unable to permeabilize their vacuoles, formation of the IgIA/IgIB containing T6SS and secretion of its effectors is believed to precede and to be required for phagosome disruption and cytosolic escape by *Francisella*. The extremely high expression at late stages of infection suggests that the FPI-encoded T6SS is required for events after phagosome permeabilization. Consistent with this, (1) most FPI genes are induced during intramacrophage growth and show high levels of expression at late time points after bacterial uptake (Golovliov et al., 1997; Wehrly et al., 2009), when most bacteria are cytosolic, and (2) we have observed that IgIC is required for intracellular growth of *F. novicida* that are micro-injected directly into the cytosol of HeLa cells.

In addition to intracellular growth in macrophages, two other conditions induce formation of fluorescent structures within Fn-IgIA-GFP or Fn-IgIA/B-split GFP: (1) placement beneath coverslips (either sealed by silicone or not) at room temperature for more than 3 hr (Figures 2A–2E) and (2) growth in broth containing 5% KCl (but not 5% NaCl) (Figures 2F–2J). The fluorescent foci do not form in Fn-IgIA-GFP with a deletion of *igIB* in response to any of the above three conditions (Figure S1), suggesting that IgIB subunits are required for assembly of the T6SS-like structure. The stimulus for assembly of fluorescent foci provided by placement beneath coverslips is unclear but could include physical stimulation, modulation of oxygen tension, or other environmental conditions. The fluorescent foci form with similar kinetics by bacteria sandwiched between a polystyrene surface and glass coverslip or between two glass surfaces but form more slowly when the glass slide is replaced with a 25 μ m gas-permeable Lumox (Starstedt) film base, consistent with a role for oxygen tension.

Whereas by fluorescence microscopy Basler et al. (2012) demonstrated highly dynamic assembly and disassembly of VipA-GFP-labeled structures of live *Vibrio*, we have not observed similar rapid disassembly of the IgIA-GFP or IgIA/B-split GFP fluorescent structures in individual live bacteria. The slower turnover of the *F. novicida* T6SS may reflect the absence of an identifiable protein in the *F. tularensis* genome to disassemble the T6SS. Although the *F. novicida* genome lacks a protein with homology to ClpV, we cannot rule out the possibility of a protein with no such sequence homology that fulfills this role. However, *F. novicida* IgIB, a VipB homolog, lacks the latter's identified ClpV-interacting motif (Pietrosiuk et al., 2011): an α -helical region at the N terminus of VipB (including a consensus sequence LLDEIM, residues 19–24 of VipB). Indeed, Protein-Protein BLAST analysis indicates that the N-terminal 56 amino acids of VipB have no sequence homology with any region of IgIB, and the N terminus of *F. novicida* IgIB has no similar α -helical region or consensus sequence. The GFP tags on IgIA and IgIB are not likely to hamper their interaction with any disassembling chaperone because (1) we observe the same slow turnover for both *F. novicida* expressing IgIA-GFP (GFP fused to the C terminus of IgIA) and *F. novicida* expressing the split GFP construct (IgIA with GFP domains 1–10 fused to its C terminus and IgIB with GFP domain 11 fused to its N terminus), and (2) for *V. cholerae*, rapid turnover was observed even for VipA-GFP (C-terminal fusion), indicating that the corresponding VipA-GFP fusion in *V. cholerae* does not prevent rapid ClpV-mediated disassembly. If *F. novicida* has a functional homolog of ClpV, then its interactions with the T6SS sheath are likely to differ markedly from those in *V. cholerae*.

Secretion of VgrG by *F. novicida* has been reported previously (Barker et al., 2009). We prepared FLAG-tagged VgrG and grew the bacteria in the presence or absence of KCl. FLAG-VgrG and IgIC are both detected in the culture supernatant in the presence, but not in the absence, of KCl (Figure 2K). Deletion of *igIA* abolishes the release of VgrG and IgIC into the culture medium (Figure 2K).

IgIA/IgIB Heterodimers Assemble to Form *Francisella* T6SS Sheaths

We purified assemblies containing IgIA-GFP or IgIA from lysates of bacteria grown in trypticase soy broth supplemented with 0.2% L-cysteine (TSBC) in the presence of KCl. Both proteins sedimented in equilibrium to below 55% sucrose on sucrose gradients. Negatively stained TEM images of the fraction containing IgIA-GFP or IgIA showed rod-shaped particles of variable length, similar to *Vibrio cholerae* T6SS sheaths with or without GFP tag (Basler et al., 2012) (Figures 2L–2M). Rod-shaped sheath particles containing IgIA-GFP, but not IgIA, are recognized by immunogold labeling for GFP (Figure S2).

We recorded cryoEM image stacks (movies) (Campbell et al., 2012) with a Gatan K2 direct electron detector (McMullan et al., 2009) operated at counting mode (Li et al., 2013) (Figure 3A); obtained a three-dimensional structure to 3.7 Å by an integrative approach that implements iterative helical real space reconstruction (IHRSR) (Egelman, 2010) within the Relion (Scheres, 2012) framework (Figure 3B); and built an atomic model of the T6SS apparatus (Figure 3C) (see also Experimental Procedures).

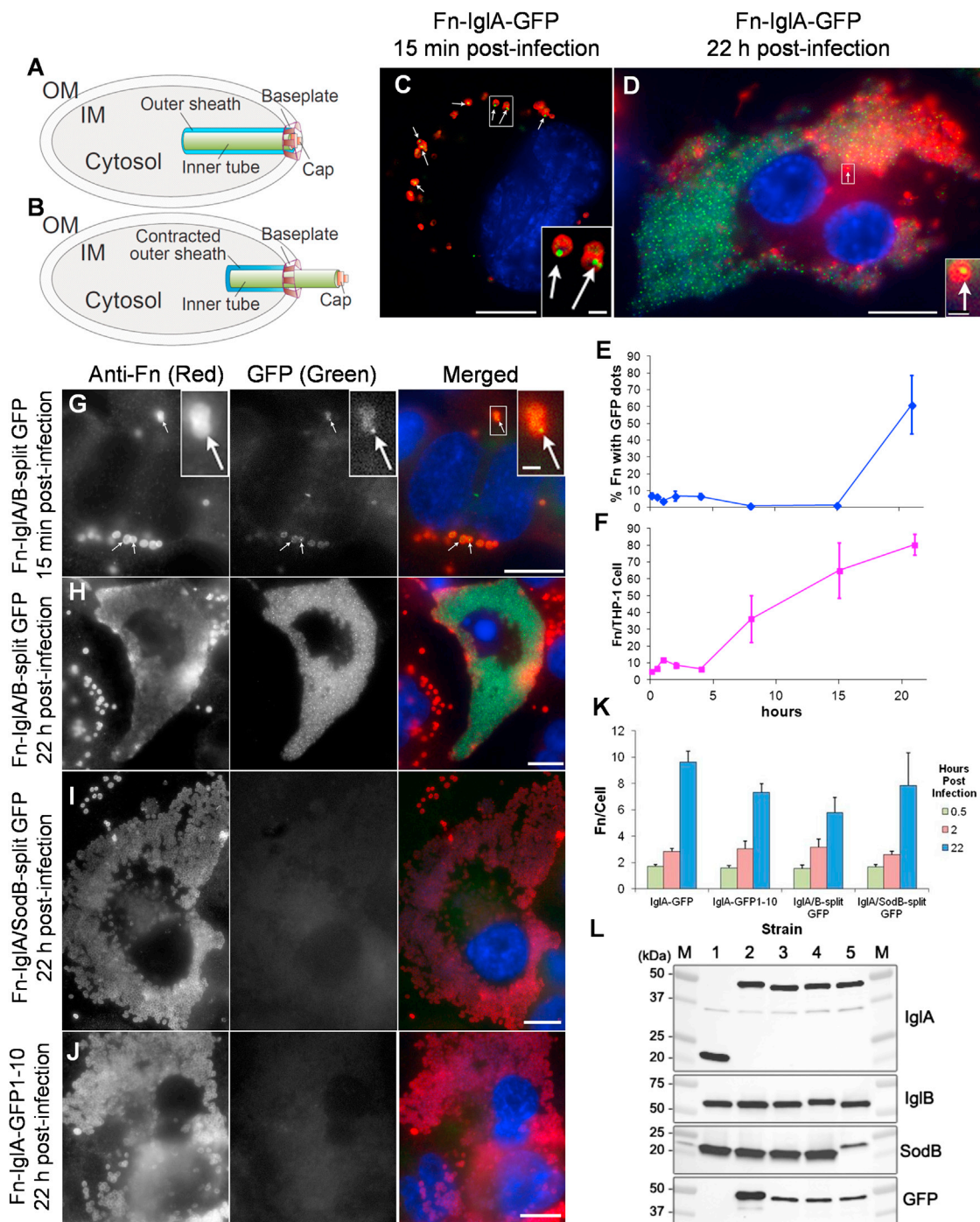


Figure 1. *F. novicida* Expressing GFP-Tagged IgIA or IgIA/B-Split GFP Form Fluorescent Foci within Macrophages, Consistent with T6SS Assembly

(A and B) Proposed T6SS model in pre-contraction (A) and post-contraction (B) conformation. IM, inner membrane; OM, outer membrane.

(C–F) *F. novicida* expressing IgIA-GFP assemble fluorescent foci after uptake by macrophages, with 10% doing so at 15 min of infection (C) and 70% at 22 hr of infection (D). *F. novicida* bacteria are stained with a red fluorescent antibody; host and bacterial DNA is stained blue with DAPI; and arrows indicate bacteria shown at higher magnification in the insets. Scale bars, 10 μ m (insets, 1 μ m). The percentage of Fn-IgIA-GFP with fluorescent foci (E) and the number of *F. novicida* per THP-1 macrophage (F) were determined at each time point. Data shown represent the mean \pm SE of measurements of at least 144 cells per time point. The experiment was done three times with similar results.

(G–J) Requirement for IgIA/B interaction for formation of the fluorescent foci was demonstrated in *F. novicida* expressing IgIA-GFP1-10/IgIB-GFP11 split GFP (Fn-IgIA/B-split GFP) and controls. At 15 min post-infection of THP-1 macrophages (G), \sim 10% of Fn-IgIA/B-split GFP form fluorescent structures at their poles, and by

(legend continued on next page)

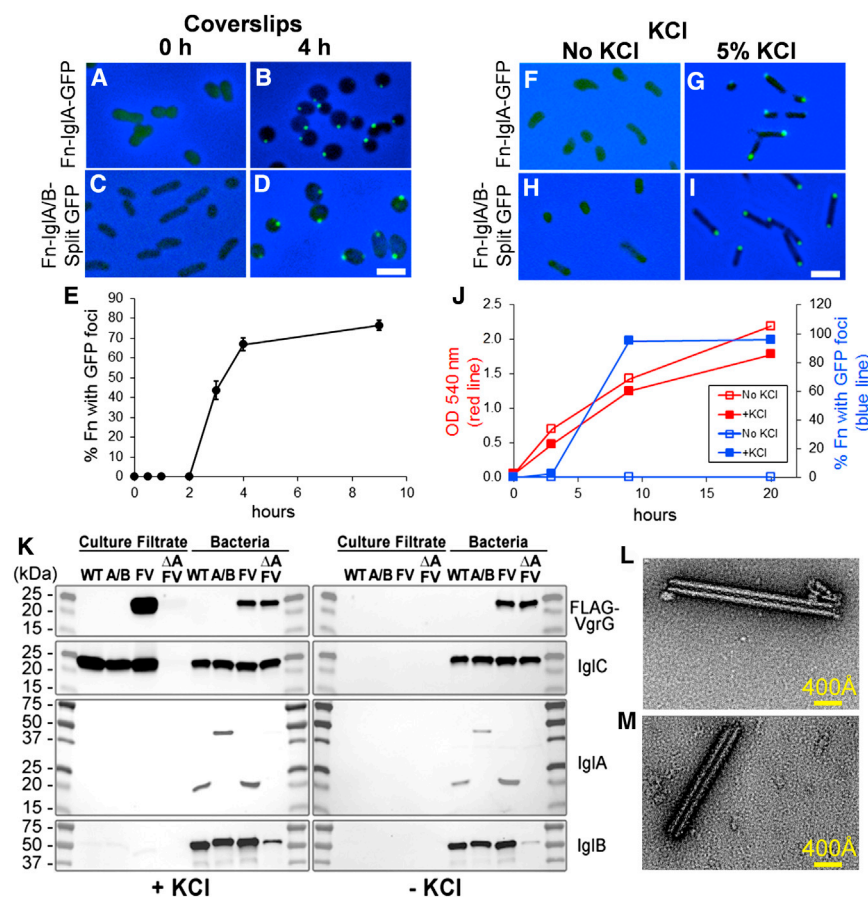


Figure 2. *F. novicida* Assemble Fluorescent Foci in Response to High KCl and Placement beneath a Coverslip and Secrete T6SS Effector Proteins in Response to Environmental Stimuli

(A–E) Placement beneath a glass coverslip: Fn-IglA-GFP (A and B) and Fn-IglA/B-split GFP (C and D) in TSBC were placed beneath a silicone sealed coverglass and imaged immediately (Fn-IglA-GFP, A; Fn-IglA/B-split GFP, C) or after 4 hr at room temperature (Fn-IglA-GFP, B; Fn-IglA/B-split GFP, D). Images shown are merged green fluorescence and phase contrast images, with phase contrast shown in blue. Bacteria exhibit either a diffuse weak fluorescence or no fluorescence immediately after placement beneath a glass coverslip (A and C) but exhibit intense fluorescence at their poles after 4 hr at room temperature (Fn-IglA-GFP, B; Fn-IglA/B-split GFP, D). Scale bar, 2 μ m. (E) Time course of formation of the fluorescent structures by Fn-IglA/B-split GFP after placement beneath a coverslip at room temperature. Data are represented as means \pm SEM.

(F–J) High KCl: Fn-IglA-GFP or Fn-IglA/B-split GFP were inoculated into TSBC at an OD 540 nm of 0.05 and grown at 37°C overnight to late exponential phase (OD 1.0–1.4) in the absence (Fn-IglA-GFP, F; Fn-IglA/B-split GFP, H) or presence of 5% KCl (Fn-IglA-GFP, G; Fn-IglA/B-split GFP, I). Bacteria exhibit only a weak diffuse fluorescence in the absence of KCl (F and H) but develop intense fluorescence at their poles in response to 5% KCl (G and I). Scale bar, 2 μ m. See also Figure S1. (J) Growth and kinetics of formation of fluorescent foci in Fn-IglA/B-split GFP in TSBC with and without 5% KCl. Fn-IglA/B-split GFP was inoculated into TSBC broth with or

without 5% KCl at an optical density of 0.05 and grown at 37°C rotating at 250 rpm. OD (red lines) and percentage of bacteria with fluorescent foci (blue lines) in the presence (solid squares) or absence (open squares) of KCl were monitored over time.

(K) Secretion in response to high KCl: VgrG and IglC are secreted by *F. novicida* with intact T6SS growing in TSBC with (left), but not without 5% KCl (right). WT, wild-type; A/B, Fn-IglA/B-split GFP; FV, Fn-FLAG-VgrG; Δ A FV, Fn-FLAG-VgrG Δ IglA.

(L–M) Sheath-like macromolecular structures purified from wild-type and IglA-GFP expressing *F. novicida*. *F. novicida* expressing native (L) or GFP-tagged (M) IglA assemble similar sheath-like macromolecular structures. Negatively stained TEM images of density gradient fractions from *F. novicida* expressing wild-type IglA (L) or IglA-GFP (M) show rod-shaped structures of variable length.

See also Figure S2.

Like contractile phage tails (Leiman and Shneider, 2012), the sheath is organized in a cylindrical, helical form with an axial 6-fold rotational symmetry (Figure 3 and Movie S1). The sheath is constructed with discs of six heterodimers of IglA/IglB proteins (Figure 3D and Movie S2). The validity of the map and the model is demonstrated by the deep grooves in α helices, well-sepa-

rated β strands, and match of side chains in the sequence and in the density map (Figures 3E and 3F).

The asymmetric unit of the helical sheath contains one copy each of IglA and IglB. The folds of the IglA/IglB proteins can be thought of as a “split” of the single protein of a bacteriophage sheath with many insertions (Figures 4A–4D and Movie S3).

22 hr after infection (H), most of the bacteria exhibit green fluorescent structures. In contrast, *F. novicida* expressing IglA-GFP1-10/SodB-GFP11 (I) and *F. novicida* expressing IglA-GFP1-10 without a GFP11 partner (J) do not form green fluorescent structures, despite their capacity to replicate extensively within the macrophages. Panels on the left show *F. novicida* stained with a red fluorescent antibody (in black and white), the middle panels show GFP green fluorescence (in black and white), and the panels on the right show merged color images with DAPI-stained host and bacterial DNA in blue. Arrows in (G) indicate bacteria with intense GFP fluorescent structures at 15 min post-infection, one of which is shown at higher magnification in the inset. Scale bars, 10 μ m (inset, 1 μ m).

(K) Kinetics of growth of IglA/B-split GFP and control strains in THP-1 macrophages. THP-1 macrophages were infected with Fn-IglA/B-split GFP or control strains, incubated at 37°C for 0.5, 2, or 22 hr, fixed with 4% paraformaldehyde, and permeabilized with 0.1% saponin, and the bacteria were stained with a red fluorescent antibody. The number of bacteria per macrophage nucleus was determined by automated counting using CellProfiler Software. All strains show capacity to grow in macrophages. Data are represented as means \pm SEM.

(L) Western immunoblot confirms expression pattern for IglA/B-split GFP constructs. Lane 1, Fn. Lane 2, Fn-IglA-GFP. Lane 3, Fn-IglA-GFP1-10. Lane 4, Fn-IglA/B-split GFP. Lane 5, Fn-IglA/SodB-split GFP. M, molecular mass standards, as indicated to the left of the figure. Primary antibody used is indicated on the right for each blot.

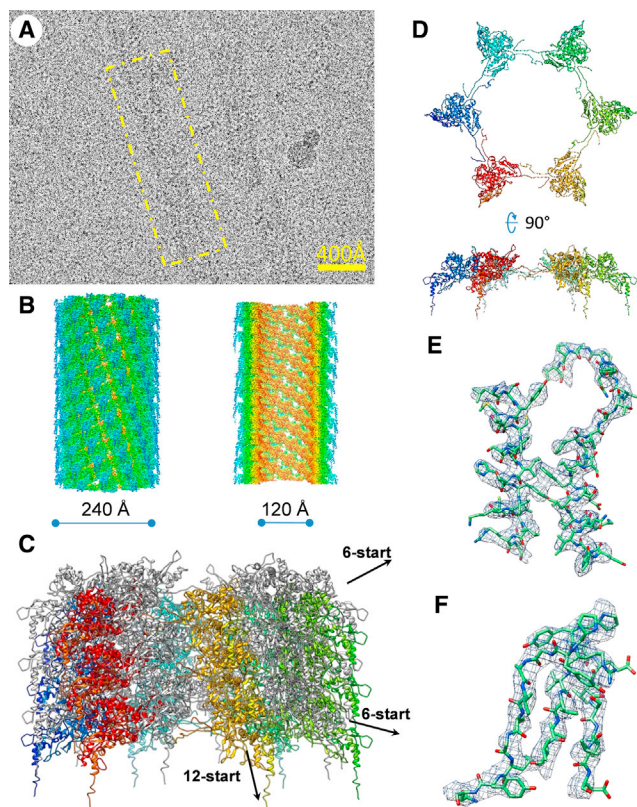


Figure 3. CryoEM and Atomic Model of *F. novicida* T6SS

(A) A representative cryoEM image of *F. novicida* T6SS recorded on a direct-electron detector. The yellow box marks one sheath.

(B) CryoEM density map of the *F. novicida* T6SS sheath displayed as shaded surface (left) and cut-away view (right), both colored according to radius. See also [Movie S1](#).

(C) Atomic model of *F. novicida* T6SS with six discs shown. The 12-start helices (ridges) are colored alternatively with rainbow colors and gray. See also [Movie S2](#).

(D) Hexagonal disc formed by six IgA/IgB heterodimers of *F. novicida* T6SS shown in two different orientations. Each heterodimer is displayed as a ribbon diagram of a different color.

(E–F) Two representative density regions (chicken-wire) with their atomic models (sticks, colored by atoms; C, green; N, blue; O, red; S, yellow).

Joining together, these two proteins form an α - β - α sandwich. The central β sheet of this sandwich is formed by interdigitation of strands from both IgA and IgB ([Figure 4E](#)). The sheath fold splits between its first and second α helices, and each of the two ends of the split is appended with an insertion (box in [Figure 4D](#)). Parts of these two insertions are disordered (C-terminal amino acids 136–184 of IgA and N-terminal amino acids 2–78 of IgB [question marks in [Figure 4D](#)]). The domain near the C terminus of IgB (cyan in [Figures 4C](#) and [4D](#)) highly resembles the C-terminal domain of the phage sheath proteins ([Aksyuk et al., 2009, 2011](#)).

***F. novicida* T6SS and Bacteriophage T4 Outer Sheaths Show Divergent Quaternary Organization Despite Secondary and Tertiary Structural Homology**

The secondary structure and tertiary structural arrangement of the *F. novicida* T6SS sheath are similar, but not identical, to

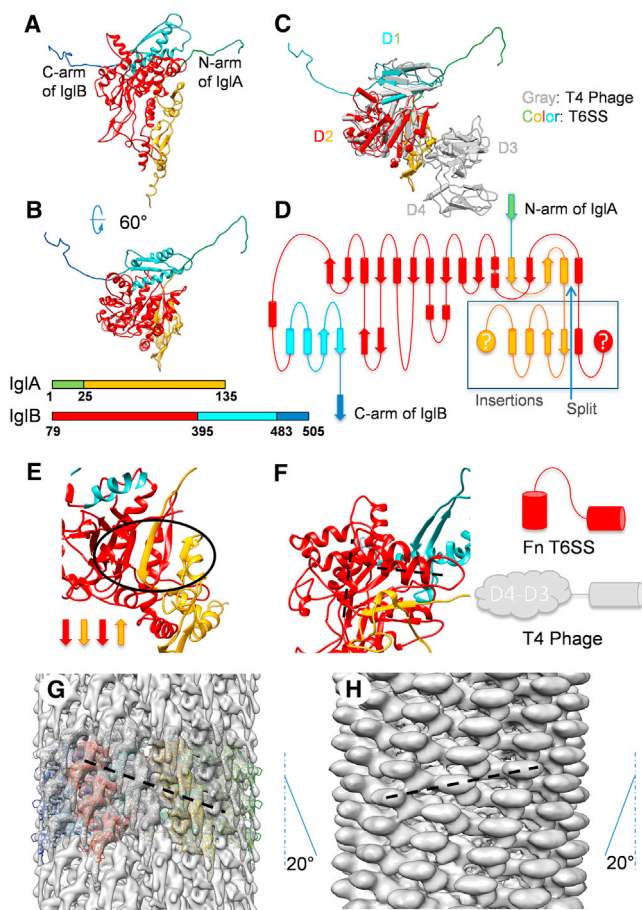


Figure 4. Atomic Model and Architecture of T6SS Sheath and Comparison with Bacteriophage T4

(A and B) Atomic model of an IgA/IgB dimer shown as ribbons with domains colored as indicated in the bars below (B).

(C) Superposition of the atomic models of the IgA/IgB dimer (colors) and bacteriophage T4 sheath (gray) ([Leiman et al., 2004](#)). See also [Movie S3](#) and [Figure S3](#). D1–D4, domains 1–4.

(D) Secondary structure diagram of an IgA/IgB dimer, colored as in (A) and (B). Elements in the box are insertions at the “split.”

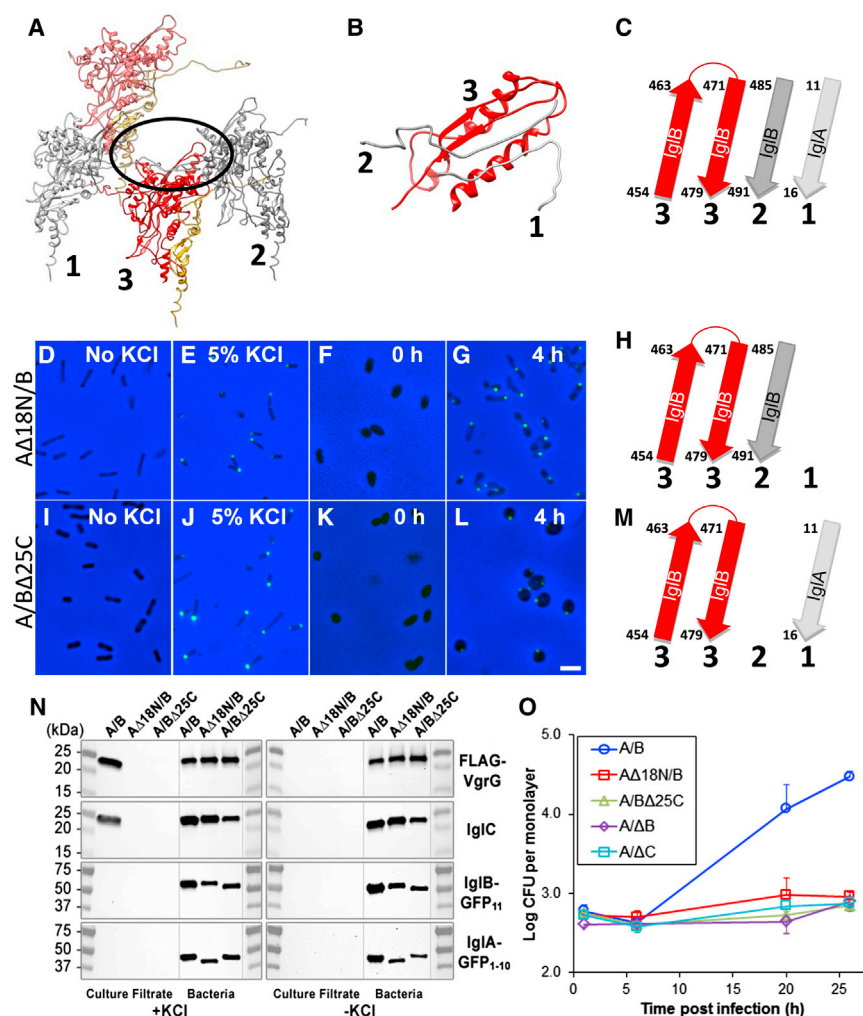
(E) The central β sheet of an IgA/IgB dimer is made of interdigitated strands (inside oval) from both subunits.

(F) Ribbon diagram of IgA/IgB centered on the third and fourth helices of IgB (marked by two dashed lines) (left) and comparison between the schematics of this vicinity in *F. novicida* T6SS and in T4 phage (right).

(G and H) Comparison between the quaternary structures of post-contraction *F. novicida* T6SS (G) and T4 phage (H) sheaths showing opposite handedness. The angles between their 12-start helices and their helical axes are marked on their sides, respectively. The semi-transparent shaded surfaces of the density map of the T6SS (G) sheaths at 10 Å resolution is fitted with six discs of ribbon models colored as in [Figure 3C](#). The density map of T4 phage sheath at 17 Å is taken from EMDB entry EMD-1086.

See also [Figure S4](#).

those of the bacteriophage T4 sheath ([Fokine et al., 2013](#)). The central β sheet of the *F. novicida* T6SS is formed by interdigitating two proteins ([Figure 4E](#)). Notably, phage T4 sheath protein has an insertion of two domains before a long helix ([Figures 4C](#) and [4F](#), see lower right schematic, and [Movie S3](#)),



whereas in T6SS sheath, this long helix is broken into two shorter helices, its third and fourth helices from its N terminus. In the case of *F. novicida*, the third helix tilts up and is almost perpendicular to the fourth helix (Figure 4F, dashed lines in ribbon diagram, and upper right schematic). In stark contrast, the quaternary structural organization of the T6SS sheath is markedly different from that of the post-contraction T4 (Leiman et al., 2004) sheath (Figures 4G and 4H; see also Figure S3). The helix with the shortest, non-zero pitch (a six-start helix, black dashed line in Figures 4G or 4H) in the T6SS sheath has a left-handed turn of 33.4° (Figure S3D) and a rise of 20.8 Å per subunit (whereas the T4 sheath has a right-handed turn of 32.9°); thus the two helical architectures mirror each other. Despite opposite handedness, layer lines in the Fourier spectra of the EM images (Figure S4) indicate that the other parameters of the helical symmetry of the *F. novicida* T6SS sheath and the post-contraction T4 sheath are similar, suggesting that this T6SS sheath structure is in its post-contraction state.

F. novicida T6SS Outer Sheath Has a Highly Interlaced Two-Dimensional Array Architecture with Augmented β Sheets that Is Essential to Secretory Function

The two-stranded β sheet of the C-terminal domain of IgIB is augmented on one side by arms that emanate from the two neighboring IgIA/IgIB dimers from a disc above (Figures 5A–5C, S3B, and S3C), forming a four-stranded sheet. By this augmentation, the arms from hundreds of copies of IgIA/IgIB interlace a two-dimensional array (Figures S3A and S3C). We hypothesized that this two-dimensional interlacing is crucial to the integrity and thus the contractility and secretory capacity of the *F. novicida* T6SS. To test this hypothesis, we carried out structure-based mutagenesis experiments for residues centered on the augmented β sheet. We prepared IgIA/B-split GFP mutant strains lacking either N-terminal amino acids 2–18 of IgIA (Fn-IgIA Δ 18N/B-split GFP) or the last 25 amino acids at the C-terminal of IgIB (Fn-IgIA/B Δ 25C-split GFP). We predicted that both mutant strains would show normal assembly of their pre-contraction T6SS organelles but that the T6SS sheath would

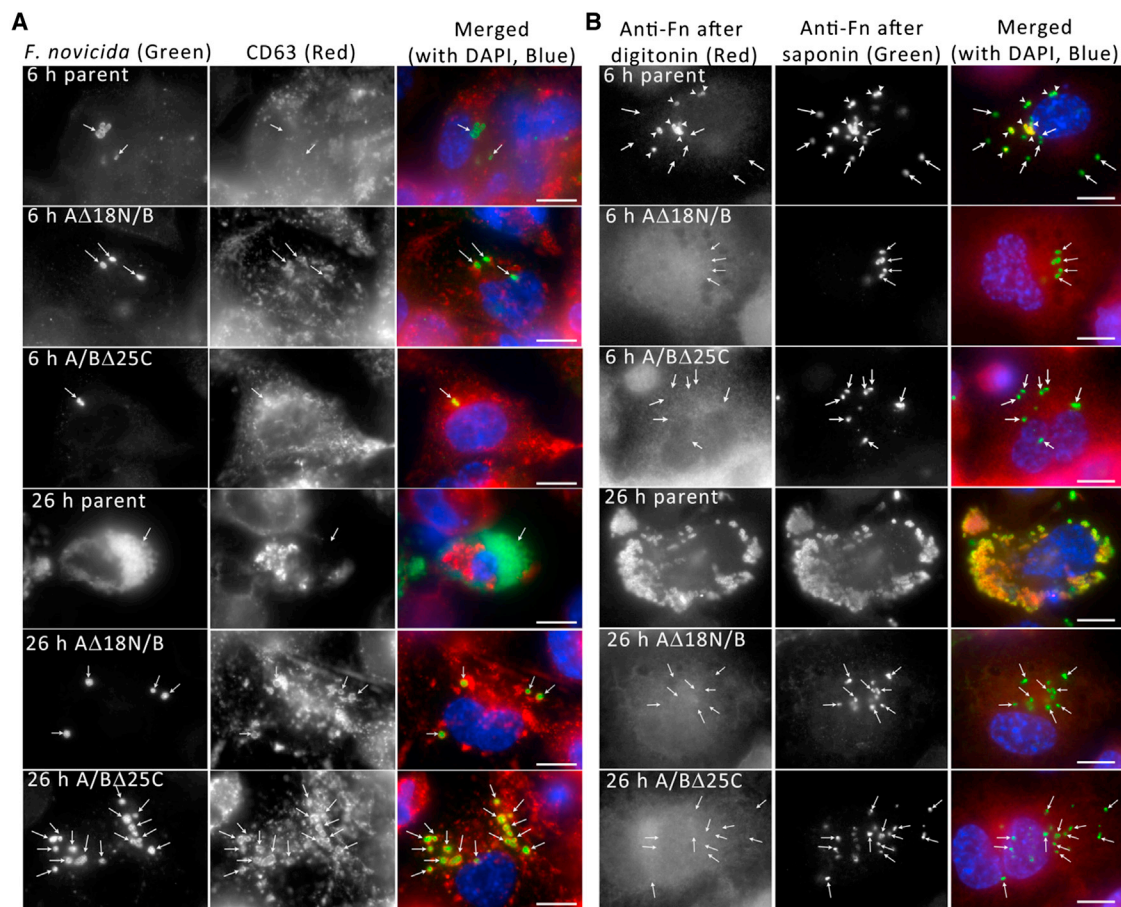


Figure 6. IgIA N-Terminal or IgIB C-Terminal Deletion Mutants Are Defective in Phagosome Escape

(A) Unlike the parental strain (Fn-IgIA/B-split GFP), Fn-IgIA Δ 18N/B-split GFP and Fn-IgIA/B Δ 25C-split GFP (stained with a green fluorescent anti-*F. novicida* antibody, shown in black and white in the left panels) are unable to escape their phagosome and remain within CD63-positive compartments (stained with a red fluorescent antibody, shown in black and white in the middle panels) in human macrophage-like THP-1 cells, both at 6 hr and 26 hr. Arrows indicate bacteria stained with the anti-*F. novicida* antibody. The panels on the right show merged color images with *F. novicida* stained green, CD63 stained red, and host and bacterial DNA stained blue with DAPI.

(B) Cytosolic versus phagosomal localization of *F. novicida* was determined using a differential digitonin permeabilization antibody staining procedure. *F. novicida* bacteria accessible to antibody after digitonin permeabilization (which permeabilizes the plasma membrane but not the phagosomal membrane) were stained with a red fluorescent anti-*F. novicida* antibody, and all bacteria were subsequently stained with a green fluorescent antibody after saponin permeabilization. Whereas many of the parental strain *F. novicida* are stained by the red fluorescent antibody after digitonin permeabilization at 6 hr post-infection (arrowheads), none of the Fn-IgIA Δ 18N/B-split GFP and Fn-IgIA/B Δ 25C-split GFP (arrows) are stained by the red fluorescent antibody either at 6 hr or 26 hr after infection. Parental bacteria that remain inaccessible to antibody after digitonin permeabilization at 6 hr are indicated by arrows. At 26 hr post-infection, the parental *F. novicida* have proliferated extensively within the cytosol, and the majority are accessible to the red fluorescent antibody after digitonin permeabilization. The Fn-IgIA Δ 18N/B-split GFP and Fn-IgIA/B Δ 25C-split GFP bacteria (indicated by arrows) show much more limited replication within the macrophage and remain inaccessible to the red fluorescent antibody. Scale bars, 10 μ m. These experiments were performed three times with similar results.

become unstable with attempted contraction and thus fail to secrete effector proteins.

Indeed, both the IgIA and IgIB truncation mutants expressing the truncated IgIA/B with the split GFP tags formed fluorescent foci in response to 5% KCl or incubation beneath coverslips (Figures 5D–5M), indicating focal multimerization of the IgIA/B-heterodimers. However, the mutants were completely defective in secretion of IgIC (Figure 5N) and had markedly impaired growth in THP-1 macrophage-like cells, with growth kinetics similar to *igIB* and *igIC* deletion mutants (Figure 5O). Like the *igIB* and *igIC* deletion mutants, the Fn-IgIA Δ 18N/B- and Fn-IgIA/B Δ 25C-

split GFP mutants remain within compartments that stain positive for the lysosomal marker CD63 (Figure 6A) and are unable to escape their phagosomes (Figure 6B).

DISCUSSION

By employing the split-GFP technology, we identified three stimuli that trigger the assembly of IgIA/IgIB sheaths in *F. novicida*: (1) late exponential phase with high bacterial density in the presence of high KCl, (2) placement beneath a coverslip, and (3) the intramacrophage environment. Although there is precedent

for demonstration of T6SS regulation by quorum sensing (Ishikawa et al., 2009; Lesic et al., 2009), salinity (Ishikawa et al., 2012), and membrane perturbation (Basler et al., 2013; Ho et al., 2013), we are unaware of prior reports of T6SS assembly induced selectively by KCl or by intracellular residence. We hypothesize that KCl is a stimulus for T6SS assembly in the intracellular environment and that higher concentrations are required in liquid culture to compensate for the absence of other intracellular stimuli. The factors stimulating T6SS when bacteria are placed beneath a coverslip are unclear and could involve physical stimuli, altered oxygen tension, or other environmental influences. We confirmed that one stimulus, high KCl in liquid culture, induced secretion of putative T6SS effector proteins, VgrG and IglC, as would be expected for induction of the secretion system. We purified sufficient amounts of IglA/IglB sheaths from bacteria stimulated with this condition for high-resolution cryoEM structural studies. Taking advantage of the latest technological breakthrough—direct electron counting—we determined the structure of this sheath to 3.7 Å, permitting the de novo atomic modeling of IglA/IglB and the confirmation of its identity as the T6SS in *F. novicida*. This structure shows a highly interlaced two-dimensional array that is critical to the secretion function.

As with other contractile nanomachines, the *F. novicida* T6SS propels its central tube by contraction of its sheath assembly. An intriguing feature of the sheath structure is its two-dimensional interlacing formed by augmented β sheets. It is likely present in the pre-contraction form of the T6SS sheath as well and plays a critical role during contraction. Our work directly reveals the importance of this interlaced structure to the contractile function of this T6SS and lays the foundation for understanding the presumably shared mechanism of other contractile nanomachines.

Results utilizing the truncation mutants of IglA/IglB prove the critical role of the interlacing formed by augmented β sheets during contraction; in addition, the intensive polymerization of IglA/IglB, as reported by the fluorescent foci, suggests that the T6SS sheath array assembles without interlacing. Therefore, an additional factor must contribute to T6SS assembly. By analogy with bacteriophages, we propose that the sheath assembles on a preassembled IglC tube, whose monomer structure is available (PDB: 2QWU). Close scrutiny of the IglB and IglC surfaces suggests a potential protein-protein interface for IglB and IglC, given favorable rotamers of residues (Figure S5). However, reliable assignment of this interaction requires the structure of pre-contraction T6SS.

It was thought, based on its limited sequence homology, that the *F. tularensis* FPI-encoded T6SS is an outlier among others (Filloux et al., 2008). Most notably, *F. tularensis* T6SS system lacks a homolog for ClpV ATPase, which is linked to T6SS disassembly (Filloux et al., 2008). Nevertheless, *Francisella* has homologs to other key T6SS proteins, including IglA/IglB, VgrG, DotU, and PdpB; *Francisella* IglC is structurally homologous to *Pseudomonas* Hcp (de Bruin et al., 2011). Remarkably, these differences and similarities coincide with differences and similarities between our structure of the *F. novicida* T6SS sheath and the other available T6SS structure (Kube et al., 2014); although the dimeric organization and the fold of the sheath proteins and the two-dimensional interlacing among dimers are the same for both, the quaternary structural organizations are different.

Whereas the turn per subunit of the contracted *Vibrio* T6SS sheath is 30.56°, giving a 3° tilt off the vertical to the 12-start helices (Kube et al., 2014), our T6SS sheath has a turn per subunit of 33.4°, giving an ~20° tilt to the 12-start helices (Figure 3G).

It is always tempting but challenging to give an explanation for such a difference. Although a facile explanation is that the *F. novicida* T6SS is an outlier, its lack of a ClpV ATPase suggests an alternative explanation. In fact, the *Vibrio* and *Pseudomonas* T6SS sheaths are severed into shorter pieces, whereas our purified *F. novicida* T6SS sheath is typically much longer, sometimes more than five times longer (Lossi et al., 2013). A few more helices are resolved in the 6 Å structure of the *Vibrio cholerae* T6SS sheath (Kube et al., 2014) than in our sheath structure. These helices belong to the part of sheath proteins that interacts with ClpV (Kube et al., 2014). Because the function of ClpV is to facilitate disassembly of the post-contraction sheath, the *Vibrio* T6SS structure might be in a state that is closer to disassembly than our structure. Our structure is closer to the immediate post-contraction state because it shares a similar turn per subunit number to post-contraction bacteriophage T4 sheath (Leiman et al., 2004). If so, then the T6SS sheath would have three states: pre-contraction, post-contraction, and pro-disassembly. This model awaits confirmation by structural analyses of a ClpV knockout mutant of *Vibrio cholerae*.

We show here that VgrG and IglC are secreted by *F. novicida* in an IglA-dependent fashion in response to environmental stimuli, confirming secretory activity of the *Francisella* FPI-encoded apparatus. Secretion of effectors through this T6SS within macrophages is required for phagosome escape and cytosolic replication because deletion mutants lacking IglA, IglB, IglC, or VgrG (Barker et al., 2009; de Bruin et al., 2011) and the contraction-incompetent mutants IglA Δ 18N/B- and IglA/B Δ 25C-split GFP presented here were all unable to escape the phagosome and markedly impaired in intramacrophage replication.

On the other hand, our Fn-IglA Δ 18N/B- and Fn-IglA/B Δ 25C-split GFP mutants stand out from other IglA and IglB mutants studied to date. Our split-GFP data suggest that the mutated proteins still interact to form IglA/IglB-heterodimers that can assemble green-fluorescent macromolecular structures (fluorescent foci), yet show loss of secretory function. This is a more precise manipulation of the protein functions owing to the availability of an atomic structure. In contrast, the previously reported mutations are not based on a structure; mutants among IglA residues 102–129 (Bröms et al., 2009) caused loss of interaction with IglB (i.e., failure to form the IglA/IglB heterodimer). Particularly, substitution of alanine for valine at residue 109 of IglA or at the corresponding residue 110 of *Vibrio* VipA was shown to abolish IglA-IglB and VipA-VipB interaction, respectively (Bröms et al., 2009). Nevertheless, our atomic model provides an explanation for such loss of interaction: Val109 of IglA is participating centrally in a hydrophobic core formed between IglA and IglB. The V109A mutation destroys this hydrophobic interaction and weakens IglA-IglB interaction. In addition to the above structure-based functional studies, our atomic model provides many other targets for further mutagenesis studies.

In conclusion, we established the identity and determined the atomic structure of an FPI-encoded T6SS in *Francisella*, the genus that includes the highly pathogenic bacterium and Tier 1

Select Agent, *F. tularensis* subsp. *tularensis*. Our atomic structure of the *F. novicida* T6SS and structure-based mutational analysis reveal the critical importance of the interlaced architecture to secretion. This atomic model will facilitate the design and testing of therapeutics targeting this and similar bacterial secretion apparatuses, which are pivotal to the virulence of many pathogenic Gram-negative bacteria.

EXPERIMENTAL PROCEDURES

Bacteria

F. tularensis subsp. *novicida* strain U112 (*F. novicida*) and the derivative strains were cultivated in TSBC. For targeted gene deletion and epitope tagging, upstream and downstream chromosomal regions flanking the gene of interest were amplified with in-frame deletion of the gene or with the gene fused to the coding sequence of an epitope tag. The amplified fragments were inserted into pMP590 (LoVullo et al., 2006) by traditional cloning method using restriction endonucleases or Gibson Assembly (New England BioLabs) and confirmed by sequencing. The resulting plasmid constructs were chemically transformed into *F. novicida* for allelic exchange. Additional information on *F. novicida* strains used in the study is provided in Table S1.

Kinetics of Formation of Fluorescent Foci

Bacteria were inoculated in TSBC with and without 5% KCl at an initial optical density at 540 nm (OD) of 0.05 and grown at 37°C rotating at 250 rpm. Optical density and percentage of bacteria with fluorescent foci were monitored over time. To observe formation of fluorescent foci beneath a glass coverslip, we placed bacteria between a glass slide and a silicone-sealed (and also unsealed) coverglass and imaged immediately or after 3–6 hr at room temperature.

Secretion of Effector Proteins

Bacteria were grown to late exponential phase in TSBC with or without 5% KCl, pelleted by centrifugation, and the supernate was filtered through a 0.45 micron filter. The culture filtrate (equivalent to 1 ml culture at an OD of 1.5) and bacterial pellet (equivalent to 5×10^7 bacteria) were analyzed by SDS-PAGE and western immunoblot. IgIA and IgIA-GFP fusion variants were detected by rabbit polyclonal antibody to His-tagged recombinant IgIA (BEI Resources) or affinity-purified rabbit polyclonal antibody to native GFP (Millipore); IgIB was detected by murine monoclonal antibody specific to His-tagged recombinant IgIB (BEI Resources); IgIC was detected by rabbit polyclonal antibody to highly purified recombinant IgIC; and FLAG-VgrG was detected by murine monoclonal antibody M2 to FLAG epitope (Sigma). Antibodies to IgIA and IgIB were obtained through the NIH Biodefense and Emerging Infections Research Resources Repository, NIAID, NIH.

Macrophage Infection and Immunofluorescent Staining

Human monocytic THP-1 cells were differentiated on poly-L-lysine-coated coverslips with phorbol 12-myristate 13-acetate (100 nM) for 3 days. *F. novicida* strains were grown overnight in TSBC to OD 540 nm of 1–1.5; opsonized with 10% human AB serum for 10 min at 37°C at an OD of 0.002; diluted in Dulbecco's Modified Eagle's Medium (DMEM) with 10% heat-inactivated fetal bovine serum (HI-FBS) to an OD 540 nm of 0.0002; and added to the monolayers of THP-1 cells in a 24-well plate. To synchronize infection, we pelleted the bacteria onto the monolayers by centrifugation of the plates at 800 g for 30 min at 4°C. The plates were warmed to 37°C for 30 min; the monolayers were washed twice with DMEM to remove non-internalized bacteria; and the second wash was replaced with fresh DMEM containing 10% HI-FBS. In experiments intended to follow growth of bacteria by determination of colony forming units (CFU), 0.1 µg/ml gentamicin was added to the culture medium to restrict extracellular growth of the bacteria. For immunofluorescence experiments, the monolayers were fixed for 30 min in 4% paraformaldehyde in PBS; washed with PBS; permeabilized with 0.1% saponin in PBS with 10 mM lysine; and stained for *F. novicida* using a chicken anti-*F. novicida* antibody (kind gift of Professor Denise Monack, Stanford University), followed by a

Texas-red-conjugated goat anti-chicken IgY antibody (Life Sciences). Host cell and bacterial DNA were stained with DAPI (1 µg/ml), and the coverslips were mounted with Prolong Gold anti-fade mounting medium (Life Sciences) and viewed with an Eclipse TE2000 (Nikon) inverted fluorescence microscope equipped with FITC, Texas red, and DAPI filter cubes and SPOT camera and software or with a SPS2 (Leica) confocal microscope. The late endosomal/lysosomal marker, CD63 (LIMP), was stained using the H5C6 hybridoma culture supernate obtained from the University of Iowa Developmental Studies Hybridoma Bank. The differential digitonin assay was performed by a modification of the assay described previously (Checroun et al., 2006) and as we have described previously (Gillespie et al., 2013). The chicken antibody to *F. novicida* was used immediately after digitonin permeabilization to detect cytosolic bacteria and a mouse IgG₃ monoclonal antibody to *F. novicida* obtained from ImmunoPrecise (Victoria, BC, Canada) was used after saponin permeabilization to detect all bacteria.

Purification of T6SS

Wild-type *F. novicida* and Fn-IgIA-GFP were grown to late exponential phase in TSBC containing 5% KCl; pelleted by centrifugation (7500 g for 15 min at 4°C); and lysed with lysozyme and 1% TX-100 detergent in 20 mM Tris HCl, (pH 7.8) with 1 mM EDTA, protease inhibitor cocktail III (1:1,000, EMD Millipore), and Benzonase nuclease (1:1,000, EMD Millipore). The lysate was centrifuged 3 times at 15,000 g for 30 min at 4°C to pellet bacterial debris, and the supernate was carefully layered onto a 10%–55% sucrose gradient overlying a 55% Optiprep cushion and centrifuged at 100,000 g for 18 hr. Fractions were collected and analyzed by TEM negative staining and by western immunoblotting. Fractions were diluted 1:50–1:500 and examined by TEM negative staining using 2% uranyl acetate. We observed that the 150 nm–200 nm sheath-like structures sedimented to just below the 55% sucrose/Optiprep interface, thereby allowing these structures to be purified away from the majority of the bacterial debris. The fractions with the greatest purity as judged by TEM negative staining were dialyzed against 20 mM Tris HCl, (pH 7.5) 0.9% NaCl (TBS) and concentrated with a 100,000 MWCO centrifugal concentrator (Amicon).

Immunogold Electron Microscopy

Fractions of T6SS purified as described above from cultures of wild-type *F. novicida* or *F. novicida* expressing IgIA-GFP were diluted 100-fold with TBS and applied to glow discharged formvar-coated nickel grids. After 5 min, the grids were washed with TBS, blocked for 30 min with 20 mM HEPES, 0.15 M NaCl containing 1% BSA (HBS-BSA), and stained with rabbit anti-GFP (1:1,000) for 60 min in the HBS-BSA. The grids were washed with HBS; stained for 60 min with 5 nm protein A gold in HBS-BSA (University of Utrecht); washed with HBS; negatively stained with 2% uranyl acetate; and examined by TEM using a JEOL 100 CXII.

Cryo Electron Microscopy, Image Processing, and Resolution Assessment

2.5 µl purified T6SS outer sheaths of wild-type *F. novicida* purified as described above was applied to a pre-irradiated, or “baked” (Miyazawa et al., 2003) 200 mesh Quantifoil grid (1.2 µm hole size) and vitrified inside an FEI vitrobot with 100% humidity. CryoEM images were collected at liquid nitrogen temperature in an FEI Titan Krios cryo electron microscope operated at 300 kV with parallel illumination using a Gatan K2 Summit direct electron detector in counting mode (Li et al., 2013) with a dosage of 25 e/Å² and a nominal magnification of 29,000× and using the Legicon package (Suloway et al., 2009). Final pixel size is 1.00 Å/pixel. The defocus range of these images is 1.5–3.5 µm underfocus. Image stacks were preprocessed according to the method described previously (Li et al., 2013).

T6SS particles were selected manually with EMAN (Ludtke et al., 1999) helix-boxer. The three-dimensional structure was reconstructed with modified (Ge et al., 2010; Ge and Zhou, 2011) IHRSR (Egelman, 2010) with Relion (Scheres, 2012) as the refinement engine (see below). Our initial guess of the helical parameters was originated from those of the post-contraction T4 sheath (Leiman et al., 2004), which we then refined to convergence with IHRSR (Egelman, 2010). An initial refinement was accomplished with EMAN-based modified IHRSR, and the resulting structures were taken as the initial reference for the

final refinement using Relion-based IHRSR. The final refinement was done using the “auto-refine” function of Relion, which automatically calculates the working resolution for each iteration and determines the final convergence (see below). The refinement for T6SS converged at 26 iterations. The box size was 640 pixels, and the overlapping was set to 64 pixels. A total of 480,000 asymmetric units were included in the refinement process and in the final reconstruction. The effective resolution of the final reconstruction was estimated to be 3.7 Å based on considerations of “gold-standard” FSC (Figure S6A) and consistency with structural features observed in the density map (Movie S4).

Implementation of IHRSR in Relion Package

We implemented IHRSR (Egelman, 2010) in the Relion 1.2 package (Scheres, 2012). The procedure is very similar to the “modified IHRSR” used in our previous studies (Ge et al., 2010; Ge and Zhou, 2011): the volume is refined for one iteration with Relion without helical symmetry, then the program refines the helical symmetry by re-implemented IHRSR module *hsearch* (though non-linear curve fitting is not implemented), the new helical symmetry is applied in real space to the volume by re-implemented IHRSR module *himpose*, and the helically symmetric volume is masked (as in Relion) and passed to the next iteration as its reference. The helical turn and rise step sizes used in *hsearch* are first set to the orientation and translation search step sizes in Relion divided by the number of helical copies in the volume, respectively (*hsearch* step-size = Relion search step-size/box size/pixel size * helical rise per subunit). Then another helical search (*hsearch*) is performed about the newly found helical parameters of the first *hsearch* with 10× finer step sizes. We implement both *hsearch* and *himpose* modules so that the volume under operation is oversampled when necessary to minimize interpolation error (Ge and Zhou, 2011).

We implemented existing and new switches to control the IHRSR behavior. Two switches to turn on the helical search and symmetrization, two switches to set cylindrical radii, two switches to set initial helical parameters, one switch to set the oversampling ratio, and one switch to set the fraction of volume in Z direction (helical axis) at the center to be considered in helical search (*hsearch*) and symmetrization (*himpose*). To save time, the oversampling ratio of the *hsearch* module is set to half that of the *himpose* module, unless *himpose* is not oversampled. For 3D classification, each class has its own bookkeeping of helical parameters. For auto-refinement, both subsets share the same helical symmetry.

For auto-refinement, the two subsets are refined independently, except that they share the same helical parameters. After each Relion refinement, each subset is subjected to *hsearch* module if so switched, the two pairs of refined helical parameters are averaged, and the averaged parameters are used for *himpose*. The FSC that is used to determine the working resolution of the refinement and to regularize the refinement is calculated between the two subsets before helical symmetrization and is “calibrated” in the attempt to account for helical symmetrization as follows. The FSC factors are converted to signal-to-noise ratio factors by $S/N = FSC / (1 - FSC)$. The latter is used to calculate the “calibrated” S/N ratio by multiplying the square root of the number of copies to be helically averaged, and the “calibrated” S/N factors are used to calculate the final “calibrated” FSC factors, which are passed on to the “maximization” step in Relion and its following iteration for regularization purposes. (See Figure S6A for a comparison between gold-standard and “calibrated” FSC curves between final maps from half datasets.)

Atomic Model Building and Refinement

A model for T6SS sheath was built de novo using Coot (Emsley et al., 2010) and was refined with CNS (Brunger, 2007) and then with Phenix (Adams et al., 2010). Non-crystallographic symmetry, i.e., the helical and 6-fold rotational symmetry, was used as a restraint among identical chains. A total of six discs were included in the working atomic model. This model was ultimately refined to 3.7 Å, with R-factor 24.4% and last shell R-factor 46.0%. The FSC curve between the model and the map crosses 0.5 at 3.75 Å (Figure S6A). To rule out potential over-fitting during model refinement, we have redone the model refinement to 4.2 Å, which is 0.5 Å less than the map resolution of 3.7 Å. The correlation (FSC) between the resulting model and the full-resolution map doesn't drop sharply at 4.2 Å, suggesting that over-fitting is unlikely, but the FSC value reaches 0.5 at 3.88 Å. The slight loss of resolution of the model

refined against the 4.2 Å map is expected because, for example, side-chain orientation might not be reliably determined at the reduced resolution.

Figures for the cryoEM maps and atomic models were prepared with UCSF Chimera package (Pettersen et al., 2004).

ACCESSION NUMBERS

The cryoEM density map and atomic model have been deposited to EMDB and PDB under the accession numbers EMD-6266 and 3J9O, respectively.

SUPPLEMENTAL INFORMATION

Supplemental Information includes six figures, one table, and four movies and can be found with this article online at <http://dx.doi.org/10.1016/j.cell.2015.02.005>.

AUTHOR CONTRIBUTIONS

D.L.C. identified conditions that triggered T6SS assembly and secretion, conducted fluorescence and immunogold EM experiments, and purified T6SS sheaths. P.G. collected, processed, and interpreted EM data and developed the atomic model. B.-Y.L. constructed the bacterial strains and performed CFU and Western Immunoblotting experiments. D.L.C., P.G., and B.-Y.L. designed and performed structure based mutagenesis experiments. All authors reviewed the data and wrote the manuscript.

ACKNOWLEDGMENTS

This project received support from National Institutes of Health grants AI065359, AI094386, and GM071940 and the NIH/NCRR/NCATS UCLA CTSI grant number UL1TR000124. P.G. was supported in part by American Heart Association Western States Affiliates Postdoc Fellowship (13POST17340020). We acknowledge the use of instruments at the Electron Imaging Center for Nanomachines supported by UCLA and by instrumentation grants from NIH (1S10OD018111) and NSF (DBI-1338135). This work used XSEDE (MCB130126), which is supported by NSF (ACI-1053575). The authors thank Denise M. Monack for the chicken anti-*F. novicida* antibody, Karl E. Klose for the *F. novicida* U112, and Francis E. Nano for the codon-optimized superfolder *gfp*.

Received: September 4, 2014

Revised: November 17, 2014

Accepted: January 28, 2015

Published: February 26, 2015

REFERENCES

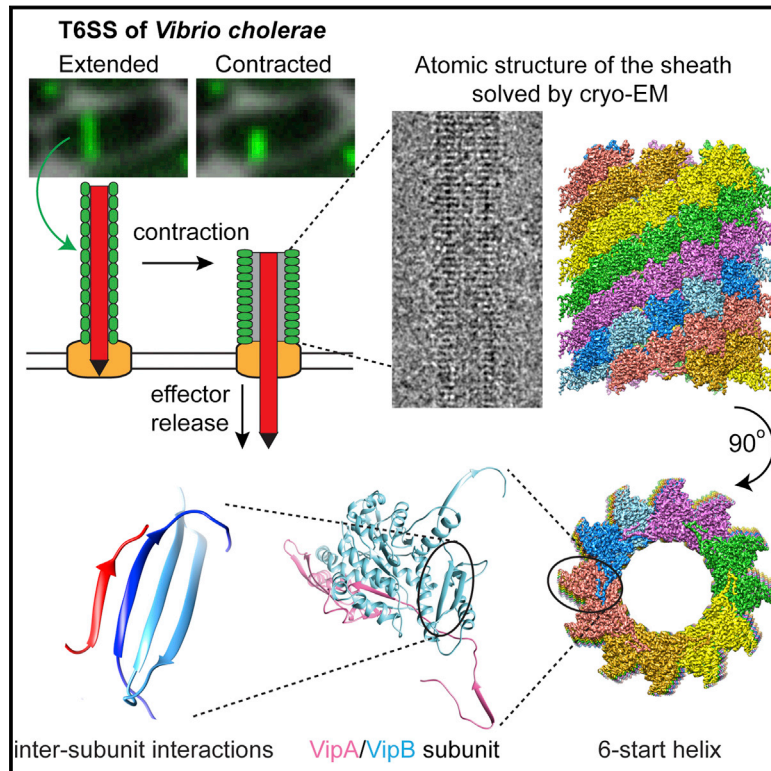
- Adams, P.D., Afonine, P.V., Bunkóczi, G., Chen, V.B., Davis, I.W., Echols, N., Headd, J.J., Hung, L.-W., Kapral, G.J., Grosse-Kunstleve, R.W., et al. (2010). PHENIX: a comprehensive Python-based system for macromolecular structure solution. *Acta Crystallogr. D Biol. Crystallogr.* 66, 213–221.
- Aksyuk, A.A., Kurochkina, L.P., Fokine, A., Forouhar, F., Mesyanzhinov, Vadim V., Tong, L., and Rossmann, M.G. (2011). Structural conservation of the myoviridae phage tail sheath protein fold. *Structure* 19, 1885–1894.
- Aksyuk, A.A., Leiman, P.G., Kurochkina, L.P., Shneider, M.M., Kostyuchenko, V.A., Mesyanzhinov, V.V., and Rossmann, M.G. (2009). The tail sheath structure of bacteriophage T4: a molecular machine for infecting bacteria. *EMBO J.* 28, 821–829.
- Barker, J.R., Chong, A., Wehrly, T.D., Yu, J.J., Rodriguez, S.A., Liu, J., Celli, J., Arulanandam, B.P., and Klose, K.E. (2009). The Francisella tularensis pathogenicity island encodes a secretion system that is required for phagosome escape and virulence. *Mol. Microbiol.* 74, 1459–1470.
- Basler, M., Pilhofer, M., Henderson, G.P., Jensen, G.J., and Mekalanos, J.J. (2012). Type VI secretion requires a dynamic contractile phage tail-like structure. *Nature* 483, 182–186.

- Basler, M., Ho, B.T., and Mekalanos, J.J. (2013). Tit-for-tat: type VI secretion system counterattack during bacterial cell-cell interactions. *Cell* 152, 884–894.
- Bladergroen, M.R., Badelt, K., and Spaink, H.P. (2003). Infection-blocking genes of a symbiotic *Rhizobium leguminosarum* strain that are involved in temperature-dependent protein secretion. *Mol. Plant Microbe Interact.* 16, 53–64.
- Bröms, J.E., Lavander, M., and Sjöstedt, A. (2009). A conserved alpha-helix essential for a type VI secretion-like system of *Francisella tularensis*. *J. Bacteriol.* 191, 2431–2446.
- Brunger, A.T. (2007). Version 1.2 of the Crystallography and NMR system. *Nat. Protoc.* 2, 2728–2733.
- Cabantous, S., and Waldo, G.S. (2006). In vivo and in vitro protein solubility assays using split GFP. *Nat. Methods* 3, 845–854.
- Campbell, M.G., Cheng, A., Briot, A.F., Moeller, A., Lyumkis, D., Veisler, D., Pan, J., Harrison, S.C., Potter, C.S., Carragher, B., and Grigorieff, N. (2012). Movies of ice-embedded particles enhance resolution in electron cryo-microscopy. *Structure* 20, 1823–1828.
- Checroun, C., Wehrly, T.D., Fischer, E.R., Hayes, S.F., and Celli, J. (2006). Autophagy-mediated reentry of *Francisella tularensis* into the endocytic compartment after cytoplasmic replication. *Proc. Natl. Acad. Sci. USA* 103, 14578–14583.
- Chong, A., and Celli, J. (2010). The francisella intracellular life cycle: toward molecular mechanisms of intracellular survival and proliferation. *Front Microbiol.* 1, 138.
- Clemens, D.L., and Horwitz, M.A. (2007). Uptake and intracellular fate of *Francisella tularensis* in human macrophages. *Ann. N Y Acad. Sci.* 1105, 160–186.
- Clemens, D.L., Lee, B.Y., and Horwitz, M.A. (2004). Virulent and avirulent strains of *Francisella tularensis* prevent acidification and maturation of their phagosomes and escape into the cytoplasm in human macrophages. *Infect. Immun.* 72, 3204–3217.
- Clemens, D.L., Lee, B.Y., and Horwitz, M.A. (2005). *Francisella tularensis* enters macrophages via a novel process involving pseudopod loops. *Infect. Immun.* 73, 5892–5902.
- Clemens, D.L., Lee, B.Y., and Horwitz, M.A. (2012). O-antigen-deficient *Francisella tularensis* Live Vaccine Strain mutants are ingested via an aberrant form of looping phagocytosis and show altered kinetics of intracellular trafficking in human macrophages. *Infect. Immun.* 80, 952–967.
- de Bruin, O.M., Ludu, J.S., and Nano, F.E. (2007). The *Francisella* pathogenicity island protein IgIA localizes to the bacterial cytoplasm and is needed for intracellular growth. *BMC Microbiol.* 7, 1.
- de Bruin, O.M., Duplantis, B.N., Ludu, J.S., Hare, R.F., Nix, E.B., Schmerk, C.L., Robb, C.S., Boraston, A.B., Hueffer, K., and Nano, F.E. (2011). The biochemical properties of the *Francisella* pathogenicity island (FPI)-encoded proteins IgIA, IgIB, IgIC, PdpB and DotU suggest roles in type VI secretion. *Microbiology* 157, 3483–3491.
- Egelman, E.H. (2010). Reconstruction of helical filaments and tubes. *Methods Enzymol.* 482, 167–183.
- Ellis, J., Oyston, P.C., Green, M., and Titball, R.W. (2002). Tularemia. *Clin. Microbiol. Rev.* 15, 631–646.
- Emsley, P., Lohkamp, B., Scott, W.G., and Cowtan, K. (2010). Features and development of Coot. *Acta Crystallogr. D Biol. Crystallogr.* 66, 486–501.
- Filloux, A., Hachani, A., and Bleves, S. (2008). The bacterial type VI secretion machine: yet another player for protein transport across membranes. *Microbiology* 154, 1570–1583.
- Fokine, A., Zhang, Z., Kanamaru, S., Bowman, V.D., Aksyuk, A.A., Arisaka, F., Rao, V.B., and Rossmann, M.G. (2013). The molecular architecture of the bacteriophage T4 neck. *J. Mol. Biol.* 425, 1731–1744.
- Ge, P., and Zhou, Z.H. (2011). Hydrogen-bonding networks and RNA bases revealed by cryo electron microscopy suggest a triggering mechanism for calcium switches. *Proc. Natl. Acad. Sci. USA* 108, 9637–9642.
- Ge, P., Tsao, J., Schein, S., Green, T.J., Luo, M., and Zhou, Z.H. (2010). Cryo-EM model of the bullet-shaped vesicular stomatitis virus. *Science* 327, 689–693.
- Gillespie, E.J., Ho, C.-L.C., Balaji, K., Clemens, D.L., Deng, G., Wang, Y.E., Elsaesser, H.J., Tamilselvam, B., Gargi, A., Dixon, S.D., et al. (2013). Selective inhibitor of endosomal trafficking pathways exploited by multiple toxins and viruses. *Proc. Natl. Acad. Sci. USA* 110, E4904–E4912.
- Golovliov, I., Ericsson, M., Sandström, G., Tärnvik, A., and Sjöstedt, A. (1997). Identification of proteins of *Francisella tularensis* induced during growth in macrophages and cloning of the gene encoding a prominently induced 23-kilodalton protein. *Infect. Immun.* 65, 2183–2189.
- Ho, B.T., Basler, M., and Mekalanos, J.J. (2013). Type 6 secretion system-mediated immunity to type 4 secretion system-mediated gene transfer. *Science* 342, 250–253.
- Ho, B.T., Dong, T.G., and Mekalanos, J.J. (2014). A view to a kill: the bacterial type VI secretion system. *Cell Host Microbe* 15, 9–21.
- Hood, R.D., Singh, P., Hsu, F., Güvener, T., Carl, M.A., Trinidad, R.R., Silverman, J.M., Ohlson, B.B., Hicks, K.G., Plemel, R.L., et al. (2010). A type VI secretion system of *Pseudomonas aeruginosa* targets a toxin to bacteria. *Cell Host Microbe* 7, 25–37.
- Ishikawa, T., Rompikuntal, P.K., Lindmark, B., Milton, D.L., and Wai, S.N. (2009). Quorum sensing regulation of the two hcp alleles in *Vibrio cholerae* O1 strains. *PLoS ONE* 4, e6734.
- Ishikawa, T., Sabharwal, D., Bröms, J., Milton, D.L., Sjöstedt, A., Uhlin, B.E., and Wai, S.N. (2012). Pathoadaptive conditional regulation of the type VI secretion system in *Vibrio cholerae* O1 strains. *Infect. Immun.* 80, 575–584.
- Kube, S., Kapitein, N., Zimniak, T., Herzog, F., Mogk, A., and Wendler, P. (2014). Structure of the VipA/B type VI secretion complex suggests a contraction-state-specific recycling mechanism. *Cell Rep.* 8, 20–30.
- Leiman, P.G., and Shneider, M.M. (2012). Contractile tail machines of bacteriophages. *Adv. Exp. Med. Biol.* 726, 93–114.
- Leiman, P.G., Chipman, P.R., Kostyuchenko, V.A., Mesyanzhinov, V.V., and Rossmann, M.G. (2004). Three-dimensional rearrangement of proteins in the tail of bacteriophage T4 on infection of its host. *Cell* 118, 419–429.
- Lesic, B., Starkey, M., He, J., Hazan, R., and Rahme, L.G. (2009). Quorum sensing differentially regulates *Pseudomonas aeruginosa* type VI secretion locus I and homologous loci II and III, which are required for pathogenesis. *Microbiology* 155, 2845–2855.
- Li, X., Mooney, P., Zheng, S., Booth, C.R., Braunfeld, M.B., Gubbens, S., Agard, D.A., and Cheng, Y. (2013). Electron counting and beam-induced motion correction enable near-atomic-resolution single-particle cryo-EM. *Nat. Methods* 10, 584–590.
- Lossi, N.S., Manoli, E., Förster, A., Dajani, R., Pape, T., Freemont, P., and Filloux, A. (2013). The HsiB1C1 (TssB-TssC) complex of the *Pseudomonas aeruginosa* type VI secretion system forms a bacteriophage tail sheathlike structure. *J. Biol. Chem.* 288, 7536–7548.
- LoVullo, E.D., Sherrill, L.A., Perez, L.L., and Pavelka, M.S., Jr. (2006). Genetic tools for highly pathogenic *Francisella tularensis* subsp. *tularensis*. *Microbiology* 152, 3425–3435.
- Ludtke, S.J., Baldwin, P.R., and Chiu, W. (1999). EMAN: semiautomated software for high-resolution single-particle reconstructions. *J. Struct. Biol.* 128, 82–97.
- McMullan, G., Chen, S., Henderson, R., and Faruqi, A.R. (2009). Detective quantum efficiency of electron area detectors in electron microscopy. *Ultramicroscopy* 109, 1126–1143.
- Miyazawa, A., Fujiyoshi, Y., and Unwin, N. (2003). Structure and gating mechanism of the acetylcholine receptor pore. *Nature* 423, 949–955.
- Nakayama, K., Takashima, K., Ishihara, H., Shinomiya, T., Kageyama, M., Kanaya, S., Ohnishi, M., Murata, T., Mori, H., and Hayashi, T. (2000). The R-type pyocin of *Pseudomonas aeruginosa* is related to P2 phage, and the F-type is related to lambda phage. *Mol. Microbiol.* 38, 213–231.
- Pettersen, E.F., Goddard, T.D., Huang, C.C., Couch, G.S., Greenblatt, D.M., Meng, E.C., and Ferrin, T.E. (2004). UCSF Chimera—a visualization system for exploratory research and analysis. *J. Comput. Chem.* 25, 1605–1612.
- Pietrosiuk, A., Lenherr, E.D., Falk, S., Bönenmann, G., Kopp, J., Zentgraf, H., Sinning, I., and Mogk, A. (2011). Molecular basis for the unique role of the

- AAA+ chaperone ClpV in type VI protein secretion. *J. Biol. Chem.* **286**, 30010–30021.
- Pukatzki, S., Ma, A.T., Sturtevant, D., Krastins, B., Sarracino, D., Nelson, W.C., Heidelberg, J.F., and Mekalanos, J.J. (2006). Identification of a conserved bacterial protein secretion system in *Vibrio cholerae* using the *Dictyostelium* host model system. *Proc. Natl. Acad. Sci. USA* **103**, 1528–1533.
- Scheres, S.H.W. (2012). RELION: implementation of a Bayesian approach to cryo-EM structure determination. *J. Struct. Biol.* **180**, 519–530.
- Silverman, J.M., Brunet, Y.R., Cascales, E., and Mougous, J.D. (2012). Structure and regulation of the type VI secretion system. *Annu. Rev. Microbiol.* **66**, 453–472.
- Suloway, C., Shi, J., Cheng, A., Pulokas, J., Carragher, B., Potter, C.S., Zheng, S.Q., Agard, D.A., and Jensen, G.J. (2009). Fully automated, sequential tilt-series acquisition with Legion. *J. Struct. Biol.* **167**, 11–18.
- Tseng, T.T., Tyler, B.M., and Setubal, J.C. (2009). Protein secretion systems in bacterial-host associations, and their description in the Gene Ontology. *BMC Microbiol.* **9** (1), S2.
- Wehrly, T.D., Chong, A., Virtaneva, K., Sturtevant, D.E., Child, R., Edwards, J.A., Brouwer, D., Nair, V., Fischer, E.R., Wicke, L., et al. (2009). Intracellular biology and virulence determinants of *Francisella tularensis* revealed by transcriptional profiling inside macrophages. *Cell. Microbiol.* **11**, 1128–1150.

Structure of the Type VI Secretion System Contractile Sheath

Graphical Abstract



Authors

Mikhail Kudryashev,
Ray Yu-Ruei Wang, ...,
Edward H. Egelman, Marek Basler

Correspondence

egelman@virginia.edu (E.H.E.),
marek.basler@unibas.ch (M.B.)

In Brief

The atomic structure of a bacterial type VI secretion system shows similarities to phage homologs in the sheath core architecture while a distinct outer layer facilitates interactions with the ClpV ATPase that enables multiple rounds of sheath use.

Highlights

- Atomic structure of the bacterial T6SS sheath was solved by cryo-EM
- β -strand-mediated intermolecular interactions stabilize six-start helical assembly
- Structural alignments with phage sheaths indicate conserved mechanism of assembly
- Arrangement of the outer domain of the sheath facilitates recycling by ClpV ATPase

Accession Numbers

EMD-2699
EMPIAR-10019
3J9G



Structure of the Type VI Secretion System Contractile Sheath

Mikhail Kudryashev,^{1,2} Ray Yu-Ruei Wang,^{3,4} Maximilian Brackmann,¹ Sebastian Scherer,² Timm Maier,⁵ David Baker,³ Frank DiMaio,³ Henning Stahlberg,² Edward H. Egelman,^{6,*} and Marek Basler^{1,*}

¹Focal Area Infection Biology, Biozentrum, University of Basel, Klingelbergstrasse 50/70, CH-4056 Basel, Switzerland

²Center for Cellular Imaging and NanoAnalytics, Biozentrum, University of Basel, Mattenstrasse 26, CH-4058 Basel, Switzerland

³Department of Biochemistry, University of Washington, 1705 NE Pacific Street, Seattle, WA 98195, USA

⁴Graduate Program in Biological Physics, Structure and Design, University of Washington, Box 357350, Seattle, WA 98195, USA

⁵Focal Area Structural Biology, Biozentrum, University of Basel, Klingelbergstrasse 50/70, CH-4056 Basel, Switzerland

⁶Department of Biochemistry and Molecular Genetics, University of Virginia, Charlottesville, VA 22908, USA

*Correspondence: egelman@virginia.edu (E.H.E.), marek.basler@unibas.ch (M.B.)

<http://dx.doi.org/10.1016/j.cell.2015.01.037>

SUMMARY

Bacteria use rapid contraction of a long sheath of the type VI secretion system (T6SS) to deliver effectors into a target cell. Here, we present an atomic-resolution structure of a native contracted *Vibrio cholerae* sheath determined by cryo-electron microscopy. The sheath subunits, composed of tightly interacting proteins VipA and VipB, assemble into a six-start helix. The helix is stabilized by a core domain assembled from four β strands donated by one VipA and two VipB molecules. The fold of inner and middle layers is conserved between T6SS and phage sheaths. However, the structure of the outer layer is distinct and suggests a mechanism of interaction of the bacterial sheath with an accessory ATPase, ClpV, that facilitates multiple rounds of effector delivery. Our results provide a mechanistic insight into assembly of contractile nanomachines that bacteria and phages use to translocate macromolecules across membranes.

INTRODUCTION

Several critical components of the type VI secretion system (T6SS) are structurally and functionally related to components of contractile tails of bacteriophages. Secreted VgrG and PAAR proteins form a complex similar to phage spike, secreted Hcp is a structural homolog of a phage tube protein, and TssE (type six secretion E) is a homolog of T4 phage baseplate protein gp25 (Leiman et al., 2009; Pukatzki et al., 2007; Shneider et al., 2013). VipA and VipB (TssB and TssC) proteins were shown to form a cog-wheel-like tubular structure in *V. cholerae* (Bönemann et al., 2009) that was noticed to resemble T4 phage gp18 polysheath (Leiman et al., 2009). The VipA/VipB sheath assembles around an inner Hcp tube and is attached to a structure called a baseplate that spans the bacterial membranes (Basler et al., 2012; Brunet et al., 2014; Zoued et al., 2013). Importantly, the VipA/VipB sheath was shown to form a long contractile

organelle in *V. cholerae* (Basler et al., 2012; Kapitein et al., 2013) and in *E. coli* (Brunet et al., 2013), suggesting that sheath contraction powers the secretion. In vivo, the contracted sheath is specifically recognized by the ClpV ATPase, which disassembles the sheath by unfolding VipB from the N terminus (Basler and Mekalanos, 2012; Kapitein et al., 2013; Pietrosiuk et al., 2011). Even though sheath contraction has been implicated in powering protein translocation across a membrane for phages, pyocins, and T6SS (Leiman and Shneider, 2012), a mechanistic understanding of this process is currently limited, mostly due to the lack of a high-resolution structure of a native and fully assembled sheath.

There is no high-resolution information available for the T6SS sheath, but several crystal structures are available for fragments of phage sheath proteins (Aksyuk et al., 2009a, 2011). However, a major limitation of these atomic structures is that monomeric proteins were used for crystallization and thus, in principle, cannot reveal atomic details of inter-subunit interactions in a native fully assembled sheath polymer. The structure of the T4 phage sheath polymer was so far solved only at low resolution using electron microscopy (Kostyuchenko et al., 2005; Leiman et al., 2004), again not providing the necessary details to fully understand sheath assembly.

Native T6SS sheath has only been isolated from *V. cholerae* in a contracted form (Basler et al., 2012). Even though the sheath was isolated without the inner Hcp tube, Hcp and other components of T6SS were shown to be necessary for sheath assembly (Basler et al., 2012; Brunet et al., 2014; Kapitein et al., 2013). Indeed, in contrast to a long and regular T6SS sheath that can be isolated from T6SS-positive *V. cholerae* (Basler et al., 2012), VipA/VipB from *P. aeruginosa* and *V. cholerae* heterologously expressed in *E. coli* only form short tubes (Bönemann et al., 2009; Kube et al., 2014; Lossi et al., 2013); electron microscopy of these tubes provided low-resolution density maps (Kube et al., 2014; Lossi et al., 2013). Nonetheless, a recent ~ 6 Å resolution structure of *V. cholerae* sheath provided insights into a possible mechanism of ClpV-specific disassembly of the contracted sheath (Kube et al., 2014).

Due to recent advances in direct electron detection cameras and software tools (Egelman, 2010; Faruqi et al., 2003; Li et al., 2013; Lu et al., 2014), it is now possible to obtain density maps

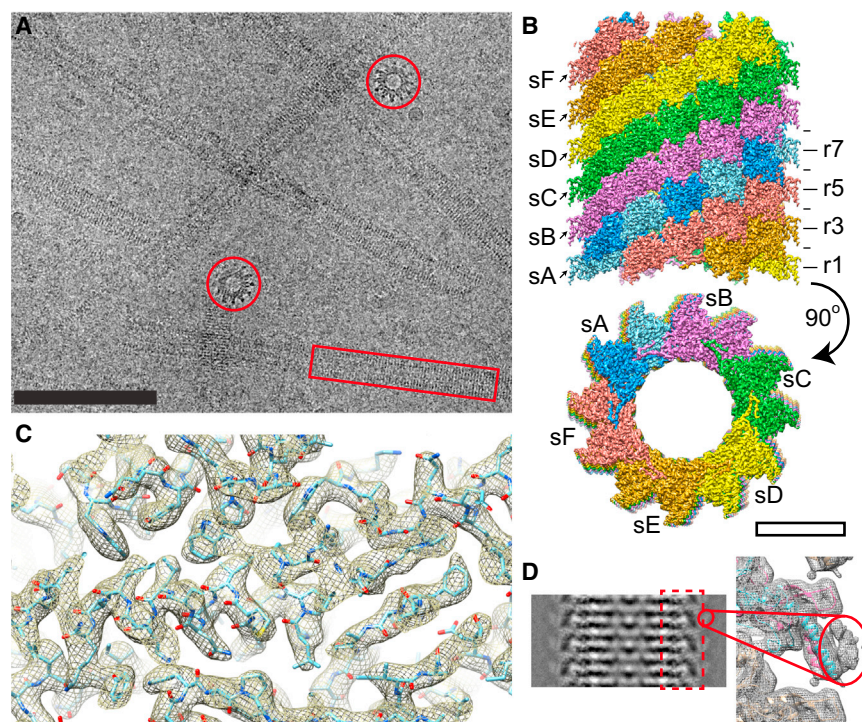


Figure 1. Cryo-EM Structure of the T6SS Sheath

(A and B) (A) A representative low-dose cryo-EM micrograph with side (red box) and top (red circle) views of the sheath. Scale bar, 100 nm; (B) assembly of the protomers into a six-start helix; s, individual strands; r, horizontal rings. Scale bar, 10 nm.

(C) An example of the atomic model fitted into the protein density.

(D) Left: a class average of the sheath showing a density on the surface; right: protein density filtered to low resolution showing density of the VipB N terminus and VipA C terminus.

See also [Figure S1](#) and [Movie S1](#).

with a resolution that allows de novo building of atomic models (Kühlbrandt, 2014). These technical advances allowed for directly generating atomic models of the subunit of the mitochondrial ribosome (Amunts et al., 2014) or the ribosome-Sec61 complex (Voorhees et al., 2014) and provided fundamental insights into mechanisms of those macromolecular machines. Here, we used the state-of-the-art electron microscopic approaches and the Rosetta density-guided structural modeling methods to reveal the structure of the contracted VipA/VipB sheath from *V. cholerae* in atomic detail.

RESULTS AND DISCUSSION

Atomic Structure of the VipA/VipB Protomer

We purified the native contracted sheath from *Vibrio cholerae* and imaged it by cryo-electron microscopy (Figure 1A). Fourier transforms of recorded images showed Thon rings up to ~ 3 Å with layer lines in single micrographs up to a resolution of 5 Å (Figure S1A). Helical reconstruction was performed by the iterative helical real space reconstruction (IHRSR) method (Egelman, 2000) with the final helical parameters being a 21.8 Å axial rise, 29.4° rotation, and a C6 rotational symmetry about the helical axis (Figures 1B, S1B, and S1C and Movie S1). Helical parameters and an overall shape of the sheath are similar to the previously reported structure (Kube et al., 2014); however, our approach allowed us to obtain a resolution of ~ 3.5 –4.0 Å, which improved up to ~ 3.2 Å for the inner and middle layers of the sheath (Figure S1D). Most of the amino acid side chains and some oxygen atoms in the backbone were resolved in the most ordered parts of the structure (Figure 1C and Movie S1). Even though the resolution of our protein density decreased for

the outer surface layer, we were able to de novo trace residues 2 to 126 (out of 168) of VipA and residues 61 to 492 of VipB (Figures 2A, 2B, and S2A–S2E). The VipA C terminus and the VipB N terminus were clearly localized to a less ordered layer on the surface of the sheath as shown in class averages of sheath images (Figures 1D, S1E, and S1F). To further improve the geometry of the side chains, the model was subject to Rosetta density-guided all-atom refinement using a physically realistic energy function (Song et al., 2013; DiMaio et al., 2015). An atomic model built into an independently generated electron microscopy (EM) map of lower resolution had a C α root-mean-square deviation (RMSD) to the original atomic model of 0.34 Å (see [Experiential Procedures](#)), suggesting that model building is highly reliable. Analysis of the conservation and coevolution of VipA/VipB protein residues shows that the conserved residues are generally facing the inner part of the protomer, variable residues are exposed on the protomer surface, and distances between most coevolving residues are within 10 Å (Figure S3 and Table S1).

The atomic model allowed us to calculate energies of protein-protein interactions using PISA (Proteins Interfaces Structures and Assemblies) (Krissinel and Henrick, 2007) and understand how the sheath structure is stabilized in its contracted form. The strongest intermolecular interaction was calculated between VipA and VipB to form a heterodimeric sheath protomer with 1:1 stoichiometry (Table 1 and Figures 2A, 2B, and S2F). Two β strands of VipA and four β strands of VipB intertwine, forming the middle layer of the sheath (domain 2, Figure 2D). VipA further binds to one side of VipB, forming 35 hydrogen bonds and 14 salt bridges. The total interfacial area for this interaction is 3,493 Å², and $\Delta G = -54.8$ kcal/mol/protomer represents more than half of all the interaction energy within the assembled sheath (Table 1).

Interprotomer Interactions

The interaction surface between VipB proteins on the same helical strand covers $\sim 2,444$ Å², represents about 20% of the total interaction energy, and stabilizes the protomers within the strand. The interface area between VipA and VipB from adjacent

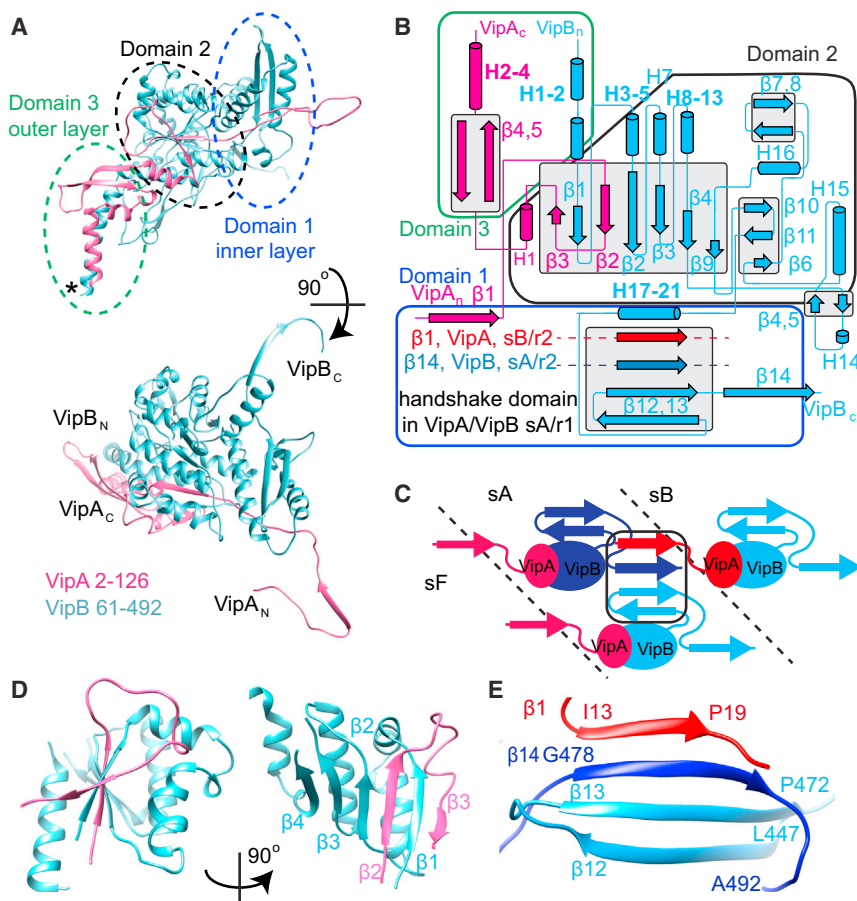


Figure 2. Atomic Model of the Sheath Protomer

(A) An atomic model for VipA (pink) and VipB (blue) with the outlined domains. Domain 3 contains untraced residues predicted to form 5 α helices (location marked with an asterisk [*]). (B–E) (B) Interactions of secondary structure elements in the protomer; (C) scheme of the handshake domain assembly by three protomers of VipA/VipB; (D) two views of domain 2, six β strands surrounded by 5 α helices stabilizing the interaction between VipA and VipB in the protomer; (E) a “handshake domain” in the domain 1 connecting four β strands: β 12 and β 13 of VipB in strand A, ring 1 (light blue) with β 14 of VipB in strand A, ring 2 (blue), and β 1 of VipA in strand B, ring 2 (red). See also Figure S2 and Movie S1.

helical strands is $1,143 \text{ \AA}^2$ and contributes $\sim 14.7 \text{ kcal/mol/protomer}$ energy to the stabilization of the individual strands within the six-start helix. Together, these interactions represent an energy of $34 \text{ kcal/mol/protomer}$ and are the major contributors to sheath stability (Table 1).

Resolution limitations of the previous study (Kube et al., 2014) led to an imprecise segmentation of a sheath subunit from the low-resolution density map (Figure S1G). Interestingly, we show that the subunits are connected by a unique set of interactions in the innermost layer of the sheath. This “handshake” domain is assembled from two anti-parallel β strands (β 12 and β 13) of one VipB molecule, one parallel β strand (β 14) of a second VipB on the same six-start helical strand, and one parallel β strand (β 1) of a VipA molecule from a neighboring strand in the six-start helix (Figures 2B, 2C, and 2E).

T6SS and Phage Sheaths Evolved from a Common Ancestor

To understand the evolution of T6SS sheath, we performed a structural alignment between VipA/VipB and a model of T4 phage sheath protein gp18 (Aksyuk et al., 2009a; Fokine et al., 2013) and a crystal structure of *Listeria innocua* phage sheath protein Lin1278 (Aksyuk et al., 2011). In contrast to sequence-based alignments that only detect homology between VipB and phage sheath proteins, we show that domains 1 and 2, composed of

both VipA and VipB, are highly conserved and the outer domains 3 and 4 are divergent (Figures 3 and S4). Domain 1 of T6SS sheath and the domain 1 of a model of gp18 or a crystal structure of Lin1278 align with RMSD of 2.7 \AA and 2.2 \AA , respectively. RMSDs between the domain 2 of the T6SS sheath and the crystal structures of the domain 2 of gp18 or Lin1278 are 3.7 \AA and 2.8 \AA , respectively.

Interestingly, the architecture of domain 1 differs between phage and T6SS. In both phage sheath proteins, the first two β strands have the same orientation as in the T6SS sheath, but the third β strand

has an opposite orientation, and the fourth β strand is missing (Figures 3A and 3B). Because the phage sheath structures were solved for monomers and not for fully assembled polymers, it is tempting to speculate that, in a fully assembled phage sheath, the corresponding handshake domain has the same architecture as in the native T6SS sheath and connects subunits and strands in the same manner as in T6SS.

The fundamental difference between phage and T6SS sheath is that phage sheath is used only once, whereas T6SS sheath is recycled in vivo by ClpV (Basler and Mekalanos, 2012; Kapitein et al., 2013). Moreover, phages act in an extracellular space, whereas the T6SS sheaths are functioning in bacterial cytoplasm. Here, we show that the major difference between phage and T6SS sheaths is in the outer layer, which is not only structurally different but also positioned differently on the sheath surface. In the case of the T4 phage sheath, the domains 3 and 4 are inserted between β 1 and H3 of VipB in the domain 2 (Figures 3A, 3B, and S4). On the other hand, the T6SS sheath has its domain 3 inserted between H1 of VipA and H2 of VipB (Figures 3A, 3B, and S4). This leads to a major difference in the angle between domain 3 and domain 2 compared to phage sheath architecture. Furthermore, the outermost layer of the phage sheaths is formed mostly by β strands (Aksyuk et al., 2009a, 2011), whereas the T6SS sheath outer layer is predicted to be composed of five α helices (Figures S2A and S2B).

Table 1. Energy of Interactions between VipA/VipB in the Sheath Assembly

	Interface Area, Å ²	Number of H-H Bonds	Number of Salt Bridges	ΔG kcal/mol	% of Interaction Energy
VipA-B main interface	3493	35	14	−54.8	57
VipB-B interaction in the strand	2444	33	14	−19.3	20
VipA-B between the strands	1143	7	2	−14.7	15
VipA-B in the horizontal ring	634	11	4	−4.5	5
VipB-B vertical interaction	454	5	2	−3.0	3

Even though the overall fold of domains 1 and 2 of phage and T6SS is conserved, the T6SS sheath has several potentially functional insertions compared to phage sheath (Figure 4A). The VipA/VipB protomer has two weakly conserved extra helices in the domain 1: VipB H17 and VipB H21. VipB H17 (aa 374–386) interacts with a loop of the next VipA in a strand (aa 18–24, originating from the handshake domain). A weakly conserved loop and a short VipB H21 interact with a loop (aa 412–415) close to VipB H19.

As hypothesized previously (Basler and Mekalanos, 2012; Kapitein et al., 2013; Kube et al., 2014), after the sheath contraction, the VipB N terminus is likely exposed on the sheath surface to allow disassembly by ClpV. Although an atomic model of an extended T6SS sheath is not available yet, it is likely that the N terminus of VipB is not accessible for binding by ClpV in the extended state to prevent disassembly of the extended sheath. We show that domain 3 is exposed on the surface of the contracted sheath, aligning the domains 3 from the neighboring strands on top of one another. This is in agreement with the recently proposed model (Kube et al., 2014); however, here we show that two helices from VipA_C and three from VipB_N are exposed on the surface. This indeed makes the VipB N terminus fully accessible for disassembly by ClpV (Figure 3D), as suggested previously (Kube et al., 2014), but raises a possibility that VipA is involved in properly positioning VipB on the sheath surface. Furthermore, our atomic model suggests that precise positioning of domain 3 could be stabilized by interactions of three T6SS-specific insertions into the surface of VipB in domain 2: short helices H8–H13, a loop R246–N276, and an outward facing hairpin β7–β8. These insertions appear to form a network of hydrophobic interactions with the domain 3 at the outer surface of the sheath (Figure 4B). Hairpin β7–β8 forms an interaction with the H8–H13 of the VipB in the neighboring strand and with the loop VipB246–276. Loop VipB246–276 interacts with the two long helices VipA H4 and VipB H1 of the domain 3 from the inside, whereas the other hairpin VipA β3–β4 stabilizes them from the outside. The two long helices are further stabilized by a helix-helix interaction with the conserved interfaces (Figure 4A).

Attachment of the Sheath to the Baseplate

Whole-cell cryo-electron tomography provided only a low-resolution structure of the sheath (Basler et al., 2012), and therefore it is not possible directly from those data to orient the VipA/VipB structure relative to a baseplate in the bacterial cell wall. However, considering the degree of structural similarity between T6SS and phage, it is likely that VipA and VipB are oriented relative to the baseplate in the same way as gp18 in T4 phage (Aksyuk et al., 2009a). In Figure 3A, and all other similar top views, the

baseplate would be located behind the plane of view; on all side views, like the inset of Figure 3A, the baseplate would be located on the bottom. This orientation of the VipA/VipB protomer suggests that two β strands per subunit are free to bind to an unknown T6SS component in the baseplate (Figure 3A). A natural interacting partner for those two β strands would be a structure similar to an “empty” 2-β-stranded handshake domain organized in a hexameric ring similarly to an actual sheath ring.

A search for structural homologs of the T6SS sheath revealed that protein NP_952040.1 from *Geobacter sulfurreducens* (PDB: 2IA7), a homolog of the T4 phage baseplate protein gp25, aligns with the T6SS sheath domain 1 with an RMSD of 2.7 Å (Figure 5A). As noted previously (Leiman and Shneider, 2012), phage sheath domain 1 has a fold that is similar to that of gp25-like protein (Figure 5B). Importantly, gp25 is positioned near the sheath in the T4 phage baseplate (Aksyuk et al., 2009b).

In a fully assembled handshake domain of T6SS sheath, the orientation of the third β strand (counting from the lumen of the sheath) is parallel to the second β strand but antiparallel in crystal structures of gp25 and its homolog (Figures 5A and S5). We detected significantly coevolving, and thus potentially interacting, residues only between the first two β strands of gp25 (Figure S5). This suggests that, similarly to the sheath handshake domain, only two β strands of gp25 are present in a native assembly. The third β strand of the gp25 could flip out of the domain and interact with yet another component of the baseplate. Therefore, gp25 could accept two additional β strands from interacting proteins in a similar mechanism to the mechanism of sheath subunit interaction.

Interestingly, T6SS component TssE was suggested to be a homolog of gp25 (Leiman et al., 2009; Lossi et al., 2011), co-purifies with the T6SS sheath in *V. cholerae* (Basler et al., 2012), and is important for sheath assembly (Basler et al., 2012; Kapitein et al., 2013). We therefore speculate that the TssE protein could be the part of the T6SS baseplate that accepts VipA-β1 and VipB-β14 strands of the first sheath ring and thus initiates the sheath assembly and also anchors the sheath to the baseplate (Figure 5C). Moreover, TssG and TssK were shown to copurify with sheath in *V. cholerae* (Basler et al., 2012), and VipB was shown to interact with TssK in *E. coli* (Zoued et al., 2013), suggesting that additional proteins are likely involved in attaching the sheath to the baseplate as well. A stable attachment of a contractile sheath to a baseplate is likely crucial for generation of the force needed to deliver substrates across target cell membranes. The sheath has to bind to the baseplate as strongly as individual sheath rings bind together—otherwise, the sheath would likely detach from the baseplate during a rapid contraction.

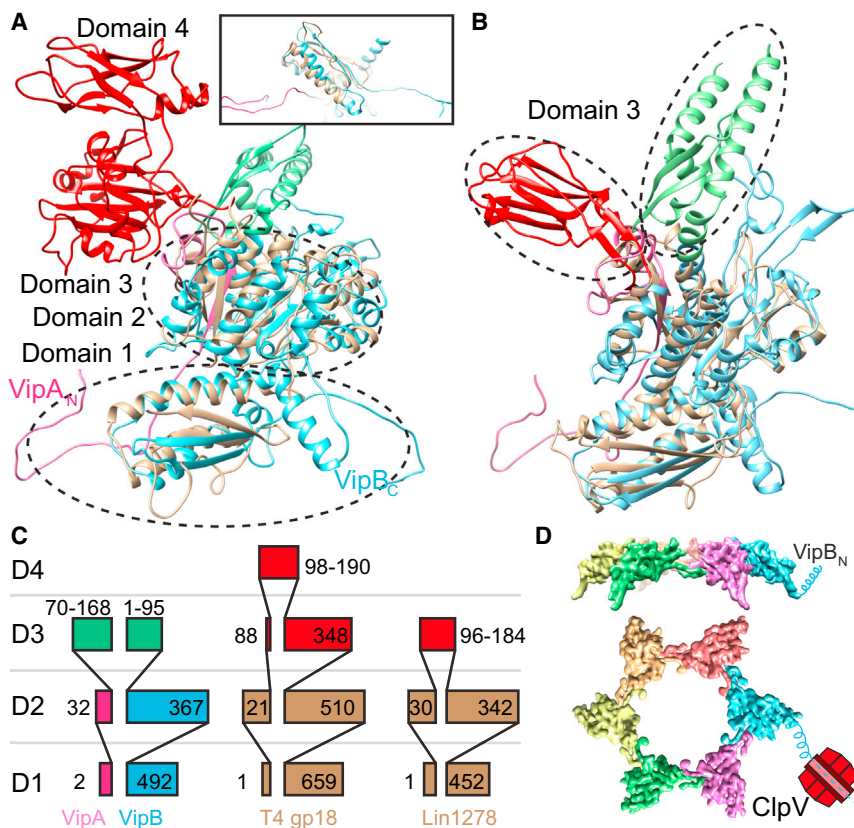


Figure 3. Structural Homology between the T6SS and Phage Sheaths

(A and B) Structural alignment of VipA/VipB (pink/blue) with (A) model of full-length T4 phage sheath gp18 (PDB: 3J2N), the inset shows a side view from the sheath lumen; (B) *L. innocua* phage sheath Lin1278 (PDB: 3LML). Structurally homologous domains 1 and 2 of phage sheaths are shown in brown; divergent domains 3 are shown in red for phage tails and in green for VipA/VipB.

(C) A scheme depicting domain organization of VipA/VipB, gp18, and Lin1278 (partially adapted from Leiman and Shneider [2012]).

(D) One ring of protomers showing N terminus of VipB exposed to the outer surface of the sheath making it accessible to be disassembled by ClpV. See also Figure S4.

Interactions in the Handshake Domain Are Critical for T6SS Sheath Assembly and Dynamics

Our structural data indicate that interactions between β strands in domain 1 are important for initiation of sheath polymerization, extension, and potentially also for sheath contraction. To test this, we generated truncated versions of VipA and VipB lacking β 1 and β 14, respectively. In a background of a fully functional VipA-msfGFP chromosomal fusion, we show that deletion of *vipB* abolishes sheath assembly and target cell killing (Figures 6A and 6C and Movie S2). As shown in Figures 6A–6C and Movie S2, sheath assembly and target cell killing can be restored by a wild-type level of expression of a full-length VipB from a plasmid, but not by a similar level of expression of a mutant lacking β 14 (VipB- Δ C). This indicates that a connection between the sheath protomers on the same strand is essential for sheath assembly and T6SS function.

To assess the role of β 1 strand of VipA, we compared dynamics of a full-length VipA-sfGFP expressed in *vipA* deletion background with dynamics of β 1 strand deletion mutant (VipA- Δ N). As shown on Figure 6D and Movie S3, the wild-type sheaths rapidly assemble and contract in almost all cells during 5 min. Sheaths with disrupted domain 1 are capable of assembling into structures resembling extended wild-type sheaths but exhibit very little dynamics (Figures 6D and 6E and Movie S3). On average, we observe only one assembly event per \sim 500 cells over 5 min. Furthermore, the time of sheath assembly is increased for the VipA- Δ N sheath to about 2 min (Figure 6E),

whereas most of wild-type sheaths fully assemble in 20 to 40 s under the same conditions. This clearly indicates that a fully assembled handshake domain is critical for efficient sheath assembly initiation and the fast assembly rate of the T6SS sheath. Interestingly, even though we inspected sheath dynamics in \sim 50,000 cells over 5 min, we identified only 5 examples of unambiguous sheath contraction and disassembly (one example is given in Figure 6E). This suggests that the ability to contract is preserved to

some degree but raises the possibility that domain 1 is involved in triggering sheath contraction in vivo. Alternatively, the rate of sheath assembly may play a role in triggering sheath contraction. Target cell killing in *vipA* deletion background was restored by expression of VipA-sfGFP, but not by expression of VipA- Δ N-sfGFP mutant (Figure 6C), suggesting that mere ability to assemble sheaths is not sufficient for T6SS-dependent killing.

Concluding Remarks

The unusual four-strand β sheet handshake domain assembled from three molecules invites comparisons with other protein polymers. In most protein filaments that have been intensively studied, such as F-actin (von der Ecken et al., 2014; Galkin et al., 2015), microtubules (Alushin et al., 2014), bacterial flagellar filaments (Yonekura et al., 2003), or type IV pili (Craig et al., 2006), subunits can be treated as compact, and the assemblies are held together by the exclusion of solvent at the buried interfaces (Miller et al., 1987). In contrast to these, type I pili from bacteria have a polymerization mechanism that involves an N-terminal extension of one subunit that becomes a β strand within a β sheet of an adjacent subunit (Waksman and Hultgren, 2009). This β sheet formed by two subunits gives a remarkable stability to the filaments and allows type I pili to resist very large shear forces (Castelain et al., 2011; Miller et al., 2006). We expect that this architecture allows the sheath to transfer a large force and remain intact during its rapid contraction.

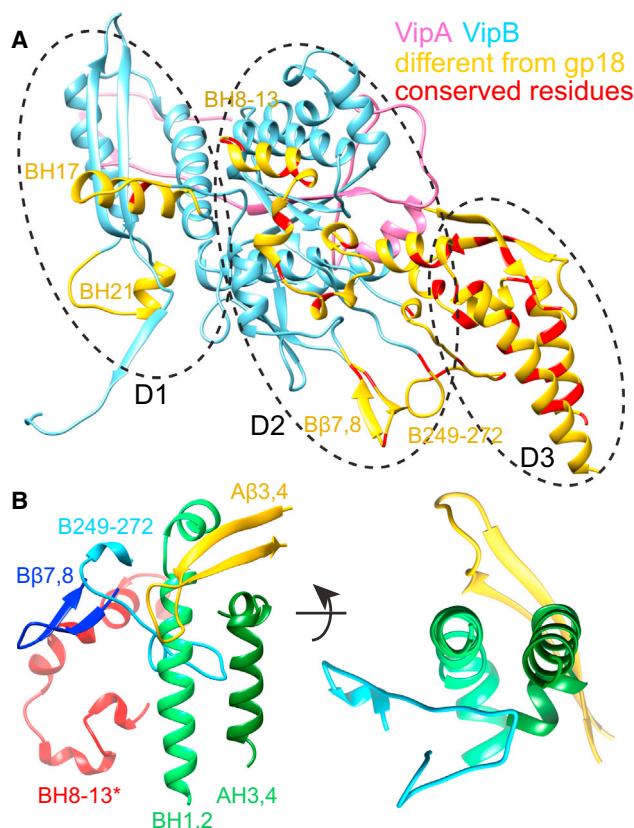


Figure 4. Divergence of the T6SS Sheath from the Phage Sheath
 (A) VipA/VipB protomer (pink/blue) with the additional insertions compared to phage sheath Lin1278 marked in yellow; residues with sequence conservation over 70% are marked in red.
 (B) Interaction network in the outer domain of VipA/VipB. BH 8–13* are part of VipB in the neighboring subunit.
 See also Figure S3.

EXPERIMENTAL PROCEDURES

Bacterial Strains and DNA Manipulations

V. cholerae 2740-80 parental and $\Delta vipA$ strains and the pBAD24-VipA-sfGFP plasmid were described previously (Basler et al., 2012). pBAD24-VipA- ΔN -sfGFP plasmid was created by replacing *vipA* gene in pBAD24-VipA-sfGFP plasmid with a gene lacking codons encoding 23 N-terminal amino acids using standard methods. *V. cholerae* 2740-80 *vipA-msfGFP* strain was created by replacing *vipA* on the chromosome with *vipA-msfGFP* fusion by *sacB*-mediated allelic exchange using the pWM91 suicide plasmid as described previously (Basler and Mekalanos, 2012; Basler et al., 2012; Bina and Mekalanos, 2001; Metcalf et al., 1996). msfGFP differs from previously used sfGFP by Val 206 to Lys substitution, which was previously described to reduce dimerization of GFP (Zacharias et al., 2002). Comparison of VipA-msfGFP to VipA-sfGFP expressed from pBAD24 plasmid in $\Delta vipA$ strain revealed no difference in dynamics of the fusion proteins (data not shown). The linker between VipA and msfGFP was 3xAla 3xGly, as used previously on pBAD24 plasmid (Basler et al., 2012). To limit effects of the fusion gene on the downstream genes in the T6SS locus, we added the last 21 bp of *vipA* at the end of *vipA-msfGFP*. *V. cholerae* 2740-80 *vipA-msfGFP* $\Delta vipB$ strain was created by replacing *vipB* with a gene encoding “MMSTTEKGRDLQA” peptide (first seven and last six residues of *vipB* fused in frame) by allelic exchange as described above and was done previously (Basler et al., 2012). Standard techniques were used to clone a PCR-amplified *vipB* or the first 477 codons of *vipB* to pBAD24

plasmid (Guzman et al., 1995) to generate pBAD24-VipB and pBAD24-VipB- ΔC plasmids, respectively. All PCR-generated products were verified by sequencing. Plasmids were transformed to *V. cholerae* by electroporation. Gentamicin-resistant *E. coli* MG1655 strain was used in bacterial killing assays. Strain list provided as Table S2.

Antibiotic concentrations used were streptomycin (100 μ g/ml), ampicillin (200 μ g/ml), and gentamicin (15 μ g/ml). Luria-Bertani (LB) broth was used for all growth conditions. Liquid cultures were grown aerobically at 37°C.

Fluorescence Microscopy

Procedures similar to those described previously (Basler et al., 2012) were used to detect fluorescence signal in *V. cholerae*. Overnight cultures of *V. cholerae* carrying pBAD24-vipA-sfGFP, pBAD24-vipA- ΔN -sfGFP, pBAD24-vipB, or pBAD24-vipB- ΔC were washed by LB and diluted 50 \times into fresh LB supplemented with ampicillin, streptomycin, and 0.003% arabinose for VipA and 0.006% arabinose for VipB and cultivated for 2.5–3.0 hr to optical density (OD) at 600 nm of about 0.8–1.2. Strains without plasmid were grown similarly, but no ampicillin and arabinose was added. Cells from 100 μ l of the culture were re-suspended in 5–10 μ l of fresh LB (to OD \sim 10), spotted on a thin pad of 1% agarose in LB, and covered with a glass coverslip. Cells were immediately imaged at room temperature using an objective heated to 37°C. Microscope configuration similar to the one described previously (Basler et al., 2013) was used: Nikon Ti-E inverted motorized microscope with Perfect Focus System and Plan Apo 100 \times Oil Ph3 DM (NA 1.4) objective lens. SPECTRA X light engine (Lumencore), ET-GFP (Chroma #49002) filter set was used to excite and filter fluorescence. sCMOS camera pco.edge 4.2 (PCO, Germany) (pixel size 65 nm) and VisiView software (Visitron Systems, Germany) were used to record images. Fiji (Schindelin et al., 2012) was used for all image analysis and manipulations as described previously (Basler et al., 2013). Contrast on compared sets of images was adjusted equally. All imaging experiments were performed with three biological replicates.

Bacterial Killing Assay

V. cholerae 2740-80 strains and *E. coli* MG1655 strain were incubated overnight at 37°C in LB supplemented with appropriate antibiotics. Cultures were washed in fresh LB, diluted 100 \times , and grown to OD 0.8–1.2 in presence of appropriate antibiotics and 0.01% arabinose for strains with pBAD24 plasmids. Cells were washed and mixed at final OD of \sim 10 in 10:1 ratio (*V. cholerae* to *E. coli*) as specified, and 5 μ l of the mixture was spotted on a dry LB agar plate containing 0.01% arabinose but no antibiotics. After 3 hr, bacterial spots were cut out and the cells were re-suspended in 0.5 ml LB. The cellular suspension was serially diluted (1:10) in LB, and 5 μ l of the suspensions were spotted on selective plates (gentamicin for *E. coli* and streptomycin for *V. cholerae*). Colonies were counted after \sim 16 hr incubation at 30°C. Three biological replicates were analyzed.

VipA/VipB Sheath Purification

Sheath was purified similarly to a previous method (Basler et al., 2012). An overnight culture of *flgG* in-frame deletion mutant of the parental *V. cholerae* 2740-80 strain (Basler et al., 2012) was diluted 1:200 into 1,000 ml of fresh LB and then shaken at 37°C for 2.5–3.0 hr to reach an OD of 1.0–1.5. Cells were cooled on ice, centrifuged for 10 min 7,000 $\times g$ and lysed in 50 ml lysis buffer (150 mM NaCl, 20 mM Tris [pH 8], lysozyme 200 μ g/ml, DNase I 50 μ g/ml, 5 mM EDTA, 0.1% SDS, 0.5% Triton X-100). Cell lysis was complete after 5–10 min incubation at 37°C. To activate DNase to cleave DNA, $MgCl_2$ was added to 10 mM final concentration and, after 2–5 min incubation at 37°C, EDTA was added to reach 15 mM final concentration. Cell debris was removed by centrifugation for 20 min at 10,000 $\times g$. Cleared lysates were subjected to ultraspeed centrifugation at 150,000 $\times g$ for 1 hr at 4°C. Pellets were re-suspended in 1 ml in TND buffer (150 mM NaCl, 20 mM Tris [pH 8], 0.5% Triton-100, 0.1% SDS), and insoluble material was removed by centrifugation for 1 min at 10,000 $\times g$. Supernatant was diluted to 50 ml in TND buffer and subjected to ultraspeed centrifugation at 150,000 $\times g$ for 1 hr at 4°C. Pellet was washed with 2 ml of PBS and resuspended in 2 ml PBS. Insoluble material was removed by centrifugation for 1 min at 10,000 $\times g$. Supernatant was diluted to 50 ml by PBS and subjected to ultraspeed centrifugation at 150,000 $\times g$ for 1 hr at 4°C. Pellet was washed by 2 ml of PBS and resuspended in 1 ml PBS, and insoluble material

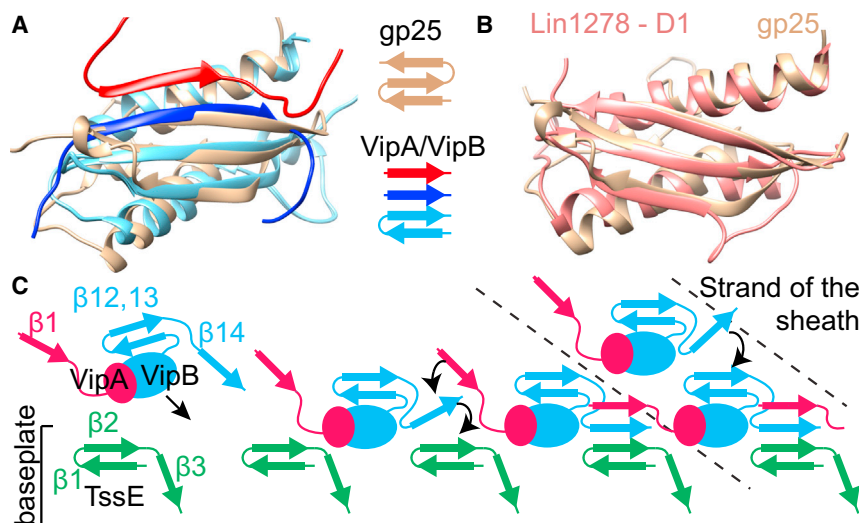


Figure 5. Evolutionary Conservation of the Handshake Interactions and Sheath Assembly Initiation

(A) Structural alignment of the gp25-like phage protein from *G. sulfurreducens* (brown, PDB: 2IA7) and a T6SS sheath handshake domain containing VipB (light blue), VipB from the next subunit on the same strand (blue), and VipA from the next strand (red).

(B) Alignment of the gp25-like phage protein from *G. sulfurreducens* (brown) and domain 1 of phage sheath Lin1278 (red).

(C) A model for sheath assembly initiation and polymerization as viewed from inside the tube: recruitment of VipA/VipB protomers (through their free β strand) to the baseplate protein TssE (providing 2 β strands); establishment of the full 4- β -stranded handshake domain starting with VipB, followed by VipA; recruitment of additional VipA/VipB protomers to the newly formed ring. See also Figure S5.

was removed by centrifugation for 1 min at $10,000 \times g$. Supernatant contained pure sheath. Purity was assessed by Coomassie stained gel, and protein concentration was measured by standard approaches.

Peptide-Specific Antibodies

Antigen-purified rabbit polyclonal antibodies raised against VipB peptide QENPPADVRSRRPL were obtained commercially (GenScript, USA). Specificity of the antibodies was tested on *V. cholerae* strains expressing or lacking *vipB*.

Cell Fractionation and Immunoblot Analysis

Cells from 250 μ l culture prepared for imaging as described above were resuspended in 100 μ l PBS and subjected to sonication (20 cycles, 100% amplitude, 0.5 s cycle) (UIS215V Hielscher Ultrasonics GmbH, Germany). Then 10 μ l of 10% SDS was added, and the sample was sonicated as before. Samples were incubated for 10 min at 95°C , centrifuged, and 17 μ l were mixed with 7 μ l 4 \times NuPAGE LDS Sample Buffer (Life Technologies) and 2 μ l 1 M DTT. Samples were heated again for 10 min at 72°C , centrifuged, and loaded on 4%–12% pre-cast polyacrylamide gels (Life Technologies) and transferred to nitrocellulose membrane (Amersham Biosciences, UK). Membrane was blocked by 5% milk in Tris buffered saline (pH 7.4) containing Tween 0.1% (TBST), incubated with primary peptide antibody for 16 hr at 4°C , washed with TBST, incubated for 1.5 hr with horseradish peroxidase-labeled anti-rabbit antibody (Jackson Lab), and washed with TBST, and peroxidase was detected by LumiGLO Chemiluminescent Substrate (Cell Signaling Technology, USA).

Cryo-Electron Microscopy

Sample was placed on holey carbon grids (Quantifoil GmbH, Germany) and plunge frozen into liquid ethane cooled down to LN_2 temperature using a Vitrobot MK4 (FEI Corp, the Netherlands). Frozen grids were stored in LN_2 and directly observed in a Titan Krios (FEI Corp, the Netherlands) operated at 300 kV and equipped with a K2 Summit direct electron detector (Gatan, Pleasanton, CA). All images were acquired in a single 2 day session at a defocus range of 0.5–1.5 μm . Images were recorded in dose fractionation mode, with a dose rate 3–4 $\text{e}^-/\text{pix}/\text{s}$, exposures per image sub-frames between 1 and 1.5 $\text{e}^-/\text{Å}^2$ and a cumulative dose for the entire image series of 30 $\text{e}^-/\text{Å}^2$. The final pixel size for the resulting $3838 \times 3710 \text{ pix}^2$ images was 1.0 $\text{Å}/\text{pix}$.

Image Processing and 3D Reconstruction

Alignment of beam-induced movement was performed by 2 dx_automator (Scherer et al., 2014) that provides on-the-fly drift correction based on the algorithm implemented by Li et al. (2013). Images recorded as movie data in “counting mode” were drift corrected with the algorithm by Li et al. (2013).

The quality of the images drastically improved after drift correction, especially at high resolution (Figure S1A). Drift on the order of 10 Å could be fixed and re-sampled in Thon rings up to 3–3.5 Å . All recorded frames up to 30 $\text{e}^-/\text{Å}^2$ were used, and no weighting was performed. From the recorded ~ 250 images, the best 77 were selected based on ice thickness and the quality of the Thon rings. Contrast transfer function (CTF) determination was performed by CTFFIND3 (Mindell and Grigorieff, 2003). This led to exclusion of one image, due to a poor fit between the theoretical and observed Thon ring pattern. The images were then multiplied by the estimated CTF in SPIDER to both correct phases and to improve the SNR. Filaments were boxed using the e2helixboxer function within EMAN2 (Tang et al., 2007), using a box width of 600 pixels for the initial alignment and 384 pixels for the final reconstruction. The SPIDER software package (Frank et al., 1996) was used for most subsequent steps. From the long boxes, overlapping segments were cut that were 600 pixels long with a shift of 30 pixels between boxes, where the shift (yielding 95% overlap) was chosen to be $\sim 1.5\times$ the axial rise per subunit. A total of 10,203 segments were obtained. The segments were then padded to 600×600 pixels and decimated to 200×200 pixels size (3 $\text{Å}/\text{pix}$) for initial alignments and reconstruction using IHRSR (Egelman, 2000). Once these were reconstructed, the original images were subsequently decimated to 300×300 pixels for further processing that included out-of-plane tilts. Finally, the initial boxes were windowed to 384×384 pixels for several cycles of IHRSR with 1.0 $\text{Å}/\text{pix}$ until convergence. At the end of each iteration, helical symmetry with a rise of 21.8 Å and a rotation of 29.4 degrees with C6 symmetry was applied. Class averages for Figures 1D and S1F were generated using Spring (Desfosses et al., 2014).

To test reproducibility of the atomic model building, a completely independent EM-density map was generated, starting from the initial micrographs followed by independent particle picking using the e2helixboxer function within EMAN2 (Tang et al., 2007). Square boxes of 400 Å length (1 $\text{Å}/\text{pix}$) were picked with a step of 30 Å . Iterative real space helical reconstruction (Egelman, 2000) was performed with Spring (Desfosses et al., 2014), starting with a featureless cylinder as an initial model. At the end of each iteration, C6 symmetry was applied to the reference. All segments were processed as one data set, and resolution estimated by Fourier Shell Correlation between the half data sets was 4.3 Å (FSC = 0.5).

Atomic Model Building

Model building was done de novo, with initial models of a single subunit built first, and then the system was refined in a symmetrical complex with all the interacting subunits present. A model of a single-subunit VipA/VipB was manually built in Coot (Emsley et al., 2010), guided by an initial partial model from Buccaneer (Cowtan, 2006), which placed a total of 513 residues into the density map. In parallel, automated model building was carried out independently

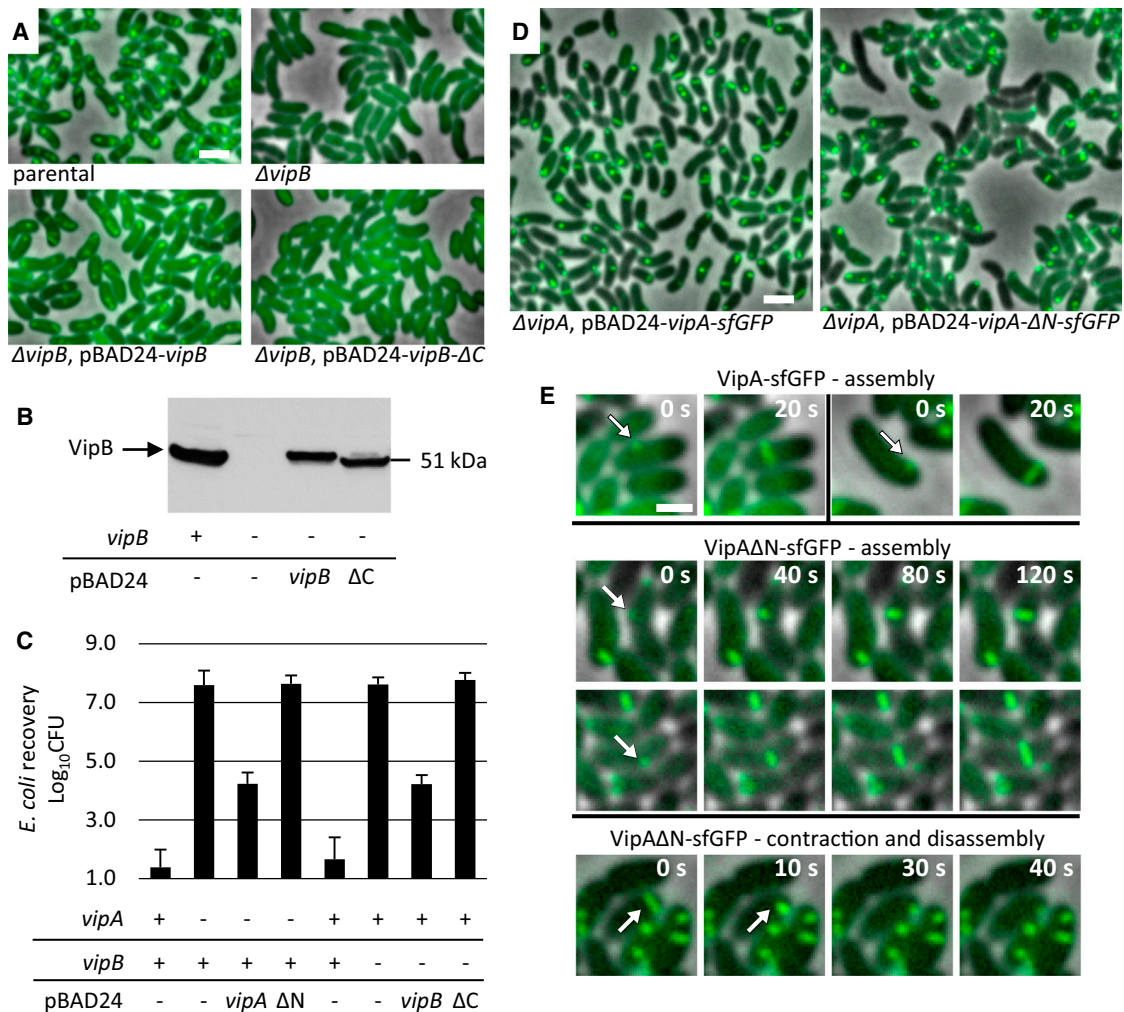


Figure 6. Handshake Domain Integrity Is Important for Sheath Dynamics

(A) Sheath assembly was detected by fluorescence microscopy. Parental strain, *V. cholerae* with VipA-msfGFP fusion encoded in the native locus. Deletion of *vipB* gene was complemented by expression of either WT *vipB* or *vipB* lacking C-terminal β strand (VipB- ΔC) from pBAD24 plasmid. 15 \times 10 μ m fields of cells are shown. Bar is 1 μ m. See also [Movie S2](#).

(B) Expression of VipB or VipB- ΔC was detected in the indicated strains prepared as for the imaging shown in (A) by western blotting using VipB-specific antibody.

(C) Level of *E. coli* killing on a plate was measured for indicated strains after 3 hr of incubation at 10:1 ratio. Presence or absence of *vipA* or *vipB* on the chromosome is indicated by “-” or “+,” respectively. Complementation was from pBAD24 plasmid carrying indicated genes. ΔN , *vipA* lacking N-terminal β strand; ΔC , *vipB* lacking C-terminal β strand. Data are represented as mean \pm SD.

(D) Sheath assembly was detected by fluorescence microscopy. Parental strain, *V. cholerae* *vipA*⁻. Deletion of *vipA* gene was complemented by expression of either WT *vipA* or *vipA* lacking N-terminal β strand (VipA- ΔN) from pBAD24 plasmid. 20 \times 20 μ m field of cells shown. Bar is 1 μ m. See also [Movie S3](#).

(E) Dynamics of sheath assembly for WT VipA (two examples, top) and VipA lacking N-terminal β strand (VipA- ΔN) (two examples, middle). An example of sheath contraction and disassembly is shown for VipA- ΔN (bottom).

using a newly developed approach (Wang et al., 2015). The automated method uses sequence-derived backbone conformations with side-chain density fit to accurately assign sequence into density maps. Starting with a map segmented to containing a single subunit, the computational method was able to place 466 residues into the density.

The two independently derived models showed reasonably good agreement: 394 residues were assigned in both models with a C α RMSD of 1.05 Å. However, there were parts of the protein assigned in each model that were unassigned in the other. Thus, to build and refine the final model, we used RosettaCM (Song et al., 2013), a comparative modeling protocol that assembles protein structures by recombining portions of several models; in this case, the inputs were the two independently traced models. RosettaCM

was guided by experimental density data, with agreement to the density map as an additional score term while building and refining models. A total of 1,000 models were generated, and a best model was selected based on the all-atom energy plus the “fit to density” energy.

Using this model, a final refinement step was carried out in the context of the symmetrical assembly, improving model geometry and relieving clashes at the symmetric interfaces (DiMaio et al., 2015). The final model shows very good agreement to the density, with 504 of 558 traced residues matching the map with real-space correlations of 0.60 or greater (using *density_tools* in Rosetta), and very good model geometry, with 0.36% Ramachandran outliers, 0% rotamer outliers, a Molprobity clash score of 2.15, and an overall Molprobity score of 1.38 (Chen et al., 2010).

To test for overfitting during model building, we uniformly perturbed the final model and refined it against the independently generated EM map. A long refinement cycle (1,000 cycles of backbone rebuilding) was used to ensure the refined model is unbiased from the model fit to the original reconstruction. The resulting model had 0.34 Å C α RMSd to the original model.

Atomic B factors were capped to 600 for heavy atoms and to 720 for H atoms. Methionine in position 1 of VipA was not included in the model due to a lack of EM density and evidence from mass spectrometry analysis of isolated sheath (data not shown) that it is not present on the N terminus.

Molecular Analysis

Interaction energy was calculated using PISA (Krissinel and Henrick, 2007). Secondary structure prediction for the Figures S2A and S2B was performed by Jnet (Cole et al., 2008). Structural alignments were performed by RaptorX (Wang et al., 2013), and the RMSD presented in the text are calculated from these alignments. Structural homologs were found using PDB Structure Navigator (<http://pdj.org/strucnavi>).

Evolutionary Constraints

Evolutionary constraints were generated by the Gremlin server (<http://gremlin.bakerlab.org/>) (Ovchinnikov et al., 2014) or FreeContact software (Kaján et al., 2014). All reliable constraints with scores over 1.5 are listed in Table S1. The distance in 3D was measured between the weighted centers of mass of the contacting residues. The distance was also estimated between the contacting residues in the neighboring protomers, and in case the inter-protomer distance was less than intra-protomer distance, the inter-protomer distance was used in Table S1. This was implemented using Matlab (Mathworks).

Coloring of the EM maps was done with Dynamo package for electron tomographic image processing (Castaño-Díez et al., 2012). The visualization of atomic models, evolutionary constraints, and rendering of the Movie S1 was performed in UCSF Chimera (Pettersen et al., 2004).

ACCESSION NUMBERS

The EM map was deposited to EMDB (<http://www.emdatabank.org/>) with an accession number EMD-2699. Electron micrographs used for processing were deposited to EMPIAR (<http://www.ebi.ac.uk/pdbe/emdb/empiar/>) with an accession number EMPIAR-10019. Atomic coordinates were deposited to PDB (<http://www.rcsb.org>) with an accession number 3J9G.

SUPPLEMENTAL INFORMATION

Supplemental Information includes five figures, two tables, and three movies and can be found with this article online at <http://dx.doi.org/10.1016/j.cell.2015.01.037>.

AUTHOR CONTRIBUTIONS

M.K. performed cryo-EM analysis, built a manual atomic model with T.M., interpreted the data, and wrote the manuscript. R.Y.-R.W., F.D., and D.B. performed automated model building and refinement and contributed to data interpretation. M. Brackmann generated new plasmids and strains, imaged sheath dynamics, performed bacterial killing assays, analyzed protein levels by western blot, and contributed to data analysis and interpretation. S.S. contributed to data collection and processing. T.M. built a manual atomic model with M.K. H.S. supervised data collection and contributed essential analytical tools. E.H.E. performed cryo-EM image analysis and made critical contributions to data interpretation. M. Basler analyzed and interpreted the data and wrote the manuscript. All authors participated in writing the manuscript.

ACKNOWLEDGMENTS

We thank Mihai Ionescu for excellent technical assistance in preparation of the sheath sample. We thank Kenneth Goldie and Bill Anderson for expert assistance with cryo-EM and Venkat Dandey for support with software. Grant sup-

port was from NIH EB001567 (to E.H.E.), Swiss systems biology initiative SystemsX.ch grant CINA, and NIH R01GM092802 (to R.Y.-R.W. and D.B.).

Received: September 5, 2014

Revised: November 17, 2014

Accepted: January 20, 2015

Published: February 26, 2015

REFERENCES

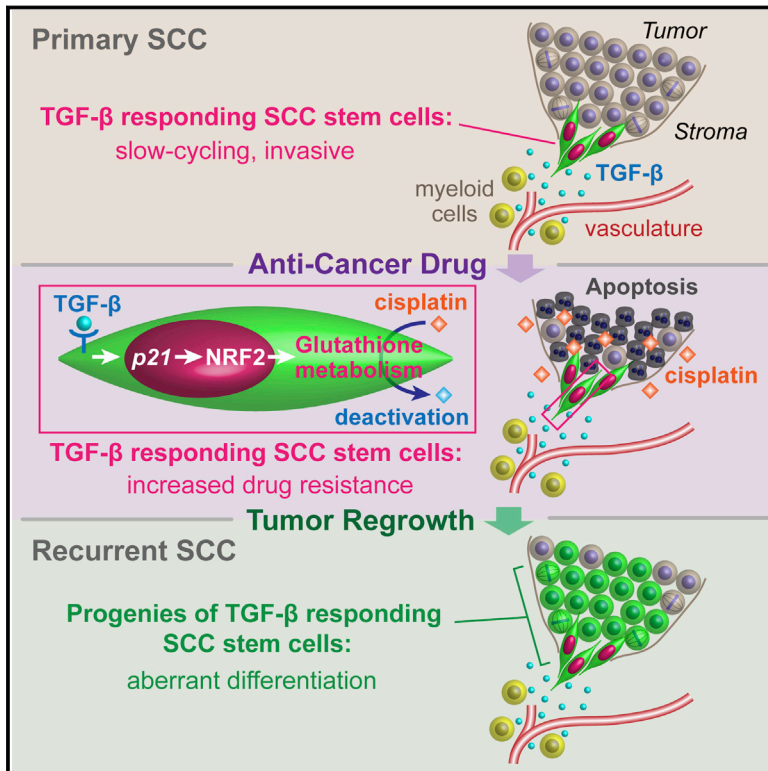
- Aksyuk, A.A., Leiman, P.G., Kurochkina, L.P., Shneider, M.M., Kostyuchenko, V.A., Mesyanzhinov, V.V., and Rossmann, M.G. (2009a). The tail sheath structure of bacteriophage T4: a molecular machine for infecting bacteria. *EMBO J.* 28, 821–829.
- Aksyuk, A.A., Leiman, P.G., Shneider, M.M., Mesyanzhinov, V.V., and Rossmann, M.G. (2009b). The structure of gene product 6 of bacteriophage T4, the hinge-pin of the baseplate. *Structure* 17, 800–808.
- Aksyuk, A.A., Kurochkina, L.P., Fokine, A., Forouhar, F., Mesyanzhinov, V.V., Tong, L., and Rossmann, M.G. (2011). Structural conservation of the myoviridae phage tail sheath protein fold. *Structure* 19, 1885–1894.
- Alushin, G.M., Lander, G.C., Kellogg, E.H., Zhang, R., Baker, D., and Nogales, E. (2014). High-resolution microtubule structures reveal the structural transitions in α -tubulin upon GTP hydrolysis. *Cell* 157, 1117–1129.
- Amunts, A., Brown, A., Bai, X.C., Llácer, J.L., Hussain, T., Emsley, P., Long, F., Murshudov, G., Scheres, S.H.W., and Ramakrishnan, V. (2014). Structure of the yeast mitochondrial large ribosomal subunit. *Science* 343, 1485–1489.
- Basler, M., and Mekalanos, J.J. (2012). Type 6 secretion dynamics within and between bacterial cells. *Science* 337, 815.
- Basler, M., Pilhofer, M., Henderson, G.P., Jensen, G.J., and Mekalanos, J.J. (2012). Type VI secretion requires a dynamic contractile phage tail-like structure. *Nature* 483, 182–186.
- Basler, M., Ho, B.T., and Mekalanos, J.J. (2013). Tit-for-tat: type VI secretion system counterattack during bacterial cell-cell interactions. *Cell* 152, 884–894.
- Bina, J.E., and Mekalanos, J.J. (2001). *Vibrio cholerae* toIC is required for bile resistance and colonization. *Infect. Immun.* 69, 4681–4685.
- Bönemann, G., Pietrosiuk, A., Diemand, A., Zentgraf, H., and Mogk, A. (2009). Remodelling of VipA/VipB tubules by ClpV-mediated threading is crucial for type VI protein secretion. *EMBO J.* 28, 315–325.
- Brunet, Y.R., Espinosa, L., Harchouni, S., Mignot, T., and Cascales, E. (2013). Imaging type VI secretion-mediated bacterial killing. *Cell Rep.* 3, 36–41.
- Brunet, Y.R., Hénin, J., Celia, H., and Cascales, E. (2014). Type VI secretion and bacteriophage tail tubes share a common assembly pathway. *EMBO Rep.* 15, 315–321.
- Castaño-Díez, D., Kudryashev, M., Arheit, M., and Stahlberg, H. (2012). Dynamo: a flexible, user-friendly development tool for subtomogram averaging of cryo-EM data in high-performance computing environments. *J. Struct. Biol.* 178, 139–151.
- Castelain, M., Ehlers, S., Klinth, J., Lindberg, S., Andersson, M., Uhlin, B.E., and Axner, O. (2011). Fast uncoiling kinetics of F1C pili expressed by uropathogenic *Escherichia coli* are revealed on a single pilus level using force-measuring optical tweezers. *Eur. Biophys. J.* 40, 305–316.
- Chen, V.B., Arendall, W.B., 3rd, Headd, J.J., Keedy, D.A., Immormino, R.M., Kapral, G.J., Murray, L.W., Richardson, J.S., and Richardson, D.C. (2010). MolProbity: all-atom structure validation for macromolecular crystallography. *Acta Crystallogr. D Biol. Crystallogr.* 66, 12–21.
- Cole, C., Barber, J.D., and Barton, G.J. (2008). The Jpred 3 secondary structure prediction server. *Nucleic Acids Res.* 36, W197–W201.
- Cowan, K. (2006). The Buccaneer software for automated model building. 1. Tracing protein chains. *Acta Crystallogr. D Biol. Crystallogr.* 62, 1002–1011.
- Craig, L., Volkmann, N., Arvai, A.S., Pique, M.E., Yeager, M., Egelman, E.H., and Tainer, J.A. (2006). Type IV pilus structure by cryo-electron microscopy and crystallography: implications for pilus assembly and functions. *Mol. Cell* 23, 651–662.

- Desfosses, A., Ciuffa, R., Gutsche, I., and Sachse, C. (2014). SPRING - an image processing package for single-particle based helical reconstruction from electron cryomicrographs. *J. Struct. Biol.* **185**, 15–26.
- DiMaio, F., Song, Y., Li, X., Brunner, M.J., Xu, C., Conticello, V., Egelman, E., Marlovits, T., Cheng, Y., and Baker, D. (2015). Atomic-accuracy models from 4.5-Å cryo-electron microscopy data with density-guided iterative local refinement. *Nat. Methods*. Published online February 23, 2015. <http://dx.doi.org/10.1038/NMETH.3286>.
- Egelman, E.H. (2000). A robust algorithm for the reconstruction of helical filaments using single-particle methods. *Ultramicroscopy* **85**, 225–234.
- Egelman, E.H. (2010). Reconstruction of helical filaments and tubes. *Methods Enzymol.* **482**, 167–183.
- Emsley, P., Lohkamp, B., Scott, W.G., and Cowtan, K. (2010). Features and development of Coot. *Acta Crystallogr. D Biol. Crystallogr.* **66**, 486–501.
- Faruqi, A.R., Cattermole, D.M., Henderson, R., Mikulec, B., and Raeburn, C. (2003). Evaluation of a hybrid pixel detector for electron microscopy. *Ultramicroscopy* **94**, 263–276.
- Fokine, A., Zhang, Z., Kanamaru, S., Bowman, V.D., Aksyuk, A.A., Arisaka, F., Rao, V.B., and Rossmann, M.G. (2013). The molecular architecture of the bacteriophage T4 neck. *J. Mol. Biol.* **425**, 1731–1744.
- Frank, J., Radermacher, M., Penczek, P., Zhu, J., Li, Y., Ladjadj, M., and Leith, A. (1996). SPIDER and WEB: processing and visualization of images in 3D electron microscopy and related fields. *J. Struct. Biol.* **116**, 190–199.
- Galkin, V.E., Orlova, A., Vos, M.R., Schröder, G.F., and Egelman, E.H. (2015). Near-atomic resolution for one state of f-actin. *Structure* **23**, 173–182.
- Guzman, L.M., Belin, D., Carson, M.J., and Beckwith, J. (1995). Tight regulation, modulation, and high-level expression by vectors containing the arabinose PBAD promoter. *J. Bacteriol.* **177**, 4121–4130.
- Kaján, L., Hopf, T.A., Kalaš, M., Marks, D.S., and Rost, B. (2014). FreeContact: fast and free software for protein contact prediction from residue co-evolution. *BMC Bioinformatics* **15**, 85.
- Kapitein, N., Bönmann, G., Pietrosiuk, A., Seyffer, F., Hausser, I., Locker, J.K., and Mogk, A. (2013). ClpV recycles VipA/VipB tubules and prevents non-productive tubule formation to ensure efficient type VI protein secretion. *Mol. Microbiol.* **87**, 1013–1028.
- Kostyuchenko, V.A., Chipman, P.R., Leiman, P.G., Arisaka, F., Mesyanzhinov, V.V., and Rossmann, M.G. (2005). The tail structure of bacteriophage T4 and its mechanism of contraction. *Nat. Struct. Mol. Biol.* **12**, 810–813.
- Krissinel, E., and Henrick, K. (2007). Inference of macromolecular assemblies from crystalline state. *J. Mol. Biol.* **372**, 774–797.
- Kube, S., Kapitein, N., Zimniak, T., Herzog, F., Mogk, A., and Wendler, P. (2014). Structure of the VipA/B type VI Secretion complex suggests a contraction-state-specific recycling mechanism. *Cell Rep.* **8**, 20–30.
- Kühlbrandt, W. (2014). Biochemistry. The resolution revolution. *Science* **343**, 1443–1444.
- Leiman, P.G., and Shneider, M.M. (2012). Contractile tail machines of bacteriophages. *Adv. Exp. Med. Biol.* **726**, 93–114.
- Leiman, P.G., Chipman, P.R., Kostyuchenko, V.A., Mesyanzhinov, V.V., and Rossmann, M.G. (2004). Three-dimensional rearrangement of proteins in the tail of bacteriophage T4 on infection of its host. *Cell* **118**, 419–429.
- Leiman, P.G., Basler, M., Ramagopal, U.A., Bonanno, J.B., Sauder, J.M., Pukatzki, S., Burley, S.K., Almo, S.C., and Mekalanos, J.J. (2009). Type VI secretion apparatus and phage tail-associated protein complexes share a common evolutionary origin. *Proc. Natl. Acad. Sci. USA* **106**, 4154–4159.
- Li, X., Mooney, P., Zheng, S., Booth, C.R., Braunfeld, M.B., Gubbens, S., Agard, D.A., and Cheng, Y. (2013). Electron counting and beam-induced motion correction enable near-atomic-resolution single-particle cryo-EM. *Nat. Methods* **10**, 584–590.
- Lossi, N.S., Dajani, R., Freemont, P., and Filloux, A. (2011). Structure-function analysis of HsiF, a gp25-like component of the type VI secretion system, in *Pseudomonas aeruginosa*. *Microbiology* **157**, 3292–3305.
- Lossi, N.S., Manoli, E., Förster, A., Dajani, R., Pape, T., Freemont, P., and Filloux, A. (2013). The HsiB1C1 (TssB-TssC) complex of the *Pseudomonas aeruginosa* type VI secretion system forms a bacteriophage tail sheathlike structure. *J. Biol. Chem.* **288**, 7536–7548.
- Lu, A., Magupalli, V.G., Ruan, J., Yin, Q., Atianand, M.K., Vos, M.R., Schröder, G.F., Fitzgerald, K.A., Wu, H., and Egelman, E.H. (2014). Unified polymerization mechanism for the assembly of ASC-dependent inflammasomes. *Cell* **156**, 1193–1206.
- Metcalfe, W.W., Jiang, W., Daniels, L.L., Kim, S.K., Haldimann, A., and Wanner, B.L. (1996). Conditionally replicative and conjugative plasmids carrying lacZ alpha for cloning, mutagenesis, and allele replacement in bacteria. *Plasmid* **35**, 1–13.
- Miller, S., Lesk, A.M., Janin, J., and Chothia, C. (1987). The accessible surface area and stability of oligomeric proteins. *Nature* **328**, 834–836.
- Miller, E., Garcia, T., Hultgren, S., and Oberhauser, A.F. (2006). The mechanical properties of *E. coli* type 1 pili measured by atomic force microscopy techniques. *Biophys. J.* **91**, 3848–3856.
- Mindell, J.A., and Grigorieff, N. (2003). Accurate determination of local defocus and specimen tilt in electron microscopy. *J. Struct. Biol.* **142**, 334–347.
- Ovchinnikov, S., Kamisetty, H., and Baker, D. (2014). Robust and accurate prediction of residue-residue interactions across protein interfaces using evolutionary information. *eLife* **3**, e02030.
- Petersen, E.F., Goddard, T.D., Huang, C.C., Couch, G.S., Greenblatt, D.M., Meng, E.C., and Ferrin, T.E. (2004). UCSF Chimera—a visualization system for exploratory research and analysis. *J. Comput. Chem.* **25**, 1605–1612.
- Pietrosiuk, A., Lenherr, E.D., Falk, S., Bönmann, G., Kopp, J., Zentgraf, H., Sinning, I., and Mogk, A. (2011). Molecular basis for the unique role of the AAA+ chaperone ClpV in type VI protein secretion. *J. Biol. Chem.* **286**, 30010–30021.
- Pukatzki, S., Ma, A.T., Revel, A.T., Sturtevant, D., and Mekalanos, J.J. (2007). Type VI secretion system translocates a phage tail spike-like protein into target cells where it cross-links actin. *Proc. Natl. Acad. Sci. USA* **104**, 15508–15513.
- Scherer, S., Kowal, J., Chami, M., Dandey, V., Arbeit, M., Ringler, P., and Stahlberg, H. (2014). 2dx_automator: implementation of a semiautomatic high-throughput high-resolution cryo-electron crystallography pipeline. *J. Struct. Biol.* **186**, 302–307.
- Schindelin, J., Arganda-Carreras, I., Frise, E., Kaynig, V., Longair, M., Pietzsch, T., Preibisch, S., Rueden, C., Saalfeld, S., Schmid, B., et al. (2012). Fiji: an open-source platform for biological-image analysis. *Nat. Methods* **9**, 676–682.
- Shneider, M.M., Buth, S.A., Ho, B.T., Basler, M., Mekalanos, J.J., and Leiman, P.G. (2013). PAAR-repeat proteins sharpen and diversify the type VI secretion system spike. *Nature* **500**, 350–353.
- Song, Y., DiMaio, F., Wang, R.Y.-R., Kim, D., Miles, C., Brunette, T., Thompson, J., and Baker, D. (2013). High-resolution comparative modeling with RosettaCM. *Structure* **21**, 1735–1742.
- Tang, G., Peng, L., Baldwin, P.R., Mann, D.S., Jiang, W., Rees, I., and Ludtke, S.J. (2007). EMAN2: an extensible image processing suite for electron microscopy. *J. Struct. Biol.* **157**, 38–46.
- von der Ecken, J., Müller, M., Lehman, W., Manstein, D.J., Penczek, P.A., and Raunser, S. (2014). Structure of the F-actin–tropomyosin complex. *Nature*. Published online December 1, 2014. <http://dx.doi.org/10.1038/nature14033>.
- Voorhees, R.M., Fernández, I.S., Scheres, S.H.W., and Hegde, R.S. (2014). Structure of the mammalian ribosome-Sec61 complex to 3.4 Å resolution. *Cell* **157**, 1632–1643.
- Waksman, G., and Hultgren, S.J. (2009). Structural biology of the chaperoneusher pathway of pilus biogenesis. *Nat. Rev. Microbiol.* **7**, 765–774.
- Wang, S., Ma, J., Peng, J., and Xu, J. (2013). Protein structure alignment beyond spatial proximity. *Sci. Rep.* **3**, 1448.

- Wang, R.Y.-R., Kudryashev, M., Li, X., Egelman, E.H., Basler, M., Cheng, Y., Baker, D., and DiMaio, F. (2015). De novo protein structure determination from near-atomic-resolution cryo-EM maps. *Nat. Methods*. Published online February 23, 2015. <http://dx.doi.org/10.1038/NMETH.3287>.
- Yonekura, K., Maki-Yonekura, S., and Namba, K. (2003). Complete atomic model of the bacterial flagellar filament by electron cryomicroscopy. *Nature* 424, 643–650.
- Zacharias, D.A., Violin, J.D., Newton, A.C., and Tsien, R.Y. (2002). Partitioning of lipid-modified monomeric GFPs into membrane microdomains of live cells. *Science* 296, 913–916.
- Zoued, A., Durand, E., Bebeacua, C., Brunet, Y.R., Douzi, B., Cambillau, C., Cascales, E., and Journet, L. (2013). TssK is a trimeric cytoplasmic protein interacting with components of both phage-like and membrane anchoring complexes of the type VI secretion system. *J. Biol. Chem.* 288, 27031–27041.

TGF- β Promotes Heterogeneity and Drug Resistance in Squamous Cell Carcinoma

Graphical Abstract



Authors

Naoki Oshimori, Daniel Oristian, Elaine Fuchs

Correspondence

fuchslb@rockefeller.edu

In Brief

Perivascular TGF- β suppresses proliferation but promotes invasion and heterogeneity in squamous cell carcinoma stem cells. These TGF- β -responding cells reprogram anti-oxidant metabolism and resist anti-cancer therapy, leading to tumor recurrence.

Highlights

- We devise a system to monitor, manipulate, and track TGF- β signaling in SCCs in vivo
- Perivascular TGF- β causes signaling-based heterogeneity among SCC stem cells
- TGF- β slows proliferation but aids in malignancy and anti-oxidant metabolism
- TGF- β -responding cells resist anti-cancer therapeutics, leading to tumor recurrence

Accession Numbers

GSE64867



TGF- β Promotes Heterogeneity and Drug Resistance in Squamous Cell Carcinoma

Naoki Oshimori,¹ Daniel Oristian,¹ and Elaine Fuchs^{1,2,*}

¹Robin Neustein Laboratory of Mammalian Cell Biology and Development, The Rockefeller University

²Howard Hughes Medical Institute

1230 York Avenue, New York, NY 10065, USA

*Correspondence: fuchslb@rockefeller.edu

<http://dx.doi.org/10.1016/j.cell.2015.01.043>

SUMMARY

Subsets of long-lived, tumor-initiating stem cells often escape cancer therapies. However, sources and mechanisms that generate tumor heterogeneity and drug-resistant cell population are still unfolding. Here, we devise a functional reporter system to lineage trace and/or genetic ablate signaling in TGF- β -activated squamous cell carcinoma stem cells (SCC-SCs). Dissecting TGF- β 's impact on malignant progression, we demonstrate that TGF- β concentrating near tumor-vasculature generates heterogeneity in TGF- β signaling at tumor-stroma interface and bestows slower-cycling properties to neighboring SCC-SCs. While non-responding progenies proliferate faster and accelerate tumor growth, TGF- β -responding progenies invade, aberrantly differentiate, and affect gene expression. Intriguingly, TGF- β -responding SCC-SCs show increased protection against anti-cancer drugs, but slower-cycling alone does not confer survival. Rather, TGF- β transcriptionally activates p21, which stabilizes NRF2, thereby markedly enhancing glutathione metabolism and diminishing effectiveness of anti-cancer therapeutics. Together, these findings establish a surprising non-genetic paradigm for TGF- β signaling in fueling heterogeneity in SCC-SCs, tumor characteristics, and drug resistance.

INTRODUCTION

Most tumors are of a clonal origin but often exhibit heterogeneity in phenotypic and functional properties including proliferation, morphology, motility, and differentiation. Such heterogeneity has also been implicated in the ability to survive therapy and seed metastases (Hanahan and Weinberg, 2011). Cumulative mutations resulting from genomic instability certainly produce heterogeneity (Greaves and Maley, 2012). However, developmental diversity of cell types is accomplished without genetic alterations, raising the possibility that cellular diversity within tumors may also arise from non-genetic factors. Contributing variations might come from the tumor microenvironment, which can

transmit gradients of signaling factors, oxygen, and metabolites to tumor cells depending upon their proximity to the local sources (Meacham and Morrison, 2013; Kreso and Dick, 2014). While the hypothesis is attractive, experimental evidence is lacking, and non-genetic mechanisms that drive tumor heterogeneity remain largely unknown.

Irrespective of the basis for tumor heterogeneity, the long-lived capacity of tumor-initiating stem cells (SCs) to self-renew, initiate, and propagate cancers place these cells at the roots of diversity. Furthermore, SCs are often few in number and can exist in slow-cycling states, which has led to speculation that cancer SCs may be the source of recurrence following anti-cancer therapy (Hope et al., 2004; Berns, 2005; Notta et al., 2011; Visvader and Stingl, 2014). Another potentially intertwined factor is the need for long-lived SCs to adjust their metabolism in order to withstand stress and reactive oxygen species (ROS) (Diehn et al., 2009). In turn, such metabolic reprogramming can alter cellular behavior and lead to cancer progression (Bigarella et al., 2014). To this end, variations in cycling rates and/or local microenvironments could generate metabolic heterogeneities in cancer SCs, which could ultimately affect tumor heterogeneity and drug resistance.

An excellent tumor model for addressing these issues is squamous cell carcinoma (SCC). Among the most common and life-threatening cancers world-wide, SCCs exhibit high rates of tumor recurrence following anti-cancer therapy. Both functionally and molecularly, populations enriched for SCC-SCs have been identified, purified, and characterized. These SCC-SC-enriched populations represent ~1%–5% of the tumor and reside at the tumor-stroma interface. They are typified by elevated integrins, and other markers, e.g. CD34, CD44, and SOX2 (Malanchi et al., 2008; Schober and Fuchs, 2011; Lapouge et al., 2012). They also express VEGFA, suggestive of enrichment at the vasculature (Beck et al., 2011). Interestingly, heterogeneity, particularly in proliferative rates, exists within SCC-SC-enriched populations (Schober and Fuchs, 2011). Whether a slow-cycling property allows some SCs to escape chemotherapy and contribute to cancer recurrence has not been explored.

Notably, SCC-SC numbers increase by ~10-fold when T β RII, an essential component of the transforming growth factor β (TGF- β) transmembrane receptor, is abrogated (Schober and Fuchs, 2011). TGF- β is a well-established inhibitor of normal epithelial cell proliferation, and conditional ablation of *Tgfb2* predisposes epithelial tissues to cancer (Lu et al., 2006; Ijichi et al., 2006; Muñoz et al., 2006; Guasch et al., 2007).

Paradoxically, although elevated TGF- β signaling in skin prevents chemical induction of benign papillomas, TGF- β enhances their malignant conversion to SCCs and promotes metastasis (Cui et al., 1996; Massagué, 2012).

Researchers often attribute these seemingly distinct effects of TGF- β to cumulative genetic changes during tumorigenesis. However, since cycling rates of SCs are heterogeneous within an SCC and since SC numbers increase in the absence of TGF- β signaling, we posited that heterogeneity in TGF- β -responsiveness might exist within SCC progenitors, and might simultaneously restrict their proliferation and promote invasion and malignant transformation. If so, TGF- β -mediated differences in cycling rates of SCC-SCs could contribute to metabolic heterogeneity, as well as ultimately, heterogeneity in response to anti-cancer therapies. Elucidating how TGF- β functions in cancer progression and metastasis is a prerequisite for ascertaining whether disrupting this pathway is prudent for metastatic therapeutics when its tumor suppressive features might co-exist.

The TGF- β signaling pathway has been extensively studied. When latent TGF- β ligands are processed and activated, they can bind to T β RII, which phosphorylates T β RI, the other essential component of this bipartite transmembrane receptor. Activated T β RI propagates the signal by phosphorylating intracellular downstream effectors, SMAD2 and SMAD3 (SMAD2/3), which complex with SMAD4, translocate to the nucleus and bind to specific DNA sequence motifs called SMAD-binding elements (SBEs). Upon binding, pSMAD2/3-SMAD4 complexes interact with additional transcriptional regulators to transactivate TGF- β -responsive target genes (Massagué, et al., 2005; Mullen et al., 2011).

The ability of TGF- β signaling to activate target genes enables the pathway to impact diverse cellular processes including not only proliferation but also differentiation, migration, apoptosis, and ECM remodeling (Derynck and Miyazono, 2008; Massagué, 2012; Oshimori and Fuchs, 2012a). Important questions now emerge regarding TGF- β 's ability to unleash its varied and temporal effects on tumor progression. Do TGF- β 's seemingly opposing actions on proliferation and invasion act sequentially or do they act simultaneously in tumor progression? Are these dissimilar events dependent upon progressively distinct genetic states that emerge during malignancy? Does TGF- β contribute to heterogeneity in the tumor microenvironment and, if so, how? Can heterogeneity in TGF- β signaling impact SCC-SCs differentially and might this allow some cancer SCs to escape anti-cancer drugs? If so, is it because of its ability to impact proliferation rates, affect metabolic states and/or alter the expression of key target genes?

To tackle these issues, we devised a strategy to monitor, track, and modify TGF- β signaling in mouse skin during malignant progression. In so doing, we've been able to delineate the temporal functions of TGF- β in SCCs as they develop and progress. Combined with transcriptional profiling, molecular, biochemical, and genetic studies, we unearth important functions for TGF- β signaling during the process and unveil its impact not only on cancer SC proliferation but also on the emergence of tumor heterogeneity and anti-cancer drug resistance. Moreover, we show that metabolic reprogramming, an emerging hallmark of

cancer, is also integrally linked to TGF- β -mediated effects on cancer SCs, and that TGF- β -regulated metabolism in particular plays a critical role in the divergent responses to anti-cancer therapies.

RESULTS

An In Vivo Reporter System for Lineage Tracing and Manipulating TGF- β Responding Cells During Malignant Progression

To identify putative TGF- β -responding cells within skin tumors, we first performed anti-phospho (active) SMAD2 immunofluorescence on mouse skin at various stages following classical carcinogenic protocols with tumor-initiator 7,12-dimethylbenz(a)anthracene (DMBA) and tumor-promoter 12-O-tetradecanoyl-phorbol-13-acetate (TPA) (Figure 1A). As reported previously (Oshimori and Fuchs, 2012b), nuclear pSMAD2 was barely detectable in interfollicular epidermis. In normal skin, it appeared transiently in follicular stem cells (SCs) at the start of a new hair cycle. As benign papillomas formed, pSMAD2 immunolabeling remained low in epithelium but was found in some stromal cells. As papillomas transitioned to malignant SCC, marked nuclear pSMAD2 appeared in epithelial cells at the invasive tumor front. Keratin 14 (K14)-Cre-mediated ablation of *Tgfb2* specifically in skin epithelium resulted in complete loss of pSMAD2 in SCCs, but not surrounding stroma. These findings underscored the efficacy of the antibody and the dependence of SMAD2/3 activation in SCCs on TGF- β /T β RI/II signaling, rather than pathways triggered by Nodal or Activins.

To monitor T β RI/II-pSMAD2 signaling in vivo, we designed a lentiviral (LV) TGF- β reporter system that used an enhancer composed of multimerized pSMAD2/3 binding elements (SBE) to drive a P2A-based bicistronic transcript encoding nuclear (NLS) mCherry and tamoxifen (Tam)-activatable CreER recombinase (herein called TGF β -CreER). We inserted a polymerase III-driven promoter in the opposite direction to simultaneously drive an shRNA to achieve knockdown (KD) of a desired transcript (Figure S1A). We first tested this reporter in primary keratinocytes (1^0 MKs) cultured from *Rosa26-lox-STOP-lox-EYFP* Cre reporter (*Rosa-YFP*) mice bred on either a *Tgfb2*^{+/+} or *Tgfb2*^{fl/fl} background (Figure S1B). Upon TGF- β treatment, reporter-transduced 1^0 MKs expressed NLS-mCherry. Tam then activated CreER in TGF- β -responding MKs, leading to constitutive *Rosa-YFP* expression. Upon *Tgfb2* ablation, cells lost TGF- β responsiveness, and in turn extinguished NLS-mCherry expression (Figure S1B).

We brought the TGF- β reporter system into an in vivo setting by injecting LV into the amniotic sac of E9.5 mouse embryos. This in utero method allowed titer-dependent (1 \rightarrow >90%) selective transduction of the unspecified surface epithelial progenitors that give rise to skin epithelia (Beronja et al., 2010). By adding a reverse tetracycline transactivator (rtTA) cassette (*PGK-rtTA3*) to our LV TGF- β reporter construct, we could transduce *TRE-Hras*^{G12V} transgenic mice (Chin et al., 1999) and then induce oncogenic Hras^{G12V} with doxycycline (Doxy) (Figure 1B).

In the first experiment, we crossed *TRE-Hras*^{G12V} and *TRE-H2BGFP* mice, and sparsely delivered TGF- β reporter to surface ectoderm of transgenic embryos. Postnatally, doxy-dependent

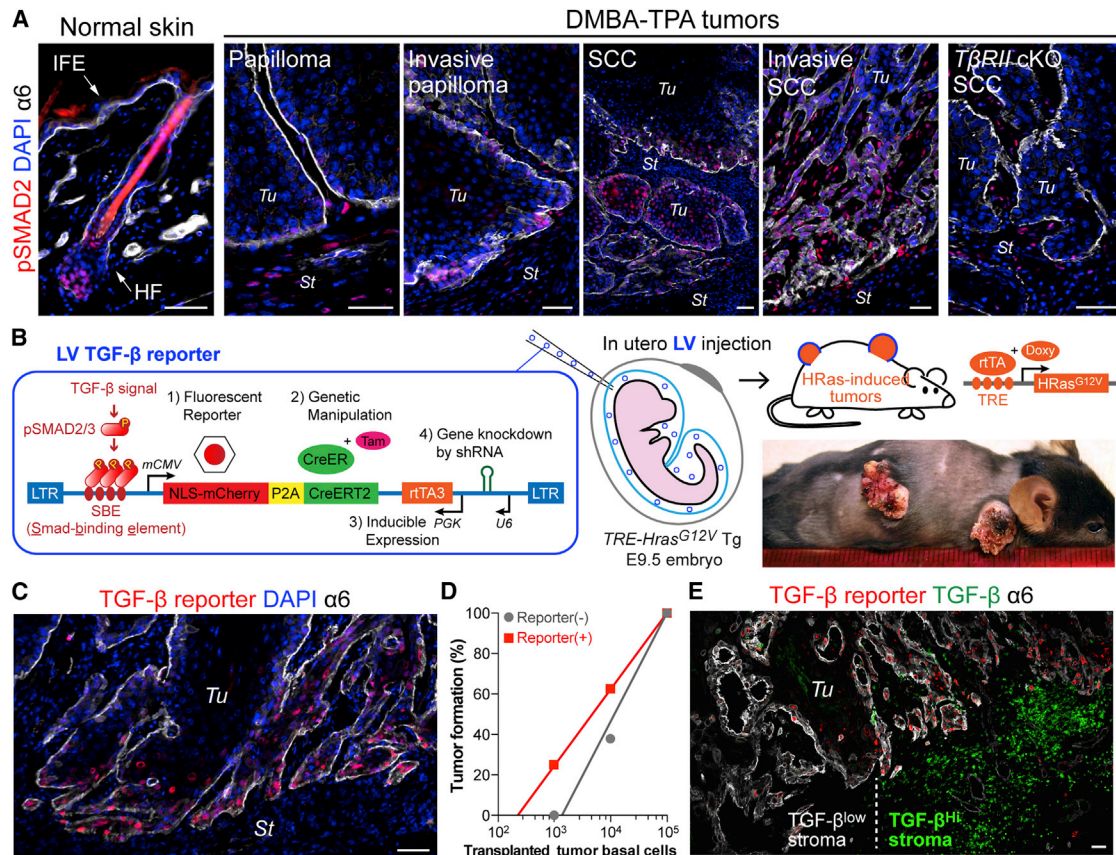


Figure 1. Lentiviral TGF- β Reporter System for Probing Malignant Transformation In Vivo

(A) pSMAD2 immunolocalization in normal mouse skin and at different stages of DMBA-TPA-induced malignant progression to SCC. Integrin $\alpha 6$ denotes the boundary of tumor epithelia (Tu) and stroma (St). IFE: interfollicular epidermis, HF: hair follicle.

(B) Schematic of LV-mediated in vivo TGF- β reporter and KO/KD system. NLS-mCherry and CreER are under the control of TGF- β signaling. shRNA and rTA3 transcription factor are under constitutive promoter regulation. LV transduction of surface epithelium of live E9.5 *TetO-Hras G^{12V} X Rosa-YFP* embryos was achieved by in utero ultrasound-guided microinjection into the amniotic sac. Doxy-induction of HRas G^{12V} initiates tumorigenesis. When desired, CreER is activated by Tam to induce recombination-dependent Rosa-YFP.

(C) Epifluorescence detection of TGF- β -pSMAD2 signaling in HRas G^{12V} SCC.

(D) Limit-dilution orthotopic transplantation of primary tumor basal cells \pm TGF- β reporter activity (10^3 and 10^4 cells; $n=8$, 10^5 cells; $n=3$).

(E) Epifluorescent TGF- β reporter activity with pan-anti-TGF- β and anti- $\alpha 6$ immunofluorescence shows that basal tumor cells with high TGF- β reporter activity are juxtaposed to stroma with high TGF- β (right). Note heterogeneity demarcated by vertical dotted line.

Scale bars, 50 μ m. See also Figure S1.

HRas G^{12V} induction occurred exclusively in LV-transduced cells. Within 1–2 months, papillomas formed, which often rapidly progressed to SCC in all or part of the tumor. Tumor epithelia were GFP $^{+}$, reflecting their derivation from rTA-expressing, LV-transduced cells (Figure S1C). Additionally, the low levels of virus used (MOI \ll 1) suggests that these tumors were clonally derived.

In remaining studies, we used *TRE-Hras G^{12V} X Rosa-YFP X Tgfr2* (+/fl or fl/fl) mice. TGF- β reporter activity (NLS-mCherry) co-localized with pSMAD2 and was particularly intense in a subset of basal tumor cells at invasive fronts (Figures 1C and S1D). Serial transplantation assays previously revealed that the tumor-stromal interface is where cells exist that have long-term, tumor-initiating potential, defined as SCC-SCs (Schober and Fuchs, 2011; Lapouge et al., 2012). To address whether the heterogene-

ity of TGF- β signaling at this interface might be relevant to SCC-SCs, we used fluorescence-activated cell sorting (FACS) to fractionate CD44 $^{+}$ $\alpha 6^{hi}$ basal tumor cells according to mCherry expression. mCherry $^{+}$ cells frequently expressed SC marker CD34 (Figure S1E). In vitro, the colony forming efficiency of TGF- β -responding basal cells was higher than non-responding counterparts, while in direct transplantation assays, FACS-purified TGF- β reporter $^{+}$ basal cells displayed \sim 5X higher tumor-initiating frequency than reporter neg counterparts (Figures 1D and S1F). Together, these data indicate that the TGF- β -responding subset of CD44 $^{+}$ CD34 $^{+}$ $\alpha 6^{hi}$ basal tumor cells was enriched for SCC-SCs.

Immunostaining revealed heterogeneity in TGF- β ligand distribution in the stroma that correlated well with basal tumor cell heterogeneity in TGF- β signaling (Figure 1E). Of the various cell

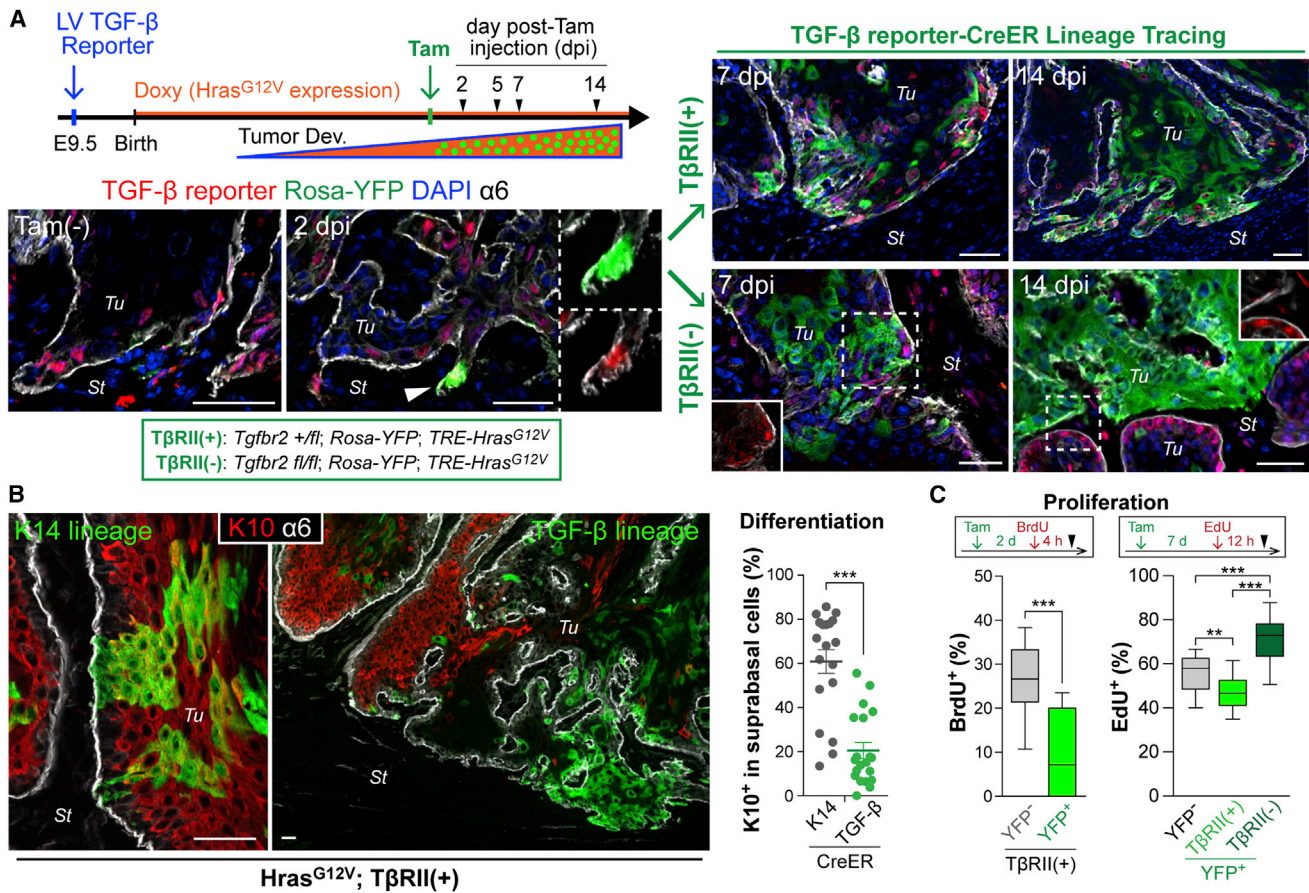


Figure 2. TGF- β Signaling-Driven Lineage Tracing during Tumor Development

(A) Experimental scheme and representative images of TGF- β signaling-driven lineage tracing. Once tumors form (>7 mm), NLS-mCherry is detected in TGF- β -responding transduced cells (Tam-). A single i.p. injection of low-dose Tam elicits *Rosa-YFP* recombination in a small subset of these cells within 2d post-Tam injection (2dpi). Note YFP/mCherry double-positive cell at invasive front. YFP-marked cells undergo clonal expansion, evident at 7 and 14 dpi, and now independent of TGF- β reporter activity (right). Note difference in clonal expansion rate and morphology based upon whether the initial marked cell is from a tumor initiated on a *Tgfb2* (fl/+) (top) or (fl/fl) (bottom) genetic background.

(B) Immunolabeling (left) and quantifications (right) show that suprabasal differentiation marker K10 preferentially marks YFP⁺ clones (n=19 analyzed) derived from K14-CreER-induced basal tumor cells. Note that TGFβ-CreER-induced lineage tracing marks TGF-β-responding basal cells that yield YFP⁺K10^{neg} clones (n=21). Data are mean ± SEM.

(C) S-phase analysis during lineage tracing. BrdU or EdU was administered at 2 or 7 dpi, respectively (see [Figures S2H and S2I](#)), and YFP^{neg} and YFP⁺ basal tumor cells were quantified for nucleotide incorporation (n = 11–15).

Data are box-and-whisker plots. Scale bars, 50 μm . See also [Figure S2](#).

types surrounding the tumor, TGF- β immunolabeling best overlapped with CD11b⁺Ly6C⁺ monocytic myeloid cells (Figure S1G), in agreement with a prior report that human peripheral blood monocytes secrete TGF- β (Grotendorst et al., 1989). Interestingly, TGF- β ⁺ cells often localized near vasculature, while nuclear pSMAD2 gave a complementary pattern in nearby SCC-SCs (Figures S1G and S1H). The spatial relation between epithelial TGF- β reporter activity and tumor vasculature was exemplified by three-dimensional (3D) microscopic imaging of the tumor-stromal interface (Movies S1 and S2). These results suggest that TGF- β ligand distribution coincides with vasculature and immune cell heterogeneity in tumor microenvironment, and this in turn, generates regional T β RI/II-pSMAD2 signaling within nearby malignant epithelial progenitors at the tumor-stroma interface.

Lineage Tracing Unveils Distinct Behaviors of TGF- β -Responding Versus Non-Responding SCC-SCs

To track the fate of TGF- β -responsive cells during early tumor progression *in vivo*, we performed TGF- β signaling-dependent lineage tracing by transducing our TGF- β reporter at low MOI as before and then administering Doxy at birth to induce tumorigenesis. Once tumors reached ~ 7 mm in size, a single low-dose of Tam was then administered systemically to trigger ~ 24 hr of CreER activity in a small subset of TGF- β -reporter-activated tumor cells (diagram in [Figure 2A](#)). Prior to Tam injection, emerging tumors showed mCherry but no YFP, underscoring the dependency of mCherry/CreER bicystronic expression on TGF- β but the reliance of CreER activation on Tam.

At 2 days post-Tam injection (dpi), single or small clusters of 2–4 YFP⁺ cells were found at the tumor-stroma interface

(Figure 2A). YFP⁺TβRII⁺ clones grew markedly over the subsequent 2 weeks and showed enrichment at invasive protrusions. Surprisingly, however, cells within these clones were highly scattered (shown).

On the *Tgfb2*^{fl/fl} background, Tam resulted in *Tgfb2* ablation specifically in the few random TGF-β-responding tumor cells that had activated CreER and YFP. YFP⁺TβRII^{neg}pSMAD2^{neg} cells underwent clonal growth faster, and clones were more tightly packed and less intrusive than TβRII⁺ counterparts (Figure 2A). Importantly, because we ablated *Tgfb2* in TGF-β-responsive cells, this difference was not attributable to microenvironmental heterogeneity but rather to intrinsic SC differences arising from loss of TGF-β signaling.

The increased scattering and invasiveness of clones derived from TGFβ-responsive tumor cells was accompanied by several features typically associated with epithelial to mesenchymal transition (EMT), including an elongated cell shape, reduced E-cadherin, and enhanced ZEB2 and HMGA2 (Figures S2A–S2D, Movie S3) (Thuault et al., 2006; Hanahan and Weinberg, 2011). By 3D reconstruction of Z-stack images, the clonal nature of the expanding colonies was still discernable, as was their close proximity to tumor vasculatures (Movie S4).

Serendipitously, additional functional lineage tracing unveiled a role for TGF-β signaling in generating aberrant differentiation during malignant progression. When Tam was given to tumors from *K14-CreER X Rosa-YFP X TRE-Hras*^{G12V} mice transduced with LV-rtTA3, many YFP⁺ clones from total basal tumor cells (K14^{hi}/K5⁺) displayed a differentiation keratin K10 suprabasally (Figure 2B). By contrast, in TGFβ-CreER-driven YFP⁺ clones, K10 was rarely detected, and leading edge cells showed reduced K5 (Figure S2E). Conversely, K13 and K18, ectopically induced in skin SCCs (Nischt et al., 1988; Yamashiro et al., 2010), were readily detected in TGFβ-CreER-driven YFP⁺ clones, but not in most K14-CreER-driven ones nor in unmarked, TGFβ-non-responsive basal tumor cells from TGFβ-CreER animals (Figures S2F and S2G).

As shown in Figures 2C and S2H, fewer TGF-β-responding (YFP⁺) basal cells were in S-phase relative to TGF-β non-responding (YFP^{neg}) basal cells. Interestingly, however, as YFP⁺ basal cells clonally expanded, their SCs remained less proliferative, suggestive of a prolonged slower-cycling state within the TGF-β lineage. By contrast, mosaic YFP⁺TβRII^{neg} basal clones showed high cycling rates compared to their YFP^{neg}TβRII⁺ neighbors (Figures 2C and S2I).

Taken together, our in vivo data provided compelling evidence that TGF-β signaling is directly responsible for generating a pool of slower-cycling SCC-SCs. Moreover, these data further suggest that TGF-β is involved in a non-genetic mechanism that underlies the emergence of tumor heterogeneity at perivascular regions and which leads to simultaneous invasiveness, cell dissemination, and aberrant differentiation, at the expense of SC proliferation and tumor growth.

TGF-β Protects SCC Progenitors From Anti-Cancer Drugs

It has long been suggested that slower-cycling SCs might be refractory to chemotherapeutic anti-proliferative cancer drugs. One of the most widely used anti-cancer drugs, cisplatin [cis-di-

aminedichloroplatinum (II)], is the standard chemotherapy for head and neck SCC, and has been used to treat advanced cutaneous SCC. However, tumor recurrence is a major problem.

To test whether TGF-β signaling might be involved in drug resistance, we first conducted a series of in vitro experiments. We prepared HRas^{G12V}-expressing 1^oMKs from *Tgfb2*^{fl/fl} X *Rosa-YFP* mice and transduced them with TGF-β reporter-CreER. After TGF-β1 ± Tam, YFP^{neg}TβRII⁺ and YFP⁺TβRII^{neg} isogenic MKs were co-cultured to assess phenotypes under identical conditions. As expected, TGF-β1 caused reporter activation and growth arrest in YFP^{neg}TβRII⁺, but not YFP⁺TβRII^{neg} MKs (Figures 3A and 3B).

Cisplatin exerts its cytotoxicity by forming DNA-cisplatin adducts that are recognized by DNA damage recognition complexes which trigger apoptosis (Kelland, 2007). Consistent with these effects, cisplatin caused apoptotic rounding and γ-H2AX (marking DNA double-strand breaks) throughout proliferating cultures (Figures 3C and 3D). Interestingly, after exposure to TGF-β1 for 24–36 hr, most YFP^{neg}TβRII⁺ cells remained spread, with markedly reduced γ-H2AX compared to YFP⁺TβRII^{neg} counterparts. Quantifications with active Caspase-3 (AcCasp3) indicated that TGF-β1 pre-treatment significantly reduced cisplatin-induced apoptotic death (Figure 3E). Moreover, an antibody recognizing DNA-cisplatin adducts showed preferential immunolabeling of YFP⁺TβRII^{neg} MKs in cisplatin-treated cultures (Figure 3F). These results suggested that TGF-β signaling enables cultured SCC-SCs to better withstand cisplatin-induced apoptosis.

TGF-β-Responding SCC Progenitors Are Responsible for Drug Resistance and Tumor Recurrence

To test TGF-β's protective qualities in vivo, we challenged tumor-bearing TGF-β reporter mice with systemic cisplatin. While few AcCasp3⁺ cells were detected in saline-injected control mice, cisplatin significantly increased apoptosis within skin tumor cells. Strikingly, fewer basal tumor cells with active TGF-β signaling were apoptotic (Figure 4A and Movie S5).

If TGF-β signaling contributes to drug therapy failure, TGF-β-responding cells should remain during treatment and outgrow their non-resistant peers over time. To test this hypothesis, we conducted TGF-β reporter-driven lineage tracing on TβRII⁺H-Ras^{G12V} tumors during systemic cisplatin treatment. To ensure that we were monitoring TGF-β reporter⁺ progeny, we carried out Tam treatment (3 doses, 12 hr each) until 1.5 days prior to cisplatin administration. Relative to saline controls, cisplatin injections resulted in a striking reduction in tumor volume within 10–12 days (Figure S3A).

Most notably, the remaining tumors, some of which already showed recurrent growth (Figure S3A), were disproportionately maintained by YFP⁺ progenies of TGF-β-responding cells (Figures 4B and 4C). This was notable since recurrent tumors still exhibited TGF-β reporter activity, and since even though overall proliferative rates of YFP⁺ SCC-SCs were elevated in these recurring tumors, the TGF-β reporter⁺ cohort of basal tumor cells still remained slower-cycling relative to TGF-β-reporter^{neg} counterparts (Figures 4C and 4D). Finally, as in the primary tumor clones derived from TGF-β reporter⁺ lineages, K10 was broadly absent in YFP⁺ suprabasal cells, suggesting that recurring

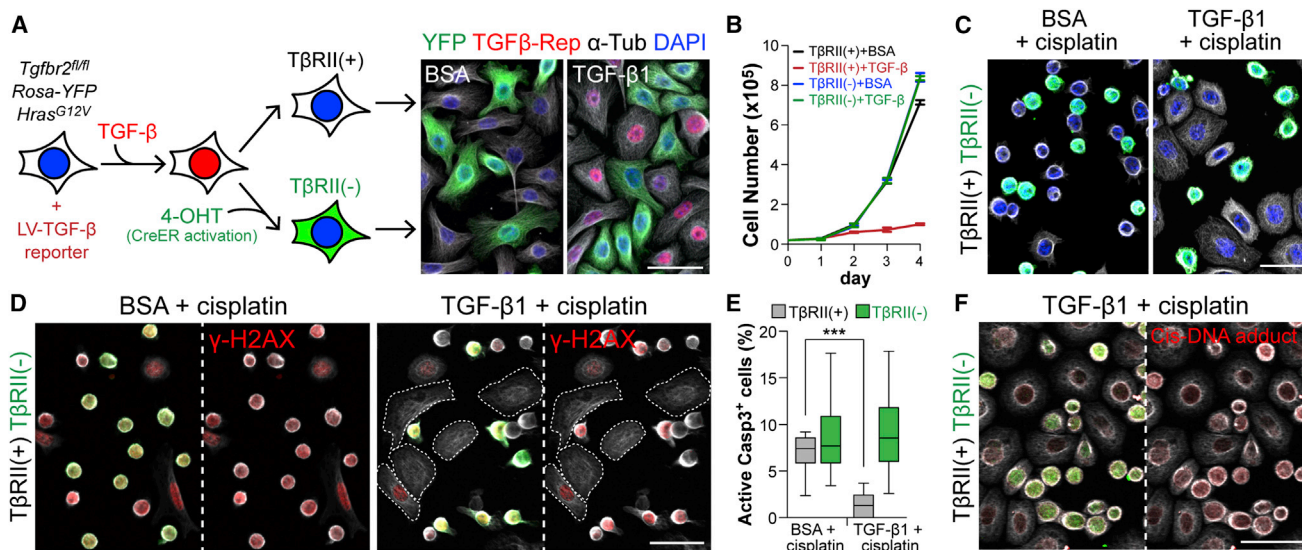


Figure 3. Active TGF-β Signaling in Basal Tumor Cells Increases Their Protection against Cisplatin-Induced Apoptosis

(A) Experimental scheme to derive isogenic HRas^{G12V}-expressing YFP^{neg}TβRII⁺ and YFP⁺TβRII^{neg} MKs from 1^o cultures. (Right) Epifluorescence of cultures ± TGF-β1. Note that only YFP^{neg}TβRII⁺ cells are TGF-β reporter⁺ (mCherry⁺).

(B) Growth curves of TβRII⁺ and TβRII^{neg} cells ± 100pM TGF-β1. Data are mean ± SEM.

(C) Immunofluorescence of BSA- or TGF-β1-pretreated (36 hr) YFP^{neg}TβRII⁺ and YFP⁺TβRII^{neg} MKs treated 10 hr with cisplatin. Note that YFP⁺TβRII^{neg} MKs frequently displayed signs of apoptotic rounding.

(D) γ-H2AX detection of DNA double-strand breaks induced by cisplatin treatment. Note that both YFP^{neg}TβRII⁺ and YFP⁺TβRII^{neg} MKs show γ-H2AX signal in control, but TGF-β1 selectively spares TβRII⁺ cells, which remain spread.

(E) Quantifications of AcCasp3⁺ cells in the same experiment as in (C) and (D) (n=15 microscopic image fields). Data are box-and-whisker plots.

(F) Immunodetection of adduct formed between cisplatin and DNA. Note that YFP⁺TβRII^{neg} cells have more cisplatin-modified DNA (red). Anti-tubulin (white). Scale bars, 50 μm.

tumors were enriched for malignant TGF-β–pSMAD2-signaling basal cells that had survived cisplatin treatment (Figure 4E).

If TGF-β signaling confers increased cisplatin protection to SCC-SCs in vivo, then ablating TGF-β signaling in these cells should confer increased sensitivity to apoptosis. To test this hypothesis, we repeated the experiment shown in Figure 4B, this time on *Tgfb2*^{+/fl} (control) and *Tgfb2*^{fl/fl} (test) backgrounds. To ensure optimal *Tgfb2* allele targeting, we extended Tam treatments until 3d prior to cisplatin. As shown in Figure 4F, loss of TGF-β signaling resulted in enhanced cisplatin sensitivity.

We obtained similar results when we transduced human SCC lines with TGF-β reporter LV and xenografted them in *Nude* mice (Figure S3B). Upon cisplatin treatment, TGF-β reporter^{neg} human basal tumor cells showed greater sensitivity than their TGF-β reporter⁺ counterparts (Figure 4G). When the experiment was repeated with TGF-β inhibitor LY364947, a dramatic increase in cisplatin sensitivity was observed (Figure 4H and S3C). Together, these findings suggest that both in mouse and human, TGF-β signaling is heterogeneous and increases protection of SCC-SCs against cisplatin.

Transcriptome Analysis Uncovers a Link between TGF-β Signaling and Glutathione Metabolism in SCC Stem Cells

The ability of TGF-β signaling to confer enhanced survival to SCC-SCs of cisplatin-treated tumors was consistent with the cancer stem cell hypothesis for tumor recurrence. A priori,

TGF-β's power could arise from its impact on slow-cycling behavior and/or its effect on transcription. To gain further insights, we used FACS and RNA sequencing (RNA-seq) to purify, transcriptionally profile and compare TGF-β-responding (mCherry⁺) versus non-responding (mCherry^{neg}) SC populations from >7 mm HRas^{G12V}-induced tumors (Figures S4A–S4C). Our purification scheme was optimized by depleting stromal cell types and dead cells, and then positively selecting for high surface expression of markers of SCC-SCs.

Independent duplicates yielded highly reproducible RNA-seq data (Figure 5A). Dendrogram analysis indicated that despite similarities across SCC-SC profiles, TGF-β reporter⁺ samples clustered together and separated from the other clustered counterpart. We defined our TGF-β-responsive SCC-SC signature as genes whose transcripts at an FPKM ≥ 1 were differentially expressed by log2 fold change ≥ |1| and which displayed a statistical significance (p < 0.05, q < 0.05) across datasets. Our signature consisted of 632 up- and 478 downregulated genes (Figure S4D).

Several noteworthy alterations were immediately evident in the TGF-β signature. Consistent with our findings thus far, cancer-related differentiation genes, e.g. *Krt13*, were upregulated. As expected, there was significant overlap with prior signatures from purified SCC-SCs but independent of TGF-β status (Schober and Fuchs, 2011; Lapouge et al., 2012). Notably however, *Sox2*, *Pitx1*, *Vegfa* and other genes typifying these SCC-SC signatures (Boumahdi et al., 2014; Siegle et al., 2014) were more enriched in the TGF-β reporter⁺ subset than in the total basal SC population.

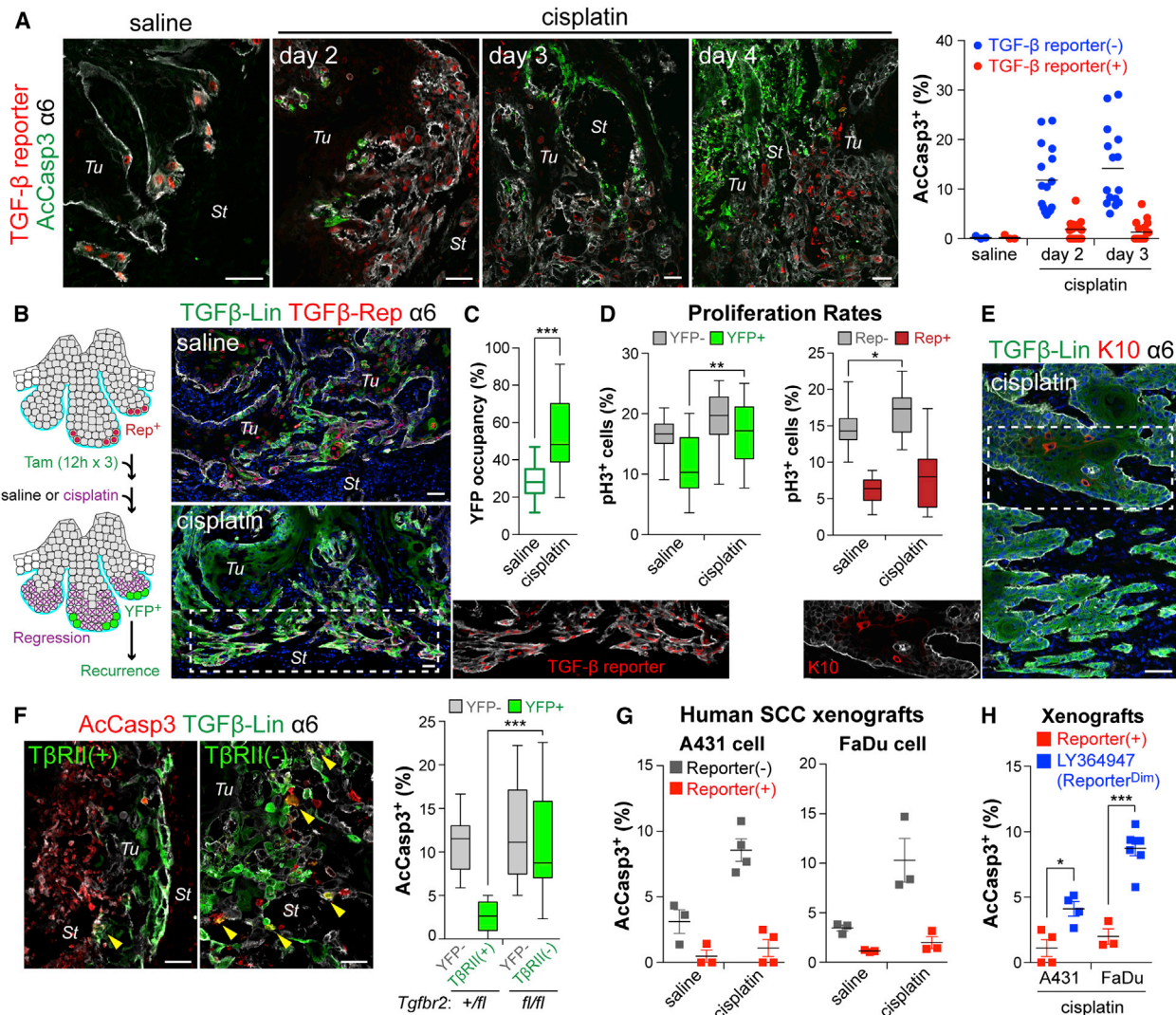


Figure 4. TGF- β -Responding SCC-SCs Show Enhanced Drug Resistance In Vivo

(A) Immunodetection of AcCasp3 (green) and TGF- β reporter (red) in tumors from mice administrated with saline or cisplatin. (Right) Quantifications revealing that TGF- β signaling protected basal tumor cells from cisplatin-induced apoptosis. (3 tumors analyzed; >15 microscopic image fields per tumor).

(B) Experimental scheme and representative examples of lineage tracing to monitor the fate of the TGF- β reporter⁺ subset of basal tumor cells after cisplatin treatment. (Right) Note that resistant SCCs are largely contributed by TGF- β -responding cells that survived cisplatin.

(C) Quantifications show that the % of YFP⁺ basal tumor cells increases after cisplatin, suggestive of their preferential survival.

(D) Quantifications of basal tumor cells in G2/M phase (phospho-H3⁺) that are YFP^{neg} vs YFP⁺ (left) and reporter^{neg} vs reporter⁺ (right). Note: although proliferation of basal tumor cells that resist cisplatin is generally elevated, TGF- β -responding SCC-SCs are still slower-cycling.

(E) Recurring tumor clones that resist cisplatin are largely YFP⁺ and express little K10, consistent with their derivation from TGF- β reporter⁺ basal cells.

(F) Quantification of apoptotic cells in cisplatin-treated tumors from LV-transduced *Tgfr2*^{+/fl} or *Tgfr2*^{fl/fl} mice treated as in (B). Note enhanced survival of TβRII⁺ progenies.

(G and H) Quantification of AcCasp3⁺ cells after cisplatin treatment of xenografts of (G) TGF- β reporter transduced human SCC cells (reporter⁺ vs reporter^{neg}), and (H) xenografts pre-treated \pm LY364947 (reporter⁺ vs reporter^{dim}) (n>3).

Data are box-and-whisker plots (C–F) and mean \pm SEM (G and H). Scale bars, 50 μ m. See also Figure S3.

There was also overlap (28%) between our TGF- β reporter⁺ SCC basal cell RNA-seq and the signature obtained from VEGF-over-expressing papilloma basal cells (Beck et al., 2011).

Gene ontology (GO) term analysis provided insights into biological processes enriched in TGF- β -responding SCC-SCs. In addition to epidermal development; lipid metabolism; and cell proliferation, “reduction and oxidation” (Redox) genes sur-

faced among top GO-terms. This was especially interesting given that the top upregulated gene pathway in KEGG analysis was “glutathione metabolism” (Figure 5A). Notably, glutathione is the most abundant intracellular antioxidant in animal cells and involves two important metabolic processes (Figure 5B) (Lushchak, 2012). The first is a reduction reaction, which prevents damage from reactive oxygen species (ROS) by exhausting

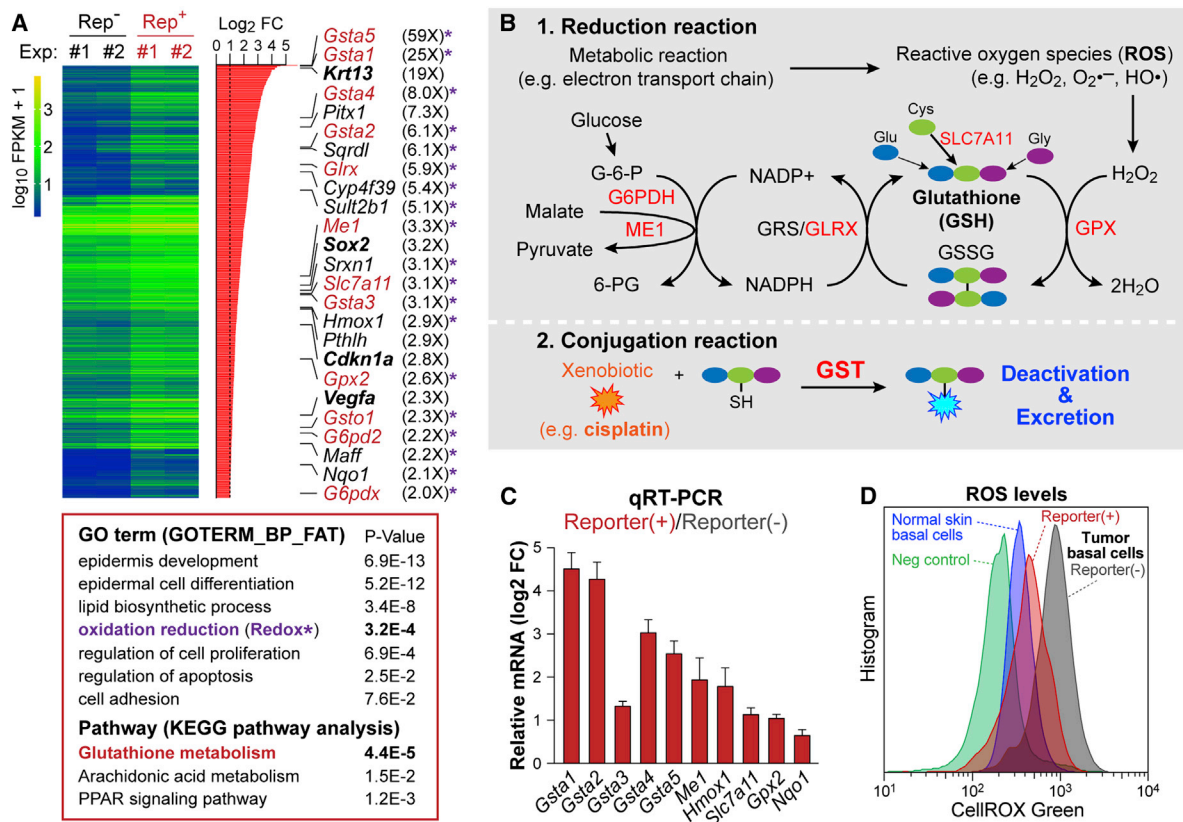


Figure 5. Transcriptional Profiling Reveals a Link between TGF- β Signaling and Glutathione Metabolism

(A) Summary of transcriptional profiling of TGF- β reporter⁺ vs reporter^{neg} tumor basal cells by RNA-seq. Significantly upregulated genes are listed on the right side; note genes involved in glutathione metabolism (red), Redox (asterisk). Other genes relevant to text are bolded. (Bottom) Gene ontology (GO: biological function) and KEGG pathway analyses.

(B) Schematic of glutathione metabolic pathway: 1) Reduction reaction; 2) Conjugation reaction. Genes in red are significantly upregulated in TGF- β reporter⁺ SCs.

(C) RNA-seq validation by qRT-PCR of independently derived in vivo tumor basal cell RNA samples. Data are mean \pm SEM.

(D) Flow cytometry analysis of ROS levels in basal cells in normal skin epidermis and tumor epithelia \pm TGF- β reporter activity. See also Figure S4.

ROS through the conversion of reduced glutathione (GSH) to its oxidized state (glutathione disulfide, GSSG). The second key process is a conjugation reaction regulated by glutathione S-transferase (GST), which is known to metabolize cisplatin (Kelland, 2007).

Our RNA-seq data indicated that genes involved in GSH-conjugation, GSH-mediated reduction and GSH-recycling processes were broadly upregulated in TGF- β reporter⁺ SCs. This list included GST genes (*Gsta1-5*, *Gsto1*) (Figure 5A). qRT-PCR on RNAs from independent tumor samples confirmed their enhanced expression in TGF- β reporter⁺ basal tumor cells (Figure 5C). Moreover, as judged by CellROX green, a cell-permeant dye that is brightly fluorescent only upon oxidation by ROS, ROS levels were significantly lower in TGF- β reporter⁺ tumor cells, consistent with the high expression of genes involved in glutathione metabolism (Figure 5D).

TGF- β Induces p21 which In Turn Stabilizes and Activates NRF2-Dependent Transcription in SCC-SCs

The myriad of glutathione metabolism genes upregulated in TGF- β -responding SCC-SCs necessitated further insights

before we could abrogate the pathway and assess the consequences to cisplatin resistance. Interestingly, the enhancer/promoters of these genes contained antioxidant response elements (AREs), which are the consensus binding motifs for transcription factor NRF2 (Gorrini et al., 2013) (Figure 6A). Additionally, as judged by immunofluorescence, nuclear NRF2 was prominent in TGF- β reporter⁺ cells at the tumor-stroma interface (Figure 6B). However, neither RNA-seq nor qRT-PCR data showed TGF- β reporter-dependent differences in NRF2 gene (*Nfe2l2*) transcription (Figure 6A), indicating that other steps must be involved in upregulating the antioxidant gene response in this SCC-SC subset.

Probing mechanism, we first considered KEAP1, which normally binds to and targets NRF2 for proteasome-mediated degradation. TGF- β activity did not affect *Keap1* mRNA levels, diminishing the likelihood that KEAP1 absence might underlie NRF2 stabilization. By contrast, cyclin-dependent kinase inhibitor p21 purportedly competes with KEAP1 for NRF2 binding (Chen et al., 2009), and *Cdkn1a*, encoding p21, is an established target of TGF- β -SMAD signaling (Seoane et al., 2004; Koinuma et al., 2009). Indeed, RNA-seq and qRT-PCR showed *Cdkn1a*

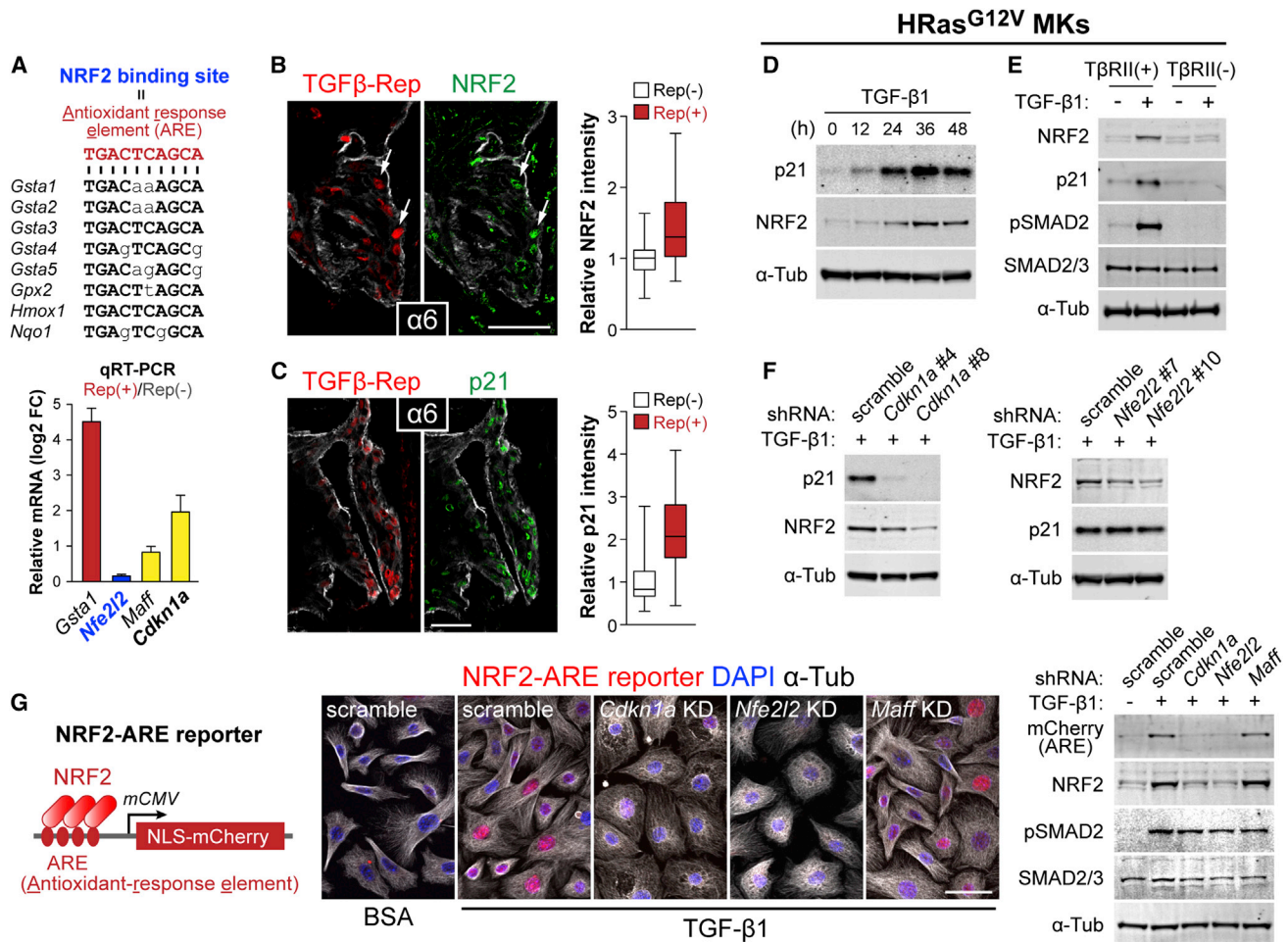


Figure 6. TGF- β Target p21 Is Required for NRF2-Dependent Activation of Antioxidant Genes

(A) Nucleotide sequence of NRF2 binding motifs within the 5'-upstream region of *Gst* and other NRF2 target genes. Nucleotides in capital letters are those shared by the antioxidant response element (ARE) consensus sequence. (bottom) qRT-PCR analysis of in vivo tumor basal cell RNA samples. Data are mean \pm SEM. (B and C) Co-expression of NRF2 or p21 (green) and TGF- β reporter (NLS-mCherry) at tumor-stroma interface of T β RII⁺ tumor sections. Fluorescent intensities of NRF2 and p21 staining in TGF- β reporter⁺ and reporter^{neg} cells were quantified (NRF2: n=78 and 57 cells, p21: n=101 and 71 cells). Data are box-and-whisker plots.

(D) Immunoblotting of lysates prepared from HRas^{G12V}-overexpressing T β RII⁺ 1⁰MKs stimulated with TGF- β 1 for indicated times.

(E) Immunoblotting of lysates prepared from HRas^{G12V}-overexpressing T β RII⁺ and T β RII^{neg} 1⁰MKs stimulated with TGF- β 1 for 36 hr.

(F) Immunoblotting of lysates prepared from 36 hr TGF- β 1-treated HRas^{G12V}-overexpressing 1⁰MKs transduced with scramble, *Cdkn1a* or *Nfe2l2* shRNAs.

(G) LV NRF2-ARE reporter. (Right) Immunofluorescence and immunoblots of NRF2-reporter transduced HRas^{G12V}-induced MKs expressing scramble (control), *Cdkn1a*, *Nfe2l2*, or *Maff* (control) shRNAs \pm TGF- β 1 stimulation (36 hr). Note that ARE-reporter activity is abolished upon *Cdkn1a* or *Nfe2l2* but not control KD. Scale bars, 50 μ m. See also Figure S5.

mRNA was upregulated in TGF- β reporter⁺ SCC-SCs in vivo (Figure 5A and 6A). Immunofluorescence further revealed a strong correlation between TGF- β signaling activity and p21 expression at the tumor-stroma interface (Figure 6C). Moreover, whereas NRF2 and p21 were readily detected in TGF- β -responding tumor cells at the tumor-stroma interface, their expression was not seen in neighboring T β RII^{neg} tumor cells derived from TGF- β -CreER activation nor in early papillomas, which do not show appreciable TGF- β signaling (Figures S5A–S5C). In vitro studies corroborated these findings (Figure S5D).

Delving deeper, we treated HRas^{G12V}-transformed 1⁰MKs with TGF- β 1 and then checked by qRT-PCR for temporal

changes in levels of select mRNAs (Figures S5E and S5F). In contrast to *Nfe2l2*, whose transcripts remained constant during the experiment, *Cdkn1a* transcripts rose 1–3 hr after TGF- β 1 treatment, reaching \sim 5X normal levels by 48 hr. Moreover by immunoblot, NRF2 and p21 were elevated upon prolonged TGF- β stimulation (Figure 6D). These effects were abrogated in T β RII^{neg} HRas^{G12V} 1⁰MKs (Figure 6E), supporting the view that p21 induced by TGF- β /pSMAD2 signaling mediates NRF2 protein stabilization.

To rigorously test the hierarchical relation between TGF- β , p21 and NRF2, we used LVs harboring *Cdkn1a* and *Nfe2l2* shRNAs (Figure S5G). *Cdkn1a* shRNAs not only efficiently depleted p21

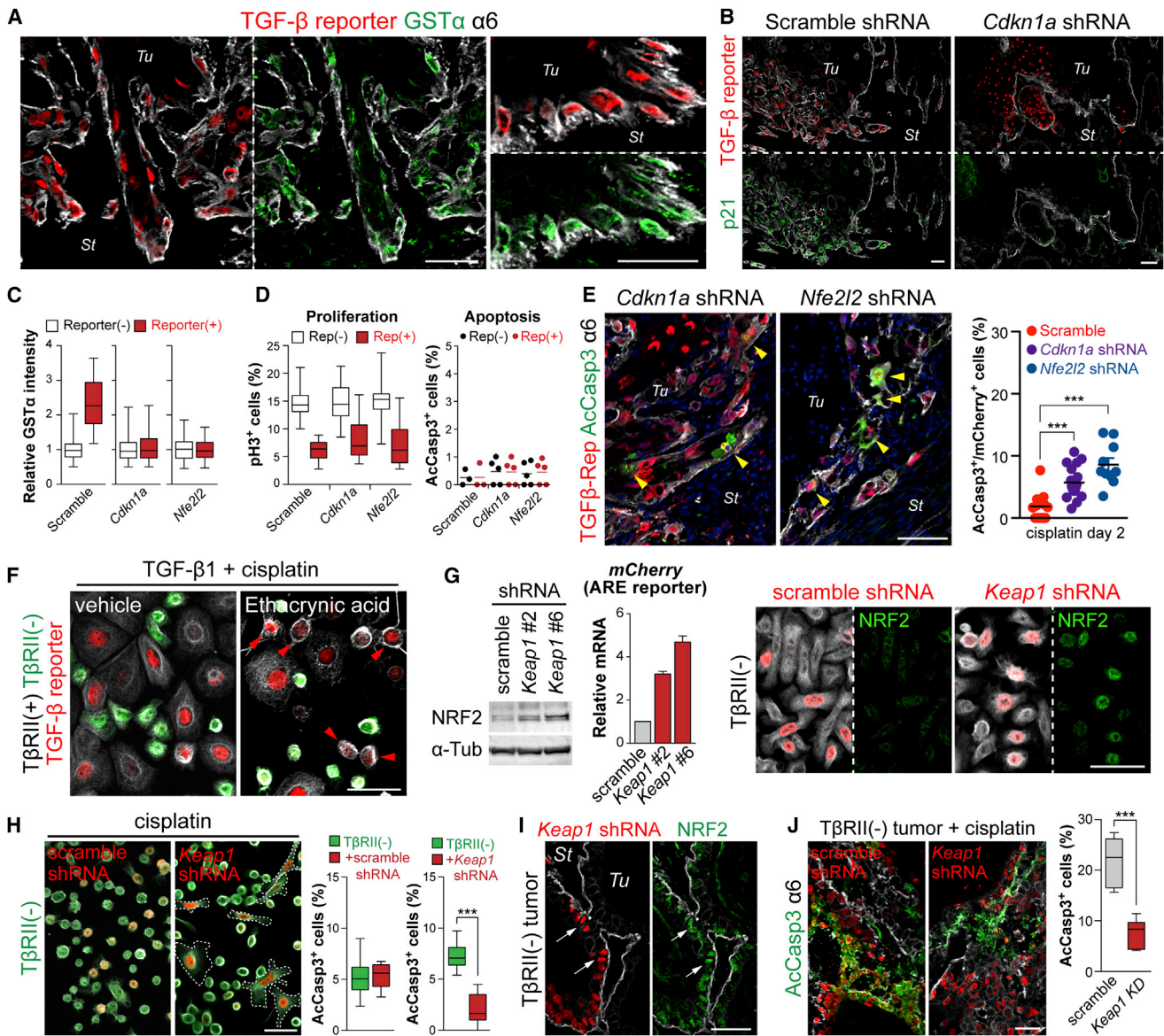


Figure 7. TGF- β -Induced Glutathione Metabolism Confers Enhanced Anti-Cancer Drug Resistance In Vivo

(A) Coimmunolabeling of TGF- β reporter and GST α in representative sections of SCCs from LV-transduced mice. Note that nuclear TGF- β reporter signal (red) and cytoplasmic GST α (green) overlap in invasive cells at the tumor-stroma interface.

(B) Immunofluorescence of T β RII⁺ tumor sections from transductions of our LV reporter harboring scramble control or *Cdkn1a* shRNAs. p21 (green) correlates well with TGF- β reporter activity (red) in scramble control and is silenced by *Cdkn1a* shRNA expression.

(C) Quantifications of GST α immunofluorescence intensities of TGF- β reporter⁺ and reporter^{neg} basal tumor cells of mice transduced with scramble, *Cdkn1a* or *Nfe2l2* shRNAs (n=144, 145 or 121 cells).

(D) Quantifications of proliferation (pH3⁺) and apoptosis (AcCasp3⁺) in basal cells from HRas^{G12V}-derived SCCs of mice transduced with LVs harboring scramble control, *Cdkn1a*, or *Nfe2l2* shRNAs.

(E) Coimmunolabeling and quantifications (n=3 tumors, >16 microscopic image fields) of AcCasp3 (green, cytoplasmic) and TGF- β reporter activity (red, nuclear) in *Cdkn1a* or *Nfe2l2* KD basal cells of SCCs from cisplatin-treated mice. Yellow arrowheads denote double-labeled cells. Note that without p21 or NRF2, TGF- β reporter⁺ cells are no longer able to resist apoptosis in response to cisplatin.

(F) TGF- β 1-pretreated MKs were exposed to cisplatin \pm a potent GST inhibitor, ethacrynic acid. Note that most YFP^{neg}T β RII⁺ MKs (red arrowheads) still exhibited robust TGF- β reporter activity, but now showed apoptotic rounding like their YFP⁺T β RII^{neg} counterparts.

(G and H) KEAP1 stabilizes NRF2 in T β RII^{neg} SCC-SCs and renders them resistant to cisplatin. (G) Immunoblotting of lysates prepared from HRas^{G12V}-over-expressing T β RII^{neg} MKs transduced with scramble or *Keap1* shRNAs. (middle) qRT-PCR of NRF2-reporter (*mCherry* mRNA) expression. (right) NRF2 immunofluorescence (green) in either scramble- or *Keap1* shRNA-transduced (H2B-RFP⁺) T β RII^{neg} cells. Note that NRF2 is readily detected in T β RII^{neg} cells only if transduced

(legend continued on next page)

but also reduced NRF2 protein in TGF- β stimulated cells (Figure 6F). By contrast, *Nfe2l2* depletion did not affect p21 levels induced by TGF- β /pSMAD2 signaling. These data place p21 downstream of TGF- β signaling and upstream of NRF2 stabilization. Indeed, as judged by immunoprecipitation, the interaction between p21 and NRF2 was dependent upon TGF- β 1 (Figure S5H).

To test the functional significance of this hierarchical relation, we created a LV NRF2 reporter (Figure 6G). NRF2 reporter activity was potently induced in 1⁰ MKs not only by the classical ROS, hydrogen peroxide (H₂O₂) (Figure S5I) but also by TGF- β stimulation (Figure S5J). Comparative analyses showed that while not as robust as the maximal effect achieved with 500 μ M H₂O₂, the effects of TGF- β 1 were comparable to 100–200 μ M H₂O₂ (Figure S5J). Moreover, NRF reporter activation by either H₂O₂ or TGF- β 1 was abolished when these cells were transduced with LVs harboring *Cdkn1a* or *Nfe2l2* shRNAs (Figures 6G and S5K). Together, these results provide compelling evidence that p21 is required for the NRF2-mediated target gene expression that occurs downstream of TGF- β /pSMAD2 signaling in SCC-SCs.

A Role for Glutathione Metabolism in the Cisplatin Resistance of TGF- β -Responding SCC-SCs

To address the physiological relevance of the p21/NRF2 pathway that we unearthed in vitro, we first showed that GST α , one of the highly upregulated glutathione pathway genes, was indeed upregulated at the protein level in TGF- β reporter⁺ cells at the tumor-stroma interface of invasive SCCs (Figure 7A). To test whether p21 mediates TGF- β -induced drug resistance, we conducted in vivo KDs by introducing *Cdkn1a* shRNAs into our LV TGF- β reporter constructs (Figure 7B). In *Cdkn1a* KD tumors, p21 expression was abrogated in TGF- β reporter⁺ cells. Importantly, GST α was also downregulated upon *Cdkn1a* KD (Figure 7C). Similar results were seen in tumors with *Nfe2l2* KD (shown). Together, these findings showed that a key component of glutathione metabolism was dependent upon NRF2 and TGF- β -regulated *Cdkn1a*.

Notably, the slow-cycling behavior of TGF- β -responding SCC-SCs was not affected appreciably by loss of either p21 or NRF2 (Figure 7D), providing a means of selectively reducing glutathione metabolism without compromising slow-cycling status in TGF- β -responding SCC-SCs. We therefore proceeded to address whether *Cdkn1a* and *Nfe2l2* KD would affect their cisplatin resistance. In the scramble control, TGF- β -responding SCC-SCs showed little apoptosis. In contrast, when mice bearing tumors knocked down for either *Cdkn1a* or *Nfe2l2* were treated with cisplatin, many basal tumor cells were double-positive for AcCasp3 and TGF- β -reporter (Figure 7E). Similarly, drug inhibition of GST increased the sensitivity of TGF- β -responding tumor cells to cisplatin in vitro (Figure 7F). Thus, under circumstances where SCC-SCs were still slow-cycling and responsive to TGF- β , the normalization of glutathione meta-

bolism was sufficient to abolish the survival advantage of TGF- β responding basal cells to cisplatin treatment.

Finally, we addressed the converse, namely whether by enhancing NRF2 stabilization, we could confer enhanced resistance of T β RII-null SCC-SCs to cisplatin. In vitro, both NRF2 protein and NRF2 reporter activity rose in T β RII-null HRas^{G12V}-transformed MKs transduced by either of two different *Keap1* shRNAs (Figure 7G). Correspondingly, this resulted in enhanced resistance to cisplatin (Figure 7H). When equal numbers of non-transduced and either scramble- or *Keap1* shRNA-transduced T β RII-null HRas^{G12V}-transformed MKs were mixed and then engrafted in vivo, tumors arose which displayed increased NRF2 specifically in *Keap1* shRNA-transduced MKs (Figure 7I). Most importantly, fewer of these basal tumor cells apoptosed after cisplatin treatment (Figure 7J). Overall, these data underscore the importance of this pathway in imparting enhanced drug resistance to TGF- β -responding SCC-SCs.

DISCUSSION

Functional and phenotypic heterogeneity among tumor cells have long been recognized, and dynamic changes in genetic, epigenetic, tumor microenvironmental and systemic factors affect subpopulations of tumor cells to acquire advantages for proliferation, survival, spread, and resistance to anti-cancer therapeutics. In studying stem cells of SCCs, we realized that they vary in cycling rates, and that SC numbers increase when TGF- β signaling is abrogated. These findings raised the possibility that TGF- β signaling might be at the root of tumor heterogeneity and that it might impact directly on cancer SCs.

In the present study, we established an in vivo LV delivery system, which allowed us to address roles of TGF- β signaling in the early stages of tumor progression. Our findings provide compelling in vivo evidence of TGF- β 's contributions to the emergence of tumor heterogeneity in the tumor-initiating cells that drive SCC. The heterogeneity in TGF- β -responsiveness is rooted in the congregation of myeloid cells near the tumor vasculature. While TGF- β is secreted in a latent form and deposited in ECM, TGF- β can be activated and released by a variety of mechanisms, which include activated integrins. The paracrine activation of T β RI/II-pSMAD2 in a subset of nearby (integrin^{hi}) SCC-SCs reflected active TGF- β signaling in these cells.

TGF- β represses normal epithelial growth, thereby functioning as an early tumor suppressor. These effects have been extensively studied, as have TGF- β 's late-stage roles in metastasis. However, in the absence of tools to explore intermediate stages of primary tumor progression, the prior speculation as to TGF- β 's dual function in these intermediate steps has been that TGF- β 's cytostatic effects are lost during tumor progression due to activation of oncogenic pathways such as Ras-MAPK, PI3K and c-Myc, which then override TGF- β 's growth inhibitory effects (Chen et al., 2002; Seoane et al., 2004; Gomis et al., 2006; Bruna

with *Keap1* shRNA. (H) Immunofluorescence of transduced YFP⁺T β RII^{neg} HRas^{G12V}-MKs treated with cisplatin for 10 hr. Note that *Keap1* KD (H2B-RFP⁺) suppresses apoptotic rounding. (right) Quantifications of AcCasp3⁺ cells in the same experiment.

(I) Anti-NRF2 (green) co-immunolabeling of *Keap1* KD (H2B-RFP⁺) cells in T β RII^{neg} HRas^{G12V} allograft tumors.

(J) AcCasp3⁺ quantifications show that *Keap1* but not scramble shRNA protects T β RII^{neg} HRas^{G12V} allograft SCC-SCs against cisplatin.

Data are box-and-whisker plots (C, D, H and J) and mean \pm SEM (E and G). Scale bars, 50 μ m. See also Figure S6.

et al., 2007). At later stages, other TGF- β responses then purportedly prevail that are unrelated to TGF- β 's cytostatic effects but which favor tumor invasion and metastasis.

By designing a functional TGF- β reporter system and coupling Cre activity to TGF- β signaling, we could monitor and compare the behaviors and fates of the subset of basal tumor SCs that activate T β RI/II-pSMAD2 signaling (or which we blocked from doing so) in developing tumors expressing HRas^{G12V}, commonly mutated in human skin cancers. Our lineage tracing analyses of the clonal growth of these cells revealed clearly that TGF- β 's cytostatic and tumor-promoting effects are not mutually exclusive. Rather, TGF- β -responding cells display morphological and biochemical features of invasiveness and malignant conversion during a period when they are in a slow-cycling proliferation state. Moreover, and most importantly, our findings show that these slow-cycling invasive tumor cells gain a marked advantage over hyperproliferative, more tightly clustered T β RII-null SCC-SCs in that they are better protected against DNA damaging agents such as cisplatin.

Cisplatin resistance is a hallmark of head and neck SCCs. Suggested mechanisms for resistance include reduced drug uptake, increased drug efflux, inactivation by GSH conjugation, increased DNA damage repair, and failure to induce apoptosis (Kelland, 2007). Another proposed route is the failure of anti-cancer therapies to target slower-cycling cancer SCs (Meacham and Morrison, 2013). Since our results show that TGF- β reporter⁺ skin tumor cells are indeed slower-cycling, it seemed plausible that at least in part, the enhanced protection against anti-proliferative cancer drugs might be attributable to the slower-cycling status of TGF- β -responding SCs. However as we learned, this was only the tip of the iceberg in what TGF- β responsiveness is able to achieve, and in fact slower-cycling status appears to be secondary to SCC-SC drug resistance.

Given that the alterations provoked by TGF- β in SCC-SCs extended beyond cycling rates, we asked whether additional changes in transcriptomes might explain the enhanced resistance of TGF- β -responding SCC-SCs to cisplatin. The TGF- β signature encompassed genes already known to play a key role in stemness. However, the signature also show-cased genes involved in glutathione metabolism. Delineating mechanism, TGF- β induced *Cdkn1a* transcription, leading to p21-mediated NRF2 stabilization and induction of a cohort of glutathione metabolism genes. Most importantly, when *Cdkn1a* or *Nfe2l2* were knocked down, SCC-SCs were still responsive to TGF- β and were still slower-cycling, but their survival in the face of cisplatin was normalized. Further bolstering the importance of this pathway, KD of *Keap1* in T β RII-null SCs resulted in not only enhanced NRF2 target gene activity but also enhanced survival in cisplatin treated SCCs.

The role of enhancing antioxidant reactions and glutathione metabolism is still obscure. Although inflammatory cells can have anti-tumorigenic roles, they can also release ROS, which is actively mutagenic, thereby accelerating the genetic evolution of nearby cancer SCs (Grivennikov et al., 2010). In the present study, we showed that even though immune cells concentrate near the vasculature, ROS levels are preferentially reduced in the subset of TGF- β -responding SCC-SCs, and that this is attributable to the TGF- β /p21/NRF2 pathway we delineated here.

In closing, since not all tumor-initiating cells localize to the perivascularity where TGF- β is concentrated, our studies show that this can be advantageous to the tumor. On the one hand, SCC-SCs that do not respond to TGF- β are faster-cycling and can greatly accelerate tumor growth and differentiation. On the other hand, TGF- β -responding SCC-SCs cycle more slowly but show enhanced invasiveness and increased glutathione metabolism, thereby increasing the likelihood not only of metastasis but also long-term survival in the face of ROS and anti-cancer drugs. Given that perivascularity is an emerging niche for many types of SCs, it will be interesting to see in the future if the mechanisms we've unearthed here will extend to other cancers. It will also be important to know whether these mechanisms are operative in human SCCs. In this regard, an analysis of the TCGA database revealed poor prognosis for patients with SCCs that upregulate this cohort of glutathione metabolism genes (Figure S6). Whether these tantalizing parallels between mouse and human SCCs will continue to hold must await future cancer databases on tumor-initiating cells as opposed to whole tumor samples. If so, these hitherto underappreciated roles for TGF- β signaling in tumor heterogeneity and anti-cancer resistance could serve as a foundation for designing chemotherapeutics that might overcome drug resistance for this devastating cancer.

EXPERIMENTAL PROCEDURES

In Vivo LV Transduction, Tumor Formation, and Drug Treatment

LV production, concentration, and ultrasound-guided in utero transduction were performed as described (Beronja et al., 2010). Briefly, female mice at day 9.5 of gestation were anesthetized with isoflurane (Hospira). In utero, 0.5 μ l LV was microinjected into each embryo's amniotic sac. To induce tumor formation, rTA3 was activated by feeding adult mice with Doxy (2 mg/kg) chow. Cre was activated by intraperitoneal (i.p.) injection of Tam (Sigma) in corn oil: TGF β -CreER, 25 μ g/g low-dose, 3 X 100 μ g/g high-dose; K14-CreER, 17.5 μ g/g. Cisplatin (Sigma) was dissolved in saline (1 mg/ml) and administered by i.p. injection (10 mg/kg). T β RI kinase inhibitor (LY364947, Tocris) was i.p. injected (1 mg/kg), 3X/wk. For limit-dilution transplantation and xenotransplantation, 1.0×10^3 – 10^5 mouse primary tumor cells and 1.0×10^5 human SCC cells were subcutaneously injected with Matrigel (BD) in *Nude* mice. Tumor size was calculated using the formula $4/3\pi \times L/2 \times W/2 \times D/2$. For cell proliferation analysis in vivo, BrdU (50 μ g/g) or EdU (25 μ g/g) was injected i.p. 4 or 12 hr before lethal administration of CO₂. All procedures were performed with IACUC-approved protocols.

In Vitro Cell Culture Experiments

Cells were cultured in E medium with 15% fetal bovine serum (FBS) and 50 μ M CaCl₂ (1⁰ MKs) or 1.5 mM CaCl₂ (human SCC lines) at 37°C, 7.5% CO₂. For stimulation experiments, media were supplemented with either recombinant mouse TGF- β 1 (100 pM = 2.5 ng/ml, R&D Systems), 4-hydroxytamoxifen (1 μ M, Sigma), cisplatin (20 μ M, Sigma), H₂O₂ (1–1,000 μ M, Fisher), or ethacrynic acid (50 μ M, Abcam). For colony formation assay, FACS-isolated 1.0×10^4 α 6^{hi}CD44⁺mCherry^{neg} and α 6^{hi}CD44⁺mCherry⁺ primary tumor basal cells were plated onto mitomycin-treated mouse 3T3 fibroblasts in 6-well dishes in E medium with 15% FBS and 300 μ M CaCl₂. Colony number was counted after 14 day culture.

Statistics

Data were analyzed and statistics performed (unpaired two-tailed Student's t test) in Prism5 (GraphPad). Significant differences between two groups were noted by asterisks or actual p values (*p < 0.05; **p < 0.01; ***p < 0.001). Quantification data were presented in mean value \pm SEM or in box and whisker plots with the dimensions of the box encompassing the 25th–75th percentile, the

horizontal bar representing the median, and the error bars representing minimum and maximum values.

ACCESSION NUMBERS

RNA-seq data have been submitted to NCBI-GEO under the accession number GSE64867.

SUPPLEMENTAL INFORMATION

Supplemental Information includes Extended Experimental Procedures, six figures, and five movies and can be found with this article online at <http://dx.doi.org/10.1016/j.cell.2015.01.043>.

ACKNOWLEDGMENTS

We thank B. Reva for helpful consultation regarding TCGA data analyses; S. Karlsson for floxed-*Tgfb2* mice; F. Costantini for *Rosa-YFP* mice; L. Chin for *TetO-Hras* mice; and L. Polak, J. LeVorse, and others for assistance in the mouse facility. We are grateful to extensive interactions and helpful discussions with former and present Fuchs lab members. We appreciate the assistance of RU's Comparative Bioscience Center (an AAALAC facility) for expert care and housing of our mice, the RU Flow Cytometry Resource Center (S. Mazel, Director) and Weill Cornell Medical College Genomics Resources Core Facility for Illumina sequencing (J. Xiang, Director). N.O. was supported by Human Frontier Science Program and the Japan Society for the Promotion of Science and is now supported by NIH K99-R00 pathway to independence award. E.F. is an investigator of the Howard Hughes Medical Institute. This work was supported by grants from the NIH and from the New York State Department of Health (NYSTEM-C029559) to E.F. and from the National Cancer Institute (K99-CA178197) to N.O.

Received: September 26, 2014

Revised: December 21, 2014

Accepted: January 13, 2015

Published: February 26, 2015

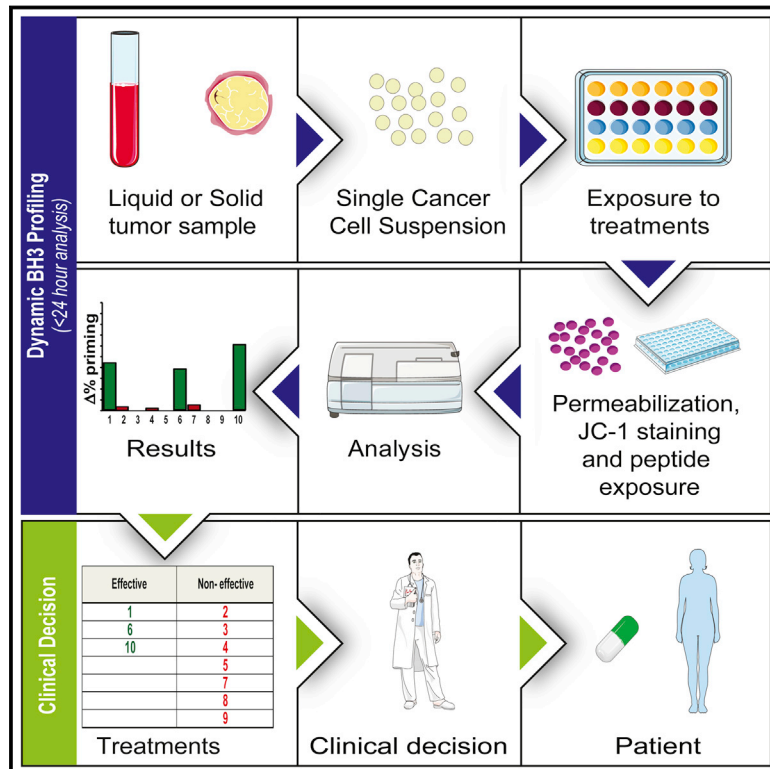
REFERENCES

- Beck, B., Driessens, G., Goossens, S., Youssef, K.K., Kuchnio, A., Caauwe, A., Sotiropoulou, P.A., Loges, S., Lapouge, G., Candi, A., et al. (2011). A vascular niche and a VEGF-Nrp1 loop regulate the initiation and stemness of skin tumours. *Nature* 478, 399–403.
- Berns, A. (2005). Stem cells for lung cancer? *Cell* 121, 811–813.
- Beronja, S., Livshits, G., Williams, S., and Fuchs, E. (2010). Rapid functional dissection of genetic networks via tissue-specific transduction and RNAi in mouse embryos. *Nat. Med.* 16, 821–827.
- Bigarella, C.L., Liang, R., and Ghaffari, S. (2014). Stem cells and the impact of ROS signaling. *Development* 141, 4206–4218.
- Boumahdi, S., Driessens, G., Lapouge, G., Rorive, S., Nassar, D., Le Mercier, M., Delatte, B., Caauwe, A., Lenglez, S., Nkusi, E., et al. (2014). SOX2 controls tumour initiation and cancer stem-cell functions in squamous-cell carcinoma. *Nature* 511, 246–250.
- Bruna, A., Darken, R.S., Rojo, F., Ocaña, A., Peñuelas, S., Arias, A., Paris, R., Tortosa, A., Mora, J., Baselga, J., and Seoane, J. (2007). High TGF β -Smad activity confers poor prognosis in glioma patients and promotes cell proliferation depending on the methylation of the PDGF-B gene. *Cancer Cell* 11, 147–160.
- Chen, C.R., Kang, Y., Siegel, P.M., and Massagué, J. (2002). E2F4/5 and p107 as Smad cofactors linking the TGF β receptor to c-myc repression. *Cell* 110, 19–32.
- Chen, W., Sun, Z., Wang, X.-J., Jiang, T., Huang, Z., Fang, D., and Zhang, D.D. (2009). Direct interaction between Nrf2 and p21(Cip1/WAF1) upregulates the Nrf2-mediated antioxidant response. *Mol. Cell* 34, 663–673.
- Chin, L., Tam, A., Pomerantz, J., Wong, M., Holash, J., Bardeesy, N., Shen, Q., O'Hagan, R., Pantginis, J., Zhou, H., et al. (1999). Essential role for oncogenic Ras in tumour maintenance. *Nature* 400, 468–472.
- Cui, W., Fowles, D.J., Bryson, S., Duffie, E., Ireland, H., Balmain, A., and Akhurst, R.J. (1996). TGF β 1 inhibits the formation of benign skin tumors, but enhances progression to invasive spindle carcinomas in transgenic mice. *Cell* 86, 531–542.
- Derynck, R., and Miyazono, K. (2008). The TGF- β family (Woodbury, New York: Cold Spring Harbor Laboratory Press).
- Diehn, M., Cho, R.W., Lobo, N.A., Kalisky, T., Dorie, M.J., Kulp, A.N., Qian, D., Lam, J.S., Ailles, L.E., Wong, M., et al. (2009). Association of reactive oxygen species levels and radioresistance in cancer stem cells. *Nature* 458, 780–783.
- Gomis, R.R., Alarcón, C., Nadal, C., Van Poznak, C., and Massagué, J. (2006). C/EBP β at the core of the TGF β cytostatic response and its evasion in metastatic breast cancer cells. *Cancer Cell* 10, 203–214.
- Gorrini, C., Harris, I.S., and Mak, T.W. (2013). Modulation of oxidative stress as an anticancer strategy. *Nat. Rev. Drug Discov.* 12, 931–947.
- Greaves, M., and Maley, C.C. (2012). Clonal evolution in cancer. *Nature* 481, 306–313.
- Grivennikov, S.I., Greten, F.R., and Karin, M. (2010). Immunity, inflammation, and cancer. *Cell* 140, 883–899.
- Grotendorst, G.R., Smale, G., and Pencev, D. (1989). Production of transforming growth factor β by human peripheral blood monocytes and neutrophils. *J. Cell. Physiol.* 140, 396–402.
- Guasch, G., Schober, M., Pasolli, H.A., Conn, E.B., Polak, L., and Fuchs, E. (2007). Loss of TGF β signaling destabilizes homeostasis and promotes squamous cell carcinomas in stratified epithelia. *Cancer Cell* 12, 313–327.
- Hanahan, D., and Weinberg, R.A. (2011). Hallmarks of cancer: the next generation. *Cell* 144, 646–674.
- Hope, K.J., Jin, L., and Dick, J.E. (2004). Acute myeloid leukemia originates from a hierarchy of leukemic stem cell classes that differ in self-renewal capacity. *Nat. Immunol.* 5, 738–743.
- Ijichi, H., Chytil, A., Gorska, A.E., Aakre, M.E., Fujitani, Y., Fujitani, S., Wright, C.V.E., and Moses, H.L. (2006). Aggressive pancreatic ductal adenocarcinoma in mice caused by pancreas-specific blockade of transforming growth factor- β signaling in cooperation with active Kras expression. *Genes Dev.* 20, 3147–3160.
- Kelland, L. (2007). The resurgence of platinum-based cancer chemotherapy. *Nat. Rev. Cancer* 7, 573–584.
- Koinuma, D., Tsutsumi, S., Kamimura, N., Taniguchi, H., Miyazawa, K., Sunamura, M., Imamura, T., Miyazono, K., and Aburatani, H. (2009). Chromatin immunoprecipitation on microarray analysis of Smad2/3 binding sites reveals roles of ETS1 and TFAP2A in transforming growth factor β signaling. *Mol. Cell. Biol.* 29, 172–186.
- Kreso, A., and Dick, J.E. (2014). Evolution of the cancer stem cell model. *Cell Stem Cell* 14, 275–291.
- Lapouge, G., Beck, B., Nassar, D., Dubois, C., Dekoninck, S., and Blanpain, C. (2012). Skin squamous cell carcinoma propagating cells increase with tumour progression and invasiveness. *EMBO J.* 31, 4563–4575.
- Lu, S.-L., Herrington, H., Reh, D., Weber, S., Bornstein, S., Wang, D., Li, A.G., Tang, C.-F., Siddiqui, Y., Nord, J., et al. (2006). Loss of transforming growth factor- β type II receptor promotes metastatic head-and-neck squamous cell carcinoma. *Genes Dev.* 20, 1331–1342.
- Lushchak, V.I. (2012). Glutathione homeostasis and functions: potential targets for medical interventions. *J. Amino Acids* 2012, 736837.
- Malanchi, I., Peinado, H., Kassen, D., Hussenet, T., Metzger, D., Chambon, P., Huber, M., Hohl, D., Cano, A., Birchmeier, W., and Huelsken, J. (2008). Cutaneous cancer stem cell maintenance is dependent on β -catenin signalling. *Nature* 452, 650–653.
- Massagué, J. (2012). TGF β signalling in context. *Nat. Rev. Mol. Cell Biol.* 13, 616–630.

- Massagué, J., Seoane, J., and Wotton, D. (2005). Smad transcription factors. *Genes Dev.* 19, 2783–2810.
- Meacham, C.E., and Morrison, S.J. (2013). Tumour heterogeneity and cancer cell plasticity. *Nature* 501, 328–337.
- Mullen, A.C., Orlando, D.A., Newman, J.J., Lovén, J., Kumar, R.M., Bilodeau, S., Reddy, J., Guenther, M.G., DeKoter, R.P., and Young, R.A. (2011). Master transcription factors determine cell-type-specific responses to TGF- β signaling. *Cell* 147, 565–576.
- Muñoz, N.M., Upton, M., Rojas, A., Washington, M.K., Lin, L., Chytil, A., Sozmen, E.G., Madison, B.B., Pozzi, A., Moon, R.T., et al. (2006). Transforming growth factor β receptor type II inactivation induces the malignant transformation of intestinal neoplasms initiated by Apc mutation. *Cancer Res.* 66, 9837–9844.
- Nischt, R., Roop, D.R., Mehrel, T., Yuspa, S.H., Rentrop, M., Winter, H., and Schweizer, J. (1988). Aberrant expression during two-stage mouse skin carcinogenesis of a type I 47-kDa keratin, K13, normally associated with terminal differentiation of internal stratified epithelia. *Mol. Carcinog.* 1, 96–108.
- Notta, F., Doulatov, S., Laurenti, E., Poepl, A., Jurisica, I., and Dick, J.E. (2011). Isolation of single human hematopoietic stem cells capable of long-term multilineage engraftment. *Science* 333, 218–221.
- Oshimori, N., and Fuchs, E. (2012a). The harmonies played by TGF- β in stem cell biology. *Cell Stem Cell* 11, 751–764.
- Oshimori, N., and Fuchs, E. (2012b). Paracrine TGF- β signaling counterbalances BMP-mediated repression in hair follicle stem cell activation. *Cell Stem Cell* 10, 63–75.
- Schober, M., and Fuchs, E. (2011). Tumor-initiating stem cells of squamous cell carcinomas and their control by TGF- β and integrin/focal adhesion kinase (FAK) signaling. *Proc. Natl. Acad. Sci. USA* 108, 10544–10549.
- Seoane, J., Le, H.-V., Shen, L., Anderson, S.A., and Massagué, J. (2004). Integration of Smad and forkhead pathways in the control of neuroepithelial and glioblastoma cell proliferation. *Cell* 117, 211–223.
- Siegle, J.M., Basin, A., Sastre-Perona, A., Yonekubo, Y., Brown, J., Sennett, R., Rendl, M., Tsigos, A., Carucci, J.A., and Schober, M. (2014). SOX2 is a cancer-specific regulator of tumour initiating potential in cutaneous squamous cell carcinoma. *Nat. Commun.* 5, 4511.
- Thuault, S., Valcourt, U., Petersen, M., Manfioletti, G., Heldin, C.-H., and Moustakas, A. (2006). Transforming growth factor- β employs HMG2 to elicit epithelial-mesenchymal transition. *J. Cell Biol.* 174, 175–183.
- Visvader, J.E., and Stingl, J. (2014). Mammary stem cells and the differentiation hierarchy: current status and perspectives. *Genes Dev.* 28, 1143–1158.
- Yamashiro, Y., Takei, K., Umikawa, M., Asato, T., Oshiro, M., Uechi, Y., Ishikawa, T., Taira, K., Uezato, H., and Kariya, K. (2010). Ectopic coexpression of keratin 8 and 18 promotes invasion of transformed keratinocytes and is induced in patients with cutaneous squamous cell carcinoma. *Biochem. Biophys. Res. Commun.* 399, 365–372.

Drug-Induced Death Signaling Strategy Rapidly Predicts Cancer Response to Chemotherapy

Graphical Abstract



Authors

Joan Montero, Kristopher A. Sarosiek, ..., Ronny Drapkin, Anthony Letai

Correspondence

anthony_letai@dfci.harvard.edu

In Brief

Dynamic BH3 Profiling takes a functional approach to precision medicine in cancer by measuring early changes in death signaling in tumor cells induced by drugs. These changes predict tumor cell killing in vitro, in vivo, and in the clinic.

Highlights

- Early death signaling predicts cytotoxicity days before cell death occurs
- Dynamic BH3 Profiling (DBP) is a functional measure of death signaling
- DBP predicts response to targeted agents in vitro and in vivo
- DBP is a potential tool for personalizing cancer therapy



Drug-Induced Death Signaling Strategy Rapidly Predicts Cancer Response to Chemotherapy

Joan Montero,¹ Kristopher A. Sarosiek,¹ Joseph D. DeAngelo,¹ Ophélie Maertens,³ Jeremy Ryan,¹ Dalia Ercan,¹ Huiying Piao,¹ Neil S. Horowitz,^{1,3} Ross S. Berkowitz,^{1,3} Ursula Matulonis,¹ Pasi A. Jänne,^{1,3} Philip C. Amrein,² Karen Cichowski,³ Ronny Drapkin,^{1,3} and Anthony Letai^{1,*}

¹Dana-Farber Cancer Institute, Harvard Medical School, Boston, MA 02215, USA

²Hematology/Oncology Department of Medicine, Massachusetts General Hospital, Boston, MA 02114, USA

³Brigham and Women's Hospital, Harvard Medical School, Boston, MA 02115, USA

*Correspondence: anthony_letai@dfci.harvard.edu

<http://dx.doi.org/10.1016/j.cell.2015.01.042>

SUMMARY

There is a lack of effective predictive biomarkers to precisely assign optimal therapy to cancer patients. While most efforts are directed at inferring drug response phenotype based on genotype, there is very focused and useful phenotypic information to be gained from directly perturbing the patient's living cancer cell with the drug(s) in question. To satisfy this unmet need, we developed the Dynamic BH3 Profiling technique to measure early changes in net pro-apoptotic signaling at the mitochondrion ("priming") induced by chemotherapeutic agents in cancer cells, not requiring prolonged ex vivo culture. We find in cell line and clinical experiments that early drug-induced death signaling measured by Dynamic BH3 Profiling predicts chemotherapy response across many cancer types and many agents, including combinations of chemotherapies. We propose that Dynamic BH3 Profiling can be used as a broadly applicable predictive biomarker to predict cytotoxic response of cancers to chemotherapeutics in vivo.

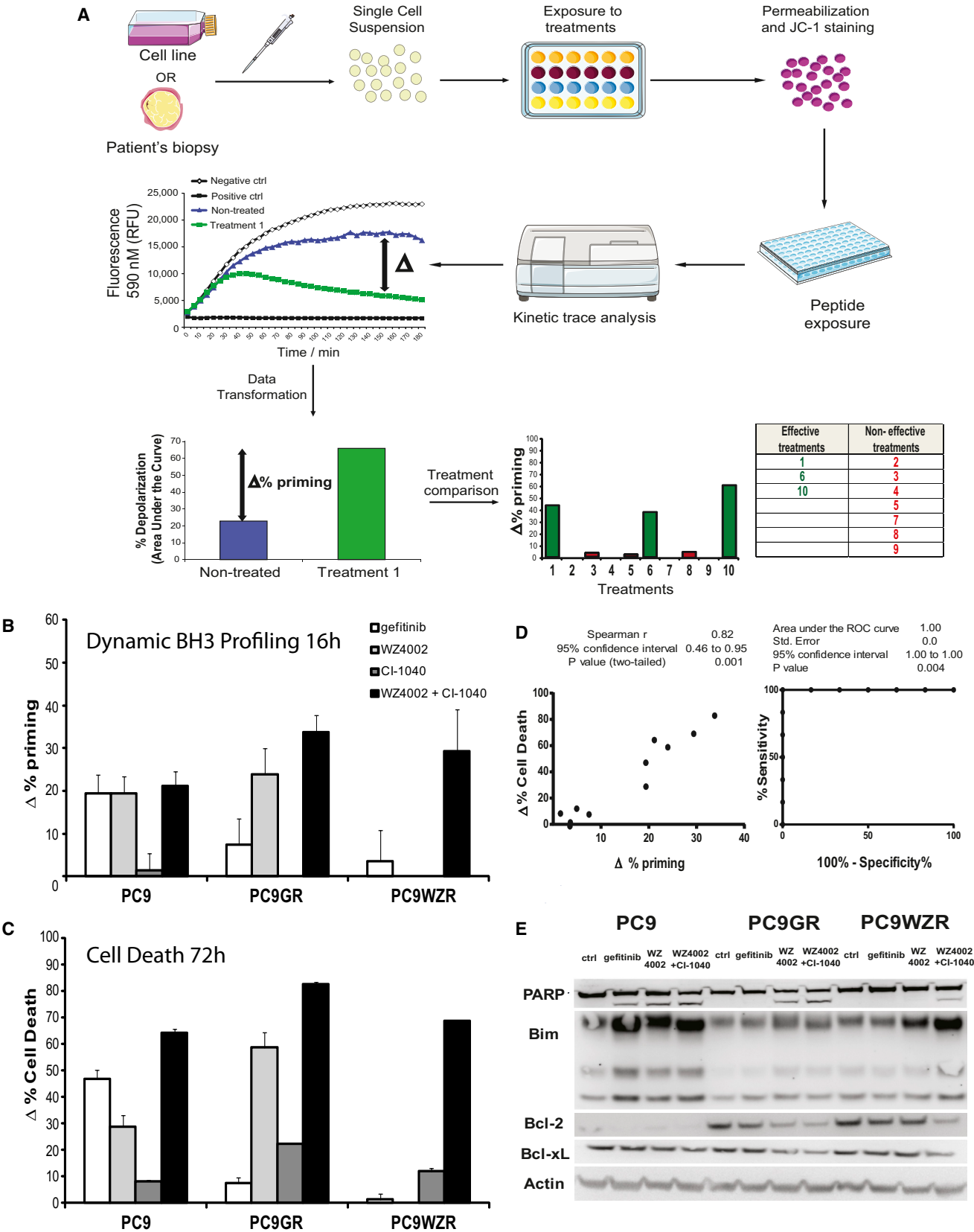
INTRODUCTION

A fundamental challenge across medicine is to assign to a patient the drug or combination of drugs that will be of greatest benefit. In oncology, this choice has historically been driven by the anatomic location and histology of the tumor. Later, therapeutic decision-making was assisted by immunohistochemistry, cytogenetics, and flow cytometric analysis of cell surface antigens. In more recent years, there are examples where gene expression signatures and specific genetic alterations have been essential to therapeutic decisions (Chapman et al., 2011; Paez et al., 2004). However, true personalization of therapy remains an elusive goal in most cases. In all too many cases, cancer patients show little benefit from therapy. Moreover, it is likely that many tumors have unrecognized sensitivity to agents for which there is simply no useful predictive biomarker to inform therapy decisions (Garraway and Jänne, 2012; Haibe-Kains et al., 2013). In this era of growing therapeutic options, there is

a comparable growing need for predictive biomarkers (Sawyers, 2008; Yaffe, 2013).

A feature common to nearly all of the biomarkers in use or in development in oncology is that they are studies performed on dead cancer cells. They are attempts to predict cancer cell behavior based on detailed analysis of components of the cell, such as DNA, RNA, or proteins (Barretina et al., 2012). In some cases, abnormalities in single genes are studied. There are spectacular examples of success with this approach, such as the use of *EGFR* mutations to guide treatment with *EGFR* inhibitors in lung cancer (Paez et al., 2004), *BRAF* mutations to guide treatment with vemurafenib in melanoma (Chapman et al., 2011), or *CKIT* mutations to guide treatment with imatinib in GIST (Joensuu et al., 2001). However, most drugs in development or approved for cancer lack a simple genetic predictor, which impedes their clinical development (Sikorski and Yao, 2010). One popular approach to this problem is to identify signatures based on huge amounts of information based on genomes, transcriptomes, or proteomes (Barretina et al., 2012; Garraway and Jänne, 2012). These strategies are relatively early in development and their power remains to be seen. Despite the abundance of information these strategies provide, they still share a weakness: they are all studies of dead cancer cells. They lack a measure of cancer cell function or response to perturbation. Studies of complex systems in and out of biology are often greatly augmented by observations of responses to strategic perturbations. Here, we present results of strategic perturbations of cancer cells with drugs and their mitochondria with peptides in a strategy we call Dynamic BH3 Profiling (DBP).

DBP interrogates the BCL-2 family of proteins that regulates commitment to the mitochondrial pathway of apoptosis, the program of cell death that is commonly used by cancer cells in response to most chemotherapeutic agents. The BCL-2 family of proteins controls mitochondrial outer membrane permeabilization (MOMP) (Certo et al., 2006; Chipuk et al., 2010). The effector proteins BAX and BAK, when activated, oligomerize to form pores in the mitochondrial outer membrane that induce release of cytochrome c and the loss of mitochondrial transmembrane potential, as well as release of SMAC/DIABLO and other proteins that trigger apoptosome formation, caspase activation, and finally apoptosis (Kluck et al., 1997; Wei et al., 2001). These effector proteins can be activated by the BH3-only proteins BIM and BID (and perhaps PUMA), also known as



(legend on next page)

activators (Sarosiek et al., 2013). Both effectors and activators can be inhibited by the anti-apoptotic members of the family, including BCL-2, BCL-X_L, MCL-1 and others (Certo et al., 2006). There is a fourth group of proteins, called sensitizers (comprising proteins like BAD, BMF, NOXA, HRK, and others) that by themselves are not able to induce BAX and BAK oligomerization but instead selectively inhibit the anti-apoptotic members of the family, thus indirectly promoting MOMP (Letai et al., 2002). The BH3 domain is a roughly 20-amino acid amphipathic alpha helix that is necessary for most of the hetero-dimeric interactions of BCL-2 family proteins that regulate apoptosis. Synthetic BH3 domain oligopeptides can execute most of the pro-apoptotic functions of pro-apoptotic BCL-2 family proteins (Certo et al., 2006).

BH3 peptides are thus a convenient, titratable reagent that can be exploited to systematically study mitochondrial readiness to undergo apoptosis. This understanding of the BCL-2 family of proteins and their interactions allowed the development of the BH3 profiling technique (Ryan et al., 2010) that identifies cancer cells' selective dependence on anti-apoptotic proteins, and also measures overall apoptotic sensitivity or "priming for death" (Deng et al., 2007a). "Priming" is a measure of how close a cell is to the threshold of apoptosis. Procedurally, priming corresponds to the sensitivity of mitochondria to BH3 peptides. The more sensitive mitochondria are to BH3 peptides, the more primed they are. We have previously found that the state of "priming" prior to therapy was an excellent predictor of chemotherapeutic response in vivo (Ni Chonghaile et al., 2011; Vo et al., 2012). Differences in priming between cancer cells and normal tissues also provide an explanation for the therapeutic index of conventional chemotherapeutic drugs that target ubiquitous elements such as DNA and microtubules.

The main principle of DBP is to expose cancer cells to short incubations with drugs of interest and measure whether the drug exposure induces an increase in priming compared to an untreated control. In this paper we use DBP to test the hypothesis that early death signaling predicts cytotoxicity, even when the cell death does not occur until days after the death signaling is measured. Our results support the model that initiation of death signaling is the main regulator of eventual commitment to cell death. Moreover, we show that we can perform these measurements on primary patient cancer cells in a way that predicts clinical response to therapy.

RESULTS

DBP Predicts Chemotherapy Sensitivity in Non-Small Cell Lung Cancer Cell Lines

Our strategy rests upon the hypothesis that it is the *initiation* of death signaling that distinguishes cells destined to be killed by an agent from those destined to survive.

We therefore rigorously tested the hypothesis that measurement of early death signaling by DBP (Figure 1A) could predict a cytotoxic response that did not occur until several days later. We first used non-small cell lung cancer (NSCLC) cell lines derived from PC9. This cell line has an exon 19 deletion in the *EGFR* gene rendering it sensitive to EGFR-specific tyrosine kinase inhibitors (TKI) like erlotinib or gefitinib. PC9GR was obtained by continuously exposing PC9 to increasing concentrations of gefitinib (Ercan et al., 2010), selecting for a T790M mutation in EGFR that renders it non-sensitive to gefitinib but still sensitive to the mutant selective EGFR TKI WZ4002 (Zhou et al., 2009). A third cell line, PC9WZR, was similarly selected for resistance to WZ4002. It possesses an EGFR T790M mutation and a *MAPK1* amplification conferring resistance to both gefitinib and WZ4002. However, PC9WZR is sensitive to the combination of WZ4002 with the MEK inhibitor CI-1040, by completely blocking the MAPK pathway (Ercan et al., 2012). This set of cell lines provided a useful initial model of differential sensitivity to targeted therapies upon which to test our strategy.

We performed DBP on each of the cell lines using a 16 hr treatment with gefitinib, WZ4002, CI-1040 or the combination WZ4002 plus CI-1040. Sixteen hours was chosen after empirically testing 4, 8, 16, 24, and 48 hr as it was the earliest time point that reliably provided a significant change in priming in PC9 cells treated with gefitinib. After testing several BH3 peptides, including BIM, HRK, and PUMA BH3, we found that BIM BH3 concentrations of 0.3 and 1 μ M provided the most useful dynamic range (Figure 1 and Figure S1). Drug concentrations were chosen based on our and others' prior experience and the dose required for a complete blockade of the MAPK pathway (Ercan et al., 2012; Ercan et al., 2010). We observed an increase in priming induced in PC9 by gefitinib, WZ4002 and WZ4002 + CI-1040, as shown by the increase in BIM BH3-induced mitochondrial depolarization ($\Delta\%$ priming). In PC9GR cells, WZ4002, but not gefitinib, increased priming. In PC9WZR cells, only the WZ4002 + CI-1040 increased mitochondrial priming

Figure 1. DBP Predicts Chemotherapy Sensitivity in PC9 Cell Lines

(A) To perform DBP we obtain a single cell suspension from a cell line or a primary sample, and we expose the cells to the different drug treatments to be tested. After this incubation, we permeabilize, stain with the fluorescent dye JC-1 and expose the cells to different BH3 peptides that will promote mitochondrial depolarization and MOMP, the ultimate event that triggers apoptosis. By comparing the non-treated cells with the treated ones, DBP will determine the $\Delta\%$ priming for each agent and identify which are most effective to induce apoptosis in that particular sample. All this analysis is performed in less than 24 hr, minimizing ex vivo culture.

(B) DBP was performed on three different PC9 cell lines: parental PC9, PC9GR (gefitinib resistant, T790M mutation present), and PC9WZR (gefitinib and WZ4002 resistant, T790M mutation present), using a 16 hr incubation of: gefitinib 1 μ M, WZ4002 100 nM, CI-1040 3 μ M (MEK inhibitor), and WZ4002+CI-1040. Results expressed as $\Delta\%$ priming (increase in priming compared to non-treated cells). Values indicate mean values \pm SEM, at least three independent experiments were performed ($n \geq 3$).

(C) Cell death measurements at 72 hr for the same cell lines under the same treatments by FACS using Annexin V/PI staining. Results are expressed as increase on cell death or $\Delta\%$ cell death, compared to non-treated cells. Values indicate mean values \pm SEM, at least three independent experiments were performed ($n \geq 3$).

(D) Plot showing correlation between $\Delta\%$ priming at 16 hr and $\Delta\%$ cell death at 72 hr. ROC curve analysis at right.

(E) Western blot analysis, showing changes in the BCL-2 family of proteins. See also Figures S1, S2 and S3.

(Figure 1B). We next measured cell death at 72 hr for the same cell lines following the same treatments using FACS analysis of Annexin V and propidium iodide (PI) staining (Figure 1C). When we compared $\Delta\%$ priming and $\Delta\%$ cell death, we observed an excellent correlation between both measurements (Figure 1D, left). The receiver operating characteristic (ROC) was also excellent, performing perfectly in this small number of tests (Figure 1D, right). Note that DBP was performed at 16 hr when no significant cell death was evident, whereas cell death was analyzed more than 2 days later (Figure S2). Thus, the early priming increase measured by DBP provided accurate, drug-specific predictions about cytotoxicity even though the death took place days later.

DBP should only be predictive if the mitochondrial apoptosis pathway is being engaged. To confirm this engagement, we analyzed PARP cleavage, as well as levels of BIM, BCL-2, and BCL-XL proteins following 24 hr of drug treatment. When cytotoxicity was observed, PARP cleavage was detected. In addition, cytotoxicity correlated with either increases in BIM, decreases in anti-apoptotic proteins, or a combination of both effects, supporting the simultaneous participation of multiple BCL-2 family proteins in the determination of cell fate (Deng et al., 2007b; Faber et al., 2011) (Figure 1E).

In order to determine if this predictive capacity of DBP could be generalized to other NSCLC models, we treated six different NSCLC cell lines with gefitinib, WZ4002, AZD6244 (MEK inhibitor), BEZ235 (PI3K/mTOR inhibitor), and the combination AZD6244 + BEZ235, that was previously described to treat murine lung cancers harboring the *KRas* G12D mutation (Engelman et al., 2008; Faber et al., 2009). We chose drug concentrations that had previously demonstrated in vitro cytotoxicity. Again, we compared the priming increase measured by DBP after 16 hr of treatment with cell death observed at 72 hr (Figure S3A). Some of the cell lines analyzed had a tendency to show less cytotoxicity than would be expected by DBP for a few drugs. It is possible that measurement of cell death at longer time points would reduce such disagreements. Nonetheless, we observed a significant correlation between $\Delta\%$ priming and $\Delta\%$ cell death when all cell lines and treatments were considered (Figure S3B). To assess if DBP provided a useful binary predictor of cytotoxicity, we performed ROC curve analysis (Pencina et al., 2008). Typically, a random classifier would present an AUC of 0.5, while a perfect classifier would have a AUC of 1. In this case, the area under the ROC curve is 0.895 (Figure S3C), comparing favorably with the ROC performance of many clinically used predictors (Burstein et al., 2011).

Note that this analysis relies not simply on measurements of the baseline priming but rather on the degree to which drugs increase priming from that baseline.

DBP Predicts Cytotoxicity in Breast Cancer Cells

To test the generalizability of our hypothesis in a different type of cancer, we performed a similar set of experiments with five different human breast cancer cell lines treated with gefitinib, lapatinib (HER2 inhibitor), MK-2206 (AKT inhibitor), AZD6244 (MEK inhibitor), BEZ235 (PI3K/mTOR inhibitor), dinaciclib (SCH 727965, CDK inhibitor), ABT-888 (PARP inhibitor), and the combination AZD6244 + BEZ235, as previously described (Faber et al., 2009). Again we observed a significant correlation between

$\Delta\%$ priming after 16 hr of treatment and $\Delta\%$ cell death at 96 hr (Figures 2A and 2B). The area under the ROC curve for this set of cell lines is 0.93 (Figure 2C), thus objectively DBP is an excellent binary predictor for breast cancer cell lines' response to chemotherapy.

Selecting the Optimal Kinase Inhibitor Using Dynamic BH3 Profiling

In clinical practice, an important application of a potentially powerful, widely applicable predictive biomarker would be to choose from among a panel of possible therapies (Sawyers, 2008). This is the central goal of what is currently commonly termed "precision medicine." We hypothesized that if we could compare the death signaling induced by several different agents in a cancer cell, we could pick the ones that would work best. To test this principle, we selected ten different cancer cell lines, chosen simply by variety and availability. For drugs, we chose nine kinase inhibitors, for their diversity of targets and known in vivo activity. We chose kinase inhibitors because of their known use of the mitochondrial apoptotic pathway to kill cancer cells (Bhatt et al., 2010; Faber et al., 2011). Our question was, among these diverse cell lines and drugs, could DBP at an early time point be used to make individualized choices of the drugs most likely to kill each cancer cell line.

For this purpose we selected drugs targeting either key membrane receptor tyrosine kinases like gefitinib (EGFR inhibitor), imatinib (ABL inhibitor), lapatinib (HER2 inhibitor), PD173074 (FGFR inhibitor), and TAE684 (ALK inhibitor) or important intracellular serine/threonine kinases including MK-2206 (AKT inhibitor), PLX4032 (*BRAF*^{V600E} inhibitor), AZD6244 (MEK inhibitor), and BEZ235 (PI3K/mTOR inhibitor). All of the compounds tested previously demonstrated cytotoxicity in cancer cell lines and/or murine cancer models, including hematological malignancies (Bhatt et al., 2010) and solid tumors (Maertens et al., 2013). We tested the panel of kinase inhibitors on several human hematological cancer cell lines: K562 (chronic myelogenous leukemia or CML), DHL6 (diffuse large B-cell lymphoma), LP1 (multiple myeloma), DHL4 (diffuse large B-cell lymphoma) and AML3 (acute myelogenous leukemia). First, we performed DBP after 16 hr exposure to the different treatments (Figure 3A). We compared the DBP results to cell death achieved at 72 hr, expressed as $\Delta\%$ cell death (Figure 3A). Each cell line demonstrated a distinct pattern of drug induced priming increase, a distinct fingerprint of pathway addiction just as there was a distinct pattern of cytotoxic response to the drug panel. Most importantly for our question, however, there was an excellent correlation of DBP with cytotoxicity days later (Figure 3B). For this set of hematological cell lines, predictive power of DBP was demonstrated by an AUC of the ROC curve of 0.83 (Figure 3C). Note that DBP identified the agent causing greatest cytotoxicity in four out of five cell lines. In the one exception, LP-1, there was little cytotoxicity induced by any of the drugs.

We next examined the predictive capacity of DBP with several diverse human solid tumor cell lines: MCF7 (breast cancer), PC9 (non-small cell lung cancer), SK-MEL-5 (melanoma), HCT116 (colon carcinoma) and MDA-MB-231 (breast cancer). We exposed the cells to the different treatments for 16 hr and performed DBP (Figure 4A), comparing it with the cell death

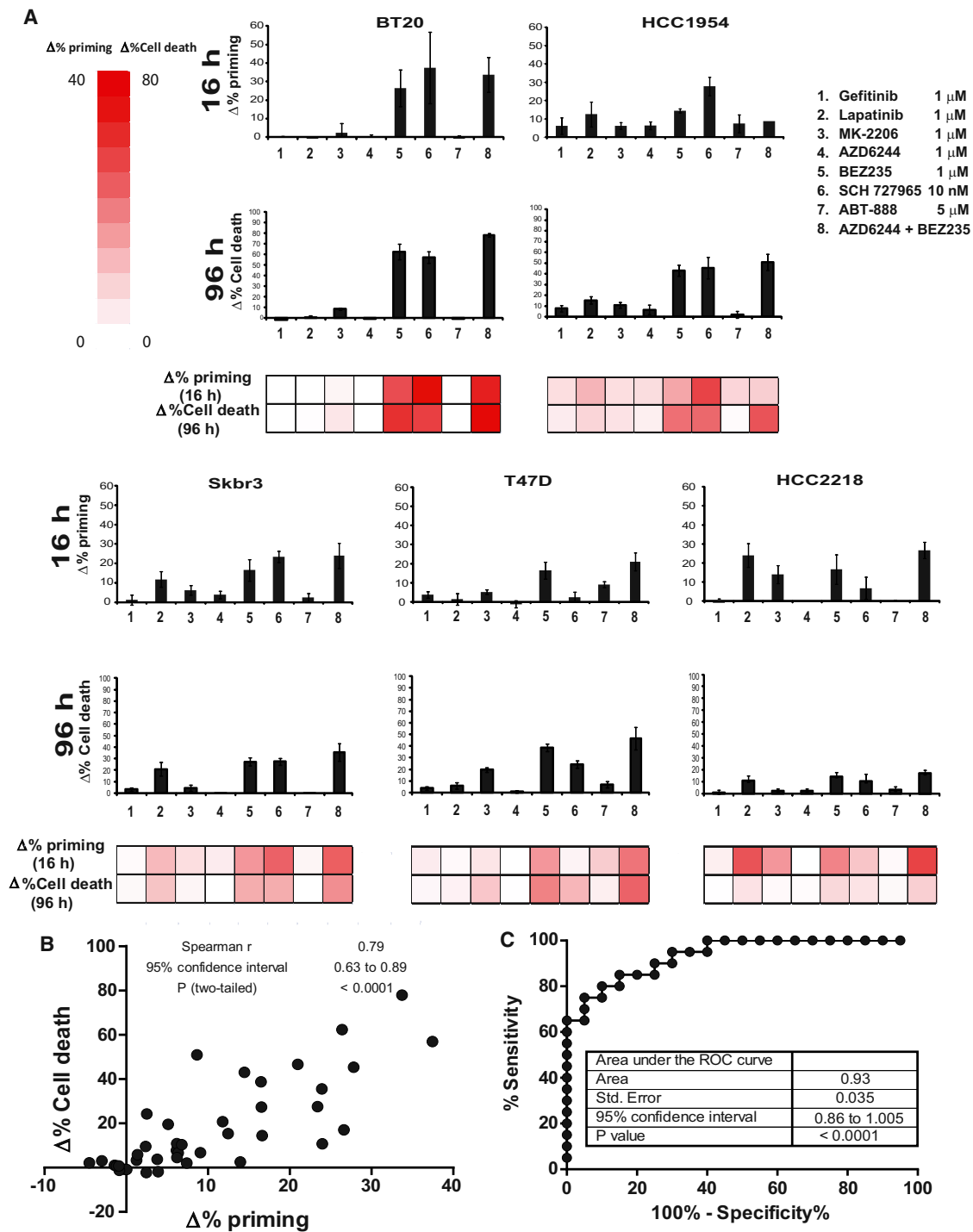


Figure 2. DBP Predicts Chemotherapy Sensitivity in Breast Cancer Cell Lines

(A) DBP was performed in five breast cancer cell lines: BT20, HCC1954, SKBR3, T47D, and HCC2218 showing different pattern of response to the treatments tested (16 hr incubation): (1) gefitinib 1 μ M, (2) lapatinib 1 μ M, (3) MK-2206 1 μ M, (4) AZD6244 1 μ M, (5) BEZ235 1 μ M, (6) dinaciclib 10 nM (SCH 727965), (7) ABT-888 5 μ M and the combination (8) AZD6244 + BEZ235. Results expressed as $\Delta\%$ priming (increase in priming compared to non-treated cells). Values indicate mean values \pm SEM, at least three independent experiments were performed ($n \geq 3$). Cell death measurements at 96 hr for the same cell lines under the same treatments by FACS using Annexin V/PI staining. Results are expressed as increase on cell death or $\Delta\%$ cell death, compared to non-treated cells. Values indicate mean values \pm SEM, at least three independent experiments were performed ($n \geq 3$).

(B) Plot showing the significant correlation between $\Delta\%$ priming at 16 hr and $\Delta\%$ cell death at 96 hr.

(C) ROC curve analysis.

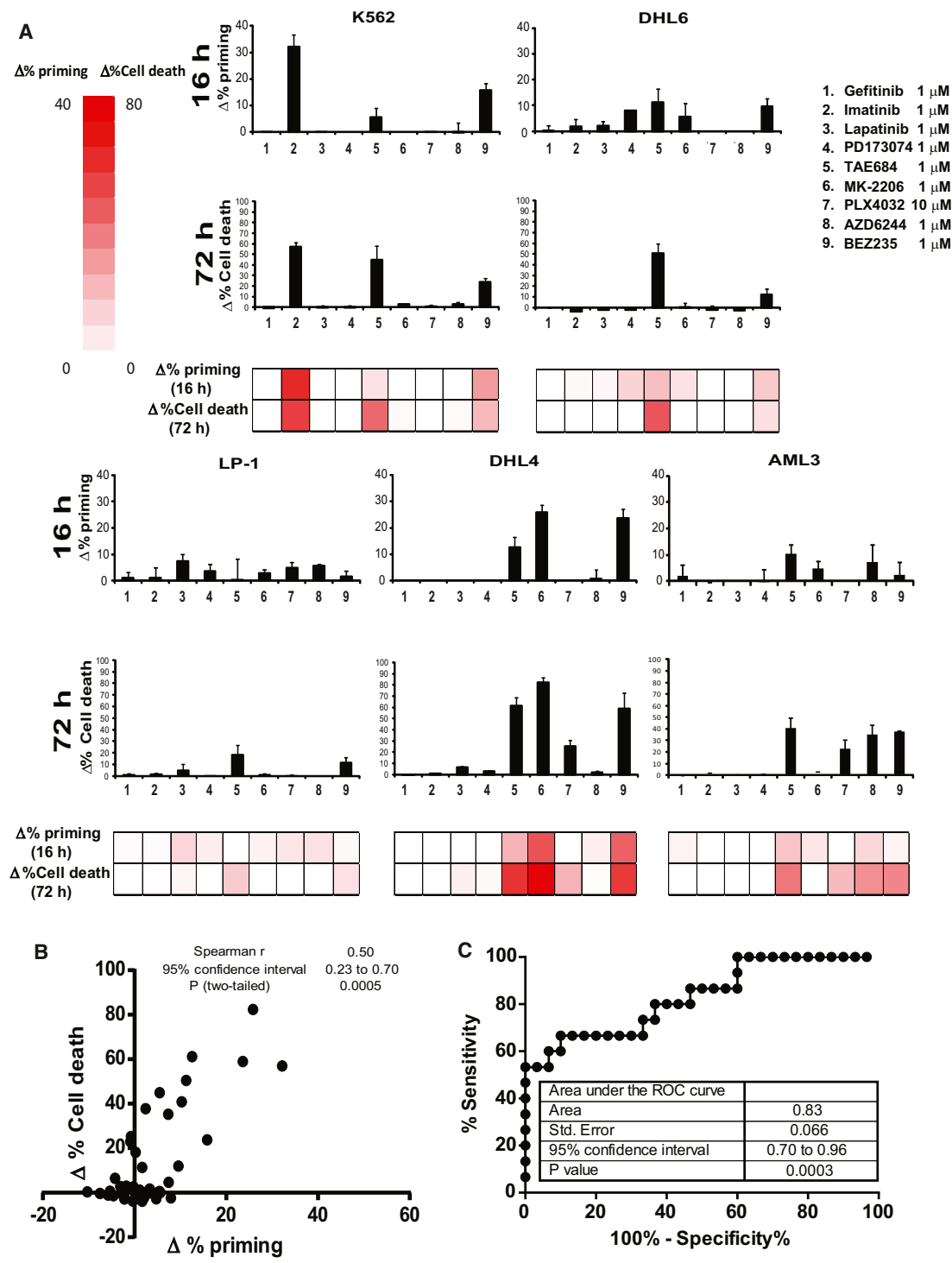


Figure 3. Identifying the Optimal Treatment in Hematological Malignancies Using DBP

We selected several drugs targeting either key membrane receptors: (1) gefitinib 1 μ M, (2) imatinib 1 μ M, (3) lapatinib 1 μ M, (4) PD173074 1 μ M and (5) TAE684 1 μ M; or important intracellular kinases: (6) MK-2206 1 μ M, (7) PLX4032 10 μ M, (8) AZD6244 1 μ M and (9) BEZ235 1 μ M, and we tested them with several human hematological cancer cell lines: K562, DHL6, LP1, DHL4, and AML3.

(A) DBP (16 hr incubation) results expressed as $\Delta\%$ priming and cell death measurements at 72 hr using Annexin V/PI staining expressed as $\Delta\%$ cell death. Values indicate mean values \pm SEM, at least three independent experiments were performed ($n \geq 3$).

(B) Plot showing the significant correlation between $\Delta\%$ priming at 16 hr and $\Delta\%$ cell death at 72 hr.

(C) ROC curve analysis shows AUC = 0.83.

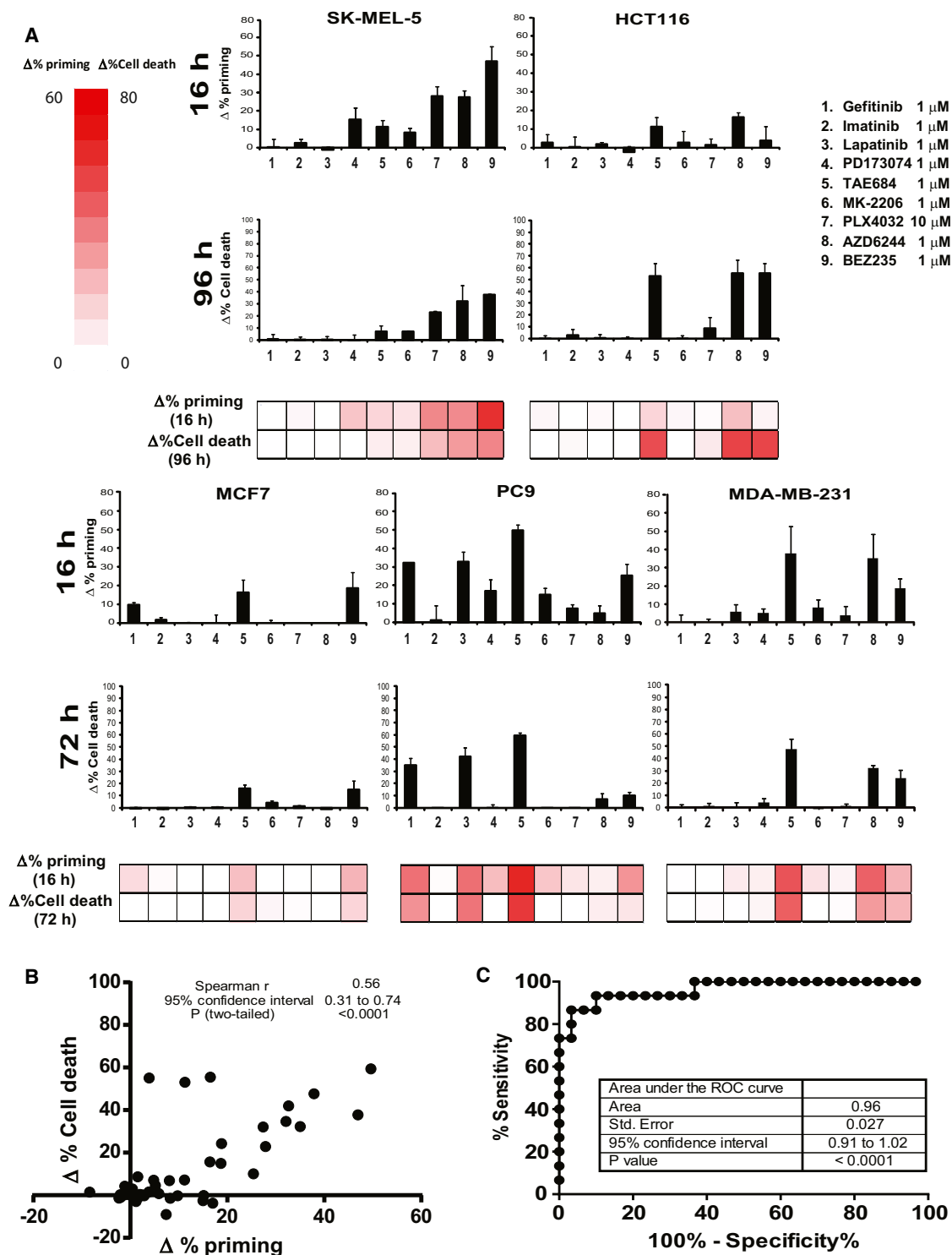


Figure 4. Identifying the Optimal Treatment in Solid Tumors Using DBP

We tested the same panel of kinase inhibitors on several human solid tumor cell lines: MCF7, PC9, SK-MEL-5, HCT116 and MDA-MB-231.

(A) DBP (16 hr incubation) results expressed as Δ% priming and cell death measurements at 72 or 96 hr (as indicated) using Annexin V/PI staining expressed as Δ% cell death. Values indicate mean values ± SEM, at least three independent experiments were performed (n ≥ 3).

(B) Plot showing the significant correlation between Δ% priming at 16 hr and Δ% cell death at 72/96 hr.

(C) The ROC curve analysis has an AUC = 0.96, indicating that DBP is an excellent binary predictor for chemotherapy response in solid tumor cell lines. See also Figure S4.

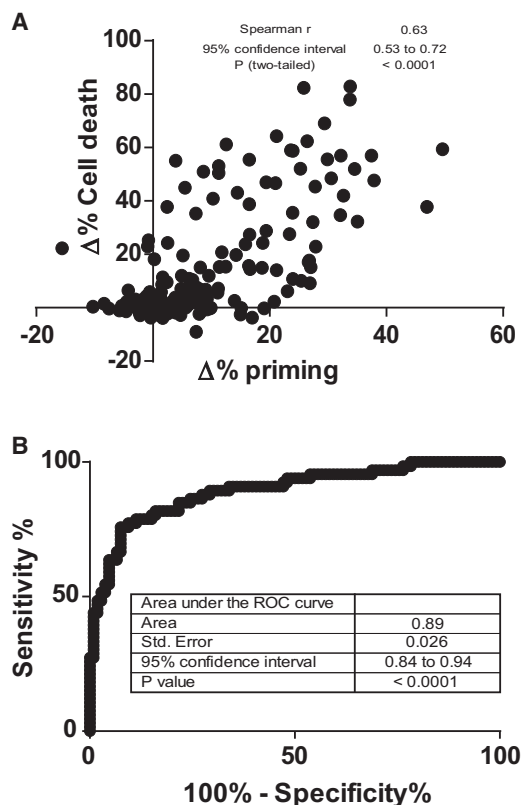


Figure 5. DBP Is a Good Binary Predictor for Cell Lines

(A) Compilation of Figures 1, 2, 3, 4 and S3 results, showing a significant correlation between $\Delta\%$ priming and $\Delta\%$ cell death for all cell lines analyzed. (B) The total area under the ROC curve is 0.89, indicating that is a good binary predictor for chemotherapy response in all the cell lines and treatments tested.

observed at 72–96 hr (Figure 4A). In some cases, a 96 hr time point was required due to slow kinetics of cytotoxicity. Similarly, as observed for hematological malignancies, the different cell lines responded differently to the drugs tested, but a significant correlation between DBP and cytotoxicity was detected (Figure 4B). SK-MEL-5 was the only one sensitive to PLX4032, as expected for a BRAF^{V600E} expressing melanoma cell line, but was also sensitive to MEK (AZD6244) and PI3K/mTOR (BEZ235) inhibition, correlating with the cell death detected three days later, at 96 hr. On the other hand, PC9, as shown previously (Figures 1 B and 1C), responded to gefitinib (Ercan et al., 2010; Faber et al., 2011) but also to lapatinib and TAE684; correlating with cell death at 72 hr. For this set of solid tumor cell lines the AUC of the ROC curve was 0.96 (Figure 4C). In three out of five cell lines, DBP clearly predicted the most cytotoxic drug. In the other two MCF7 and HCT116, there was nearly equal maximum response of the same two drugs in both DBP and cytotoxicity.

Throughout this paper, we use loss of fluorescence from an indicator compound, JC-1, that is sensitive to the electropotential gradient across the inner mitochondrial membrane. We have previously shown that this JC-1 signal provides a good surrogate for permeabilization of the outer mitochondrial membrane (Ryan et al., 2010). To verify that this surrogacy is maintained in DBP,

we compared measuring MOMP by JC-1 or by efflux of cytochrome c as read on a flow cytometer (Ryan and Letai, 2013) (Figure S4). Our results show good agreement between the two techniques, supporting the use of JC-1 fluorescence as a surrogate for MOMP in the context of DBP.

To test the generalizability of the principle that early drug-induced priming changes predict eventual cytotoxicity across a wide variety of both solid and liquid cancers and a wide variety of agents, we combined the data of Figures 1, 2, 3, 4 and Figure S3. We observed that there is a significant correlation between $\Delta\%$ priming and $\Delta\%$ cell death (Figure 5A). Note that liquid tumors in general have a greater cytotoxic response per change in priming, perhaps explained by the higher baseline mitochondrial apoptotic priming we observe in hematologic cancer cell lines compared to solid tumor cell lines. In addition, the ROC analysis suggests that DBP could be a good binary predictor for cytotoxicity across a wide range of pathway inhibitors and cancer, with an AUC for the ROC curve of 0.89 (Figure 5B). These results suggest the most significant hurdle that must be cleared for a drug to cause cytotoxicity is simply the initiation of death signaling. Regardless of the pathway inhibited and regardless of the cell of origin of the cancer, early drug-induced death signaling predicts later cytotoxicity.

Choosing the Best Treatment among Several Options

A predictive biomarker can be used to identify the best therapy among many treatment options for a single patient. To test the ability of DBP to identify the most effective therapy among a myriad of treatment options we turned to an allograft melanoma model. Mouse melanomas harboring compound mutations in *Braf* and *Nf1* readily grow as allografts and are resistant to selective BRAF inhibitors but sensitive to (combined) MEK/mTORC1 inhibition (Maertens et al., 2013). To ask whether DBP could discriminate among the in vivo efficacy of several therapies on the same tumor model, we exposed *Braf/Nf1* mutant melanoma cells to different targeted agents for 16 hr: PLX4720 (a PLX4032 analog that inhibits mutant BRAF^{V600E}), PD0325901 (referred to as PD-901, a MEK inhibitor), GDC-0941 (a PI3K inhibitor), and rapamycin (an mTOR inhibitor), as single agents or in combination. Of all the treatments tested, PD-901 in combination with rapamycin induced the greatest increase in priming (Figure 6A). These findings correlate well with the preclinical data previously generated using this tumor model (Figure 4C Maertens et al., 2013). More specifically, of all (combination) therapies tested in vivo, the PD-901/rapamycin combination caused the greatest tumor shrinkage, as summarized in Figure 6B. Across all of the treatments, we observed a significant correlation between DBP results and the in vivo data obtained in the *Braf/Nf1* mutant allografts (Figure 6C). These results suggest that DBP can be used as a predictive biomarker to select among treatment options to identify treatments that will provide best in vivo benefit.

Identifying the Best-Responding Patients to a Single Therapy in a Patient Cohort

Predictive biomarkers can also be used to stratify likelihood of response to a single therapy among many patients. This can be described as a companion diagnostic use. Having thoroughly supported the hypothesis that early death signaling detected by

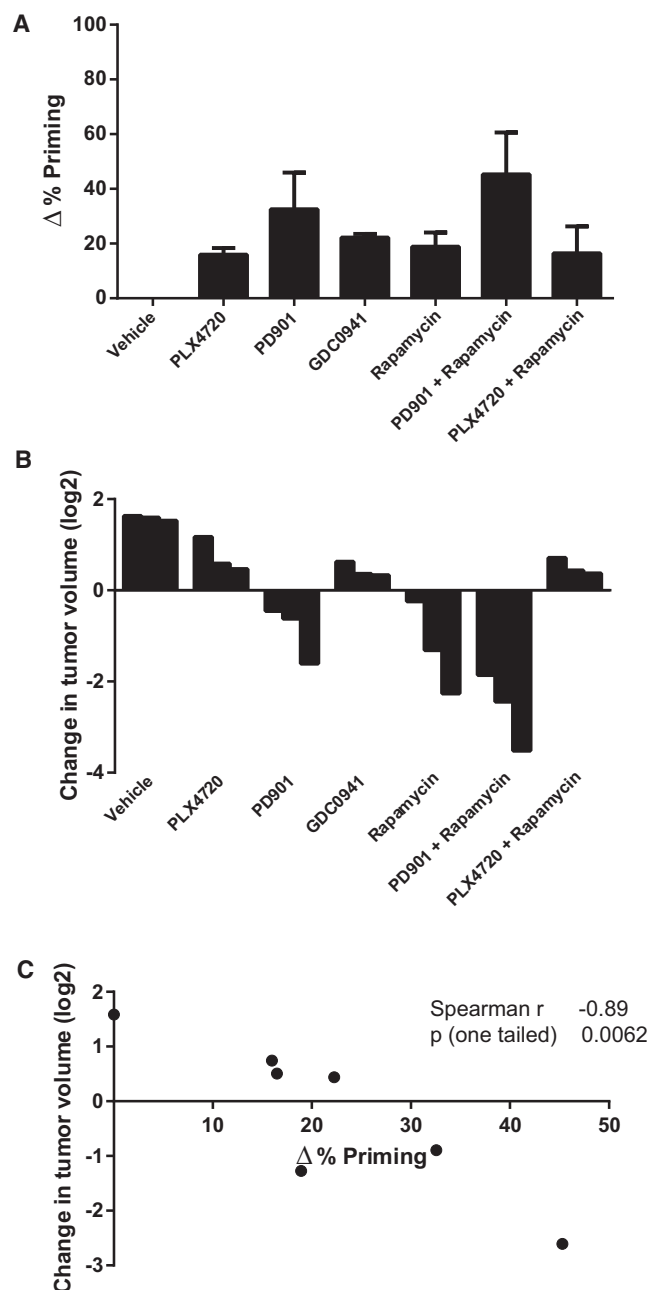


Figure 6. DBP Can Identify the Best In Vivo Treatment among Several Options

Braf/Nf1 mutant melanoma cells were treated ex vivo with PLX4720 1 μ M, PD0325901 (referred to as PD-901) 0.25 μ M, GDC-0941 1 μ M, rapamycin 0.1 μ M, PD-901 + rapamycin, and PLX4720 + rapamycin.

(A) DBP (16 hr incubation) results expressed as Δ% priming. Values indicate mean values \pm SEM, at least three independent experiments were performed ($n \geq 3$).

(B) In vivo response for this *Braf/Nf1* mutant allograft melanoma model (adapted from Figure 4C Maertens et al., 2013) expressed as change in tumor volume (log2) after 7 days of treatment.

(C) Correlation between Δ% priming and change in tumor volume.

DBP predicts cytotoxicity in vitro, it was important to test whether our tool can likewise discriminate between clinical sensitivity and resistance to anti-cancer therapies using primary patient samples. We chose treatment of chronic myelogenous leukemia (CML) with imatinib as a first test of this principle. CML cells possess a t(9;22) translocation creating a BCR-ABL fusion protein that results in constitutively active ABL kinase activity. CML is typically sensitive to inhibitors of ABL kinase including imatinib (Sawyers, 1999).

To demonstrate the correlation between imatinib's inhibition of ABL and an increase in apoptotic priming, we treated two human CML cell lines with different concentrations of imatinib. After 16 hr of treatment, we observed that the dephosphorylation of ABL, and its downstream target CRKL correlated with an increase in priming. Note that frank cell death began days later, at 72 hr (Figure S5).

We treated bone marrow cells obtained from 24 CML patients for 16 hr with imatinib, performed DBP, and recorded the change in priming induced. Initial resistance to imatinib is very rare in CML, so we compared samples of patients who were newly started on imatinib, all of whom entered at least a complete hematologic remission ("sensitive", Figure 7A), with samples from patients obtained when they were known to be refractory to imatinib ("resistant", Figure 7A). Samples from patients that were sensitive to imatinib showed a significantly higher Δ% priming compared to those that did not respond (Figure 7A). We next tested the ability of DBP to segregate clinical sensitivity and resistance in a binary fashion with ROC analysis (Figure 7B). The area under the ROC curve was 0.89, $p = 0.016$, supporting the ability of DBP to discriminate clinical sensitivity and resistance. There was variability in the quality of the tracings obtained, likely due to variability in the viability of the thawed patient samples. When we applied criteria only to accept tracings for which there was at least a difference of 100 relative fluorescent units between our positive control (FCCP) and negative control, we observed similar results, with an AUC of 0.88. This came at the cost of excluding seven samples from analysis based on the criteria (Figure S6). Basically, every newly diagnosed patient with CML will be started on imatinib or another tyrosine kinase inhibitor, and nearly all will have at least a complete hematologic remission. Thus, there is little need for a new predictive biomarker to guide administration of tyrosine kinase inhibitors in CML. Nonetheless, this study demonstrates the principal that DBP can distinguish clinical sensitivity and resistance to a targeted agent.

DBP Predicts Carboplatin Response in Ovarian Cancer Patients

Although our testing was focused on using DBP with targeted agents, pro-death signaling resulting from treatment with classical cytotoxic chemotherapies should be predictive of cellular response since these drugs also largely kill via the mitochondrial apoptotic pathway. We obtained 16 primary ovarian adenocarcinomas from surgical resection. We treated a single cell suspension of these tumors with carboplatin, the standard front-line therapy, ex vivo for 16 hr and performed DBP. We detected a robust Δ% priming (>20%) in six of the patient specimens.

All analyzed patients were then treated with carboplatin in combination with taxol in the clinic. We then collected and

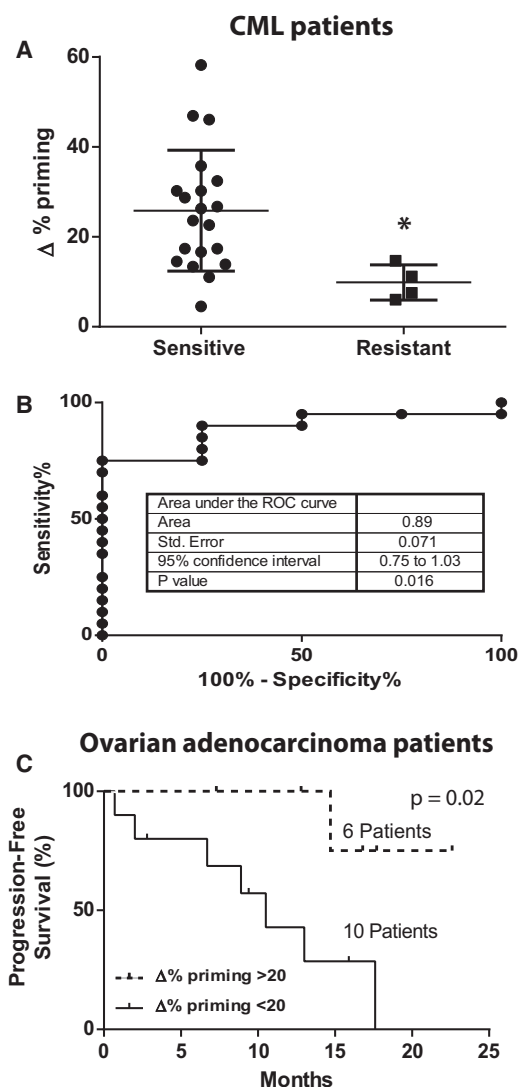


Figure 7. DBP Can Stratify In Vivo Drug Response to Imatinib in a Cohort of CML Patients and to Carboplatin in Ovarian Adenocarcinoma Patients

(A) 24 frozen Ficoll purified bone marrow primary CML samples were treated for 16 hr with imatinib 1 and 5 μ M, and DBP was then performed. Results are expressed as $\Delta\%$ priming. Values indicate mean \pm SEM. Unpaired t-test, two-tailed, * $p < 0.05$.

(B) A ROC curve analysis for this set of samples. The AUC is 0.89.

(C) 16 ovarian adenocarcinoma patient samples were analyzed by DBP with carboplatin. We treated the samples for 16 hr with carboplatin 100 μ g/ml, and DBP was then performed. Shown is a Kaplan-Meier plot of the patients' progression-free survival in response to carboplatin and taxol. A significant difference was observed between those patients whose samples showed a $\Delta\%$ priming $>20\%$ from those that were $<20\%$, as assessed by Mantel-Cox statistical analysis.

See also Figures S5 and S6, and Table S1.

analyzed the clinical data on the patients to assess progression free survival using an abnormal and rising CA-125 as an index for progression. Patients with ovarian adenocarcinomas that exhibited a robust $\Delta\%$ priming ($>20\%$) experienced a significantly

longer progression free survival to those patients who did not (Figure 7C).

DISCUSSION

Here, we tested and supported the hypothesis that the initiation of death signaling is sufficient to determine eventual commitment to cell death. By detecting early death signaling, DBP can predict in vitro and in vivo cytotoxic response in varied cancers to varied classes of chemotherapeutic agents, agents which have in common only their ability to kill cancer cells via the mitochondrial pathway of apoptosis. While this provides basic mechanistic information about the events between drug treatment and commitment to cell death, we anticipate that its greatest utility might be in prediction of cancer patients' response to therapy in the clinic. Over the past decade, an ever-growing number of therapies have been approved for use in medical oncology. But every tumor is distinct, with its own particular signaling network and pathway addiction yielding a distinct pattern of sensitivity to cancer therapeutics. The task of precision cancer medicine is to match a tumor to those agents that will most effectively eliminate it (Garraway and Jänne, 2012; Sawyers, 2008; Yaffe, 2013).

An analogous problem was faced in the previous century in the world of clinical microbiology. As the number of antibiotics proliferated, it became more challenging to identify the best drug for a particular isolate of bacteria. The very practical solution that emerged was to simply grow a lawn of bacteria and expose the isolate to all available antibiotics in the form of drug-soaked disks. Antibiotics were then chosen from those that caused the greatest elimination of bacteria. This practice is still the standard and has not been displaced by any modern technology, including genomics, proteomics or systems biology. While this method reveals little about signaling pathways and genetics of bacteria, it is supremely useful because it functionally summarizes the contribution of many genes and pathways to the phenotype that is most pertinent, the response of the viable bacterium to antibiotics. A version of this assay has been the mainstay of clinical microbiology for many decades.

Analogous ex vivo approaches have been attempted in oncology but with little success. A typical strategy was to expose a patient's tumor to drugs and place it into ex vivo culture for 3–14 days followed by evaluation of cell death, proliferation, or colony formation (Burstein et al., 2011). The biggest difficulty was the requirement for ex vivo culture of cancer cells. Many cancer cells simply rapidly die in ex vivo culture. Those that survive can undergo arrest or other phenotypic changes that accompany the transfer from a comfortable in vivo niche to an ex vivo plastic dish in 21% oxygen. In addition, if the culture is prolonged, there can be selection for non-tumor cells or clones that are poorly representative of the patient's tumor. The result, in any case, was a series of studies that did not provide sufficient predictive power to be clinically useful. Exciting new ex vivo cell culture strategies using more modern techniques require weeks to months (Crystal et al., 2014). Their utility in guiding patient care will doubtless be tested in the coming years. Patient-derived xenograft (PDX) mouse models are being tested as a newer venue for functional assessment of tumor cell response to therapy (Hidalgo et al.,

2014). However, the time (months) and expense that are required to establish PDX models may limit their utility in clinical medicine.

Here, we have taken a different approach. Appreciating the tremendous advantages of perturbing the actual patient tumor cell with the actual therapy of interest, we instead have prioritized making observations early enough that long term ex vivo culture is not needed. While we have found that death signaling can be detected as early as 4 hr after treatment, depending on the drug, we have found that a 16 hr incubation is sufficient for most agents to produce measurable death signaling in responding cells.

We demonstrated that DBP can be exploited to select among many therapies the one that is best for a single tumor (Figure 6). We also demonstrated that DBP can select among many patients those that are most likely to respond to a single therapy (Figure 7). These are the two major functions of a clinically useful predictive biomarker, and it is notable that DBP can perform them both. Of equal importance, the clinical and in vivo experiments of Figure 7 demonstrate that useful predictive observations of both liquid (CML) and solid (ovarian) primary human tumors is consistent with a simple 16 hr monolayer culture.

We anticipate that DBP may be used to make personalized choices of therapy for patients. One could use DBP to choose agents among a panel of candidate drugs for one individual patient. Alternatively, one could use DBP to stratify a panel of patients to identify those most likely to respond to an individual drug. In the case of drugs that have activity only in a subset of a particular disease, we believe DBP can more efficiently stratify patient selection for clinical trials or clinical use by prospectively identifying those whose tumors are most likely to respond. In addition, while our focus here was on cancer cells, it is important to realize that this approach is also applicable to the study of non-malignant cells. As such, it can be used as a probe of sensitivities of cells in normal biology to a variety of insults, or as a toxicology tool to predict the toxicity of novel agents to normal tissues.

While we have focused mainly on single agent therapies in our proofs of principle studies, a strength of this approach is that it should work for both single agent and combination therapies. In fact, we explicitly demonstrated this in Figures 1, 2, and S3. Given the nearly universal emergence of resistance to single agent targeted therapies, even when there is an excellent initial response, strategies for the rational choice of personalized combination therapies is of great importance. We can envision two ways DBP could be used to fashion such strategies. One is to simply expose tumor cells to the combinations as we did in Figures 1, 2, and S3. Another is to test a panel of single agents via DBP and combine two or more with good single agent activity.

A tremendous amount of information has been collected on cancer cells in the past few years, and the amount is likely to continue to grow exponentially. Much of this information is now genetic, with whole cancer genomes being sequenced (Barretina et al., 2012). In addition, there are technologies that garner an abundance of gene expression information and those that capture protein expression (Kornblau et al., 2009). It remains to be seen how widely these technologies will be useful in better assigning therapy to patients. However, despite the huge amounts of information acquired, one common limitation of these studies

is that they all represent static observations of dead cells. That means that a tremendous amount of the functional complexity of the cell has been lost to study. With DBP, we anticipate that a small number of strategic perturbations (drug and peptide exposures) on viable cells will yield vastly fewer bits of information, but that a great proportion of the bits will be clinically actionable.

EXPERIMENTAL PROCEDURES

Cell Lines and Treatments

RPMI 1640 media supplemented with 10% heat inactivated fetal bovine serum (GIBCO) 10 mM L-Glutamine and 100 U/ml penicillin and 100 µg/ml streptomycin was used for the culture of the cell lines used. The cells were cultured at 37°C in a humidified atmosphere of 5% CO₂.

Isolation and Treatment of Primary CML Cells

Thirty primary CML samples from bone marrow biopsies viably frozen in 90% FBS/10%DMSO were obtained from the Pasquarello Tissue Bank at Dana-Farber Cancer Institute and from Dr. Philip C. Amrein at the Massachusetts General Hospital. Cells were thawed and resuspended in complete RPMI media and washed with fresh media, counted by trypan blue exclusion and plated in a 12-well plate, 1 million cells/well, and treated with imatinib 1 and 5 µM. DBP failed on five samples due to failure of mitochondria to maintain transmembrane polarization and 1 sample analysis was discarded for not having complete clinical information. After a 16 hr incubation at 37°C in a humidified atmosphere of 5% CO₂, Dynamic BH3 Profile analysis was performed. Clinical response data were compiled by clinicians; patients are considered responders when complete hematologic response was observed.

Ovarian Primary Tumors

Fresh primary tumors obtained from routine resections after patients signed an informed consent approved by the Institutional Review Board (DFCI#02-051), were used for preparation of viable single-cell suspensions. Tumors were first mechanically dissociated and digested for 1 hr at 37°C in 1 mg/ml collagenase/dispase (Roche Diagnostics). Cells were then filtered through a cell strainer and cell viability was assessed by trypan blue exclusion. Cells were then frozen in freezing buffer (fetal bovine serum with 10% DMSO). For DBP, cells were thawed and resuspended in complete RPMI media with 100 U/ml of DNase I and incubated 15 min at room temperature. Then the cells were washed with fresh media, counted by trypan blue exclusion, and plated in a 12-well plate, 0.2–0.5 M cells/well and treated with carboplatin 100 µg/ml. After a 16 hr incubation at 37°C in a humidified atmosphere of 5% CO₂, Dynamic BH3 Profile analysis was performed blinded to clinical outcome. Clinical response data were compiled by clinicians 6–24 months after sample acquisition.

Dynamic BH3 Profiling

2 × 10⁴ cells/well were normally used, but 4 × 10⁴ cells/well were used for primary CML and AML. 15 µl of BIM BH3 peptide (final concentration of 0.03, 0.1, 0.3, 1, and 3 µM) in T-EB (300 mM Trehalose, 10 mM HEPES-KOH [pH 7.7], 80 mM KCl, 1 mM EGTA, 1 mM EDTA, 0.1% BSA, 5 mM succinate) were deposited per well in a black 384-well plate (BD Falcon no. 353285). Single-cell suspensions were washed in T-EB before being resuspended at 4× their final density. One volume of the 4× cell suspension was added to one volume of a 4× dye solution containing 4 µM JC-1, 40 µg/ml oligomycin, 0.02% digitonin, 20 mM 2-mercaptoethanol in T-EB. This 2× cell/dye solution stood at RT for 10 min to allow permeabilization and dye equilibration. A total of 15 µl of the 2× cell/dye mix was then added to each treatment well of the plate, shaken for 15 s inside the reader, and the fluorescence at 590 nm monitored every 5 min at RT. Percentage loss of Ψ_m for the peptides is calculated by normalization to the solvent only control DMSO (0% depolarization) and the positive control FCCP (100% depolarization). Individual DBP analysis were performed using triplicates for DMSO, FCCP, and the different BIM BH3 concentrations used, and the expressed values stand for the average of three different readings. In cases where SD was >10%, the outlying reading was discarded. % priming stands for the maximum % depolarization obtained from the different BIM BH3

concentrations tested; typically 0.03, 0.1, 0.3, 1, and 3 μ M. $\Delta\%$ priming stands for the difference between treated cells minus non-treated cells ($\% \text{ priming}^{\text{treated}} - \% \text{ priming}^{\text{non-treated}}$). See also [Figure S1](#).

Cell Viability Assays

Cells were stained with fluorescent conjugates of Annexin-V (BioVision) and/or propidium iodide (PI) and analyzed on a FACS Canto machine (BD). Viable cells are annexin-V negative and PI negative, and cell death is expressed as 100% - viable cells. $\Delta\%$ cell death stands for the difference between treated cells minus non-treated cells ($\% \text{ cell death}^{\text{treated}} - \% \text{ cell death}^{\text{non-treated}}$).

Immunoblotting

Total cell lysates were prepared in 1% Chaps buffer (5 mM MgCl₂, 137 mM NaCl, 1 mM EDTA, 1 mM EGTA, 1% Chaps, 20 mM Tris-HCl [pH 6.5], and protease inhibitors [Complete, Roche]). Cells were washed twice, resuspended with 50–100 μ l of CHAPS lysis buffer, and kept on ice for 30 min. Then, the cellular suspension was centrifuged at 16,100 g for 5 min, and the supernatant used to perform the immunoblotting analysis.

Twenty micrograms of protein were loaded on NuPAGE 10% Bis-Tris polyacrylamide gels (Invitrogen). The following antibodies were used to detect proteins on the membrane (dilution 1:1,000): Actin (Chemicon, MAB1501), PARP-1 (cell signaling, #9542), BCL-2 (Epitomics, #1017-1), BIM (Cell Signaling, #2933), and BCL-xL (Cell signaling, #2762).

Statistical Analysis

Statistical significance of the results was analyzed using Student's t-tail test using GraphPad Prism 5.0 software. * $p < 0.05$ and ** $p < 0.01$ were considered significant. SEM stands for Standard Error of the Mean. For ROC curve analysis cell lines were considered responsive to treatment when $\Delta\%$ cell death $>10\%$; CML clinical samples when the patient achieved a complete hematologic response after treatment; for ovarian adenocarcinoma biopsies, clinical response data were compiled by clinicians 6–24 months after sample acquisition.

SUPPLEMENTAL INFORMATION

Supplemental Information includes Extended Experimental Procedures, six figures, and one table and can be found with this article online at <http://dx.doi.org/10.1016/j.cell.2015.01.042>.

AUTHOR CONTRIBUTIONS

The study was conceived and designed by A.L. and J.M. [Figure 2](#) analyses were performed by J.D.D. under supervision of J.M. and A.L. P.C.A. provided CML patient samples and relevant clinical correlation. Ovarian adenocarcinoma patient samples and clinical correlation were obtained from N.S.H., H.P., R.S.B., U.M., and R.D.; K.A.S. processed these samples. Drug-resistant NSCLC cell lines were obtained from D.E. and P.A.J.; melanoma murine allograft cells and relevant in vivo data were obtained from O.M. and K.C. All other experiments were performed by J.M. with technical assistance from J.R. under supervision of A.L. [Figures 6](#) and [7C](#) were prepared by K.A.S., all others by J.M. The manuscript was prepared by A.L. and J.M. with input from most authors.

ACKNOWLEDGMENTS

We gratefully acknowledge funding from the Beatriz de Pinós programme from la Generalitat de Catalunya in Spain (J.M.), and NIH grants RO1CA129974, RO1CA135257, P01CA068484, and P01CA139980. A.L. is a Leukemia and Lymphoma Society Scholar. R.D. would like to thank the Dr. Miriam and Sheldon G. Adelson Medical Research Foundation (AMRF) and NIH grant U01CA152990. We thank the Pasquarello Tissue Bank and the DFCI Flow Cytometry. We also thank Richard P. Oakley Jr. and <http://www.servier.com/Powerpoint-image-bank> (licensed under Creative Commons Attribution 3.0 Unported License) for allowing us to use some images to elaborate [Figure 1](#) and the Graphical Abstract.

Received: June 10, 2014

Revised: October 3, 2014

Accepted: January 12, 2015

Published: February 26, 2015

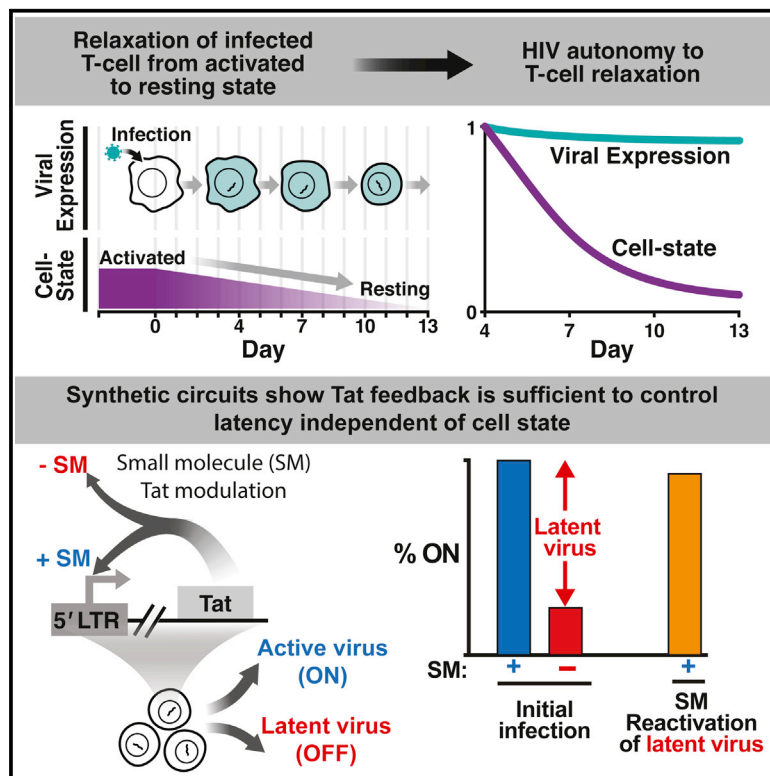
REFERENCES

- Barretina, J., Caponigro, G., Stransky, N., Venkatesan, K., Margolin, A.A., Kim, S., Wilson, C.J., Lehár, J., Kryukov, G.V., Sonkin, D., et al. (2012). The Cancer Cell Line Encyclopedia enables predictive modelling of anticancer drug sensitivity. *Nature* 483, 603–607.
- Bhatt, A.P., Bhende, P.M., Sin, S.H., Roy, D., Dittmer, D.P., and Damania, B. (2010). Dual inhibition of PI3K and mTOR inhibits autocrine and paracrine proliferative loops in PI3K/Akt/mTOR-addicted lymphomas. *Blood* 115, 4455–4463.
- Burstein, H.J., Mangu, P.B., Somerfield, M.R., Schrag, D., Samson, D., Holt, L., Zelman, D., and Ajani, J.A.; American Society of Clinical Oncology (2011). American Society of Clinical Oncology clinical practice guideline update on the use of chemotherapy sensitivity and resistance assays. *J. Clin. Oncol.* 29, 3328–3330.
- Certo, M., Del Gaizo Moore, V., Nishino, M., Wei, G., Korsmeyer, S., Armstrong, S.A., and Letai, A. (2006). Mitochondria primed by death signals determine cellular addiction to antiapoptotic BCL-2 family members. *Cancer Cell* 9, 351–365.
- Chapman, P.B., Hauschild, A., Robert, C., Haanen, J.B., Ascierto, P., Larkin, J., Dummer, R., Garbe, C., Testori, A., Maio, M., et al.; BRIM-3 Study Group (2011). Improved survival with vemurafenib in melanoma with BRAF V600E mutation. *N. Engl. J. Med.* 364, 2507–2516.
- Chipuk, J.E., Moldoveanu, T., Llambi, F., Parsons, M.J., and Green, D.R. (2010). The BCL-2 family reunion. *Mol. Cell* 37, 299–310.
- Crystal, A.S., Shaw, A.T., Sequist, L.V., Friboulet, L., Niederst, M.J., Lockerman, E.L., Frias, R.L., Gainor, J.F., Amzallag, A., Greninger, P., et al. (2014). Patient-derived models of acquired resistance can identify effective drug combinations for cancer. *Science* 346, 1480–1486.
- Deng, J., Carlson, N., Takeyama, K., Dal Cin, P., Shipp, M., and Letai, A. (2007a). BH3 profiling identifies three distinct classes of apoptotic blocks to predict response to ABT-737 and conventional chemotherapeutic agents. *Cancer Cell* 12, 171–185.
- Deng, J., Shimamura, T., Perera, S., Carlson, N.E., Cai, D., Shapiro, G.I., Wong, K.K., and Letai, A. (2007b). Proapoptotic BH3-only BCL-2 family protein BIM connects death signaling from epidermal growth factor receptor inhibition to the mitochondrion. *Cancer Res.* 67, 11867–11875.
- Engelman, J.A., Chen, L., Tan, X., Crosby, K., Guimaraes, A.R., Upadhyay, R., Maira, M., McNamara, K., Perera, S.A., Song, Y., et al. (2008). Effective use of PI3K and MEK inhibitors to treat mutant Kras G12D and PIK3CA H1047R murine lung cancers. *Nat. Med.* 14, 1351–1356.
- Ercan, D., Zejnullahu, K., Yonesaka, K., Xiao, Y., Capelletti, M., Rogers, A., Lifshits, E., Brown, A., Lee, C., Christensen, J.G., et al. (2010). Amplification of EGFR T790M causes resistance to an irreversible EGFR inhibitor. *Oncogene* 29, 2346–2356.
- Ercan, D., Xu, C., Yanagita, M., Monast, C.S., Pratilas, C.A., Montero, J., Butaney, M., Shimamura, T., Sholl, L., Ivanova, E.V., et al. (2012). Reactivation of ERK signaling causes resistance to EGFR kinase inhibitors. *Cancer Discov.* 2, 934–947.
- Faber, A.C., Li, D., Song, Y., Liang, M.C., Yeap, B.Y., Bronson, R.T., Lifshits, E., Chen, Z., Maira, S.M., García-Echeverría, C., et al. (2009). Differential induction of apoptosis in HER2 and EGFR addicted cancers following PI3K inhibition. *Proc. Natl. Acad. Sci. USA* 106, 19503–19508.
- Faber, A.C., Corcoran, R.B., Ebi, H., Sequist, L.V., Waltman, B.A., Chung, E., Incio, J., Digumarthy, S.R., Pollack, S.F., Song, Y., et al. (2011). BIM expression in treatment-naïve cancers predicts responsiveness to kinase inhibitors. *Cancer Discov.* 1, 352–365.
- Garraway, L.A., and Jänne, P.A. (2012). Circumventing cancer drug resistance in the era of personalized medicine. *Cancer Discov.* 2, 214–226.

- Haibe-Kains, B., El-Hachem, N., Birkbak, N.J., Jin, A.C., Beck, A.H., Aerts, H.J., and Quackenbush, J. (2013). Inconsistency in large pharmacogenomic studies. *Nature* 504, 389–393.
- Hidalgo, M., Amant, F., Biankin, A.V., Budinská, E., Byrne, A.T., Caldas, C., Clarke, R.B., de Jong, S., Jonkers, J., Mælandsmo, G.M., et al. (2014). Patient-derived xenograft models: an emerging platform for translational cancer research. *Cancer Discov* 4, 998–1013.
- Joensuu, H., Roberts, P.J., Sarlomo-Rikala, M., Andersson, L.C., Tervahartiala, P., Tuveson, D., Silberman, S., Capdeville, R., Dimitrijevic, S., Druker, B., and Demetri, G.D. (2001). Effect of the tyrosine kinase inhibitor STI571 in a patient with a metastatic gastrointestinal stromal tumor. *N. Engl. J. Med.* 344, 1052–1056.
- Kluck, R.M., Bossy-Wetzell, E., Green, D.R., and Newmeyer, D.D. (1997). The release of cytochrome c from mitochondria: a primary site for Bcl-2 regulation of apoptosis. *Science* 275, 1132–1136.
- Kornblau, S.M., Tibes, R., Qiu, Y.H., Chen, W., Kantarjian, H.M., Andreeff, M., Coombes, K.R., and Mills, G.B. (2009). Functional proteomic profiling of AML predicts response and survival. *Blood* 113, 154–164.
- Letai, A., Bassik, M.C., Walensky, L.D., Sorcinelli, M.D., Weiler, S., and Korsmeyer, S.J. (2002). Distinct BH3 domains either sensitize or activate mitochondrial apoptosis, serving as prototype cancer therapeutics. *Cancer Cell* 2, 183–192.
- Maertens, O., Johnson, B., Hollstein, P., Frederick, D.T., Cooper, Z.A., Mesiaen, L., Bronson, R.T., McMahon, M., Granter, S., Flaherty, K., et al. (2013). Elucidating distinct roles for NF1 in melanomagenesis. *Cancer Discov* 3, 338–349.
- Ni Chonghaile, T., Sarosiek, K.A., Vo, T.T., Ryan, J.A., Tammareddi, A., Moore, Vdel.G., Deng, J., Anderson, K.C., Richardson, P., Tai, Y.T., et al. (2011). Pre-treatment mitochondrial priming correlates with clinical response to cytotoxic chemotherapy. *Science* 334, 1129–1133.
- Paez, J.G., Jänne, P.A., Lee, J.C., Tracy, S., Greulich, H., Gabriel, S., Herman, P., Kaye, F.J., Lindeman, N., Boggon, T.J., et al. (2004). EGFR mutations in lung cancer: correlation with clinical response to gefitinib therapy. *Science* 304, 1497–1500.
- Pencina, M.J., D'Agostino, R.B., Sr., D'Agostino, R.B., Jr., and Vasan, R.S. (2008). Evaluating the added predictive ability of a new marker: from area under the ROC curve to reclassification and beyond. *Stat Med* 27, 157–172, discussion 207–112.
- Ryan, J., and Letai, A. (2013). BH3 profiling in whole cells by fluorimeter or FACS. *Methods* 61, 156–164.
- Ryan, J.A., Brunelle, J.K., and Letai, A. (2010). Heightened mitochondrial priming is the basis for apoptotic hypersensitivity of CD4+ CD8+ thymocytes. *Proc. Natl. Acad. Sci. USA* 107, 12895–12900.
- Sarosiek, K.A., Chi, X., Bachman, J.A., Sims, J.J., Montero, J., Patel, L., Flanagan, A., Andrews, D.W., Sorger, P., and Letai, A. (2013). BID preferentially activates BAK while BIM preferentially activates BAX, affecting chemotherapy response. *Mol. Cell* 51, 751–765.
- Sawyers, C.L. (1999). Chronic myeloid leukemia. *N. Engl. J. Med.* 340, 1330–1340.
- Sawyers, C.L. (2008). The cancer biomarker problem. *Nature* 452, 548–552.
- Sikorski, R., and Yao, B. (2010). Visualizing the landscape of selection biomarkers in current phase III oncology clinical trials. *Sci. Transl. Med.* 2, 34ps27.
- Vo, T.T., Ryan, J., Carrasco, R., Neuberg, D., Rossi, D.J., Stone, R.M., Deangelo, D.J., Frattini, M.G., and Letai, A. (2012). Relative mitochondrial priming of myeloblasts and normal HSCs determines chemotherapeutic success in AML. *Cell* 151, 344–355.
- Wei, M.C., Zong, W.X., Cheng, E.H., Lindsten, T., Panoutsakopoulou, V., Ross, A.J., Roth, K.A., MacGregor, G.R., Thompson, C.B., and Korsmeyer, S.J. (2001). Proapoptotic BAX and BAK: a requisite gateway to mitochondrial dysfunction and death. *Science* 292, 727–730.
- Yaffe, M.B. (2013). The scientific drunk and the lamppost: massive sequencing efforts in cancer discovery and treatment. *Sci. Signal.* 6, pe13.
- Zhou, W., Ercan, D., Chen, L., Yun, C.H., Li, D., Capelletti, M., Cortot, A.B., Chirieac, L., Iacob, R.E., Padera, R., et al. (2009). Novel mutant-selective EGFR kinase inhibitors against EGFR T790M. *Nature* 462, 1070–1074.

A Hardwired HIV Latency Program

Graphical Abstract



Authors

Brandon S. Razooky, Anand Pai, ..., Igor M. Rouzine, Leor S. Weinberger

Correspondence

leor.weinberger@gladstone.ucsf.edu

In Brief

Although HIV latency is currently thought to arise when an infected cell transitions from an activated to a resting state that is non-permissive to viral expression, a combination of modeling and synthetic control of HIV Tat positive feedback demonstrates that latency establishment operates autonomously from cell state.

Highlights

- HIV expression persists even when primary cells transition from activated to resting
- Tat positive-feedback circuitry drives this autonomy from cell-state relaxation
- Orthogonal activation of Tat shows that the circuitry suffices for autonomous latency



A Hardwired HIV Latency Program

Brandon S. Razooky,^{1,2,5,6} Anand Pai,^{1,3,5} Katherine Aull,² Igor M. Rouzine,¹ and Leor S. Weinberger^{1,3,4,*}

¹The Gladstone Institutes (Virology and Immunology), San Francisco

²Biophysics Graduate Group

³Department of Biochemistry and Biophysics,

⁴QB3

California Institute of Quantitative Biosciences, University of California, San Francisco, 94158

⁵Co-first author

⁶Present address: Laboratory of Immune Cell Epigenetics and Signaling, The Rockefeller University, New York, NY 10065, USA

*Correspondence: leor.weinberger@gladstone.ucsf.edu

<http://dx.doi.org/10.1016/j.cell.2015.02.009>

SUMMARY

Biological circuits can be controlled by two general schemes: environmental sensing or autonomous programs. For viruses such as HIV, the prevailing hypothesis is that latent infection is controlled by cellular state (i.e., environment), with latency simply an epiphenomenon of infected cells transitioning from an activated to resting state. However, we find that HIV expression persists despite the activated-to-resting cellular transition. Mathematical modeling indicates that HIV's Tat positive-feedback circuitry enables this persistence and strongly controls latency. To overcome the inherent crosstalk between viral circuitry and cellular activation and to directly test this hypothesis, we synthetically decouple viral dependence on cellular environment from viral transcription. These circuits enable control of viral transcription without cellular activation and show that Tat feedback is sufficient to regulate latency independent of cellular activation. Overall, synthetic reconstruction demonstrates that a largely autonomous, viral-encoded program underlies HIV latency—potentially explaining why cell-targeted latency-reversing agents exhibit incomplete penetrance.

INTRODUCTION

Diverse biological systems, both natural and engineered, face the challenge of surviving in variant and unpredictable environmental conditions. One strategy is to sense surrounding conditions and respond with environment-specific developmental programs—there is a 1:1 correspondence between explicit sensor-actuators and the extremely reduced form of this scheme in which sensing and actuation are so tightly coupled that environment entirely actuates the program (Bull and Vogt, 1979). An alternate strategy foregoes environmental sensing and actuation, instead relying on autonomous programs (Knedler, 1947), for example programs that intrinsically generate heterogeneity in phenotypes and allow probabilistic “bet hedging” (Cohen,

1966). For many systems, such as bacteriophage- λ , it is unclear whether environmental sensor-actuator schemes or autonomous programs are employed (Arkin et al., 1998; St-Pierre and Endy, 2008; Zeng et al., 2010). The ensuing debates carry evolutionary significance since sensor-actuator regulation can be driven by crosstalk from coincidental signals and hence tied to unrelated epiphenomena, whereas autonomous circuits are invariably subjected to direct natural selection pressures. In other words, if a phenotype is controlled by sensor-actuator regulation, it can be an “epiphenomenon,” but if autonomously regulated, the phenotype is invariably evolutionary hardwired and directly selected for.

For HIV, the debate is clinically relevant; it remains unclear whether the host-cell environment or autonomous viral circuitry controls proviral latency, a long-lived viral dormancy state that is the chief barrier to curative therapy (Richman et al., 2009; Weinberger and Weinberger, 2013). Upon infecting CD4⁺ T lymphocytes, HIV either actively replicates to rapidly produce progeny virions or can enter a long-lived quiescent state (proviral latency), from which it subsequently reactivates. These latently infected cells form a viral reservoir, forcing patients to remain on lifelong suppressive therapy. The prevailing view (Coffin and Swanstrom, 2013; Siliciano and Greene, 2011) holds that proviral latency results from HIV transcription being controlled by the host-cell activation state (i.e., environment) since relaxation of activated lymphocytes to a resting-memory state is correlated with increased epigenetic silencing of the HIV promoter and increased cytoplasmic sequestration of transcription factors that activate HIV transcription (Pearson et al., 2008; Tyagi et al., 2010). In this model, HIV infects activated T cells, which allow active viral replication, and if these cells “relax” to resting-memory T cells, which generally restrict HIV infection, viral latency ensues (Figure 1, left).

In contrast to the cellular control hypothesis, there is circumstantial evidence for an alternate model wherein latency is controlled by viral gene-regulatory circuitry (Ho et al., 2013; Jeeninga et al., 2008; Weinberger et al., 2005) without strict dependence on cellular state (Figure 1, right). HIV encodes a transcriptional master circuit that is driven by the HIV Tat protein, which amplifies expression from the viral promoter within the HIV long terminal repeat (LTR), establishing positive feedback. Critically, minimal Tat positive-feedback circuits can recapitulate latency, and stochastic fluctuations between a

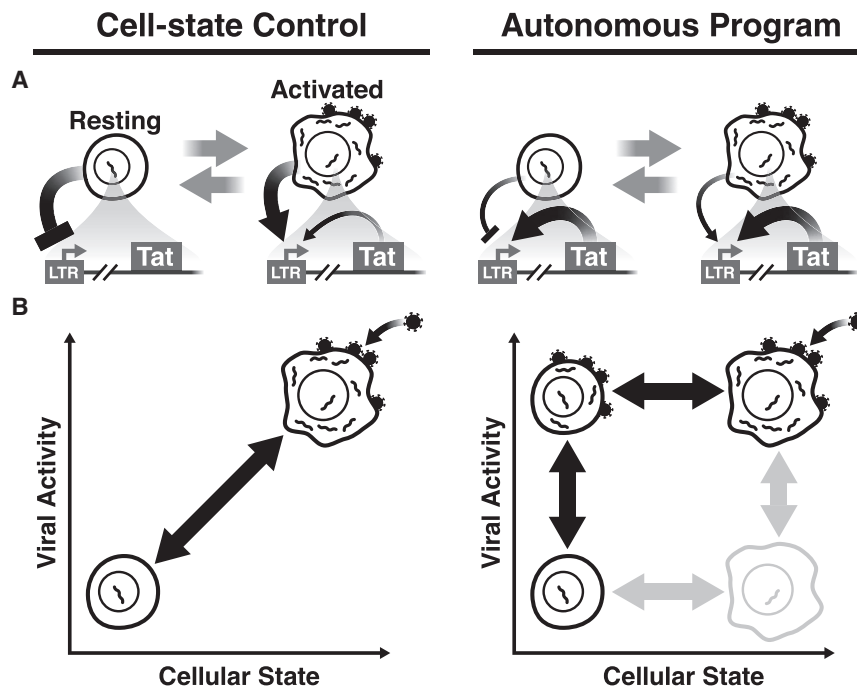


Figure 1. Two Models of HIV Latency Regulation: Cell-State Control versus Autonomous Programming

(A) (Left) The prevailing hypothesis of HIV proviral latency regulation. As $CD4^+$ T cells relax from an activated state (permissive to infection) to a resting-memory state, the host-cell environment silences HIV gene expression, restricting Tat transactivation of the LTR. (Right) The alternate hypothesis that HIV Tat positive feedback is robust to changes of the host-cell environment and operates autonomously despite changes in cell state. The overlapping nature of cellular and viral regulatory circuits confounds testing between these hypotheses (i.e., the LTR actuates Tat feedback but doubles as a sensor of the host-cell environment). (B) If cell state and viral circuitry can be orthogonalized (i.e., decoupled), the influence of cellular state on viral latency can be analyzed via an orthogonal 2D graphical correlation. (Left) If cellular state dominates regulation of viral latency, resting cells would inhibit viral circuitry while active cells would induce viral gene expression, generating a strong correlation between cell state and viral activity. (Right) If an autonomous latency circuit regulates latency, both latent and active viral expression could be generated in either resting cells or activated T cells, producing little correlation between cell state and viral activity.

transcriptionally on and off state in the Tat circuit are sufficient to drive a phenotypic bifurcation between active and latent expression, even in non-resting cells (Weinberger et al., 2005). However, there is also evidence that cellular factors modulate stochastic HIV expression to drive latency (Burnett et al., 2009), confounding the hypothesis that latency is controlled by an autonomous viral circuit.

Here, we test between the cell-state and autonomous-circuit hypotheses for latency establishment. If latency is regulated by host-cell state, viral expression should be tightly correlated with cell state, whereas if the latency circuit is hardwired to function autonomously, then cellular state would be uncorrelated with viral expression and tuning viral circuitry, independent of cell state, would be sufficient to control HIV latency (Figure 1B). Surprisingly, we find that viral expression is robust to cellular-activation state in primary T cells, and mathematical models indicate that this autonomy results from intrinsic properties of the HIV Tat positive-feedback circuit. However, directly testing circuit autonomy to cell state is confounded by overlap between cellular and viral networks—the same transcription factors that alter cellular activation also activate the HIV LTR, triggering Tat positive feedback (Karn, 2011). To circumvent this overlap, we synthetically reconstruct the Tat circuit to decouple viral dependence on the cellular environment from viral transcriptional regulation (i.e., decouple viral sensing and actuation). The refactored circuits chemically modulate viral expression independent of cellular activation levels and show that Tat circuitry is sufficient to overcome cell-driven silencing of HIV transcription during cellular relaxation from active to resting. Overall, the results argue that the Tat circuit is hardwired to establish latency largely autonomous of cellular state.

RESULTS

Donor-Derived Primary T Lymphocytes Maintain Robust HIV Expression during Cellular Relaxation from Activated to Resting

To test the prevailing “epiphenomenon” hypothesis of HIV latency establishment, we α CD3/CD28 pre-activated donor-derived primary human $CD4^+$ T lymphocytes (to achieve a $CD25^+CD69^+$ phenotype), infected them with full-length HIV-1 virus, and then removed activation stimuli, allowing infected cells to relax to a resting ($CD25^-CD69^-$) state (Figure 2A). The virus used (HIV-d2GFP) encodes a short-lived 2-hr half-life GFP (d2GFP) reporter to enable rapid detection of viral transcriptional silencing and is *env* mutated (i.e., single-replication round) to avoid confounding the data with expansion of the infected cell population. Infected cells were sampled periodically over 2 weeks for cellular activation status (as quantified by CD25 and CD69) alongside viral-GFP expression.

Surprisingly, viral expression appears remarkably robust during the cellular transition from activated to resting (Figures 2B and 2C–2H). Despite drastic decline in cellular activation both in CD25 (Figures 2D and 2G) and in CD69 (Figures 2C and 2F), viral activity (quantified by GFP expression of productively infected cells) remained relatively unchanged (Figures 2B, 2E, and 2H). The resilience of viral gene expression despite cellular relaxation is not due to differential relaxation of productively infected cells compared to the overall population, as productively infected cells relax at the same rate as the overall population (Figure S1).

Since human primary cells represent a mixed co-culture (i.e., infected and uninfected subsets of cells), which may obfuscate the interpretation of results (Jordan et al., 2003), we also

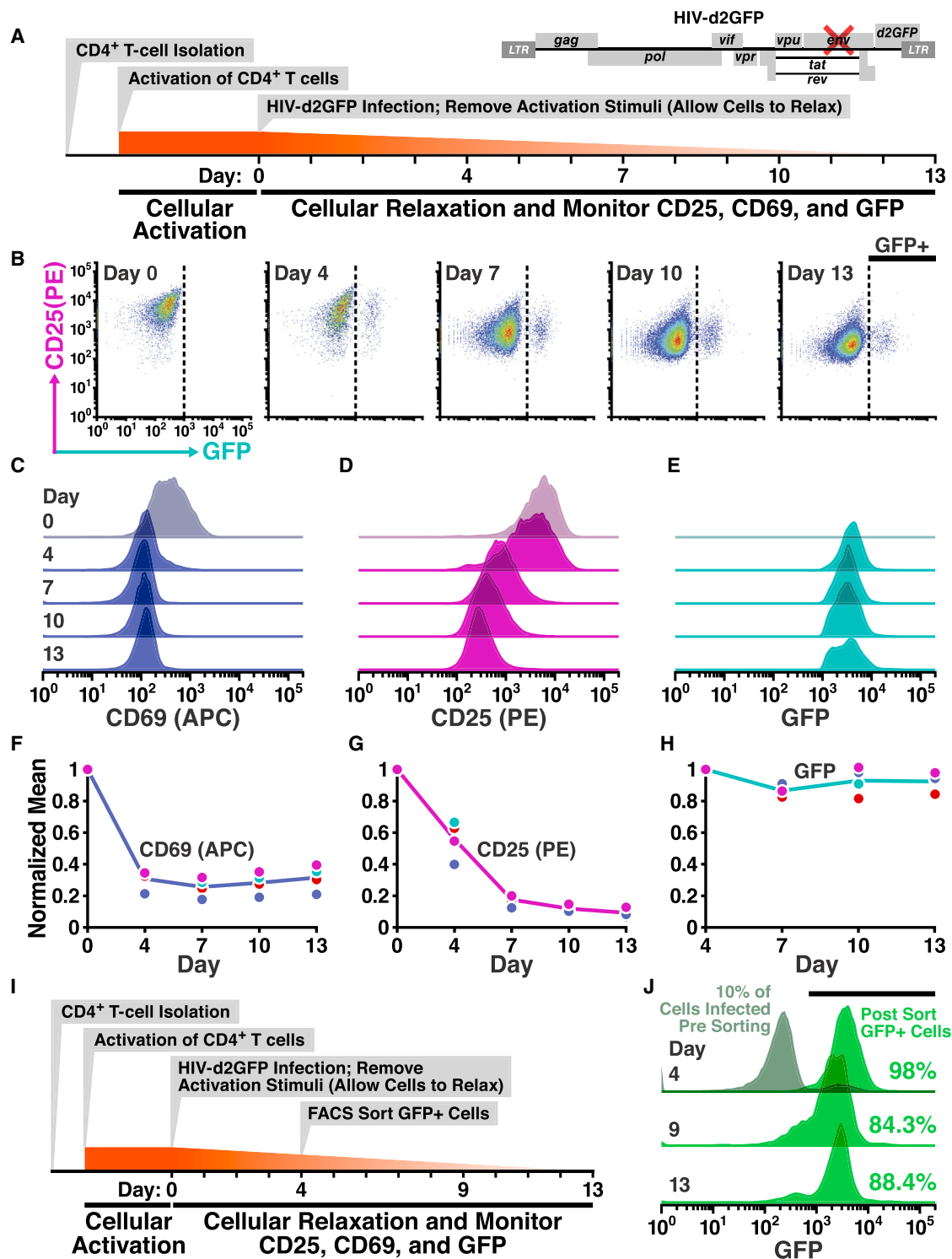


Figure 2. HIV Expression Is Autonomous to Changes in Cellular State: Transitioning of Primary T Lymphocytes from Activated to Resting Does Not Silence HIV Expression

(A) Schematic of activation, infection, and long-term observations of relaxing primary CD4⁺T cells with full-length HIV-d2GFP. Donor-derived primary cells were activated with α CD3/CD28 beads in the presence of rIL-2 for 3 days, following which beads were removed and the cells were infected. At indicated time points, cells were collected for flow-cytometry-based measurement of CD25/CD69 levels and GFP expression. Data shown (in B–E) are representative of duplicate infections performed with cells from two donors.

(legend continued on next page)

performed a refined version of the experiment by isolating HIV-infected cells through FACS sorting and tracking this purified population of infected lymphocytes as cells relaxed to resting (Figure 2I). As before, even after 2 weeks of culture, ~90% of cells maintain high-level viral expression (Figure 2J) despite cellular relaxation to resting (Figure S1). Collectively, these two experiments show that, despite a 10-fold decline in CD4⁺ T cell activation levels, the impact on viral gene expression is minimal, suggesting that viral circuitry is largely autonomous to cellular state.

Computational Analysis Predicts that Tat Feedback Circuitry Can Autonomously Generate Active and Latent Infection across a Broad Range of Cellular-Activation States

To investigate how viral transcription remains robust despite cell-state changes, we employ a simplified computational model of HIV transcriptional regulation (Figure 3A) based on previous studies (Weinberger et al., 2008). This model builds off the standard two-state model of transcription (Kepler and Elston, 2001; Paulsson, 2004) and allows the LTR promoter to stochastically toggle between a transcriptionally non-permissive state (LTR_{OFF}) and a transcriptionally permissive state (LTR_{ON}) at rates k_{off} and k_{on} , respectively. In the LTR_{ON} state, Tat protein can transactivate the promoter, enhancing transcriptional elongation at a rate k_{transact} . These parameters (k_{off} , k_{on} , and k_{transact}) have been quantified by single-cell analysis (Dar et al., 2012; Singh et al., 2010; Weinberger et al., 2008), and measurements at thousands of HIV integration sites across the human genome show k_{on} to be the predominant parameter that alters LTR activity in the regime required for latency (Dar et al., 2012), i.e., the weak expression regime. Potent cell-state activators, such as tumor necrosis factor α (TNF α), which acts through the same pathway as α CD3/CD28 activation, maximally stimulate LTR activity by increasing k_{on} by 1.5- to 2-fold (Dar et al., 2012, 2014; Jordan et al., 2001).

To determine whether relaxation of activated T cells (i.e., decreases in k_{on}) can drive LTR-Tat circuit shutoff and latency, we simulated infection of activated T cells and examined how tuning k_{on} alters the fraction of trajectories in the ON state; i.e., initial conditions were LTR_{ON} = 1, and all other molecular species = 0 (see Table S1), thereby allowing efficient Tat turn-on in activated cells with subsequent stochastic circuit shutoff. The simplified model recapitulates previous results showing a phenotypic bifurcation in Tat levels (Weinberger et al., 2005), with a fraction of trajectories remaining ON and a fraction turning OFF (Figure 3B) for any given k_{on} across a broad range of values

(Figure 3C). Indeed, for LTR activities within three orders of magnitude (Figure S2), any trajectory can maintain either an ON or OFF state purely by altering the level of Tat without a change in basal LTR activity. Thus, the model predicts that, at a given cellular-activation state (k_{on} value), circuit activity could be toggled ON and OFF simply by supplying Tat alone (e.g., *in trans*) without activating the LTR or changing the cellular-activation state (e.g., via TNF α). Moreover, the ON fraction can also be altered by changing Tat abundance—and hence feedback strength—through Tat half-life modulation (Figure S2).

Next, we directly examined how decreases in k_{on} influenced circuit activity. For all 2-fold decreases in k_{on} (over three orders of magnitude), there is >90% robustness in the percentage of trajectories in the ON state (Figure 3D). 2-fold decreases in LTR activity were examined because removal of cell-state activators (e.g., TNF α), result in 1.5- to 2-fold reductions in LTR activity (Dar et al., 2012; Jordan et al., 2001), but comparable circuit robustness was observed for all 4-fold and even 1-Log reductions in k_{on} (Figure S2). In fact, the simplified nature of the computational model allows derivation of an analytical “closed-form” solution for the fraction of ON trajectories as a function of time for all parameters (see Extended Experimental Procedures), thereby enabling phase-plane analysis of the ON fraction as a function of k_{on} and k_{transact} (Figure S2). This phase-plane sensitivity analysis demonstrates that—throughout the physiological parameter regime of $k_{\text{transact}} > k_{\text{on}}$ (Dar et al., 2012; Molle et al., 2007)—even if an infected cell lives far longer than the *in vivo* lifetime of 40 hr (Perelson et al., 1996), k_{on} modulation cannot substantially alter the ON fraction. To be completely sure that these results were not a peculiarity of the specific model used, we also examined an alternate positive-feedback model topology (Weinberger et al., 2005)—which encodes substantially more molecular detail but is experimentally validated—and we observed similar circuit robustness to decreases in k_{on} (Figure S2). Analytical solution shows that this robustness results from the strong positive feedback ($k_{\text{transact}} > k_{\text{on}}$), since changes in k_{on} produce small corrections. Notably, despite the circuit’s robustness to cellular relaxation (k_{on} decreases), high values of k_{on} do generate less-frequent latency in both the simplified model (Figure 3C) and the complex models (Weinberger et al., 2005). In fact, the analytical solution quantifies how increases in k_{on} (e.g., via NF κ B stimulation) reactivate the circuit from a latent state (Equation 12, Extended Experimental Procedures).

Overall, the results demonstrate robustness of LTR-Tat circuit activity to cellular relaxation (i.e., reductions in k_{on}), consistent with primary cell observations (Figure 2), but, critically, also

(B) Flow cytometry time course of CD25 and GFP levels taken on indicated days post infection. Dotted line indicates gating for productively infected cells (GFP⁺). (C–E) Histograms of cellular activation levels CD25 (C) and CD69 (D) of the entire population alongside GFP expression from productively infected cells (cells in GFP⁺ gate in B) over the course of 13 days post infection (17 days post cellular activation). (F–H) Cellular activation levels and GFP levels for all replicates over the experimental time course. Each dot indicates the time point from an independent infection and represents the geometric mean of the distribution as seen in C–E. Solid line connects the mean of the replicates. CD25 and CD69 normalized to day 0 (maximal); GFP normalized to day 4 when viral activity is first observed. (I) Schematic of FACS-based isolation of productively infected cells. 4 days post infection, GFP⁺ cells were isolated and cultured (repeated for two donors). (J) Histograms of isolated GFP⁺ cells over time. Numbers indicate the proportion of cells that fall within the gate for positive GFP expression (marked by horizontal black bar). Day 4: Gray histogram shows the infected population prior to FACS-based separation. Viral titer was calibrated to achieve 10% infection (fraction of gray histogram that is GFP⁺ at day 4). Histogram in green (for days 4, 9, and 13) shows the GFP expression in the isolated productively infected cells (post sort). All data shown above are from donor 1.

See Figure S1 for results from donor 2 and CD25 expression decline during the experiment.

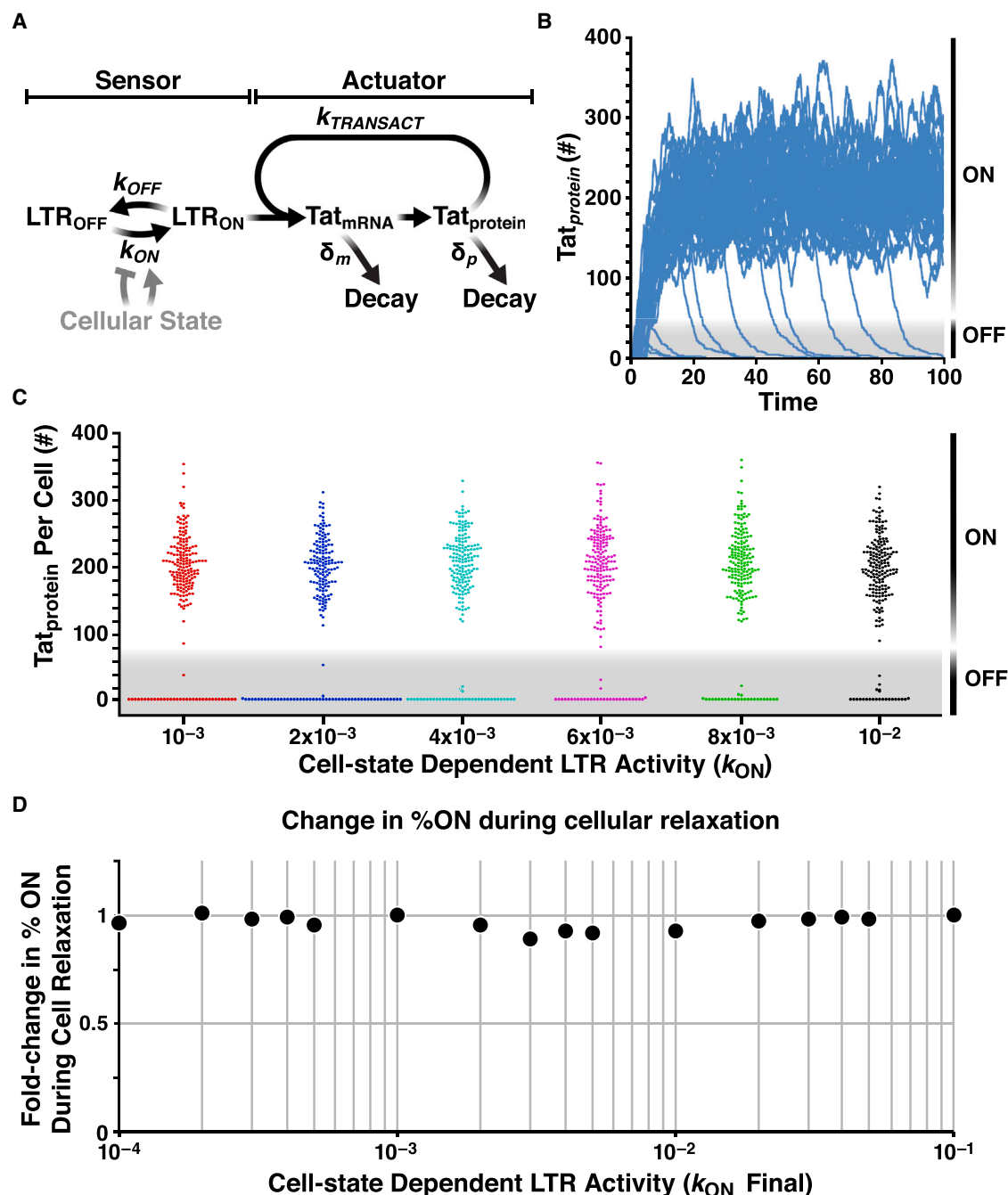


Figure 3. Computational Analysis Predicts that Tat Positive-Feedback Circuitry Underlies HIV Autonomy to Cell State

(A) Schematic of a simplified model of the Tat-feedback circuit. The LTR promoter can toggle between a state where transcriptional elongation is stalled (LTR_{OFF}) and a state where elongation proceeds (LTR_{ON}) at rates k_{OFF} and k_{ON} , respectively, (Dar et al., 2012; Singh et al., 2010, 2012) and Tat protein transactivates the promoter by enhancing transcriptional elongation at a rate $k_{transact}$ (Razooky and Weinberger, 2011). Tat protein and mRNA decay at rates δ_m and δ_p , respectively.

(B) Stochastic Monte-Carlo simulations ("Gillespie" algorithm) of Tat protein levels (in arbitrary number of molecules) in individual cells over time (from reaction scheme in A). Each trajectory represents an individual cell; 100 single-cell trajectories shown (initial conditions for all species equal zero at time $t = 0$, except $LTR_{ON} = 1$); see [Extended Experimental Procedures](#) for reaction rates.

(C) Bee-Swarm plots of circuit activity (Tat levels at $t = 200$) over a range of k_{ON} values. Each data point represents a single-cell trajectory, (200 trajectories shown per k_{ON} value). The width of the collection of cells (dots) having zero level of Tat (bottom of each k_{ON} value simulated) shows that high values of k_{ON} do generate less frequent latency (smaller number of dots). Compare, for example, the spread of red dots ($k_{ON} = 10^{-3}$) and black dots ($k_{ON} = 10^{-2}$) at 0.

(legend continued on next page)

show sensitivity of latency to changes in Tat abundance or changes in Tat half-life. Below, we experimentally test these computational predictions: (1) that LTR-Tat circuit activity between latent and active can be toggled by Tat levels alone (i.e., independent of cellular-activation state), (2) that Tat is more effective at activation from latency than cell-state modifiers, and (3) that cellular relaxation to resting does not silence Tat positive-feedback circuitry.

A Minimal Synthetic Circuit Shows that Viral Reactivation from Latency Can Be Toggled Independent of Cellular Activation

To test whether HIV gene-regulatory circuitry can control proviral latency without changes in cellular-activation state, we developed synthetic circuits in which viral expression could be toggled independent of cell state. The synthetic circuits are based upon a minimal model of the HIV latency circuit and encode a transcriptional positive-feedback loop in which HIV Tat amplifies expression from the HIV LTR promoter (Jordan et al., 2001; Weinberger et al., 2005). The minimal LTR-Tat circuit is sufficient to recapitulate latent gene expression; stimulation with cell-state modifiers reactivates proviral expression from a non-expressive “OFF” state to a high-level “ON” state.

The minimalist synthetic toggle circuit encodes Tat fused to a controllable proteolysis tag, FKBP (Banaszynski et al., 2006), under the control of the HIV LTR (Figure 4A). FKBP degradation is reversibly inhibited by a small molecule, Shield-1, allowing Tat half-life to be rapidly tuned. The Tat-FKBP fusion was also tagged with a photo-switchable fluorescent protein, Dendra-2 (Gurskaya et al., 2006), which allows for light-based pulse-chase experiments (Zhang et al., 2007) to measure Tat half-life destabilization in single cells (Figure S3). In this minimal LTR-Tat-Dendra-FKBP viral vector, Tat half-life is reduced to 2.5 hr in the absence of Shield-1 (a ~3.3-fold reduction from its native half-life) but returns to its native 8 hr half-life (Weinberger and Shenk, 2007) in the presence of 1 μ M Shield-1.

Simulations predict that changes in Tat half-life should be sufficient to toggle HIV positive feedback between ON and OFF at a majority of viral integration sites (Figure S2). As predicted, altering the Tat half-life by addition or removal of Shield-1 was sufficient to toggle between latent and active expression across an array of integration sites (Figure 4B). The observed reactivation is not due to pleiotropic effects of Shield-1 since Tat-Dendra fusion proteins lacking FKBP are insensitive to Shield-1 (Figure S3). Moreover, the increased expression levels cannot simply be due to an increase in the half-life of the reporter (Dendra-2), as the expression increases are substantially greater than the 3.3-fold increase in half-life caused by Shield-1 (Figure S3). To be completely sure that reporter half-life changes were not accounting for the increased expression, we also decoupled the fluorescent reporter half-life from the Tat half-life by creating a polycistronic system in which the reporter protein and Tat are transcriptionally fused, but not translationally fused (Figure S4).

The polycistronic system corroborates the finding that Tat positive feedback is sufficient to control viral switching from an inexpressive OFF to expressive ON state (Figure S4). Thus, in both the translational and transcriptional fusions, Shield-1 toggles the circuit between ON and OFF. These data indicate that tuning Tat positive feedback is sufficient to toggle HIV gene expression between a quiescent state and an actively expressing state and that viral expression can be activated without activating cell state.

Tat Induction Alone Is More Efficient Than Cell-State Activation for Reactivating Latent Clones

One caveat of using tunable proteolysis systems to toggle the Tat circuit is that a minimal level of Tat protein must be present in the off state—i.e., modulating protein half-life when protein concentration is zero has no effect. Thus, the Tat-FKBP approach is unable to test whether Tat can reactivate latent cells that are fully silenced. To circumvent this obstacle and test whether Tat induction is sufficient to reactivate completely silenced LTRs, we developed a set of open-loop circuits, based on the Tet-On system (Gossen and Bujard, 1992), that induce Tat expression de novo. These systems allow tight induction of Tat expression upon Doxycycline (Dox) addition. To examine the effects of Tat induction on HIV gene expression, these circuits were incorporated into cells that encoded an HIV LTR promoter driving the mCherry fluorescent reporter (Figure 4C), and a library containing 33 distinct LTR clonal integration sites was examined.

The Tet-On circuits show that Tat by itself is sufficient to toggle cells between OFF and ON and to control the mean levels of LTR expression despite the large clonal variation (Figure 4D). Importantly, a number of clones (clones 1–3) exhibit no detectable LTR expression in the absence of Tat induction—the conventional threshold for latency. But, inducing Tat expression is sufficient to fully reactivate these clones without the need for any cell-state activation signals.

Next, to test the effects of cell-state activation, Tet-inducible isoclonal populations were exposed to an array of standard cell-state modifiers. These agents are potent activators of T lymphocytes (Pazin et al., 1996) and also of the LTR (Jordan et al., 2001; Karn, 2011). For example, TNF α strongly activates T cell state by stimulating nuclear localization of the nuclear factor of activated T cells (NFAT) and by stimulating recruitment of the p50-RelA heterodimer to promoters containing NF- κ B-binding sites (Karin and Lin, 2002). If cell-state activation were the dominant factor controlling latency, then cell-state modulators should strongly reactivate latent mCherry expression in the Tet-inducible system. Strikingly, cell-state activation alone only slightly increases LTR expression and the percentage of cells in the ON state, across the library of 33 distinct integration sites (Figure 4E). In contrast, induction of Tat (by Dox) drastically increases the percentage of cells in the ON state to near 100% (Figure 4E). This dramatic difference between direct Tat induction versus cell-state modifiers demonstrates that $k_{transact} > k_{on}$ for the HIV circuitry and indicates that Tat-mediated transactivation is far

(D) Fold change in percentage of trajectories in ON state for 2-fold reductions in k_{on} . Circuit activity (%ON) is largely robust to reductions in LTR activity (i.e., k_{on}) over three orders of magnitude. Phase-plane analysis (i.e., sensitivity analysis) from a closed-form analytical solution shows that this behavior is robust across the physiological parameter regime ($k_{transact} > k_{on}$). See also Figure S2 and Table S1.

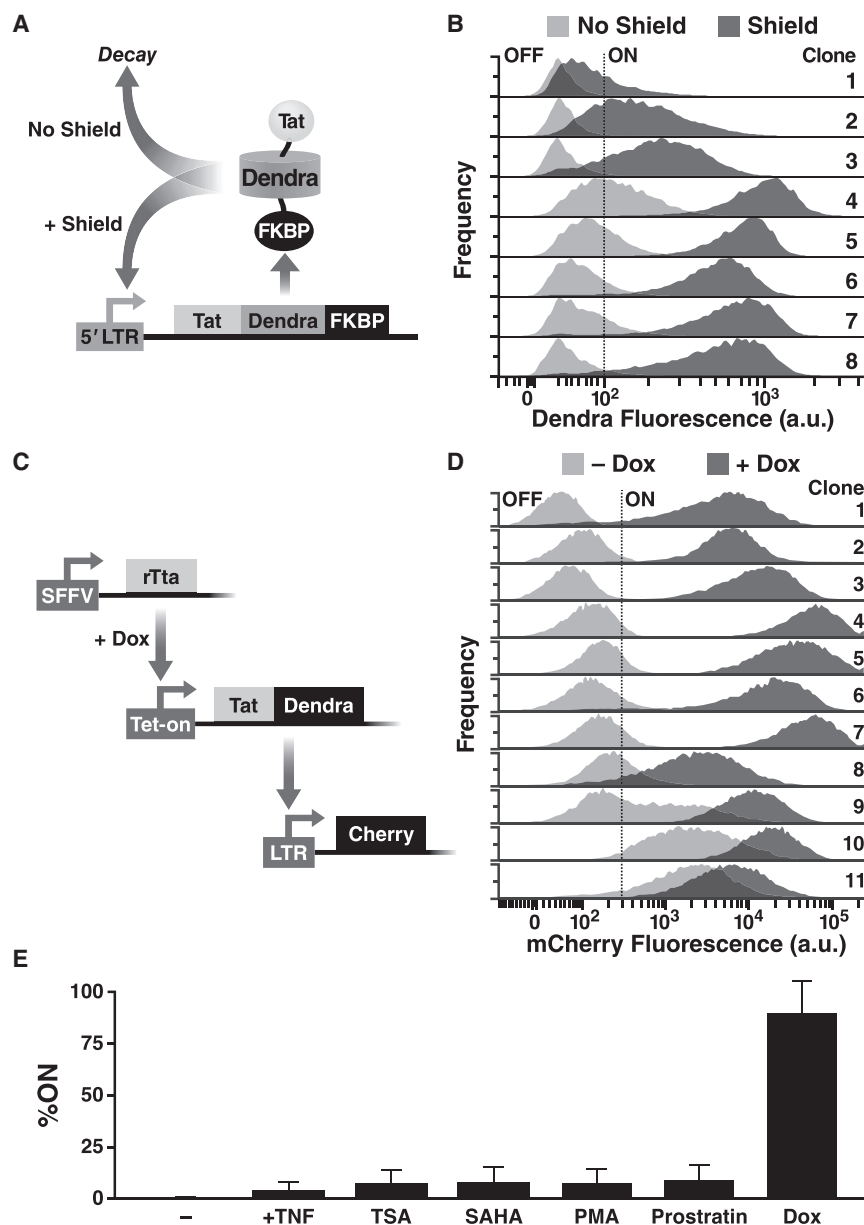


Figure 4. Synthetic Tuning of Tat Circuit Activity Is Sufficient to Control Latent HIV Expression in the Absence of Cellular Activation

(A) Schematic of the minimal LTR-Tat-Dendra-FKBP lentiviral circuit. In the absence of Shield-1, the Tat-Dendra-FKBP fusion protein is rapidly degraded, diminishing positive feedback. When Shield-1 is added, FKBP-mediated proteolysis is blocked, allowing Tat levels to increase and enabling strong Tat positive feedback.

(B) Flow cytometry histograms of eight isoclinal populations of Jurkat cells infected with LTR-Tat-Dendra-FKBP in the absence of Shield-1 (light gray histograms) or the presence of 1 μ M Shield-1 (dark gray histograms). Gating of the Dendra-positive region (right of black-dashed line) was set relative to naive, un-transduced Jurkat cells. See also Figures S3 and S4.

(C) Schematic of the synthetic system (left) and flow cytometry data of the LTR expression in cells transduced with the synthetic circuit (right). The synthetic circuit is composed of an rTta activator constitutively expressed from an SFFV promoter. In the presence of Dox, rTta protein activates the Tet-On promoter to drive expression of the Tat-Dendra fusion protein. Tat transactivates expression from the HIV-1 LTR promoter, and LTR activity is measured by mCherry expression.

(D) LTR mCherry expression is shown for 11 representative isoclinal populations in the absence of Dox (light gray histograms) or after Dox addition (dark gray histograms).

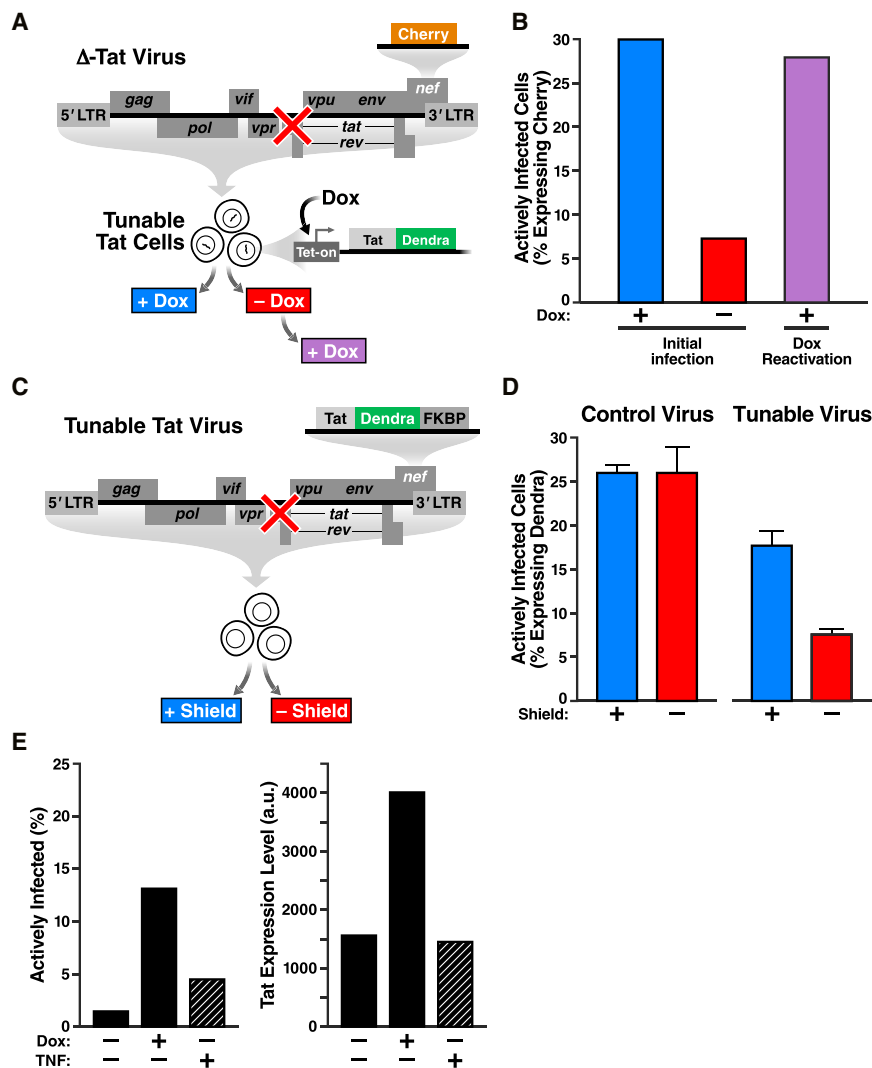
(E) Flow cytometry analysis of a library containing 33 distinct LTR clonal integration sites subjected to Dox and a panel of standard cell-state modifiers: TNF α , phorbol myristate acetate (PMA), PMA-ionomycin, suberanilohydroxamic acid (SAHA/vorinostat), trichostatin A (TSA), or prostratin. Error bars show SD.

stronger an effect than the switching of the LTR to an ON state through cell-state modifications. Collectively, these data (Figure 4E) indicate that activating cell-state alone is not sufficient to control HIV transcription. These results in no way exclude a role for cellular state in HIV reactivation in vivo. Rather, the sufficiency of Tat-mediated viral reactivation without cell-state modification emphasizes the autonomy of the HIV Tat circuit.

Refactoring of Full-Length Replicating HIV Indicates that Latency Establishment and Reactivation Depend on Viral-Circuit Activity and Are Largely Independent of Cellular Activation

We next tested whether viral circuitry could control latency in full-length replicating virus. First, we developed a decoupled system in

cassette and provide in *trans* complementation of Tat for a reengineered Tat-deleted full-length virus, the Δ Tat-Cherry virus. The Δ Tat-Cherry virus was constructed from a full-length HIV molecular clone containing a Tat deletion (Huang et al., 1994) and encodes an mCherry fluorescent reporter within *nef* (Figure 5A). In these inducible Tat cells, viral gene expression can be toggled on even if initial Tat levels are zero and virus replicates only in the presence of Dox and, as with conventional strains, virus is inhibited by HIV protease inhibitors (Figure S5). Inducing Tat expression in these cells during infection with Δ Tat-Cherry virus shows a ~400% increase in active infection compared to non-induced Δ Tat Cherry-infected cells (Figure 5B), indicating that absence of Dox drives the virus to enter latency in agreement with findings that Tat protein can inhibit establishment of latency (Donahue et al.,



Tat expression level (Dendra). Again, TNF α by itself leaves expression level unchanged over that in absence of treatment. Addition of Dox leads to >2-fold increase in expression. Also see Figure S5 for the experiment repeated with Dox and a panel of cell-state modifiers.

2012). Strikingly, subsequent induction of Tat expression by Dox fully reactivates latent virus to levels observed in the initial infection with Dox (Figure 5B). Further, Dox was far more effective in reactivating latent virus than any of the standard cell-state modifiers: TNF α , PMA, PMA-ionomycin, SAHA/vorinostat, TSA, or prostratin (Figure S5). Hence, latent provirus can be reactivated by Tat induction alone, without altering cellular-activation state, demonstrating that Tat is sufficient to control latent reactivation in full-length HIV.

Next, to check whether Tat induction in *cis* (i.e., within the positive-feedback loop) could also control latency in full-length virus, we reengineered the Δ Tat-Cherry virus to encode either the Tat-Dendra-FKBP cassette, referred to as “Tat-FKBP virus” (Figure 5C), or a control Tat-Dendra cassette, referred to as “Tat-Dendra control virus,” or simply “control virus” (Figure S5). As previously established in these *nef*-reporter viruses, actively replicating infections express reporter, while latent infections

Figure 5. Tat Feedback Circuitry Is Sufficient to Control Active-versus-Latent Infection in Full-Length Viruses

(A) Schematic of experiment: A Jurkat cell line in which Tat-Dendra is expressed only in the presence of Dox, “inducible Tat cells,” was infected with full-length Δ Tat-Cherry virus in the presence (+) or absence (-) of Dox to score for latency and to score reactivation. Dox- infections were subsequently induced by Dox.

(B) Percent of cells actively infected (actively expressing mCherry) 2 days post infection. 30% of cells were actively infected in the presence of Dox (blue), while only 7% of cells were actively infected in the absence of Dox (red). Upon subsequent Dox incubation of the Dox- infection, 28% of cells reactivated to active infection (purple), indicating that virtually all latent cells can be reactivated with Tat induction.

(C) Experiment schematic: CEM T cells were infected with either full-length Tat-FKBP virus or control virus in the presence or absence of Shield-1.

(D) Percent of cells actively infected (actively expressing Dendra) 2 days post infection. For the control virus infection, 25.8% \pm 1.0% of cells exhibit active infection in the presence of 1 μ M Shield-1 (blue), while 26.0% \pm 2.7% exhibit active infection in the absence of Shield-1 (red). For the Tat-FKBP virus infection, 17.5% \pm 1.7% of cells exhibit active infection in the presence of 1 μ M Shield-1 (blue), while 7.5% \pm 1.0% of cells exhibit active infection in the absence of Shield-1 (red). Infections were performed in triplicate. Error bars = 1 SD. Control virus infection and Tat-FKBP virus infection are independent experiments (infection titers of the two are different).

(E) Comparison of viral circuit versus cell-state activation by quantifying the percentage of delta-Tat virus infections that enter the active state. In the absence of TNF α or Dox, 2% of cells generate active HIV replication. Dox addition increases active infections to ~13%, while

are quantified by absence of reporter expression (Jordan et al., 2003; Pearson et al., 2008). In control HIV infections, Shield-1 has no measureable effect on active-versus-latent infection (Figure 5D). In striking contrast, in Tat-FKBP virus infections, modulating Tat positive-feedback strength with Shield-1 alters the percentage of actively infected cells by 141%, i.e., >2-fold (Figure 5D). The reduction in actively infected cells is not due to reduced input virus since equivalent titers of virus (i.e., MOIs) were used in the presence and absence of Shield-1 and the lack of measureable difference in infection in control HIV infections indicates that Shield-1 is not inducing abortive infections and that hypothetical pleiotropic effects of Shield-1 cannot explain the difference in active-versus-latent infection. Overall, these results show that modulating viral feedback strength is sufficient to control the establishment of active-versus-latent infection in full-length replicating virus.

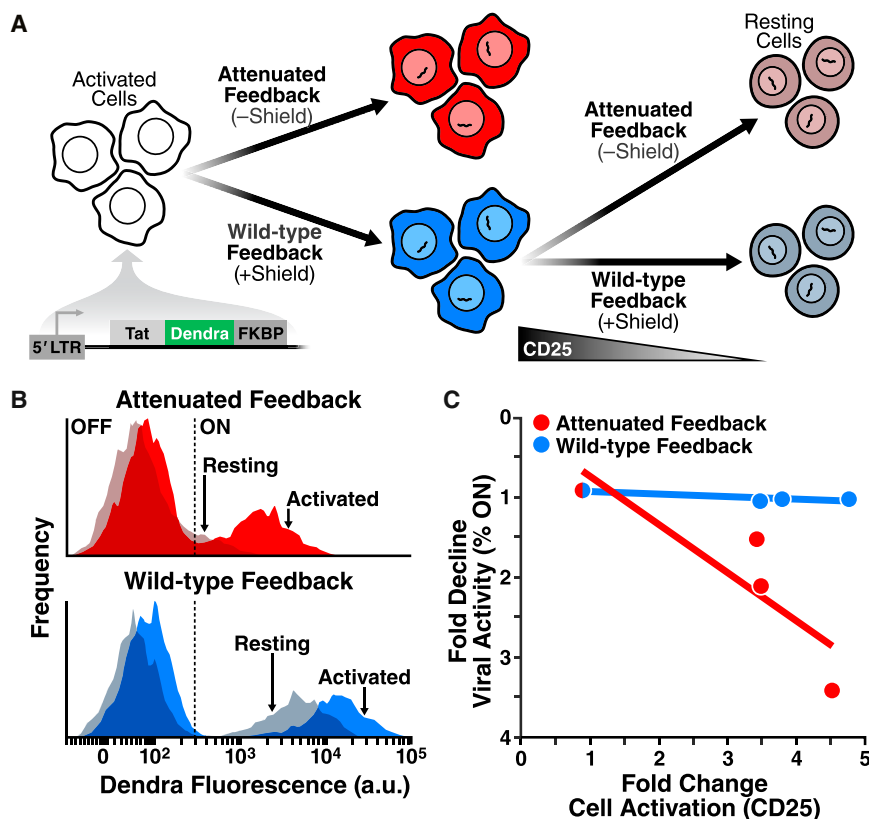


Figure 6. Tat Feedback Circuitry Is Sufficient to Autonomously Regulate Viral Expression during the Activated-to-Resting Transition in Primary T Cells

(A) Experiment schematic: Donor-derived primary CD4⁺ T lymphocytes were activated and infected with LTR-Tat-Dendra-FKBP in either the presence of Shield-1 (blue, wild-type feedback) or without Shield (red, attenuated feedback), and cells were allowed to relax back to resting (as measured by CD25 surface expression) in the presence/absence of Shield-1 (i.e., under wild-type/attenuated feedback).

(B) Flow cytometry analysis of viral expression (Dendra fluorescence) in primary CD4⁺ T lymphocytes during transition from activated to resting in absence of Shield-1 (attenuated feedback; top) or presence of Shield-1 (wild-type feedback; bottom); activated are lymphocytes shown as opaque histograms, and resting lymphocytes are shown as translucent histograms.

(C) Plot of the fold change in the number of active infections for varying cellular state (fold change cell activation as measured by CD25 surface expression; see also Figure S6). If feedback strength is wild-type (blue data points; blue trend line), the fold change in viral activity is uncorrelated with changing cell state. In the presence of attenuated feedback, the percentage of active infections is dependent on cell state. Each data point is normalized against the percent of active infections in the lowest cell-state activation data point.

Tat Induction Is >300% More Effective Than Cellular Activation for Reactivating Full-Length Latent HIV

To directly compare the effects of tuning viral circuitry to altering cellular-activation state, inducible Tet-Tat-Dendra cells were infected with Δ Tat virus in the presence of Dox or TNF α (Figure 5E). Modifying cellular activity with TNF α , in the absence of Tat induction, leads to a 1.5-fold change in the percentage of active infections (from 2% to 4% active infection), whereas Tat induction drastically increases, by >300%, the proportion of infections that are active (Figure 5E). Similar results were seen in reactivating latent cells post infection (Figure S5): inducible Tet-Tat-Dendra cells were infected with Δ Tat virus and 3 days post infection were treated with either Dox or standard cell-state modulators (as well as combination of the two). Tat induction through Dox was significantly more effective at reactivation than the cell-state modifiers. Thus, as seen with the minimal-synthetic circuits (Figure 4), perturbing viral circuitry provides substantially more potent reactivation of latency than targeting cell state alone.

Tat Circuitry Is Sufficient to Autonomously Regulate Viral Expression during the Activated-to-Resting Transition in Human Primary T Lymphocytes

As a final test, we directly examined the model prediction that Tat circuitry alone is sufficient to explain the resilience of HIV transcription to cellular silencing during cellular relaxation from activated to resting (Figure 3D). Activated primary CD4⁺ T cells were transduced with LTR-Tat-Dendra-FKBP virus and allowed to relax from an active to a resting-memory state while Tat pos-

itive-feedback strength was either maintained or attenuated by removing Shield-1 (Figure 6A).

When Tat positive feedback is attenuated (by absence of Shield-1) as lymphocytes relax from activated to memory, significant silencing of HIV gene expression occurs (Figure 6B, red histograms). However, when Tat positive-feedback strength is maintained at wild-type levels (via Shield-1 addition), only a slight shift in HIV gene expression occurs as lymphocytes transition from active to memory (Figure 6B, blue histograms). Quantifying the relaxation of cellular activation alongside viral latency reveals a remarkable relationship: if Tat feedback is attenuated, the cellular-activation state tightly controls entry to latency by significantly reducing the percentage of cells in active infection (Figure 6C, red); however, when Tat feedback is active (the case in Figure 2), the cellular activation state has no bearing on entrance into latency as the percentage of cells in active infection remains constant (Figure 6C, blue)—i.e., the intact feedback circuit allows viral gene expression to act completely independent of cellular-activation state. Thus, active Tat feedback appears to buffer HIV from global transcriptional silencing as primary lymphocytes transition from active to resting memory.

DISCUSSION

Beginning with observations that HIV gene expression is largely autonomous to cellular relaxation (Figure 2), computationally guided synthetic reconstruction revealed Tat positive feedback as the core mechanism underlying viral autonomy

(Figures 3–5). Strikingly, Tat feedback alone is sufficient to overcome cell-driven silencing of HIV transcription during cellular relaxation from active to resting in primary T cells (Figure 6). These findings are consistent with patient-cell latent-reactivation experiments showing that direct addition of Tat activates viral expression and reverses latency in resting CD4⁺ T cells without requiring cellular activation (Lassen et al., 2006; Lin et al., 2003). Thus, in patient cells, Tat-mediated positive feedback also appears to regulate latency independent of cell state.

The data herein cannot discount one variant of the cell-state hypothesis which proposes that latency is established when HIV infects relaxing cells which are at an activation level just above a first threshold required for HIV infection and integration but below a second threshold required to sustain active Tat expression and viral replication. However, there are difficulties with this hypothesis. While the presence of two thresholds is plausible, the second (Tat activation) threshold being higher than the first (infection) threshold is not consistent with existing data. For example, although global activation of primary CD4⁺ T cells is required for efficient infection, HIV can be reactivated from latency in primary cells without globally activating the cells (Xing et al., 2012). Similarly, the reactivation of HIV in resting T cells using Tat protein (Lassen et al., 2006; Lin et al., 2003) indicates that extremely low levels of cellular activation (i.e., in resting/quiescent cells) are still amenable to robust viral expression. Thus, since resting cells are at an activation level non-permissive to infection (Pan et al., 2013) but are sufficiently activated for Tat to function, the putative Tat-activation threshold is *lower* than the infection threshold and the two-threshold scenario appears unlikely.

If cellular relaxation does not lead to the establishment of HIV latency, how is HIV latency established? Previous studies demonstrated the intrinsic ability of the Tat positive-feedback circuit to rapidly and stochastically establish latency (Weinberger et al., 2005), consistent with recent primate studies showing that latency is rapidly established within the first 3 days of infection (Whitney et al., 2014) and with cell-culture models showing latency establishment immediately upon infection (Calvanese et al., 2013; Dahabieh et al., 2013). Given that resting CD4⁺ T lymphocytes are highly resistant to direct HIV infection (Pan et al., 2013), the rapid establishment of latency is difficult to reconcile with the cell-state epiphenomenon theory; productively infected cells live <2 days in vivo (Perelson et al., 1997), while the process of T cell transitioning from active to memory is a slow and low-probability process (Youngblood et al., 2013) occurring during and after vigorous expansion of effector lymphocytes that only begins weeks after infection (Kuroda et al., 1999). The alternate model examined here (Figure 3), wherein intrinsic (stochastic) viral circuitry autonomously regulates HIV latency, also provides a mechanistic basis for recent observations in patient cells (Ho et al., 2013), showing that: (1) a significant fraction of latent proviruses are not induced even if cells are reactivated from a resting-memory state, and (2) a second identical cellular stimulation (of already activated cells) induces additional latent proviruses to reactivate. These results indicate that viral reactivation is probabilistic. While particularly puzzling for the cellular-control hypothesis, probabi-

listic reactivation is consistent with HIV latency being regulated by an autonomous viral-encoded circuit influenced by stochastic gene-expression fluctuations, which provides rationale for targeting viral gene-expression circuitry to reactivate latent HIV (Dar et al., 2014).

To be completely clear, the viral-encoded latency model does not exclude a role for cellular state in regulating HIV proviral latency. In fact, the Tat-feedback model predicts that latency establishment is sharply reduced at higher cellular activation levels (Figure 3C) and that cellular activation probabilistically reactivates latent virus (Equation 12 in Extended Experimental Procedures). Experimentally, cellular activation clearly rescues attenuated feedback (Figure 6B). Similarly, the ability of Tat expression to reactivate latent virus independent of cellular activation (Figures 4 and 5) does not imply that in vivo latent reactivation occurs absent cellular activation. Rather, the results herein demonstrate—contrary to prevailing dogma—that there is also an underlying viral program that autonomously regulates proviral latency.

A viral-encoded latency program naturally raises questions on the evolutionary origin and function of HIV latency. While sensor-actuator circuitry would have been consistent with either the epiphenomenon hypothesis or evolutionary hardwiring, an autonomous regulatory circuit is invariably hardwired and must be selectively maintained—especially in a rapidly evolving virus under strong selection. So, how would latency be beneficial in the natural history of lentiviral infection? In a companion paper (Rouzine et al., 2015 [this issue of *Cell*]), we propose that latency may provide a fitness advantage by acting as a viral “bet-hedging” strategy to enhance net viral transmission probability. An associated aspect is the decision-making architecture behind latency: Tat positive feedback maintains strong expression levels robust to cellular perturbations, while large stochastic fluctuations exhibited by the LTR promoter enable the system to probabilistically switch (Dar et al., 2012). Notably, this architecture has been theoretically proposed to be an unreliable environmental sensor in fluctuating environments (Brandman et al., 2005), suggesting that HIV’s circuit architecture is precisely the *opposite* configuration that would be required for a reliable environmental sensor—a reliable sensor would respond faithfully to environmental changes—and similar stochastic positive-feedback circuitry has been proposed for autonomous decision making in other biological systems (Jilkine et al., 2011). Overall, viral evolution appears to have selected for circuitry that both maintains remarkable autonomy from environmental cues and simultaneously drives probabilistic on-off decision making.

EXPERIMENTAL PROCEDURES

Primary-Cell Isolation and Cell-Culture Conditions

Primary CD4⁺ T cells were isolated from peripheral blood obtained from Stanford Blood Bank (Palo Alto, CA) using RosetteSep Human CD4⁺ T Cell Enrichment Cocktail from STEMCELL Technologies and Ficoll as described (Terry et al., 2009). Once isolated, cells were either cultured as described (Terry et al., 2009) or frozen in 10% DMSO, 90% culture media at a density of 10⁷ per ml. For infections, primary CD4⁺ T cells were pre-activated for 2–3 days with α CD3/CD28 beads (Dynabeads, Life Technologies) as per manufacturer’s instructions. Cell activation was measured

by flow cytometry with anti-CD25-PE-conjugated antibody and anti-CD69-APC-conjugated antibody from BD Biosciences. Primary CD4⁺ T lymphocytes, Jurkat T Lymphocytes, and CEMs were all cultured in RPMI 1640 (supplemented with L-glutamine, 10% fetal bovine serum, and 1% penicillin-streptomycin) in a humidified environment at 37°C and 5% CO₂. Jurkats and CEM were maintained by passage between 2 × 10⁵ and 2 × 10⁶ cells/ml. Primary cell media was supplemented with 20 U/ml r-IL2 (Peprotech, 200-02).

Computational Modeling

A simplified two-state model of Tat positive feedback was constructed from experimental data of LTR toggling (Dar et al., 2014; Dar et al., 2012; Singh et al., 2010; Singh et al., 2012) and simulated using the Gillespie algorithm (Gillespie, 1977) to test how altering LTR basal transcription rate or Tat protein stability would affect the activity of the circuit. The chemical reaction scheme and parameters used are described in Table S1. The outputs from simulations are the different molecular species in arbitrary numbers. Stochastic simulations were run in Mathematica using the xSSA package (<http://www.wolfram.com/mathematica/> and <http://www.xlr8r.info/SSA/>). Initial conditions for all species were set to 0, except for LTR_{ON}, which was set to 1, and simulations were run to time = 200 (arbitrary time units); 500 simulation runs were conducted for each parameter set. See Extended Experimental Procedures for further details and explanation of simulations for the more complex model (Figure S2).

Recombinant Virus Production and Infections

Lentivirus was packaged in 293T cells and isolated as described (Dull et al., 1998; Weinberger et al., 2005). HIV-d2GFP (Jordan et al., 2003) was packaged with dual-tropic *env*-encoding plasmid pSVIII-92HT593.1 (NIH AIDS Reagents Program). Before infecting primary cells, activation beads were removed and cells were mixed with appropriate amount of virus (to get <10% infection) in 100 μl media and spinoculated at 32°C for 2 hr at 1,000 × g.

To generate the isoclonal populations with engineered viral circuits, lentivirus was added to Jurkat T Lymphocytes at a low MOI to ensure a single integrated copy of proviral DNA in infected cells. Cells were stimulated with tumor necrosis factor α (TNFα) and Shield-1 for 18 hr before sorting for Dendra-expressing cells. Isoclonal and polyclonal populations were created as described (Weinberger et al., 2005). Sorting and analysis of cells infected was performed on a FACSAria II. The same procedure was followed to create the LTR-Tat-Dendra and LTR-mCherry-IRES-Tat-FKBP cell lines. Inducible Tat cells were generated by transducing Jurkat cells with Tet-Tat-Dendra and SFFV-rTta lentivirus at high MOI. The cells were incubated in Dox for 24 hr and then FACS sorted for Dendra⁺ cells to create a polyclonal population. To create the Tet-Tat-Dendra + LTR-mCherry cells, the polyclonal population was infected with LTR-mCherry lentivirus at a low MOI. Before sorting for mCherry⁺ and Dendra⁺ cells, Dox was added at 500 ng/ml for 24 hr, and single cells were FACS sorted and expanded to isolate isoclonal populations. The same procedure was followed for the Tet-Tat-Dendra-FKBP + LTR-mCherry populations; however, 24 hr before the sort, 1 μM Shield-1 and 500 ng/ml Dox was added to the culture. All inducible Tat or control HIV infection experiments were performed by incubating 5 × 10⁵ CEM cells in the same titer of inducible Tat or the same titer of control HIV in the presence or absence of Shield-1 and taking a flow cytometry time point after 48 hr. Δ-Tat mCherry infections were carried out using 10⁵–10⁶ inducible Tat (Jurkat) cells in the presence or absence of 500 ng/ml doxycycline.

Flow Cytometry and Analysis

Flow cytometry data were collected on a BD FACSCalibur DxP8, BD LSR II, or HTFC Intellicyt for stably transduced lines and primary cells and on a BD FACSAria II for replication-competent virus assays and sorting. All flow cytometry experiments on replication-competent virus were performed in BSL3 conditions (safety information available upon request). Flow cytometry data were analyzed in FlowJo and using customized MATLAB code.

SUPPLEMENTAL INFORMATION

Supplemental Information includes Extended Experimental Procedures, six figures, and one table and can be found with this article online at <http://dx.doi.org/10.1016/j.cell.2015.02.009>.

AUTHOR CONTRIBUTIONS

B.S.R., A.P., and L.S.W. designed research and wrote the paper. B.S.R., A.P., and K.A. executed the experiments and analyzed the data. I.M.R., B.S.R., and L.S.W. performed mathematical analysis.

ACKNOWLEDGMENTS

We are grateful to M. Thompson, O. Weiner, J. Toettcher, J. Miranda, A. Weinberger, M. Ott, E. Verdin, A. Frankel, M. Simpson, and G. Süel for comments, helpful discussions, and providing reagents. B.S.R. was supported by an NSF graduate research fellowship (GRFP, grant 1144247). This work was supported by NIH award R01-AI109593 and, in part, by the Center for Synthetic and Systems Biology at UCSF (P50GM081879), the NIH Delaney CARE Collaboratory of AIDS Researchers for a Cure (U19AI096113), and UCSF-GIVI CFAR (P30AI027763 and S10RR028962-01). L.S.W. acknowledges support from NIH Director's New Innovator Award Program (DP2-OD006677), the Alfred P. Sloan Foundation, and the Pew Scholar's in the Biomedical Sciences.

Received: September 2, 2014

Revised: December 9, 2014

Accepted: February 5, 2015

Published: February 26, 2015

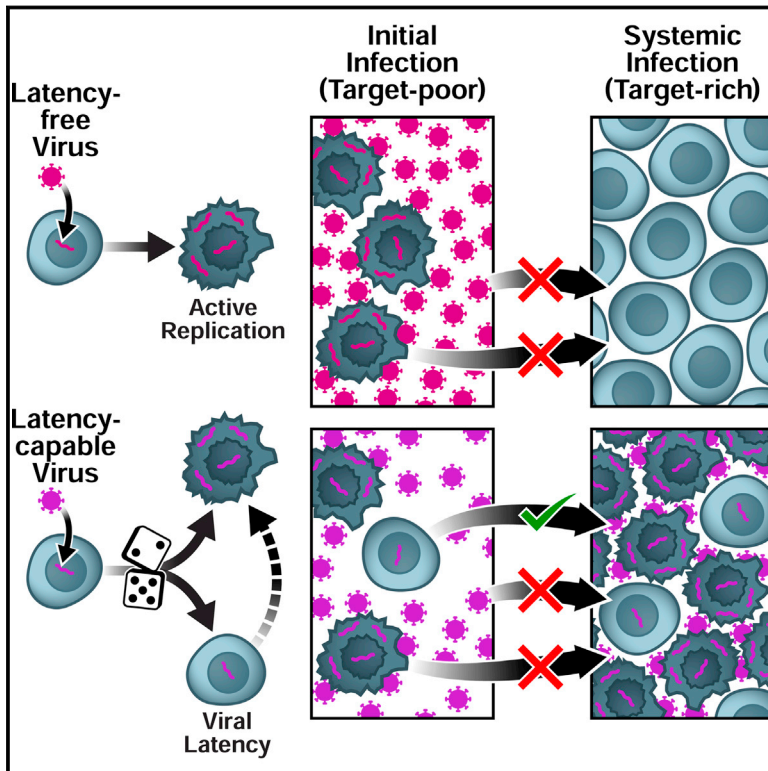
REFERENCES

- Arkin, A., Ross, J., and McAdams, H.H. (1998). Stochastic kinetic analysis of developmental pathway bifurcation in phage lambda-infected *Escherichia coli* cells. *Genetics* 149, 1633–1648.
- Banaszynski, L.A., Chen, L.C., Maynard-Smith, L.A., Ooi, A.G., and Wandless, T.J. (2006). A rapid, reversible, and tunable method to regulate protein function in living cells using synthetic small molecules. *Cell* 126, 995–1004.
- Brandman, O., Ferrell, J.E., Jr., Li, R., and Meyer, T. (2005). Interlinked fast and slow positive feedback loops drive reliable cell decisions. *Science* 310, 496–498.
- Bull, J.J., and Vogt, R.C. (1979). Temperature-dependent sex determination in turtles. *Science* 206, 1186–1188.
- Burnett, J.C., Miller-Jensen, K., Shah, P.S., Arkin, A.P., and Schaffer, D.V. (2009). Control of stochastic gene expression by host factors at the HIV promoter. *PLoS Pathog.* 5, e1000260.
- Calvanese, V., Chavez, L., Laurent, T., Ding, S., and Verdin, E. (2013). Dual-color HIV reporters trace a population of latently infected cells and enable their purification. *Virology* 446, 283–292.
- Coffin, J., and Swanstrom, R. (2013). HIV pathogenesis: dynamics and genetics of viral populations and infected cells. *Cold Spring Harb. Perspect. Med.* 3, a012526.
- Cohen, D. (1966). Optimizing reproduction in a randomly varying environment. *J. Theor. Biol.* 12, 119–129.
- Dahabieh, M.S., Ooms, M., Simon, V., and Sadowski, I. (2013). A doubly fluorescent HIV-1 reporter shows that the majority of integrated HIV-1 is latent shortly after infection. *J. Virol.* 87, 4716–4727.
- Dar, R.D., Razoooky, B.S., Singh, A., Trimeloni, T.V., McCollum, J.M., Cox, C.D., Simpson, M.L., and Weinberger, L.S. (2012). Transcriptional burst frequency and burst size are equally modulated across the human genome. *Proc. Natl. Acad. Sci. USA* 109, 17454–17459.
- Dar, R.D., Hosmane, N.N., Arkin, M.R., Siliciano, R.F., and Weinberger, L.S. (2014). Screening for noise in gene expression identifies drug synergies. *Science* 344, 1392–1396.

- Donahue, D.A., Kuhl, B.D., Sloan, R.D., and Wainberg, M.A. (2012). The viral protein Tat can inhibit the establishment of HIV-1 latency. *J. Virol.* 86, 3253–3263.
- Dull, T., Zufferey, R., Kelly, M., Mandel, R.J., Nguyen, M., Trono, D., and Naldini, L. (1998). A third-generation lentivirus vector with a conditional packaging system. *J. Virol.* 72, 8463–8471.
- Gillespie, D.T. (1977). Exact Stochastic Simulation of Coupled Chemical-Reactions. *J. Phys. Chem.* 81, 2340–2361.
- Gossen, M., and Bujard, H. (1992). Tight control of gene expression in mammalian cells by tetracycline-responsive promoters. *Proc. Natl. Acad. Sci. USA* 89, 5547–5551.
- Gurskaya, N.G., Verkhusa, V.V., Shcheglov, A.S., Staroverov, D.B., Chepurnykh, T.V., Fradkov, A.F., Lukyanov, S., and Lukyanov, K.A. (2006). Engineering of a monomeric green-to-red photoactivatable fluorescent protein induced by blue light. *Nat. Biotechnol.* 24, 461–465.
- Ho, Y.C., Shan, L., Hosmane, N.N., Wang, J., Laskey, S.B., Rosenbloom, D.I., Lai, J., Blankson, J.N., Siliciano, J.D., and Siliciano, R.F. (2013). Replication-competent noninduced proviruses in the latent reservoir increase barrier to HIV-1 cure. *Cell* 155, 540–551.
- Huang, L.M., Joshi, A., Willey, R., Orenstein, J., and Jeang, K.T. (1994). Human immunodeficiency viruses regulated by alternative trans-activators: genetic evidence for a novel non-transcriptional function of Tat in virion infectivity. *EMBO J.* 13, 2886–2896.
- Jeeninga, R.E., Westerhout, E.M., van Gerven, M.L., and Berkhout, B. (2008). HIV-1 latency in actively dividing human T cell lines. *Retrovirology* 5, 37.
- Jilkine, A., Angenent, S.B., Wu, L.F., and Altschuler, S.J. (2011). A density-dependent switch drives stochastic clustering and polarization of signaling molecules. *PLoS Comput. Biol.* 7, e1002271.
- Jordan, A., Defechereux, P., and Verdin, E. (2001). The site of HIV-1 integration in the human genome determines basal transcriptional activity and response to Tat transactivation. *EMBO J.* 20, 1726–1738.
- Jordan, A., Bisgrove, D., and Verdin, E. (2003). HIV reproducibly establishes a latent infection after acute infection of T cells in vitro. *EMBO J.* 22, 1868–1877.
- Karin, M., and Lin, A. (2002). NF-kappaB at the crossroads of life and death. *Nat. Immunol.* 3, 221–227.
- Karn, J. (2011). The molecular biology of HIV latency: breaking and restoring the Tat-dependent transcriptional circuit. *Curr. Opin. HIV AIDS* 6, 4–11.
- Kepler, T.B., and Elston, T.C. (2001). Stochasticity in transcriptional regulation: origins, consequences, and mathematical representations. *Biophys. J.* 81, 3116–3136.
- Knedler, J.W. (1947). *Masterworks of Science—Digests of 13 Great Classics* (Garden City, NY: Doubleday & Company).
- Kuroda, M.J., Schmitz, J.E., Charini, W.A., Nickerson, C.E., Lifton, M.A., Lord, C.I., Forman, M.A., and Letvin, N.L. (1999). Emergence of CTL coincides with clearance of virus during primary simian immunodeficiency virus infection in rhesus monkeys. *J. Immunol.* 162, 5127–5133.
- Lassen, K.G., Ramyar, K.X., Bailey, J.R., Zhou, Y., and Siliciano, R.F. (2006). Nuclear retention of multiply spliced HIV-1 RNA in resting CD4+ T cells. *PLoS Pathog.* 2, e68.
- Lin, X., Irwin, D., Kanazawa, S., Huang, L., Romeo, J., Yen, T.S., and Peterlin, B.M. (2003). Transcriptional profiles of latent human immunodeficiency virus in infected individuals: effects of Tat on the host and reservoir. *J. Virol.* 77, 8227–8236.
- Molle, D., Maiuri, P., Boireau, S., Bertrand, E., Knezevich, A., Marcello, A., and Basyuk, E. (2007). A real-time view of the TAR:Tat:P-TEFb complex at HIV-1 transcription sites. *Retrovirology* 4, 36.
- Pan, X., Baldauf, H.M., Keppler, O.T., and Fackler, O.T. (2013). Restrictions to HIV-1 replication in resting CD4+ T lymphocytes. *Cell Res.* 23, 876–885.
- Paulsson, J. (2004). Summing up the noise in gene networks. *Nature* 427, 415–418.
- Pazin, M.J., Sheridan, P.L., Cannon, K., Cao, Z., Keck, J.G., Kadonaga, J.T., and Jones, K.A. (1996). NF-kappa B-mediated chromatin reconfiguration and transcriptional activation of the HIV-1 enhancer in vitro. *Genes Dev.* 10, 37–49.
- Pearson, R., Kim, Y.K., Hokello, J., Lassen, K., Friedman, J., Tyagi, M., and Karn, J. (2008). Epigenetic silencing of human immunodeficiency virus (HIV) transcription by formation of restrictive chromatin structures at the viral long terminal repeat drives the progressive entry of HIV into latency. *J. Virol.* 82, 12291–12303.
- Perelson, A.S., Neumann, A.U., Markowitz, M., Leonard, J.M., and Ho, D.D. (1996). HIV-1 dynamics in vivo: virion clearance rate, infected cell life-span, and viral generation time. *Science* 271, 1582–1586.
- Perelson, A.S., Essunger, P., Cao, Y., Vesanen, M., Hurley, A., Saksela, K., Markowitz, M., and Ho, D.D. (1997). Decay characteristics of HIV-1-infected compartments during combination therapy. *Nature* 387, 188–191.
- Razooky, B.S., and Weinberger, L.S. (2011). Mapping the architecture of the HIV-1 Tat circuit: A decision-making circuit that lacks bistability and exploits stochastic noise. *Methods* 53, 68–77.
- Richman, D.D., Margolis, D.M., Delaney, M., Greene, W.C., Hazuda, D., and Pomerantz, R.J. (2009). The challenge of finding a cure for HIV infection. *Science* 323, 1304–1307.
- Rouzine, I., Weinberger, A.D., and Weinberger, L.S. (2015). An evolutionary role for HIV latency in enhancing viral transmission. *Cell* 160, this issue, 1002–1012.
- Siliciano, R.F., and Greene, W.C. (2011). HIV latency. *Cold Spring Harb. Perspect. Med.* 1, a007096.
- Singh, A., Razooky, B., Cox, C.D., Simpson, M.L., and Weinberger, L.S. (2010). Transcriptional bursting from the HIV-1 promoter is a significant source of stochastic noise in HIV-1 gene expression. *Biophys. J.* 98, L32–L34.
- Singh, A., Razooky, B.S., Dar, R.D., and Weinberger, L.S. (2012). Dynamics of protein noise can distinguish between alternate sources of gene-expression variability. *Mol. Syst. Biol.* 8, 607.
- St-Pierre, F., and Endy, D. (2008). Determination of cell fate selection during phage lambda infection. *Proc. Natl. Acad. Sci. USA* 105, 20705–20710.
- Terry, V.H., Johnston, I.C., and Spina, C.A. (2009). CD44 microbeads accelerate HIV-1 infection in T cells. *Virology* 388, 294–304.
- Tyagi, M., Pearson, R.J., and Karn, J. (2010). Establishment of HIV latency in primary CD4+ cells is due to epigenetic transcriptional silencing and P-TEFb restriction. *J. Virol.* 84, 6425–6437.
- Weinberger, L.S., and Shen, T. (2007). An HIV feedback resistor: auto-regulatory circuit deactivator and noise buffer. *PLoS Biol.* 5, e9.
- Weinberger, A.D., and Weinberger, L.S. (2013). Stochastic fate selection in HIV-infected patients. *Cell* 155, 497–499.
- Weinberger, L.S., Burnett, J.C., Toettcher, J.E., Arkin, A.P., and Schaffer, D.V. (2005). Stochastic gene expression in a lentiviral positive-feedback loop: HIV-1 Tat fluctuations drive phenotypic diversity. *Cell* 122, 169–182.
- Weinberger, L.S., Dar, R.D., and Simpson, M.L. (2008). Transient-mediated fate determination in a transcriptional circuit of HIV. *Nat. Genet.* 40, 466–470.
- Whitney, J.B., Hill, A.L., Sanisetty, S., Penaloza-MacMaster, P., Liu, J., Shetty, M., Parenteau, L., Cabral, C., Shields, J., Blackmore, S., et al. (2014). Rapid seeding of the viral reservoir prior to SIV viraemia in rhesus monkeys. *Nature* 512, 74–77.
- Xing, S., Bhat, S., Shroff, N.S., Zhang, H., Lopez, J.A., Margolick, J.B., Liu, J.O., and Siliciano, R.F. (2012). Novel structurally related compounds reactivate latent HIV-1 in a bcl-2-transduced primary CD4+ T cell model without inducing global T cell activation. *J. Antimicrob. Chemother.* 67, 398–403.
- Youngblood, B., Hale, J.S., and Ahmed, R. (2013). T-cell memory differentiation: insights from transcriptional signatures and epigenetics. *Immunology* 139, 277–284.
- Zeng, L., Skinner, S.O., Zong, C., Sippy, J., Feiss, M., and Golding, I. (2010). Decision making at a subcellular level determines the outcome of bacteriophage infection. *Cell* 141, 682–691.
- Zhang, L., Gurskaya, N.G., Merzlyak, E.M., Staroverov, D.B., Mudrik, N.N., Samarkina, O.N., Vinokurov, L.M., Lukyanov, S., and Lukyanov, K.A. (2007). Method for real-time monitoring of protein degradation at the single cell level. *Biotechniques* 42, 446, 448, 450.

An Evolutionary Role for HIV Latency in Enhancing Viral Transmission

Graphical Abstract



Authors

Igor M. Rouzine, Ariel D. Weinberger, Leor S. Weinberger

Correspondence

ariel.weinberger@wyss.harvard.edu (A.D.W.),
leor.weinberger@gladstone.ucsf.edu (L.S.W.)

In Brief

HIV latency allows the virus to evade eradication under modern treatment regimens. Now, it appears that there is an evolutionary advantage to latency as well. Latency may have remained hardwired into the HIV genome to enhance lentiviral transmission across the target-cell-poor mucosa.

Highlights

- Mathematical model proposes evolutionary basis for HIV latency
- Hardwired latency circuit enhances HIV transmission across target-cell-poor mucosa
- Predicted optimal latency rate for HIV transmission matches measured levels
- Model predictions are testable in primates by modulating latency rates or CD8 levels



An Evolutionary Role for HIV Latency in Enhancing Viral Transmission

Igor M. Rouzine,¹ Ariel D. Weinberger,^{2,*} and Leor S. Weinberger^{1,3,4,*}

¹Gladstone Institutes (Virology and Immunology), San Francisco, CA 94158, USA

²Wyss Institute for Biologically Inspired Engineering, Harvard University, Boston, MA 02115, USA

³Department of Biochemistry and Biophysics

⁴QB3, California Institute for Quantitative Biosciences

University of California, San Francisco, San Francisco, CA 94158, USA

*Correspondence: ariel.weinberger@wyss.harvard.edu (A.D.W.), leor.weinberger@gladstone.ucsf.edu (L.S.W.)

<http://dx.doi.org/10.1016/j.cell.2015.02.017>

SUMMARY

HIV latency is the chief obstacle to eradicating HIV but is widely believed to be an evolutionary accident providing no lentiviral fitness advantage. However, findings of latency being “hardwired” into HIV’s gene-regulatory circuitry appear inconsistent with latency being an evolutionary accident, given HIV’s rapid mutation rate. Here, we propose that latency is an evolutionary “bet-hedging” strategy whose frequency has been optimized to maximize lentiviral transmission by reducing viral extinction during mucosal infections. The model quantitatively fits the available patient data, matches observations of high-frequency latency establishment in cell culture and primates, and generates two counterintuitive but testable predictions. The first prediction is that conventional CD8-depletion experiments in SIV-infected macaques increase latent cells more than viremia. The second prediction is that strains engineered to have higher replicative fitness—via reduced latency—will exhibit lower infectivity in animal-model mucosal inoculations. Therapeutically, the theory predicts treatment approaches that may substantially enhance “activate-and-kill” HIV-cure strategies.

INTRODUCTION

HIV actively replicates in CD4⁺ T lymphocytes but can also enter a long-lived quiescent state termed proviral latency in memory CD4⁺ T cells (Chun et al., 1997a; Finzi et al., 1997). The population of latently infected cells is relatively small in patients (~1 in 10⁶ CD4⁺ T cells) and does not generate significant viral RNA (Pierson et al., 2000). However, latently infected cells provide a critical viral reservoir, which enables lentiviral persistence even during prolonged antiretroviral therapy (ART). Further, if patients interrupt ART, persisting latent viruses reactivate, driving HIV to pre-treatment viral loads within weeks (Richman et al., 2009). Consequently, latency is the chief barrier to a curative HIV therapy.

While latency enables HIV to avoid extinction during ART, the benefit of latency prior to the ART era—during the centuries of natural lentiviral infections—remains unclear. In fact, latency appears to have been deleterious prior to ART since latently infected cells produce no virus and decrease patient viral loads. Given latency’s reduction of lentiviral replicative fitness, the prevailing hypothesis is that latency is an evolutionary accident—an epiphenomenon that only results when lentiviruses infect CD4⁺ T cells that are transitioning from activated to quiescent memory states (Coffin and Swanstrom, 2013; Eisele and Siliciano, 2012; Han et al., 2007). Latency is therefore viewed to be an infrequent bystander effect that only occurs after a viral-driven adaptive immune response initiates and CD4⁺ T lymphocytes begin to form memory subsets. Yet, a recent study in *Rhesus macaques* indicates that latency reaches high levels within the first 3 days of infection (Whitney et al., 2014), which is prior to the generation of an SIV-specific adaptive immune response (Kuroda et al., 1999).

If latency were a non-beneficial viral trait or epiphenomenon, one would expect it to have been lost due to natural selection or genetic drift, given lentiviruses’ rapid evolutionary rates. Yet, a companion study (Razooky et al., 2015 [this issue of *Cell*]) demonstrates that the ability to establish latency is “hardwired” into HIV’s gene-regulatory circuitry. This study matches recent data showing that ~50% of cell-culture infections—in which adaptive immune responses are absent—result in lentiviral latency (Calvanese et al., 2013; Dahabieh et al., 2013). Further, HIV’s auto-regulatory Tat circuit appears optimized to amplify stochastic fluctuations in viral gene expression, producing fluctuations that are sufficient to induce a probabilistic switch to latency (Burnett et al., 2009; Weinberger et al., 2005; Weinberger et al., 2008). In general, stochastic expression noise is thought to be selected against and thus filtered out of regulatory circuits when not beneficial (Batada and Hurst, 2007; Fraser et al., 2004). The persistence of a hardwired latency circuit suggests an unknown selective advantage, which outweighs latency’s putative fitness cost of reducing long-term viral loads.

One possible selective benefit is that—by providing a long-lived viral reservoir—latency could enhance lentiviral survival during unfavorable environmental conditions. Similar “bet-hedging” hypotheses (Cohen, 1966) have been proposed for bacteriophage- λ lysogeny (Arkin et al., 1998) and bacterial persistence (Balaban, 2011). However, lentiviral latency would only provide a bet-hedging advantage if there were risks of viral extinction due

to environmental fluctuations. In reality, lentiviruses appear in little danger of population crashes, as they evade immune clearance and maintain high viral loads of $\sim 10^5$ particles/ml of blood plasma for years (and lentiviruses clearly did not evolve under pressure from antiretroviral drugs). Further, lentiviruses only infect a small percentage ($\sim 1\%$ – 2%) of available target cells, making target-cell fluctuations unimportant during chronic infection. Nevertheless, viral loads remain low during one phase of the lentiviral lifecycle: initial mucosal infection.

The probability of successful mucosal infection is low, with $<1\%$ of unprotected sex acts between HIV-discordant couples resulting in self-propagating systemic HIV infections (Fraser et al., 2007; Gray et al., 2001; Wawer et al., 2005). When successful infections do occur, they expand from single founder sequences (Kearney et al., 2009; Keele et al., 2008), indicating that only one variant in the transmitted quasispecies avoids extinction. Further, animal models of HIV capture a consistent ~ 6 day delay from experimental mucosal inoculation to self-propagating infection (Haase, 2011; Zhang et al., 1999), which implies that the first days of lentiviral infection provide conditions unsuitable for viral growth.

The unfavorable conditions of early lentiviral infections typically occur in the mucosa, where $>90\%$ of HIV infections initiate (Haase, 2011). HIV's evolutionary precursor in non-human primates (SIV) also spreads through mucosal transmission—via sexual activity or fighting with subsequent communal wound licking (Santiago et al., 2005). Mucosal challenge experiments in primates with large inoculations provide direct evidence that the mucosa are initially unfavorable to lentiviral growth: large inoculations of $\sim 10^9$ infectious units (by TCID₅₀) initially burn out within ~ 5 days (Miller et al., 2005). Quantitatively, each initially infected cell lives for ~ 1 day (Markowitz et al., 2003), so the number of actively infected cells after 5 days scales with $(R_0^{\text{muc}})^5$ —wherein R_0^{muc} is the basic reproductive ratio during early mucosal infection. Since actively infected cells crash within ~ 5 days (Miller et al., 2005), $(R_0^{\text{muc}})^5$ approaches 0, implying that $R_0^{\text{muc}} < 1$ during initial mucosal infection.

Here, we quantitatively test the hypothesis that latency provides a bet-hedging advantage that increases the probability of successful lentiviral transmission despite reducing viral loads during systemic infection (Figure 1A). The key point is that increasing the probability of latency (p_{lat}) increases the probability that each initially infected cell survives initial mucosal infection. Yet, increasing p_{lat} also decreases viral loads in systemically infected hosts, which reduces the inoculum transmitted to new hosts. With a higher per-cell survival rate but fewer initially infected cells, the question is whether latency's fitness benefits outweigh its costs—which would establish latency as an evolutionarily beneficial trait that is maintained by natural selection.

RESULTS AND DISCUSSION

Mathematical Models of Lentiviral Transmission and Rationale for Models

Three classes of mathematical models are developed to quantify the net impact of latency on lentiviral transmission (Figure S1). Each class of models generalizes the well-parameterized basic model of viral dynamics (Nowak and May, 2000) to include

both proviral latency and the conditions of early mucosal infection (i.e., $R_0^{\text{muc}} < 1$) during which latency may be critical (Experimental Procedures).

The first class of models tracks initial lentiviral infection in the mucosa alone (Extended Experimental Procedures, Section A). Given the small numbers of infected cells during initial mucosal infection, the established model of mucosal infection is stochastic (Pearson et al., 2011). We analyze this experimentally parameterized stochastic model—and a deterministic approximation to this model—to quantify how the probability of viral extinction in the mucosa depends on the probability of latency (p_{lat}).

The second class of models extends the single-compartment model into a two-compartment model (Figure 1B) that tracks both initial infection in the mucosa and systemic infection in the lymphoid tissue (Extended Experimental Procedures, Section B). Importantly, the initial and systemic infection model compartments only differ in a single experimentally measured parameter: R_0 (Figure 1B and Table S1). Collectively, the models predict an optimal value of p_{lat} ($p_{\text{lat}}^{\text{opt}} = 0.5$) that matches latency frequencies measured in cell culture (Calvanese et al., 2013; Dahabieh et al., 2013) and is consistent with latency levels measured in mucosal primate infections (Whitney et al., 2014). However, the large value of p_{lat} does not match the low frequencies of latency observed in chronically infected patients (Chun et al., 1997b; Ho et al., 2013).

The third class of models incorporates a canonical immune response (Nowak and May, 2000) into the two-compartment model (Extended Experimental Procedures, Section C)—since a key difference between cell-culture models and chronic infection is the presence of an adaptive immune response. Each immune parameter added is either tied to a distinct patient-measured value or has been measured previously in the literature (Table S2). With no added free parameters, the immune model fits all available patient data and predicts the same robust $p_{\text{lat}}^{\text{opt}}$ value.

Latency's Net Evolutionary Impact Is the Product of Its Impact on Both Initial Infection and Systemic Infection

To calculate the optimal p_{lat} value, the two-compartment models track latency's net evolutionary impact across both mucosal and systemic infections. While the nonlinear models are complex, we decouple latency's net impact on viral transmission into a product of two factors: (1) the average initial inoculum of infected cells per mucosal inoculation (I_0), and (2) the probability that an initially infected cell establishes systemic infection (p_{estab}) (Figure 1A). This product can be derived analytically when the number of infected cells is Poisson distributed and when each infected cell lineage is statistically independent. Under these two assumptions, the probability of lentiviral transmission per-mucosal inoculation ($p_{\text{transmission}}$) reduces to:

$$p_{\text{transmission}} = 1 - e^{-p_{\text{estab}} I_0} \approx p_{\text{estab}} I_0 \quad [1]$$

The equality in Equation [1] is a direct calculation of the Poisson probability that at least one infected cell in the inoculum I_0 establishes systemic infection. Critically, $p_{\text{transmission}} < 10^{-2}$ since $< 1\%$ of lentiviral infections result in self-propagating infections (Gray et al., 2001; Wawer et al., 2005). Given the equality, $p_{\text{transmission}} < 10^{-2}$ immediately implies that $p_{\text{estab}} I_0 < \sim 10^{-2}$.

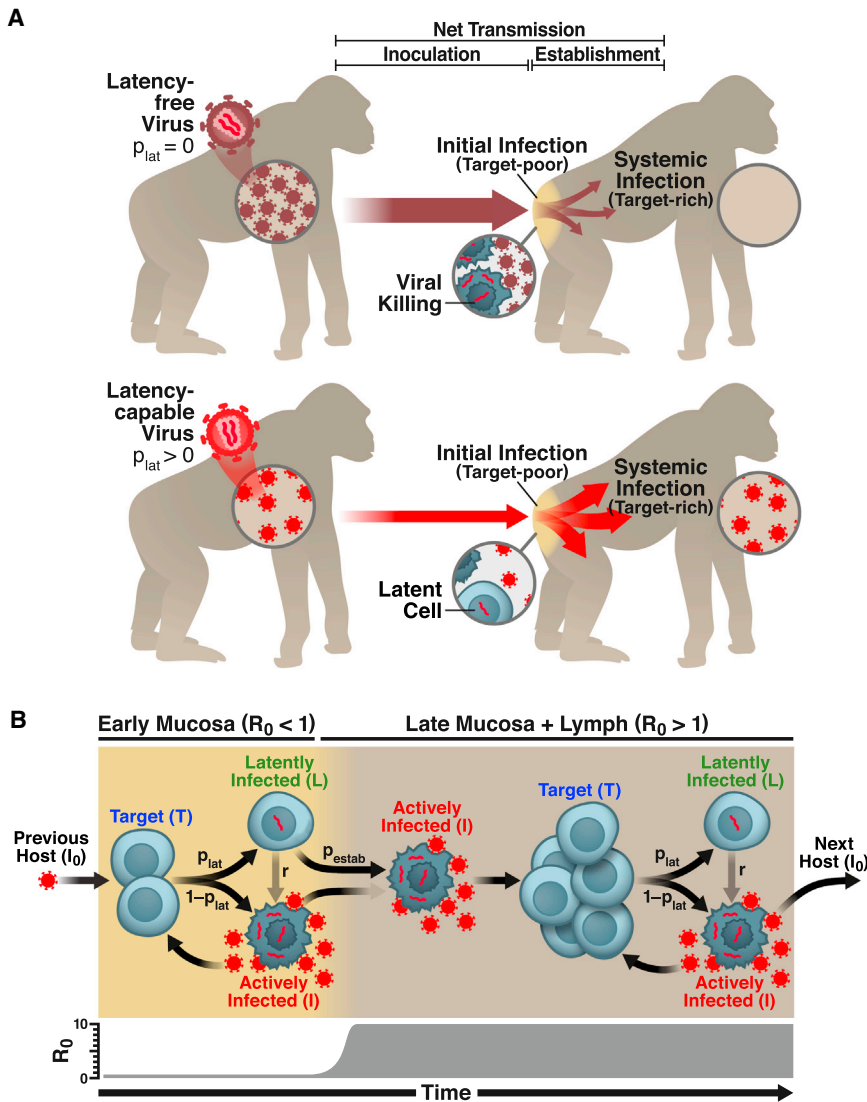


Figure 1. HIV Latency as a Bet-Hedging Strategy for Maximizing Viral Transmission

(A) Schematic of the lentiviral transmission process. Lentiviral transmission is illustrated as a two-compartment process, beginning with viral inoculation in the mucosa and progressing—in some cases—to systemic infection in the lymphoid tissue, where $>98\%$ of CD4^+ T cells reside (Murphy, 2011). The parameter p_{lat} reflects the probability that an HIV-infected cell enters latency. An HIV strain incapable of entering latency ($p_{\text{lat}} = 0$) would generate increased viral loads during systemic infection, transferring more virions to new hosts. However, the latency-incapable virions would rapidly destroy the small CD4^+ T cell population initially present in the mucosa of the new host—reducing the probability of systemic infection (upper). In contrast, an HIV strain capable of entering latency ($p_{\text{lat}} > 0$) would generate lower viral loads during systemic infection, transferring fewer virions to new hosts. Yet, the relatively few transferred virions would not destroy all mucosal target cells. By entering long-lived latency in some mucosal cells, the latency-capable strain would increase its probability of surviving initial infection to establish systemic infection (lower).

(B) Schematic of the two-compartment model of lentiviral transmission. The two major processes controlling the probability of lentiviral transmission ($p_{\text{transmission}}$) are: (1) the inoculum of infected cells (I_0) and (2) the probability that an infected cell in the inoculum survives initial infection to establish systemic infection (p_{estab}). (Right to left) HIV enters a host mucosal site, but due to the small number of permissive target cells in the early mucosa (prior to day 6), $R_0 < 1$. To successfully establish systemic infection, the virus must avoid extinction until $R_0 > 1$. Critically, the likelihood of an actively infected cell or a free viral particle surviving until day 6 to initiate systemic infection is negligible since virus-producing cells die within 40 hr of infection and viral progeny are cleared from the system ~ 100 -fold more rapidly. In contrast, latently infected cells

are long-lived and can reactivate once $R_0 > 1$ to initiate systemic viral expansion. Therefore, despite reducing long-term viral loads, latency may increase $p_{\text{transmission}}$ by increasing viral survival during initial infection. This would make latency evolutionarily beneficial at the population scale.

See also Figure S1.

Having used the equality to establish that $p_{\text{estab}} I_0 < \sim 10^{-2}$, we can discard the quadratic and higher-order terms in the Taylor Series expansion of $e^{-p_{\text{estab}} I_0}$ with negligible impact. This leads to the subsequent approximation (i.e., linearization) in Equation [1]: $p_{\text{transmission}} \approx p_{\text{estab}} I_0$.

Given Equation [1], the overall goal of determining whether latency's benefits outweigh its costs reduces to quantifying latency's impact on p_{estab} and I_0 .

Latency Increases the Probability that an Initially Infected Cell Survives Mucosal Infection and Establishes Systemic Infection

To quantify latency's impact on p_{estab} , we begin by tracking lentiviral survival during mucosal infection alone. As noted above, the first 5 days of mucosal infection are characterized by a

lack of detectable actively infected cells (Li et al., 2005; Miller et al., 2005), indicating that R_0 in the mucosa (R_0^{muc}) is initially < 1 (Extended Experimental Procedures, Section D). $R_0^{\text{muc}} < 1$ is also consistent with the infrequency of successful mucosal transmissions ($p_{\text{transmission}} < 0.01$) and the ~ 6 -day delay before systemic infection when lentiviral infections do establish (Miller et al., 2005).

Both deterministic differential equations models (Figure 2A) and stochastic Monte-Carlo models (Figures S2A and S2B) capture the fitness advantage of latency in the mucosa. Model simulations are performed with $R_0 < 1$ and an inoculated dose of virus that results in a few dozen initially infected cells, matching animal mucosal experiments (Haase, 2011; Miller et al., 2005; Zhang et al., 1999). The quantitative models show that—in the absence of latency—all virions and infected cells are driven

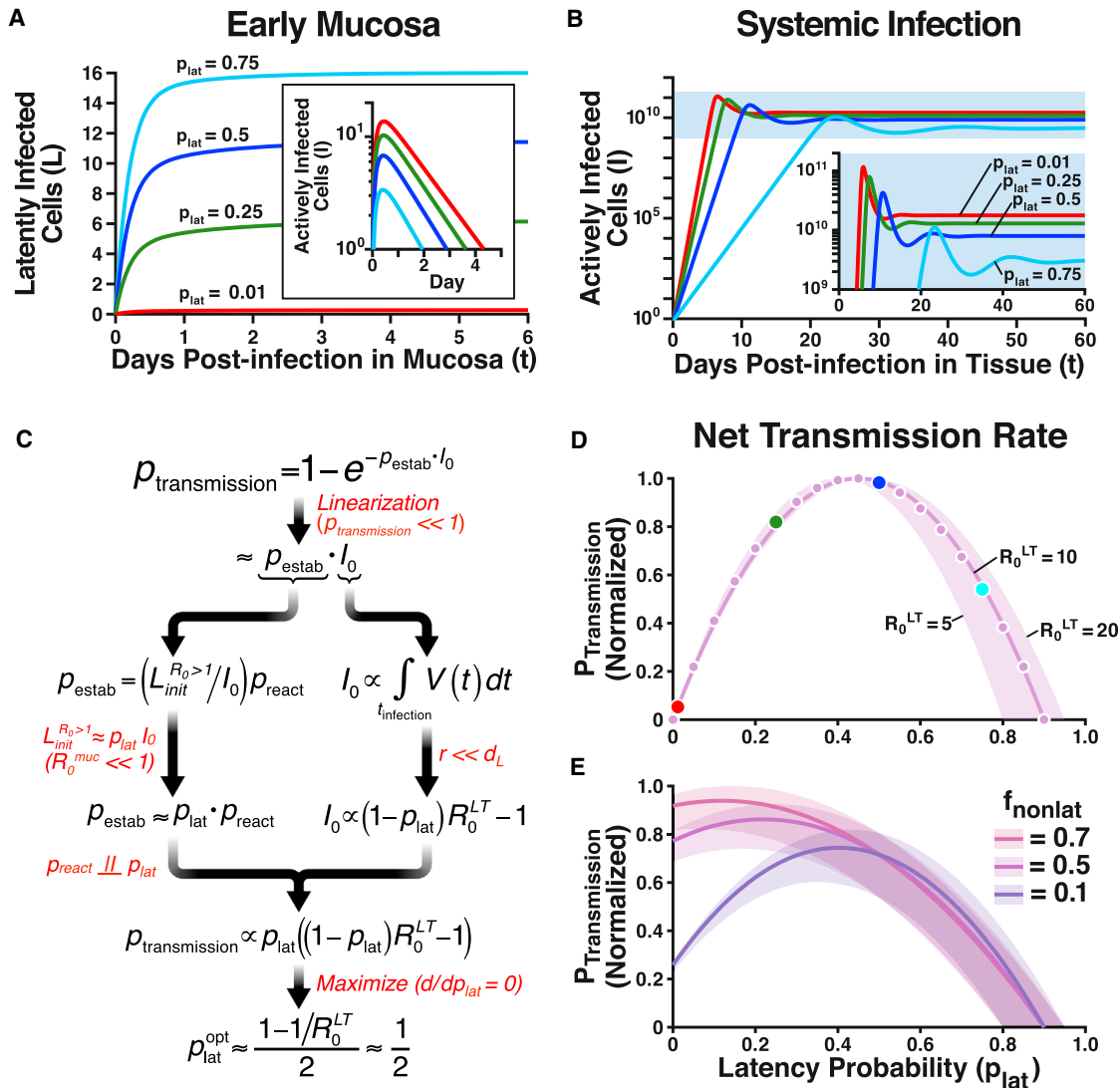


Figure 2. An Evolutionary Optimum for Latency

(A) Numerical solutions to Equation [6] showing the dynamics of latently infected cells in early mucosal infection ($R_0^{\text{muc}} = 0.25$). As p_{lat} increases, the number of surviving latently infected cells increases. (Inset) The dynamics of actively infected cells in early mucosal infection showing that as p_{lat} increases, actively infected cells reach extinction more rapidly.

(B) In systemic infection, ($R_0^{LT} = 10$), increases in p_{lat} decrease the virus load (and, therefore, the viral dose transmitted to the next host). Dynamics in (A and B) are calculated numerically from Equation [6], using the parameters in Table S1 ($r = 0$).

(C) Schematic flowchart of the derivation of the (optimal) latency probability $p_{\text{lat}}^{\text{opt}}$ that maximizes $p_{\text{transmission}}$. Red text indicates key assumptions made at each step of the derivation. For example, $R_0^{\text{muc}} \ll 1$ implies that the vast majority of latently infected cells during initial infection are produced in the first generation, leading to the approximation $L_{\text{init}}^{R_0 > 1} \approx p_{\text{lat}} I_0$. The results of the analytic derivation quantify the tradeoff of latency: increasing p_{lat} linearly increases p_{estab} but decreases I_0 by the factor $(1 - p_{\text{lat}})$. Since this tradeoff is almost equally balanced, the optimal latency probability, $p_{\text{lat}}^{\text{opt}}$, approximately equals 0.5.

(D) Normalized probability of host-to-host transmission ($p_{\text{transmission}}$) as a function of p_{lat} . Results shown are obtained either analytically, from Equation [5] (magenta line), or numerically using the plateau levels of actively infected cells (I) and latently infected cells (L) simulated in A and B (magenta dots). As in C, the probability of transmission is maximized when $p_{\text{lat}} \sim 0.5$.

(E) Normalized probability of host-to-host transmission when systemic infections emerge from non-latent routes (e.g., dendritic cells) with probability $f_{\text{nonlat}} > 0$ (Equations [S12 and S13]). The maximum probability of transmission occurs at slightly lower p_{lat} values, but $p_{\text{lat}}^{\text{opt}}$ is still large.

See also Figure S2.

extinct in the first 5 days of mucosal infection (Figures 2A, inset, and S2A). In contrast, low levels of latency enable viral survival (Figures 2A and S2B). To test the robustness of these predictions across all $R_0 < 1$ and $I_0 < 100$, a continuous-time branching-pro-

cess model was developed (Grimmett and Stirzaker, 1992). The branching-process model (Extended Experimental Procedures, Section A) directly computes the viral extinction probability as a function of time, providing an efficient alternative to averaging

thousands of Monte-Carlo simulations for each R_0 and I_0 . In the absence of latency, the viral extinction probability approaches 1 by day 5 of mucosal infection, except in the small slice when $R_0 \approx 1$ (Figures S2C and S2D)—which does not match the levels of R_0 inferred from animal mucosal challenge experiments (Miller et al., 2005).

For completeness, the surviving number of mucosally infected cells was directly computed using a Wright-Fisher model (Hartl and Clark, 2007; Extended Experimental Procedures, Section A). The Wright-Fisher simulations demonstrate that the surviving number of mucosally infected cells increases approximately linearly with p_{lat} for each I_0 (Figures S2E–S2G). This linear dependence can also be derived analytically. Given that $R_0^{\text{muc}} < 1$ during initial mucosal infection, the majority of latently infected cells are produced in the first generation of infection (Extended Experimental Procedures, Section A). Since these cells are unlikely to reactivate during the short duration of initial infection, the number of latently infected cells that survive mucosal infection is $\approx p_{\text{lat}} I_0$, the latent fraction of the inoculum. Thus, both simulations and analytics indicate that increasing p_{lat} approximately linearly increases the number of infected cells that survive initial mucosal infection.

Given that latency appears to increase viral survival in the early mucosa, we next tested whether latency increases the probability of systemic infection, which mainly occurs in the lymphoid tissue where >98% of CD4⁺ T cells reside (Murphy, 2011). To do so, the Wright-Fisher model was extended into a two-compartment model that directly captures the two typical stages of lentiviral infection: early mucosal infection and systemic (lymphoid) infection (Extended Experimental Procedures, Section B). Only a single parameter value is assumed to differ between the early mucosal and systemic infection compartments. While R_0^{muc} is parameterized to be <1, R_0 during systemic infection in the lymphoid tissue (R_0^{LT}) is set to 10 to match its value in chronically infected patients (Nowak and May, 2000).

The two-compartment model fits the available human and animal data of early infections, showing that: (1) only a small fraction of mucosal infections result in systemic infections (Fraser et al., 2007), (2) successful systemic infections emerge after ~5–7 days (Haase, 2011), and (3) systemic infections initiate from single “founder” infected cells (Kearney et al., 2009; Keele et al., 2008). More importantly, the two-compartment model directly shows that latency increases the probability (p_{estab}) of systemic infection—with p_{estab} maximized when $p_{\text{lat}} > 0.6$ (Figure S2H; Extended Experimental Procedures, Section E).

Latency Decreases the Inoculum in a New Host

While increasing p_{lat} increases the probability of systemic lymphoid infection for any given inoculum of initially infected cells (I_0), the probability of lentiviral infection also depends on I_0 itself. Critically, I_0 is proportional to the viral load of the transmitting patient (Extended Experimental Procedures, Equation S4). Thus, we can quantify latency’s impact on I_0 by measuring latency’s impact on viral loads in systemically infected patients.

To track latency’s effect on systemic viral loads, we simulated the deterministic model in the lymphoid compartment alone (i.e., $R_0 = 10$). Initial mucosal infection was not tracked in these simu-

lations because of the data showing that systemic infections emerge from single “founder” viruses independent of the inoculum (Kearney et al., 2009; Keele et al., 2008). These data indicate that mucosal dynamics affect the probability of systemic infection, but not the level once established. Thus, we assumed the existence of a single founder infected cell and solved Equation [6] numerically. Assuming successful systemic establishment, the systemic infection model shows that increasing p_{lat} decreases long-term viral loads (Figure 2B). Consequently, increasing the frequency of latency (p_{lat}) decreases infection inocula (I_0) at the population scale.

The Evolutionarily Optimal Probability of Latency Is ~0.5

Given Equation [1], if latency’s benefit to p_{estab} exceeds its cost to I_0 , then latency increases the probability of lentiviral transmission ($p_{\text{transmission}}$). Mathematically, this net evolutionary benefit of latency can only occur if the (evolutionarily optimal) value of p_{lat} that maximizes $p_{\text{transmission}}$ is greater than 0. Here, we test whether the maximizing value of p_{lat} is greater than 0, directly quantifying latency’s net evolutionary benefit.

We first derive p_{estab} as a function of p_{lat} . After initial mucosal infection, only latently infected cells persist, with the number of surviving latently infected cells defined to be $L_{\text{init}}^{R_0 > 1}$. As noted above, due to $R_0^{\text{muc}} < 1$, the majority of mucosal latent infections emerge in the first generation of infection, making $L_{\text{init}}^{R_0 > 1} \approx p_{\text{lat}} I_0$ (Figures 2A, S2F, and S2G). At least one of these surviving infected cells must be reactivated (with probability p_{react}) to establish systemic infection. Thus, the *per-inoculum* probability of establishing systemic infection is:

$$p_{\text{estab}} = \left(\frac{L_{\text{init}}^{R_0 > 1}}{I_0} \right) p_{\text{react}} \approx p_{\text{lat}} p_{\text{react}} \quad [2]$$

Equation [2] emerges from the result that only latently infected cells survive initial infection in the mucosa (Figures 2A and S2A–S2E). To demonstrate robustness, below we introduce a “leakage” probability ($f_{\text{nonlatent}}$) that reflects the fraction of systemic infections that are established by non-latent cells—including Langerhans dendritic cells, actively infected cells, and free virions.

We next solve for I_0 as a function of p_{lat} . As noted above, the average infectious dose (i.e., I_0) that can be transmitted to a new individual is directly proportional to the time integral of the viral load— $\int V(t)dt$, Equation [S4]—over the duration of systemic infection (Nowak and May, 2000). Analytically solving this time integral yields (Extended Experimental Procedures, Section B):

$$I_0 \approx \text{const}(p_{\text{lat}}) [(1 - p_{\text{lat}}) R_0^{\text{LT}} - 1] \quad [3]$$

The constant term in Equation [3] only implies constant in p_{lat} —it may depend on other parameters. Further, Equation [3] is solved under the assumption that latently infected cells rarely reactivate prior to cell death (i.e., $r < d_{\text{L}}$ in Table S1). This conservative assumption reduces the optimal level of latency by presuming that latently infected cells generally die before contributing to viral loads. Given this maximal fitness cost, latency reduces the reproductive ratio during systemic infection, R_0^{LT} , by the factor $(1 - p_{\text{lat}})$.

By combining Equations [1–3], $p_{\text{transmission}}$ emerges as a function of p_{lat} (Figure 2C):

$$p_{\text{transmission}} \approx p_{\text{estab}} I_0 \approx \text{const}(p_{\text{lat}}) p_{\text{react}} p_{\text{lat}} [(1 - p_{\text{lat}}) R_0^{\text{LT}} - 1] \quad [4]$$

Equation [4] shows that, for each value of R_0^{LT} , the probability of viral transmission has an optimum at a specific p_{lat} . To analytically derive this optimum, we make the simplifying assumption that p_{react} is constant in p_{lat} . This makes $p_{\text{transmission}} \propto p_{\text{lat}} [(1 - p_{\text{lat}}) R_0^{\text{LT}} - 1]$. Differentiating the simplified transmission probability with respect to p_{lat} yields the following optimal probability of latency, denoted $p_{\text{lat}}^{\text{opt}}$:

$$p_{\text{lat}}^{\text{opt}} \approx \frac{1 - (1/R_0^{\text{LT}})}{2} \quad [5]$$

Strikingly, for a typical value of $R_0^{\text{LT}} \sim 10$ (Nowak and May, 2000), $p_{\text{lat}}^{\text{opt}} \approx 0.5$ is the probability of latency that maximizes lentiviral transmission (Figure 2C).

In agreement with these analytic derivations, numerical solutions also show that $p_{\text{transmission}}$ has an optimum at $p_{\text{lat}} \approx 0.5$ (Figure 2D). The numerical simulations are generated by directly calculating $\int V(t)dt$ in model runs, rather than approximating it via Equation [3]. Sensitivity analyses show that this optimum at $p_{\text{lat}} \approx 0.5$ exists across the entire observed range of R_0^{LT} values (Figure 2D).

Large Optimal Latency Probability Is Robust to Changes in Model Assumptions

The main prediction of a large $p_{\text{lat}}^{\text{opt}}$ value remains valid even if one removes key mathematical assumptions. In particular, the two-compartment Wright-Fisher model (Extended Experimental Procedures, Section B) inverts the assumption that p_{react} is constant in p_{lat} , allowing p_{react} to strongly decrease in p_{lat} . Even in this extreme scenario—in which latency has a substantial fitness cost beyond its reduction of viral loads during systemic infection— $p_{\text{lat}}^{\text{opt}} > 1/3$ (Figure S2I). Similarly, the large $p_{\text{lat}}^{\text{opt}}$ value remains valid when one relaxes the assumption that only latently infected cells seed systemic infections. To show this, we analytically re-calculated $p_{\text{lat}}^{\text{opt}}$ when a fraction ($f_{\text{nonlatent}}$) of successful infections are established via non-latent routes (Extended Experimental Procedures, Section E). Even if 80% of lentiviral transmissions are established via non-latent routes, $p_{\text{lat}}^{\text{opt}} = 0.1$. More generally, as long as $f_{\text{nonlatent}}$ is less than 100%, latency remains evolutionarily beneficial (Figures 2E and S2J).

Strikingly, relaxing other model assumptions increases the large $p_{\text{lat}}^{\text{opt}}$ value. For example, relaxing the assumption that latently infected cells die prior to reactivation (i.e., $r < d_l$) reduces the cost of latency during systemic infection and therefore increases the optimal latency probability. In fact, if $r \geq d_l$, $p_{\text{lat}}^{\text{opt}} = 1$ (Extended Experimental Procedures, Section E). Further, if lentiviral transmissibility saturates at high viral loads (Fraser et al., 2007)—so that latency's decrease of steady-state viral loads does not decrease I_0 —then $p_{\text{lat}}^{\text{opt}}$ would again equal 1, due to the absence of a cost to latency (Extended Experimental Procedures, Section E).

Simplified Two-Compartment Model Fits the High Frequencies of Latency Measured in Experimental Models

The predicted value of $p_{\text{lat}}^{\text{opt}} \sim 0.5$ matches the latency frequencies of 50% (Dahabieh et al., 2013) or higher (Calvanese et al., 2013) measured in cell culture. $p_{\text{lat}}^{\text{opt}} \sim 0.5$ is also consistent with a recent in vivo study in *Rhesus macaques*, in which a large reservoir of latently infected cells is documented on day 3 of mucosal infection (Whitney et al., 2014). However, $p_{\text{lat}}^{\text{opt}} \sim 0.5$ is inconsistent with the low latency frequencies measured in chronically infected patients. Only 1 in 10^6 – 10^7 patient CD4⁺ T cells appear to be latently infected (Chun et al., 1997a; Sedaghat et al., 2007). This has led to estimates of $p_{\text{lat}} \sim 10^{-5}$ – 10^{-4} (Rong and Perelson, 2009a; Sedaghat et al., 2007). While more recent studies indicate that the latency frequency in patient cells is ~ 60 -fold higher (Ho et al., 2013), this still leaves $p_{\text{lat}} < 0.5$ during chronic infection. Below, we show that the dichotomy between latency's high frequency in early infection and cell culture and latency's low frequency in chronic infection can be explained by the onset of the adaptive immune response.

Mathematical Models Incorporating the Immune Response Are Required to Explain the Divergent Latency Frequencies between Experimental Models and Patients

Unlike early mucosal infections or cell-culture infections, chronic lentiviral infections contain an HIV-specific adaptive immune response (Turnbull et al., 2009). Previous work has shown that this adaptive immune response must be incorporated into the basic model of viral dynamics (De Boer and Perelson, 1998; Nowak and May, 2000) to fit the 2–3 log drop in viral loads between the viral peak during acute infection and the viral set point established during chronic infection (Stafford et al., 2000). We hypothesized that incorporating a canonical adaptive immune response (De Boer and Perelson, 1998; Nowak and May, 2000) would also be necessary to observe the reduced level of latently infected cells documented during chronic infection.

A substantial body of literature suggests that the model assumptions that p_{lat} and r are constant must be relaxed to account for the adaptive immune response. In particular, the activation levels of CD4⁺ T cells appear to increase during chronic infection in vivo, as is measured by the expression levels of three activation markers (Li et al., 2005) and the increased turnover rates of CD4⁺ T cells (Mohri et al., 1998). While the exact mechanism is unknown, one potential driver of CD4⁺ T cell activation is the body's homeostatic response to the depletion of CD4⁺ T cells during acute infection (Mohri et al., 1998). Another potential mechanism is CD8⁺ T cells' secreting activating cytokines such as TNF- α (Murphy, 2011). Whatever the mechanism, cellular activation factors sharply decrease p_{lat} and sharply activate HIV transcription (Calvanese et al., 2013; Chun et al., 1998; Siliciano and Greene, 2011), for example, by accumulating transcription factors (e.g., NF- κ B) that activate the HIV LTR promoter. Further, in the companion study (Razooky et al., 2015), mathematical modeling shows that cellular activation levels bias HIV circuit output (i.e., p_{lat} and r), even though latency is hardwired into the circuit.

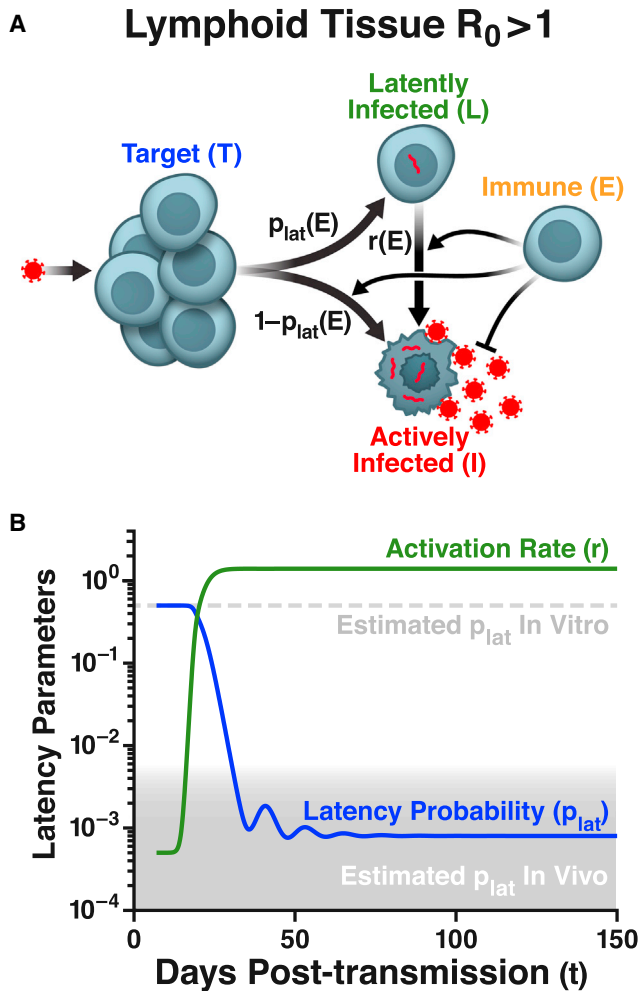


Figure 3. Incorporating the Immune Response Explains the Divergent HIV-Latency Frequencies between Experimental Models and Patients

(A) Extended model of systemic HIV infection, which includes CD8⁺ T cells (E) that kill actively infected cells (or suppress viral replication) and activate latently infected cells (Equations [S9] and [S10]).

(B) The latency probability (p_{lat}) and reactivation rate (r) change dramatically around the time of the viremia peak due to the immune response (e.g., due to bystander cytokine activation by immune cells, Equation [S10]). Inclusion of immune cells into the model is capable of interpreting the low incidence of latently infected cells in chronically infected patients.

Since an adaptive immune response is associated with an increase in CD4⁺ T cell activation levels (Li et al., 2005) that reduces p_{lat} and increases r (Calvanese et al., 2013; Chun et al., 1998; Siliciano and Greene, 2011), we hypothesized that the adaptive-immune response could be responsible for the reduced p_{lat} levels in chronically infected patients (Figure 3A). This hypothesis was quantitatively tested by allowing p_{lat} and r to vary as functions of the effector CD8⁺ T cell concentration, $E[t]$ (Extended Experimental Procedures, Section C). Before the initiation of the adaptive-immune response (i.e., before chronic infection), the model naturally generates high latency probabilities of ~ 0.5 and low reactivation rates, as in the simplified

models above. However, after the viremia peak, cellular activation (Li et al., 2005) and cell death (Doitsch et al., 2010) become substantial, increasing $r[E[t]]$ to high levels and decreasing $p_{\text{lat}}[E[t]]$ to low levels (Figure 3B). As a result, the immune model mechanistically explains the divergent latency frequencies measured between experimental models (cell culture and non-human primates) and chronically infected patients (Figure 3B).

Models Incorporating the Immune Response Fit Available Patient Data while Retaining the Robust Optimal Latency Prediction

While the immune-response model interprets the low levels of p_{lat} measured during chronic infection, validation against all available patient data is a critical test of the model. Thus, we tested whether the model could recapitulate extant patient data on: (1) viral loads before ART (Fraser et al., 2007), (2) effector T cell concentrations before ART (Turnbull et al., 2009), (3) latently infected cells before ART (Chun et al., 1997b), and (4) latently infected cells after ART (Finzi et al., 1999). Strikingly, the extended immune-response model is able to fit these four data plateaus (Figure 4A), using established parameter estimates (Table S2). In particular, the immune-response model reproduces the depressed latent reservoir of $\sim 10^6$ cells measured in chronically infected patients. Further, the model captures the ~ 1 log drop in the latent reservoir under ART (Figure 4A), because ART leads to antigen depletion. This causes the immune-cell population to contract and the reactivation rate $r(t)$ to decrease to its low background level. To be sure that these fits were not artifacts due to model complexity, we also tested simplified immune response models (Extended Experimental Procedures, Section E). While these simplified models fit the four steady-state plateaus, they cannot reproduce the pre-steady-state kinetics measured in patients (Figure S3). In contrast, the full immune model fits both steady-state and pre-steady-state kinetics (Figure 4A, inset), including the viral decay kinetics measured in patients who undergo ART (Markowitz et al., 2003).

Critically, the level of the adaptive immune response does not change the prediction of the simplified model (i.e., the model without an immune response) that the initial latency probability $p_{\text{lat}}(0)$ has a large optimum of ~ 0.5 (Figures 4B and S3). As a result, the prediction of the high optimal latency probability is directly applicable to natural lentiviral hosts even if they exhibit depressed immune responses. Further, as in the simplified models lacking an immune response, the large $p_{\text{lat}}^{\text{opt}}$ value is preserved even when a large fraction of systemic infections are mediated by non-latent cells (Extended Experimental Procedures, Section E). The optimal latency prediction is also robust to perturbations of epidemiological assumptions, such as the monotonic dependence of lentiviral transmission on viral loads (Extended Experimental Procedures, Section E). Overall, the robustness of $p_{\text{lat}}^{\text{opt}}$ in the immune model matches the robustness of $p_{\text{lat}}^{\text{opt}}$ in the simplified models.

Experimental Depletion of CD8⁺ T Cells in SIV-Infected Macaques Will Increase the Latent Reservoir ~ 3 Logs More Than Viremia

The immune model argues that CD8⁺ T cells depress the latent reservoir during chronic infection—either directly (e.g., through

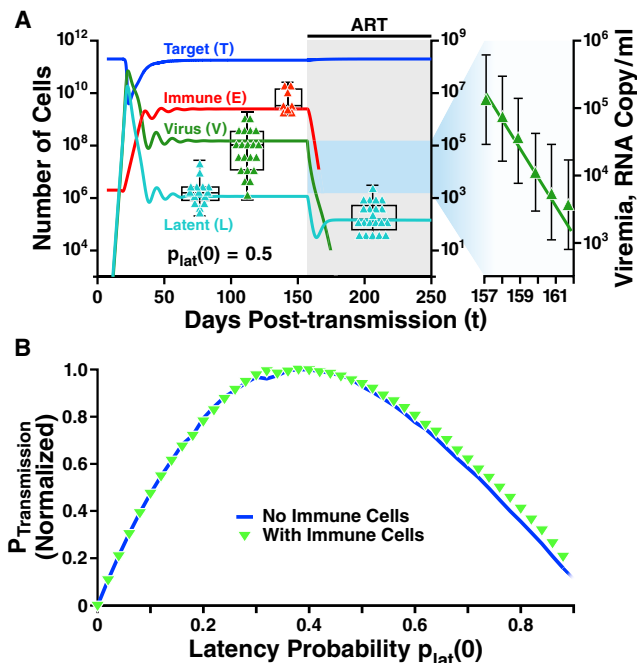


Figure 4. The Extended Immune-Response Model Fits the Available In Vivo Data and Does Not Change the Optimal Latency Probability for Resting Cells, $p_{\text{lat}}^{\text{opt}}(0)$

(A) Dynamics of cell compartments during systemic infection calculated from Equations [S9] and [S10]. Antiretroviral therapy (ART) initiated during steady-state infection causes a decline of the latent reservoir (L). The saturation of the fall in the latent reservoir is due to the decline in immune cells (E) during ART. (Data points across human patients) Virus load prior to ART (Fraser et al., 2007) (green triangles); latent cells prior to ART (Chun et al., 1997b) and after highly active ART (Finzi et al., 1997) (cyan triangles); effector CD8 T cells (Turnbull et al., 2009) (red triangles). For each data set (triangles), box-and-whisker plots show the upper and lower quartiles of the patient data. (Blowout) Virus load after the onset of ART (Markowitz et al., 2003) (green triangles, error bars show SD).

(B) Normalized transmission rate $p_{\text{transmission}}$ as a function of $p_{\text{lat}}(0)$ calculated from the dynamics in A and Equation [1]. Two cases are shown for comparison: with immune cells (E, green triangles) and without immune cells ($E = N = 0$, blue curve). Inclusion of immune cells into the model only weakly affects the prediction of a large optimal latency probability for resting cells, $p_{\text{lat}}^{\text{opt}}(0) \sim 0.5$. Model parameters in A and B are in Tables S1 and S2 (with $R_0^{\text{LT}} = 15$ and $p_{\text{lat}}(0) = 0.5$ in A). See also Figure S3.

secreted cytokines) or indirectly (e.g., through activation of downstream cell types that secrete factors). Thus, a direct test of the model can be achieved by depleting CD8⁺ T cells with anti-CD8 antibodies. CD8 depletion should increase the latency probability (p_{lat}) toward its original high value of ~ 0.5 and concomitantly decrease the reactivation rate (r) toward its original low value. In fact, the model quantitatively predicts the outcome of this experiment. Whereas previous CD8 depletion studies have already measured an ~ 1 – 3 log increase in the number of actively infected cells following CD8 depletion in SIV-infected *Rhesus macaques* (Jin et al., 1999; Metzner et al., 2000; Schmitz et al., 1999), the model predicts that the latent reservoir will increase by ~ 5 logs following CD8 depletion (Figure 5A). Thus, the increase in the latent reservoir would be ~ 3 logs greater than the increase in actively infected cells and viremia

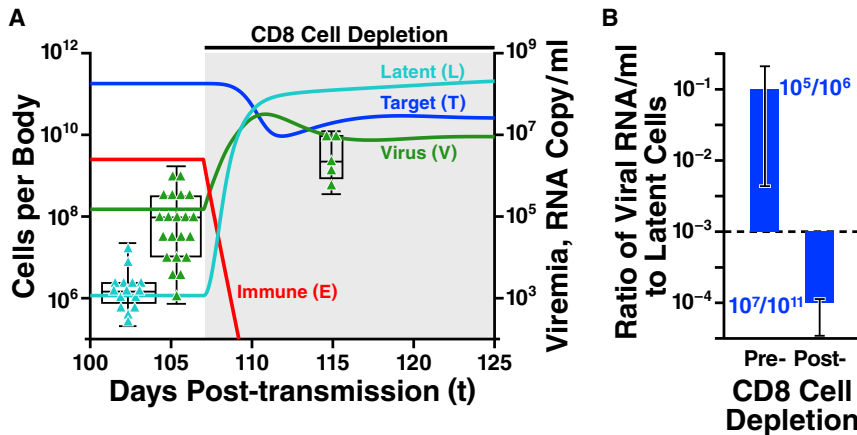
(Figure 5B). A corollary prediction is that CD8 depletion during early pre-peak infection (Matano et al., 1998), prior to a high-level adaptive immune response, will only increase the latent reservoir ~ 2 - to 3 -fold and will thus be harder to reliably measure (Figure S4). Notably, these experimental tests of the model require viral outgrowth assays (Finzi et al., 1997) since directly measuring proviral DNA will only report on actively infected cells, which outnumber latently infected cells by orders of magnitude. A viral outgrowth assay post-CD8 depletion would provide quantitative verification of the model and would consequently test the model's output that latency is a viral bet-hedging strategy tuned by natural selection.

Viral Strains Engineered to Have Higher Replicative Fitness—via Reduced Latency—Will Exhibit Lower Infectivity in Animal-Model Mucosal Inoculations

A more direct experimental test of the model would involve mucosal challenge experiments using recombinant SIV strains engineered to have substantially reduced latency probabilities. Engineering strains with reduced latency efficiencies appears possible since different HIV-1 clades are already known to exhibit different latency frequencies. These clade-specific differences appear to be driven by *cis* elements within the HIV-1 LTR (Jeeninga et al., 2008; van der Sluis et al., 2011). The model directly predicts that the reduced-latency recombinants will establish self-propagating systemic infections less frequently than the wild-type strains maintaining high latency frequencies. Further, these reduced latency strains could be quantitatively tested for increased replicative fitnesses via competitive growth assays with wild-type strains. If decreasing latency both increased replicative fitness and decreased successful lentiviral transmission, this would directly show that proviral latency provides a bet-hedging advantage that increases viral transmission despite reducing steady-state viral loads.

Proviral Latency Contrasted with Alternate Mechanisms of Initial Viral Survival

A natural question is whether alternatives to latently infected CD4⁺ T cells exist that also increase the probability of initial viral survival in the mucosa. One proposed non-latent route is dendritic cell migration from the mucosa to the target-cell rich lymphoid tissue (Kahn and Walker, 1998; Wu and KewalRamani, 2006). More specifically, Langerhans dendritic cells present in the mucosa can be infected by HIV and are prone to migration to the lymphoid tissue, where they can support subsequent dissemination of HIV by *cis* transfer (Peressin et al., 2014). Yet, Langerhans cells' dissemination of HIV may be partially blocked by neutralizing antibodies (Su et al., 2012). Follicular dendritic cells may provide another route of viral survival; however, these cells do not migrate to the mucosa (Murphy, 2011). In contrast to dendritic cells, proviral latent cells are neither impacted by neutralizing antibodies (being quiescent) nor blocked by the mucosal barrier, which has been proposed to be a viral bottleneck (Haaland et al., 2009). Latency can thus act as a type of "Trojan horse" for the virus. More fundamentally, even if alternative routes of initial viral survival exist, the results of this study (i.e., $p_{\text{lat}}^{\text{opt}} > 0$) remain robust as long as latency seeds some fraction of systemic infections (Figures 2E and S2J).



simulation example in A. The maximal expected errors (vertical bars) are estimated from the whisker box borders in A (the two middle quartiles). Since the dynamic balance between actively infected cells and latently infected cells is modulated by p_{lat} and r , the depletion of immune cells affecting p_{lat} and r is predicted to change this balance and disproportionately increase the latent reservoir. See also Figures S4 and S5.

Suppressing Latent Reactivation in the First Week of Infection Could Substantially Reduce the Latent Reservoir, Enhancing “Kick-and-Kill” Therapy

The model presents a potential therapeutic strategy that exploits the need for latently infected cells to reactivate to both establish systemic infection and dramatically increase the size of the latent reservoir (Figure S5). Thus, if the early reactivation rate were reduced—for example, by suppressing antigen-presenting cell (APC) migration (Peressin et al., 2014) or HIV transcriptional reactivation (Weinberger et al., 2008)—systemic infection would be rendered less likely and the latent reservoir size would be substantially decreased (Figure S5). While a caveat of this proposed approach is detection and treatment within the first week of infection, similar early treatments have been achieved; for a review, see Haase (2011). Critically, a substantially smaller latent reservoir of $\sim 10^2$ cells would require the reactivation of far fewer latent cells by imperfect “shock-and-kill” strategies (Archin et al., 2012; Deeks, 2012). As a result, suppression of reactivation during the first week of infection followed by shock and kill could substantially enhance the chances of HIV eradication.

Implications for Alternate Antiviral Therapy Approaches

A further implication of the result that latency is a hardwired, evolutionarily maintained trait is that it may be easier to control HIV by increasing, rather than purging, the latent reservoir (Dar et al., 2014; Weinberger and Weinberger, 2013; Weinberger et al., 2008). Current shock-and-kill therapies are fighting natural selection in attempting to reactivate each of $\sim 10^5$ latent cells. In contrast, discovering a non-toxic compound that switches 90%–95% of actively infected cells to latency would drive HIV’s basic reproductive ratio (R_0) below 1, making HIV infection unsustainable. While still a hypothetical avenue, enhancing viral latency may provide a viable alternative if shock-and-kill strategies fail to achieve their goal of complete eradication.

EXPERIMENTAL PROCEDURES

A Simplified Two-Compartment Model to Quantify the Net Impact of Latency on Lentiviral Transmission

All models described in the main text are variations of the well-parameterized basic model of viral dynamics (Nowak and May, 2000) expanded to include latent infections (Rong and Perelson, 2009a, 2009b; Sedaghat et al., 2007, 2008). Absent an immune response, the deterministic form of the models is captured by the following ordinary differential equations:

$$\begin{aligned}
 \text{Uninfected 'target' cells } \frac{dT}{dt} &= \underbrace{b}_{\text{replenishment}} - \underbrace{d_T T}_{\text{natural death}} - \underbrace{kVT}_{\text{infection}} \\
 \text{Actively infected cells } \frac{dI}{dt} &= \underbrace{(1 - p_{lat})kVT}_{\text{active infection}} - \underbrace{d_I I}_{\text{death}} + \underbrace{rL}_{\text{reactivation}} \\
 \text{Latently infected cells } \frac{dL}{dt} &= \underbrace{p_{lat}kVT}_{\text{latent infection}} - \underbrace{d_L L}_{\text{death}} - \underbrace{rL}_{\text{reactivation}} \\
 \text{Virus } \frac{dV}{dt} &= \underbrace{nd_I I}_{\text{production}} - \underbrace{cV}_{\text{clearance}}
 \end{aligned} \quad [6]$$

In the model above, uninfected “target” cells (T) are produced at rate b , decay at rate d_T , and can be infected by virus particles (V) at rate k . Upon viral infection, target cells become either latently infected cells (L) with probability p_{lat} or become actively infected (virus-producing) cells (I) with probability $1 - p_{lat}$. Latently infected cells reactivate into actively infected cells at rate r or die at the (slow) rate d_L . Actively infected cells produce “burst sizes” of n virions as they die at rate d_I . Virions decay at the relatively fast rate c . All parameter values are given in Table S1; Table S2 contains parameters for the model extended to include an adaptive immune response (Extended Experimental Procedures, Section C).

Critically, the infection models can be simplified by re-parameterizing the equations in terms of the basic reproductive ratio: $R_0 = bkn/cd_T$. This “non-dimensionalization” enables us to capture the disparate dynamics between mucosal infection (Figure 2A) and systemic infection (Figure 2B) by simulating the same model for both infection stages and only varying a single parameter, R_0 . Further, R_0^{muc} is experimentally bounded to be < 1 from the viral dynamics during initial infection (Miller et al., 2005), and R_0^{LT} is similarly measured to be ~ 10 during systemic infection (Nowak and May, 2000). As a result, no assumptions about unknown parameter values are needed to obtain the optimal latency probability (p_{lat}^{opt}). More directly, Equation [5] shows that (p_{lat}^{opt}) only depends on R_0^{LT} .

(for detailed derivations and tests of the models, see [Extended Experimental Procedures](#)).

SUPPLEMENTAL INFORMATION

Supplemental Information includes Extended Experimental Procedures, five figures, and two tables and can be found with this article online at <http://dx.doi.org/10.1016/j.cell.2015.02.017>.

ACKNOWLEDGMENTS

We are grateful to Lani Wu and Stephen Altschuler for input and discussions; to Alan Perelson, Warner Greene, Eric Verdin, Anand Pai, Brandon Razooky, and John Coffin for helpful comments; and to Abhyudai Singh for generating preliminary data. We are also grateful to the graphics department at the Gladstone Institutes for artistic expertise and help with figure schematics. This work was supported by the Alfred P. Sloan Foundation, the Wyss Institute Technology Development Fellowship, the NIH Director's Pioneer Award Program (DP1 OD017181), as well as NIH awards R21AI109611, F32AI102520, and U19AI096113 as part of the Delaney Collaboratory for AIDS Research and Eradication (CARE).

Received: September 2, 2014

Revised: December 11, 2014

Accepted: February 10, 2015

Published: February 26, 2015

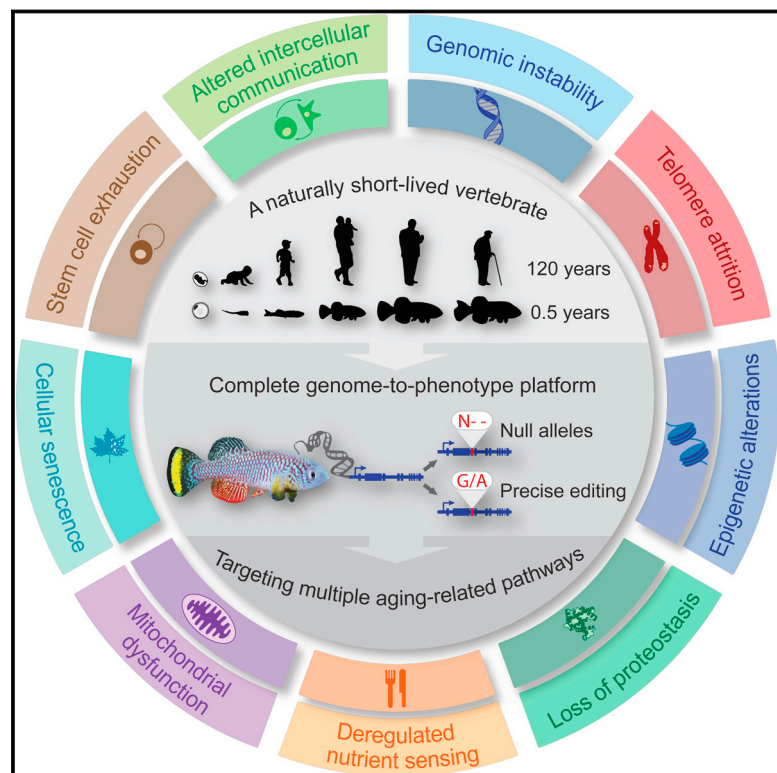
REFERENCES

- Archin, N.M., Liberty, A.L., Kashuba, A.D., Choudhary, S.K., Kuruc, J.D., Crooks, A.M., Parker, D.C., Anderson, E.M., Kearney, M.F., Strain, M.C., et al. (2012). Administration of vorinostat disrupts HIV-1 latency in patients on antiretroviral therapy. *Nature* **487**, 482–485.
- Arkin, A., Ross, J., and McAdams, H.H. (1998). Stochastic kinetic analysis of developmental pathway bifurcation in phage lambda-infected *Escherichia coli* cells. *Genetics* **149**, 1633–1648.
- Balaban, N.Q. (2011). Persistence: mechanisms for triggering and enhancing phenotypic variability. *Curr. Opin. Genet. Dev.* **21**, 768–775.
- Batada, N.N., and Hurst, L.D. (2007). Evolution of chromosome organization driven by selection for reduced gene expression noise. *Nat. Genet.* **39**, 945–949.
- Burnett, J.C., Miller-Jensen, K., Shah, P.S., Arkin, A.P., and Schaffer, D.V. (2009). Control of stochastic gene expression by host factors at the HIV promoter. *PLoS Pathog.* **5**, e1000260.
- Calvanese, V., Chavez, L., Laurent, T., Ding, S., and Verdin, E. (2013). Dual-color HIV reporters trace a population of latently infected cells and enable their purification. *Virology* **446**, 283–292.
- Chun, T.-W., Stuyver, L., Mizell, S.B., Ehler, L.A., Mican, J.A.M., Baseler, M., Lloyd, A.L., Nowak, M.A., and Fauci, A.S. (1997a). Presence of an inducible HIV-1 latent reservoir during highly active antiretroviral therapy. *Proc. Natl. Acad. Sci. USA* **94**, 13193–13197.
- Chun, T.W., Carruth, L., Finzi, D., Shen, X., DiGiuseppe, J.A., Taylor, H., Hermankova, M., Chadwick, K., Margolick, J., Quinn, T.C., et al. (1997b). Quantification of latent tissue reservoirs and total body viral load in HIV-1 infection. *Nature* **387**, 183–188.
- Chun, T.W., Engel, D., Mizell, S.B., Ehler, L.A., and Fauci, A.S. (1998). Induction of HIV-1 replication in latently infected CD4+ T cells using a combination of cytokines. *J. Exp. Med.* **188**, 83–91.
- Coffin, J., and Swanstrom, R. (2013). HIV pathogenesis: dynamics and genetics of viral populations and infected cells. *Cold Spring Harb. Perspect. Med.* **3**, a012526.
- Cohen, D. (1966). Optimizing reproduction in a randomly varying environment. *J. Theor. Biol.* **12**, 119–129.
- Dahabieh, M.S., Ooms, M., Simon, V., and Sadowski, I. (2013). A doubly fluorescent HIV-1 reporter shows that the majority of integrated HIV-1 is latent shortly after infection. *J. Virol.* **87**, 4716–4727.
- Dar, R.D., Hosmane, N.N., Arkin, M.R., Siliciano, R.F., and Weinberger, L.S. (2014). Screening for noise in gene expression identifies drug synergies. *Science* **344**, 1392–1396.
- De Boer, R.J., and Perelson, A.S. (1998). Target cell limited and immune control models of HIV infection: a comparison. *J. Theor. Biol.* **190**, 201–214.
- Deeks, S.G. (2012). HIV: Shock and kill. *Nature* **487**, 439–440.
- Doitsh, G., Cavrois, M., Lassen, K.G., Zepeda, O., Yang, Z., Santiago, M.L., Hebbeler, A.M., and Greene, W.C. (2010). Abortive HIV infection mediates CD4 T cell depletion and inflammation in human lymphoid tissue. *Cell* **143**, 789–801.
- Eisele, E., and Siliciano, R.F. (2012). Redefining the viral reservoirs that prevent HIV-1 eradication. *Immunity* **37**, 377–388.
- Finzi, D., Hermankova, M., Pierson, T., Carruth, L.M., Buck, C., Chaisson, R.E., Quinn, T.C., Chadwick, K., Margolick, J., Brookmeyer, R., et al. (1997). Identification of a reservoir for HIV-1 in patients on highly active antiretroviral therapy. *Science* **278**, 1295–1300.
- Finzi, D., Blankson, J., Siliciano, J.D., Margolick, J.B., Chadwick, K., Pierson, T., Smith, K., Lisiewicz, J., Lori, F., Flexner, C., et al. (1999). Latent infection of CD4+ T cells provides a mechanism for lifelong persistence of HIV-1, even in patients on effective combination therapy. *Nat. Med.* **5**, 512–517.
- Fraser, H.B., Hirsh, A.E., Giaever, G., Kumm, J., and Eisen, M.B. (2004). Noise minimization in eukaryotic gene expression. *PLoS Biol.* **2**, e137.
- Fraser, C., Hollingsworth, T.D., Chapman, R., de Wolf, F., and Hanage, W.P. (2007). Variation in HIV-1 set-point viral load: epidemiological analysis and an evolutionary hypothesis. *Proc. Natl. Acad. Sci. USA* **104**, 17441–17446.
- Gray, R.H., Wawer, M.J., Brookmeyer, R., Sewankambo, N.K., Serwadda, D., Wabwire-Mangen, F., Lutalo, T., Li, X., vanCott, T., and Quinn, T.C.; Rakai Project Team (2001). Probability of HIV-1 transmission per coital act in monogamous, heterosexual, HIV-1-discordant couples in Rakai, Uganda. *Lancet* **357**, 1149–1153.
- Grimmett, G., and Stirzaker, D. (1992). *Probability and Random Processes*, Second Edition (Oxford University Press).
- Haaland, R.E., Hawkins, P.A., Salazar-Gonzalez, J., Johnson, A., Tichacek, A., Karita, E., Manigart, O., Mulenga, J., Keele, B.F., Shaw, G.M., et al. (2009). Inflammatory genital infections mitigate a severe genetic bottleneck in heterosexual transmission of subtype A and C HIV-1. *PLoS Pathog.* **5**, e1000274.
- Haase, A.T. (2011). Early events in sexual transmission of HIV and SIV and opportunities for interventions. *Annu. Rev. Med.* **62**, 127–139.
- Han, Y., Wind-Rotolo, M., Yang, H.C., Siliciano, J.D., and Siliciano, R.F. (2007). Experimental approaches to the study of HIV-1 latency. *Nat. Rev. Microbiol.* **5**, 95–106.
- Hartl, D.L., and Clark, A.G. (2007). *Principles of population genetics*, Fourth Edition (Sunderland, Mass: Sinauer Associates).
- Ho, Y.C., Shan, L., Hosmane, N.N., Wang, J., Laskey, S.B., Rosenbloom, D.I., Lai, J., Blankson, J.N., Siliciano, J.D., and Siliciano, R.F. (2013). Replication-competent noninduced proviruses in the latent reservoir increase barrier to HIV-1 cure. *Cell* **155**, 540–551.
- Jeeninga, R.E., Westerhout, E.M., van Gerven, M.L., and Berkhout, B. (2008). HIV-1 latency in actively dividing human T cell lines. *Retrovirology* **5**, 37.
- Jin, X., Bauer, D.E., Tuttleton, S.E., Lewin, S., Gettie, A., Blanchard, J., Irwin, C.E., Safrit, J.T., Mittler, J., Weinberger, L., et al. (1999). Dramatic rise in plasma viremia after CD8(+) T cell depletion in simian immunodeficiency virus-infected macaques. *J. Exp. Med.* **189**, 991–998.
- Kahn, J.O., and Walker, B.D. (1998). Acute human immunodeficiency virus type 1 infection. *N. Engl. J. Med.* **339**, 33–39.
- Kearney, M., Maldarelli, F., Shao, W., Margolick, J.B., Daar, E.S., Mellors, J.W., Rao, V., Coffin, J.M., and Palmer, S. (2009). Human immunodeficiency virus type 1 population genetics and adaptation in newly infected individuals. *J. Virol.* **83**, 2715–2727.

- Keele, B.F., Giorgi, E.E., Salazar-Gonzalez, J.F., Decker, J.M., Pham, K.T., Salazar, M.G., Sun, C., Grayson, T., Wang, S., Li, H., et al. (2008). Identification and characterization of transmitted and early founder virus envelopes in primary HIV-1 infection. *Proc. Natl. Acad. Sci. USA* 105, 7552–7557.
- Kuroda, M.J., Schmitz, J.E., Charini, W.A., Nickerson, C.E., Lifton, M.A., Lord, C.I., Forman, M.A., and Letvin, N.L. (1999). Emergence of CTL coincides with clearance of virus during primary simian immunodeficiency virus infection in rhesus monkeys. *J. Immunol.* 162, 5127–5133.
- Li, Q., Duan, L., Estes, J.D., Ma, Z.M., Rourke, T., Wang, Y., Reilly, C., Carlis, J., Miller, C.J., and Haase, A.T. (2005). Peak SIV replication in resting memory CD4⁺ T cells depletes gut lamina propria CD4⁺ T cells. *Nature* 434, 1148–1152.
- Markowitz, M., Louie, M., Hurley, A., Sun, E., Di Mascio, M., Perelson, A.S., and Ho, D.D. (2003). A novel antiviral intervention results in more accurate assessment of human immunodeficiency virus type 1 replication dynamics and T-cell decay in vivo. *J. Virol.* 77, 5037–5038.
- Matano, T., Shibata, R., Siemon, C., Connors, M., Lane, H.C., and Martin, M.A. (1998). Administration of an anti-CD8 monoclonal antibody interferes with the clearance of chimeric simian/human immunodeficiency virus during primary infections of rhesus macaques. *J. Virol.* 72, 164–169.
- Metzner, K.J., Jin, X., Lee, F.V., Gettie, A., Bauer, D.E., Di Mascio, M., Perelson, A.S., Marx, P.A., Ho, D.D., Kostrikis, L.G., and Connor, R.I. (2000). Effects of in vivo CD8(+) T cell depletion on virus replication in rhesus macaques immunized with a live, attenuated simian immunodeficiency virus vaccine. *J. Exp. Med.* 191, 1921–1931.
- Miller, C.J., Li, Q., Abel, K., Kim, E.Y., Ma, Z.M., Wietgreffe, S., La Franco-Scheuch, L., Compton, L., Duan, L., Shore, M.D., et al. (2005). Propagation and dissemination of infection after vaginal transmission of simian immunodeficiency virus. *J. Virol.* 79, 9217–9227.
- Mohri, H., Bonhoeffer, S., Monard, S., Perelson, A.S., and Ho, D.D. (1998). Rapid turnover of T lymphocytes in SIV-infected rhesus macaques. *Science* 279, 1223–1227.
- Murphy, K. (2011). *Janeway's Immunobiology*, Eighth Edition (London, New York: Garland Science).
- Nowak, M., and May, R. (2000). *Virus dynamics: mathematical principles of immunology and virology* (Oxford, New York: Oxford University Press).
- Pearson, J.E., Krapivsky, P., and Perelson, A.S. (2011). Stochastic theory of early viral infection: continuous versus burst production of virions. *PLoS Comput. Biol.* 7, e1001058.
- Peressin, M., Proust, A., Schmidt, S., Su, B., Lambot, M., Biedma, M.E., Laumond, G., Decoville, T., Holl, V., and Moog, C. (2014). Efficient transfer of HIV-1 in trans and in cis from Langerhans dendritic cells and macrophages to autologous T lymphocytes. *AIDS* 28, 667–677.
- Pierson, T., McArthur, J., and Siliciano, R.F. (2000). Reservoirs for HIV-1: mechanisms for viral persistence in the presence of antiviral immune responses and antiretroviral therapy. *Annu. Rev. Immunol.* 18, 665–708.
- Razooky, B.S., Pai, A., Aull, K., Rouzine, I.M., and Weinberger, L.S. (2015). A hardwired HIV latency program. *Cell* 160, this issue, 990–1001.
- Richman, D.D., Margolis, D.M., Delaney, M., Greene, W.C., Hazuda, D., and Pomerantz, R.J. (2009). The challenge of finding a cure for HIV infection. *Science* 323, 1304–1307.
- Rong, L., and Perelson, A.S. (2009a). Modeling HIV persistence, the latent reservoir, and viral blips. *J. Theor. Biol.* 260, 308–331.
- Rong, L., and Perelson, A.S. (2009b). Modeling latently infected cell activation: viral and latent reservoir persistence, and viral blips in HIV-infected patients on potent therapy. *PLoS Comput. Biol.* 5, e1000533.
- Santiago, M.L., Range, F., Keele, B.F., Li, Y., Bailes, E., Bibollet-Ruche, F., Fruteau, C., Noë, R., Peeters, M., Brookfield, J.F., et al. (2005). Simian immunodeficiency virus infection in free-ranging sooty mangabeys (*Cercopithecus atys*) from the Taï Forest, Côte d'Ivoire: implications for the origin of epidemic human immunodeficiency virus type 2. *J. Virol.* 79, 12515–12527.
- Schmitz, J.E., Kuroda, M.J., Santra, S., Sasseville, V.G., Simon, M.A., Lifton, M.A., Racz, P., Tenner-Racz, K., Dalesandro, M., Scallion, B.J., et al. (1999). Control of viremia in simian immunodeficiency virus infection by CD8⁺ lymphocytes. *Science* 283, 857–860.
- Sedaghat, A.R., Siliciano, J.D., Brennan, T.P., Wilke, C.O., and Siliciano, R.F. (2007). Limits on replenishment of the resting CD4⁺ T cell reservoir for HIV in patients on HAART. *PLoS Pathog.* 3, e122.
- Sedaghat, A.R., Siliciano, R.F., and Wilke, C.O. (2008). Low-level HIV-1 replication and the dynamics of the resting CD4⁺ T cell reservoir for HIV-1 in the setting of HAART. *BMC Infect. Dis.* 8, 2.
- Siliciano, R.F., and Greene, W.C. (2011). HIV latency. *Cold Spring Harbor Perspect. Med.* 1, a007096.
- Stafford, M.A., Corey, L., Cao, Y., Daar, E.S., Ho, D.D., and Perelson, A.S. (2000). Modeling plasma virus concentration during primary HIV infection. *J. Theor. Biol.* 203, 285–301.
- Su, B., Xu, K., Lederle, A., Peressin, M., Biedma, M.E., Laumond, G., Schmidt, S., Decoville, T., Proust, A., Lambot, M., et al. (2012). Neutralizing antibodies inhibit HIV-1 transfer from primary dendritic cells to autologous CD4⁺ T lymphocytes. *Blood* 120, 3708–3717.
- Turnbull, E.L., Wong, M., Wang, S., Wei, X., Jones, N.A., Conrod, K.E., Aldam, D., Turner, J., Pellegrino, P., Keele, B.F., et al. (2009). Kinetics of expansion of epitope-specific T cell responses during primary HIV-1 infection. *J. Immunol.* 182, 7131–7145.
- van der Sluis, R.M., Pollakis, G., van Gerven, M.L., Berkhout, B., and Jeeninga, R.E. (2011). Latency profiles of full length HIV-1 molecular clone variants with a subtype specific promoter. *Retrovirology* 8, 73.
- Wawer, M.J., Gray, R.H., Sewankambo, N.K., Serwadda, D., Li, X., Laeyendecker, O., Kiwanuka, N., Kigozi, G., Kiddugavu, M., Lutalo, T., et al. (2005). Rates of HIV-1 transmission per coital act, by stage of HIV-1 infection, in Rakai, Uganda. *J. Infect. Dis.* 191, 1403–1409.
- Weinberger, A.D., and Weinberger, L.S. (2013). Stochastic fate selection in HIV-infected patients. *Cell* 155, 497–499.
- Weinberger, L.S., Burnett, J.C., Toettcher, J.E., Arkin, A.P., and Schaffer, D.V. (2005). Stochastic gene expression in a lentiviral positive-feedback loop: HIV-1 Tat fluctuations drive phenotypic diversity. *Cell* 122, 169–182.
- Weinberger, L.S., Dar, R.D., and Simpson, M.L. (2008). Transient-mediated fate determination in a transcriptional circuit of HIV. *Nat. Genet.* 40, 466–470.
- Whitney, J.B., Hill, A.L., Sanisetty, S., Penaloza-MacMaster, P., Liu, J., Shetty, M., Parenteau, L., Cabral, C., Shields, J., Blackmore, S., et al. (2014). Rapid seeding of the viral reservoir prior to SIV viraemia in rhesus monkeys. *Nature* 512, 74–77.
- Wu, L., and KewalRamani, V.N. (2006). Dendritic-cell interactions with HIV: infection and viral dissemination. *Nat. Rev. Immunol.* 6, 859–868.
- Zhang, Z., Schuler, T., Zupancic, M., Wietgreffe, S., Staskus, K.A., Reimann, K.A., Reinhart, T.A., Rogan, M., Cavert, W., Miller, C.J., et al. (1999). Sexual transmission and propagation of SIV and HIV in resting and activated CD4⁺ T cells. *Science* 286, 1353–1357.

A Platform for Rapid Exploration of Aging and Diseases in a Naturally Short-Lived Vertebrate

Graphical Abstract



Authors

Itamar Harel, Bérénice A. Benayoun, ..., Steven E. Artandi, Anne Brunet

Correspondence

abrunet1@stanford.edu

In Brief

Aging is the number one risk factor for many human pathologies, yet it is challenging to study as existing vertebrate models are relatively long lived. The development of an integrative genome-to-phenotype platform in a naturally short-lived vertebrate, the African turquoise killifish, opens the door to high-throughput in vivo modeling of vertebrate aging and complex human diseases.

Highlights

- The turquoise killifish is the shortest-lived vertebrate species bred in the lab
- A complete genome-to-phenotype platform for this emerging model
- Telomerase-deficient fish display the fastest onset of related human pathologies
- A resource of targeted aging- and disease-related genes and available fish lines

Accession Numbers

JNBZ00000000
SRP041421
SRP045718



A Platform for Rapid Exploration of Aging and Diseases in a Naturally Short-Lived Vertebrate

Itamar Harel,¹ Bérénice A. Benayoun,¹ Ben Machado,¹ Param Priya Singh,¹ Chi-Kuo Hu,¹ Matthew F. Pech,^{2,3} Dario Riccardo Valenzano,^{1,5} Elisa Zhang,¹ Sabrina C. Sharp,¹ Steven E. Artandi,^{2,3,4} and Anne Brunet^{1,4,*}

¹Department of Genetics, Stanford University, Stanford, CA 94305, USA

²Department of Medicine, Stanford University School of Medicine, Stanford, CA 94305, USA

³Biochemistry Department, Stanford University School of Medicine, Stanford, CA 94305, USA

⁴Glenn Laboratories for the Biology of Aging at Stanford, Stanford, CA 94305, USA

⁵Present address: Max Planck Institute for Biology of Ageing, Cologne 50931, Germany

*Correspondence: abrunet1@stanford.edu

<http://dx.doi.org/10.1016/j.cell.2015.01.038>

SUMMARY

Aging is a complex process that affects multiple organs. Modeling aging and age-related diseases in the lab is challenging because classical vertebrate models have relatively long lifespans. Here, we develop the first platform for rapid exploration of age-dependent traits and diseases in vertebrates, using the naturally short-lived African turquoise killifish. We provide an integrative genomic and genome-editing toolkit in this organism using our de-novo-assembled genome and the CRISPR/Cas9 technology. We mutate many genes encompassing the hallmarks of aging, and for a subset, we produce stable lines within 2–3 months. As a proof of principle, we show that fish deficient for the protein subunit of telomerase exhibit the fastest onset of telomere-related pathologies among vertebrates. We further demonstrate the feasibility of creating specific genetic variants. This genome-to-phenotype platform represents a unique resource for studying vertebrate aging and disease in a high-throughput manner and for investigating candidates arising from human genome-wide studies.

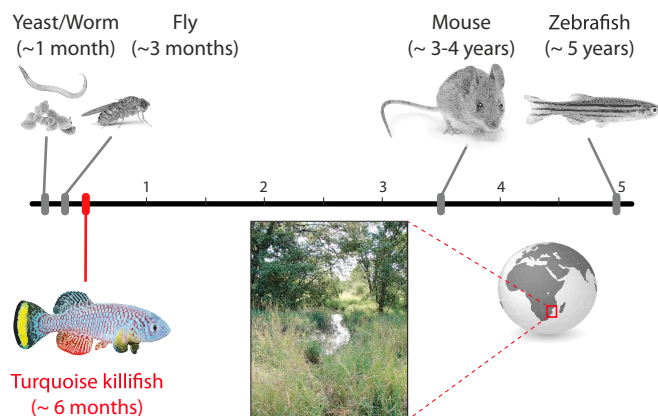
INTRODUCTION

Aging is the number one risk factor for many human pathologies, including diabetes, cancer, cardiovascular, and neurodegenerative diseases (Niccoli and Partridge, 2012). Thus, delaying aging could help postpone the onset of these devastating ailments and increase healthspan. Because aging affects multiple organs and systems in humans (López-Otín et al., 2013), it is one of the most challenging processes to model in the lab. So far, the study of aging has been dominated by non-vertebrate short-lived model organisms, such as yeast (*C. cerevisiae*), worm (*C. elegans*), and fly (*D. melanogaster*), which has allowed the identification of remarkably conserved aging-related pathways, such as the TOR and Insulin/IGF pathways (Kenyon, 2010). However,

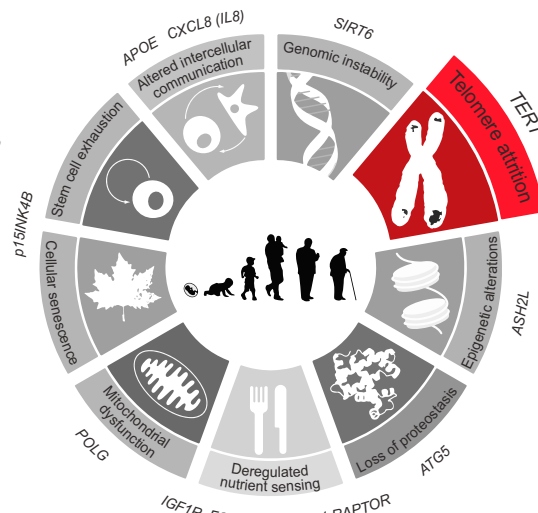
some important aspects of human aging and disease phenotypes cannot be faithfully recapitulated in invertebrate models, as they lack specific organs and systems (e.g., blood, bones, and an adaptive immune system) that are crucial components of human aging and age-related pathologies. Vertebrate model systems, namely the mouse (*M. musculus*) and zebrafish (*D. rerio*), have also been exploited to probe genes involved in aging and age-related diseases. However, experimental studies have been hampered by the relatively long lifespan of mice and zebrafish (maximal lifespan of 3–4 and 5 years, respectively [Tacutu et al., 2013]) and high costs of maintenance, especially for mice. Mouse models with accelerated onset of age-associated disease (e.g., neurodegeneration) can partially address this issue (Trancikova et al., 2011), but these models uncouple the disease phenotype from its main risk factor—aging—and they remain expensive to use. Thus, a new vertebrate model is needed to better understand the principles of vertebrate aging and to study age-related diseases in the context of aging.

The African turquoise killifish *Nothobranchius furzeri* is a naturally short-lived vertebrate that lives in ephemeral water ponds in Zimbabwe and Mozambique (Figure 1A), where water is only present during a brief rainy season. This fish species has likely evolved a compressed life cycle (as short as 30–40 days from egg to egg-laying adult) to adapt to its transient habitat. The turquoise killifish is currently the shortest-lived vertebrate that can be bred in captivity (Genade et al., 2005; Valenzano et al., 2006), with a lifespan of 4–6 months in optimal laboratory conditions (6 to 10 times shorter than the lifespan of mice and zebrafish, respectively). Importantly, despite its short lifespan, this fish recapitulates typical age-dependent phenotypes and pathologies such as decline in fertility, sarcopenia, cognitive decline, and cancerous lesions (Di Cicco et al., 2011; Genade et al., 2005; Valenzano et al., 2006). It also displays a conserved response to environmental stimuli known to affect the aging rate in other species, such as dietary restriction (Terzibasi et al., 2009). These characteristics make this fish an attractive model organism to study vertebrate aging, physiology, and age-dependent diseases throughout organismal lifespan (Di Cicco et al., 2011). Furthermore, the turquoise killifish telomeres are similar in length to those of humans (6–8 kb) (Hartmann et al., 2009), unlike laboratory mouse telomeres, which are

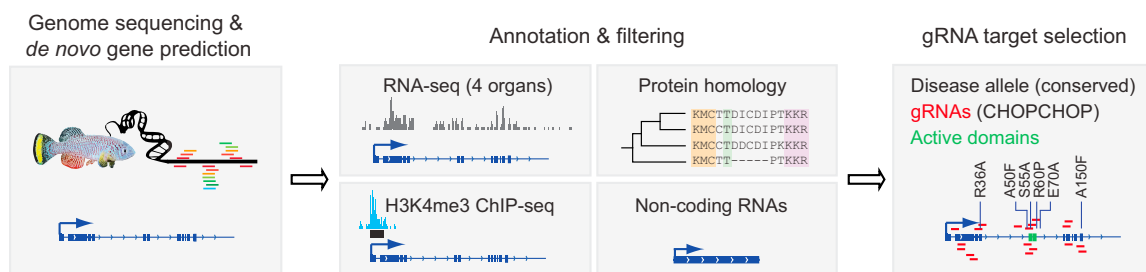
A Vertebrate and non-vertebrate genetic aging models



B Targeted genes encompassing the 9 “hallmarks of aging”



C Genomic pipeline



D Genome-editing pipeline

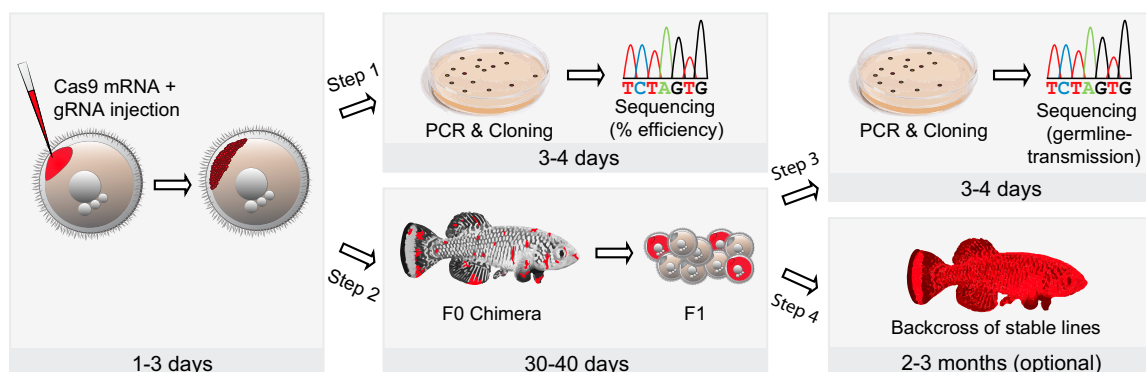


Figure 1. A Versatile Platform for Rapid Exploration of Aging and Longevity Genes in the Naturally Short-Lived Turquoise Killifish

(A) Lifespan of non-vertebrate and vertebrate model systems widely used for aging and disease research (top), when compared to the lifespan of the turquoise killifish (bottom). The turquoise killifish originates from ephemeral water ponds in Zimbabwe and Mozambique (bottom).

(B) Examples of genes encompassing the hallmarks of human aging (modified with permission from López-Otín et al. [2013]).

(C) Genomic pipeline to generate CRISPR/Cas9 gRNAs in a new model organism using our newly created genomic tools (de-novo-assembled turquoise killifish genome, epigenome, and transcriptome). Gene models and gRNA selection are available via CHOPCHOP.

(D) CRISPR/Cas9 genome-editing pipeline to generate stable mutant fish lines in the turquoise killifish. Overall, the total time for generating a stable mutant line in the lab (i.e., steps 1–4) is about 2–3 months.

very long (50–150 kb) (Lee et al., 1998). Thus, findings from aging studies in the turquoise killifish should be relevant for vertebrate aging, including humans. The rapid timescale of aging in

this species should not only facilitate the causative identification of factors regulating vertebrate lifespan but also allow longitudinal studies.

The turquoise killifish has additional advantages as a model system. Contrary to many other fish, including zebrafish, the turquoise killifish has an XY-based sexual determination (Valenzano et al., 2009). Furthermore, there exists a highly inbred strain of the turquoise killifish (the GRZ strain, used in this study), as well as a number of wild-derived strains (Terzibasi et al., 2008). The availability of multiple strains provides an important advantage for genetic studies and for mapping traits that are different between strains (e.g., color, maximal lifespan) (Kirschner et al., 2012; Valenzano et al., 2009). Collectively, these characteristics of the turquoise killifish—coupled with the ease of rapidly generating many offspring and low maintenance costs—make this fish a promising vertebrate model, uniquely fit to address aging and age-related diseases (Genade et al., 2005; Valenzano et al., 2006).

For the African turquoise killifish to become a widely used vertebrate model compatible with high-throughput approaches, key tools need to be created. Although preliminary genetic tools have been developed in the turquoise killifish, including genetic linkage maps (Kirschner et al., 2012; Reichwald et al., 2009; Valenzano et al., 2009), and Tol2-based transgenesis (Hartmann and Englert, 2012; Valenzano et al., 2011), the lack of a sequenced genome and ability to manipulate endogenous genes has drastically limited the use of this organism. The RNA-guided CRISPR (clustered regularly interspaced short palindrome repeats) associated Cas9 nuclease (Jinek et al., 2012) has recently emerged as an effective approach for introducing targeted mutations in a variety of model organisms, such as yeast, worms, flies, zebrafish, and mice, as well as several non-model organisms (for a detailed list see Hsu et al. [2014]). However, genome-editing approaches have never been reported in the African turquoise killifish, probably because of the lack of a sequenced genome.

Here, we create the first platform for the rapid exploration of aging and aging-related diseases in vertebrates by developing new genomic and genome-editing tools in a promising vertebrate model, the naturally short-lived African turquoise killifish. As a proof of principle for the versatility of this platform, we generate a suite of mutated alleles for 13 genes encompassing the hallmarks of aging and report six stable lines to date. We characterize a loss-of-function mutation in the gene encoding the protein component of telomerase and show that telomerase-deficient turquoise killifish recapitulate characteristics of human pathologies. This platform should allow high-throughput studies on aging and longevity in vertebrates, as well as longitudinal modeling of human diseases. Our platform should also enable systematic examination of unexplored candidates identified in human genomic studies.

RESULTS

A Platform for the Study of “Hallmarks of Aging” Genes in Vertebrates

We sought to create a versatile platform to rapidly model human aging and diseases in the short-lived turquoise killifish (Figure 1A). A recent review has categorized nine “hallmarks of aging” (López-Otín et al., 2013), including telomere attrition, deregulated nutrient sensing, and stem cell exhaustion (Figure 1B). We selected 13 genes encompassing those hallmarks (e.g., the protein

subunit of telomerase [*TERT*], insulin-like growth factor 1 receptor [*IGF1R*], and S6 kinase [*RPS6KB1*]) with the overall goal of generating mutant alleles for each of them (Figure 1B).

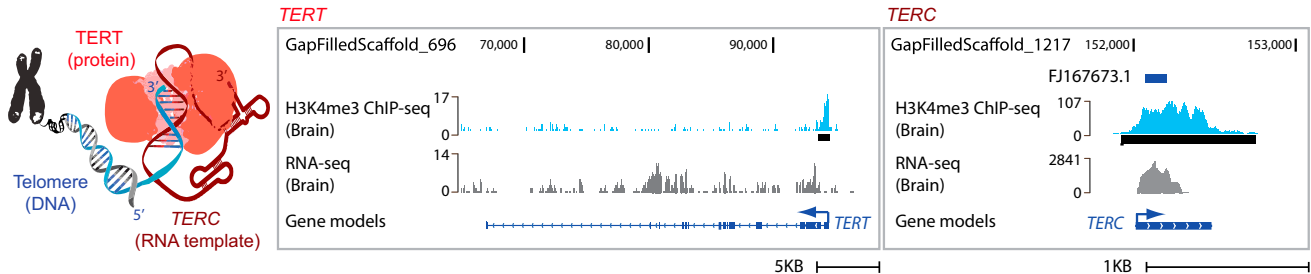
Because the turquoise killifish is an emerging model, the first step was to identify genes in this organism. To this end, we generated a wide range of genomic data sets and designed a tailored genomic pipeline. We built gene models, using our recently assembled turquoise killifish genome (Figure 1C). We verified the accuracy of gene models and analyzed mRNA expression pattern using our RNA sequencing (RNA-seq) data sets from four tissues (Figure 1C). We generated an H3K4me3 chromatin immunoprecipitation sequencing (ChIP-seq) data set to define transcriptional start sites (TSSs) and further support annotations, especially for non-coding RNAs (Rinn and Chang, 2012) (Figure 1C). Additional support for protein-coding gene annotation was obtained using protein homology (Figure 1C). Finally, we designed guide RNA (gRNA) targets for CRISPR/Cas9 genome editing (Figure 1C and Table S1). The genome of the turquoise killifish and the RNA-seq and H3K4me3 ChIP-seq datasets are provided as resources (accession numbers JNBZ00000000, SRP041421, and SRP045718, respectively). The full description and analysis of the genome will be reported elsewhere (D.R.V., B.A.B., P.P.S., and A.B., unpublished data). The gene models and gRNA design are made available via the CHOPCHOP platform (<https://chopchop.rc.fas.harvard.edu/>) (Montague et al., 2014). Together, these data sets provide an integrative resource for the scientific community, not only to target specific genes in the turquoise killifish, but also for comparative genomics and evolutionary studies of aging and longevity.

We then designed a CRISPR/Cas9 genome-editing strategy in the turquoise killifish. Based on our tailored genomic pipeline, we generated two to five independent gRNA sequences for each gene (Table S1). We then microinjected a mixture of Cas9 mRNA and gRNAs (Hwang et al., 2013; Jao et al., 2013) into fertilized turquoise killifish eggs at the single-cell stage (Figure 1D). Cas9 is known to introduce double-strand breaks that are repaired by non-homologous end joining (NHEJ), resulting in genome editing (small deletions or insertions, also known as indels) (Hsu et al., 2014). Successful editing was assessed in a subset of eggs by cloning and sequencing of the targeted region 72 hr after injection (Figure 1D, step 1). The gRNAs that resulted in successful editing were then used to generate F0 chimeras that were crossed with wild-type fish to generate F1 embryos (Figure 1D, step 2). Successful germline transmission was assessed on pooled F1 embryos, usually 45–60 days after initial injection (Figure 1D, Step 3). F1 embryos from successful F0 chimeras (founders) were raised to adulthood, and fish with desired alleles were maintained as stable lines and further backcrossed to minimize potential off-target editing by Cas9 (Figure 1D, step 4). We will first describe our results with *TERT* as a paradigm for modeling telomere attrition and then present the general toolbox of 13 mutant alleles in genes involved in the hallmarks of aging.

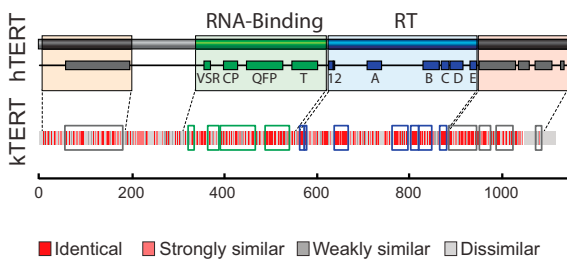
Modeling Telomere Attrition

Telomerase, which comprises the protein component TERT and the RNA component *TERC*, elongates telomeres after replication, thereby maintaining telomere length (Figure 2A). Telomeres

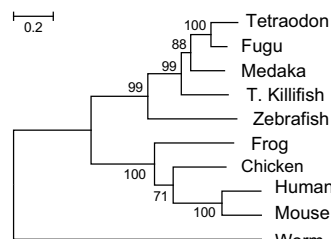
A Telomerase components



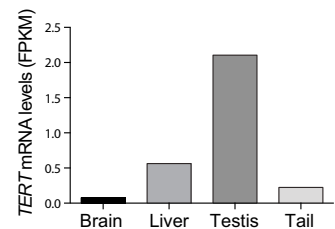
B TERT protein domain conservation



C TERT evolutionary divergence



D TERT mRNA expression (RNA-Seq)



E Successful genome-editing

TERT Exon2 - 10% [5/50]

TGCCCGGTGGCTGAGCAGAGCAGCGTGGATCAGGGAGAGTT	WT
TGCCCGGTGGCTGAGCAGAGCAGCGTGGATCAGGGAGAGTT	Δ15
TGCCCGGTGGCTGAGCAGAGCAGCGTGGATCAGGGAGAGTT	Δ7
TGCCCGGTGGCTGAGCAGAGCAGCGTGGATCAGGGAGAGTT	Δ3
TGCCCGGTGGCTGAGCAGAGCAGCGTGGATCAGGGAGAGTT	Δ8

gRNA, PAM, Stable lines

F *TERT* Δ8 deletion is transcribed, and leads to a premature stop codon

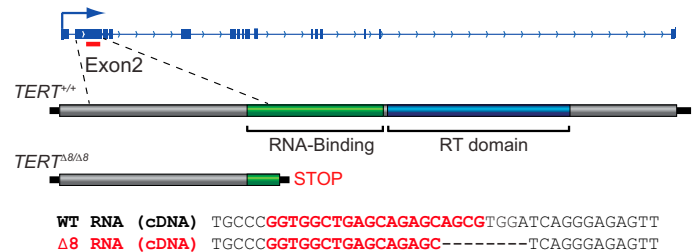


Figure 2. Example of Rapid Genome Editing of *TERT*, the Protein Component of Telomerase, in the Turquoise Killifish

(A) The telomerase complex and gene model prediction for *TERT* and *TERC* using genomic and epigenomic profiling.

(B) Conservation of *TERT* protein domains between human (hTERT) and the turquoise killifish (kTERT).

(C) *TERT* protein sequence divergence predicts evolutionary tree. Scale: substitution per site. Number on nodes: level of confidence.

(D) Relative expression of *TERT* mRNA in brain, liver, testis, and tail using RNA-seq. FPKM, fragments per kilobase of exon per million fragments mapped.

(E) Successful editing of the turquoise killifish *TERT* gene. The wild-type (WT) sequence, as well as the length of deletions (Δ), is indicated relative to the protospacer adjacent motif (PAM, in gray) and the guide RNA sequence (gRNA, in red). The deletions that gave rise to stable lines (Δ3 and Δ8) are indicated (in yellow with black outline).

(F) Top: location of the gRNA successfully targeting *TERT* exon 2 (red line), which is upstream of the exons encoding *TERT* catalytic domains. *TERT* Δ8 allele is predicted to generate a protein with a premature stop codon. Bottom: the *TERT* Δ8 allele is successfully transcribed to RNA, as measured by RT-PCR followed by cDNA sequencing. RT, reverse-transcriptase.

shorten during vertebrate aging, including in the turquoise killifish (Artandi and DePinho, 2010; Hartmann et al., 2009), and are considered to be a good biomarker of biological age (Boonekamp et al., 2013). In humans, mutations in *TERT* or other genes in the telomere-protecting complex result in a spectrum of diseases characterized by tissue homeostasis failure, such as dyskeratosis congenita (Armanios, 2009). Dyskeratosis congenita patients exhibit multiple symptoms resembling aspects of premature aging, including bone marrow failure and pulmonary fibrosis (Armanios, 2009), reduced fertility (Bessler et al., 2010),

and several types of cancers (Alter et al., 2009). Because of their long telomeres, *TERT*-deficient laboratory mice have to be bred for four to six generations for disease phenotypes to manifest (Lee et al., 1998) and are therefore not ideal to model human *TERT* deficiency or telomere attrition during aging.

We first asked whether telomerase components are conserved in the turquoise killifish (Figure 2A). The *TERT* gene model (Figure 2A) allowed us to predict a putative *TERT* protein sequence in the turquoise killifish. The predicted *TERT* protein was conserved, particularly in the RNA binding and the reverse

transcriptase (RT) catalytic domains (Figure 2B). The sequence divergence between *TERT* from the turquoise killifish and other species precisely matched the evolutionary tree (Figure 2C), confirming that the predicted *TERT* protein indeed corresponds to turquoise killifish *TERT*. Interestingly, our RNA-seq data revealed that *TERT* mRNA expression was enriched in the testis relative to other tissues in the turquoise killifish, similar to what is observed in humans (Bessler et al., 2010) (Figure 2D). *TERC*, the RNA component of telomerase, as well as other genes encoding proteins associated with telomerase (e.g., *DYSKERIN*) or involved in the protection of telomeres (e.g., *TRF2* from the Shelterin complex), were also present and expressed in the turquoise killifish (Figures 2A and S1). Thus, telomerase components are well conserved between human and the turquoise killifish.

To edit the *TERT* gene in the turquoise killifish, we designed two gRNAs with a targeting region within the *TERT* exon 2—a long exon located upstream to both catalytic domains of *TERT* (the RNA binding and the RT domains) (Figure 2F, top). One of the two gRNAs led to the generation of a range of deletions in the targeted region of the *TERT* gene (from 3 bp to 15 bp), with a frequency of 10% (Figure 2E). By raising the injected embryos to sexual maturity (~40 days), we obtained four F0 chimeras. Crossing each of these four chimeras with wild-type fish allowed us to generate stable lines with two different types of deletion in *TERT*: 3 bp ($\Delta 3$) and 8 bp ($\Delta 8$) (Figure 2E). The $\Delta 8$ *TERT* allele was successfully transcribed, as assessed by PCR amplification and sequencing of cDNA from heterozygous fish (Figure 2F, bottom). The $\Delta 8$ *TERT* allele is predicted to give rise to a premature stop codon in the *TERT* protein, N-terminal to the catalytic domains (Figure 2F). These results demonstrate the feasibility for rapid genome manipulation in the turquoise killifish, with a total time from injection to stable line of about 2 months.

A *TERT*-Deficient Line in the Turquoise Killifish Exhibit Loss of Telomerase Function and Are Outwardly Normal

We characterized the fish harboring the $\Delta 8$ *TERT* allele, which is predicted to result in a *TERT* protein without catalytic activity. To reduce the frequency of potential off-target mutations, we backcrossed *TERT* $^{\Delta 8/+}$ fish for three generations. We then crossed these heterozygous fish with each other to generate *TERT* $^{\Delta 8/\Delta 8}$ homozygous individuals (generation 1 of homozygous individuals, G1) (Figure 3A). The ratio of adult G1 *TERT* $^{\Delta 8/\Delta 8}$ mutants followed the expected Mendelian ratio ($p = 0.8809$, χ^2 test) (Figure 3A), indicating no embryonic or juvenile (fry) lethality. Furthermore, G1 *TERT* $^{\Delta 8/\Delta 8}$ embryos and adult fish were outwardly normal (Figures 3B and S2A). We asked whether the *TERT* $^{\Delta 8/\Delta 8}$ allele was a true loss of function using the Telomere Repeat Amplification Protocol (TRAP) (Figure 3C). In this assay, tissue extracts are incubated with a radiolabeled oligonucleotide template, followed by PCR amplification of elongated products and autoradiography (Figure 3C). This protocol allowed us to assess telomerase enzymatic activity in liver extracts from *TERT* $^{+/+}$ (wild-type) and *TERT* $^{\Delta 8/\Delta 8}$ homozygous siblings (Figure 3D). Whereas liver extracts from wild-type fish showed robust telomerase activity, we failed to detect any telomerase activity in extracts from *TERT* $^{\Delta 8/\Delta 8}$ fish (Figure 3D). Thus, the $\Delta 8$ allele of *TERT*, which is predicted to generate a truncated

TERT protein, leads to a complete loss of telomerase activity and outwardly normal individuals.

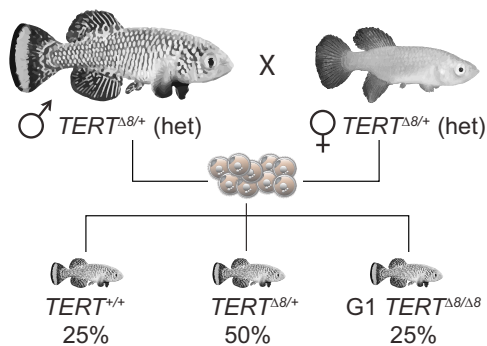
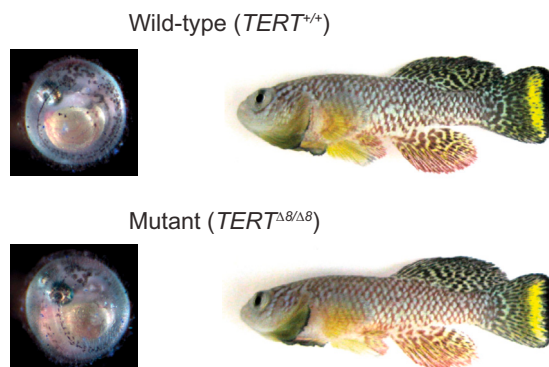
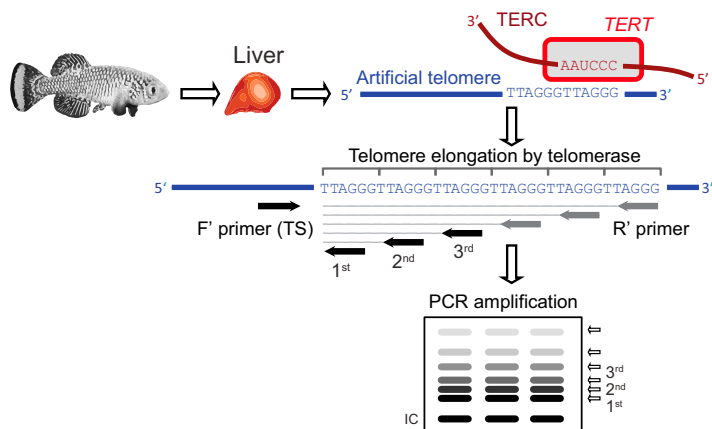
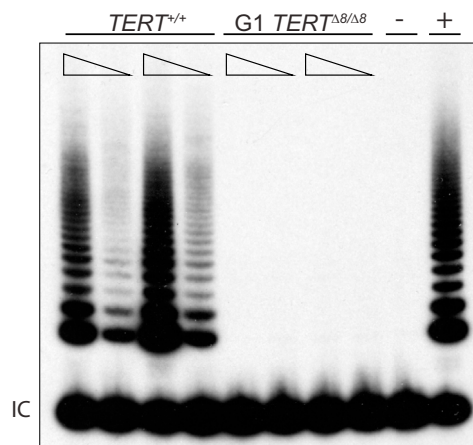
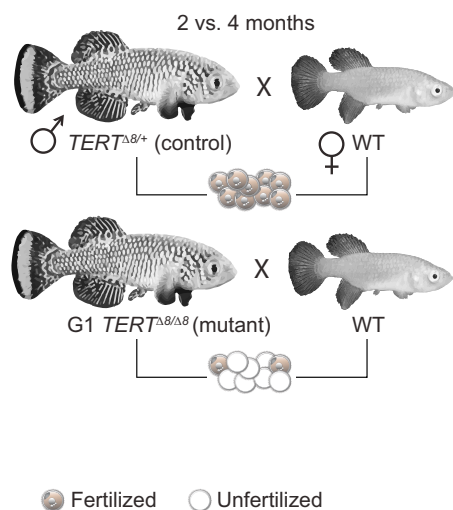
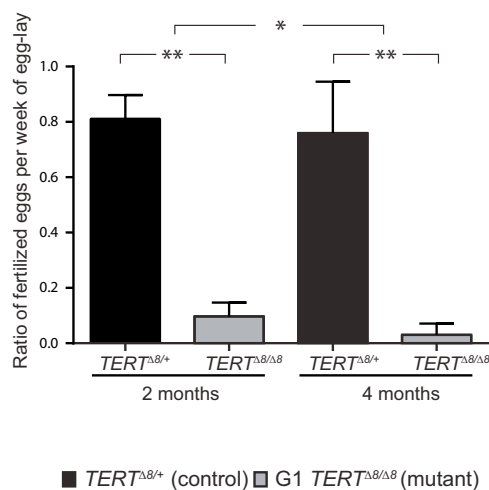
TERT-Deficient Fish Have Age-Dependent Defects in the Germline

Most human patients with haploinsufficiency for telomerase develop normally but exhibit a broad spectrum of tissue homeostasis failure (Armanios, 2009), especially in highly proliferative tissues such as blood, skin, intestine, and male germline (Bessler et al., 2010). *TERT* is highly expressed in the germline (Bessler et al., 2010) and is considered to be particularly important for maintaining the “immortality” of the germline (Zuccherro and Ahmed, 2006). We first tested the fertility of young (2-month-old) G1 *TERT* $^{\Delta 8/\Delta 8}$ males compared to control (heterozygous) siblings by crossing them to young wild-type females (Figure 3E). Whereas control heterozygous male fish were able to fertilize the majority of eggs (81%), G1 *TERT* $^{\Delta 8/\Delta 8}$ males only fertilized 9% of eggs, indicating a dramatic reduction in fertility (Figure 3F, $p < 0.01$, Wilcoxon signed-rank test). Older G1 *TERT* $^{\Delta 8/\Delta 8}$ males (4 month old) showed a further decline in fertility (Figure 3F, $p < 0.05$, Wilcoxon signed-rank test, comparison between age groups). Consistently, the testes of older G1 *TERT* $^{\Delta 8/\Delta 8}$ males were atrophied and had an almost complete loss of germ cells compared to age-matched wild-type controls (Figure 3G, black arrowheads). Germ cells were present in younger G1 *TERT* $^{\Delta 8/\Delta 8}$ males (Figure 3G, inserts), suggesting an age-dependent defect of the germline. Similarly, G1 *TERT* $^{\Delta 8/\Delta 8}$ females also had atrophied ovaries (Figure S2B) and laid fewer eggs than wild-type controls (average of 7 ± 4 and 74 ± 25 eggs respectively, Figure S2B). Thus, G1 *TERT* $^{\Delta 8/\Delta 8}$ fish show premature defects in their germline, resulting in infertility.

G1 *TERT* $^{\Delta 8/\Delta 8}$ fish also displayed defects in other highly proliferative tissues, including blood (overall decrease in tested blood cell types, Figure S2C) and intestine (villi atrophy in some gut regions, Figure S2C). Furthermore, as previously reported in mouse models for *TERT* (Artandi and DePinho, 2010; Hao et al., 2005), *TERT*-deficient fish exhibited epithelial adenomatous changes (decreased polarity and increased nuclear/cytoplasmic ratio) (Figure S2D), which could represent a first step toward intestinal cancers such as those found in dyskeratosis congenita patients (Alter et al., 2009). In contrast, G1 *TERT* $^{\Delta 8/\Delta 8}$ fish did not exhibit significant defects in low-proliferative tissues such as heart, muscle, liver, and kidney (Figure S2E). As the *TERT* $^{\Delta 8/\Delta 8}$ turquoise killifish model exhibits phenotypes in the first generation (as opposed to several generations in laboratory mice [Lee et al., 1998]) and within 2 months (as opposed to 6–8 months in zebrafish [Anchelin et al., 2013; Henriques et al., 2013]), it is currently the fastest system to study telomere attrition pathologies in vertebrates.

TERT-Deficient Fish Exhibit Signs of “Genetic Anticipation”

To further explore the effect of *TERT* deficiency on the germline, we tested whether the offspring of *TERT*-deficient fish exhibit signs of “genetic anticipation.” Genetic anticipation is a phenomenon in which symptoms of a genetic disorder are increased in severity or become apparent at an earlier age in the next generation, mostly due to cumulative damage in the germline.

A Design to create first generation (G1) *TERT* mutant fish**B** G1 *TERT*^{Δ8/Δ8} fish are outwardly normal**C** TRAP assay**D** Telomerase activity**E** Design to test male fertility**F** Male fertility**G** Testis histology

(legend on next page)

Dyskeratosis congenita patients show genetic anticipation: offspring of affected individuals often exhibit earlier onset and more severe symptoms, as well as shorter telomeres (Savage and Alter, 2009). To test whether *TERT*^{Δ8/Δ8} fish also showed signs of genetic anticipation, we crossed the G1 *TERT*^{Δ8/Δ8} homozygous fish to generate G2 *TERT*^{Δ8/Δ8} embryos (Figure 4A). Whereas G1 *TERT*^{Δ8/Δ8} embryos were similar to wild-type embryos (see Figure 3B), G2 *TERT*^{Δ8/Δ8} embryos showed gross developmental abnormalities (Figure 4B, right) and all died prior to hatching (Figure 4C). Thus, the severity of phenotype between generations increases. To test whether telomere length is indeed shorter in G2 *TERT*^{Δ8/Δ8} embryos compared to wild-type or G1 *TERT*^{Δ8/Δ8} embryos, we used Terminal Restriction Fragment (TRF) Southern blot on genomic DNA isolated from *TERT*^{+/+}, G1 *TERT*^{Δ8/Δ8}, or G2 *TERT*^{Δ8/Δ8} individual live embryos using a radio-labeled telomeric probe. These Southern blots revealed that the average length of telomeres was shorter in G2 *TERT*^{Δ8/Δ8} embryos than in wild-type embryos (~1.5 kb versus ~6 kb, respectively) (Figure 4D, left) and G1 *TERT*^{Δ8/Δ8} embryos (Figures 4D, right, and S3). The dramatic telomere shortening in the G2 generation of *TERT*-deficient fish, coupled with the increase in severity of phenotype, is consistent with genetic anticipation and germline defects. Thus, we have successfully generated a vertebrate model for telomerase deficiency that rapidly recapitulates several characteristics of the corresponding human disease. Our results also provide a proof of principle for the use of genome editing in a naturally short-lived vertebrate as a powerful way to quickly test the function of a gene involved in human disease and aging.

Site-Specific Precise Editing: Generating a Disease-Causing Nucleotide Mutation in *TERT* and Inserting a Short Sequence in *POLG*

A large proportion of human diseases are not caused by deletions but by single nucleotide mutations that result in amino acid changes (non-synonymous mutations) (Abecasis et al., 2012). Therefore, we tested the feasibility of editing a specific amino acid residue, taking advantage of homology-directed repair (HDR) instead of the less precise NHEJ (Figure 5A). To this end, we co-injected Cas9 mRNA, one gRNA, and a single-strand DNA (ssDNA) template with a mutation at the desired site to modify the corresponding genomic residue via HDR (Fig-

ure 5A) (Bedell et al., 2012). In human *TERT*, almost all of the disease-associated mutations are non-synonymous (Podlevsky et al., 2008), and many are conserved in the turquoise killifish (Figure 5B). We selected an evolutionary conserved lysine (K902 in human *TERT*) whose mutation to arginine (Parry et al., 2011) or asparagine (Armanios et al., 2005) gives rise to dyskeratosis congenita. This lysine residue corresponds to K836 in the turquoise killifish (Figure 5B). To specifically edit K836, we designed a single gRNA in the proximity of the region encoding this amino acid and an ssDNA template containing two point mutations: one that changes K836 to R and another that prevents Cas9 from further targeting the edited site (Hsu et al., 2014) (Figure 5C, top). Direct sequencing indeed revealed nucleotide changes leading to the K836R mutation in the turquoise killifish *TERT* (Figure 5C, bottom).

We next tested the feasibility of precisely knocking in a short exogenous sequence using HDR (Figure 5A), this time targeting another candidate gene, the mitochondrial DNA Polymerase γ (*POLG*). We designed a gRNA targeting exon 2 of *POLG* and an ssDNA template containing short homology arms and an exogenous NdeI restriction sequence (Figure 5D, top). We chose to target exon 2 of *POLG*, as it has a very high targeting efficiency (90%, Figure S4). Direct sequencing or digestion with NdeI revealed in-frame knockin of the NdeI restriction site into the genomic sequence of turquoise killifish *POLG* (Figure 5D, bottom). Thus, precise genome editing allowed us to generate a specific human disease-causing mutation in the turquoise killifish *TERT* gene and knockin an exogenous sequence in the *POLG* gene.

A Toolbox of Turquoise Killifish Mutants Encompassing the Hallmark of Aging

We next sought to use our platform to target various candidate genes within the hallmarks of aging pathways (López-Otín et al., 2013), including cellular senescence and stem cell exhaustion (*p15/INK4B*), mitochondrial dysfunction (*POLG*), deregulated nutrient sensing (*IGF1R*, *RAPTOR*, *RPS6KB1*, and *FOXO3*), epigenetic alterations (*ASH2L*), genomic instability (*SIRT6*), loss of proteostasis (*ATG5*), and intercellular communication (*IL8* and *APOE*) (Figures 6A and S4 and Table S1). We targeted genes whose deficiency is expected to either promote longevity (*IGF1R*, *RAPTOR*, and *RPS6KB1*) or accelerate signs of aging (*TERT* and *POLG*) (López-Otín et al., 2013). Although some

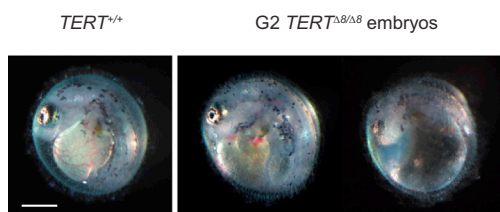
Figure 3. *TERT*^{Δ8/Δ8} Fish Show No Telomerase Activity and Exhibit a Progressive Loss of Fertility in the First Generation

- (A) Intercrossing of *TERT*^{Δ8/+} heterozygous (het) fish to generate generation 1 (G1) *TERT*^{Δ8/Δ8} fish. G1 *TERT*^{Δ8/Δ8} fish are observed at the expected Mendelian ratios (no difference between expected and observed frequencies, $p = 0.8809$, χ^2 test).
- (B) G1 *TERT*^{Δ8/Δ8} embryos (left) and adults (right) are outwardly normal.
- (C) Schematic for TRAP. Telomerase enzymatic activity in liver is evaluated by the ability of tissue extract to add telomeric repeats to radio-labeled artificial telomeres in vitro.
- (D) Telomerase enzymatic activity as measured by the TRAP assay in *TERT*^{+/+} and G1 *TERT*^{Δ8/Δ8} fish liver samples. IC: TRAP internal control product. Representative of three independent experiments.
- (E) Experimental design to assess male fertility. *TERT*^{Δ8/+} (control) and G1 *TERT*^{Δ8/Δ8} (mutant) males, at two different age groups (2 and 4 months), were mated with young (2 months) wild-type (WT) females. Fertilized eggs (gray) were counted after 1 week.
- (F) Ratio of fertilized eggs per week of egg lay in *TERT*^{Δ8/+} (control) and G1 *TERT*^{Δ8/Δ8} (mutant). Mean + SD of >70 eggs, generated from 4 to 5 crosses per age group. Wilcoxon signed-rank test, * $p < 0.05$ and ** $p < 0.01$. For the comparison between age groups, standardized values to age-matched controls were used.
- (G) Histological sections of testis from *TERT*^{+/+} (control) and G1 *TERT*^{Δ8/Δ8} fish at 4 to 5 months (4 m, full-size image) and 2 months (2 m, insert). Sz, spermatozoa (mature sperm); St, spermatids. Scale bar, 50 μ m. Representative of $n \geq 6$ individuals from each genotype (4 to 5 months) and $n = 2$ individuals from each genotype (2 months). Presence of germ cells in the testis of control fish (top, white arrowheads). Deficiency of germ cells in the testis of *TERT*-deficient fish (bottom, black arrowheads).

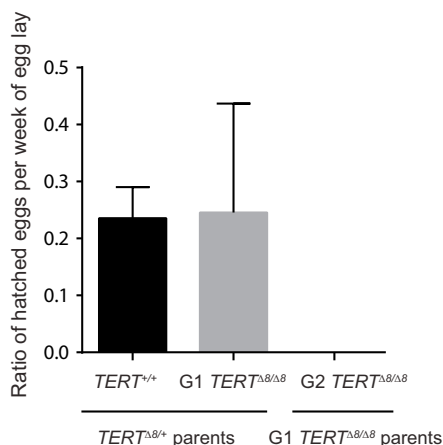
A Design to create second generation (G2) *TERT* mutant fish



B G2 *TERT*^{Δ8/Δ8} embryos suffer from gross abnormalities



C Ratio of successful hatching per genotype



D Telomere length measurement

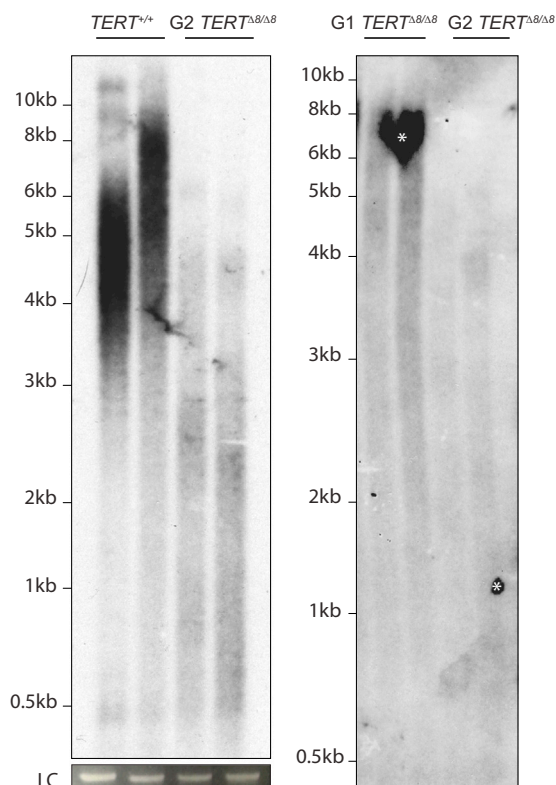


Figure 4. *TERT*-Deficient Turquoise Killifish Exhibit Genetic Anticipation

(A) Experimental design. G1 *TERT*^{Δ8/Δ8} (left) or *TERT*^{+/+} (right) fish were intercrossed to generate generation 2 (G2) *TERT*^{Δ8/Δ8} or *TERT*^{+/+} fish, respectively. The development of embryos was assessed until hatching.

(B) Representative images of *TERT*^{+/+} and G2 *TERT*^{Δ8/Δ8} embryos at an equivalent developmental stage. Scale bar, 300 μm.

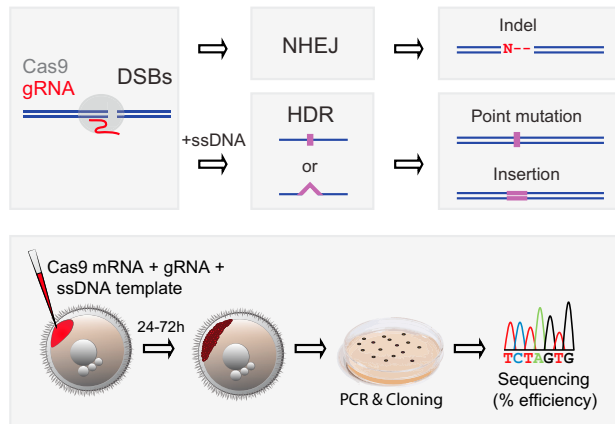
(C) Ratio of successful hatching per week of egg lay for the indicated genotypes. Mean + SD of >70 embryos for each parental genotype (*TERT*^{Δ8/+} versus G1 *TERT*^{Δ8/Δ8}).

(D) Telomere length measurement using TRF Southern blot. Left: *TERT*^{+/+} and G2 *TERT*^{Δ8/Δ8} embryos. Representative of three experiments. LC: loading control for genomic DNA. Right: G1 *TERT*^{Δ8/Δ8} and G2 *TERT*^{Δ8/Δ8} embryos. Expanded version is in Figure S3. White asterisk: non-specific probe binding.

genes have already been shown to regulate lifespan in both invertebrates and vertebrates (*IGF1R* and *RPS6KB1*) (Kenyon, 2010), others have not yet been tested in vertebrates (*ASH2L* and *FOXO3*) (Figure 6B). Importantly, some genes do not have obvious orthologs in yeast or invertebrates (*p15INK4B*, *IL8*, and *APOE*) (Figure 6B). Finally, several genes have been implicated in human diseases, including *APOE* (Alzheimer's disease [Rhinn et al., 2013]), *TERT* (dyskeratosis congenita [Armanios, 2009]), and *p15INK4B* (cancer [Okamoto et al., 1995]).

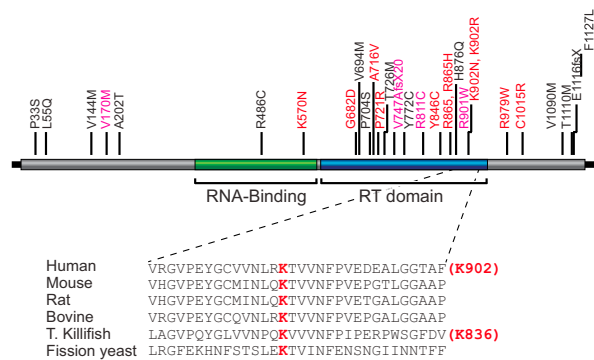
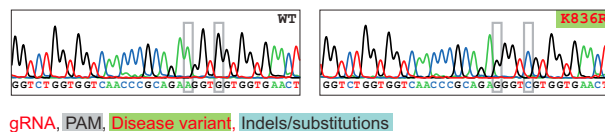
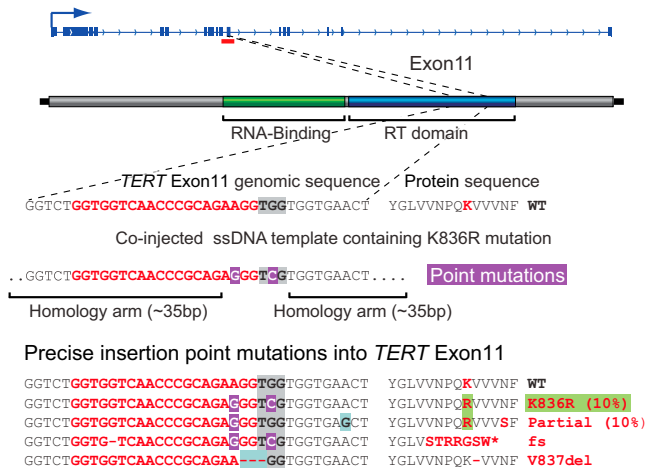
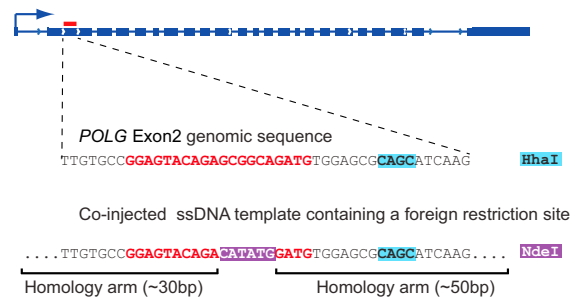
For each of these 13 genes, we assembled gene models and predicted protein sequences, analyzed mRNA expression patterns in four tissues, and profiled the H3K4me3 epigenetic landscape to determine TSSs (Figures 6C and S4). We designed two to five gRNA sequences for each gene (Table S1), which was sufficient to identify at least one successful gRNA (Figures 6B, 6C, and S4 and Table S1). The efficiency of targeting ranged from 0% to 90% depending on the gRNA (Figures 6 and S4 and Table S1). So far, we have

A Precise genome-editing pipeline



B Disease-associated variants of human TERT

Identical, Similar in turquoise killifish

C Generating a human disease variant in the killifish *TERT*D Precise insertion of short sequences in the killifish *POLG*Precise insertion of NdeI site into *POLG* Exon 2

TTGTGCCGGAGTACAGAGCGGCGAGATGTTGGAGCCGAGCATCAAG WT
 TTGTGCCGGAGTACAGAGCGGCGAGATGTTGGAGCCGAGCATCAAG NdeI KI (10%)
 TTGTGCCGGAGTACAGAGCGGCGAGATGTTGGAGCCGAGCATCAAG Partial (20%)
 TTGTGCCGGAGTACAGAGCGGCGAGATGTTGGAGCCGAGCATCAAG Δ1
 TTGTGCCGGAGTACAGAGCGGCGAGATGTTGGAGCCGAGCATCAAG Δ14

DNA digestion from non-injected or injected embryos

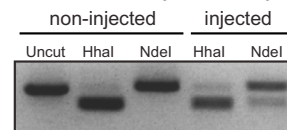


Figure 5. Precise Generation of Human Disease Mutation in *TERT* and Insertion of a Short Sequence in *POLG*

(A) Genome-editing pipeline for specific point mutations and insertions. ssDNA: ssDNA template. NHEJ: non-homologous end joining. HDR: homology-directed repair.

(B) Top: disease-associated variants in hTERT. Conservation of the disease-causing residues between human TERT and turquoise killifish TERT is color coded (red, identical; pink, similar in turquoise killifish TERT). Bottom: K902 in human TERT is evolutionary conserved and corresponds to K836 in turquoise killifish TERT.

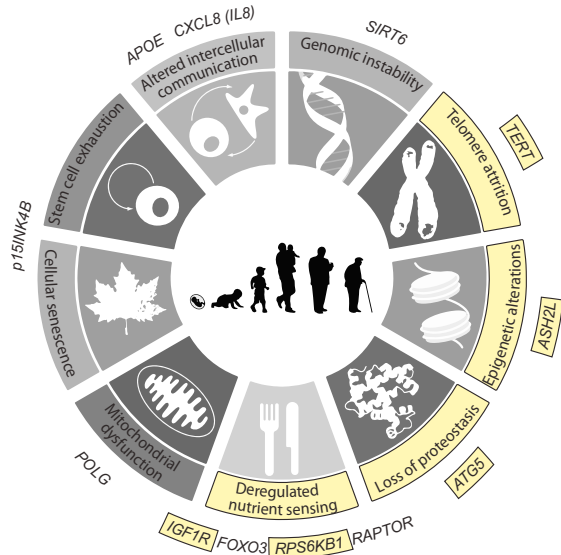
(C) Top: location of a selected gRNA (red line) in close proximity to K836 in exon 11 of the turquoise killifish *TERT* and core sequence of the co-injected ssDNA template. Bottom: precise editing of specific codons leading to the nucleotide change (A to G) corresponding to the K836R mutation. An example chromatogram is shown at the bottom. The K836R mutation is highlighted with green background. fs, frame shift; del, deletion.

(D) Location of the gRNA targeting exon 2 of the turquoise killifish *POLG*, and core sequence of the co-injected ssDNA template to introduce an exogenous NdeI site. Bottom: precise insertion of the NdeI restriction sequence, as shown by direct sequencing or restriction digestion. Representative of two independent experiments.

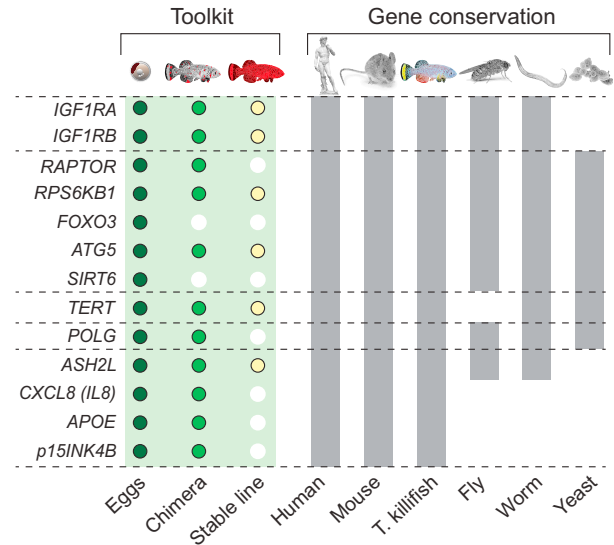
generated chimeras (F0, adult) for 11 genes (Figure 6B). We have examined germline transmission for five of them (*IGF1RA*, *IGF1RB*, *ATG5*, *ASH2L*, and *RPS6KB1*) and report

the targeted alleles (Figures 6C and S4). We also have stable lines for a subset of these alleles (Figures 6B and S4 and Table S1).

A Targeted genes and pathways with stable lines

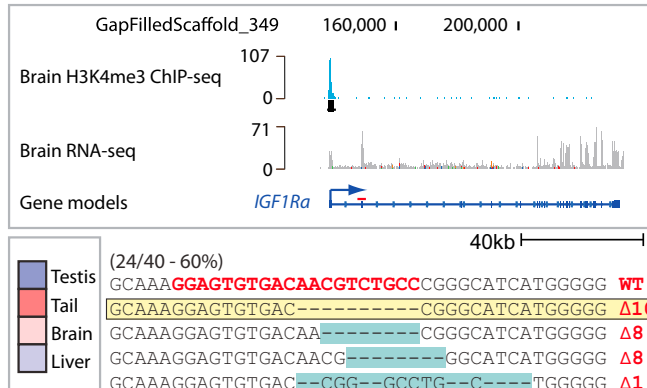


B Targeted genes and evolutionary conservation

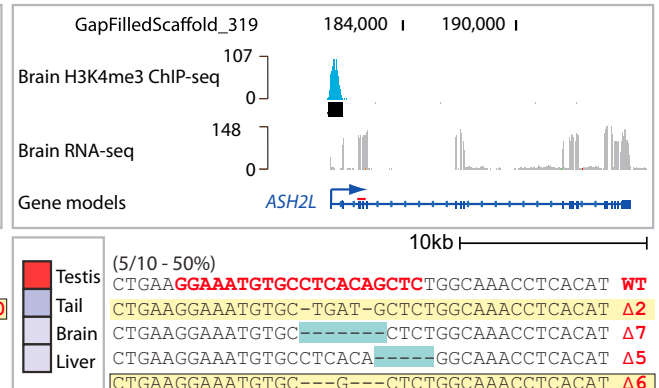


C Selected examples of targeted genes

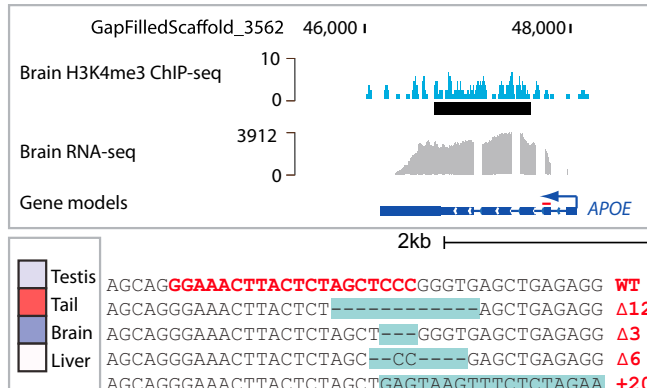
IGF1RA



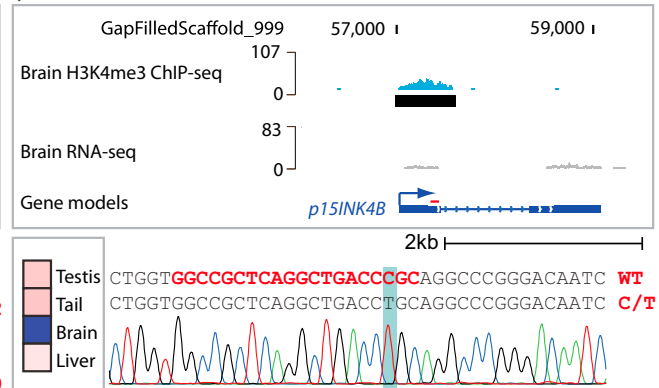
ASH2L



APOE



p15INK4B



gRNA, Indels/substitutions, Germline transmitted (pooled F1 embryos), Stable lines, Normalized RNA expression

(legend on next page)

The platform and toolbox we have developed—genome, genomic data sets, gene models, and efficient gRNAs—as well as the mutant fish lines, will be made available to the community. To facilitate future design of gRNAs in the turquoise killifish, we have uploaded the sequenced genome and gene models into CHOPCHOP (Montague et al., 2014), thereby providing easy access for the community. Together, our results highlight the ease and versatility of our platform for generating mutants in the turquoise killifish, which will greatly facilitate high-throughput aging studies and disease modeling in vertebrates.

DISCUSSION

The Turquoise Killifish: A New Vertebrate Model for Systematic Studies on Aging and Longevity

Here, we developed a platform in a naturally short-lived vertebrate, the turquoise killifish, for the systematic exploration of aging and age-related diseases. The field of aging will greatly benefit from the study of species beyond conventional model systems (Bolker, 2012). Many exceptionally long-lived vertebrates, such as the naked mole rat (~30 years), the Brandt's bat (~30 years), capuchin monkey (~50 years), rock fish (~150 years), and the bow-headed whale (~200 years) (Tacutu et al., 2013) have already allowed comparative genomics, proteomics, and cellular studies (Austad, 2010; Gorbunova et al., 2014). However, long-lived species are not well suited for genetic manipulation, longitudinal, or lifespan studies. The turquoise killifish, with its naturally short lifespan, well-characterized aging traits, low costs, and ease of maintenance in the laboratory, is highly suited for rapid experimental aging research in vertebrates. Furthermore, the turquoise killifish is currently the shortest living vertebrate with a sequenced genome, which will be valuable for comparative studies.

Fish provide several advantages as laboratory species. They are amenable to high-throughput approaches such as genetic and drug screens (Schartl, 2014). Fish also display a range of unique traits. For example, zebrafish, the primary fish model, is widely used for developmental processes due to its unique characteristics (e.g., fast and stereotypic embryonic development). Other fish have been used for specific traits, including social behaviors (cichlids [Fernald, 2012]) and adaptive evolution (sticklebacks [Jones et al., 2012]). Our genome and genome-editing platform in the turquoise killifish should help transition this fish to a more widely studied model, providing a unique opportunity for high-throughput aging and longitudinal studies. It will be important to characterize aging in the mutants we have already generated, as well as generating additional ones. Finally, the genome-to-phenotype platform we present here could serve

as a paradigm for how to rapidly develop a wide range of species into model organisms.

A Proof-of-Concept Model for Telomerase-Related Pathologies in the Turquoise Killifish

By targeting the *TERT* gene in the turquoise killifish, we have developed the fastest system so far for studying telomerase pathologies in vertebrates. Similar to what is observed in dyskeratosis congenita patients, *TERT*-deficient fish exhibit defects in highly proliferative tissues (male germline, intestine, and blood) in the first generation and as early as 2 months of age. This killifish *TERT* model should help untangle the interaction between aging and telomerase pathologies, which is largely unknown despite the fact that telomere attrition rate is a good predictor of accelerated aging in humans (Boonekamp et al., 2013). Although *TERT*-deficient killifish exhibit specific age-dependent defects, we have not observed premature death by 4–5 months of age. This might indicate that the defects in regeneration of specific tissues are not limiting for lifespan under these conditions, although they may be detrimental under more stressful conditions (e.g., injuries or end of life). It will be important to characterize lifespan, regeneration, and telomere length in this *TERT* model during aging. It will also be interesting to compare the phenotypes of this *TERT* deletion model with models mimicking in killifish the *TERT* mutations found in human patients.

The killifish model fills a unique niche in the wide range of existing models of telomerase deficiency. Cellular models have been extremely helpful to understand telomerase biology and pathologies (Batista and Artandi, 2013), but they cannot easily recapitulate systemic defects or tissue interactions. Invertebrate models, which have provided crucial insights into telomerase function (Raices et al., 2005), lack some of the organs affected by telomere pathologies in humans (e.g., bona fide blood) (Gomes et al., 2010). The main vertebrate model system, the laboratory mouse, has been the most widely used to understand the role of telomerase in specific pathologies, particularly cancer (Artandi and DePinho, 2010). However, in laboratory mouse strains, phenotypes are only manifested after several generations because of their extremely long telomeres. This issue can be solved by using the *castaneus* strain, which has shorter telomeres (Hao et al., 2005), but changing genetic background is time consuming. Recent studies in zebrafish have been promising, with *TERT*-deficient zebrafish demonstrating a range of phenotypes, including gastrointestinal atrophy, premature infertility, and death (Anchelin et al., 2013; Henriques et al., 2013), although it took those fish at least 6–8 months to exhibit most phenotypes. While the turquoise killifish *TERT* model is still limited by the number of available tools, it should

Figure 6. A Toolkit for Vertebrate Aging and Age-Related Disease Research

(A) Genes that were successfully edited in the nine hallmarks of aging. Genes and pathways for which we chose to generate stable lines are indicated in yellow with a black outline.

(B) Detailed stages of editing completion in specific genes, color-coded as indicated. Presence of orthologs in different species is indicated in gray.

(C) Selected examples of targeted genes depicting detailed genomic, epigenomic, and expression information (upper box), relative expression in tissues (lower left box), and types of observed indels and substitutions (lower right box). Germline-transmitted alleles assessed in pooled F1 embryos are in yellow. Stable lines are in yellow with a black outline. Whenever assessed, the targeting efficiency in eggs was indicated as a percentage. For *ASH2L*, the $\Delta 6$ stable line was generated by a separate pair of founders and was not part of the efficiency calculation. Example of a sequencing chromatogram showing the substitution in *p15INK4B*.

be well suited for rapid exploration of telomere pathologies and screening for potential treatments that can delay these pathologies.

A Toolkit for Modeling Complex Human Diseases, Traits, and Drug Responses

The advent of personalized medicine and high-throughput human genetic studies is providing an overwhelming influx of new variants associated with specific human diseases, traits, and responses to drugs (pharmacogenetics). However, functional validation for most of these genes and variants is lagging behind. One way to study these candidates has been to generate induced pluripotent stem cells (iPSCs) harboring mutations derived from patients or engineered *de novo* (Hockemeyer et al., 2011). Although this approach allows high-throughput studies, it does not recapitulate the complex interactions between tissues, such as endocrine and paracrine communication, as well as complex responses to environment or drugs. The turquoise killifish model could greatly facilitate *in vivo* high-throughput studies of new candidate genes or alleles, while modeling the integrative and non-cell-autonomous interactions that are characteristic of aging and pathological conditions.

Recent genomic studies have revealed that many human diseases are caused by deleterious non-synonymous variants (Abecasis et al., 2012), and this is also likely the case for aging and longevity. For example, most disease-causing mutations in human *TERT* are due to variants leading to a single amino acid residue change (Podlevsky et al., 2008). Here, we show the feasibility of editing specific sequences in turquoise killifish genes. Such directed knockin approach will also be particularly helpful for the systematic exploration of variants in human longevity candidate genes, such as *IGF1R*, which is among ~200 predicted candidates identified by genetic association studies of longevity (Tacutu et al., 2013). This approach could also facilitate introduction of epitope tags, *loxP* sites, or artificial stop codons at endogenous genomic loci.

Overall, our study provides a rapid pipeline for genotype-to-phenotype analyses in a new vertebrate model with a compressed timescale of aging. It also renders available as a resource the *de novo* sequenced genome of the turquoise killifish and mutant lines of this fish. This comprehensive platform opens the possibility of screening for genetic and drug interactions in an integrative system. In addition, it offers a promising venue for high-throughput modeling of aging and complex human diseases *in vivo*.

EXPERIMENTAL PROCEDURES

Additional details are provided in the [Extended Experimental Procedures](#).

Gene Model Prediction, Conservation, and Phylogeny

Gene models were obtained from two independent sources: (1) a *de novo* whole-genome shotgun assembly (GenBank JNBZ000000000) and (2) a *de novo* transcriptome assembly from four adult fish tissues (brain, liver, testis, and tail) using Oases (Schulz et al., 2012) (Sequence Read Archive [SRA] SRP041421). For the *de novo* transcriptome assembly, putative annotations were obtained by unidirectional blastx to the Swissprot database. The detailed genome assembly and annotation will be reported elsewhere (D.R.V., B.A.B., P.P.S., and A.B., unpublished data).

Strand-Specific RNA-Seq Expression Analysis

RNA extraction was performed using the Nucleospin kit (Machery-Nagel), followed by rRNA removal (RiboZero Magnetic Gold Kit, Epicenter). Double-strand cDNA was ligated with barcoded adapters and amplified using Illumina PCR primers (P1.0 and 2.0, Illumina) prior to sequencing. Expression data were analyzed by mapping RNA-seq reads onto gene models using Tophat2 v2.0.4 and Cufflinks v2.0.2.

H3K4me3 ChIP-Seq

H3K4me3 ChIP-seq experiments were performed according to Benayoun et al. (2014) on whole-brain tissue isolated from adult male fish (SRA SRP045718).

CRISPR/Cas9 Target Prediction for Guide RNA Selection

For each selected gene, we identified conserved regions in the coding sequence using multiple vertebrate orthologs using <http://genome.ucsc.edu/>. Conserved regions that were upstream of functional or active protein domains were selected for targeting. gRNA target sites were identified using ZIFIT (<http://zifit.partners.org/>) (Hwang et al., 2013) or CHOPCHOP (<https://chopchop.rc.fas.harvard.edu/>) (Montague et al., 2014).

Guide RNA Synthesis

Initial experiments were performed using the DR274 guide RNA expression vector (Addgene, 42250) (Hwang et al., 2013). In subsequent experiments, hybridized oligonucleotides were used as an *in vitro* transcription template. gRNAs were *in vitro* transcribed and purified using the MAXIscript T7 kit (Life Technologies).

Production of Cas9 mRNA

Initial experiments were performed using the MLM3613 Cas9 expression vector (Addgene, 42251) (Hwang et al., 2013). In subsequent experiments, the pCS2-nCas9n expression vector was used (Addgene, 47929) (Jao et al., 2013). Capped and polyadenylated Cas9 mRNA was *in vitro* transcribed and purified using either the mMESSAGE mMACHINE T7 ULTRA or SP6 kits (Life Technologies).

Single-Stranded DNA Template for Homology-Directed Repair

For homology-directed repair (HDR) experiments, ssDNA templates were designed to contain short homology arms (30 bp–50 bp) surrounding the gRNA target. The ssDNA templates were commercially synthesized and purified prior to injection (QIAquick Nucleotide Removal Kit, QIAGEN) (Bedell et al., 2012).

Microinjection of Turquoise Killifish Embryos and Sequencing of Targeted Sites

Microinjection of turquoise killifish embryos was performed according to Valenzano et al. (2011). Cas9-encoding mRNA (200–300 ng/μl) and gRNA (30 ng/μl) were mixed with phenol-red (2%) and co-injected into one-cell-stage fish embryos. For HDR experiments, the ssDNA template (20 μM) was also co-injected. Three days after injection, genomic DNA was extracted from five to ten pooled embryos. The genomic area encompassing the targeted site (~600 bp) was PCR amplified. Endonuclease digestions or DNA sequencing was used for analysis (Table S1).

Fish husbandry, telomerase activity and telomere length measurements, fertility, histology, and blood count analyses are provided in the [Extended Experimental Procedures](#).

ACCESSION NUMBERS

Sequencing and genome data have been deposited to the GenBank (JNBZ000000000). RNA-seq (SRP041421) and H3K4me3 ChIP-seq (SRP045718) data were submitted to SRA (Sequence Read Archive).

SUPPLEMENTAL INFORMATION

Supplemental Information includes Extended Experimental Procedures, four figures, and one table and can be found with this article online at <http://dx.doi.org/10.1016/j.cell.2015.01.038>.

AUTHOR CONTRIBUTIONS

I.H. and A.B. designed the study and wrote the manuscript. I.H. performed experiments with help from B.M. B.A.B. generated gene models with help from P.P.S. and E.Z. B.A.B. also analyzed all data sets generated by D.R.V. (genomic), C.-K.H. (transcriptomic), and I.H. (epigenomic). P.P.S. performed the protein domain conservation analysis. M.F.P. and S.E.A. helped I.H. with the telomerase-related assays. S.C.S. helped I.H. with injections. All authors commented on the manuscript.

ACKNOWLEDGMENTS

We thank Summer Thyme, John Geisinger, Franklin Zhong, and Michael Basisk for stimulating scientific discussion and members of the Brunet lab, especially Lauren Booth and Ashley Webb, for critical discussion and feedback on the manuscript. We thank Brock Martin and Andrew Connolly for histology advice and Elizabeth Pollina for help with the epigenomic data set. We thank Tessa Montague, Eivind Valen, and James Gagnon for incorporating the genome into the CHOPCHOP search engine. This work was supported by NIH DP1AG044848 and the Glenn Laboratories for the Biology of Aging (A.B.), the Damon Runyon, Rothschild, and HFSP fellowships (I.H.), and the Dean's fellowship, Stanford (B.A.B.).

Received: November 10, 2014

Revised: January 15, 2015

Accepted: January 23, 2015

Published: February 12, 2015

REFERENCES

- Abecasis, G.R., Auton, A., Brooks, L.D., DePristo, M.A., Durbin, R.M., Handsaker, R.E., Kang, H.M., Marth, G.T., and McVean, G.A.; 1000 Genomes Project Consortium (2012). An integrated map of genetic variation from 1,092 human genomes. *Nature* 491, 56–65.
- Alter, B.P., Giri, N., Savage, S.A., and Rosenberg, P.S. (2009). Cancer in dyskeratosis congenita. *Blood* 113, 6549–6557.
- Anchelin, M., Alcaraz-Pérez, F., Martínez, C.M., Bernabé-García, M., Mulero, V., and Cayuela, M.L. (2013). Premature aging in telomerase-deficient zebrafish. *Dis. Model. Mech.* 6, 1101–1112.
- Armanios, M. (2009). Syndromes of telomere shortening. *Annu. Rev. Genomics Hum. Genet.* 10, 45–61.
- Armanios, M., Chen, J.L., Chang, Y.P., Brodsky, R.A., Hawkins, A., Griffin, C.A., Eshleman, J.R., Cohen, A.R., Chakravarti, A., Hamosh, A., and Greider, C.W. (2005). Haploinsufficiency of telomerase reverse transcriptase leads to anticipation in autosomal dominant dyskeratosis congenita. *Proc. Natl. Acad. Sci. USA* 102, 15960–15964.
- Artandi, S.E., and DePinho, R.A. (2010). Telomeres and telomerase in cancer. *Carcinogenesis* 31, 9–18.
- Austad, S.N. (2010). Cats, “rats,” and bats: the comparative biology of aging in the 21st century. *Integr. Comp. Biol.* 50, 783–792.
- Batista, L.F., and Artandi, S.E. (2013). Understanding telomere diseases through analysis of patient-derived IPS cells. *Curr. Opin. Genet. Dev.* 23, 526–533.
- Bedell, V.M., Wang, Y., Campbell, J.M., Poshusta, T.L., Starker, C.G., Krug, R.G., 2nd, Tan, W., Penheiter, S.G., Ma, A.C., Leung, A.Y., et al. (2012). In vivo genome editing using a high-efficiency TALEN system. *Nature* 491, 114–118.
- Benayoun, B.A., Pollina, E.A., Ucar, D., Mahmoudi, S., Karra, K., Wong, E.D., Devarajan, K., Daugherty, A.C., Kundaje, A.B., Mancini, E., et al. (2014). H3K4me3 breadth is linked to cell identity and transcriptional consistency. *Cell* 158, 673–688.
- Bessler, M., Wilson, D.B., and Mason, P.J. (2010). Dyskeratosis congenita. *FEBS Lett.* 584, 3831–3838.
- Bolker, J. (2012). Model organisms: There's more to life than rats and flies. *Nature* 491, 31–33.
- Boonekamp, J.J., Simons, M.J., Hemerik, L., and Verhulst, S. (2013). Telomere length behaves as biomarker of somatic redundancy rather than biological age. *Aging Cell* 12, 330–332.
- Di Cicco, E., Tozzini, E.T., Rossi, G., and Cellerino, A. (2011). The short-lived annual fish *Nothobranchius furzeri* shows a typical teleost aging process reinforced by high incidence of age-dependent neoplasias. *Exp. Gerontol.* 46, 249–256.
- Fernald, R.D. (2012). Social control of the brain. *Annu. Rev. Neurosci.* 35, 133–151.
- Genade, T., Benedetti, M., Terzibasi, E., Roncaglia, P., Valenzano, D.R., Cattaneo, A., and Cellerino, A. (2005). Annual fishes of the genus *Nothobranchius* as a model system for aging research. *Aging Cell* 4, 223–233.
- Gomes, N.M., Shay, J.W., and Wright, W.E. (2010). Telomere biology in Metazoa. *FEBS Lett.* 584, 3741–3751.
- Gorbunova, V., Seluanov, A., Zhang, Z., Gladyshev, V.N., and Vijg, J. (2014). Comparative genetics of longevity and cancer: insights from long-lived rodents. *Nat. Rev. Genet.* 15, 531–540.
- Hao, L.Y., Armanios, M., Strong, M.A., Karim, B., Feldser, D.M., Huso, D., and Greider, C.W. (2005). Short telomeres, even in the presence of telomerase, limit tissue renewal capacity. *Cell* 123, 1121–1131.
- Hartmann, N., and Englert, C. (2012). A microinjection protocol for the generation of transgenic killifish (Species: *Nothobranchius furzeri*). *Dev. Dyn.* 241, 1133–1141.
- Hartmann, N., Reichwald, K., Lechel, A., Graf, M., Kirschner, J., Dorn, A., Terzibasi, E., Wellner, J., Platzer, M., Rudolph, K.L., et al. (2009). Telomeres shorten while Tert expression increases during ageing of the short-lived fish *Nothobranchius furzeri*. *Mech. Ageing Dev.* 130, 290–296.
- Henriques, C.M., Carneiro, M.C., Tenente, I.M., Jacinto, A., and Ferreira, M.G. (2013). Telomerase is required for zebrafish lifespan. *PLoS Genet.* 9, e1003214.
- Hockemeyer, D., Wang, H., Kiani, S., Lai, C.S., Gao, Q., Cassady, J.P., Cost, G.J., Zhang, L., Santiago, Y., Miller, J.C., et al. (2011). Genetic engineering of human pluripotent cells using TALE nucleases. *Nat. Biotechnol.* 29, 731–734.
- Hsu, P.D., Lander, E.S., and Zhang, F. (2014). Development and applications of CRISPR-Cas9 for genome engineering. *Cell* 157, 1262–1278.
- Hwang, W.Y., Fu, Y., Reyon, D., Maeder, M.L., Tsai, S.Q., Sander, J.D., Peterson, R.T., Yeh, J.R., and Joung, J.K. (2013). Efficient genome editing in zebrafish using a CRISPR-Cas system. *Nat. Biotechnol.* 31, 227–229.
- Jao, L.E., Wente, S.R., and Chen, W. (2013). Efficient multiplex biallelic zebrafish genome editing using a CRISPR nuclease system. *Proc. Natl. Acad. Sci. USA* 110, 13904–13909.
- Jinek, M., Chylinski, K., Fonfara, I., Hauer, M., Doudna, J.A., and Charpentier, E. (2012). A programmable dual-RNA-guided DNA endonuclease in adaptive bacterial immunity. *Science* 337, 816–821.
- Jones, F.C., Grabherr, M.G., Chan, Y.F., Russell, P., Mauceli, E., Johnson, J., Swofford, R., Pirun, M., Zody, M.C., White, S., et al.; Broad Institute Genome Sequencing Platform & Whole Genome Assembly Team (2012). The genomic basis of adaptive evolution in threespine sticklebacks. *Nature* 484, 55–61.
- Kenyon, C.J. (2010). The genetics of ageing. *Nature* 464, 504–512.
- Kirschner, J., Weber, D., Neuschl, C., Franke, A., Böttger, M., Zielke, L., Powalsky, E., Groth, M., Shagin, D., Petzold, A., et al. (2012). Mapping of quantitative trait loci controlling lifespan in the short-lived fish *Nothobranchius furzeri*—a new vertebrate model for age research. *Aging Cell* 11, 252–261.
- Lee, H.W., Blasco, M.A., Gottlieb, G.J., Horner, J.W., 2nd, Greider, C.W., and DePinho, R.A. (1998). Essential role of mouse telomerase in highly proliferative organs. *Nature* 392, 569–574.
- López-Otín, C., Blasco, M.A., Partridge, L., Serrano, M., and Kroemer, G. (2013). The hallmarks of aging. *Cell* 153, 1194–1217.
- Montague, T.G., Cruz, J.M., Gagnon, J.A., Church, G.M., and Valen, E. (2014). CHOPCHOP: a CRISPR/Cas9 and TALEN web tool for genome editing. *Nucleic Acids Res.* 42, W401–W407.

- Niccoli, T., and Partridge, L. (2012). Ageing as a risk factor for disease. *Curr. Biol.* 22, R741–R752.
- Okamoto, A., Hussain, S.P., Hagiwara, K., Spillare, E.A., Rusin, M.R., Demetrick, D.J., Serrano, M., Hannon, G.J., Shiseki, M., Zariwala, M., et al. (1995). Mutations in the p16INK4/MTS1/CDKN2, p15INK4B/MTS2, and p18 genes in primary and metastatic lung cancer. *Cancer Res.* 55, 1448–1451.
- Parry, E.M., Alder, J.K., Qi, X., Chen, J.J., and Armanios, M. (2011). Syndrome complex of bone marrow failure and pulmonary fibrosis predicts germline defects in telomerase. *Blood* 117, 5607–5611.
- Podlevsky, J.D., Bley, C.J., Omana, R.V., Qi, X., and Chen, J.J. (2008). The telomerase database. *Nucleic Acids Res.* 36, D339–D343.
- Raices, M., Maruyama, H., Dillin, A., and Karlseder, J. (2005). Uncoupling of longevity and telomere length in *C. elegans*. *PLoS Genet.* 1, e30.
- Reichwald, K., Lauber, C., Nanda, I., Kirschner, J., Hartmann, N., Schories, S., Gausmann, U., Taudien, S., Schilhabel, M.B., Szafranski, K., et al. (2009). High tandem repeat content in the genome of the short-lived annual fish *Nothobranchius furzeri*: a new vertebrate model for aging research. *Genome Biol.* 10, R16.
- Rhinn, H., Fujita, R., Qiang, L., Cheng, R., Lee, J.H., and Abeliovich, A. (2013). Integrative genomics identifies APOE ϵ 4 effectors in Alzheimer's disease. *Nature* 500, 45–50.
- Rinn, J.L., and Chang, H.Y. (2012). Genome regulation by long noncoding RNAs. *Annu. Rev. Biochem.* 81, 145–166.
- Savage, S.A., and Alter, B.P. (2009). Dyskeratosis congenita. *Hematol. Oncol. Clin. North Am.* 23, 215–231.
- Schartl, M. (2014). Beyond the zebrafish: diverse fish species for modeling human disease. *Dis. Model. Mech.* 7, 181–192.
- Schulz, M.H., Zerbino, D.R., Vingron, M., and Birney, E. (2012). Oases: robust de novo RNA-seq assembly across the dynamic range of expression levels. *Bioinformatics* 28, 1086–1092.
- Tacutu, R., Craig, T., Budovsky, A., Wuttke, D., Lehmann, G., Taranukha, D., Costa, J., Fraifeld, V.E., and de Magalhães, J.P. (2013). Human Ageing Genomic Resources: integrated databases and tools for the biology and genetics of ageing. *Nucleic Acids Res.* 41, D1027–D1033.
- Terzibasi, E., Valenzano, D.R., Benedetti, M., Roncaglia, P., Cattaneo, A., Domenici, L., and Cellerino, A. (2008). Large differences in aging phenotype between strains of the short-lived annual fish *Nothobranchius furzeri*. *PLoS ONE* 3, e3866.
- Terzibasi, E., Lefrançois, C., Domenici, P., Hartmann, N., Graf, M., and Cellerino, A. (2009). Effects of dietary restriction on mortality and age-related phenotypes in the short-lived fish *Nothobranchius furzeri*. *Aging Cell* 8, 88–99.
- Trancikova, A., Ramonet, D., and Moore, D.J. (2011). Genetic mouse models of neurodegenerative diseases. *Prog. Mol. Biol. Transl. Sci.* 100, 419–482.
- Valenzano, D.R., Terzibasi, E., Cattaneo, A., Domenici, L., and Cellerino, A. (2006). Temperature affects longevity and age-related locomotor and cognitive decay in the short-lived fish *Nothobranchius furzeri*. *Aging Cell* 5, 275–278.
- Valenzano, D.R., Kirschner, J., Kamber, R.A., Zhang, E., Weber, D., Cellerino, A., Englert, C., Platzer, M., Reichwald, K., and Brunet, A. (2009). Mapping loci associated with tail color and sex determination in the short-lived fish *Nothobranchius furzeri*. *Genetics* 183, 1385–1395.
- Valenzano, D.R., Sharp, S., and Brunet, A. (2011). Transposon-mediated transgenesis in the short-lived African killifish *Nothobranchius furzeri*, a vertebrate model for aging. *G3 (Bethesda)* 1, 531–538.
- Zuccherro, T., and Ahmed, S. (2006). Genetics of proliferative aging. *Exp. Gerontol.* 41, 992–1000.

The Cellular and Molecular Basis of Direction Selectivity of A δ -LTMRs

Michael Rutlin, Cheng-Ying Ho, Victoria E. Abraira, Colleen Cassidy, Ling Bai, C. Jeffery Woodbury,^{*} and David D. Ginty^{*}

^{*}Correspondence: woodbury@uwyo.edu (C.J.W.), david_ginty@hms.harvard.edu (D.D.G.)

<http://dx.doi.org/10.1016/j.cell.2015.02.013>

(Cell 159, 1640–1651; December 18, 2014)

The author Ling Bai was inadvertently omitted from the author list when the above article was originally published. The author list has been revised online.